



TECHNISCHE UNIVERSITÄT MÜNCHEN

TUM School of Engineering and Design

Nonlinear Flight Control Strategies for Urban Air Mobility

Pranav Bhardwaj, M.Sc.

Vollständiger Abdruck der von der TUM School of Engineering and Design der Technischen Universität München zur Erlangung eines

Doktors der Ingenieurwissenschaften (Dr.-Ing.)

genehmigten Dissertation.

Vorsitz: Prof. Dr.-Ing. Agnes Jocher

Prüfende der Dissertation: 1. Prof. Dr.-Ing. Florian Holzapfel
2. Prof. Dr. Sophie Armanini

Die Dissertation wurde am 16.10.2023 bei der Technischen Universität München eingereicht und durch die TUM School of Engineering and Design am 20.02.2024 angenommen.

Abstract

The emergence of Urban Air Mobility (UAM) has necessitated the demand for effective flight control approaches that can adequately satisfy the requirements pertaining to operation of novel aircraft configurations in urban airspace. To address the aforementioned demand, this thesis presents methods to facilitate design of unified flight control strategies for all flight phases – hover, transition, and wingborne of Vertical Take-Off and Landing (VTOL) transition aircraft that are commonly being developed within the UAM ecosystem. To begin with, the dynamics of VTOL transition aircraft are studied and aspects pertaining to motion control of these vehicles are elaborated. A modular, configuration-agnostic Integrated Reference Model (IRM) architecture is then developed, which incorporates the capability of continuous desired behavior specification and enables an inherently intuitive aircraft response to pilot inceptor inputs over the complete flight envelope. The proposed integrated reference model design is employed in an Incremental Nonlinear Dynamic Inversion (INDI) control framework and verified in flight tests. Furthermore, design methodology for the jerk-level physical reference model is proposed, which accommodates state dependent damping terms, noise-attenuation filters, input/output channel dynamics, and high order effector dynamics to produce appropriate feedforward commands and reference trajectories consistent with aircraft physics as well as the control system architecture. The advantages of utilizing the jerk-level reference model in an extended INDI controller framework are highlighted through linear analysis, simulations, and experimental tests. The final contribution of this dissertation involves design of a configuration-independent unified trajectory control strategy for VTOL transition/VTOL aircraft. The trajectory control law is derived by dynamic inversion of kinematic jerk error dynamics, which are devoid of model uncertainties. The structure of the unified trajectory control framework is designed such that it can interface with any kind of aircraft configuration-dependent inner loop controller with minimal effort.

Acknowledgment

I wish to convey my profound gratitude to my advisor Prof. Dr.-Ing. Florian Holzapfel for his unwavering support and invaluable guidance since the beginning of my research journey, empowering me to take important responsibilities, trusting my ability to work independently, and motivating me to strive for excellence. I am deeply grateful to Prof. Dr. Sophie Armanini for her keen interest in my work, and a thorough review of this thesis. I would like to thank the chair of the exam committee Prof. Dr.-Ing. Agnes Jocher. My heartfelt thanks to Prof. Dr.-Ing. Stephan Myszchik for involving me in exciting collaborations, engaging in insightful discussions, and consistently providing encouragement, a support he continues to offer.

I am very grateful to my friends and colleagues at the Institute of Flight System Dynamics for cultivating a superb working environment. Special thanks to Stefan Raab, Jiannan Zhang, Valentin Marvakov, Jorg Angelov, and Maximilian Söpper for the numerous technical conversations, countless flight tests, incredible support, and most importantly the cheerful atmosphere that you guys created during our joint projects. I would like to thank Venkata Sravan Akkinapalli, who always found time to give his expert advice on tackling any issues in experiments. Gratitude to the C2Land project team, specially Simon Scherer for their support. I had the privilege of supervising numerous outstanding students, and I extend my thanks to all of them. Michael Marb and Philipp Müller deserve a special mention for their remarkable work.

Many thanks to my friends who have been supportive during all these years. I cannot thank my parents enough for their love and unconditional support throughout my academic journey. My achievements are a testament to the inspiration they have always given to me. A special thanks to Pranay, my brother, for all the love and help he has always provided, even when I didn't realize I needed it.

Last but not the least, I want to express my utmost appreciation to my wife, Anchal, who I love and who has been my pillar of strength for the past several years. Thank you for your immense patience, empathy, and encouragement without which I would not have made it.

Garching, September 19, 2023

Pranav Bhardwaj

Contents

- Abstract** **i**
- Acknowledgment** **iii**
- Table of Contents** **v**
- List of Figures** **ix**
- List of Tables** **xiii**
- Acronyms** **xv**
- Symbols and Indices** **xvii**
 - Symbols xvii
 - Indices xviii
- 1 Introduction** **1**
 - 1.1 Motivation and Background 1
 - 1.2 State of the Art 5
 - 1.2.1 Reference Model 7
 - 1.2.2 Jerk level Physical Reference Model 11
 - 1.2.3 Trajectory Control 14
 - 1.3 Mission Statement and Objectives 19
 - 1.4 Contributions 20
 - 1.5 Outline 21
 - 1.6 List of Publications 22
- 2 Dynamics and Control of Vertical Take-off and Landing Transition Aircraft** **25**
 - 2.1 Control Frame 27
 - 2.2 Aircraft Translation Dynamics 30
 - 2.3 Translation Motion in the Control Frame 35
 - 2.3.1 Acceleration due to Transport Rate in the Control Frame 35
 - 2.3.2 Acceleration due to Earth’s Rotation in the Control Frame 36
 - 2.3.3 Acceleration due to Rigid Body Rotation in the Control Frame 37
 - 2.3.4 Lateral Motion in the Control Frame 39
 - 2.3.5 Vertical Motion in the Control Frame 47
 - 2.4 Aircraft Rotational Dynamics 49

2.5	Design Reference Model	50
2.5.1	Pilot Inceptor Interpretation	53
2.5.2	DRM Kinematics and Control	56
2.6	Maneuverability Phase Planes	63
2.7	Summary	71
3	Integrated Nonlinear Reference Model for Vertical Take-Off and Landing Transition Aircraft	73
3.1	Preliminaries	74
3.1.1	Incremental Nonlinear Dynamic Inversion	75
3.1.2	Reference Model	83
3.2	Research Environment	89
3.2.1	Aircraft Configuration	89
3.2.2	Controller Structure	95
3.3	Modular Integrated Reference Model architecture	102
3.3.1	Pilot Inceptor – Control Variables	103
3.3.2	Command Transformation	106
3.3.3	Reference Model Core	116
3.3.4	Compliance Enforcement between Reference Variables	137
3.4	Verification	147
3.4.1	Simulation Results	147
3.4.2	Experimental Results	155
3.5	Summary	158
4	Jerk-Level Physical Reference Model	161
4.1	Extended Incremental Nonlinear Dynamic Inversion	163
4.2	Jerk-level Reference Model	169
4.2.1	Jerk-level Reference Model Structure: SISO system	172
4.2.2	Jerk-level Reference Model Structure: MIMO system	175
4.3	Jerk level Reference Model in an Extended INDI Control Architecture . .	180
4.4	Analysis and Verification	183
4.4.1	Linear Analysis - SISO case	183
4.4.2	MUAD Analysis	192
4.4.3	Consideration of High-pass/Estimation filter	195
4.4.4	Consideration of Time Delays	199
4.4.5	Consideration of Residual Effector Dynamics	206
4.4.6	Treatment of Unstable Systems	211
4.4.7	Experimental Verification	213
4.5	Summary	216
5	Unified Trajectory Control for VTOL Transition Aircraft	219
5.1	Jerk-level Translation Dynamics in the Control Frame	221
5.1.1	Improper Jerk	223
5.1.2	Order Analysis of terms in Jerk-level Dynamics	225
5.1.3	Jerk Translation Equations of Motion	230

5.1.4	Nonlinear Jerk-level Error Dynamics	231
5.2	Unified Trajectory Control Law	238
5.2.1	Desired Trajectory Parameters in $G(x)$	240
5.2.2	Measurements and Estimated Terms in $G(x)$	247
5.2.3	Error Terms in $G(x)$	249
5.2.4	Error Feedback Controller	252
5.2.5	State-space Formulation: Jerk Error Dynamics and Unified Trajectory Control Law	253
5.3	Unified Trajectory Controller Framework	255
5.4	Interface Module to Multicopter Configurations	261
5.5	Verification	263
5.5.1	Reference Configuration	263
5.5.2	Inner Loop Controller	265
5.5.3	Simulation Results	268
5.6	Summary	273
6	Conclusion	275
6.1	Dynamics and Control of Vertical Take-off and Landing Transition Aircraft	276
6.2	Integrated Nonlinear Reference Model for Vertical Take-Off and Landing Transition Aircraft	277
6.3	Jerk-Level Physical Reference Model	278
6.4	Unified Trajectory Control for VTOL Transition Aircraft	280
6.5	Future Work	282
A	Coordinate Frames and Transformations	I
A.1	Coordinate Frame Definitions	I
A.2	Frame Transformations	IV
B	Angular Rotation Rates	V
C	Miscellaneous	IX
C.1	Order Analysis of Improper Accelerations	X
C.1.1	Acceleration due to Transport Rate	X
C.1.2	Acceleration due to Earth's Rotation	XI
D	Design Plant Adaptation in Jerk-level Reference Model	XV

List of Figures

1.1	Aircraft configurations for Urban Air Mobility	2
1.2	Reference Model following control	8
1.3	Generic representation of a closed loop system	13
1.4	Method breakdown for Trajectory/path-following control	16
1.5	Take-Off trajectories in Means of Compliance for Special Condition VTOL [135]	18
2.1	Powered lift parallel to the body vertical axis [141]	27
2.2	Rotation from North East Down (NED) frame to Control frame [142] . . .	28
2.3	Relative angles between O , C and K frames in the horizontal plane	40
2.4	Lateral Motion Schematic for hover flight	41
2.5	Lateral translation/Turning in different flight phases of a VTOL transition aircraft	42
2.6	Lateral Motion Schematic for forward velocity flight	43
2.7	Lateral Motion Schematic for full flight envelope	43
2.8	Rotation from Control frame to Body frame [142]	45
2.9	Effect of vertical load factor command in bank angle command generation	46
2.10	Vertical Motion Schematic for full flight envelope	48
2.11	Requirements for moderate-amplitude pitch (roll) attitude changes — hover and low speed [84, p. 78]	52
2.12	Requirements for moderate-amplitude pitch (roll) attitude changes — hover and low speed [84, p. 78]	52
2.13	Definition of Moderate-Amplitude Criterion Parameters [84, p. 78]	52
2.14	Requirements for moderate-amplitude heading changes — hover and low speed [84, p. 79]	53
2.15	Design Reference Model	54
2.16	Pilot inceptor interpretation for full flight envelope of a VTOL transition aircraft	55
2.17	Transfer of vertical load factor generation from powered to aerodynamic lift during transition phase	59
2.18	DRM pitch angle responses for step-input command maneuvers	65
2.19	DRM pitch rate responses for pitch angle step-input command maneuvers	66
2.20	Required control maneuverability phase plane - roll axis	67
2.21	Required control maneuverability phase plane - pitch axis	68

2.22	Required control maneuverability phase plane - yaw axis	68
2.23	Unstable bank angle and roll rate response for the phase-plane design point [100, 175] from the HQ-Level 1 zone	70
2.24	Stable bank angle and roll rate response using control design limits for the phase-plane design point [100, 175] from the HQ-Level 1 zone	70
3.1	MIMO System Transformation [90]	80
3.2	Generalized Linear Reference Model structure for a MIMO system	84
3.3	Linear phase plane based envelope protection in a second order linear RM	87
3.4	Comparison of limitation mechanism in a linear second order RM	88
3.5	Tilt-rotor VTOL transition aircraft configuration	90
3.6	Incremental Nonlinear Dynamic Inversion controller structure	96
3.7	Integrated Reference Model architecture	102
3.8	Inceptor assignment in all flight phases of the VTOL transition aircraft [87, 148]	104
3.9	Transformation of forward velocity flight phases control variables to RM core commands [82]	107
3.10	Hybrid Throttle inceptor command variable mapping	109
3.11	Kinematic velocity dependent phase-plane envelope protection for turn rate	112
3.12	Virtual Control Inputs concept diagram	117
3.13	Reference Model Core interface definition	118
3.14	Translation Reference Model	119
3.15	Reference Dynamics inversion in the Translation Reference Model	120
3.16	Effect of C_{V_k} on rate of convergence to boundary limits	127
3.17	Rotation Reference Model	128
3.18	Cross-wind disturbance rejection for all flight phases	136
3.19	Blending parameter hysteresis over absolute kinematic velocity	139
3.20	<i>Command Transformation</i> unit	140
3.21	Kinematic Velocity and bank angle tracking during turn flight in a constant wind field	144
3.22	Lateral Velocity command response and tracking error during turn flight in a constant wind field	145
3.23	Forward velocity tracking in hover flight phase	147
3.24	Lateral velocity tracking in hover flight phase	148
3.25	Vertical velocity and Heading angle rate tracking in hover flight phase	149
3.26	Coupled velocity and heading angle rate maneuvers in hover flight phase	150
3.27	Forward velocity commands and tracking in Transition/re-transition	151
3.28	Vertical channel tracking in wingborne flight	152
3.29	Lateral channel tracking in wingborne flight	153
3.30	Transition to wingborne flight phase in a cross-wind field	154
3.31	Flight path visualization during automated mission	155

3.32	Reference velocity and attitude angle tracking in automated flight mission	156
3.33	Lateral and vertical position deviation in automated flight mission . . .	157
4.1	Effector Dynamics consideration in the continuous extension of INDI . .	167
4.2	Feedforward generation in the Jerk-level reference model for a MIMO system	171
4.3	Jerk-level reference model structure for a SISO system	173
4.4	Delay and Higher order effects inclusion in the jerk-level reference model structure for a SISO system	174
4.5	Jerk level reference model for a MIMO system	176
4.6	Extended INDI control architecture with jerk-level reference model [90]	181
4.7	Jerk level reference model - transfer functions in a SISO case	185
4.8	Jerk-level RM in a closed Loop system for a SISO case	188
4.9	Frequency domain illustration of the effect of model uncertainty in A_v on tracking error	191
4.10	Added dynamics by the model uncertainty A_v on the loop transfer characteristics $G_{y_{cmd} \rightarrow y}(s)$ with feedforward	194
4.11	Added dynamics by the model uncertainty A_v on the loop transfer characteristics $G_{y_{cmd} \rightarrow y}(s)$ without feedforward	195
4.12	Effect of the inclusion of G_L in RM on the transfer characteristics $G_{y_R \rightarrow \hat{y}}$	197
4.13	3 – 2 – 1 – 1 maneuver simulation to illustrate effect of the inclusion of G_L in RM	199
4.14	Delay emulation in the Jerk level reference model for a SISO system . . .	201
4.15	Effect of the inclusion of G_D in RM on the transfer characteristics $G_{y_R \rightarrow \hat{y}}$	203
4.16	Reference response characteristics based on the transfer function $G_{y_{cmd} \rightarrow y_R}$	204
4.17	Impact of the delay magnitude in Input Output delay emulation G_D of the RM on unit step response of the controlled SISO system	204
4.18	Bi-level control design objective in the Jerk level reference model	205
4.19	Real vs. Estimated system response corresponding to bi-level control objectives	206
4.20	Jerk level reference model in a closed loop SISO system with second order effector dynamics	207
4.21	Effect of the inclusion of R_u in RM on the transfer characteristics $G_{y_R \rightarrow \hat{y}}$	210
4.22	Effect of inclusion of Input/Output delay emulation G_D and higher order effect emulation G_L in the RM on the transfer characteristics $G_{y_R \rightarrow \hat{y}}$ for control of an unstable SISO system	212

4.23	Impact of the consideration of Input/Output delay emulation G_D and higher order effect emulation G_L in the RM on the tracking performance for control of an unstable SISO system	213
4.24	System view for RPM control system of the Lift Thrust Unit	214
4.25	RPM controller of the LTU	214
4.26	Comparison of RPM control in case of only feedforward against the case with both feedforward and feedback active	216
5.1	Magnitudes of the triple cross product terms in the C -frame Jerk-level translation dynamics	226
5.2	Magnitudes of $(\vec{\omega}_K^{IO})_C$	229
5.3	Trajectory tracking error variables	233
5.4	Guidance and control function framework	241
5.5	Aircraft configuration-agnostic Unified Trajectory Controller Framework	256
5.6	Simplified Inner Loop controller used in the verification of the Unified Trajectory controller	265
5.7	Full Mission Trajectory tracking in the horizontal plane	268
5.8	Three dimensional visualization of the Automated Trajectory Flight Mission	269
5.9	Lateral channel tracking in the Automated Trajectory Flight Mission . . .	270
5.10	Bank angle tracking in the Automated Trajectory Flight Mission	271
5.11	Vertical channel tracking in the Automated Trajectory Flight Mission . .	271
5.12	Forward channel tracking in the Automated Trajectory Flight Mission . .	272
5.13	Pitch angle tracking in the Automated Trajectory Flight Mission	273
A.1	Body-fixed Frame [141]	I
A.2	Aerodynamic Frame [141]	II
A.3	Kinematic Frame [141]	III
C.1	Magnitudes of $(\vec{a}_{tr}^R)_C$	XI
C.2	Magnitudes of $(\vec{a}_{e,rot}^R)_C$	XIII

List of Tables

1.1	Flight phases and their corresponding major lift generators	10
1.2	Geometric guidance and control functions classification for hover and forward flight phase	15
2.1	List of assumptions taken in derivation of translation dynamics	30
2.2	List of assumptions for simplification of translation dynamics	34
2.3	Control variables governing the kinematic lateral motion of a VTOL transition aircraft	39
2.4	Moderate-amplitude pitch (roll) attitude changes (attitude quickness) . .	52
2.5	Moderate-amplitude heading changes (attitude quickness)	53
3.1	Magnitude of parameters for simulations of the second order linear reference model	87
3.2	Control Effectors of the tilt-rotor VTOL transition aircraft	90
3.3	Flight phase specific Control Variables set intended for manual flight operation of the tilt-rotor VTOL transition aircraft	105
3.4	Interface definition for the Reference Model Core components	118
3.5	Sources of control force generation in all flight phases of the tilt-rotor VTOL transition aircraft	121
4.1	Magnitude of parameters used in the linear analysis of the jerk-level RM with the extended INDI controller	191
4.2	Transfer functions for envelopes of Maximum Unnoticeable Added Dynamics[208]	193
4.3	Magnitude of parameters used in the linear analysis of the jerk-level RM including delay emulation with the extended INDI controller	203
4.4	Magnitude of parameters used in the linear analysis of the jerk-level RM with the extended INDI controller for an unstable system	211
5.1	Magnitude and Range of states for order analysis	227
5.2	Ranges of accelerations contributing to Coriolis jerk due to $(\vec{\omega}_K^{IO})_C$	228
5.3	Maximum magnitude for the vector components of Coriolis jerk due to $(\vec{\omega}_K^{IO})_C$	229
5.4	Maximum magnitude of jerk emanating from specific forces in C -frame due to $(\vec{\omega}_K^{IO})_C$	230
5.5	Trajectory tracking error variables for each flight phase	233
5.6	Composition of the nonlinear term $G(x)$ for each flight phase	251

LIST OF TABLES

5.7	Inputs to the <i>Rotation matrices generator</i> unit	256
5.8	Outputs of the <i>Rotation matrices generator</i> unit	257
5.9	Inputs to the <i>Rotation rate acceleration jerk calculation</i> unit	257
5.10	Rotation rates for the unified trajectory control law	258
5.11	Inputs to the <i>Translation states transformation</i> unit	258
5.12	Outputs from the <i>Translation states transformation</i> unit	259
5.13	Control variable sets produced by the Interface module for the Unified Trajectory Controller	262
A.1	Body-fixed frame [143]	I
A.2	Aerodynamic frame [143]	II
A.3	Kinematic frame [143]	III
C.1	Magnitude of states for order analysis of acceleration due to transport rate	X
C.2	Range of components of acceleration due to transport rate in <i>C</i> -frame . . .	X
C.3	Magnitude of states for order analysis of the <i>x</i> -component of acceleration due to transport rate and Earth's rotation	XII
C.4	Range of components of acceleration due to Earth's rotation in <i>C</i> -frame .	XIII

Acronyms

AC	Attitude Control
ACAH	Attitude Command Attitude Hold
AoA	Angle-of-Attack
ATOL	Auto Take-Off and Landing
CA	Control Allocation
CAN	Controller Area Network
CG	Center of Gravity
COTS	Commercial Off-The-Shelf
CV	Control Variable
DC	Direct Current
DEP	Distributed Electric Propulsion
DI	Dynamic Inversion
DRM	Design Reference Model
EASA	European Union Aviation Safety Agency
EC	Error Controller
ECEF	Earth Centered Earth Fixed
ECI	Earth Centered Inertial
EIU	Engine Interface Unit
EOM	Equations of Motion
EST	Estimation module
eVTOL	Electric Vertical Take-Off and Landing
FCC	Flight Control Computer
FSD	Institute of Flight System Dynamics
HMI	Human Machine Interface
HQ	Handling Quality
ICAO	International Civil Aviation Organisation
ICE	Internal Combustion Engine
IMU	Inertial Measurement Unit
INDI	Incremental Nonlinear Dynamic Inversion
IRM	Integrated Reference Model
LHS	Left Hand Side
LOS	Line of Sight
LQG	Linear Quadratic Gaussian
LQR	Linear Quadratic Regulator

LTU	Lift Thrust Unit
LTV	Linear Time-Varying
MAV	Micro Aerial Vehicle
MIL	Model-in-the-Loop
MIMO	Multi-Input Multi-Output
MOC	Means of Compliance
MTE	Mission Task Element
MTOW	Maximum Take-Off Weight
MUAD	Maximum Unnoticeable Added Dynamics
NDI	Nonlinear Dynamic Inversion
NED	North East Down
OBPM	On-board Plant Model
PCH	Pseudo Control Hedging
PD	Proportional Derivative
PI	Proportional Integral
PID	Proportional Integral Derivative
PSs	Problem Statements
RCAH	Rate Control Attitude Hold
RCDH	Rate Command Direction Hold
RHS	Right Hand Side
RM	Reference Model
SC-VTOL	Special Condition VTOL
SISO	Single Input Single Output
SPI	Serial Peripheral Interface
TUM	Technische Universität München
UAM	Urban Air Mobility
UART	Universal Asynchronous Receiver-Transmitter
UAV	Unmanned Aerial Vehicle
UCE	Usable Cue Environment
V/STOL	Vertical/Short Take-off and Landing
VCI	Virtual Control Input
VTO	Vertical Take-Off
VTOL	Vertical Take-Off and Landing
VTP	Virtual Target Point

Symbols and Indices

Symbols

C	Aerodynamic coefficient
D	Aerodynamic drag force
E	Energy
K	Gain
L	Aerodynamic lift force
L	Luenberger gain
Q	Aerodynamic side force
S	Surface Area
T	Thrust in N
X	External force along the x -axis
Y	External force along the y -axis
Z	External force along the z -axis
Φ	Euler bank angle
Ψ	Euler heading angle
Θ	Euler pitch angle
\bar{c}	Chord of a lifting surface, $\bar{c} \in \mathbb{R}$
\bar{q}	Dynamic pressure
A	System state matrix
B	Control effectiveness matrix
C	Gain matrix
C	System output matrix
F	Force vector defined in a cartesian frame, $\mathbf{F} \in \mathbb{R}^3$
F	Nonlinear function describing dynamics of a physical system
K	Diagonal gain matrix
M	Moments vector defined in a cartesian frame, $\mathbf{M} \in \mathbb{R}^3$
V	Velocity vector defined in a cartesian frame, $\mathbf{V} \in \mathbb{R}^3$
Ω	Angular rate skew-symmetric matrix
Φ	Euler attitude angles vector, $\Phi \in \mathbb{R}$
ω	Angular rate vector
c	Constraints for control allocation
n	Load factors defined in a cartesian frame, $\mathbf{n} \in \mathbb{R}^3$

\mathbf{r}	Position vector
\mathbf{x}, x	System state vector, System state
\mathbf{y}	System Output vector
χ	Flight course angle
δ	Effector deflection angle
η	Elevator deflection angle or denotes an entity related to the elevator
γ	Flight climb angle
\mathbf{I}	Moment of inertia matrix, $\mathbf{I} \in \mathbb{R}^{3 \times 3}$
\mathbf{M}	Frame rotation matrix, $\mathbf{M} \in \mathbb{R}^{3 \times 3}$
\mathbf{p}	Linear momentum vector of a rigid body defined in a cartesian frame
\mathbf{u}	Control input vector
\mathbf{G}	Matrix of linear transfer functions
G	Linear transfer function
T	Mechanical Torque, $T \in \mathbb{R}$
μ	Bank angle
ω	Natural frequency of a linear transfer function
ω	Angular rate
\bar{T}	Thrust level
ρ	Density
σ	Sigmoid function having magnitude in the range $[0, 1]$, $\sigma \in \mathbb{R}$
λ	Blending variable having magnitude in the range $[0, 1]$, $\lambda \in \mathbb{R}$
ε	Horizontal side slip angle
ζ	Damping ratio of a linear transfer function
i	Angle of incidence of an aerodynamic surface
k	Force or Moment coefficient for a thrust unit, $k \in \mathbb{R}$
k	Rise rate of a sigmoid function, $k \in \mathbb{R}$
m	Mass in kg
n	Load factor
n	Size of dimensions of a matrix
p	Roll rate
q	Pitch rate
r	Yaw rate
s	Semi-span of a Lifting surface, $s \in \mathbb{R}$
t	Time variable
u	Velocity vector component along the x -axis
v	Velocity vector component along the y -axis
w	Velocity vector component along the z -axis
x	x -axis of a reference frame
y	System Output
y	y -axis of a reference frame
z	z -axis of a reference frame
$ V $	Absolute velocity in m/s

Indices

<i>A</i>	Aerodynamic frame
<i>A</i>	Aerodynamic center of an aircraft
<i>B</i>	Body fixed frame
<i>C</i>	Control frame
<i>D</i>	Desired path frame
<i>D</i>	Refers to a parameter related to aerodynamic drag
<i>E</i>	Earth centered Earth fixed frame
<i>F</i>	Footpoint on the desired aircraft trajectory
<i>G</i>	Center of gravity of a rigid body
<i>H</i>	Horizontal tail frame
<i>H</i>	Reference point of the horizontal tail
<i>I</i>	Inertial frame
<i>K</i>	Kinematic frame
<i>L</i>	Related to left hand side
<i>L</i>	Refers to a parameter related to aerodynamic lift
<i>MCA</i>	Specifies the minimum control airspeed
<i>M</i>	Describes an entity derived from an assumed model
<i>M</i>	Specifies a variable related to a motor
<i>O</i>	North-East-Down frame
<i>P</i>	Specifies a point on an aircraft
<i>P</i>	Denotes parameters related to dynamics of propulsion/thrust unit
<i>Q</i>	Aerodynamic side Force
<i>R</i>	Related to right hand side
<i>R</i>	Reference point of an aircraft
<i>R</i>	Reference variable
<i>T</i>	Trajectory frame
<i>T</i>	Total sum of a physical quantity originating from multiple sources
<i>T</i>	Transpose of a matrix
<i>V</i>	Vertical tail frame
<i>W</i>	Reference Point of the wing body
<i>W</i>	Wing-body frame
\bar{K}	Kinematic frame rotated by kinematic bank angle about the kinematic x-axis
<i>act</i>	Describes an entity that belongs to an actuator
<i>alw</i>	Specifies the allowable limit of a variable obtained from aircraft configuration data
<i>a</i>	Denotes parameters related to actuator dynamics
<i>bck</i>	Denotes a variable pertaining to the re-transition phase to hover flight for a VTOL transition aircraft
<i>cmd</i>	Describes a commanded variable
<i>c</i>	Describes an entity that can be generated by the control effectors
<i>c</i>	Describes an entity that relates to the constraints for control allocation

<i>fwd</i>	Denotes a variable pertaining to the forward speed flight phases of a VTOL transition aircraft
<i>f</i>	Denotes a filtered variable
<i>g</i>	Describes a gravitational entity
<i>hvr</i>	Denotes a variable pertaining to the hover flight phase
<i>h</i>	Describes an entity that belongs to the horizontal tail
<i>kin</i>	Denotes the kinetic energy
<i>k</i>	<i>k</i> -th component of a vector
<i>lo</i>	Lower limit of a variable
<i>l</i>	Refers to a coefficient for the roll moment
<i>max</i>	Denotes the maximum value of a variable
<i>min</i>	Denotes the minimum value of a variable
<i>m</i>	Denotes the mean of a quantity
<i>m</i>	Refers to a coefficient for the pitch moment
<i>n</i>	Refers to a coefficient for the yaw moment
<i>o, R</i>	Denotes a variable of the outer loop reference model
<i>pot</i>	Denotes the potential energy
<i>pred</i>	Describes a predicted variable
<i>p</i>	Specifies a preferred solution of the Control Allocation
<i>p</i>	Describes a variable derived from pilot inceptor deflection
<i>sat</i>	Denotes a variable containing saturation limits
<i>tr</i>	Describes a variable related to the transition phase
<i>up</i>	Upper limit of a variable
<i>vel</i>	Denotes a variable related to velocity
<i>v</i>	Describes an entity that belongs to the virtual control inputs
<i>wb</i>	Describes a variable related to the wingborne phase
<i>w</i>	Describes an entity that belongs to the wing-body
<i>x</i>	x-component of a vector in a Cartesian frame
<i>y</i>	y-component of a vector in a Cartesian frame
<i>z</i>	z-component of a vector in a Cartesian frame

Chapter 1

Introduction

1.1 Motivation and Background

Infatuation with the ability to fly has captivated the human kind through the entirety of its evolutionary journey. One of the earliest recorded attempts to fly was made by *Eilmer of Malmesbury, The Flying Monk*, who attached wings to his hands and feet and then jumped off a tower only to glide for a few meters before crashing to the ground. Numerous similar failed attempts could not demotivate our species to relinquish the desire to fly. So strong is the affinity to flight, that a mere 12 seconds flight by the Wright Brothers in December 1903, provided a lift-off to the aerospace industry that transcended in to a moon landing in July, 1969. To put it into perspective, it only took 66 years, which is at times even shorter than a healthy person's life span, from flying a wooden structure 37 meters above ground to leaving the planet and land on the moon.

The meteoric upsurge of the aviation industry stimulated the era of the air transportation boom. According to International Civil Aviation Organisation (ICAO), commercial airliners transported 4.5 billion passengers covering a total of 8,686 billion revenue passenger-kilometers in the year 2019 [1]. Commercial airlines not only connect continents and countries, but also provide a fast and reliable medium of transport between cities in the same country. Operation of the commonly used commercial fixed wing aircraft for transportation requires establishment of massive airport infrastructure. Helicopters have originated as an infrastructure non-intensive alternative for a better part in the second-half of the 20th century. The predilection for helicopters is induced by their Vertical Take-Off and Landing (VTOL) capability, which can provide reachability to remote and urban areas (inside cities) where fixed wing aircraft cannot operate. Consequently, they are employed for use-cases like emergency operations, search and rescue, cargo delivery, medical ambulance as well as urban transport. However, low efficiency in forward flight and high maintenance costs of complex mechanical parts increase the operating costs of helicopters. Additionally, they exhibit high noise and vibration levels that limits their usability in noise-sensitive areas as well as cause discomfort to the passengers [2].

1.1 Motivation and Background

In the last decade, advancement in battery technology and electric propulsion [3] along with the higher costs of aviation fuel in comparison to the electric energy sources [4] have ushered an era of Electric Vertical Take-Off and Landing (eVTOL) aircraft. Electric energy costs 50% cheaper for an equivalent amount of energy generated by aviation grade fuel [5]. For a conventional fuel powered Internal Combustion Engine (ICE) rotorcraft, fuel costs constitute approximately 20% of the total operational costs [6], and considering the 2x decrease in pure energy costs, an eVTOL can potentially provide a reduction of 10% in operating costs. This concession does not yet factor in the increase in overall powered-lift efficiency due to improvement in motor and propulsive efficiencies, which are estimated to have multipliers of 3.3 and 2.4, respectively [5].

Besides the financial advantage, use of electric propulsion drastically reduces the complexity in power transmission as compared to mechanical drive trains. Hence, powered-lift systems employing rotors with collective and variable pitch control are replaced by a simplified system having constant pitch propellers with variable rotational speed control for regulating thrust. The reduction of complexity in the power train not only enhances the life-cycle of the propulsion system but also lowers the maintenance efforts. Moreover, adoption of electric propulsion delivers the option of using multiple propulsors electrically connected to the primary energy source in a Distributed Electric Propulsion (DEP) system [7]. Consequently, the propulsion units can be sized and oriented in different constellations to maximize the attainable moment set of the given configuration [8] and capitalize on aerodynamic-propulsive interaction for increased lift performance [9, 10].



(a) *Dragonfish Lite* [11]



(b) *PWOne* [12]



(c) *VoloCity* [13]



(d) *Lilium Jet* [14]



(e) *Joby Aviation* [15]



(f) *Prosperity I* [16]

Figure 1.1: *Aircraft configurations for Urban Air Mobility*

Inspired by the financial benefits and technological advantage that electric propulsion offers, there has been an exponential rise in both manned and unmanned novel aircraft configurations. As illustrated in Fig. 1.1, the configurations are some form of an eVTOL aircraft with different structure. For example the first image (Fig. 1.1a) is *Autel Robotics*

Dragonfish Lite—an unmanned sub-5 kg Maximum Take-Off Weight (MTOW) VTOL tilt-rotor transition aircraft while the Fig. 1.1b shows *Phoenix-Wings PWO*, which is also an unmanned VTOL transition aircraft, however it comprises a pusher rotor. Although, both vehicles perform similar operations, the powered lift and traction units are arranged in very dissimilar layouts by virtue of the distributive capability of electric propulsion systems. Beyond the unmanned drones, several solutions for manned transportation are also coming up. *VoloCity* by *Volocopter* in Fig. 1.1c is an eVTOL, which can be sub-classified as a multicopter. These type of aircraft only utilize the powered-lift propulsion units for generating vertical lift and tilt the vertical lift vector by varying rotational speeds of a specific combination of rotors to generate moments throughout the full flight envelope. Alternatively, some eVTOL transition vehicles have also been developed which comprise of a hybrid combination of powered and aerodynamic lift capability. These aircraft are capable of VTOL and additionally accelerate to higher airspeed with or without reconfiguration such that aerodynamic lift can be harnessed to perform a wingborne flight like traditional fixed-wing aircraft. Some examples are *Lilium jet* from *Lilium GmbH*, *pre-production prototype* from *Joby Aviation* and *Prosperity I* from *Autoflight* as shown in Figures 1.1d – 1.1f.

Powered by the VTOL ability and the potential of the electric propulsion technology, these novel aircraft configurations are being predicated to bring the next revolution in the aviation industry – Urban Air Mobility (UAM) [17–19]. European Union Aviation Safety Agency (EASA) defines UAM as

UAM is a new safe, secure and more sustainable air transportation system for passengers and cargo in urban environments, enabled by new technologies and integrated into multimodal transportation systems. The transportation is performed by electric aircraft taking off and landing vertically, remotely piloted or with a pilot on board [20].

UAM is not only limited to intercity/intracity passenger mobility, but also comprises of emergency assistance and cargo delivery services. Manned, remotely piloted and autonomous unmanned aircraft form a part of the UAM ecosystem to realize the targeted services [19]. UAM could face considerable safety, regulatory, certification, financial and social acceptance challenges regardless of the ample counts of use cases that it delivers [19, 21]. Furthermore, UAM infrastructure requires operation of different novel aircraft configurations such as the ones shown in Fig. 1.1 in urban environments with close proximity to other aircraft and humans. Therefore, motion control is of primary importance and UAM operations impose further challenges on flight control.

Based on the demands of UAM, three main Problem Statements (PSs) are recognized that stimulate the development of methods proposed in this thesis in order to successfully deliver suitable flight control strategies.

PS.1 Changing dynamics and relative degree of the system

Firstly, challenges arise from the aircraft configurations used for the purpose of UAM. In order to increase range while maintaining VTOL function, several aircraft reconfigure within the flight mission. Consequently, the envelope of these

configurations spans over a huge range of dynamic pressure, thereby incorporating inherent nonlinearities in the dynamics of the system. In case of VTOL transition aircraft these nonlinearities are predominantly imposed by the **changing relative degree** of the system. Additionally, the majority of these aircraft possess redundant actuators facilitated by DEP and redistribution of control inputs to generate desired forces and moments is naturally nonlinear.

PS.2 Uniform behavior over complete flight envelope

The ultimate goal of UAM is to provide a fully autonomous air transport solution. However, in the near future piloted vehicles will co-exist with unmanned aircraft [22]. Therefore, uniform piloting response over complete flight envelope in tandem with the cockpit Human Machine Interface (HMI) needs to be assured by the flight control software. This requirement primarily occurs in transition vehicles for which **interpretation of pilot inceptor commands must be unified across the full flight envelope**, although command variables for motion control of the aircraft might vary.

PS.3 Precision tracking and disturbance rejection

Urban airspace can feature sudden wind gusts generated by interaction of turbulent wind with structures in densely built areas [23, 24]. In order to attain **precise desired trajectory-following** in high air traffic and obstacle presence in close vicinity at low altitudes, flight control algorithms must be capable of providing stringent rejection to the disturbance effects of the urban atmosphere.

Linear control theory has been applied extensively for development of flight control laws [25–27]. A fundamental disadvantage of linear flight control laws is that their design is based on the approximation of a higher order system around certain equilibrium points in the flight envelope whereby nonlinearities of the system in consideration are automatically neglected. It is evident from the identified challenges that classical linear control strategies can not present a satisfactory solution to the implicit nonlinear problem posed by flight control in UAM.

The aim of this thesis is to design nonlinear control strategies that unify flying behavior and provide precise path control over the entire envelope of the complex aircraft configurations being developed in the UAM ecosystem. Specifically, consistency of aircraft response to pilot commands during transition between different flight phases is addressed. Due to the constricted airspace that these aircraft would be operated in, inconsistency in aircraft response can be detrimental. For the same reason, precise trajectory-following with strong disturbance rejection is necessary. Although, official aviation standards that would define requirements/limits for the mentioned aspects are currently under development, the strategies proposed in this thesis are sufficiently **modular** and **parametric** such that they can be adapted to conform with requirements formulated in the future.

Having established the background, motivation and recognized the challenges for flight control in realization of UAM, an extensive literature review of the current state of the art is presented, which lists the available techniques and their applications.

1.2 State of the Art

In the scope of flight control, linear control laws are designed on the basis of approximate linear aircraft dynamics at certain equilibrium flight conditions [25]. The resultant controllers are intended to achieve the desired performance at these operating points. However, the assumptions used during the linear controller development may be violated if the aircraft deviates from the design operating points. The class of aircraft being designed for UAM exhibit highly nonlinear attributes that emanate from DEP based airframe design [11–15] (Fig. 1.1), extensive range of dynamic pressure encountered within the flight envelope and reconfiguration executed during flight [28–32] for transition between different flight phases.

Nonlinear control strategies have been extensively applied for control of multi-rotor [33–35] and VTOL transition capable aircraft configurations [36–39]. One of the most prominently used approach is Nonlinear Dynamic Inversion (NDI), which is also designated as feedback linearization [40, 41]. As the name suggests, the goal of feedback linearization is to convert a nonlinear dynamic system in to a linear form by using plant feedback [42, p. 148]. In consequence of linearization through plant feedback, the nonlinearities of the system are canceled and the resulting closed-loop dynamics yield a simplified input-output relation as a multiple integrator form [40, p. 208].

A dynamic inversion control method coupled with gain scheduled Proportional Integral (PI) error controller improved performance as compared to the commonly used linear PI controllers for a tail-sitter VTOL transition vehicle in [43]. NDI has been applied in several theoretical and experimental frameworks for multicopters [44–47] as well as VTOL transition aircraft [36, 48–50] to develop flight control strategies. In [44], a cascaded dynamic inversion controller was implemented for a quadrotor using input-output linearization, which mitigated strong inter-axis coupling effects in the quadrotor dynamics. In addition to a quadrotor platform, NDI was also applied to hexarotor and octorotor platforms in [47]. Consistent closed-loop response was achieved across all configurations by elimination of nonlinearities in the rigid body dynamics using a common NDI control structure while requiring major changes only in Control Allocation (CA). Moreover, experimental verification of a position controller using a two-loop Dynamic Inversion (DI) strategy was performed for a quadcopter [45, 46]. By commanding direct body-fixed rotation rate commands to the inner loop, higher control bandwidth and better tracking accuracy was achieved through the dynamic inversion based controller.

Likewise, translational motion control of a Vertical/Short Take-off and Landing (V/STOL) aircraft was demonstrated in hover as well as forward flight using NDI [49]. The proposed algorithm was capable of resolving effector redundancy along with blending of required effectors between hover and forward flight. In [50] NDI coupled with a wing-tilt angle weighted CA was employed to deal with the nonlinear coupling between the pitch angle and the airspeed during the transition flight phase for a VTOL tilt-wing Unmanned Aerial Vehicle (UAV). Nevertheless, use of NDI poses severe disadvantages. Firstly, reliance on an accurate plant model is an immense drawback of NDI based control laws. Since the plant is not known exactly in practical applications,

parametric uncertainties in the model used for inversion along with control saturations decrease the performance as well as the robustness of the controller [40]. Moreover, application of NDI to non-minimum phase systems can cause instability in the dynamics, which are rendered unobservable by the feedback linearization. These unobservable dynamics are referred to as the internal dynamics of the system [51]. Lastly, NDI cannot be applied to control input non-affine systems directly.

Several authors have presented solutions to alleviate the drawbacks of NDI. Inner-loop (rotational acceleration loop) DI controllers were coupled with outer-loop controllers established on robust strategies like singular value (μ) synthesis [52] and Linear Quadratic Gaussian (LQG) control [53] to enhance the robustness of NDI in presence of model uncertainties. However, the tedious iterative process for selection of input weights of μ -synthesis and quadratic weight matrices for LQG diminished the intuitiveness and ease of implementation of a DI controller. Pseudo Control Hedging (PCH) [54] was shown to successfully curb the loss of robustness in NDI [51, 55] due to control input saturations. Nonetheless, use of PCH did not alleviate issues related to model mismatch.

In this matter, Incremental Nonlinear Dynamic Inversion (INDI) [56, 57] brings the benefit of reducing model dependency as compared to NDI while retaining its performance. Knowledge of aircraft parameters, mainly the state variant terms, are replaced by state derivative measurements or estimations. Additionally, feedback of effector position is also required. Consequently, the requisite of an accurate plant model in the control design is relaxed. INDI can also be applied to input non-affine systems in a straight-forward manner. To the best of the author's knowledge, INDI was first introduced by Smith as a simplified approach to NDI [56]. A longitudinal control law designed for a nonlinear aircraft model exhibited excellent robustness properties and utilized rotational acceleration as well as effector position feedback. Similarly, INDI was presented as a modified version of NDI with a special implementation of accelerometers to aid in rotational acceleration estimation [57]. Special focus was put on reconfiguration ability of the control law in case of actuator failures. The application of INDI to an input non-affine system was exhibited for rate control of a helicopter [58]. The proof of robustness of INDI against model uncertainties, with the exception of the control input matrix uncertainty, was derived in [59]. Moreover, problems in practical implementations of INDI were also identified. The proof of increase in robustness compared with NDI was only valid under the assumptions of small controller sampling time and instantaneously fast actuator dynamics which are often violated in real life applications. Apart from the necessity of state derivatives and actuator position feedback, sensitivity of INDI to measurement noise and time delays was also established.

INDI adaptive controller was applied to a quadrotor Micro Aerial Vehicle (MAV) where delays occurring in estimated rotational accelerations caused by employing second order filters were addressed in the control design [60]. In [61], INDI control law displayed better external disturbance properties than a Proportional Integral Derivative (PID) control law for a MAV in flight tests. Similarly, an INDI based velocity tracking controller was developed and flight tested for a hexarotor [62]. An integrated CA was proposed for allocating Euler angles to the inner loop and control input commands simultaneously. Additionally, complementary filtering was used to estimate rotational

and linear accelerations to compensate for the phase lag introduced by the measurement filters. Correspondingly, INDI control laws were also designed for several fixed wing aircraft configurations [63–66] and flight tested successfully for a CS-25 certified aircraft [67]. The INDI-related literature covered so far only lists its application to aircraft operating in one flight phase - hover in case of multirotors or wingborne for fixed-wing aircraft.

As elaborated in the background for the dissertation, hybrid aircraft concepts possessing VTOL transition capability are a vital element in the UAM ecosystem in addition to the multirotor platforms. The benefit of using nonlinear inversion strategies for such aircraft is two-fold. Firstly, the inter-axis nonlinear coupling between the control axes of these aircraft are implicitly accounted. Moreover, the broad range of flight envelope is naturally managed without the need of gain scheduling. Lombaerts et al. explicitly document the advantage offered by INDI over NDI in control of a quad tiltrotor eVTOL [68] and an eVTOL with separate lift and cruise propulsion units [69]. It was noted that the controller synthesis becomes less dependent on knowledge of accurate aerodynamic derivatives, which are not easily known for such UAM vehicles. Likewise, INDI control law for the full envelope of a tilt rotor UAV was developed in [70] and [71]. The logic for use of the incremental strategy was attributed to its effectiveness for control non-affine systems and ability to counteract drastic nonlinearities in a transition vehicle without the need of accurate model knowledge. Additionally, INDI method has also been implemented for attitude and position control of tailsitter hybrid aircraft concept and tested in outdoor flight experiments [72].

Resulting from this comprehensive literature review of dynamic inversion motivated techniques, INDI clearly emerges as a proficient, robust and versatile control strategy for development of novel configurations being developed in the field of UAM. Therefore, in this work, modular functions complementing the INDI control method and its further extensions will be developed. As previously stated, the fundamental idea of DI and by association INDI is to cancel the inherent nonlinear behavior of the controlled system and replace it with a desired behavior specified by the control designer. Consequently, the inversion control law can be utilized for a model following control approach in which a **Reference Model (RM)** defines the reference aircraft response/behavior to commanded control variables.

1.2.1 Reference Model

The primary function of a reference model is to provide desired command variable trajectories, which not only adhere to constraints on bandwidth, damping or similar characteristics of the pilot command response but are also consistent with the physical capabilities of the system. Fundamentally, RM incorporates a command mapping function, which interprets pilot stick commands as physical control variables. Additionally, desired control variable trajectories are produced by the command regulation function, which accommodates handling qualities, command response bandwidth or any further flying qualities metrics [73]. Within the context of dynamic inversion based control techniques, the command to the linearized system can only be specified through the

control variable's derivative of the order corresponding to the relative degree of the system [51]. Hence, the reference state trajectories are required to be continuous and adequately smooth such that all the derivatives until the order equal to the relative degree are defined. Figure 1.2 illustrates a generic architecture for a reference model following control law.

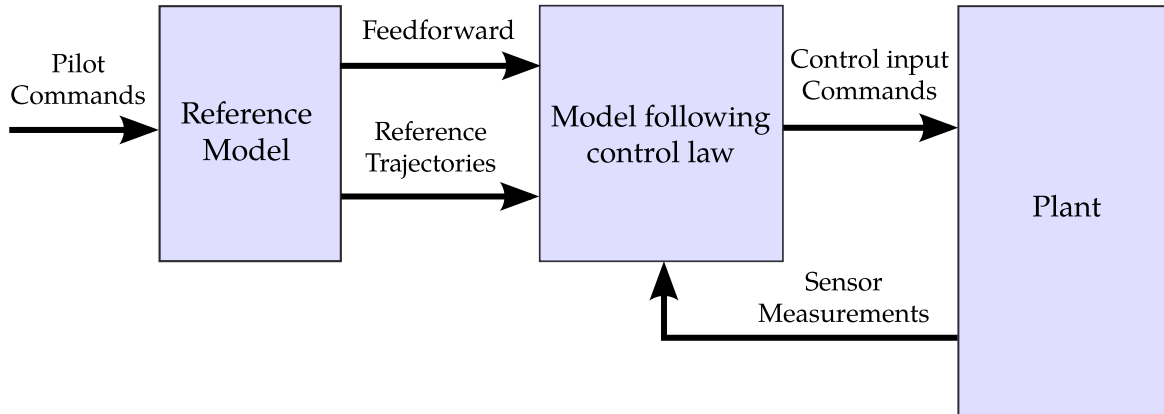


Figure 1.2: *Reference Model following control*

Smooth reference signals can be generated either through linear or non-linear reference models. In addition to the pilot command mapping component, a linear reference model comprises of a transfer function element having the order equal to the relative degree of the corresponding channel of the system. Accordingly, linear RMs are also referred to as command filters in literature [45, 74, 75]. The parameters of the transfer function are chosen such that the RM does not produce non-physical reference signals. Linear RMs have been applied for different applications [46, 58, 62, 67, 75, 76] within the context of dynamic inversion based flight control. In [62], a linear first-order RM and a second-order RM were employed for the velocity and attitude control loops respectively. Flight tests were performed with the resulting incremental dynamic inversion control law for a hexacopter. Likewise, linear RMs denoted as command filters were utilized for the inner loop of a NDI autopilot of an air-to-air missile [75]. A second order linear RM was coupled with a command module to facilitate Rate Control Attitude Hold (RCAH) and Attitude Control (AC) modes in the flight testing of INDI control law for a CS-25 certified aircraft [67]. Application of a linear RM poses a major downside that it constrains the natural nonlinear characteristics of an aircraft to track a linear transient response. Some attempts have been made to bring linear reference models closer to physical reality. Third order outer loop (position to angular rate and thrust) along with second order inner loop (incorporating motor dynamics) reference models were used in a dynamic inversion control law for position control of a quadcopter [46]. Furthermore, second-order reference models for roll and yaw angle were supplemented with turn coordination constraints in [76], and additionally pseudo control hedging was employed to account for actuator dynamics. Similarly, PCH was also implemented in a first-order RM for the INDI rate control law of a helicopter to prohibit generation of physically unfeasible reference signals [58]. However, nonlinearities induced due to inter-axis couplings, state-dependent damping effects, aerodynamic properties, system architecture related higher order effects or other aircraft dynamics are not accounted.

Alternatively, nonlinear reference models were designed to aid in defining physically viable references by integrating aircraft dynamics knowledge in the RM design [66, 77–80]. A nonlinear RM was applied for control of a tail-controlled missile in a NDI control architecture [77]. The closed-loop system was able to harness the full capability of the plant by applying knowledge of nominal plant dynamics and actuator dynamics within the RM. Likewise, nonlinear reference model architectures were proposed for a general aviation aircraft [78] and a fighter aircraft [79]. The work in [79] was focused on maximizing performance by defining desired trajectories that inherently accounted for the physics of the plant. Additionally, the structure put forward in [78] also incorporated phase plane based envelope protections. Similar phase plane based envelope protections were also incorporated in RM for an incremental backstepping controller by [81]. Furthermore, a physical dynamic inversion approach utilizing a physically integrated RM was presented, which decouples the definition of the reference dynamics and the error regulation [80]. Use of the proposed RM design not only reduced the feedback control efforts but also offered a direct method to integrate handling qualities requirements in the control design. Subsequently, a reference model structure including an incremental short period plant model was introduced with an INDI control law for the longitudinal channel of a piloted fixed wing turboprop demonstrator [66]. Control variables were varied over the envelope and pilot stick deflection to sustain an intuitive aircraft response over the complete flight operation.

As a summary of the given literature concerning nonlinear reference models, it can be stated that through a physical imitation of the nonlinear aircraft behavior nonlinear RMs produce considerable advantages over their linear counterparts. The reference signals produced by the nonlinear reference models are physically motivated and therefore lie within the capabilities of the aircraft. In doing so, the control effort and by association the tracking error is reduced. A nonlinear RM can be observed as an idealized replica of the aircraft running onboard the Flight Control Computer (FCC). Information about flight dynamics, effector dynamics with absolute and rate saturations along with envelope protections can be integrated in the RM in a parametric structure, which also delivers the potential of updating aircraft knowledge if needed.

Nonetheless, in the research activities presented earlier, reference models (linear or nonlinear) were developed for aircraft operating in one flight phase – hover or wingborne. No deliberation was put on the effect that varying flight phases cause in aircraft dynamics. As noted previously, aircraft configurations having capability of operating in multiple flight phases are an essential constituent in the domain of UAM. Henceforth, for any UAM worthy flight control strategy, consideration of multiple flight phases is crucial. Omission of the current flight phase information from a reference model can lead to physically inconsistent commands to any kind of dynamic inversion law for a typical VTOL transition aircraft configuration, which is one of the important focus in this dissertation.

Linear reference models were employed in a cascaded control architecture for control of a tilt-rotor UAV [70]. Reference dynamics did not account for changing flight phases. Transition mode logics were used to switch between outer loop controllers for hover and forward flight. Correspondingly, the virtual pseudo control commands to the inner loop

also varied depending on the flight phase of the UAV. To the best of author's knowledge, a reference model design with a uniform pseudo control command and reference trajectory interface for all flight phases of a VTOL transition aircraft was first presented by the author himself in [82]. Furthermore, linear reference models with uniform interfaces to dynamic inversion controllers were presented in [68, 69]. An attitude controller was developed for a hovering quad tiltrotor eVTOL vehicle [68]. ADS-33 handling qualities requirements were incorporated in the NDI control strategy through linear RMs. Simulation tests proved that handling qualities criteria were fulfilled in hover and low speed flight phases for small and moderate amplitudes of attitude changes. This control strategy was expanded to higher dynamic pressure flight phase in [69]. In addition to linear RMs, command filtering module was applied to provide additional control modes like Attitude Command Attitude Hold (ACAH), Rate Command Direction Hold (RCDH), RCAH and so on. Additionally, flight configuration dependent blending of the reference transfer function bandwidths was also proposed. However, merely changing the natural frequencies of the linear reference filters does not account for the nonlinearities that manifest in the operation of a VTOL transition aircraft.

Through the literature covered so far, the following challenges are recognized for designing a reference model architecture, which can be incorporated in the control strategy for a VTOL transition aircraft. Firstly, changing relative degree of the system implies that the reference pseudo controls also vary according to the flight phase. As listed in Table 1.1, three main flight phases are recognized for a transition aircraft, namely – hover, transition and wingborne. Therefore, up to three different controllers are required depending on the flight stage. In such a case, a switching algorithm or a blending mechanism that generates consistent control input commands during transition between different flight phases would be necessary. Moreover, same set of pilot stick command variables cannot sustain an intuitive aircraft response for all phases in which the considered aircraft operate. Subsequently, a uniform wind disturbance rejection behavior needs to be specified since it also varies drastically between hover and wingborne phases. The solution for these identified barriers is presented in this research work through a **modular configuration independent integrated reference model architecture** that can be applied for most of the configurations being pitched in the UAM sphere with minimal changes.

Flight Phase	Major lift generator
Hover	Lift Thrust Unit (LTU)
Transition	Mixed Lift - LTUs & Aerodynamic Lift surfaces
Wingborne	Aerodynamic Lift surfaces

Table 1.1: *Flight phases and their corresponding major lift generators*

Exclusive of the adoption in the flight control software, there are further benefits that the inclusion of the reference model brings. The handling and flying qualities requirements can be explicitly considered in the RM design in addition to the physics of the vehicle. Since, the controller tracks the behavior specified by the reference model, the requirements included in the RM are implicitly fulfilled. In addition, the RM can be flown in simulators very early in the aircraft design phase, thereby demonstrating the closed-loop behavior of the aircraft with respect to pilot inceptor commands. Rigid body dynamics, aerodynamic effects and propulsion characteristics are integrated in such a behavior specification model, also known as Design Reference Model (DRM) [83]. The advantage brought about by the DRMs is that the behavior of novel aircraft configurations can be validated in the scope of intended aircraft operations without having a detailed system design.

Beyond its use as a validation tool, the author proposes to employ the DRM in the baseline aircraft control effector sizing. This process entails the derivation of a set of design points specifying required effector forces and moments obtained through DRM simulations. The estimation of the required control forces and moments is constrained through maneuverability requirements. For hover phase such requirements are acquired from standards like ADS-33E-PRF [84] whereas for wingborne flight from MIL-STD-1797A [85]. In this manner, the DRM influences the aircraft design through a top-down approach. The aircraft requirements are directly translated into aircraft design requirements through the design reference model. Consequently, expensive design iterations in the development phase can be avoided. A notable benefit of assimilating the design reference model in the aircraft development process is that this design specification can later be transformed to a reference model implemented for the flight control software. Therefore, requirement specification and physical behavior reside concurrently in the model-following control strategy.

1.2.2 Jerk level Physical Reference Model

As previously noted, implementation of INDI makes assumptions of high controller sampling rate and fast actuators, which renders the linearization error trivial even when the state dependent term, more commonly known as the "A-part", is neglected. The assumptions on which this hypothesis is based does not always hold in practical applications. Especially in terms of transition aircraft, propulsive effectors as well as aerodynamic effectors can be used simultaneously in transition flight regimes. The dynamic characteristics of these effectors vary drastically and need to be accounted for explicitly in the control strategy. Therefore, a continuous extension to the INDI was proposed in [86, 87], which was derived by inversion of the direct time derivative of the physical system instead of a linear approximation of plant dynamics obtained by the Taylor's expansion. As a result, a control input derivative was computed in the control law rather than a control input increment. The control effector dynamics was then incorporated specifically in the calculation of the control input increment from the control effector rate. As compared to the INDI control strategy, no additional sensor feedback was required in the proposed continuous extension.

Nonetheless, the state term was still neglected in the derivation of the continuous incremental law. The ignored term can have considerable impact for fixed wing aircraft that have high aerodynamic damping effects along with slow actuators. Coupled with a low control frequency, the assumption of neglecting the state dependent terms turns invalid. The integrator chain of the feedback-linearized system amplifies the errors made by neglecting such terms, even if an ideal case of perfect model knowledge without any external disturbances is considered. Notwithstanding the fact that disregarding the state variant terms is well-founded since the system is not known accurately in reality, yet no benefit is acquired from any known aircraft parameters. Compensation of the errors caused by neglecting these terms is generally achieved through a feedback error controller [51, 76, 88]. Moreover, consideration of the state dependent effects in the feedback architecture of a sensor based NDI approach was also introduced in [89]. Alternatively, this dissertation proposes to include the influence of identifiable disturbances–state dependent terms within a physically realizable feedforward to the extended INDI control law.

In literature, linear RMs are also employed to generate feedforward commands [46, 58, 62, 67, 75, 76]. The feedforward commands constituted in these implementations are of the order of the relative degree of the system, which does not concur with the extended INDI architecture. While this aspect can easily be overcome by employing a linear filter of one higher order, still the feedforward signals produced are just high-pass filtered component of the command variables. Such feedforward commands do not hold a major physical significance. Similar shortcomings were also recognized in physically motivated nonlinear reference models [77–80]. Although, these physical reference models harnessed the information of aircraft dynamics to produce meaningful command variable reference trajectories, the feedforward command generation did not incorporate the effect of the state dynamics.

In the extended INDI, a pseudo control derivative command, which lies one order higher than the relative degree of the system, is allocated to a control input rate command. The effector command is then computed in an actuator dynamics consideration module and the feedback of the current actuator state [86, 87]. Since the direct path from a pilot command to an actuator command is constituted through a pseudo control derivative, the feedforward from the reference model also requires to be at this dynamic level. However, such higher order reference models which produce physically motivated feedforward commands in the context of flight controls could not be found during the literature research. The author presented initial work elaborating the incorporation of feedforward pseudo control derivative in the design of a higher order jerk level reference model in [90]. The reason for specifying the jerk level originates from the fact that usually the relative degree of a physical system such as an aircraft [76, 88] yields translation and rotational accelerations as the pseudo controls. As stated earlier, the RM for the extended INDI law operates at one order higher than the relative degree of the system, which is the derivative of the accelerations–commonly called jerk [91].

Besides the state dynamics, another important element that can be considered in the reference model is the input/output channel dynamics. One constituent of these dynamics is the latency/time delay that occurs in the flight control system. Apart from

the process delay, major components that contribute to the cumulative time delay are transport delay, sensor delay [92] and time synchronization delays. The sensor delay is mainly composed of delay due to anti-aliasing filters [93], analog to digital conversion [94] or any low-pass filters used for noise cancellation. This information is usually defined in data-sheets for Commercial Off-The-Shelf (COTS) sensor products used in flight control. Transport and sensor delays are constant for a given system architecture containing specific sensors and computing platforms. On the other hand, the process of syncing data between the components of a flight control system causes a variable delay. This time synchronization delay depends on the arbitration of the data packets in to communication protocols being used such as Controller Area Network (CAN) bus, Serial Peripheral Interface (SPI), Universal Asynchronous Receiver-Transmitter (UART) and others. Since the synchronization delay can vary in every FCC calculation interval, only a range of this delay can be accurately estimated. However, the transport and sensor delay along with other higher order effects of any filters used are known with good precision in a flight control system. Although, these elements do not constitute the physical behavior of an aircraft, still they are a significant part of the closed loop system (shown in Fig. 1.3) that affects its performance. To the best of author's knowledge and based on the sources related to reference model covered, there have been no attempts to accommodate these constant delays and known effects in the reference model design.

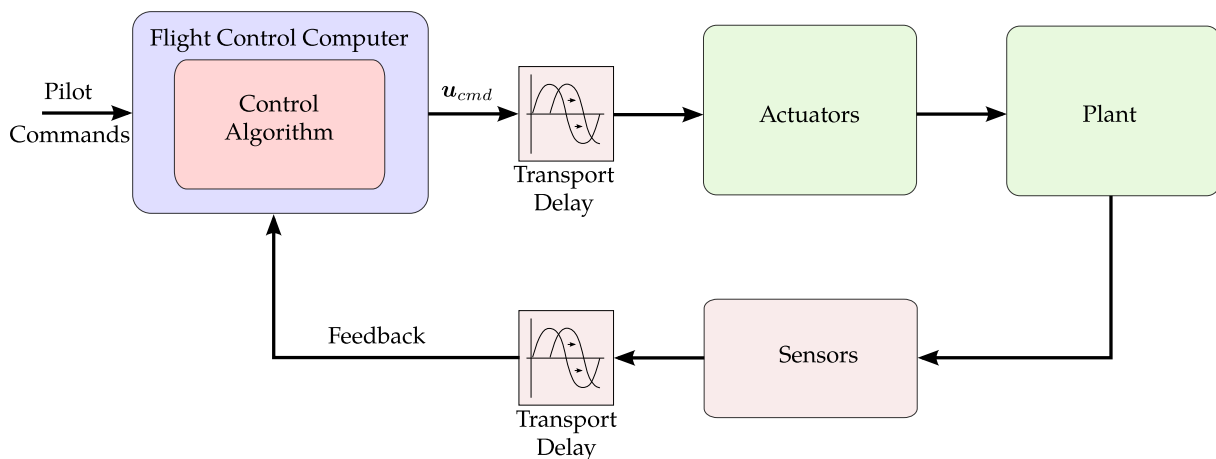


Figure 1.3: *Generic representation of a closed loop system*

To perform exact cancellation of the effector dynamics exhibiting higher than first order behavior, implementation of a non-causal filter was required in the extended INDI [86, 87]. Although, in real application the second order dynamics can be treated with an equivalent first order cancellation, the missing filter still has a residual effect. Since most aircraft effectors can be modeled with first or second order dynamics, a solution to counteract this residual effect is significant. Therefore, treatment of higher order effector dynamics within the RM has also been analyzed in this work.

Following from the sources and arguments presented for a jerk level physical reference model, the challenges identified include development of a RM framework which is compliant with the continuous form of INDI law. The second challenge is to define an approach that accommodates the effect of state reliant terms, which are neglected by the

extended incremental law, within the reference model. Furthermore, inclusion of known input/output channel dynamics in the generation of reference states was also detected as a significant limitation from the current state of the art. Subsequently, consideration of higher than first order effector dynamics, which require a non-causal filter for exact cancellation of the actuator dynamics in the extended incremental dynamic inversion law is also determined as a potential problem. An attempt has been made to resolve these problems through a jerk level physical reference model in this thesis.

1.2.3 Trajectory Control

Urban airspace comprises of substantial challenges characterized by atmospheric perturbations due to unsteady temporal and spatial wind-fields [95], boundary layer around urban structures, turbulence due to canyon effects and thermal bursts [23, 96, 97]. Urban topology constituting high-rise buildings, power-lines and other structures [96] further restricts the availability of airspace conducive to aircraft operations. Apart from these static obstacles, avoidance of other flying vehicles is ascertained to be essential in traffic management for UAM [95, 98]. Owing to the dynamic environmental conditions, narrow operating volume and congestion in the urban airspace, stringent bounds on the deviation of an aircraft from the desired position need to be maintained at all times. Henceforth with the advent of Urban Air Mobility, the urgency of developing high precision and comfort driven trajectory/path-following control techniques has intensified. A secure UAM solution not only requires small UAVs and manned aircraft to operate flawlessly in close proximity to each other but also other components of an urban environment. Therefore, high accuracy in path tracking is crucial to facilitate a safe mission flight in the context of UAM.

Before diving into the state of the art for trajectory control techniques, the definitions of the terms utilized in the background of trajectory control are presented, which are in accordance to the interpretations outlined in [99]. In the terminology of flight control, *trajectory* refers to the time history of any state of the system under examination. However, in this section trajectory is used in connection to geometric guidance and control, and therefore it denotes the time history of the geometric path of a system. Accordingly, the objective of *trajectory control* is to track a desired position in space under a time constraint. Alternatively, the time constraint is omitted in *path-following control* and the problem is reduced to tracking the reference path independent of time. In literature, conflicting definitions for trajectory control have been detected where it is used to indicate either position control or flight path control [100–102] rather than a geometric tracking method. For clarification Table 1.2 displays the functions incorporated in trajectory and path-following control pertaining to the field of geometric guidance and control for a VTOL transition aircraft.

In contrast to the three flight phases classified in Table 1.1 for a VTOL transition aircraft depending on the main force generator, the flight phase distinction in relation to geometric guidance and control is reduced to two phases—hover and forward flight phase. The transition and wingborne phases are treated as one forward flight phase since the path kinematics in these cases of non-negative kinematic velocity (ground

Features	Guidance Functions	
	Trajectory control	Path-following control
3-D Geometric position tracking in hover	✓	✓
Kinematic velocity control in hover (time constraint)	✓	–
3-D Geometric path tracking in forward flight	✓	✓
Kinematic velocity control in forward flight (time constraint)	✓	–

Table 1.2: *Geometric guidance and control functions classification for hover and forward flight phase*

speed) are governed by same set of equations. Hence, the only distinction, with respect to path kinematics, that remains in the full flight envelope of a transition aircraft is the hover state. Since the aircraft can have zero kinematic velocities in hover, the normal path kinematic equations of motion [51, 99] do not apply, owing to the singularities produced by zero ground speed. As the framework for trajectory and path-following control functions is derived based on the path kinematics, it is comprehensible to make the classification of flight phases dependent on them. Alternatively, it is still appropriate to follow the flight phase definition of Table 1.1 for inner loop control development, since this classification originates from the type of control force producers in each phase.

Even in the hover and forward flight phases, the difference between trajectory and path-following control is characterized by the time constraint i.e. trying to reach a desired point a given time instant. In practice, the additional time constraint is enforced through the kinematic velocity control. On the grounds of limited airspace in urban areas, precise tracking in lateral and vertical direction from the reference trajectory is highly desirable. Comparatively, control of deviation along the desired trajectory, which corresponds to a timing constraint is not as critical. Nonetheless, in this dissertation the derived control strategy caters to the four-dimensional trajectory tracking problem. Since the three dimensional geometric position and path tracking features remain common to both guidance functions, the derived controller can then simply be modified to a path-following solution depending upon the requirement of the application. Additionally, changing from the trajectory control solution to path-following or vice-versa in flight depending on the current flight phase is also possible. Special attention is devoted to develop a control strategy which is adequately modular for application to any aircraft platform.

Methods used to realize the guidance functions listed in Table 1.2 can be broadly classified into two categories [103] – geometric methods and control techniques, as illustrated in Fig. 1.4. The geometric methods, whether pure pursuit [104–106] or Line

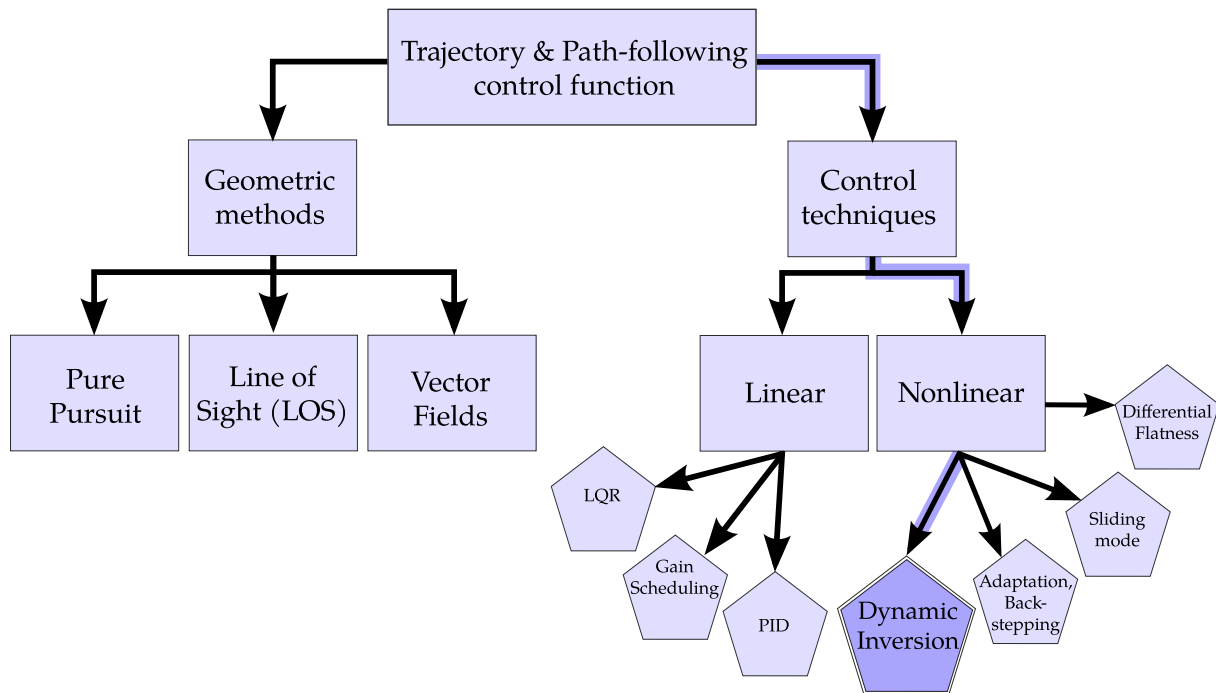


Figure 1.4: Method breakdown for Trajectory/path-following control

of Sight (LOS) guidance laws [107, 108], focus on following a Virtual Target Point (VTP) on the desired path [103]. By pursuing the VTP, the aircraft is directed to the desired path. For trajectory control, the VTP comprises of a reference velocity along the three-dimensional desired path definition. Alternately, the aircraft position is projected on the desired path using a "virtual distance" parameter to yield the VTP in case of path-following. The aforementioned geometric methods do not accommodate vertical channel and hence only provide two-dimensional guidance, which is not suitable for the application desired in this work. Another option is the vector field based technique [109–111] within the geometric methods category. In this technique, desired track angle command is generated to drive the aircraft towards the path. However, the vector field method relies on knowledge about the type of path - circular or straight, and does not incorporate any feedforward elements. Moreover, this approach is normally applied for horizontal guidance problems.

Control techniques is the second category introduced in [103], which focuses on driving the deviation of the system from the desired trajectory to zero. Therefore, the first step is to compute the error with respect to the reference path. In case of trajectory control, the position error can be directly calculated using the current aircraft position and the desired point which is uniquely defined on the reference trajectory due to the time specification. However, in path-following the calculation of tracking error is more complex. The error computation has been executed by employing Serret-Frenet frame [112–114] projections [114–116] on the path or by projecting the current aircraft position on to the planned path [117, 118]. Furthermore, a propagation algorithm was proposed for footpoint determination in case of continuous, nonlinear three dimensional trajectories [119]. After determination of the tracking error, different control strategies

can be employed for regulating the deviation from the desired trajectory to zero. In this case, commonly used linear control techniques include PID control [120–123], gain-scheduling [124] and Linear Quadratic Regulator (LQR) [123, 125]. Nonetheless, these control laws neglect the inherent nonlinearities that exist in the vehicle path dynamics, which generally would contribute to inferior tracking performance as compared to nonlinear methods.

Nonlinear control strategies exhibit a superior efficacy in exploiting the full physical capabilities, thereby improving the control authority utilization of an aircraft. Additionally, the dynamic behavior of the inner loop controllers can also be accounted in order to establish a reliable interface with the trajectory/path-following controllers. Some of the nonlinear control techniques applied for trajectory/path-following involve adaptation [126, 127], dynamic inversion [100, 128], backstepping [113, 129, 130], sliding mode control [131, 132], and nonlinear guidance laws [133, 134]. A substantial shortcoming in the preceding literature is that the proposed frameworks only cater to vehicles flying in one flight phase. Moreover, most of the trajectory/path-following control solutions dealt with two dimensional path tracking tasks only. Since the approach presented in this dissertation is a unified three dimensional trajectory/path following control strategy for all flight phases of a VTOL transition aircraft, it differs significantly from the state of the art covered so far.

The requirement about the three dimensional trajectory/path-following control originates from the current state of the take-off and landing performance requirements published in the proposed Means of Compliance (MOC) with the Special Condition VTOL (SC-VTOL) [135] defined in MOC-SUBPART B-FLIGHT under the section MOC VTOL.2115 Take-off performance. In addition to take-off trajectory specifications for conventional take-off and elevated conventional take-off paths, Vertical Take-Off (VTO) path definitions were also defined for urban environments as illustrated in Fig. 1.5. Further provisions for flight missions in urban airspace were made by specifying reference volumes inside which the aircraft shall operate at all times for take-off and landing. The resultant trajectories must be executable in atmospheric conditions having relative wind magnitude of 17 kts. This excerpt of requirements certainly brings out the necessity of an integrated three dimensional path following control strategy which tightly follows the desired path definition even in case of severe atmospheric disturbances.

Another important feature of the control architecture developed in this thesis is its modular aspect. The proposed trajectory control can be modified to link with an inner loop controller of any type of aircraft with minimal effort. Configuration independent trajectory control strategies have been presented in literature. A modular trajectory controller concept was presented in [99], which employed NDI to transform full nonlinear kinematic error dynamics for path-following control of a fixed wing aircraft. This control strategy was derived for the second order error dynamics and hence produced specific force commands for the consecutive inner loop controllers. Successful flight tests were performed using the guidance control architecture that comprised of a way-point trajectory generation module [118] and the modular configuration independent trajectory controller for a DA 42 M-NG general aviation aircraft. Nonetheless, the higher order dynamics of the actuators are neglected by employing direct force control for the

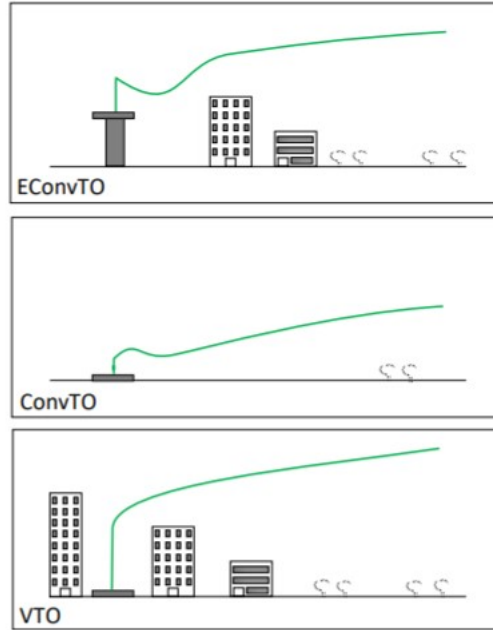


Figure 1.5: Take-Off trajectories in Means of Compliance for Special Condition VTOL [135]

inner loop system. Therefore, the approach was extended in [136] to incorporate jerk error dynamics for trajectory control. Specific force derivatives were commanded to the inner loop controller. Clearly, this interface is ideal for an extended INDI [86, 87] based inner loop controller. In addition to account for the effector dynamics, jerk regulation in the trajectory controller also resulted in generation of smooth control inputs. Moreover, it was established in [137] that jerk has a higher impact on the subjective perception of motion strength as compared to acceleration, hence jerk minimal motion delivers the advantage of increased passenger comfort. Subsequently, [138] concluded that jerk is one of the predominant sources causing loss in efficiency of robotic manipulators and therefore minimization of jerk is usually included as a cost function in trajectory planning. This benefit can also be exploited in the scope of aircraft effectors. In [139], a combination of differential flatness and INDI was used to develop a trajectory tracking controller. Angular jerk and snap feedforward were generated through the differential flat quadcopter dynamics. The acceleration commands for the INDI controller were computed by a Proportional Derivative (PD) controller. However, this approach does not compare with the modular and configuration-neutral technique being developed in this thesis for all flight phases of a transition aircraft. The generation of feedforward angular jerk and snap through differential flatness needs prior knowledge of quadcopter model. Moreover, linear acceleration commands are produced for the INDI control loop as compared to the linear jerk commands that are proposed for the trajectory/path controller in this work.

Additionally, the aforementioned modular trajectory control strategies are only valid in forward velocity phases ($V_K > 0$) since they are designed for fixed wing aircraft. Consequently, they cannot be used for VTOL transition aircraft configurations whose flight envelope also encompass zero kinematic velocity flight in the hover phase. Moreover, the lateral channel in the hover phase constitutes of two additional control degrees of

freedom, which are the bearing angle and lateral position. However, in the forward flight phase the lateral position and direction demand is achieved through flight course angle change and eventually a bank angle change.

Similar to the trajectory tracking controller in [139], the combined approach of differential flatness and INDI was applied for trajectory control of a tail-sitter flying wing [140]. However, the feedforward generation of the angular jerk through the differential flatness approach employed an aerodynamic model of the tail-sitter. Additionally, linear acceleration commands were provided to inner INDI control loop. Ultimately, this approach is widely different from the **configuration-agnostic, modular and unified jerk-level trajectory controller** designed in this thesis. The technique presented in this work is capable of operating in the complete flight envelope of a VTOL transition aircraft. One of the important factors that allow to design this approach is the choice of a valid frame of operation for the control law in the complete flight envelope. Additionally, employment of kinematic error dynamics for generation of subsequent commands to the inner loops give freedom from the requirement of any aircraft model knowledge. Hence, this trajectory/path-following controller can be applied to any aircraft with marginal effort.

1.3 Mission Statement and Objectives

This dissertation addresses the challenges that have been perceived in nonlinear flight control for the class of aircraft configurations being developed to realize urban air mobility. An extensive literature review of the current solutions being applied to overcome such challenges revealed the gaps which still have to be closed. Ergo, the following objectives are established based on these gaps

- 1 Study of rigid body dynamics of a Vertical Take-off and Landing Transition aircraft:** Owing to the vast envelope in which the type of effectors utilized for primary control of such a hybrid configuration are subject to change, it is crucial to establish an appropriate aircraft motion behavior in each flight phase and determine the means to achieve this behavior.
- 2 Selection of a practical combination of pilot command variables to realize uniform aircraft response over full flight envelope.**
- 3 Unified, platform agnostic and a modular reference model architecture.**
- 4 Identification of precisely known higher order effects in the closed loop system architecture:** In addition to the physical characteristics of the system, influence of elements like sensors, communication buses and measurement filters plays a significant role in the system behavior. Therefore, any accurately available knowledge of these effects can be incorporated in the reference model.
- 5 Integration of aircraft model parameters and system architecture (software and hardware) related effects in a jerk-level physical reference model.**

- 6 Allowable uncertainty margin estimation for aircraft parameters incorporated in the higher order reference model.**
- 7 Derivation of jerk-level position error dynamics:** To be calculated in an appropriate coordinate frame such that a unified trajectory control law can be developed for VTOL transition type hybrid aircraft.
- 8 Development of a unified trajectory controller, which does not require any model knowledge.**
- 9 Interfacing of the trajectory control module with inner loop controllers:** A mandatory task in order to test the feasibility of the designed trajectory control method.
- 10 Code-compliant implementation of the proposed controller modules:** To ensure that the developed software is of adequate quality so that it can be run on real FCCs.
- 11 Testing of the developed control law modules as an integrated unit.**

1.4 Contributions

Beyond the state of the art and technology, this thesis makes the following contributions to mitigate the shortcomings that have been identified through the literature review.

- C.1** Derivation of required maneuverability phase planes through Design Reference Model simulations for a VTOL transition aircraft.
Using the Design Reference Model, phase planes specifying the required rotational accelerations and jerk to achieve different handling quality levels in the hover flight phase of a generic VTOL transition aircraft are derived. In this process, the estimation of the required rotational acceleration and jerk is constrained through maneuverability requirements for the hover and low speed phases defined in the Aeronautical Design Standard for Military Rotorcraft ADS-33E-PRF [84].
- C.2** Integrated Nonlinear Reference Model Structure for Vertical Take-Off and Landing transition aircraft.
 - C.2.1** Flight phase dependent mappings for pilot command variables contained within the reference model.
 - C.2.2** Sequential desired rotation rate calculation in a unified control structure.
The INDI controller framework used with the integrated reference model employs a unified control allocation scheme to allocate load factors and rotational accelerations simultaneously. Although the integrated reference model is interfaced with a unified control structure, the generation of the desired body rotation rates is still performed analogous to a cascaded sequence by employing the virtual control inputs. The virtual control inputs are calculated within the control allocation module depending on the demand of the load factors for the full flight envelope.

- C.2.3 Reference Model core design to facilitate use of same set of variables for the whole flight envelope.
 - C.2.4 Definition of an explicit wind disturbance rejection behavior over the complete flight envelope within the Reference Model core design.
 - C.2.5 Approaches to enforce compliance between different reference variables.
- C.3 Jerk-level Physical Reference Model design.
- C.3.1 Feedforward pseudo control derivative generation for input non-affine systems.
 - C.3.2 Inclusion of measurement/estimation filter effects in the reference model design to achieve phase conformity between external reference and estimated plant states.
 - C.3.3 Integration of time-delays from the input/output channel dynamics within reference model design to facilitate phase match between external reference and estimated plant states.
 - C.3.4 Consideration of higher than first order effector dynamics in the generation of external reference states and feedforward pseudo control rate.
- C.4 Unified trajectory control module for Vertical Take-Off and Landing transition aircraft.
- C.4.1 Derivation of nonlinear jerk-level position error dynamics with respect to the desired path.
 - C.4.2 Unified trajectory control law for all flight phases of a VTOL transition aircraft.
 - C.4.3 Configuration-agnostic design of the unified trajectory control framework.
 - C.4.4 Interface function for trajectory controller with inner loop control law incorporating conversion of specific force rate commands to attitude angle rate commands for a multicopter platform.

1.5 Outline

The structure of this dissertation is divided into chapters based on the contribution list specified in the previous section. To begin with, Chapter 2 elucidates the concepts related to the dynamics of VTOL transition aircraft. The derivations performed in this chapter lay the foundation for the design of the integrated reference model as well as the unified trajectory controller proposed in this research. Furthermore, an aircraft configuration agnostic structure of a Design Reference Model DRM is presented. The DRM is employed to derive maneuverability phase planes based on handling quality requirements for the hover flight phase.

An integrated reference model architecture intended to be utilized with an INDI controller framework is presented in Chapter 3. In addition to specifying a switch-free and continuous reference behavior specification, the integrated RM also facilitates an intuitive aircraft response to pilot inceptor input over the complete flight envelope of

a VTOL transition aircraft. Unified set of pseudo controls to the inner loop, reference trajectory compliance and explicit definition of wind disturbance rejection are some of the main topics covered within the scope of this chapter.

Chapter 4 presents a jerk-level physical reference model, which specifies desired aircraft behavior for a controller based on the continuous extension of the INDI control strategy. The jerk-level RM incorporates state dependent damping effects, information about dynamics of measurement/estimation filters, transport delays and higher order effector dynamics to produce a physically appropriate feedforward command as well as reference external state trajectories.

An aircraft configuration agnostic unified trajectory controller is developed in Chapter 5. Nonlinear jerk-level position error dynamics specified in the desired path frame are employed to derive the control law for the unified trajectory control law. The trajectory control module provides specific force rate commands in the control frame together with the heading acceleration command in all flight phases of a VTOL transition aircraft. Moreover, special interfacing module generating Euler attitude angles or rate commands, required by Euler attitude angle command based controllers, is also defined within the scope of the chapter.

1.6 List of Publications

Some elements of the research presented in this thesis along with scientific work beyond the scope of this dissertation have been published by the author as a main or co-contributor in the following articles.

- [1] P. Bhardwaj, S. A. Raab, J. Zhang, and F. Holzapfel, "Integrated Reference Model for a Tilt-rotor Vertical Take-off and Landing Transition UAV," in *2018 Applied Aerodynamics Conference*.
- [2] P. Bhardwaj, V. S. Akkinapalli, J. Zhang, S. Saboo, and F. Holzapfel, "Adaptive Augmentation of Incremental Nonlinear Dynamic Inversion Controller for an Extended F-16 Model," in *AIAA Scitech 2019 Forum*.
- [3] P. Bhardwaj, S. A. Raab, J. Zhang, and F. Holzapfel, "Thrust command based Integrated Reference Model with Envelope Protections for Tilt-rotor VTOL Transition UAV," in *AIAA Aviation 2019 Forum*.
- [4] P. Bhardwaj, S. A. Raab, and F. Holzapfel, "Higher Order Reference Model for Continuous Dynamic Inversion Control," in *AIAA Scitech 2021 Forum*.
- [5] P. Bhardwaj, P. Müller, and F. Holzapfel, "Design Plant Adaptation in Jerk-level Reference Model," in *AIAA SCITECH 2022 Forum*.
- [6] J. Zhang, P. Bhardwaj, S. A. Raab, S. Saboo, and F. Holzapfel, "Control Allocation Framework for a Tilt-rotor Vertical Take-off and Landing Transition Aircraft Configuration," in *2018 Applied Aerodynamics Conference*.

-
- [7] J. Zhang, P. Bhardwaj, S. A. Raab, and F. Holzapfel, "Control Allocation Framework with SVD-based Protection for a Tilt-rotor VTOL Transition Air Vehicle," in *AIAA Aviation 2019 Forum*.
- [8] S. A. Raab, J. Zhang, P. Bhardwaj, and F. Holzapfel, "Proposal of a Unified Control Strategy for Vertical Take-off and Landing Transition Aircraft Configurations," in *2018 Applied Aerodynamics Conference*.
- [9] S. A. Raab, J. Zhang, P. Bhardwaj, and F. Holzapfel, "Consideration of Control Effector Dynamics and Saturations in an Extended INDI Approach," in *AIAA Aviation 2019 Forum*.
- [10] P. Piprek, M. M. Marb, P. Bhardwaj, and F. Holzapfel, "Trajectory/Path-Following Controller Based on Nonlinear Jerk-Level Error Dynamics," *Applied Sciences*, vol. 10, no. 23, 2020.
- [11] P. Panchal, S. Myschik, K. Dmitriev, P. Bhardwaj, and F. Holzapfel, "Handling Complex System Architectures with a DO-178C/DO-331 Process-Oriented Build Tool," in *2022 IEEE/AIAA 41st Digital Avionics Systems Conference (DASC)*, pp. 1–8, 2022.
- [12] M. Wang, N. Chu, P. Bhardwaj, S. Zhang, and F. Holzapfel, "Minimum-Time Trajectory Generation of eVTOL in Low-Speed Phase: Application in Control Law Design," *IEEE Transactions on Aerospace and Electronic Systems*, vol. 59, no. 2, pp. 1260–1275, 2023.

Chapter 2

Dynamics and Control of Vertical Take-off and Landing Transition Aircraft

Concepts pertaining to the dynamics of *vertical take-off and landing transition aircraft* are presented in this chapter. Given the large flight envelope of the transition vehicles, challenges of varying relative degree, additional control degrees of freedom and inter-axis couplings are encountered during the process of designing a control strategy for these aircraft. This chapter introduces a frame of reference, called the Control (C) frame, which simplifies the formulation of the aircraft translation dynamics over all the flight phases – hover, transition and wingborne, thereby providing the possibility of defining a unified control strategy. Derivation of the translation dynamics in the C -frame, along with their utilization for the lateral and vertical motion control of a VTOL transition aircraft are presented. Furthermore, the architecture of a Design Reference Model (DRM) is demonstrated, which acts as a flyable specification to assist in the validation of aircraft behavior against requirements for handling qualities, inceptor interpretation, flight mission and more, within the scope of the intended aircraft operation at an early stage when a detailed system design is unavailable. The DRM is further utilized to derive maneuverability phase planes from the handling quality requirements for the hover flight phase. The purpose of the maneuverability phase planes is to assist in the preliminary sizing of the lift thrust units as well as their spatial configuration during the aircraft design process.

The attractiveness of VTOL transition aircraft follows from the fact that they combine enhanced geographical accessibility through their vertical take-off and landing ability with extended flight range by capitalizing on the increased fuel (electric or conventional) efficiency in wingborne flight. Accordingly, such an aircraft can operate in different

flight phases during a mission. Notably the main flight phases for a VTOL transition aircraft include – **hover**, **wingborne** in conjunction with the **transition** flight phase that encompasses the transit from hover to wingborne or vice-versa.

Flight dynamics of hover and wingborne flight vary considerably. Some of the major differences involve:

1. **Mechanism of lift generation** is entirely different in the given flight phases. As mentioned in Table 1.1, LTUs provide direct lift control in hover flight, however in the wingborne phase aerodynamic lift is regulated through the angle of attack and airspeed. Transition phase control utilizes the effects of both powered and aerodynamic lift. Simply put, the relative degree of the vertical channel changes over the flight envelope.
2. Heading orientation is an explicit **control degree of freedom** in the hover flight phase, which is decoupled from the kinematic flight path. However, in the wingborne flight phase the heading orientation is implicitly controlled by realization of the aerodynamic side-slip minimization constraint for reducing drag.
3. In the hover phase, a significant **inter-axis coupling** between the lateral and the vertical channel exists. In order to generate a lateral displacement, the vertical powered-lift vector (in the body fixed frame) needs to be tilted in the desired direction and simultaneously the required lift magnitude increases in order to maintain the altitude. Similar force coupling also exists between the vertical and the pitch channel, when the pitch angle is used for position control in hover (in absence of traction units). In addition to these effects, motion in wingborne phase exhibits strong coupling between the translation and rotation channels, firstly due to the reason that the aerodynamic lift control is realized through the pitch rotation. Moreover, lateral translation is usually only possible through bank-to-turn maneuvers, which require simultaneous body rotation rate commands in all axes to produce a coordinated turn. Consequently, the constraints governing the **specification of desired body rotation rate commands** vary significantly between these flight phases. Naturally, additional inter-axis couplings also exist in these phases, nevertheless only the major differences between the two phases are highlighted here.
4. Aircraft dynamics denoted in different **frames of reference** have been utilized for the purpose of flight control in hover and wingborne phases according to the literature [45–47, 51, 55]. A combination of NED and body-fixed frames is commonly used for control of translation dynamics in multicopters [45–47], which corresponds to the hover phase. Use of body-fixed frame (shown in Fig. A.1) is fairly intuitive in this case because the direct-lift control effectors are generally configured parallel to the body vertical axis as illustrated through a generic VTOL configuration in the Fig. 2.1. However, use of the body frame is not perceptible for describing the kinematic motion of an aircraft in the wingborne phase. Therefore, command variables defined in the kinematic frame (shown in Fig. A.3) are often utilized for control of wingborne translation dynamics [51, 55]. Nonetheless, the variables defined in the kinematic frame cannot be used for the hover phase because the kinematic frame is not defined for zero kinematic velocities.

Development of a unified control strategy for VTOL transition aircraft requires explicit consideration of these differences. Choice of an appropriate frame of reference has an important role not merely for defining control variables, but also in establishing the approach for treatment of various inter-axis couplings as well as external disturbance rejection behavior in a unified control scheme. In this regard, Control (C) frame was proposed by the author in previous publications [82, 87]. This chapter further establishes the utility of the C -frame in creating control strategy specific components like the trajectory control module for autonomous flight and generating desired command variable trajectories for manual flight.

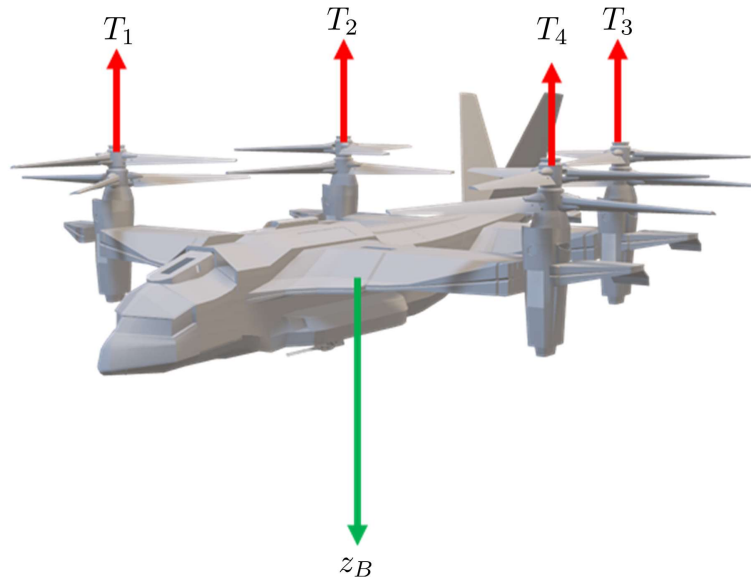


Figure 2.1: Powered lift parallel to the body vertical axis [141]

2.1 Control Frame

The Control (C) frame is defined as the frame obtained by the rotating NED frame (O) along the vertical z_O -axis through the heading angle Ψ . Figure 2.2 illustrates the frame rotation from the NED to the control frame for a model of a lift to cruise VTOL configuration [142]. The considered aircraft configuration comprises of four LTUs for generating vertical powered lift and one traction unit for generating forward thrust to gain airspeed. Furthermore, it comprises of ailerons and V-tail control surfaces that combine the effect of elevator and rudder for generating control moments in the wingborne phase. This configuration is strictly intended for visualization of different aspects pertaining to the dynamics of a VTOL transition aircraft in this chapter. Reference configurations employed to exhibit the effectiveness of the algorithms developed in this dissertation will be introduced later chapters.

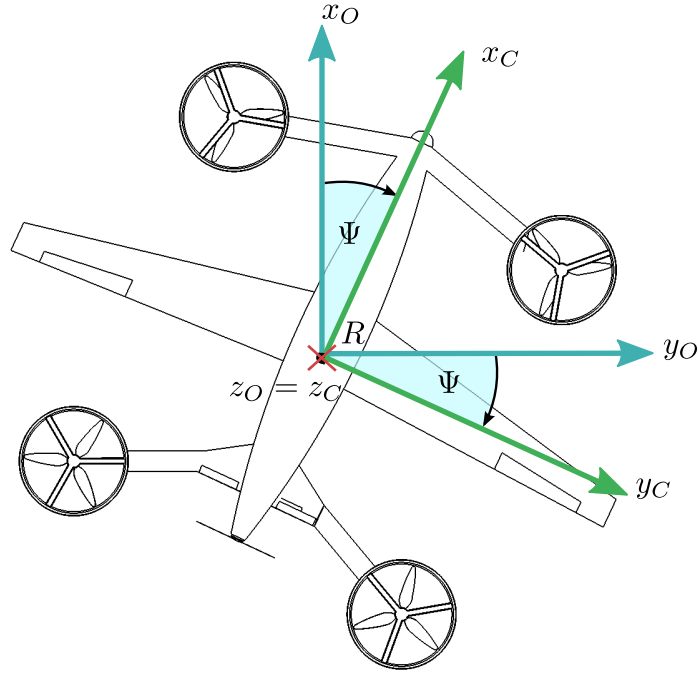


Figure 2.2: Rotation from NED frame to Control frame [142]

In order to transform physical variables denoted in the NED-frame to their counterparts in the control frame, the frame rotation matrix \mathbf{M}_{CO} is defined by using the heading angle Ψ

$$\mathbf{M}_{CO} = \mathbf{M}_{OC}^T = \begin{bmatrix} \cos \Psi & \sin \Psi & 0 \\ -\sin \Psi & \cos \Psi & 0 \\ 0 & 0 & 1 \end{bmatrix}. \quad (2.1)$$

This rotation matrix represents the rotation of a vector defined in the NED-frame to a vector denoted in the C -frame. By means of the orthonormal property of the frame rotation matrices, the inverse transformation matrix \mathbf{M}_{OC} is directly obtained by the transpose of \mathbf{M}_{CO} . In addition to the frame transformation, the angular rate of the control frame with respect to the O -frame ($\vec{\omega}^{OC}$) _{C} is one of the requisites for the derivation of the translation dynamics expressed in the control frame. The first step in the derivation of this angular rate is to calculate the differential of the frame rotation matrix \mathbf{M}_{CO}

$$\dot{\mathbf{M}}_{CO}^C = \begin{bmatrix} -\sin \Psi \cdot \dot{\Psi} & \cos \Psi \cdot \dot{\Psi} & 0 \\ -\cos \Psi \cdot \dot{\Psi} & -\sin \Psi \cdot \dot{\Psi} & 0 \\ 0 & 0 & 0 \end{bmatrix} \quad (2.2)$$

on which the following skew-symmetric angular rate matrix decomposition [143] for any two arbitrary frames A and B is applied

$$\dot{\mathbf{M}}_{AB}^A = \mathbf{M}_{AB} \cdot \left(\boldsymbol{\Omega}^{AB} \right)_{BB}, \quad (2.3)$$

where $(\Omega^{AB})_{BB}$ is a skew-symmetric matrix, which constitutes the elements of angular rotational rate vector $(\vec{\omega}^{AB})_B$

$$(\Omega^{AB})_{BB} = \begin{bmatrix} 0 & -(\omega_K^{AB})_z & (\omega_K^{AB})_y \\ (\omega_K^{AB})_z & 0 & -(\omega_K^{AB})_x \\ -(\omega_K^{AB})_y & (\omega_K^{AB})_x & 0 \end{bmatrix}_{BB}. \quad (2.4)$$

Subsequently, frame rotation matrix derivative in Eq. (2.2) is reformulated using the skew-symmetric matrix decomposition from Eq. (2.3)

$$\dot{\mathbf{M}}_{CO}^C = \mathbf{M}_{CO} \cdot (\Omega^{CO})_{OO}. \quad (2.5)$$

The skew symmetric matrix $(\Omega^{CO})_{OO}$ is defined in the NED-frame. In order to transform the notation frame of this matrix to the C -frame, the relation in Eq. (2.5) is post-multiplied with the rotation matrix \mathbf{M}_{OC}

$$\dot{\mathbf{M}}_{CO}^C \cdot \mathbf{M}_{OC} = \mathbf{M}_{CO} \cdot \underbrace{(\Omega^{CO})_{OO}}_{(\Omega^{CO})_{CC}} \cdot \mathbf{M}_{OC}$$

and the rotation matrix derivative $\dot{\mathbf{M}}_{CO}^C$ is formulated as

$$\dot{\mathbf{M}}_{CO}^C = (\Omega^{CO})_{CC} \cdot \mathbf{M}_{CO}. \quad (2.6)$$

By comparison of the resultant expression in Eq. (2.6) with the frame rotation matrix in Eq. (2.1) and its derivative from Eq. (2.2), the following relation emanates

$$\dot{\mathbf{M}}_{CO}^C = \underbrace{\begin{bmatrix} 0 & \dot{\Psi} & 0 \\ -\dot{\Psi} & 0 & 0 \\ 0 & 0 & 0 \end{bmatrix}}_{(\Omega^{CO})_{CC}} \cdot \underbrace{\begin{bmatrix} \cos \Psi & \sin \Psi & 0 \\ -\sin \Psi & \cos \Psi & 0 \\ 0 & 0 & 1 \end{bmatrix}}_{\mathbf{M}_{CO}}. \quad (2.7)$$

Elements of the angular rate vector $(\vec{\omega}_K^{CO})_C$ are determined through a comparison of the matrix $(\Omega^{CO})_{CC}$ with the structure of a generic angular rate skew-symmetric matrix

$$(\Omega^{CO})_{CC} = \begin{bmatrix} 0 & -(\omega_K^{CO})_z & (\omega_K^{CO})_y \\ (\omega_K^{CO})_z & 0 & -(\omega_K^{CO})_x \\ -(\omega_K^{CO})_y & (\omega_K^{CO})_x & 0 \end{bmatrix}_{CC} = \begin{bmatrix} 0 & \dot{\Psi} & 0 \\ -\dot{\Psi} & 0 & 0 \\ 0 & 0 & 0 \end{bmatrix}_{CC} \quad (2.8)$$

Consequently, the angular rate vector describing the rotation of the C -frame relative to the O frame $(\vec{\omega}_K^{OC})_C$ is constructed using the corresponding elements from the skew symmetric matrix $(\Omega^{CO})_{CC}$

$$\begin{aligned} (\vec{\omega}_K^{OC})_C &= -(\vec{\omega}_K^{CO})_C = - \begin{bmatrix} (\omega_K^{CO})_x \\ (\omega_K^{CO})_y \\ (\omega_K^{CO})_z \end{bmatrix}_C, \\ (\vec{\omega}_K^{OC})_C &= \begin{bmatrix} 0 \\ 0 \\ \dot{\Psi} \end{bmatrix}. \end{aligned} \quad (2.9)$$

The kinematic quantities introduced here are further utilized in the next section for the derivation of the VTOL translation dynamics denoted in the C -frame.

2.2 Aircraft Translation Dynamics

The goal of this section is to determine the Equations of Motion (EOM) using the principle of conservation of linear momentum specified by Newton's second law for the translation states namely

(\vec{r}^R)	Aircraft position
$(\dot{\vec{r}}_K^R)^E$	Aircraft velocity with respect to the ECEF frame
$(\ddot{\vec{r}}_K^R)^{EC}$	Aircraft acceleration derived with respect to the control frame.

Subsequent derivation is agnostic of any notation frame. Thereafter, the derived equations can be denoted in any frame of choice. The following assumptions have been taken in the derivation of the translation equations of motion

Assumption	Implication
A.2.1 The aircraft is a rigid body	$(\dot{\vec{r}}^{RP})^B = 0$
A.2.2 The mass of the aircraft is quasi-stationary	$\dot{m} \approx 0$
A.2.3 The rotation rate of earth is constant	$(\dot{\vec{\omega}}^{IE})^I = 0$

Table 2.1: List of assumptions taken in derivation of translation dynamics

Assumption **A.2.1** indicates that the relative position of any point with respect to another point on the rigid body aircraft remains constant over time. Therefore, any aero-elastic phenomenon are neglected within the context of translation dynamics. For the intended applications in this work, the change in the aircraft mass is lower than the 5% threshold within a time interval of 60 seconds [99], which is considered as the convention for the validity of the assumption **A.2.2**. To initiate with the derivation of the translation EOM, consider a point P on an aircraft having reference point R

$$(\vec{r}^P) = (\vec{r}^R) + (\vec{r}^{RP}), \quad (2.10)$$

where $(\vec{r}^P) \in \mathbb{R}^3$ and $(\vec{r}^R) \in \mathbb{R}^3$ denote the position vector of the point P and aircraft reference point R respectively. The relative position vector of P with respect to R is given by $(\vec{r}^{RP}) \in \mathbb{R}^3$. The time derivative of the position terms in Eq. (2.10) with respect to the the inertial frame produces

$$(\dot{\vec{r}}^P)^I = (\dot{\vec{r}}^R)^I + (\dot{\vec{r}}^{RP})^I, \quad (2.11)$$

$$(\dot{\vec{r}}^R)^I = (\dot{\vec{r}}^R)^E + (\vec{\omega}_K^{IE}) \times (\vec{r}^R), \quad (2.12)$$

$$(\dot{\vec{r}}^{RP})^I = \boxed{(\dot{\vec{r}}^{RP})^B} + (\vec{\omega}_K^{IB}) \times (\vec{r}^{RP}).$$

=0 ∴ **A.2.1:Rigid Body**

The angular rate $(\vec{\omega}_K^{IB}) \in \mathbb{R}^3$ comprises of

$$(\vec{\omega}_K^{IB}) = (\vec{\omega}_K^{IE}) + (\vec{\omega}_K^{EO}) + (\vec{\omega}_K^{OB}), \quad (2.13)$$

in which $(\vec{\omega}_K^{IE}) \in \mathbb{R}^3$ denotes the rotation rate of the earth, $(\vec{\omega}_K^{EO}) \in \mathbb{R}^3$ represents the transport rate owing to the earth's ellipsoid and $(\vec{\omega}_K^{OB}) \in \mathbb{R}^3$ is the rigid body rotational rate of the aircraft. By combining the expressions in Eq. (2.11), velocity of the aircraft point P is determined

$$(\dot{\vec{r}}^P)^I = (\dot{\vec{r}}^R)^E + (\vec{\omega}_K^{IE}) \times (\vec{r}^R) + (\vec{\omega}_K^{IB}) \times (\vec{r}^{RP}). \quad (2.14)$$

Further, the time derivative of the velocity $(\dot{\vec{r}}^P)^I$ yields

$$\begin{aligned} (\ddot{\vec{r}}^P)^{II} &= \underbrace{(\ddot{\vec{r}}^R)^{EI}}_{= 0 \text{ : A.2.3: Constant earth rotation rate}} + \underbrace{(\vec{\omega}_K^{IE})^I \times (\dot{\vec{r}}^R)^I}_{\text{highlighted}} + (\vec{\omega}_K^{IE}) \times \underbrace{(\dot{\vec{r}}^R)^I}_{\text{highlighted}} + \underbrace{(\vec{\omega}_K^{IB})^I}_{\text{highlighted}} \times (\dot{\vec{r}}^{RP})^I \\ &\quad + (\vec{\omega}_K^{IB}) \times \underbrace{(\dot{\vec{r}}^{RP})^I}_{\text{highlighted}}. \end{aligned}$$

The derivatives in the highlighted terms, calculated with reference to the inertial frame (I), are transformed with respect to **control (C)**, **Earth Centered Earth Fixed (ECEF)** and the **body (B)** frame

$$\begin{aligned} (\ddot{\vec{r}}^P)^{II} &= \underbrace{(\ddot{\vec{r}}^R)^{EC}}_{\text{highlighted}} + \underbrace{(\vec{\omega}_K^{IC})}_{\text{highlighted}} \times (\dot{\vec{r}}^R)^E + (\vec{\omega}_K^{IE}) \times \underbrace{\left[(\dot{\vec{r}}^R)^E + (\vec{\omega}_K^{IE}) \times (\vec{r}^R) \right]}_{\text{highlighted}} + \quad (2.15) \\ &\quad \underbrace{(\vec{\omega}_K^{IB})^I}_{\text{highlighted}} \times (\dot{\vec{r}}^{RP})^I + (\vec{\omega}_K^{IB}) \times \underbrace{\left[(\dot{\vec{r}}^{RP})^B + (\vec{\omega}_K^{IB}) \times (\vec{r}^{RP}) \right]}_{\text{highlighted}}, \end{aligned}$$

which results in

$$\begin{aligned} (\ddot{\vec{r}}^P)^{II} &= (\ddot{\vec{r}}^R)^{EC} + \underbrace{(\vec{\omega}_K^{IC})}_{\text{highlighted}} \times (\dot{\vec{r}}^R)^E + (\vec{\omega}_K^{IE}) \times (\dot{\vec{r}}^R)^E + \\ &\quad (\vec{\omega}_K^{IE}) \times \left[(\vec{\omega}_K^{IE}) \times (\vec{r}^R) \right] + (\vec{\omega}_K^{IB})^B \times (\dot{\vec{r}}^{RP}) + (\vec{\omega}_K^{IB}) \times \left[(\vec{\omega}_K^{IB}) \times (\vec{r}^{RP}) \right]. \end{aligned}$$

Expansion of the angular rate $(\vec{\omega}_K^{IC}) = (\vec{\omega}_K^{IE}) + (\vec{\omega}_K^{EC})$ results in

$$\begin{aligned} (\ddot{\vec{r}}^P)^{II} &= (\ddot{\vec{r}}^R)^{EC} + \underbrace{(\vec{\omega}_K^{IE})}_{\text{highlighted}} \times (\dot{\vec{r}}^R)^E + \underbrace{(\vec{\omega}_K^{EC})}_{\text{highlighted}} \times (\dot{\vec{r}}^R)^E + (\vec{\omega}_K^{IE}) \times (\dot{\vec{r}}^R)^E + \\ &\quad (\vec{\omega}_K^{IE}) \times \left[(\vec{\omega}_K^{IE}) \times (\vec{r}^R) \right] + \underbrace{(\vec{\omega}_K^{IB})^B}_{\text{highlighted}} \times (\dot{\vec{r}}^{RP}) + \quad (2.16) \\ &\quad (\vec{\omega}_K^{IB}) \times \left[(\vec{\omega}_K^{IB}) \times (\vec{r}^{RP}) \right]. \quad \approx (\vec{\omega}_K^{EB})^B \end{aligned}$$

The highlighted term in the equation above can be expanded according to $(\vec{\omega}_K^{IB})^B = (\vec{\omega}_K^{IE})^B + (\vec{\omega}_K^{EB})^B$. The earth rotation acceleration in the body-fixed frame yields $(\vec{\omega}_K^{IE})^B = (\vec{\omega}_K^{IE})^I + (\vec{\omega}_K^{BI}) \times (\vec{\omega}_K^{IE})$, which upon utilizing the assumption **A.2.3** of constant earth

rotation rate loses the first term and the remaining cross product is neglected on account of low magnitude. Consequently, the approximation $(\dot{\vec{\omega}}_K^{IB})^B \approx (\dot{\vec{\omega}}_K^{EB})^B$ holds, which is substituted in Eq. (2.16) to get

$$\begin{aligned} (\ddot{\vec{r}}^P)^{II} = & (\ddot{\vec{r}}^R)^{EC} + (\vec{\omega}_K^{EC}) \times (\dot{\vec{r}}^R)^E + 2 \cdot (\vec{\omega}_K^{IE}) \times (\dot{\vec{r}}^R)^E + \\ & (\vec{\omega}_K^{IE}) \times [(\vec{\omega}_K^{IE}) \times (\dot{\vec{r}}^R)] + (\dot{\vec{\omega}}_K^{EB})^B \times (\vec{r}^{RP}) + (\vec{\omega}_K^{IB}) \times [(\vec{\omega}_K^{IB}) \times (\vec{r}^{RP})] \end{aligned} \quad (2.17)$$

the absolute acceleration of a point P $(\ddot{\vec{r}}^P)^{II} \in \mathbb{R}^3$ on the rigid body aircraft.

The translational equations of motion for an aircraft are derived using Newton's Second Law of motion

In an inertial reference frame, the summation of all external forces acting on a body is equal to the time rate of change of the linear momentum of the body [144]

which is expressed as

$$\left(\frac{d}{dt}\right)^I (\vec{p})^I(t) = \sum \vec{F}, \quad (2.18)$$

where $(\vec{p})^I \in \mathbb{R}^3$ is the linear momentum vector and $\vec{F} \in \mathbb{R}^3$ represents the vector of external forces acting on the rigid body. In order to obtain the expression for the sum of external forces acting on the rigid body aircraft, consider the linear momentum of the point P

$$\left(d\vec{p}\right)^I(\vec{r}^P, t) = (\dot{\vec{r}}(\vec{r}^P, t))^I \cdot dm, \quad (2.19)$$

which is integrated to obtain the linear momentum of the entire rigid body

$$(\vec{p})^I(t) = \int_m (\dot{\vec{r}}(\vec{r}^P, t))^I \cdot dm. \quad (2.20)$$

Subsequently, the sum of forces acting on the rigid body is obtained by substituting the expression for linear momentum from Eq.(2.20) in the definition of Newton's second law given by Eq.(2.18)

$$\sum \vec{F} = \left(\frac{d}{dt}\right)^I (\vec{p})^I(t) = \left(\frac{d}{dt}\right)^I \int_m (\dot{\vec{r}}(\vec{r}^P, t))^I \cdot dm. \quad (2.21)$$

By consideration of the quasi-stationary mass assumption **A.2.2** in Eq.(2.21) the time differential can be brought under the mass integral using the Leibniz integral rule, thereby resulting in the following expression for the sum of external forces

$$\sum \vec{F} = \int_m \left(\frac{d}{dt}\right)^I \cdot [(\dot{\vec{r}}(\vec{r}^P, t))^I] \cdot dm = \int_m (\ddot{\vec{r}}^P)^{II} \cdot dm. \quad (2.22)$$

Here the dependence of the absolute acceleration $(\ddot{\vec{r}}^P)^{II}$ of point P on the position vector $(\vec{r})^P$ and time t is omitted to have better readability. Subsequently, by inserting the absolute acceleration from Eq.(2.17) in the sum of external forces from Eq.(2.22)

leads to

$$\begin{aligned} \sum \vec{F} = & \int_m \left[(\ddot{\vec{r}}^R)^{EC} + (\vec{\omega}_K^{EC}) \times (\dot{\vec{r}}^R)^E + 2 \cdot (\vec{\omega}_K^{IE}) \times (\dot{\vec{r}}^R)^E \right] \cdot dm + \\ & \int_m \left[(\vec{\omega}_K^{IE}) \times [(\vec{\omega}_K^{IE}) \times (\vec{r}^R)] \right] \cdot dm + \\ & \int_m \left[(\dot{\vec{\omega}}_K^{EB})^B \times (\vec{r}^{RP}) + (\vec{\omega}_K^{IB}) \times [(\vec{\omega}_K^{IB}) \times (\vec{r}^{RP})] \right] \cdot dm. \end{aligned} \quad (2.23)$$

Thereupon, the mass-invariant terms are drawn out of the integral

$$\begin{aligned} \sum \vec{F} = & \left[(\ddot{\vec{r}}^R)^{EC} + (\vec{\omega}_K^{EC}) \times (\dot{\vec{r}}^R)^E + 2 \cdot (\vec{\omega}_K^{IE}) \times (\dot{\vec{r}}^R)^E \right] \int_m \cdot dm + \\ & (\vec{\omega}_K^{IE}) \times [(\vec{\omega}_K^{IE}) \times (\vec{r}^R)] \int_m \cdot dm + \\ & (\dot{\vec{\omega}}_K^{EB})^B \times \int_m (\vec{r}^{RP}) \cdot dm + (\vec{\omega}_K^{IB}) \times [(\vec{\omega}_K^{IB}) \times \int_m (\vec{r}^{RP}) \cdot dm]. \end{aligned} \quad (2.24)$$

The position vector $(\vec{r}^{RP}) \in \mathbb{R}^3$ specifying the relative position of the point P with respect to the reference point R is divided into two parts $(\vec{r}^{RP}) = (\vec{r}^{RG}) + (\vec{r}^{GP})$, constituting the position of the center of gravity G relative to the reference point $(\vec{r}^{RG}) \in \mathbb{R}^3$ and the relative position of the point P in comparison to the center of gravity (\vec{r}^{GP}) . This decomposed position vector is replaced in the force equation from Eq.(2.24)

$$\begin{aligned} \sum \vec{F} = & \left[(\ddot{\vec{r}}^R)^{EC} + (\vec{\omega}_K^{EC}) \times (\dot{\vec{r}}^R)^E + 2 \cdot (\vec{\omega}_K^{IE}) \times (\dot{\vec{r}}^R)^E \right] \int_m \cdot dm + \\ & (\vec{\omega}_K^{IE}) \times [(\vec{\omega}_K^{IE}) \times (\vec{r}^R)] \int_m \cdot dm + (\dot{\vec{\omega}}_K^{EB})^B \times \int_m [(\vec{r}^{RG}) + (\vec{r}^{GP})] \cdot dm + \\ & (\vec{\omega}_K^{IB}) \times [(\vec{\omega}_K^{IB}) \times \int_m [(\vec{r}^{RG}) + (\vec{r}^{GP})] \cdot dm]. \end{aligned} \quad (2.25)$$

By the definition of the center of gravity, it follows that

$$\int_m (\vec{r}^{GP}) \cdot dm = 0 \quad (2.26)$$

and additionally through the rigid body property

$$\int_m (\vec{r}^{RG}) \cdot dm = (\vec{r}^{RG}) \cdot \int_m dm = (\vec{r}^{RG}) \cdot m \quad (2.27)$$

the expression in Eq. (2.25) transforms to

$$\begin{aligned} \sum \vec{F} = & m \cdot \left[(\ddot{\vec{r}}^R)^{EC} + (\vec{\omega}_K^{EC}) \times (\dot{\vec{r}}^R)^E + 2 \cdot (\vec{\omega}_K^{IE}) \times (\dot{\vec{r}}^R)^E \right] + \\ & m \cdot (\vec{\omega}_K^{IE}) \times [(\vec{\omega}_K^{IE}) \times (\vec{r}^R)] + \\ & m \cdot \left[(\dot{\vec{\omega}}_K^{EB})^B \times (\vec{r}^{RG}) + (\vec{\omega}_K^{IB}) \times [(\vec{\omega}_K^{IB}) \times (\vec{r}^{RG})] \right] \end{aligned} \quad (2.28)$$

in which the angular rate specifying the transport rate for non-flat earth $(\vec{\omega}_K^{EO})$ is separated from the angular rate $(\vec{\omega}_K^{EC})$ by means of

$$(\vec{\omega}_K^{EC}) = (\vec{\omega}_K^{EO}) + (\vec{\omega}_K^{OC}). \quad (2.29)$$

Consequently, the component breakdown in Eq. (2.29) is substituted in the sum of external forces from Eq. (2.28) to yield

$$\begin{aligned}
 (\vec{f}_T^R) = \frac{\sum \vec{F}^R}{m} = & \left[(\ddot{\vec{r}}^R)^{EC} + (\vec{\omega}_K^{OC}) \times (\dot{\vec{r}}^R)^E + \boxed{(\vec{\omega}_K^{EO}) \times (\dot{\vec{r}}^R)^E} \right] + \vec{a}_{tr}^R \\
 & \left[\boxed{2 \cdot (\vec{\omega}_K^{IE}) \times (\dot{\vec{r}}^R)^E + (\vec{\omega}_K^{IE}) \times [(\vec{\omega}_K^{IE}) \times (\dot{\vec{r}}^R)^E]} \right] + \vec{a}_{e,rot}^R \\
 & \left[\boxed{(\vec{\omega}_K^{EB})^B \times (\dot{\vec{r}}^{RG}) + (\vec{\omega}_K^{IB}) \times [(\vec{\omega}_K^{IB}) \times (\dot{\vec{r}}^{RG})]} \right] + \vec{a}_{b,rot}^{RG}.
 \end{aligned} \tag{2.30}$$

where (\vec{f}_T^R) denotes the total external specific forces acting on the reference point of the rigid body aircraft, $\vec{a}_{tr}^R \in \mathbb{R}^3$ represents the acceleration generated due to the transport rate by virtue of the ellipsoid earth. The Coriolis acceleration generated by earth's rotation $2 \cdot (\vec{\omega}_K^{IE}) \times (\dot{\vec{r}}^R)^E$ and the centrifugal acceleration induced by earth's rotation $(\vec{\omega}_K^{IE}) \times [(\vec{\omega}_K^{IE}) \times (\dot{\vec{r}}^R)^E]$ at point R constitute the total acceleration due to the earth's rotation depicted by $\vec{a}_{e,rot}^R \in \mathbb{R}^3$ and $\vec{a}_{b,rot}^{RG} \in \mathbb{R}^3$ denotes the acceleration caused by the rigid body rotation due to the difference between the position of the reference point R and the center of gravity G .

In general aviation practice [144, 145], the assumptions enumerated in Table 2.2 are adopted to simplify the translation equations of motion derived in Eq. (2.30).

Assumption	Implication
A.2.4 Flat earth, $(\vec{\omega}_K^{EO}) = \mathbf{0}$	$\vec{a}_{tr}^R = \mathbf{0}$
A.2.5 Non-rotating earth, $(\vec{\omega}_K^{IE}) = \mathbf{0}$	$\vec{a}_{e,rot}^R = \mathbf{0}$
A.2.6 Reference point R lies at the center of gravity G , $(\dot{\vec{r}}^{RG}) = \mathbf{0}$	$\vec{a}_{b,rot}^{RG} = \mathbf{0}$

Table 2.2: List of assumptions for simplification of translation dynamics

Thereupon, use of the assumptions **A.2.4–A.2.6** on the expression specified in Eq. (2.30) results in the simplified translation dynamics

$$(\vec{f}_T^R) = (\ddot{\vec{r}}^R)^{EC} + (\vec{\omega}_K^{OC}) \times (\dot{\vec{r}}^R)^E. \tag{2.31}$$

However, in the subsequent derivations, all the terms in the translation equations of motion from Eq. (2.30) will be considered.

2.3 Translation Motion in the Control Frame

The rigid body aircraft translation dynamics derived in Eq. (2.30) are not specified in any frame. In order to achieve the objective of devising a unified control strategy for all flight phases of a VTOL transition aircraft, the control (C) frame is adopted. Henceforth, the derived translation equations of motion are denoted in the C -frame. Furthermore, the derivatives of the position vector are hereafter represented in terms of velocity vectors to simplify the notations. The acceleration components \vec{a}_{tr}^R , $\vec{a}_{e,rot}^R$, $\vec{a}_{b,rot}^{RG}$ are also transformed to the C -frame based on the composition of the terms presented in Eq. (2.30)

$$\left(\vec{f}_T^R\right)_C = \left(\dot{\vec{V}}^R\right)_C^{EC} + \left(\vec{\omega}_K^{OC}\right)_C \times \left(\vec{V}^R\right)_C + \left(\vec{a}_{tr}^R\right)_C + \left(\vec{a}_{e,rot}^R\right)_C + \left(\vec{a}_{b,rot}^{RG}\right)_C. \quad (2.32)$$

Kinematic acceleration due to transport rate $\left(\vec{a}_{tr}^R\right)_O$, denoted in the NED frame, is transformed to the control frame through the rotation matrix M_{CO}

$$\left(\vec{a}_{tr}^R\right)_C = M_{CO} \cdot \left\{ \left(\vec{\omega}_K^{EO}\right)_O \times \left(\vec{V}_K^R\right)_O^E \right\}. \quad (2.33)$$

Similarly, the total acceleration due to earth's rotation

$$\left(\vec{a}_{e,rot}^R\right)_C = M_{CO} \cdot \left\{ 2 \cdot \left(\vec{\omega}_K^{IE}\right)_O \times \left(\vec{V}_K^R\right)_O^E + \left(\vec{\omega}_K^{IE}\right)_O \times \left[\left(\vec{\omega}_K^{IE}\right)_O \times \left(\vec{r}^R\right)_O \right] \right\} \quad (2.34)$$

and acceleration due difference between the reference point and the center of gravity

$$\left(\vec{a}_{b,rot}^{RG}\right)_C = M_{CB} \cdot \left\{ \left(\vec{\omega}_K^{EB}\right)_B^B \times \left(\vec{r}^{RG}\right)_B + \left(\vec{\omega}_K^{IB}\right)_B \times \left[\left(\vec{\omega}_K^{IB}\right)_B \times \left(\vec{r}^{RG}\right)_B \right] \right\} \quad (2.35)$$

are denoted in the C -frame by application of appropriate frame rotation matrices M_{CO} and M_{CB} from Eqs. (2.1) and (A.1) respectively. In the upcoming sections, the three acceleration sources are assessed by elaborating the terms that appear in them.

2.3.1 Acceleration due to Transport Rate in the Control Frame

As observed in Eq. (2.33), the acceleration $\left(\vec{a}_{tr}^R\right)_C \in \mathbb{R}^3$ develops through the transport rate due to the ellipsoidal earth [143]

$$\left(\vec{\omega}_K^{EO}\right)_O = \begin{bmatrix} \dot{\lambda} \cdot \cos \phi \\ -\dot{\phi} \\ -\dot{\lambda} \cdot \sin \phi \end{bmatrix}_O \quad (2.36)$$

where $\dot{\lambda}$ and $\dot{\phi}$ are the geodetic longitude and latitude rates specified in the position differential equations (C.1). Upon substitution of $\left(\vec{\omega}_K^{EO}\right)_O \in \mathbb{R}^3$ and the frame rotation matrix $M_{CO} \in \mathbb{R}^{3 \times 3}$ from Eq. (2.1) along with the application of the distributive property of an orthogonal matrix over a cross product in Eq. (2.33) yields

$$\left(\vec{a}_{tr}^R\right)_C = \left(\vec{\omega}_K^{EO}\right)_C \times \left(\vec{V}_K^R\right)_C^E = \left(\Omega^{EO}\right)_{CC} \cdot \left(\vec{V}_K^R\right)_C^E \quad (2.37)$$

2.3 Translation Motion in the Control Frame

where $(\vec{V}_K^R)_E^C \in \mathbb{R}^3$ represents the kinematic velocity vector in the control frame, the angular rate $(\vec{\omega}_K^{EO})_C \in \mathbb{R}^3$ constitutes

$$(\vec{\omega}_K^{EO})_C = \begin{bmatrix} \dot{\lambda} \cdot \cos \phi \cdot \cos \Psi - \dot{\phi} \cdot \sin \Psi \\ -\dot{\phi} \cdot \cos \Psi - \dot{\lambda} \cdot \cos \phi \cdot \sin \Psi \\ -\dot{\lambda} \cdot \sin \phi \end{bmatrix}, \quad (2.38)$$

and $(\Omega^{EO})_{CC} \in \mathbb{R}^{3 \times 3}$ emerges as a skew symmetric matrix that incorporates the elements of the angular rate vector in Eq. (2.38) according to the structure

$$(\Omega^{EO})_{CC} = \begin{bmatrix} 0 & -\omega_{K,z}^{EO} & \omega_{K,y}^{EO} \\ \omega_{K,z}^{EO} & 0 & -\omega_{K,x}^{EO} \\ -\omega_{K,y}^{EO} & \omega_{K,x}^{EO} & 0 \end{bmatrix}_{CC}. \quad (2.39)$$

By substituting the resulting skew symmetric matrix and elements of the kinematic velocity denoted in the control frame in Eq. (2.37), the kinematic acceleration due to the transport rate in the C -frame originates

$$(\vec{a}_{tr}^R)_C = \begin{bmatrix} \dot{\lambda} \cdot (v_K^R)_C^E \cdot \sin \phi - (w_K^R)_C^E \cdot \sigma_1 \\ (w_K^R)_C^E \cdot \sigma_2 - \dot{\lambda} \cdot (u_K^R)_C^E \cdot \sin \phi \\ (u_K^R)_C^E \cdot \sigma_1 - (v_K^R)_C^E \cdot \sigma_2 \end{bmatrix}_C. \quad (2.40)$$

where the temporary variables σ_1 and σ_2 denote the expressions

$$\begin{aligned} \sigma_1 &= \dot{\phi} \cdot \cos \Psi + \dot{\lambda} \cdot \sin \Psi \cdot \cos \phi \\ \sigma_2 &= \dot{\phi} \cdot \sin \Psi - \dot{\lambda} \cdot \cos \Psi \cdot \cos \phi \end{aligned} \quad (2.41)$$

2.3.2 Acceleration due to Earth's Rotation in the Control Frame

Angular velocity of the Earth Centered Earth Fixed (ECEF) frame with respect to the Earth Centered Inertial (ECI) frame $(\vec{\omega}_K^{IE}) \in \mathbb{R}^3$ specifies the rotation of the Earth [143]. In the NED frame, the angular velocity $(\vec{\omega}_K^{IE})_O \in \mathbb{R}^3$ is determined by

$$(\vec{\omega}_K^{IE})_O = \omega_E \cdot \begin{bmatrix} \cos \phi \\ 0 \\ -\sin \phi \end{bmatrix}_O \quad \text{where} \quad \omega_E \approx \frac{2\pi}{86400} \text{ rad/s} \quad (2.42)$$

is the rotation rate of the earth about its axis. The angular velocity $(\vec{\omega}_K^{IE})_O \in \mathbb{R}^3$ is denoted in the C -frame by transformation through the rotation matrix $M_{CO} \in \mathbb{R}^{3 \times 3}$

$$(\vec{\omega}_K^{IE})_C = \omega_E \cdot \begin{bmatrix} \cos \phi \cdot \cos \Psi \\ -\cos \phi \cdot \sin \Psi \\ -\sin \phi \end{bmatrix}_C \quad (2.43)$$

Analogous to the derivation of $(\vec{a}_{tr}^R)_C \in \mathbb{R}^3$ in Eq. (2.37), the total acceleration of the aircraft reference point due to earth's rotation in the control frame is determined

$$(\vec{a}_{e,rot}^R)_C = \underbrace{2 \cdot (\vec{\omega}_K^{IE})_C \times (\vec{V}_K^R)_C^E}_{\text{Coriolis acceleration due to Earth's rotation}} + \underbrace{(\vec{\omega}_K^{IE})_C \times [(\vec{\omega}_K^{IE})_C \times (\vec{r}^R)_C]}_{\text{Centrifugal acceleration due to Earth's rotation}}, \quad (2.44)$$

in which the cross products are reformulated as matrix multiplications

$$(\vec{a}_{e,rot}^R)_C = 2 \cdot (\Omega^{IE})_{CC} \cdot (\vec{V}_K^R)_C^E + [(\Omega^{IE})_{CC}]^2 \cdot (\vec{r}^R)_C. \quad (2.45)$$

Here $(\Omega^{IE})_{CC} \in \mathbb{R}^{3 \times 3}$, exhibited in (B.1), is a skew symmetric matrix, which is employed in Eq. (2.45) to illustrate all the terms that constitute the total acceleration of the aircraft reference point due to earth's rotation indicated in the control frame

$$(\vec{a}_{e,rot}^R)_C = 2 \cdot \omega_E \cdot \begin{bmatrix} (v_K^R)_C^E \cdot \sin \phi - (w_K^R)_C^E \cdot \sin \Psi \cdot \cos \phi \\ - (u_K^R)_C^E \cdot \sin \phi - (w_K^R)_C^E \cdot \cos \Psi \cdot \cos \phi \\ \cos \phi \cdot \left((u_K^R)_C^E \cdot \sin \Psi + (v_K^R)_C^E \cdot \cos \Psi \right) \end{bmatrix} + \quad (2.46)$$

$$\omega_E^2 \cdot \begin{bmatrix} -\sin \phi \cdot (x_C^R \cdot \sin \phi + z_C^R \cdot \cos \Psi \cdot \cos \phi) - \sin \Psi \cdot (\cos \phi)^2 \cdot \sigma_1 \\ \sin \phi \cdot (y_C^R \cdot \sin \phi - z_C^R \cdot \sin \Psi \cdot \cos \phi) - \cos \Psi \cdot (\cos \phi)^2 \cdot \sigma_1 \\ \cos \phi \cdot (-x_C^R \cdot \cos \Psi \cdot \sin \phi + y_C^R \cdot \sin \Psi \cdot \sin \phi - z_C^R \cdot \cos \phi) \end{bmatrix}$$

where

$$\sigma_1 = y_C^R \cdot \cos \Psi + x_C^R \cdot \sin \Psi.$$

2.3.3 Acceleration due to Rigid Body Rotation in the Control Frame

Acceleration $(\vec{a}_{b,rot}^{RG})_C \in \mathbb{R}^3$, specified by Eq. (2.35), is induced at the aircraft reference point R due to rigid body rotation when the reference point and the center of gravity G of the aircraft do not coincide. In Eq. (2.35), the rotational accelerations $(\vec{\omega}_K^{EB})_B^B \in \mathbb{R}^3$ and rates $(\vec{\omega}_K^{IB})_B \in \mathbb{R}^3$ are expanded according to

$$(\vec{\omega}_K^{EB})_B^B = (\vec{\omega}_K^{EO})_B^B + (\vec{\omega}_K^{OB})_B^B = \begin{bmatrix} (\dot{\omega}_{K,x}^{EO}) \\ (\dot{\omega}_{K,y}^{EO}) \\ (\dot{\omega}_{K,z}^{EO}) \end{bmatrix}_B + \begin{bmatrix} \dot{p}_K \\ \dot{q}_K \\ \dot{r}_K \end{bmatrix} \quad (2.47)$$

$$(\vec{\omega}_K^{IB})_B = (\vec{\omega}_K^{IO})_B + (\vec{\omega}_K^{OB})_B = \begin{bmatrix} (\omega_{K,x}^{IO}) \\ (\omega_{K,y}^{IO}) \\ (\omega_{K,z}^{IO}) \end{bmatrix}_B + \begin{bmatrix} p_K \\ q_K \\ r_K \end{bmatrix}$$

for comprehending the effect of rigid body rotational accelerations $(\vec{\omega}_K^{OB})_B^B \in \mathbb{R}^3$ and rates $(\vec{\omega}_K^{OB})_B \in \mathbb{R}^3$ on translation acceleration

$$(\vec{a}_{b,rot}^{RG})_C = \mathbf{M}_{CB} \cdot \left\{ \left((\vec{\omega}_K^{EO})_B^B + (\vec{\omega}_K^{OB})_B^B \right) \times (\vec{r}^{RG})_B + \left((\vec{\omega}_K^{IO})_B + (\vec{\omega}_K^{OB})_B \right) \times \left[\left((\vec{\omega}_K^{IO})_B + (\vec{\omega}_K^{OB})_B \right) \times (\vec{r}^{RG})_B \right] \right\}. \quad (2.48)$$

2.3 Translation Motion in the Control Frame

The elements of the angular acceleration $(\vec{\omega}_K^{EO})_B^B \in \mathbb{R}^3$ and rate $(\vec{\omega}_K^{IO})_B \in \mathbb{R}^3$ appearing in Eq. (2.47) are shown in the Eqs. (B.6) and (B.4) respectively. The cross products in Eq. (2.48) are replaced by matrix multiplications with the skew symmetric matrices for body angular acceleration $(\dot{\Omega}^{OB})_{BB}^B \in \mathbb{R}^{3 \times 3}$ and body angular rate $(\Omega^{OB})_{BB} \in \mathbb{R}^{3 \times 3}$ according to the generic skew symmetric matrix form in Eq. (2.4)

$$(\dot{\Omega}^{OB})_{BB}^B = \begin{bmatrix} 0 & -\dot{r}_K & \dot{q}_K \\ \dot{r}_K & 0 & -\dot{p}_K \\ -\dot{q}_K & \dot{p}_K & 0 \end{bmatrix}_{BB}, \quad (\Omega^{OB})_{BB} = \begin{bmatrix} 0 & -r_K & q_K \\ r_K & 0 & -p_K \\ -q_K & p_K & 0 \end{bmatrix}_{BB}, \quad (2.49)$$

and in a similar manner for the remaining angular acceleration $(\dot{\Omega}^{EO})_{BB}^B \in \mathbb{R}^{3 \times 3}$ and angular velocity $(\Omega^{IO})_{BB} \in \mathbb{R}^{3 \times 3}$, thereby resulting in the following relation

$$(\vec{a}_{b,rot}^{RG})_C = \mathbf{M}_{CB} \cdot \left\{ \left[(\dot{\Omega}^{EO})_{BB}^B + (\dot{\Omega}^{OB})_{BB}^B \right] \cdot (\vec{r}^{RG})_B + \left[(\Omega^{IO})_{BB} + (\Omega^{OB})_{BB} \right]^2 \cdot (\vec{r}^{RG})_B \right\} \quad (2.50)$$

The composition of the translation acceleration due to rigid body rotation $(\vec{a}_{b,rot}^{RG})_C \in \mathbb{R}^3$ based on the major effects from rigid body rotational acceleration and rate is obtained by performing an element-wise decomposition of the expression in Eq. (2.50) without the skew-symmetric matrices $(\dot{\Omega}^{EO})_{BB}^B$ and $(\Omega^{IO})_{BB}$

$$(\vec{a}_{b,rot}^{RG})_C = \begin{bmatrix} \cos \Theta \cdot \sigma_3 + \cos \Phi \cdot \sin \Theta \cdot \sigma_2 + \sin \Phi \cdot \sin \Theta \cdot \sigma_1 \\ \cos \Phi \cdot \sigma_1 - \sin \Phi \cdot \sigma_2 \\ \cos \Phi \cdot \cos \Theta \cdot \sigma_2 - \sin \Theta \cdot \sigma_3 + \cos \Theta \cdot \sin \Phi \cdot \sigma_1 \end{bmatrix} \quad (2.51)$$

where

$$\begin{aligned} \sigma_1 &= \dot{r}_K \cdot x_B^{RG} - \dot{p}_K \cdot z_B^{RG} - y_B^{RG} \cdot (p_K^2 + r_K^2) + p_K \cdot q_K \cdot x_B^{RG} + q_K \cdot r_K \cdot z_B^{RG}, \\ \sigma_2 &= \dot{p}_K \cdot y_B^{RG} - \dot{q}_K \cdot x_B^{RG} - z_B^{RG} \cdot (p_K^2 + q_K^2) + p_K \cdot r_K \cdot x_B^{RG} + q_K \cdot r_K \cdot y_B^{RG}, \\ \sigma_3 &= \dot{q}_K \cdot z_B^{RG} - \dot{r}_K \cdot y_B^{RG} - x_B^{RG} \cdot (q_K^2 + r_K^2) + p_K \cdot q_K \cdot y_B^{RG} + p_K \cdot r_K \cdot z_B^{RG}. \end{aligned} \quad (2.52)$$

Ultimately, by utilizing the acceleration sources elaborated in the Eqs. (2.40), (2.46) and (2.50), the rigid body translation equations of motion from Eq. (2.30) are denoted in the control frame

$$(\vec{f}_T^R)_C = (\vec{V}_K^R)_C^{EC} + (\vec{\omega}_K^{OC})_C \times (\vec{V}_K^R)_C^E + (\vec{a}_{tr}^R)_C + (\vec{a}_{e,rot}^R)_C + (\vec{a}_{b,rot}^{RG})_C \quad (2.53)$$

At this point, arguments justifying the choice of the reference frame in the development of unified control strategies are presented. In the forward velocity phases - transition and wingborne, formulation of the translation control problem in the kinematic frame (K) is a viable option. Contrarily, it does not accomplish the aspiration of a unified controller for both hover and forward velocity phases since the K -frame is not defined for the hover phase, which encompasses flight conditions with zero kinematic velocity ($V_K = 0$). Therefore, subsequent sections discuss aspects of lateral and vertical motion for complete flight envelope in the proposed control frame to establish its utility for the manual and trajectory control architectures further developed in this work.

2.3.4 Lateral Motion in the Control Frame

Kinematic motion along the aircraft lateral axis for all the flight phases can be exactly determined through the variables enlisted in the Table 2.3. Important to note that velocity commands are the highest level of control variables considered in this evaluation. Lateral position commands can also be applied, however for streamlining this analysis only the velocity command is considered. Moreover, the position loop is completely kinematic and hence can be added straightaway around the velocity control loop. Besides the lateral velocity, the heading angle rate appears as an additional degree of freedom in specifying the aircraft motion especially in the hover flight phase. While observing the aircraft motion in the C -frame, the heading angle rate is decoupled from the kinematic motion in the absence of the forward velocity $(u_K^R)^E$. The significance of this inter-axis coupling relation in unifying the lateral motion control over full flight envelope is discussed in detail later. In the hover phase, the lateral translation maneuvers are specified through lateral velocity commands in the C -frame $(v_K^R)^E$ and additionally heading angle rate $\dot{\Psi}$ command can be used to orient the aircraft independently.

Hover flight Phase	Forward velocity flight phase
Lateral kinematic velocity $(v_K^G)^E$	Course angle rate $\dot{\chi}_K$
Heading angle rate $\dot{\Psi}$	Bank angle Φ

Table 2.3: Control variables governing the kinematic lateral motion of a VTOL transition aircraft

In the forward velocity phases the lateral translation is accomplished through the kinematic course angle rate $\dot{\chi}_K$, which can directly be converted to a desired bank angle using a kinematic relation such as the one derived in Eq. (2.69) afterwards. It is important to emphasize that the desired behavior of the kinematic lateral motion is agnostic of the magnitude of the dynamic pressure. Simply stated, the aircraft behavior for lateral motion is defined like a fixed-wing configuration (bank-to-turn) for forward velocity flight phases – transition and wingborne. Even though the mechanism of lift generation differs between these two phases, and the heading angle rate can theoretically be used as an additional degree of control as long as the powered lift is active in the low dynamic pressure regime of the transition flight phase. However, a decoupled heading angle rate control is not used in order to avoid a non-intuitive skid-to-turn behavior.

In order to comprehend the lateral motion in the forward velocity phases, the first step is to visualize the angles between NED (O), control (C) and kinematic (K) frames in the horizontal plane as illustrated in Fig. 2.3. The kinematic course angle

$$\chi_K = \arctan \left[\frac{(v_K^G)^E}{(u_K^G)^E} \right] \quad (2.54)$$

2.3 Translation Motion in the Control Frame

is not valid for zero kinematic velocities. However, the heading $\Psi \in \mathbb{R}$, which specifies the rotation of the C -frame in comparison to the NED frame, is valid for all flight phases. Moreover, the relation between the kinematic course angle $\chi_K \in \mathbb{R}$ and the yaw angle Ψ

$$\chi_K = \Psi + \varepsilon \quad (2.55)$$

only utilizes the horizontal kinematic side slip angle $\varepsilon \in \mathbb{R}$ which can be determined through the velocities denoted in the C -frame

$$\varepsilon = \arctan \left[\frac{(v_K^G)_C^E}{(u_K^G)_C^E} \right]. \quad (2.56)$$

Inherently, it follows from Eq. (2.55) that

$$\dot{\Psi} = \dot{\chi}_K - \dot{\varepsilon} \quad (2.57)$$

where $\dot{\varepsilon} \in \mathbb{R}$ is the horizontal kinematic side slip angle rate

$$\dot{\varepsilon} = \frac{(\dot{u}_K^G)_C^{EC} \cdot (v_K^G)_C^E - (u_K^G)_C^E \cdot (\dot{v}_K^G)_C^{EC}}{[(u_K^G)_C^E]^2 + [(v_K^G)_C^E]^2}. \quad (2.58)$$

Here the velocities $(u_K^G)_C^E \in \mathbb{R}$, $(v_K^G)_C^E \in \mathbb{R}$ denoted in the C -frame are computed by the rotation of their corresponding NED-frame states along the vertical z_O -axis by the bearing angle Ψ using the frame rotation matrix M_{CO} formulated in Eq. (2.1). The terms $(\dot{u}_K^G)_C^{EC} \in \mathbb{R}$, $(\dot{v}_K^G)_C^{EC} \in \mathbb{R}$ represent the kinematic accelerations with respect to the control

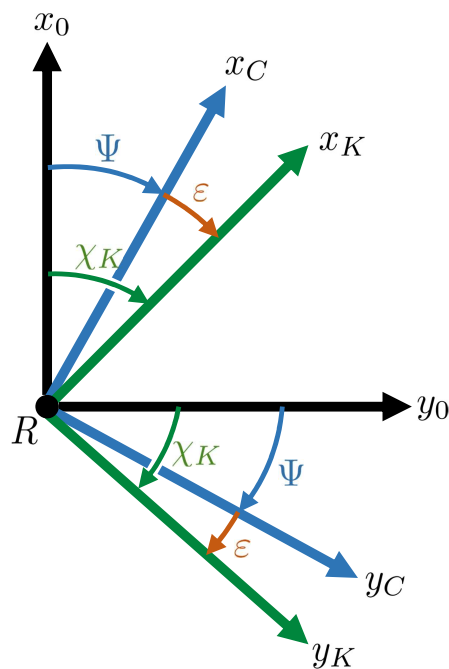


Figure 2.3: Relative angles between O , C and K frames in the horizontal plane

frame and denoted in the control frame. In a steady state flight condition, horizontal accelerations in C -frame are negligible $(\dot{u}_K^R)_C^{EC}, (\dot{v}_K^R)_C^{EC} \approx 0$ and thus Eq. (2.58) results in $\dot{\epsilon} \approx 0$ as well. Consequently, for a steady state flight Eq. (2.57) resolves to

$$\dot{\Psi} = \dot{\chi}_K \quad (2.59)$$

Considering the relation between yaw angle rate and course angle rate, an individual component breakdown of the terms in the translation dynamics from Eq. (2.53)

$$\begin{bmatrix} \dot{u}_K^R \\ \dot{v}_K^R \\ \dot{w}_K^R \end{bmatrix}_C^{EC} + \begin{bmatrix} - (v_K^R)_C^E \cdot \dot{\Psi} \\ (u_K^R)_C^E \cdot \dot{\Psi} \\ 0 \end{bmatrix} = \begin{bmatrix} f_x \\ f_y \\ f_z \end{bmatrix}_C^R + \begin{bmatrix} \cos \Psi & \sin \Psi & 0 \\ -\sin \Psi & \cos \Psi & 0 \\ 0 & 0 & 1 \end{bmatrix} \cdot \begin{bmatrix} 0 \\ 0 \\ g \end{bmatrix}_O \quad (2.60)$$

exhibits the unification of the hover and the forward velocity phases for lateral motion through the side specific force $(f_y^R)_C$ equation

$$(\dot{v}_K^R)_C^{EC} + (u_K^R)_C^E \cdot \dot{\Psi} = (f_y^R)_C. \quad (2.61)$$

Note that the acceleration terms $(\vec{a}_{tr}^R)_C, (\vec{a}_{e,rot}^R)_C$ and $(\vec{a}_{b,rot}^{RG})_C$ are ignored in this analysis for simplification and to facilitate an evaluation of the major effects only.

In the hover flight phase, lateral acceleration $(\dot{v}_K^R)_C^{EC}$ command is derived from a demand for lateral displacement. This acceleration command forms one of the constituents of the lateral specific force command, which is allocated to a bank angle command as presented by the schematic diagram in Fig. 2.4. Moreover, the aircraft nose can be rotated through by commanding the heading angle rate $\dot{\Psi}$ separately without triggering a substantial inter-axis coupling $((u_K^R)_C^E \cdot \dot{\Psi})$ in the lateral channel. Subsequently, the lateral displacement is attained through the lateral specific force $(f_y^R)_C$ generated by means of the tilted powered-lift vector due to the bank angle as exhibited in Fig. 2.5a.

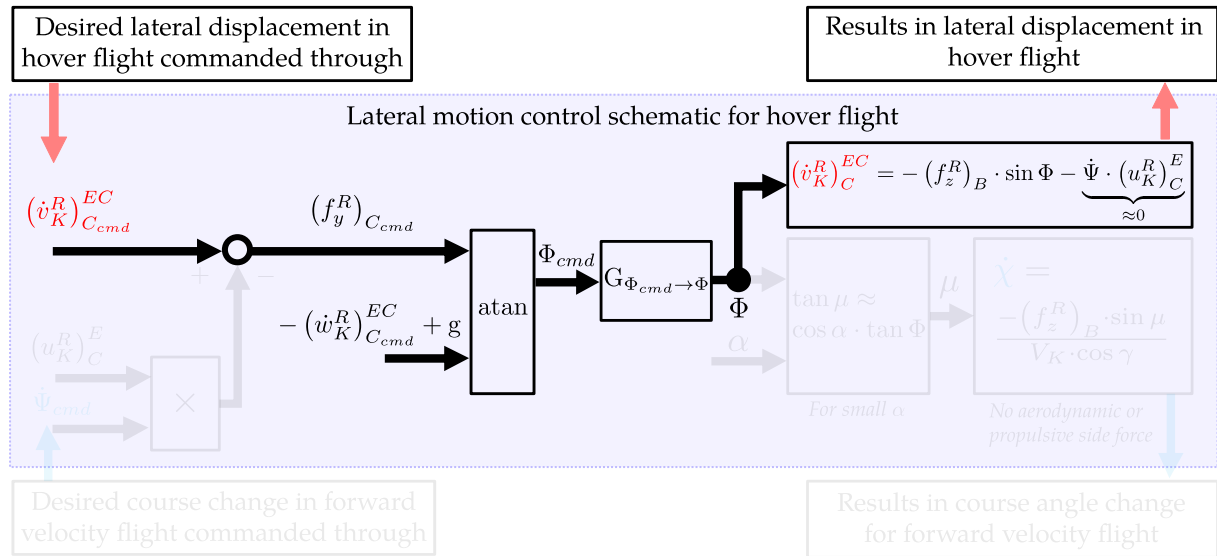
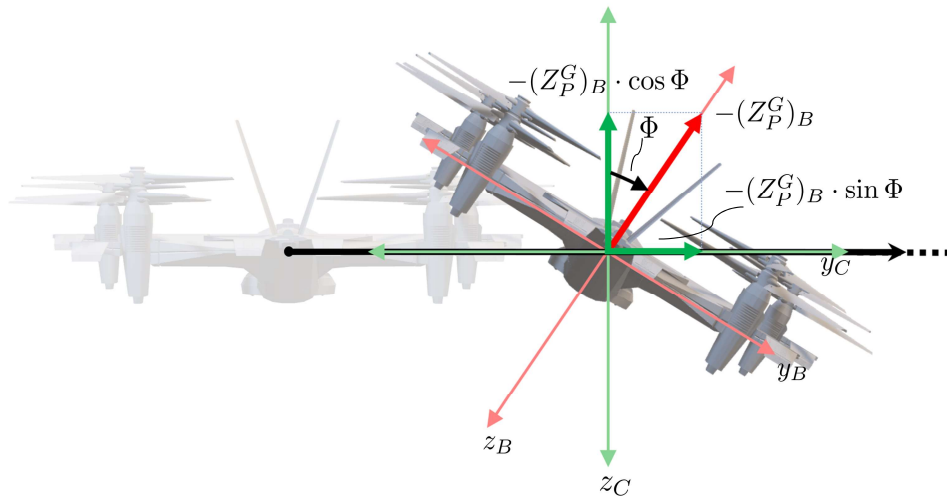
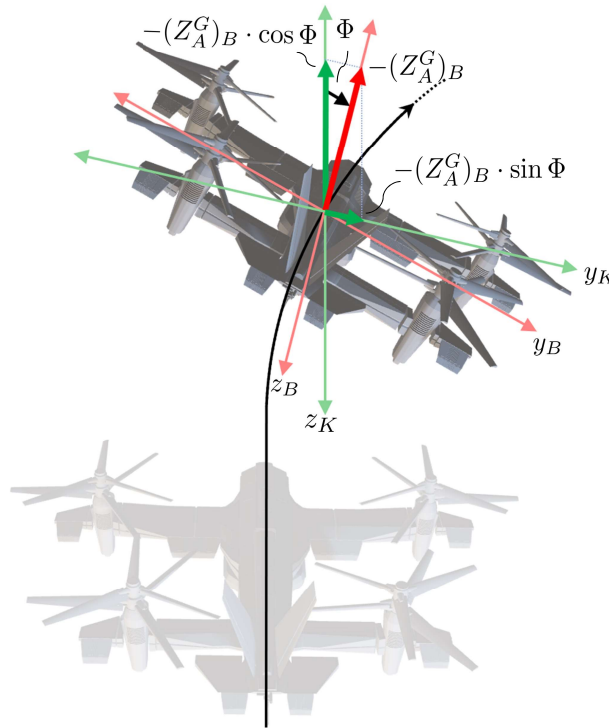


Figure 2.4: Lateral Motion Schematic for hover flight


 (a) *Hover flight phase*

 (b) *Forward velocity flight phases*
Figure 2.5: *Lateral translation/Turning in different flight phases of a VTOL transition aircraft*

For the forward velocity flight phases, lateral maneuvering is realized through the second constituent of the y -specific force demand constructed from the inter-axis coupling term $((u_K^R)^E_C \cdot \dot{\Psi})$. Given a desired course angle rate $\dot{\chi}_K$, the yaw angle rate command $\dot{\Psi}_{cmd}$ is computed through Eqs. (2.57), (2.59) with consideration of appropriate assumptions. The demand in the lateral specific force $(f_y^R)^E_C, cmd$ is then obtained by the product of the heading angle rate command $\dot{\Psi}_{cmd}$ with the forward velocity $(u_K^R)^E_C$. Furthermore, a bank angle command is produced from the desired lateral specific force command which is then commanded to the inner loop controller as demonstrated by the diagram

in Fig. 2.6. The achieved bank angle produces a centripetal force by tilting the mixed or aerodynamic lift vector (depending on the current flight phase), thereby curving the flight path to achieve the desired course angle rate as depicted by the visualization in Fig.2.5b. Assumptions of small angle of attack and absence of aerodynamic or propulsive side control forces (in the y_B axis) are made for the schematic in Fig. 2.6.

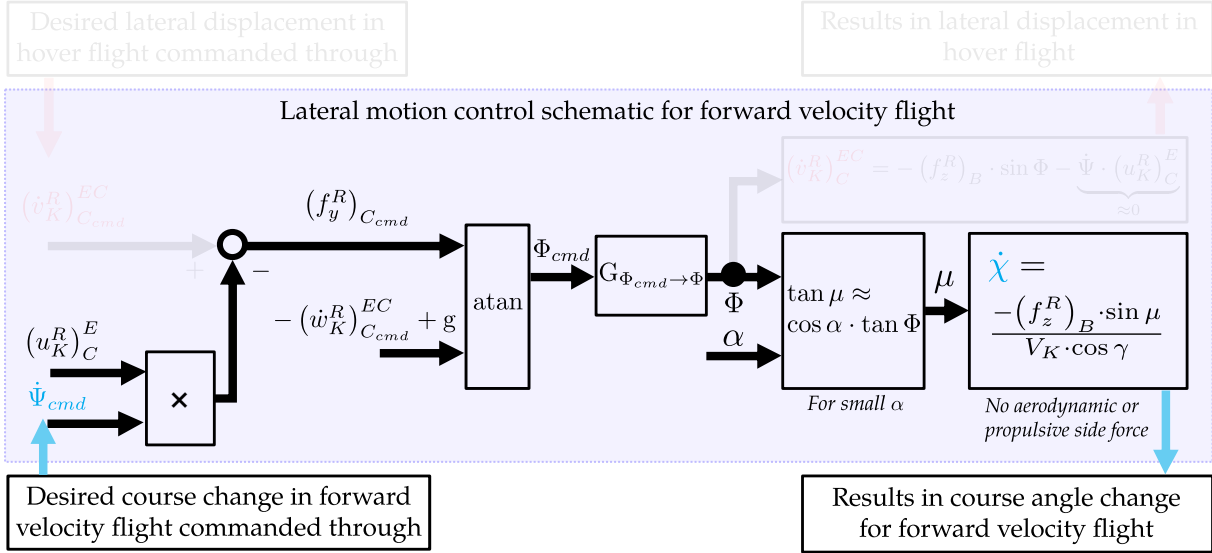


Figure 2.6: Lateral Motion Schematic for forward velocity flight

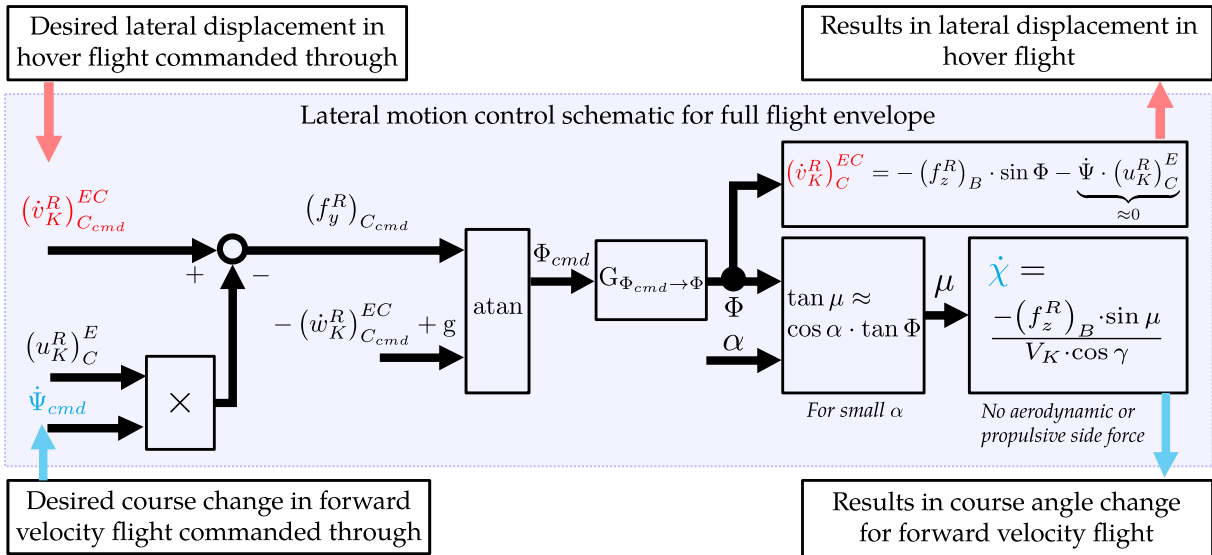


Figure 2.7: Lateral Motion Schematic for full flight envelope

Therefore, the lateral displacement, heading and course angle can be controlled without dealing with the singularity of kinematic course angle χ_K at zero kinematic velocity by employing C -frame lateral velocity $(v_K^R)_C^E$ and yaw angle rate $\dot{\Psi}$ as the control variables for the lateral-directional axes in the full flight envelope of a VTOL transition

aircraft. The strategy for the full flight envelope is illustrated by the Fig. 2.7. Generation of bank angle command plays an important role in the lateral motion and it will be discussed next.

Majority of the aircraft configurations being developed in the UAM ecosystem, similar to the example aircraft illustrated in Fig. 2.8, comprise of propulsors that produce forces in the longitudinal and vertical body frame (B) axes along with the conventional aerodynamic control surfaces. Consequently, as already stated, the lateral specific force in C -frame can be generated by tilting the vertical lift (propulsive or aerodynamic) through the bank angle. Body-fixed specific forces are transformed to C -frame specific forces according to

$$\begin{bmatrix} f_x \\ f_y \\ f_z \end{bmatrix}_C^R = \begin{bmatrix} \cos \Theta & \sin \Phi \cdot \sin \Theta & \cos \Phi \cdot \sin \Theta \\ 0 & \cos \Phi & -\sin \Phi \\ -\sin \Theta & \sin \Phi \cdot \cos \Theta & \cos \Phi \cdot \cos \Theta \end{bmatrix} \cdot \begin{bmatrix} f_x \\ f_y \\ f_z \end{bmatrix}_B^R. \quad (2.62)$$

Commonly, aircraft do not possess any control effectors that can produce a lateral body fixed force, hence $(f_y^R)_B \in \mathbb{R}$ is neglected in Eq. (2.62) such that the side specific force in C -frame $(f_y^R)_C \in \mathbb{R}$ is only a function of bank angle and body vertical specific force

$$(f_y^R)_C = - (f_z^R)_B \cdot \sin \Phi. \quad (2.63)$$

Additionally, compensation of the vertical specific force demand in the control frame can be achieved only through the vertical lift. The longitudinal body specific force $(f_x^R)_B$ couples into the C -frame vertical channel through the pitch angle, however it is not actively used for controlling the vertical axis variables. Thereupon, neglecting the term corresponding to $(f_x^R)_B$ in Eq. (2.63) produces

$$(f_z^R)_C = (f_z^R)_B \cdot \cos \Phi \cdot \cos \Theta. \quad (2.64)$$

For wingborne flight, the neglect of the $(f_x^R)_B$ term is valid under the assumption that longitudinal thrust is commanded in a decoupled manner to generate the airspeed for sustaining aerodynamic lift. Moreover, the vertical force can be produced directly through the control effectors in powered lift flight. Therefore, the relation in Eq. (2.64) is applicable for full flight envelope.

As stated previously, the control frame lateral specific force $(f_y^R)_C$ is generated by banking the aircraft. Thus, the expression for bank angle is computed by division of Eq. (2.63) and Eq. (2.64)

$$\tan \Phi = \frac{(f_y^R)_C \cdot \cos \Theta}{-(f_z^R)_C} \quad (2.65)$$

in which the substitution of $(f_z^R)_C$ by the vertical translation equation of motion from Eq.(2.60) delivers

$$\Phi = \arctan \left[\frac{(f_y^R)_C \cdot \cos \Theta}{-(\dot{w}_K^R)_C^{EC} + g} \right] \quad (2.66)$$

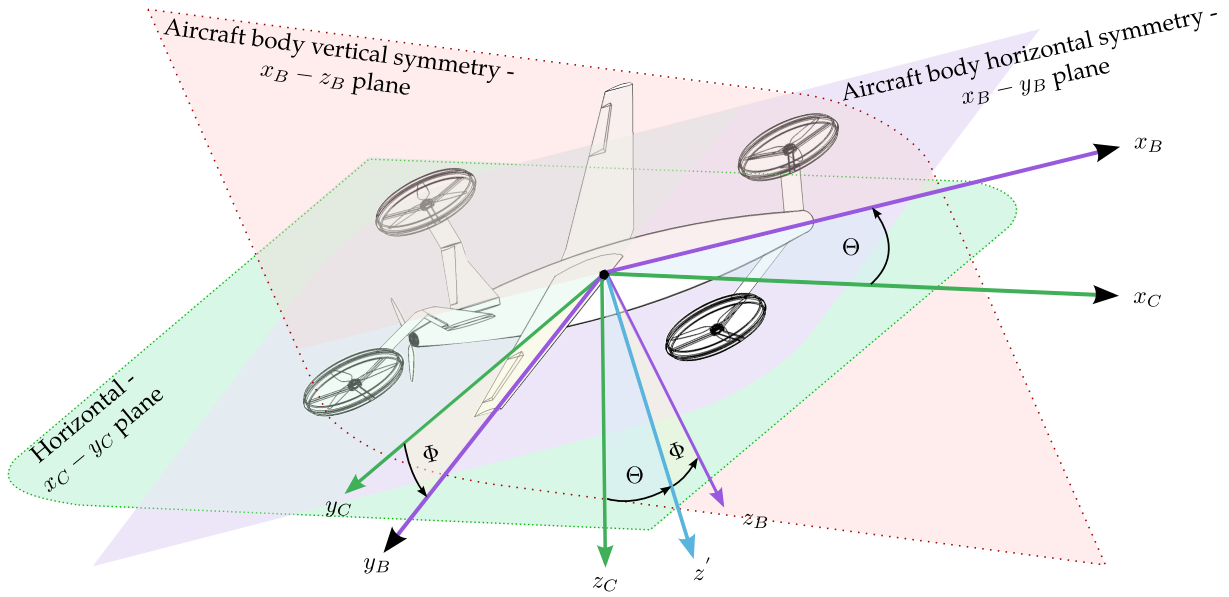


Figure 2.8: Rotation from Control frame to Body frame [142]

a relation for bank angle which also involves the control frame vertical acceleration $(\dot{w}_K^R)^{EC}$. Subsequently, the bank angle command emanates from further use of Eq. (2.61) for a given lateral acceleration and yaw angle rate command

$$\Phi_{cmd} = \arctan \left[\frac{\left[(\dot{w}_K^R)^{EC}_{Ccmd} + (u_K^R)^E_C \cdot \dot{\Psi}_{cmd} \right] \cdot \cos \Theta}{-(\dot{w}_K^R)^{EC}_{Ccmd} + g} \right]. \quad (2.67)$$

In order to assess the effect of the vertical acceleration on the allocation of the lateral specific force $(f_y^R)_C$ to a bank angle, simulations for the lateral motion schematic from Fig. 2.7 are performed with two scenarios

Case 1 Consideration of vertical acceleration command $(\dot{w}_K^R)^{EC}_{Ccmd}$,

Case 2 No consideration of the vertical acceleration command in the bank angle command specification.

The test cases are executed for a no-wind condition with steady state forward velocity $(u_K^R)^{EC}$, thus the approximation of equality between the heading angle rate and the course angle rate in Eq. (2.59) holds. Figure 2.9 illustrates the results for the two cases. A heading angle rate of 10 *deg/s* is commanded and the lateral specific force command $(f_y)_{Ccmd}$ is determined using the Eq. (2.61). When the heading angle rate and likewise the bank angle reaches a steady state value, vertical velocity command $(w_K^R)^{EC}_{Ccmd}$ is applied. The bank angle command is determined by Eq. (2.66) for the first case. It is observed in the bank angle response plot from Fig. 2.9 that the bank angle command value reduces at the instant of execution of the vertical velocity command and then it slowly converges back to the initial command value. The physical reason for the drop in bank angle is attributed to the inherent vertical-lateral force coupling in conventional aircraft where the centripetal acceleration is generated by tilting the lift vector (powered

or aerodynamic) through the bank angle

$$V \cdot \dot{\chi} \cdot \cos \gamma = - \left(f_z^R \right)_B \cdot \underbrace{\sin \mu}_{\approx \Phi} . \quad (2.68)$$

Pertaining to the first case under study, the vertical acceleration demand is fulfilled by an increase in the lift vector that further leads to an increase in centripetal acceleration. Subsequently, the increase in the centripetal acceleration increases the turn rate generated at a given bank angle since the turn rate is built with

$$\dot{\chi} = \dot{\Psi} = \frac{- \left(f_z^R \right)_B \cdot \sin \Phi}{V \cdot \cos \gamma} . \quad (2.69)$$

Since the controlled variable in this analysis is the heading rate, the bank angle needs to reduce in order to maintain a steady state yaw angle rate $\dot{\Psi}$. Consequently, the true yaw angle rate denoted by the red signal in yaw angle rate response, does not see a drastic change.

In the second test case, the vertical acceleration term is omitted from the bank angle command calculation in Eq. (2.67)

$$\Phi_{cmd} = \arctan \left[\frac{\left[\left(\dot{w}_K^R \right)_{C_{cmd}}^{EC} + \left(u_K^R \right)_C^E \cdot \dot{\Psi}_{cmd} \right] \cdot \cos \Theta}{g} \right] . \quad (2.70)$$

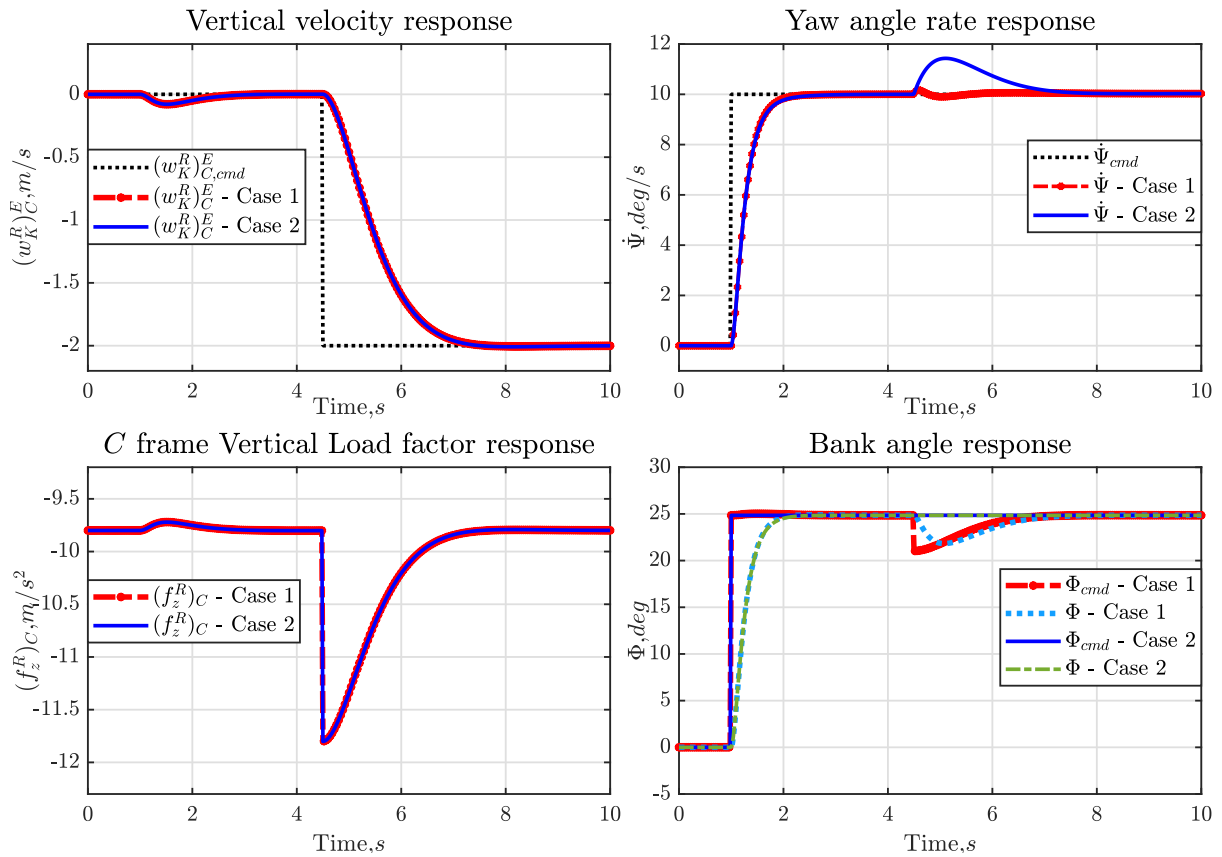


Figure 2.9: Effect of vertical load factor command in bank angle command generation

It is evident from the bank angle response plots in Fig. 2.9 that the vertical velocity maneuver has no effect on the bank angle response. Nevertheless, a substantial increase is observed in the heading angle rate during the build-up of the vertical load factor because the heading rate is generated with Eq. (2.69). While this behavior is acceptable for a manually piloted aircraft, where the pilot perceives the stick deflection as a bank angle command and does not anticipate that the vertical channel commands would cause a change in the bank angle of the aircraft, however it is not the desired behavior for a trajectory following control mode since it deteriorates the course angle rate tracking in a level turn maneuver.

It can be concluded from these results that for the lateral motion control the bank angle command to the inner loop in Eq. (2.67) is preferred for precise flight trajectory control since it maintains the desired turn rate by accounting for the vertical channel acceleration. However, in case of manual flight operation the bank angle command computed in Eq. (2.70) is more favorable to retain the intuitiveness of the aircraft response for the pilot.

In these simulations, lateral displacement maneuvers in hover flight that require generation of lateral acceleration $(\dot{v}_K^R)_{C_{cmd}}^{EC}$ are not performed, however the conclusions with regard to bank angle command computation still hold because the command generation depends on the full specific force command rather than its individual components.

Finally, the strategy presented in this section allows to not only achieve the lateral displacement in hover phase but to also specify the path dynamics of the aircraft by utilization of heading rate in the forward velocity flight unifiedly through the lateral specific force in the C -frame. Additionally, the bearing of the aircraft can also be specified using the $\dot{\Psi}$ command variable in hover.

2.3.5 Vertical Motion in the Control Frame

The flight controllers for the vertical channel in the wingborne phase are conventionally derived in the kinematic frame, however similar to the kinematic course angle in Eq. (2.54), the kinematic climb angle

$$\gamma_K = \arctan \left[\frac{(w_K^G)_O^E}{(u_K^G)_O^E} \right] \quad (2.71)$$

is not valid for zero kinematic velocities, and thus not suitable for the hover flight phase. Needless to say, the kinematic frame is also not suitable to develop a unified strategy for the vertical channel control. Consequently, the analysis of the vertical dynamics in control frame is continued. Isolating z_C axis equation of motion from Eq. (2.60)

$$(\dot{w}_K^R)_C^{EC} = (f_z^R)_C + g = -\ddot{h}. \quad (2.72)$$

exhibits that there are no inter-axis coupling terms associated with the generation of the vertical specific force $(f_z^R)_C \in \mathbb{R}$ in the control frame. The term $(\dot{w}_K^R)_C^{EC} \in \mathbb{R}$ represents the vertical acceleration derived in reference to the C -frame and denoted in the same frame, $g \in \mathbb{R}$ indicates the acceleration due to gravity and $\ddot{h} \in \mathbb{R}$ represents the height acceleration.

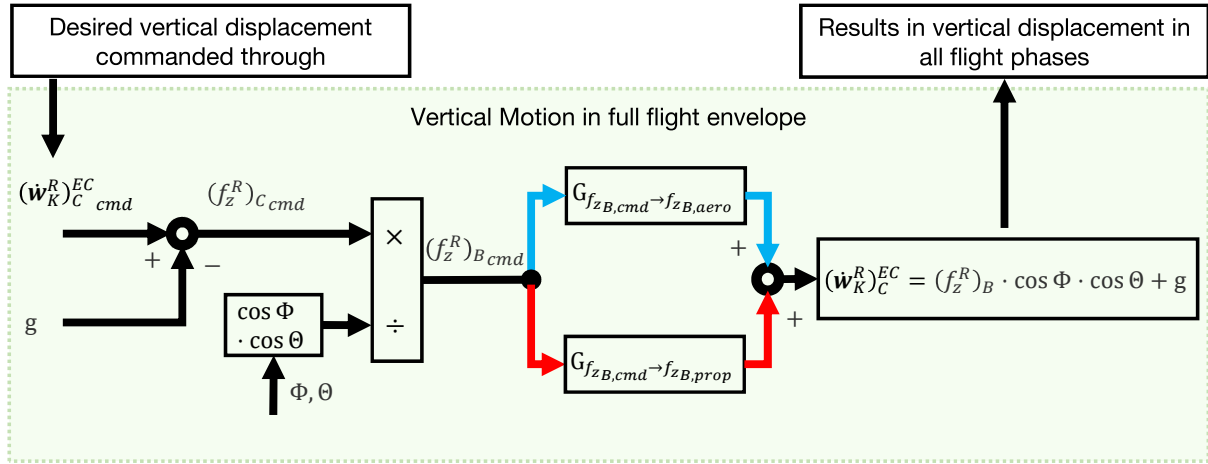


Figure 2.10: Vertical Motion Schematic for full flight envelope

As shown in Fig. 2.10, a vertical acceleration command $(\dot{w}_K^R)_C^{EC}$, computed from the desired vertical displacement, yields the control frame vertical specific force $(f_z^R)_{C\,cmd}$ command by inclusion of the gravitational acceleration g . Furthermore, $(f_z^R)_{C\,cmd}$ is converted to a body frame specific force $(f_z^R)_{B\,cmd}$ demand in the inner loop which is directly commanded through either the powered lift in hover or through the pitch channel when sufficient aerodynamic lift is available. For the body frame specific force $(f_z^R)_B$, the inter-axis coupling with the lateral channel that mainly emanates from the bank angle, as shown in Eq. (2.64), is addressed by the inner loop control. Therefore, any vertical displacement commands in all phases are easily achievable through a $(f_z^R)_C$ command derived either from the higher level control variables commanded by the pilot or a trajectory/path-following controller.

Ultimately, through the aspects presented for the lateral and vertical motion control of a VTOL transition aircraft, it is observed that by specifying the control problem in the C -frame, unified control strategies for a VTOL transition vehicle can be formulated. Moreover, such a control strategy also facilitates division of the designed control architecture in to modular configuration-agnostic and configuration-dependent units. The aircraft configuration-agnostic unit is derived from the concepts described for the lateral and vertical motion control in the sections before. The outputs of the configuration agnostic unit contain desired variables defined in the control frame, and serve as input to the aircraft configuration-specific control unit. Within the configuration dependent part of the control strategy, the desired variables are either converted to another physical variable or directly allocated to the control effectors to produce the desired effect. The C -frame translation dynamics presented in this section will be employed in the design of an integrated modular reference model structure, and the unified trajectory controller later in the chapters 3 and 5 respectively. In the next section, the aircraft rotational dynamics are presented briefly before introducing the concept of the Design Reference Model.

2.4 Aircraft Rotational Dynamics

Contrary to the translation dynamics, the rotational dynamics of a VTOL transition aircraft remain agnostic of the flight phase with the exception in the generation of control moments. Differential thrust along with drag moment from the LTUs is utilized to meet the desired moments demand in all axes for the hover and transition phases. In the wingborne phase, conventional control surfaces are employed to produce the desired moments. However, the propagation of moments to body angular rates is governed by the same angular momentum dynamics.

In addition to the assumption **A.2.2** for quasi-stationary mass, the derivation of the angular momentum dynamics employs the assumption

A.2.8 Mass distribution of the aircraft is assumed to be quasi-stationary which implies that $(\dot{\mathbf{I}}^R)^B \approx 0$.

A detailed derivation of the rotational momentum dynamics has been extensively covered in various sources [143, 144, 146] and therefore will not be presented here. Applying the law of conservation of angular momentum with consideration of assumptions **A.2.2** and **A.2.8**, the angular momentum dynamics are obtained

$$\left(\frac{d}{dt}\right)^B \cdot (\vec{\omega}_K^{IB})_B = (\mathbf{I}_{BB}^R)^{-1} \cdot \left[(\vec{M}_T^R)_B - (\vec{\omega}_K^{IB})_B \times \mathbf{I}_{BB}^R \cdot (\vec{\omega}_K^{IB})_B + m \cdot (\vec{r}^{RG})_B \times \left(\left(\dot{\vec{V}}_K^R \right)_B^{IB} + (\vec{\omega}_K^{IB})_B \times (\vec{V}_K^R)_B^I \right) \right], \quad (2.73)$$

where $(\vec{M}_T^R)_B \in \mathbb{R}^3$ represents the sum of all external moments at the reference point R incorporating aerodynamic and propulsive moments for any aircraft configuration. The term $(\vec{\omega}_K^{IB})_B \times \mathbf{I}_{BB}^R \cdot (\vec{\omega}_K^{IB})_B$ signifies the inertia coupling. The last term in Eq. (2.73) manifests when the reference point does not lie at the center of gravity G .

The generation of angular body acceleration, as described by the moment dynamics in Eq. (2.73), further yields angular body rates $(\vec{\omega}_K^{IB})_B$. Assumptions of flat non-rotating earth is frequently applied in flight control [99, 136, 143] are considered here, thereby rendering $(\vec{\omega}_K^{IB})_B = (\vec{\omega}_K^{OB})_B$. The rotational rate vector $(\vec{\omega}_K^{OB})_B$ comprises of the roll rate p_K , pitch rate q_K and yaw rate r_K , which describe the rotation of the body fixed frame compared to the NED frame (O). Correspondingly, the angular orientation of the aircraft (body frame) with respect to the O-frame is quantified through the Euler angles [143, 144, 146]. Given the body rotational rates $(\vec{\omega}_K^{OB})_B$, the attitude dynamics are specified by the strap-down equation

$$\begin{bmatrix} \dot{\Phi} \\ \dot{\Theta} \\ \dot{\Psi} \end{bmatrix} = \begin{bmatrix} 1 & \sin \Phi \tan \Theta & \cos \Phi \tan \Theta \\ 0 & \cos \Phi & -\sin \Phi \\ 0 & \frac{\sin \Phi}{\cos \Theta} & \frac{\cos \Phi}{\cos \Theta} \end{bmatrix} \cdot \begin{bmatrix} p_K \\ q_K \\ r_K \end{bmatrix}. \quad (2.74)$$

Besides the Euler angles, quaternions [146, 147] offer another option to quantify the attitude of an aircraft, which exclude the singularity occurring at a pitch angle of 90° . However, maneuvers that demand such extreme attitude angles do not lie within the scope of this thesis. Henceforth, Euler angles are used to define the attitude of the aircraft.

As noted previously, excluding the production of control moments, the rotational dynamics do not alter in the full flight envelope of a VTOL transition aircraft. Nonetheless, the desired behavior of the aircraft rotational motion differs substantially with varying flight phases. As an instance, attitude/rate commands produced to meet any specific force demands are not subject to additional constraints such as turn coordination, turn compensation in the hover flight phase however, these constraints are essential to define meaningful desired rotation rate trajectories in the forward velocity phases. The approach for generation of rotational rate commands for all flight phases is covered in the chapter presenting the integrated reference model.

In the next section, the rotational dynamics presented here along with the body frame translation dynamics are used to create a Design Reference Model (DRM) for the hover phase of a generic lift-to-cruise VTOL transition configuration such as the one illustrated in Fig. 2.8. Note that the aircraft shown in Fig. 2.8 is only for illustration purposes. The structure of the DRM is designed to be configuration agnostic with the option of incorporating aircraft configuration-specific properties as modular elements.

2.5 Design Reference Model

The Design Reference Model demonstrates a flyable behavior specification, which contains rigid body dynamics, propulsion attributes and aerodynamic properties of an aircraft. Moreover, it serves as an instrument to validate the aircraft behavior against requirements for Handling Quality (HQ) levels, inceptor interpretation, flight mission and more, within the scope of the intended aircraft operation at an early stage when a detailed system design is unavailable.

In addition to the use of the DRM as a validation utility, the author proposes to use it as a tool for baseline control effector sizing in the early aircraft design. This process entails the derivation of maneuverability phase planes comprising of design points, which specify required rotational accelerations and jerk for different handling quality levels. These phase planes are obtained through DRM simulations. Within the bounds of this thesis, the extraction of the maneuverability phase planes is primarily focused for the hover and low speed flight regime. Thereafter, the derived phase planes can serve as a valuable input to the preliminary effector sizing in the aircraft design process attributed to the fact that several aircraft designs proposed in the UAM sphere contain multiple LTUs which must be configured (both in their magnitude and spatial positioning) to satisfy the requirements pertaining to maneuverability. Since the phase planes inherently contain the magnitudes of physical parameters required to satisfy maneuverability requirements, consideration of these values early in the aircraft design process also tends to prevent any costly design iterations at a later stage.

Note that the maneuverability phase planes do not directly relate to effector parameters but rather define requirements for baseline control effector sizing in terms of physical parameters i.e. body rotational acceleration and jerk. Hence, the aircraft design process must strive for a configuration that can fulfill the requirements on the magnitude of these physical parameters, and in addition also retain buffer for external disturbance rejection. The method can also be extended to the high forward-speed flight phases, however that aspect is not covered in this work. The estimation of the required angular acceleration and jerk is constrained through maneuverability requirements for the hover and low speed phases, acquired from the Aeronautical Design Standard for Military Rotorcraft ADS-33E-PRF [84].

In this respect, an Euler attitude angle and vertical velocity pilot command driven design reference model was utilized. The underlying reason for choosing attitude commands as the interpretation for the pilot stick deflections stems from the **Required Response-Types for hover and low speed - near earth** [84, p. 67], which broadly specify ACAH response-type for Usable Cue Environment (UCE) ≥ 2 . Subsequently, the maneuverability requirements in terms of attitude quickness for moderate amplitude changes are chosen. Although termed as moderate amplitude requirements for military rotorcraft, the change in angle magnitude defined in these requirements ranges from 5° to 60° , which are adequate for the entire operational envelope of aircraft functioning within the UAM environment. Moreover, within the attitude quickness requirements handling quality classification is based only on Mission Task Element (MTE) while the Target Acquisition and Tracking classification is omitted since it is of no relevance for the application considered in this research.

Table 2.4 outlines the attitude quickness requirement for the roll and pitch angle. The handling quality level is assessed based on the ratio of the peak rate to the peak of the change in angle resulting from a step input commanded of the corresponding angle as shown in Figures 2.11 and 2.12. The definition of the peaks for each physical quantity is illustrated in Fig. 2.13. The subjective desired behavior is to achieve the required attitude change without any sign reversals in the pilot inceptor input.

Analogously, Table 2.5 details the attitude quickness requirement for changes in the heading angle. The definition of peak angle and rate are consistent with the ones specified in Fig. 2.13. Additionally, the classification of handling quality levels based on the magnitude of the ratio of the peak yaw angle change to peak yaw rate is made according to Fig. 2.14.

Components pertaining to different aspects of the DRM are elucidated in the upcoming sections. As demonstrated in Fig. 2.15, the structure of the design reference model is quite modular. Consequently, it can be used to establish a behavior specification for completely dissimilar configurations such as a multicopter, tilt-rotor transition or a lift-to-cruise transition aircraft. There is a clear distinction between the configuration specific and agnostic components, which reduces the effort of adapting the DRM to a any particular aircraft configuration.

Source **ADS-33 3.3.3 Moderate-amplitude pitch (roll) attitude changes (attitude quickness)**[84, p. 11]

Contents *The ratio of peak pitch (roll) rate to change in pitch (roll) attitude, $q_{pk}/\Delta\theta_{pk}$ ($p_{pk}/\Delta\phi_{pk}$), shall meet the limits specified in Figure 8 (regenerated in the Figures 2.11 and 2.12). The required attitude changes shall be made as rapidly as possible from one steady attitude to another without significant reversals in the sign of the cockpit control input relative to the trim position. The attitude changes required for compliance with this requirement shall vary from 5 deg in pitch (10 deg in roll) to the limits of the Operational Flight Envelope or 30 deg in pitch (60 deg in roll), whichever is less. It is not necessary to meet this requirement for Response-Types that are designated as applicable only to UCE = 2 or 3.*

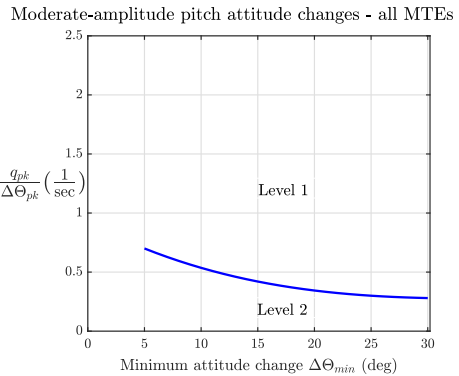
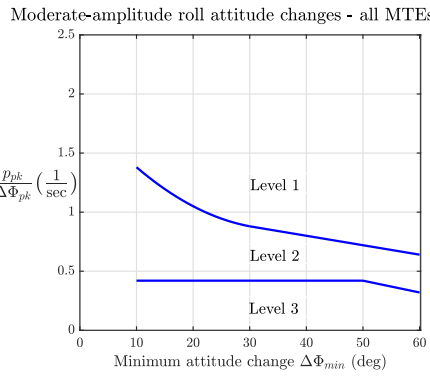


Figure 2.11: Requirements for moderate-amplitude pitch (roll) attitude changes — hover and low speed [84, p. 78]

Figure 2.12: Requirements for moderate-amplitude pitch (roll) attitude changes — hover and low speed [84, p. 78]

Visualization

Definition of Moderate-amplitude Criterion Parameters

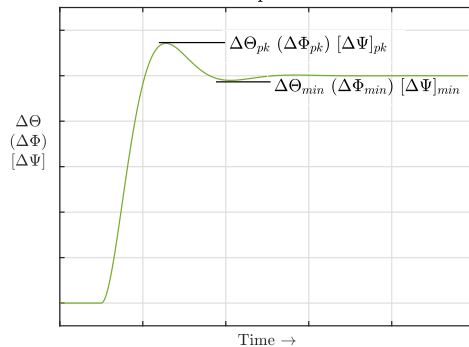


Figure 2.13: Definition of Moderate-Amplitude Criterion Parameters [84, p. 78]

Table 2.4: Moderate-amplitude pitch (roll) attitude changes (attitude quickness)

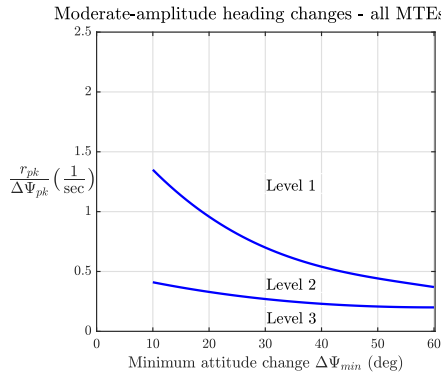
Source	ADS-33 3.3.6 Moderate-amplitude heading changes (attitude quickness)[84, p. 12]
Contents	<i>The ratio of peak yaw rate to change in heading, $r_{pk}/(\Delta\Psi_{pk})$, shall meet the limits specified in Figure 10 (regenerated in the Fig. 2.14). The required heading changes shall be made as rapidly as possible from one steady heading to another and without significant reversals in the sign of the cockpit control input relative to the trim position. It is not necessary to meet this requirement for Response-Types that are designated as applicable only to UCE = 2 or 3.</i>
Visualization	
	Figure 2.14: Requirements for moderate-amplitude heading changes — hover and low speed [84, p. 79]

Table 2.5: Moderate-amplitude heading changes (attitude quickness)

2.5.1 Pilot Inceptor Interpretation

The first element is the pilot inceptor interpretation. As illustrated in the Fig. 2.16, a dual inceptor design is chosen. The right stick, also called the Thrust stick, follows a hybrid design, similar to the design described in [83, 87, 148, 149] for UAVs as well as piloted aircraft. The full deflection range of the hybrid Thrust inceptor comprises of two areas – spring centered and spring-free region, which are separated by an indentation at the boundary of the two regions to facilitate a haptic feedback to the pilot, thereby providing situational awareness. The two regions of the Thrust inceptor associate with the flight phases of a transition aircraft. The spring centered region is employed to achieve translation in the horizontal plane for the the powered lift as well as the mixed lift flight phase. For the Thrust stick up-down axis, the positive (up) deflection is mapped to a traction system command, which provides acceleration along the positive body x -axis, whereas the negative (down) deflection is mapped to a pitch up command in order to translate backwards. However, for a multicopter configuration with no traction thrust units the Thrust stick up-down deflections in the spring-centered region are interpreted as pitch angle commands only. The positive (up) deflection is interpreted

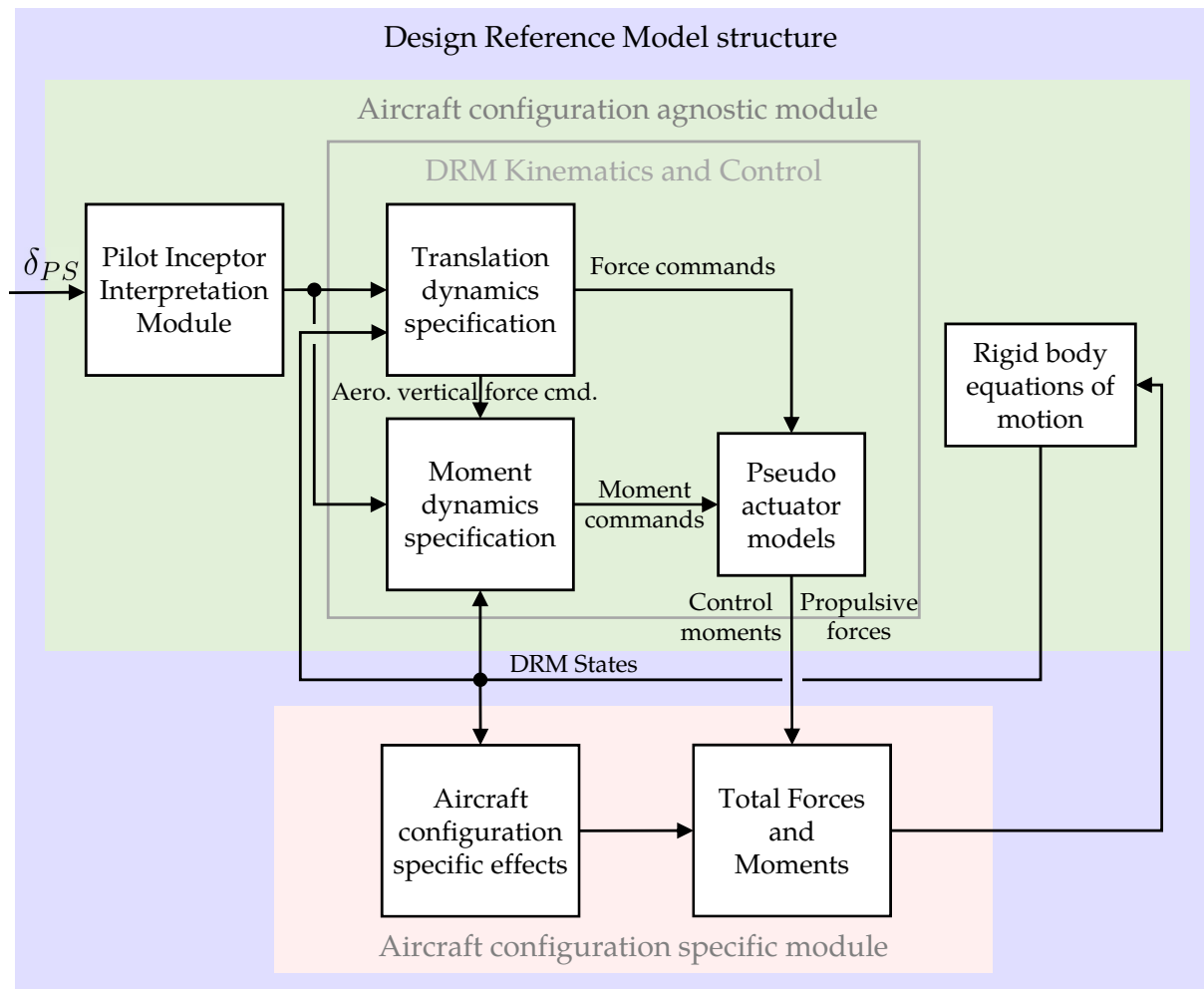


Figure 2.15: *Design Reference Model*

as a pitch down (negative pitch angle) command to accelerate forward and the negative (down) deflection zone is transformed to pitch up (positive pitch angle) command to achieve backward acceleration.

The side-ward deflections of the Thrust stick is mapped to a bank angle command in the low forward speed flight phase. The sign of the bank angle command corresponds to the side-wards deflection direction of the hybrid Thrust inceptor. As soon as the aircraft flies beyond the speed threshold that defines this low speed phase, the stick deflection mapping to the bank angle command magnitude is faded out. The speed range within which the low speed threshold can be defined is governed by the aircraft configuration. However, the magnitude of the low speed threshold itself is a design choice established through feedback from piloted simulator tests. Although, the high speed phases are not the focus of this discussion, but for the sake of completion it must be noted that the side-wise degree of freedom is restricted physically in this hybrid inceptor design, therefore the Thrust inceptor behaves exactly like a throttle lever in the wingborne phase.

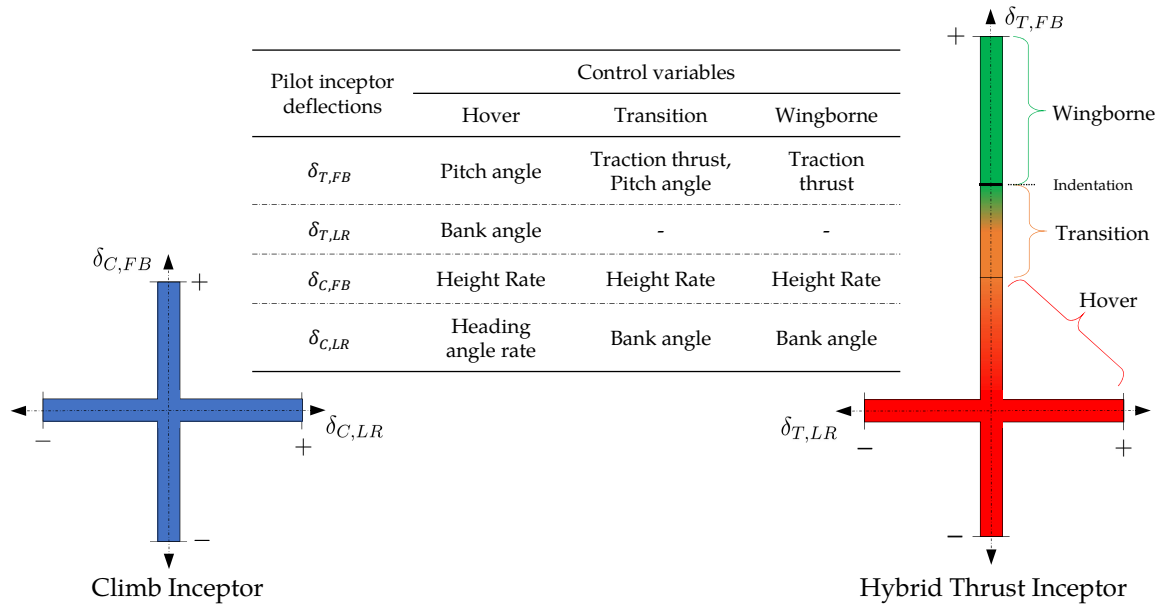


Figure 2.16: Pilot inceptor interpretation for full flight envelope of a VTOL transition aircraft

Conversely, the Climb stick is proposed to be a spring centered inceptor for all flight phases. The up-down deflection of the Climb stick is always mapped to a height rate command, which coincides with the vertical axis of the NED frame as well as the C -frame, such that a positive height rate corresponds to an increase in height perpendicular to the horizontal ground level. Furthermore, the vertical deflection of the Climb stick is mapped to the height rate command in a manner that it corresponds to the stick behavior of a conventional fixed-wing aircraft. Therefore, pulling the Climb stick (vertical negative deflection as in Fig. 2.16) always leads to an increase in the lift force. The resource used to increase the lift force could either be the propulsive lift by increasing the rotational speed of the LTUs in hover phase or the aerodynamic lift by increasing the aerodynamic angle of attack in wingborne phase. Nonetheless, the consequent effect that the pilot perceives when they pull the Climb stick is an upwards acceleration.

Subsequently, the pilot always achieves a rotation of the aircraft nose around the body vertical z_B -axis by deflecting the Climb inceptor laterally. Hence, the control variable in the low forward speed phase, defined through the low speed threshold discussed earlier, is a heading angle rate $\dot{\Psi}$. Beyond the low speed regime, the Climb stick's side-ward deflections are construed as bank angle commands bringing about the rotation of the aircraft nose through bank-to-turn maneuvers.

After the control variables commands are computed from the pilot inceptor deflections, the desired behavior of the interpreted control variable commands is specified through the DRM kinematics and control module.

2.5.2 DRM Kinematics and Control

As depicted in the Fig. 2.15, the DRM Kinematics and Control module comprises of translation dynamics, moment dynamics and pseudo actuator models for forces and moments. The DRM does not constitute a simulation of the true control inputs such as rotational speed of the thrust units or actuator deflections of the aerodynamic control surfaces, rather provides a flyable aircraft specification that considers directly the control forces and moments produced by the effectors. Given the fact that the DRM structure proposed here is used to acquire maneuverability phase planes for the hover flight phase, the description of the components is limited to that flight phase in this section.

The control variable commands to the translation dynamics include the traction system thrust command and the height rate command. As mentioned earlier, the DRM only emulates control forces and moments rather than true control inputs, therefore the traction system thrust command $(X_{cmd}^G)_B \in \mathbb{R}$ is directly applied to the traction thrust actuator

$$(X_P^G)_B = G_X(s) \cdot (X_{cmd}^G)_B, \quad (2.75)$$

where the actuator $G_X(s)$ is modeled as having first order dynamics with rate and absolute saturation. It is assumed that the force produced by the traction system acts directly at the center of gravity G of the aircraft. In a case where the commanded thrust $(X_{cmd}^G)_B$ does not lead to any saturation, the actuator can be represented as a first order element in the Laplace domain

$$G_X(s) = \frac{K_{X,act}}{s + K_{X,act}}. \quad (2.76)$$

However, the full representation of the traction force actuator with all saturations can be realized through the following set of equations

$$\begin{aligned} (\dot{U}_X^G)_B &= K_{X,act} \cdot [(X_{cmd}^G)_B - (X_P^G)_B], \\ (\dot{X}_P^G)_B &= (\dot{U}_X^G)_B, \quad (\dot{X}_{P,min}^G)_B \leq (\dot{U}_X^G)_B \leq (\dot{X}_{P,max}^G)_B, \\ (X_P^G)_B &= (U_X^G)_B, \quad (X_{P,min}^G)_B \leq (U_X^G)_B \leq (X_{P,max}^G)_B, \quad (U_X^G)_B(0) = 0. \end{aligned} \quad (2.77)$$

Additionally, the configuration-specific aerodynamic drag force is modeled as

$$(D_x)_B = \frac{1}{2} \cdot \rho \cdot [(u_A^G)_B^E]^2 \cdot C_{D_x} \cdot S_x, \quad (2.78)$$

where $\rho \in \mathbb{R}$ is the air density, $(u_A^G)_B^E \in \mathbb{R}$ denotes the aerodynamic velocity along the body x_B -axis, $C_{D_x} \in \mathbb{R}$ is the drag coefficient in the body-fixed frame and $S_x \in \mathbb{R}$ represents the cross-section area perpendicular to the forward body axis. By addition of the configuration-specific aerodynamic drag force from Eq. (2.78) to the control force by the traction system in Eq. (2.77) and consideration of the gravitational component, the total external forward force in the body frame is obtained

$$(X^G)_B = (X_P^G)_B + (D_x)_B - m \cdot g \cdot \sin \theta. \quad (2.79)$$

Since in the given configuration, no effector produces forces in the lateral body translation channel directly, the external force in this axis manifests majorly through the aerodynamic drag and the gravity

$$\left(Y^G\right)_B = \left(D_y\right)_B + m \cdot g \cdot \sin \phi \cdot \cos \theta. \quad (2.80)$$

Similar to the longitudinal drag force, the drag force in the lateral body-fixed direction is defined by using the aerodynamic velocity along the body y_B -axis $\left(v_A^G\right)_B^E \in \mathbb{R}$, lateral drag coefficient in the body-fixed frame $C_{D_y} \in \mathbb{R}$ and the cross-section area perpendicular to the lateral body axis $S_y \in \mathbb{R}$

$$\left(D_y\right)_B = \frac{1}{2} \cdot \rho \cdot \left[\left(v_A^G\right)_B^E\right]^2 \cdot C_{D_y} \cdot S_y \quad (2.81)$$

Ultimately, the vertical force dynamics of the DRM are presented. As previously stated, a height rate is commanded by the pilot, for which the desired vertical acceleration is determined

$$\left(\ddot{h}_K^G\right)_{C_{cmd}}^{EC} = K_{\dot{h}} \cdot \left[\left(\dot{h}_K^G\right)_{C_{cmd}}^E - \left(\dot{h}_K^G\right)_C^E\right], \quad (2.82)$$

where the parameter $K_{\dot{h}}$ represents the desired bandwidth of the height rate, which is selected based on the *Height response characteristics* requirement from Aeronautical Design Standard for Military Rotorcraft ADS-33E-PRF [84, p. 13]. Commanded height rate and the height rate response produced by the DRM are denoted by $\left(\dot{h}_K^G\right)_{C_{cmd}}^E$ and $\left(\dot{h}_K^G\right)_C^E$ respectively. Thereafter, the C -frame vertical specific force command is determined analogous to the relation in Eq. (2.72)

$$\left(f_z^G\right)_{C_{cmd}} = -\left(\ddot{h}_K^G\right)_{C_{cmd}}^{EC} + g. \quad (2.83)$$

Next, the required body frame vertical specific force is obtained using the inverse of the transformation in Eq. (2.64)

$$\left(f_z^G\right)_{B_{cmd}} = \frac{\left(f_z^G\right)_{C_{cmd}}}{\cos \Phi \cdot \cos \Theta} \quad (2.84)$$

As addressed in subsection 2.3.5, the physical source of the vertical specific force generation changes from powered lift to aerodynamic lift over increasing dynamic pressure for a transition aircraft. Hence, the vertical specific force command increment intended to be generated through powered lift $\Delta\left(f_{zP,cmd}^G\right)_B \in \mathbb{R}$ is specified

$$\Delta\left(f_{zP,cmd}^G\right)_B = \left(f_z^G\right)_{B_{cmd}} - \left(f_z^G\right)_B, \quad (2.85)$$

by employing feedback of the total vertical specific force in the body frame. Consequently, the required propulsive lift increment $\Delta\left(Z_{P,cmd}^G\right)_B$ is obtained after multiplication with the aircraft mass. Similar to the pseudo actuator for the traction system thrust described in Eq. (2.77), the actuator dynamics for the vertical thrust produced by the LTUs are

also modeled as first order dynamics containing absolute and rate saturations

$$\begin{aligned} (\dot{U}_Z^G)_B &= K_{Z,act} \cdot \Delta(Z_{P,cmd}^G)_B, \\ (\dot{Z}_P^G)_B &= (\dot{U}_Z^G)_B, \quad (\dot{Z}_{P,min}^G)_B \leq (\dot{U}_Z^G)_B \leq (\dot{Z}_{P,max}^G)_B, \\ (Z_P^G)_B &= (U_Z^G)_B, \quad (Z_{P,min}^G)_B \leq (U_Z^G)_B \leq (Z_{P,max}^G)_B, \quad (U_Z^G)_B(0) = 0. \end{aligned} \quad (2.86)$$

Thereupon, the total external vertical force is constituted by the summation of the propulsive, the aerodynamic lift, drag and the gravitational forces

$$(Z^G)_B = (Z_P^G)_B + (Z_A^G)_B + (D_z)_B + m \cdot g \cdot \cos \phi \cdot \cos \theta, \quad (2.87)$$

where the configuration dependent aerodynamic forces are modeled as

$$\begin{aligned} (Z_A^G)_B &= -\frac{1}{2} \cdot \rho \cdot \left[(u_A^G)_B^E \right]^2 \cdot S \cdot C_L \cdot \cos \alpha_A \\ (D_z)_B &= \frac{1}{2} \cdot \rho \cdot \left[(w_A^G)_B^E \right]^2 \cdot S_z \cdot (C_{D_z} + C_L \cdot \sin \alpha_A) \end{aligned} \quad (2.88)$$

Note that only the major aerodynamic effects are captured in the DRM since in-depth information about aircraft parameters is not available at the initial stage of the design process for which the design reference model is intended. Comprehensive knowledge about simulation modeling pertaining to different VTOL and transition aircraft is available in [150–152].

By utilizing the feedback of the total vertical specific force in Eq. (2.85), the information of the additional aerodynamic lift is implicitly accounted for in the computation of the incremental specific force to be generated by the powered lift. Consequently, as the aerodynamic lift increases during transition, the required incremental vertical specific force by the powered lift decreases. This phenomenon is illustrated by the Fig. 2.17 where transition from hover to wingborne flight is simulated. In the hover flight phase, the vertical specific force, specified as $(f_{z_p}^G)_B$, is produced completely by the lift thrust units. Since, no commands in the vertical axis were simulated, the powered lift produces a vertical specific force that counters the acceleration due to gravity. As the aircraft gains aerodynamic speed, the fraction of the lift produced by the aerodynamic surfaces starts increasing and the powered lift subsequently reduces on account of the propulsive vertical specific force command generated in Eq. (2.85). Once the aircraft accelerates beyond the stall speed, the aerodynamic lift can sustain the weight of the aircraft which corresponds to the production of an aerodynamic vertical specific force equivalent to the gravitational acceleration. Therefore, the command to the propulsive lift generators is terminated, and the vertical channel can then be controlled by regulating the aerodynamic lift through the aerodynamic angle of attack. Note that the simulation described in Fig. 2.17 was performed at a zero pitch angle to isolate the effect of aerodynamic lift on the vertical specific force during transition from the rotational kinematics. More details about the the procedures and additional considerations required to completely define the desired behavior of a VTOL transition aircraft while moving from low-speed phase to high-speed phases or vice-versa will be addressed with in the scope of the integrated reference model in chapter 3.

Employing the total external forces denoted in the body-fixed frame as provided by the Eqs. (2.79), (2.80) and (2.87), the translation equations of motion for the B -frame [27, 51, 144, 145, 153] supply the velocity calculation besides also accounting for the acceleration due to body angular rates

$$\left(\dot{\vec{V}}_K^G\right)_B^{EB} = \frac{\Sigma(\vec{F}^G)_B}{m} + \mathbf{M}_{BO} \cdot (\vec{g})_O - (\vec{\omega}_K^{OB})_B \times \left(\vec{V}_K^G\right)_B^E, \quad (2.89)$$

where $\left(\dot{\vec{V}}_K^G\right)_B^{EB} \in \mathbb{R}^3$ represents the acceleration at the center of gravity derived with respect to the body-fixed frame and denoted in the body-fixed frame, $\left(\vec{V}_K^G\right)_B^E \in \mathbb{R}^3$ depicts the velocity of the aircraft center of gravity indicated in the B -frame, $\mathbf{M}_{BO} \in \mathbb{R}^{3 \times 3}$ is the rotation matrix from the O -frame to the B -frame, specified in the Eq. (A.2), and $\Sigma(\vec{F}^G)_B \in \mathbb{R}^3$ signifies a vector comprising of the sum of external forces from Eqs. (2.79), (2.80) and (2.87) along the co-ordinate axes of the body-fixed frame.

Following the translation dynamics, the desired behavior specification of the rotational states for the hover flight phase is presented. Additionally, critical parameters requisite to the generation of the maneuverability phase planes for each rotational axis are highlighted. Firstly, Euler attitude rate commands are computed through the attitude control commands (interpreted from the pilot inceptor deflections) to the moment dynamics as illustrated in Fig. 2.15. Roll angle and pitch angle commands are com-

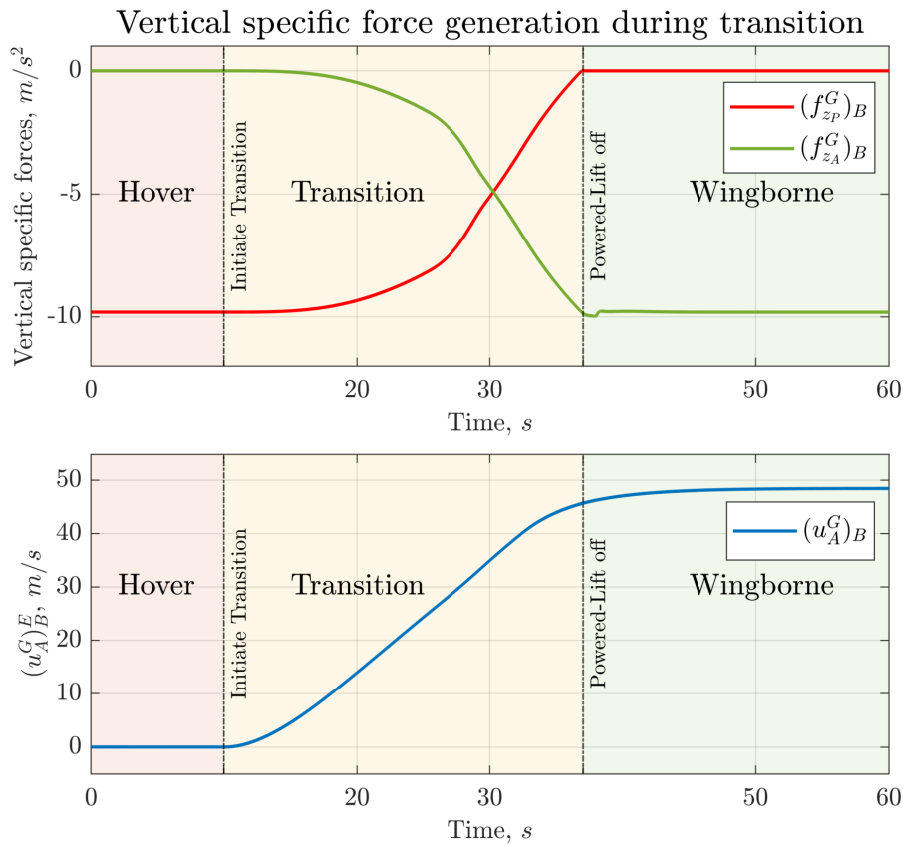


Figure 2.17: Transfer of vertical load factor generation from powered to aerodynamic lift during transition phase

puted based on the Thrust stick deflections commanded by the pilot while the heading angle rate $\dot{\Psi}_{cmd}$ command is mapped from the sideways deflection of the Climb inceptor. Subsequently, the bank and pitch angle rate commands $\dot{\Phi}_{cmd} \in \mathbb{R}$, $\dot{\Theta}_{cmd} \in \mathbb{R}$ are calculated

$$\begin{aligned}\dot{\Phi}_{cmd} &= K_{\Phi} \cdot (\Phi_{cmd} - \Phi), \\ \dot{\Theta}_{cmd} &= K_{\Theta} \cdot (\Theta_{cmd} - \Theta),\end{aligned}\quad (2.90)$$

where the bandwidths $K_{\Phi} \in \mathbb{R}$ and $K_{\Theta} \in \mathbb{R}$ for the bank angle and pitch angle response respectively, are chosen based on the pitch, roll attitude response bandwidth requirements specified in Aeronautical Design Standard for Military Rotorcraft ADS-33E-PRF [84, p. 15,18]. Thereupon, body rotational rate commands $(\vec{\omega}_K^{OB})_{B_{cmd,hvr}} \in \mathbb{R}^3$ are calculated by inverting the Euler strapdown equation introduced in Eq. (2.74)

$$\begin{aligned}(\vec{\omega}_K^{OB})_{B_{cmd,hvr}} &= \begin{bmatrix} p_{cmd} \\ q_{cmd} \\ r_{cmd} \end{bmatrix}_{hvr} = \begin{bmatrix} 1 & 0 & -\sin \Theta \\ 0 & \cos \Phi & \sin \Phi \cdot \cos \Theta \\ 0 & -\sin \Phi & \cos \Phi \cdot \cos \Theta \end{bmatrix} \cdot \begin{bmatrix} \dot{\Phi} \\ \dot{\Theta} \\ \dot{\Psi} \end{bmatrix}_{cmd},\end{aligned}\quad (2.91)$$

and the desired body rotational accelerations are obtained using a proportional error element for three rotational axes

$$(\vec{\omega}_K^{OB})_{B_{des}}^B = \mathbf{K}_{\omega} \cdot \left[(\vec{\omega}_K^{OB})_{B_{cmd,hvr}} - (\vec{\omega}_K^{OB})_B \right].\quad (2.92)$$

Remember that the Euler attitude angle bandwidths were chosen in accordance with the attitude response bandwidth requirements specified in Aeronautical Design Standard for Military Rotorcraft ADS-33E-PRF [84, p. 15,18]. Thereafter, the diagonal bandwidth matrix $\mathbf{K}_{\omega} \in \mathbb{R}^{3 \times 3}$ for the generation of the desired rotational accelerations is established through the principle of time-scale separation [154, 155].

As discussed previously, the maneuverability phase planes comprise of design points, which indicate required rotational accelerations and jerk for different handling quality levels. Accordingly, the maximum and minimum values of the desired rotational accelerations determined in Eq. (2.92) ought to be varied in order to assess the handling quality level in accordance with the moderate amplitude attitude change requirements stated in the Tables 2.4 and 2.5. Hence, the commanded rotational accelerations are obtained from the desired quantities in Eq. (2.92) based on the saturations

$$(\vec{\omega}_K^{OB})_{B_{cmd}}^B = \begin{cases} (\vec{\omega}_K^{OB})_{B_{des}}^B, & \text{if } (\vec{\omega}_K^{OB})_{B_{min}}^B \leq (\vec{\omega}_K^{OB})_{B_{des}}^B \leq (\vec{\omega}_K^{OB})_{B_{max}}^B \\ (\vec{\omega}_K^{OB})_{B_{min}}^B, & \text{if } (\vec{\omega}_K^{OB})_{B_{des}}^B < (\vec{\omega}_K^{OB})_{B_{min}}^B \\ (\vec{\omega}_K^{OB})_{B_{max}}^B, & \text{if } (\vec{\omega}_K^{OB})_{B_{des}}^B > (\vec{\omega}_K^{OB})_{B_{max}}^B \end{cases}\quad (2.93)$$

Since the structural design of the aircraft is not finalized at an early baseline design phase, the actuator dynamics are specified for the rotational accelerations rather than at the moment level to evade the use of moment of inertia, thereby sustaining a configuration-agnostic structure of the rotational dynamics in the DRM. Thereupon, the incremental

rotational accelerations are computed in accordance with

$$\Delta(\vec{\omega}_K^{OB})_{B_{cmd}}^B = (\vec{\omega}_K^{OB})_{B_{cmd}}^B - (\vec{\omega}_K^{OB})_B^B. \quad (2.94)$$

Equivalent to the definition of the actuator dynamics for the traction force and powered lift in Eqs. (2.77) and (2.86), the actuator dynamics for rotational accelerations intended to be generated by the LTUs are also modeled with first order dynamics [35, 60] having rate and absolute saturations

$$\begin{aligned} \dot{U} &= K_{\dot{\omega},act} \cdot \Delta(\vec{\omega}_K^{OB})_{B_{cmd}}^B, \\ (\vec{\omega}_{K_P}^{OB})_B^{BB} &= \dot{U}, \quad (\vec{\omega}_{K_P}^{OB})_{B_{min}}^{BB} \leq \dot{U} \leq (\vec{\omega}_{K_P}^{OB})_{B_{max}}^{BB}, \\ (\vec{\omega}_{K_P}^{OB})_B^B &= U, \quad (\vec{\omega}_K^{OB})_{B_{min}}^B \leq U \leq (\vec{\omega}_K^{OB})_{B_{max}}^B, \quad U(0) = 0. \end{aligned} \quad (2.95)$$

In addition to the bounds of the rotational accelerations employed in Eq. (2.93), limits on the rotational jerk $(\vec{\omega}_{K_P}^{OB})_{B_{min}}^{BB} \in \mathbb{R}^3$, $(\vec{\omega}_{K_P}^{OB})_{B_{max}}^{BB} \in \mathbb{R}^3$ are applied in the propulsive angular acceleration effector dynamics with the objective of assessing the handling qualities for different limits of rotational jerk produced by the propulsion units.

As the dynamic pressure increases, the effectiveness of the aerodynamic control surfaces also increases, which can be harnessed to produce moments. In the design reference model, the rotational acceleration increment demand from Eq. (2.94) is simultaneously commanded to the aerodynamic effectors together with the propulsion units. The reasoning behind this idea is that as the aircraft accelerates to higher dynamic pressures the control surfaces become more effective and can take over as the primary moment generators. Contrary to the propulsion units, the aerodynamic control surface effectors are commonly modeled as second order systems [51, 156]. Therefore, the actuation dynamics for rotational accelerations generated by the aerodynamic surfaces are also emulated as second order systems

$$\ddot{U} = K_{\ddot{\omega},D} \cdot \left[K_{\dot{\omega},P} \cdot \Delta(\vec{\omega}_K^{OB})_{B_{cmd}}^B - (\vec{\omega}_{K_A}^{OB})_{B_{act}}^B \right], \quad (2.96)$$

$$(\vec{\omega}_{K_A}^{OB})_B^B = U, \quad (\vec{\omega}_{K_A}^{OB})_B^{BB} = \dot{U}, \quad (\vec{\omega}_{K_A}^{OB})_B^{BBB} = \ddot{U}. \quad (2.97)$$

Even though the flight phases having substantial control effectiveness of the aerodynamic control surfaces are not covered within the scope of the derivation of the maneuverability phase planes, this aspect has been presented here for the purpose of completeness.

Furthermore, the sum of the propulsive and aerodynamic control angular accelerations in Eqs. (2.95) and (2.96) yields the total rotational accelerations produced by control effectors

$$(\vec{\omega}_{K_{ctrl}}^{OB})_B^B = (\vec{\omega}_{K_P}^{OB})_B^B + (\vec{\omega}_{K_A}^{OB})_B^B, \quad (2.98)$$

which by further integration lead to the angular rates $(\vec{\omega}_{K_{ctrl}}^{OB})_B \in \mathbb{R}^3$ resulting from the rotational accelerations produced by the control effectors.

Ultimately, the total control moments can be calculated using the inverse of the angular momentum dynamics from Eq. (2.73) given that a preliminary estimate of the aircraft moment of inertia \mathbf{I}_{BB}^G is available

$$\left(\overline{\mathbf{M}}_{ctrl}^G\right)_B = \mathbf{I}_{BB}^G \cdot \left(\dot{\vec{\omega}}_{Kctrl}^{OB}\right)_B + \left(\vec{\omega}_{Kctrl}^{OB}\right)_B \times \left[\mathbf{I}_{BB}^G \cdot \left(\vec{\omega}_{Kctrl}^{OB}\right)_B\right]. \quad (2.99)$$

In addition to the assumptions applied for the angular momentum dynamics in Eq. (2.73), the preceding equation also presumes **A.2.4** flat earth, **A.2.5** non-rotating earth and **A.2.6** reference point at the same position as the center of gravity to be true.

The rationale for keeping the control angular acceleration $\left(\dot{\vec{\omega}}_{Kctrl}^{OB}\right)_B \in \mathbb{R}^3$ generation decoupled from model-specific parameters like moment of inertia is to avoid implicit consideration of an aircraft configuration in the derivation of the maneuverability phase planes. If that was not the case, then the actuation dynamics could also be directly specified on the moment level in the DRM.

The total external moments comprise of the gravitational, aerodynamic and control moments. The gravitational moment is zero by virtue of the assumption **A.2.6**. The aerodynamic moments incorporate moments generated due to airflow and damping moments due to body rotational rates. Exhaustive description on the process of modeling of these aerodynamic moments is defined in the section 3.2.1, and also provided by [150–152]. Finally, the sum of total external moment is

$$\sum \left(\overline{\mathbf{M}}^G\right)_B = \left(\overline{\mathbf{M}}_{ctrl}^G\right)_B + \left(\overline{\mathbf{M}}_A^G\right)_B. \quad (2.100)$$

Since in the hover flight phase, the magnitude of these aerodynamic moments is negligible therefore they are insignificant in the composition of the maneuverability phase planes for this flight phase. Subsequently, the rotational dynamics are governed by the simplified rotational equations of motion

$$\left(\dot{\vec{\omega}}_K^{OB}\right)_B = \left(\mathbf{I}_{BB}^G\right)^{-1} \cdot \left[\sum \left(\overline{\mathbf{M}}^G\right)_B - \left(\vec{\omega}_K^{OB}\right)_B \times \left(\mathbf{I}_{BB}^G \cdot \left(\vec{\omega}_K^{OB}\right)_B\right)\right]. \quad (2.101)$$

The rotational rates propagated through the integration of the angular accelerations are fed back to compute the desired rotational accelerations as defined in Eq. (2.92). Likewise, the angular accelerations from Eq. (2.101) are employed to calculate the incremental rotational acceleration commands given by Eq. (2.94).

2.6 Maneuverability Phase Planes

The design reference model architecture demonstrated so far is now used to generate the maneuverability phase planes for the rotational motion in the hover flight phase. The saturations defined for computation of body angular acceleration commands in Eq. (2.93) along with the limits of control angular jerk for the first order actuator dynamics in Eq. (2.95) are harnessed for this purpose.

As indicated in the Tables 2.4 and 2.5, the moderate amplitude attitude quickness requirements are defined for a range of $[0^\circ, 60^\circ]$ in case of roll and yaw angle maneuvers, whereas $[0^\circ, 30^\circ]$ for pitch angle maneuvers. However, within the scope of this work, amplitude for all attitude angle maneuvers is limited to $[0^\circ, 30^\circ]$ subject to the reason that this range is sufficient for any civilian application appropriate to UAM. The generalized algorithm for determination of handling qualities level during any Euler attitude angle step maneuver, and further generation of required control maneuverability phase planes based on the detected handling quality level for each set of angular acceleration-jerk limitations is presented in a pseudocode.

Algorithm 1 Required Control Maneuverability phase plane generation

Let $z_0 = (\dot{\omega}_0, \ddot{\omega}_0)$ be the initial point on a phase plane for the assessment of the HQ level. The x -coordinate of any point on the phase plane describes the unsigned limit for the body angular acceleration and the y -coordinate denotes the body angular jerk.

▷ Declare variables pertaining to row identifiers of HQ-level datasets

Declare: $r_init_lvl[1, 2, 3]$, $r_end_lvl[1, 2, 3] = 0$

for $k_{\ddot{\omega}} = 1, 2, \dots, k_{\ddot{\omega}_{max}}$ **do**

Given a $\Delta\ddot{\omega}$, the limits for the angular jerk are assigned. The increment $\Delta\ddot{\omega}$ is chosen by programmer based on the resolution with which the boundary between different HQ-levels needs to be estimated.

$\ddot{\omega}_{max} = k_{\ddot{\omega}} \cdot \Delta\ddot{\omega}$ ▷ Maximum limit for Angular jerk

$\ddot{\omega}_{min} = -\ddot{\omega}_{max}$ ▷ Minimum limit for Angular jerk

for $k_{\dot{\omega}} = 1, 2, \dots, k_{\dot{\omega}_{max}}$ **do**

Given a $\Delta\dot{\omega}$, the limits for the angular acceleration are assigned.

$\dot{\omega}_{max} = k_{\dot{\omega}} \cdot \Delta\dot{\omega}$ ▷ Maximum limit for Angular acceleration

$\dot{\omega}_{min} = -\dot{\omega}_{max}$ ▷ Minimum limit for Angular acceleration

for $k_{sim} = 1, 2, \dots, 6$ **do**

Each simulation iteration defines the magnitude of a attitude angle step input command y_{cmd} . In this analysis, the step input command magnitudes are specified as $20^\circ, -20^\circ, 25^\circ, -25^\circ, 30^\circ, -30^\circ$.

$y_{cmd}, \dot{\omega}_{max}, \dot{\omega}_{min}, \ddot{\omega}_{max}$ and $\ddot{\omega}_{min}$ written to the simulation environment.

try

Simulate the DRM with the updated parameters

catch Out of Bounds Exception in the DRM state trajectories

Continue to the next simulation iteration.

end try

```

function REQUIREMENT ASSESSMENT
    Input: logData                ▷ Simulated time series data
    Output: hqlvl                 ▷ Array of HQ-level for all step commands
    Identify unstable or diverging cases—discarded as a failure case.
    Identify the first peak of the attitude angle state trajectory  $\Delta\theta_{pk}$ .
    Identify the first peak of the corresponding body angular rate  $\Delta\omega_{pk}$ .
     $R_{\omega \rightarrow \theta} = \frac{\Delta\omega_{pk}}{\Delta\theta_{pk}}$ 
    Identify the minima after the first peak of the attitude angle  $\Delta\theta_{min}$ .
    Estimate HQ-level based on the charts specified in Tables 2.4 and 2.5.
end function
    ▷ Define array containing assessed HQ-level for all step commands
    hqlvl [ksim] = HQ-level
end for
if all(hqlvl == 1) then
    function GENERATE MANEUVERABILITY-HQ DATASETS
        Input: hqlvl                ▷ HQ-level array
        Input: k $\ddot{\omega}$ , k $\dot{\omega}$           ▷ Current for-iterator states
        Input: k $\ddot{\omega}_{max}$ , k $\dot{\omega}_{max}$     ▷ Maximum for-iterator states
        Input:  $\Delta\ddot{\omega}$ ,  $\Delta\dot{\omega}$       ▷ Phase-plane resolution parameters
        Output: lvl_set             ▷ Dataset of the intended HQ-level
        ▷ Update initial row id of the HQ-level dataset
        r_init_lvl = r_end_lvl + 1
        ▷ Update final row id of the HQ-level dataset
        r_end_lvl = r_init_lvl + k $\dot{\omega}_{max}$  - k $\dot{\omega}$ 
        ▷ Add angular acceleration values to the HQ-level dataset
        lvl_set(r_init_lvl : r_end_lvl, 1) = [k $\dot{\omega}$  : k $\dot{\omega}_{max}$ ] ·  $\Delta\dot{\omega}$ 
        ▷ Add angular jerk values to the HQ-level dataset
        lvl_set(r_init_lvl : r_end_lvl, 2) = [k $\ddot{\omega}$  : k $\ddot{\omega}_{max}$ ] ·  $\Delta\ddot{\omega}$ 
    end function
    lvl1_mat = lvl_set
    break the for loop
else if all(hqlvl > 0) && any(hqlvl < 3) && any(hqlvl == 2) then
    call function GENERATE MANEUVERABILITY-HQ DATASETS
    lvl2_set = lvl_set
else if all(hqlvl > 0) && any(hqlvl == 3) then
    call function GENERATE MANEUVERABILITY-HQ DATASETS
    lvl3_set = lvl_set
end if
end for
end for

```

As reflected in Algorithm 1, the DRM is simulated with varying limits of the body angular acceleration $(\vec{\omega}_{K_P}^{OB})_B^B \in \mathbb{R}^3$ and jerk $(\vec{\omega}_{K_P}^{OB})_B^{BB} \in \mathbb{R}^3$ generated by the lift thrust units for each Euler angle attitude. In order to assess the handling quality level for one

set of angular acceleration-jerk limits, six simulations are performed with attitude angle step input commands of 20° , -20° , 25° , -25° , 30° , and -30° . For illustrative purposes, Fig. 2.18 depicts the pitch angle responses for the aforementioned step command magnitudes with varying limits of pitch acceleration and jerk. Only stable cases are plotted in the referred figure. The peak and minimum change in pitch angle are specifically marked for every simulated response since the requirement assessment function in Algorithm 1 is dependent on them.

Additionally, the peak change in the corresponding body rate response is also required for determining the handling quality level. Therefore, continuing the exemplification with the pitch channel, the peak change in the every pitch rate response Fig. 2.19 is also recorded. Finally, through the ratio between the peak rate change and the peak angle change along with the minima of the angle response are employed to evaluate the handling quality level for one step angle input command case.

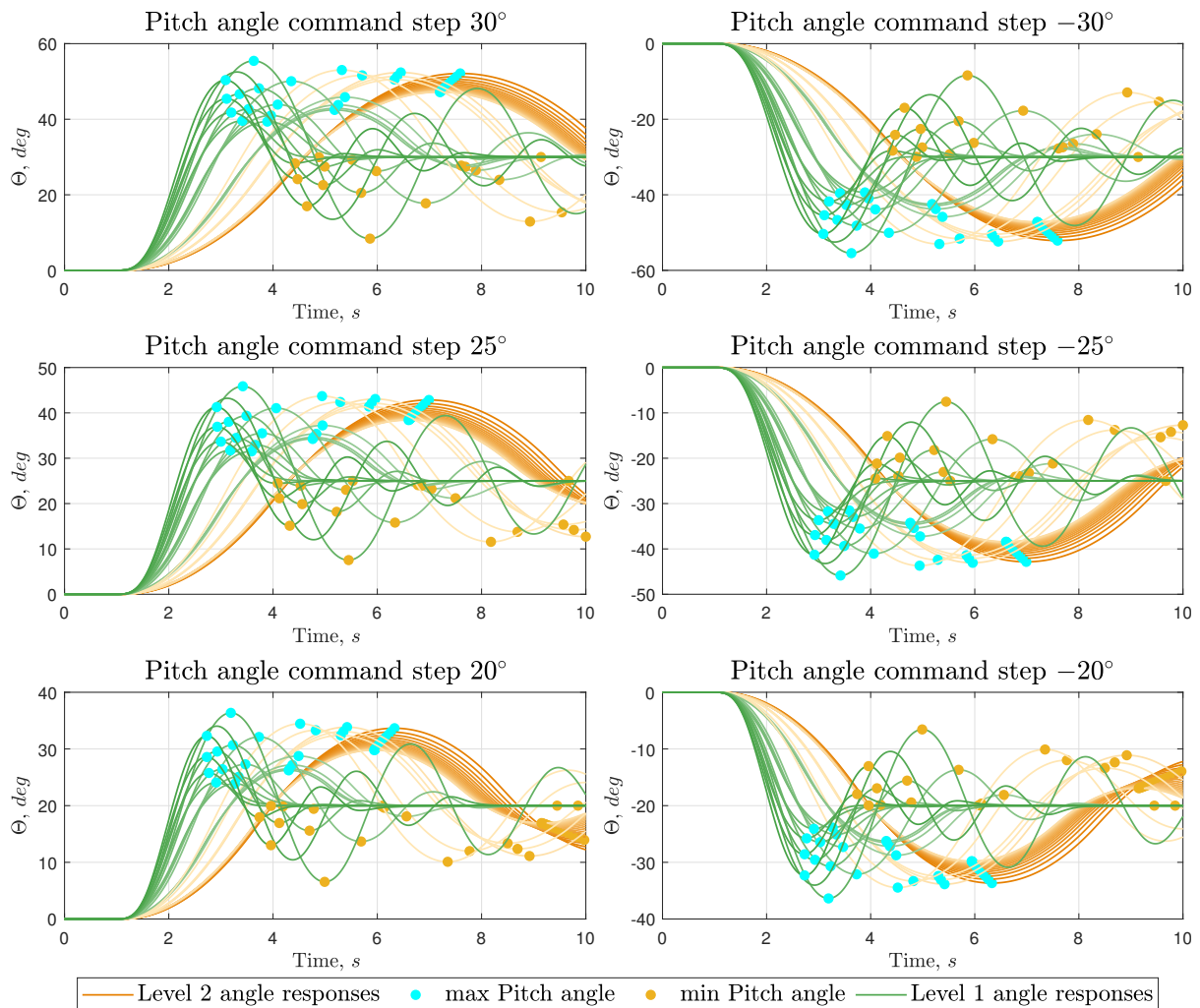


Figure 2.18: DRM pitch angle responses for step-input command maneuvers

However, the handling quality level for one set of the angular acceleration-jerk limit values is not directly determined through the response to one step input angle command. The lowest handling quality level among the six response cases is deemed as the HQ-level for that set of limits. Therefore, in order to have Level-1 HQ, all the command cases must pass the Level-1 criteria of any attitude quickness requirements.

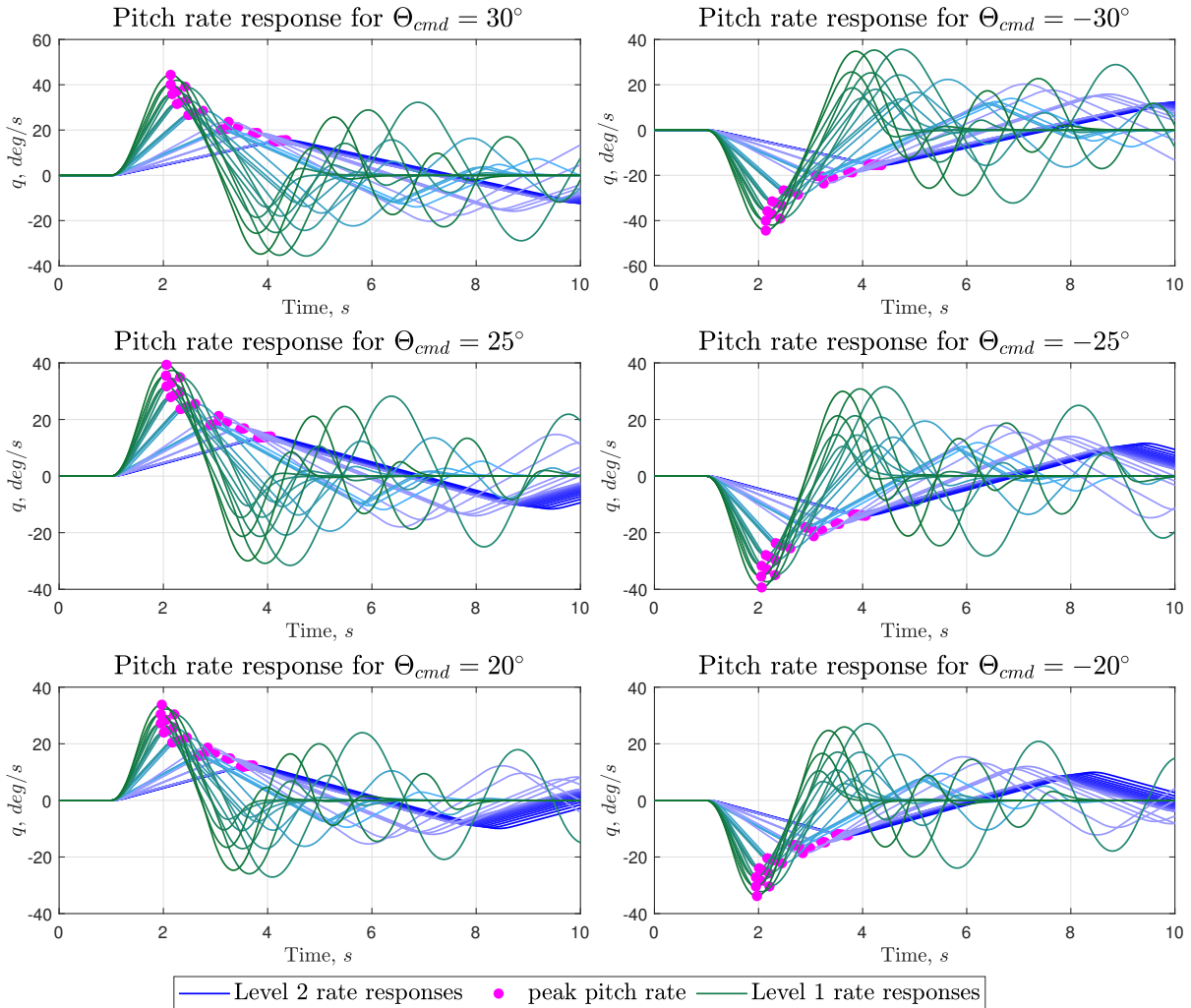


Figure 2.19: DRM pitch rate responses for pitch angle step-input command maneuvers

As it is intuitively clear, the results from the pitch channel simulations also demonstrate that with increase in the pitch acceleration and jerk limits (generated by propulsors), the pitch angle response improves from handling quality Level-2 to Level-1 in accordance with the pitch attitude quickness requirement noted in Table 2.4. Figure 2.18 demonstrates the noticeable decrease in the rise time as well as settling time of the pitch angle step response, which is entirely driven by the increase in the attainable body rotational acceleration and jerk by the LTUs. Other physical parameters as well as control bandwidths are kept constant in the closed loop DRM system.

The effect of changing angular acceleration limits is clearly distinguishable in the pitch rate responses displayed in Fig. 2.19. Pitch rate responses corresponding to Level 2 handling qualities have linear ramp up-down trajectories, which is the cause of high rise time witnessed in the pitch angle responses. With increasing magnitude of the rotational acceleration-jerk limits, the peak change in the body angular rate response also increases.

Consequently, the ratio of peak rate change to peak angle change increases, which primarily improves the HQ-level when assessed pursuant to the attitude quickness requirements.

Even though the Climb inceptor’s side-wards deflection is mapped to a heading angle rate command in the original behavior specification, a heading angle command is employed for the derivation of the maneuverability phase plane for the yaw channel instead because the attitude quickness requirement is defined in terms of heading angle rather than heading rate in the Aeronautical Design Standard for Military Rotorcraft ADS-33E-PRF [84]. The heading rate command is calculated from the heading angle command similar to the method utilized in Eq. (2.90) for the calculation of the bank and pitch angle rate commands.

Ultimately, the datasets extracted by the Algorithm 1 from the DRM simulations are utilized to obtain the required control maneuverability phase planes. These phase planes for the three rotational axes are exhibited in Figures 2.20, 2.21 and 2.22. Each phase plane comprises of the body rotational acceleration and jerk as its x and y axes respectively. Remember that the quantities depicted in these planes pertain to the propulsive component of the total producible rotational acceleration and jerk by the control effectors. Consequently, every phase plane maps the regions for each handling quality level, which can be achieved if the propulsion units of the given configuration can produce body angular acceleration and jerk corresponding to that region.

As stated earlier, any other parameters apart from the limits of the angular acceleration and jerk generated by the propulsion systems are not altered in the DRM for the derivation of the required control maneuverability phase planes. **Simply put, any data point on the generated phase planes indicates the handling quality levels that can be achieved, given that the considered LTU configuration can produce an angular**

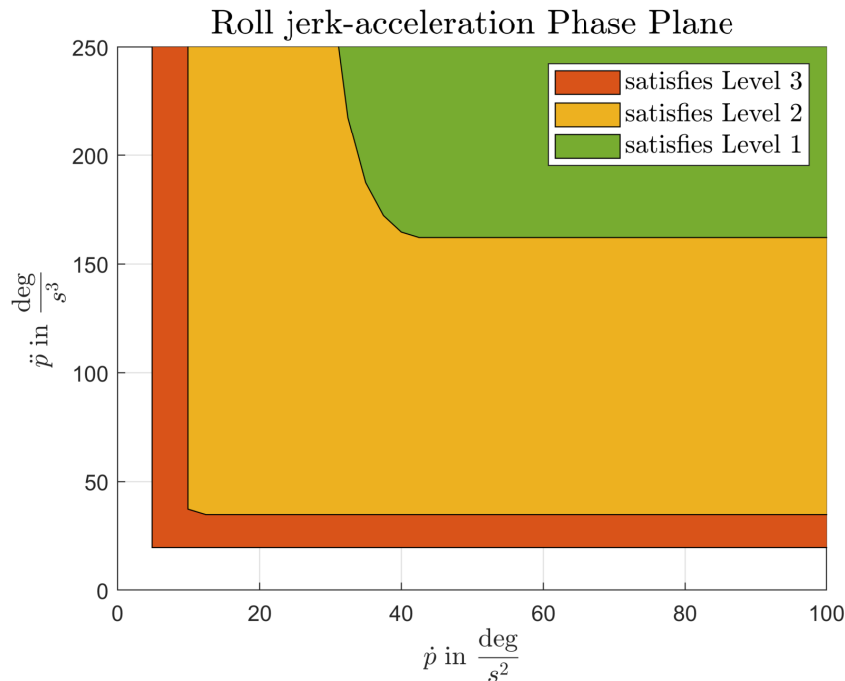


Figure 2.20: Required control maneuverability phase plane - roll axis

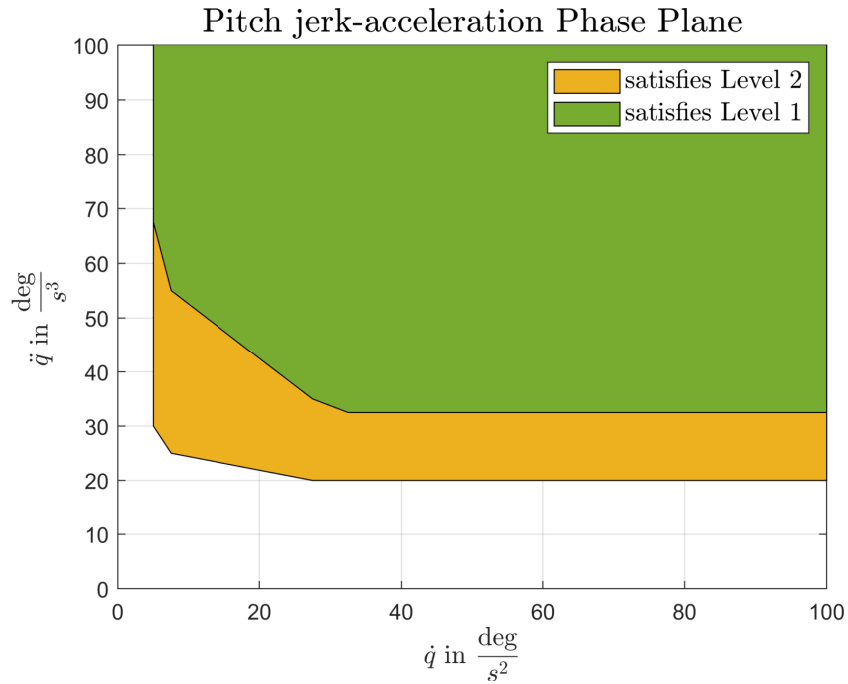


Figure 2.21: Required control maneuverability phase plane - pitch axis

acceleration and jerk equal to or greater than the magnitudes specified by that point. This statement has been emphasized to highlight that the data exhibited by the phase planes directly relates to the physical limits of the effectors, and gives no statement on the stability of the closed loop system. Since the stability of the closed loop design specification can also be affected by the magnitude of these limits, it is important to point out this distinction.

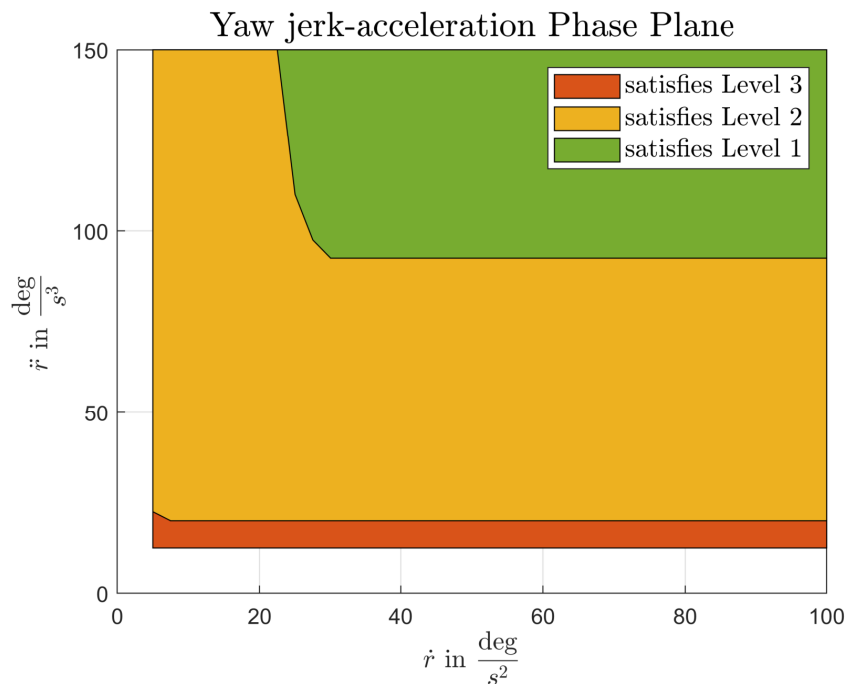


Figure 2.22: Required control maneuverability phase plane - yaw axis

As an instance, DRM simulations run using roll acceleration-jerk limits chosen from the design point [100, 175] in the right side of the green zone (Level 1) in Fig. 2.20 yield unstable bank angle responses. The bank angle and roll rate response for such a case are exhibited in Fig. 2.23. It does not imply that the chosen design point is invalid for sizing the propulsion units. **Stable attitude angle response can still be achieved by choosing appropriate attitude rate command (in Eq. (2.90)) saturations during the control design.** Accordingly, when artificial limits are applied on the bank angle rate command, which relates to the control design aspect of the closed loop behavior, stable roll channel responses are obtained as shown in Fig. 2.24 without changing any parameter in the configuration dependent part of the DRM. Likewise, this observation applies to the phase planes for pitch and yaw axes in Figures 2.21 and 2.22.

Besides the rotational acceleration and jerk limits obtained from any design point in the maneuverability phase planes, additional buffer in the design limits needs to be considered for external disturbance rejection and engine failure cases to achieve the desired handling quality levels. However, this aspect is not a part of the current analysis, and would lie in the scope of future works.

The Maneuverability Phase Planes derived in this section using the Design Reference Model framework from section 2.5 provide the realization of the contribution **C.1 Derivation of required maneuverability phase planes through Design Reference Model simulations for a VTOL transition aircraft.**

2.6 Maneuverability Phase Planes

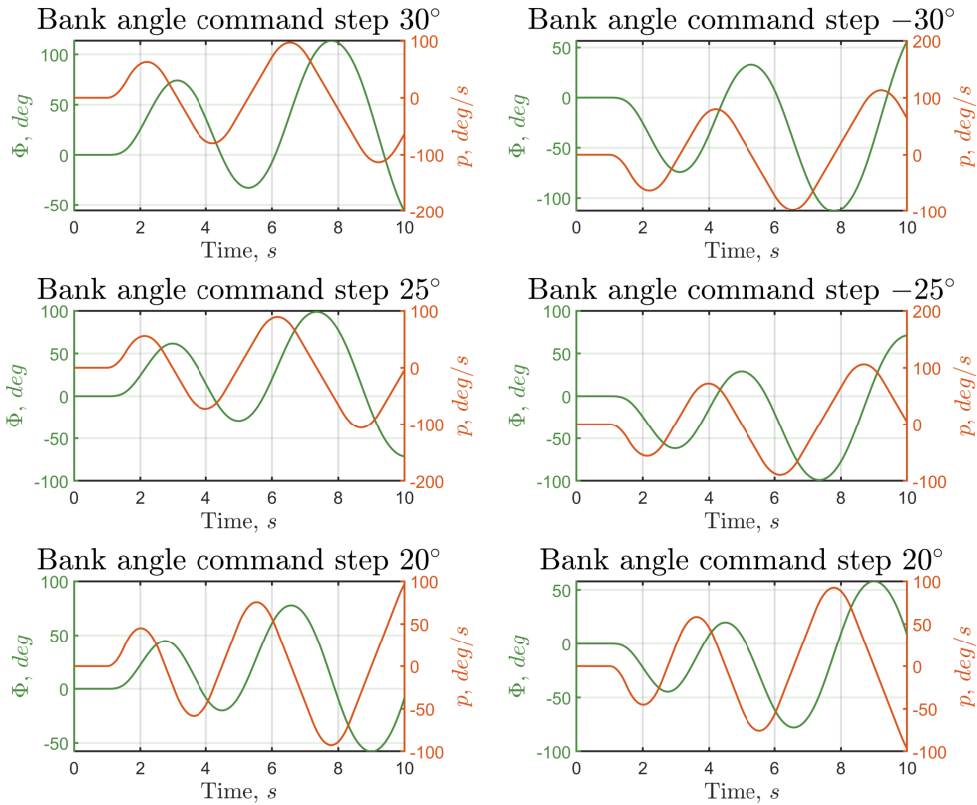


Figure 2.23: Unstable bank angle and roll rate response for the phase-plane design point [100, 175] from the HQ-Level 1 zone

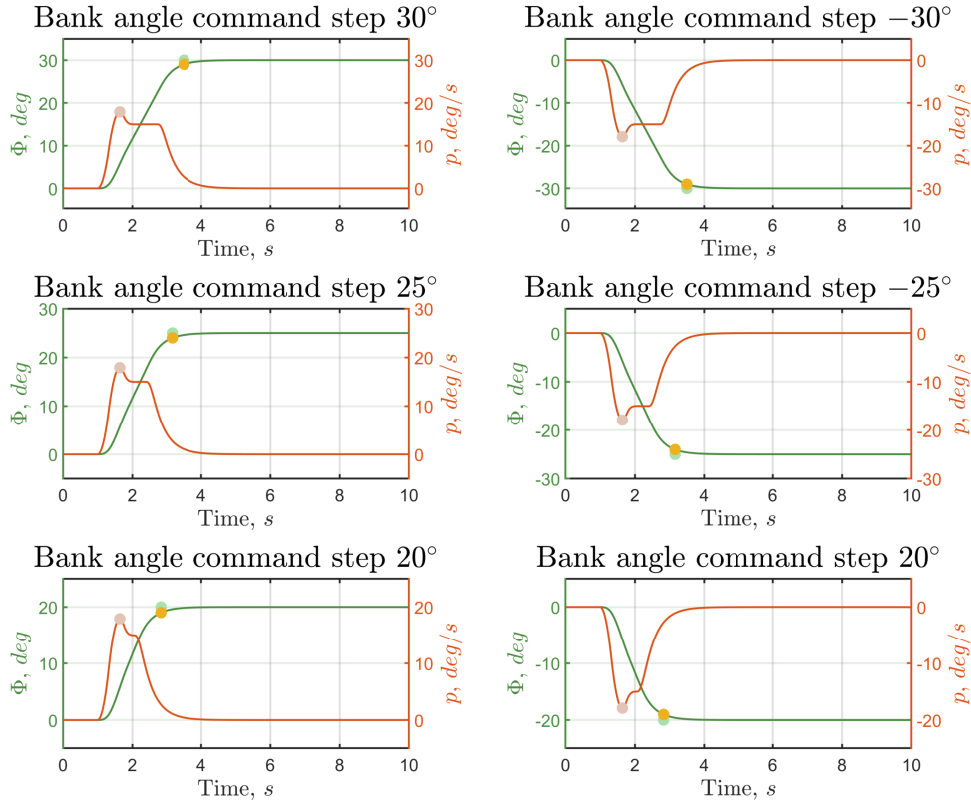


Figure 2.24: Stable bank angle and roll rate response using control design limits for the phase-plane design point [100, 175] from the HQ-Level 1 zone

2.7 Summary

This chapter describes the concepts related to the dynamics of vertical take-off and landing transition aircraft. Most importantly, the translation dynamics denoted in the control frame are derived, which facilitate an easier formulation of the control problem over all the flight phases of the VTOL transition aircraft. The C -frame translation dynamics are further employed to define unified control strategies for lateral and vertical motion control in the full flight envelope without requiring any flight phase specific switching procedures for aircraft motion control.

Furthermore, the framework of an aircraft configuration agnostic Design Reference Model (DRM) is proposed. The DRM provides a flyable specification of the intended aircraft, which can be employed to validate aircraft behavior from the perspective of handling qualities, inceptor interpretation, flight mission, and more. Pilot inceptor interpretation for an attitude and height rate command control strategy is presented. The thrust inceptor employs a hybrid design which assists in an intuitive pilot operation for all flight phases. Moreover, the motion control concept details are also described for the hover flight. Instead of including real effectors, the effector dynamics are incorporated at the control forces and moment level in the DRM.

Ultimately, the process of obtaining maneuverability phase planes from the DRM is elaborated. The derived phase planes define the required rotational acceleration and jerk that must be generated by the control effectors (LTUs for the hover flight phase) to achieve the handling quality levels according to the attitude quickness requirements from the Aeronautical Design Standard for Military Rotorcraft ADS-33E-PRF [84]. The phase planes are defined at the rotational acceleration and the jerk level in order to remain independent from any aircraft configuration specific parameters. The effects of external disturbances and failure cases are not included in the analysis performed here. Therefore, these aspects have to be considered separately in the future works. Additionally, future works shall include employment of the maneuverability phase planes in the preliminary sizing of the lift thrust units as well as their spatial configuration during the initial aircraft design process.

Chapter 3

Integrated Nonlinear Reference Model for Vertical Take-Off and Landing Transition Aircraft

This chapter introduces a *modular, configuration-agnostic integrated reference model architecture* for a vertical take-off and landing transition aircraft. One of the novel attributes incorporated in the proposed reference model structure is the continuous desired behavior specification capability for all the flight phases including the transition regimes. Thereupon, a unified control strategy can be formulated without the requisite of any switching procedures between flight phase specific control algorithms. The integrated reference model is embedded in an incremental nonlinear dynamic inversion (INDI) control framework. It is imperative for a unified strategy that same set of reference pseudo controls and external states are interfaced with the INDI controller for all flight phases. Concurrently, preserving an instinctively equivalent aircraft response to the pilot inceptor inputs is also crucial. With these constraints in consideration, selection of the control variables is performed. Furthermore, flight phase dependent compliance enforcement among the reference variables, and sequential desired rotation rate computation in a unified structure is addressed. Explicit consideration of the wind disturbance rejection behavior conforming to the current flight state is also encompassed within the integrated reference model.

The problem statements outlined in the motivation for this dissertation highlight the nonlinearities imposed by varying relative degree of the system along with the need for modifying pilot stick interpretation to maintain an intuitive aircraft behavior in every flight phase of transition aircraft configurations, which are predominant in the UAM ecosystem. The integrated reference model presents a potential solution to these challenges. The proposed reference model facilitates the operation of a unified, flight phase agnostic INDI controller in the full flight envelope of VTOL transition aircraft.

Therefore, preliminaries about the INDI control law for a generic nonlinear system are presented first. The concepts of the incremental control law bring about the particulars of the required RM interfaces with the controller.

Secondly, a feasible control variable choice, which aids in the constitution of a consistent response to pilot stick commands is presented. The chosen control variables also adhere to the realization of a fixed reference model interface with the INDI controller over the whole flight envelope. Consequently, an identical group of reference pseudo controls as well as external states are produced by the RM independent of the flight phases, despite the fact that the control variables mapped to the inceptor deflections vary according to the current flight phase. Subsequently, the control variables specific to each phase are transformed to a uniform set of command variables for the RM core module in all phases by a commands transformation module.

Thereafter, flight phase independent component of the integrated reference model called the reference model core module is presented. It comprises of the outer loop reference model, which specifies the reference translation dynamics in terms of load factors and velocities denoted in the control frame. Reference body angular acceleration, angular rate and Euler attitude trajectories are generated by the inner loop reference model. Desired rotation rate command specification for all flight phases of the VTOL transition vehicle is performed in the inner loop reference model. Moreover, explicit consideration about wind disturbance rejection behavior is also treated in the inner loop reference model.

Besides the basic structure of the integrated reference model, approaches to maintain conformity between different reference variables are also covered. These techniques involve blending of control variables and rotation rate commands along with flight phase dependent slaving of reference states. Plant state feedback is also involved to assist in accurate mapping of the control variables especially in flight conditions with high wind gradients.

Similar attempts to define control variables that unify the pilot stick interpretation over the complete flight envelope were also made in literature [157], however the inceptor design and the corresponding the control variable definitions are quite different from what is presented in this work. Initial results pertaining to the modular, integrated reference model architecture discussed here were first presented by the author in [82, 87].

3.1 Preliminaries

The preliminaries pertaining to the incremental nonlinear dynamic inversion control strategy are elucidated in this section. The incremental control law is derived while outlining the assumptions employed in the procedure. Moreover, concepts pertaining to generation and protection of the desired trajectories by a reference model are also covered.

3.1.1 Incremental Nonlinear Dynamic Inversion

For a generalized derivation of the INDI control technique, a generic nonlinear, time invariant, Multi-Input Multi-Output (MIMO) system with non-affine inputs is observed

$$\begin{aligned}\dot{\mathbf{x}}(t) &= \mathbf{f}(\mathbf{x}(t), \mathbf{u}(t)), \\ \mathbf{y}(t) &= \mathbf{h}(\mathbf{x}(t)),\end{aligned}\tag{3.1}$$

where $\mathbf{x}(t) = [x_1(t), x_2(t), \dots, x_{n_x}(t)]^T \in \mathbb{R}^{n_x}$ denotes the states of the system, $\mathbf{u}(t) = [u_1(t), u_2(t), \dots, u_{n_u}(t)]^T \in \mathbb{R}^{n_u}$ represents the control input vector, $\mathbf{y}(t) = [y_1(t), y_2(t), \dots, y_{n_y}(t)]^T \in \mathbb{R}^{n_y}$ presents the system outputs, $\mathbf{f}_{n_x \times 1} : D_{\mathbf{x}, \mathbf{u}} \rightarrow \mathbb{R}^{n_x}$ represents the plant dynamics and the function $\mathbf{h}_{n_y \times 1} : D_{\mathbf{x}} \rightarrow \mathbb{R}^{n_y}$ signifies the output dynamics of the given system. With an aim of improving the readability, the dependence of the states, control inputs and system outputs on time is not shown hereafter. The vector fields \mathbf{f} and \mathbf{h} comprise of state and control input dependent nonlinear functions

$$\begin{aligned}\mathbf{f}(\mathbf{x}, \mathbf{u}) &= [f_1(\mathbf{x}, \mathbf{u}), f_2(\mathbf{x}, \mathbf{u}), \dots, f_{n_x}(\mathbf{x}, \mathbf{u})]^T, \\ \mathbf{h}(\mathbf{x}) &= [h_1(\mathbf{x}), h_2(\mathbf{x}), \dots, h_{n_y}(\mathbf{x})]^T,\end{aligned}\tag{3.2}$$

The following assumptions specify additional attributes of the generic nonlinear system described in Eq. (3.1)

A.3.1 The nonlinear functions constituting the vector fields \mathbf{f} and \mathbf{h} of the generic nonlinear system are continuous and sufficiently smooth.

A.3.2 Accurate measurement or estimation of the state vector \mathbf{x} is available.

A.3.3 The system is minimum phase.

The ultimate target of any control strategy is to drive a given system's output to a desired set point. The specified set point is reached by manipulating the system states through the control inputs. Therefore, the relation between the system output and the control input needs to be ascertained. With this aim, each output channel is derived

$$\begin{aligned}y_i &= h_i(\mathbf{x}) && \triangleq L_f^0 h \\ \dot{y}_i &= \left(\frac{\partial h_i(\mathbf{x})}{\partial \mathbf{x}} \right)^T \cdot \dot{\mathbf{x}} && = \left(\frac{\partial h_i(\mathbf{x})}{\partial \mathbf{x}} \right)^T \cdot \mathbf{f}(\mathbf{x}, \mathbf{u}) \triangleq L_f h(\mathbf{x}, \mathbf{u}) \\ \ddot{y}_i &= \left(\frac{\partial L_f h(\mathbf{x}, \mathbf{u})}{\partial \mathbf{x}} \right)^T \cdot \dot{\mathbf{x}} && = \left(\frac{\partial L_f h}{\partial \mathbf{x}} \right)^T \cdot \mathbf{f}(\mathbf{x}, \mathbf{u}) \triangleq L_f^2 h(\mathbf{x}, \mathbf{u}) \\ &\vdots \\ y_i^{(k)} &= \left(\frac{\partial L_f^{k-1} h(\mathbf{x}, \mathbf{u})}{\partial \mathbf{x}} \right)^T \cdot \dot{\mathbf{x}} && = \left(\frac{\partial L_f^{k-1} h}{\partial \mathbf{x}} \right)^T \cdot \mathbf{f}(\mathbf{x}, \mathbf{u}) \triangleq L_f^k h(\mathbf{x}, \mathbf{u})\end{aligned}\tag{3.3}$$

until an order (k) for which the condition holds that

$$\frac{\partial}{\partial \mathbf{u}} [L_f^k h(\mathbf{x}, \mathbf{u})] \neq \mathbf{0}.\tag{3.4}$$

The minimum order of an output derivative [158, 159] for which the condition in Eq. (3.4) is valid yields the relative degree r_i of the corresponding output channel

$$r_i \triangleq \min \left\{ k : \frac{\partial}{\partial \mathbf{u}} [L_f^k h(\mathbf{x}, \mathbf{u})] \neq \mathbf{0} \right\}.\tag{3.5}$$

Accordingly, vector relative degree [160] for a MIMO system like the general nonlinear system presented in Eq. (3.1) can be defined.

Definition 3.1.1 (Vector Relative Degree). The nonlinear MIMO system (3.1) has a vector relative degree $[r_1, r_2, \dots, r_{n_y}]$ at a point $(\mathbf{x}_0, \mathbf{u}_0)$ iff

1. $\frac{\partial}{\partial \mathbf{u}} [L_{\mathbf{f}}^k h_i(\mathbf{x}, \mathbf{u})] = \mathbf{0} \quad \forall \quad k < r_i, \quad i = 1, 2, \dots, n_y$ and $(\mathbf{x}_0, \mathbf{u}_0)$ in a vicinity of $(\mathbf{x}_0, \mathbf{u}_0)$
2. $\frac{\partial}{\partial \mathbf{u}} [L_{\mathbf{f}}^{r_i} h_i(\mathbf{x}_0, \mathbf{u}_0)] \neq \mathbf{0} \quad \forall \quad i = 1, 2, \dots, n_y$

Considering the definition of relative degree, it can be deduced that the Lie derivatives of the scalar outputs with respect to the vector field \mathbf{f} , derived in the Eq. (3.3), do not depend on the control inputs \mathbf{u} until the order $r_i - 1$

$$L_{\mathbf{f}}^k h_i(\mathbf{x}, \mathbf{u}) = L_{\mathbf{f}}^k h_i(\mathbf{x}) \quad \forall \quad k < r_i, \quad i = 1, 2, \dots, n_y. \quad (3.6)$$

Further, a coordinate transformation of the nonlinear dynamic system is carried out to obtain linear input/output dynamics. Although, a linear input-output relation for an input non-affine system is not achievable, a coordinate transformation is conducted nonetheless to establish a transformed system, which is then utilized to derive the incremental control law. Diffeomorphism [40–42, 51, 160], a generalized concept of coordinate transformation is employed for this purpose.

Definition 3.1.2 (Diffeomorphism [40]). A function $\Phi : \mathbb{R}^n \rightarrow \mathbb{R}^n$, defined in a region Ω , is called a diffeomorphism if it is smooth, and if its inverse Φ^{-1} exists and is smooth.

The map Φ is a global diffeomorphism if the domain Ω spans the complete space \mathbb{R}^n . However, global diffeomorphism is unlikely to be encountered, therefore a local diffeomorphism is often pursued. A local diffeomorphism specifies coordinate transformation in the locality of a point $\mathbf{x} = \mathbf{x}_0 \in \Omega$. Local diffeomorphism for a nonlinear function $\Phi(\mathbf{x})$ is verifiable through the existence of a non-singular Jacobian matrix $\nabla \Phi$ at the point $\mathbf{x} = \mathbf{x}_0$.

Thereupon, coordinate transformation $\Phi(\mathbf{x})$ is defined for the MIMO system [161] declared in Eq. (3.1)

$$\begin{array}{c}
 \text{Output Channel 1} \\
 \boxed{
 \begin{array}{l}
 \Phi_1(\mathbf{x}) = \xi_1^1 = y_1 = L_f^0 h_1 \\
 \Phi_2(\mathbf{x}) = \xi_2^1 = \dot{y}_1 = L_f^1 h_1 \\
 \vdots \\
 \Phi_{r_1}(\mathbf{x}) = \xi_{r_1}^1 = y_1^{(r_1-1)} = L_f^{r_1-1} h_1
 \end{array}
 } \\
 \\
 \text{Output Channel 2} \\
 \boxed{
 \begin{array}{l}
 \Phi_{r_1+1}(\mathbf{x}) = \xi_2^1 = y_2 = L_f^0 h_2 \\
 \Phi_{r_1+2}(\mathbf{x}) = \xi_2^1 = \dot{y}_2 = L_f^1 h_2 \\
 \vdots \\
 \Phi_{r_1+r_2}(\mathbf{x}) = \xi_{r_2}^2 = y_2^{(r_2-1)} = L_f^{r_2-1} h_2
 \end{array}
 } \\
 \\
 \text{Output Channel } n_y \\
 \boxed{
 \begin{array}{l}
 \Phi_{r_1+r_2+\dots+r_{n_y-1}+1}(\mathbf{x}) = \xi_1^{n_y} = y_m = L_f^0 h_m \\
 \Phi_{r_1+r_2+\dots+r_{n_y-1}+2}(\mathbf{x}) = \xi_2^{n_y} = \dot{y}_m = L_f^1 h_m \\
 \vdots \\
 \Phi_r(\mathbf{x}) = \xi_{r_{n_y}}^{n_y} = y_m^{(r_{n_y}-1)} = L_f^{r_{n_y}-1} h_m
 \end{array}
 } \\
 \\
 \text{State transformation} \\
 \boxed{
 \begin{array}{l}
 z_1 = \Phi_1(\mathbf{x}) \\
 z_2 = \Phi_2(\mathbf{x}) \\
 \vdots \\
 z_r = \Phi_r(\mathbf{x})
 \end{array}
 } \tag{3.7}
 \end{array}$$

where r is the sum of the relative degrees of all outputs $r = r_1 + r_2 + \dots + r_{n_y}$. Remember that the nonlinear state transformation $z = \Phi(\mathbf{x})$ in Eq. (3.7) is valid only if it is at least a local diffeomorphism which means that the mapping has to be uniquely invertible in the region where the transformation is carried out. In order to guarantee local invertibility, the Jacobian matrix $\nabla\Phi(\mathbf{x})$ must be non-singular which implies that its rows have to be linearly independent. The structure of the Jacobian matrix for the derived mapping $z = \Phi(\mathbf{x})$ is presented in Eq. (C.2). Since the first r rows of every Jacobian contain Lie derivatives $L_f^k h_i$, it can be proven that these rows are linearly independent [160, p. 389]. If the given system has full relative degree i.e. the sum of the relative degrees of all outputs is equal to the number of states $r = n_x$, then the Jacobian $\nabla\Phi$ is quadratic and consequently a diffeomorphism. However, if the system does not have full relative degree $r < n_x$, then $n_x - r$ additional rows are required to sustain a diffeomorphism. Therefore additional $n_x - r$ functions $\boldsymbol{\eta} = [\eta_1(\mathbf{x}), \eta_2(\mathbf{x}), \dots, \eta_{n_x-r}(\mathbf{x})]^T$ are chosen such that the rows of $\nabla\Phi_i$, $(r+1) \leq i \leq n_x$ are linearly independent to each other as well as to the r -rows that have already been selected. The additional states are defined as

$$\begin{array}{l}
 \eta_1 = z_{r+1} = \Phi_{r+1}(\mathbf{x}) \\
 \eta_2 = z_{r+2} = \Phi_{r+2}(\mathbf{x}) \\
 \vdots \\
 \eta_{n_x-r} = z_{n_x} = \Phi_{n_x}(\mathbf{x}) .
 \end{array} \tag{3.8}$$

These states are often referred to as **internal states** [161, 162] since they are rendered unobservable by the feedback linearization.

Ultimately, the complete state transformation corresponds to

Full state transformation

$$\mathbf{z} = \Phi(\mathbf{x}) = \begin{bmatrix} z_{r_1} \\ z_{r_2} \\ \vdots \\ z_{r_{n_y}} \\ z_{r+1} \\ z_{r+2} \\ \vdots \\ z_{n_x} \end{bmatrix} = \begin{bmatrix} \xi^1 \\ \xi^2 \\ \vdots \\ \xi^{n_y} \\ \eta_1 \\ \eta_2 \\ \vdots \\ \eta_{n_x-r} \end{bmatrix} \left. \begin{array}{l} \xi \\ \eta \end{array} \right\} \quad (3.9)$$

Transformed states

$$\begin{aligned}
 z_{r_1} = \xi^1 &\implies \begin{bmatrix} z_1 \\ z_2 \\ \vdots \\ z_{r_1} \end{bmatrix} = \begin{bmatrix} \xi_1^1 \\ \xi_2^1 \\ \vdots \\ \xi_{r_1}^1 \end{bmatrix} & z_{r_2} = \xi^2 &\implies \begin{bmatrix} z_{r_1+1} \\ z_{r_1+2} \\ \vdots \\ z_{r_1+r_2} \end{bmatrix} = \begin{bmatrix} \xi_1^2 \\ \xi_2^2 \\ \vdots \\ \xi_{r_2}^2 \end{bmatrix} \dots \\
 z_{r_{n_y}} = \xi^{n_y} &\implies \begin{bmatrix} z_{r_1+r_2+\dots+r_{n_y-1}+1} \\ z_{r_1+r_2+\dots+r_{n_y-1}+2} \\ \vdots \\ z_{r_1+r_2+\dots+r_{n_y-1}+r_{n_y}} \end{bmatrix} = \begin{bmatrix} \xi_1^{n_y} \\ \xi_2^{n_y} \\ \vdots \\ \xi_{r_{n_y}}^{n_y} \end{bmatrix}
 \end{aligned}$$

The dynamics of the nonlinear input non-affine system, when expressed using the state transformation $\Phi(\mathbf{x})$ yield the **MIMO normal form** [160, 163, 164] which constitutes the following n_y blocks

$$\begin{array}{ccc}
 \dot{\xi}_1^1 = \xi_2^1 & \dot{\xi}_1^2 = \xi_2^2 & \dots \quad \dot{\xi}_1^{n_y} = \xi_2^{n_y} \\
 \dot{\xi}_2^1 = \xi_3^1 & \dot{\xi}_2^2 = \xi_3^2 & \dots \quad \dot{\xi}_2^{n_y} = \xi_3^{n_y} \\
 \vdots & \vdots & \dots \quad \vdots \\
 \dot{\xi}_{r_1}^1 = a_1(\boldsymbol{\xi}, \boldsymbol{\eta}, \mathbf{u}) & \dot{\xi}_{r_2}^1 = a_2(\boldsymbol{\xi}, \boldsymbol{\eta}, \mathbf{u}) & \dots \quad \dot{\xi}_{r_{n_y}}^1 = a_{n_y}(\boldsymbol{\xi}, \boldsymbol{\eta}, \mathbf{u})
 \end{array} \quad (3.10)$$

where

$$a_i(\boldsymbol{\xi}, \boldsymbol{\eta}, \mathbf{u}) = L_f^i h_i[\mathbf{x}, \mathbf{u}] = F_i(\mathbf{x}, \mathbf{u}) = \boldsymbol{\nu} \quad (3.11)$$

denote the **pseudo controls** $\boldsymbol{\nu} \in \mathbb{R}^{n_y}$ for each output channel i , where $1 \leq i \leq n_y$. As stated earlier, each output channel is derived in Eq. (3.3) till the order of its relative degree r_i , which corresponds to the quantity that can directly be influenced by the system's control inputs \mathbf{u} . The variables indicated in Eq. (3.11) are the r_i -th derivative

of each output and since they are at the dynamic level of the real control inputs, they are designated as pseudo controls. Desired set-point values of the lower order derivatives, which lie within the physical capabilities of the considered system can be tracked as long as the required demand in the corresponding pseudo control is fulfilled.

Along with the dynamics defined in Eq. (3.10), the normal form also comprises of the set of additional (internal) dynamics

$$\dot{\eta} = \mathbf{q}(\xi, \eta). \quad (3.12)$$

One can select the additional states η in a manner that their time derivatives do not depend on the control input \mathbf{u} [159]

$$\dot{\eta}_k = \left(\frac{\partial \Phi_{r+k}(\mathbf{x})}{\partial \mathbf{x}} \right)^T \cdot \dot{\mathbf{x}} = \left(\frac{\partial \Phi_{r+k}(\mathbf{x})}{\partial \mathbf{x}} \right)^T \cdot \mathbf{f}(\mathbf{x}, \mathbf{u}) \triangleq L_f \Phi_{r+k}(\mathbf{x}, \mathbf{u}),$$

$$L_f \Phi_{r+k}(\mathbf{x}, \mathbf{u}) = L_f \Phi_{r+k}(\mathbf{x}) \quad \forall 1 \leq k \leq n_x - r \text{ and all } \mathbf{x} \text{ in a vicinity of } \mathbf{x}_0 \quad (3.13)$$

if the control effectiveness distribution for the given nonlinear system is involutive in the neighborhood of \mathbf{x}_0 [165, 166]. In this case, the internal dynamics are independent of the control input \mathbf{u}

$$\dot{\eta} = \mathbf{q}(\xi, \eta) \quad (3.14)$$

and the resultant transformed system dynamics are referred to as **input-normalized Byrnes-Isidori normal form**. However, involutiveness of the control effectiveness distribution is not always fulfilled [159]. Ergo, stability and boundedness of the internal dynamics remains critical for the realization of feedback linearization. Such proofs are extensively covered in the literature [42]. Another well-known method to establish local stability of the internal dynamics is to prove that the **zero dynamics** with origin at $\eta = 0$ are asymptotically stable [160, 165, 166]. Detailed stability proofs related to internal dynamics of feedback linearized systems can also be found in the given references.

Ultimately, by gathering the terms corresponding to the r_i -th derivative of each output channel from the normal form in Eq. (3.10), the generic nonlinear system is reformulated into a new transformed system

$$\nu_i = F_i(\mathbf{x}, \mathbf{u}) = \dot{\xi}_{r_i}^i = \overset{(r_i)}{y_i} \quad \text{where} \quad i = 1, 2, \dots, n_y \quad (3.15)$$

$$\boldsymbol{\nu} = \mathbf{F}(\mathbf{x}, \mathbf{u})$$

that comprises of the reformulated system dynamics $\mathbf{F}_{n_y \times 1} : D_{\mathbf{x}, \mathbf{u}} \rightarrow \mathbb{R}^{n_y}$ and r_i integrators for each channel. The transformed system uses effector control inputs \mathbf{u} along with the full state feedback \mathbf{x} to generate the pseudo control trajectories $\boldsymbol{\nu}$. Figure 3.1 shows the reformulation of the general nonlinear system from Eq. (3.1) to the transformed system in Eq. (3.15). For ease of visualization, the system transformation is illustrated for a MIMO system having full relative degree, which implies that the sum of the relative degrees of all channels r is equal to the number of system states n_x , and hence there are no internal states.

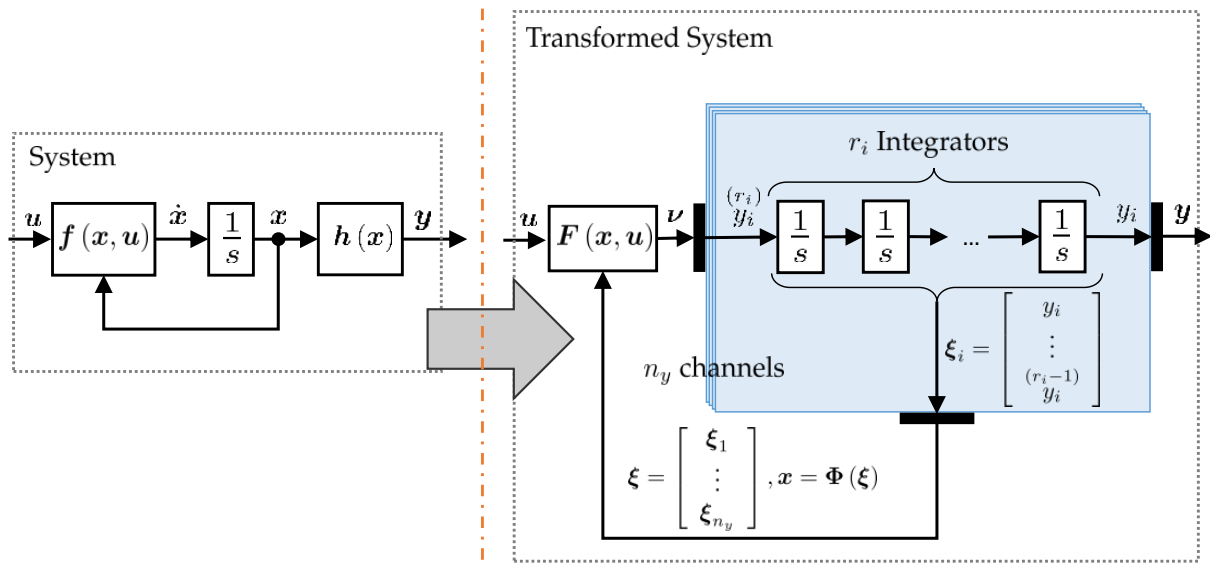


Figure 3.1: MIMO System Transformation [90]

Given the desired pseudo controls, the transformed system dynamics in Eq. (3.15) can be solved to compute the required control inputs \mathbf{u} . However, the function \mathbf{F} that describes the pseudo control dynamics is not necessarily affine in the control input \mathbf{u} , and hence not explicitly solvable for it. Even if the direct inversion of the function \mathbf{F} was possible, an assumed model $\hat{\mathbf{F}}$ of the transformed system would be required for inversion as in nonlinear dynamic inversion (NDI). However, as indicated through the extensive literature review in the state of the art section 1.2, model uncertainties can drastically reduce the robustness of the model based control strategy. Moreover, computation of control input commands from Eq. (3.15) directly is not feasible if the aforementioned system contains redundant control effectors.

To overcome these restrictions, the incremental nonlinear dynamic inversion INDI control strategy has been proposed and applied in many flight control applications [56, 57, 59, 60, 72, 82, 88]. Contrary to the inversion of an assumed system model as in NDI, deriving the incremental control law does not require inversion of the full plant dynamics. Instead, localized dynamics of the transformed system in Eq. (3.15) are inverted. These local dynamics are specified at the current state \mathbf{x}_0 and control input \mathbf{u}_0 and derived through Taylor series expansion [167] of the transformed dynamics with respect to the dependent variables i.e. system state vector \mathbf{x} and control effector inputs \mathbf{u} . The consequent locally linearized system dynamics from Taylor's expansion are employed to compute incremental control inputs $\Delta\mathbf{u}$. Ensuing formulation of the control law involves feedback of the state derivatives and effector positions. Therefore, requirement of model knowledge is replaced with the state derivative feedback in the incremental approach, thereby enhancing robustness against model mismatch [59].

The first step in the incremental control law derivation is the to obtain a first order approximation of the pseudo control dynamics from Eq. (3.15) at the current state \mathbf{x}_0 and control input \mathbf{u}_0 using the Taylor series expansion

$$\begin{aligned}\boldsymbol{\nu} &= \mathbf{F}(\mathbf{x}, \mathbf{u}), \\ \boldsymbol{\nu} &= \mathbf{F}(\mathbf{x}_0, \mathbf{u}_0) + \left. \frac{\partial \mathbf{F}}{\partial \mathbf{x}} \right|_{(\mathbf{x}_0, \mathbf{u}_0)} \cdot (\mathbf{x} - \mathbf{x}_0) + \left. \frac{\partial \mathbf{F}}{\partial \mathbf{u}} \right|_{(\mathbf{x}_0, \mathbf{u}_0)} \cdot (\mathbf{u} - \mathbf{u}_0) + \dots h.o.t\end{aligned}\quad (3.16)$$

while the higher order terms are neglected yielding a linear approximation of the transformed system dynamics

$$\boldsymbol{\nu} = \overset{\boldsymbol{\nu}_0}{\mathbf{F}(\mathbf{x}_0, \mathbf{u}_0)} + \overset{\mathbf{A}_\nu(\mathbf{x}_0, \mathbf{u}_0)}{\left. \frac{\partial \mathbf{F}}{\partial \mathbf{x}} \right|_{(\mathbf{x}_0, \mathbf{u}_0)}} \cdot \Delta \mathbf{x} + \overset{\mathbf{B}_\nu(\mathbf{x}_0, \mathbf{u}_0)}{\left. \frac{\partial \mathbf{F}}{\partial \mathbf{u}} \right|_{(\mathbf{x}_0, \mathbf{u}_0)}} \cdot \Delta \mathbf{u}.\quad (3.17)$$

The value of the pseudo control variables at the current time step $\mathbf{F}(\mathbf{x}_0, \mathbf{u}_0)$ is denoted by $\boldsymbol{\nu}_0 \in \mathbb{R}^{n_y}$. Moreover, the Jacobian matrix of the pseudo control dynamics function \mathbf{F} with respect to the state vector \mathbf{x} yields the local system matrix $\mathbf{A}_\nu(\mathbf{x}_0, \mathbf{u}_0) \in \mathbb{R}^{n_y \times n_x}$. Likewise, the gradient of the transformed system dynamics with reference to the control input \mathbf{u} provides the local control effectiveness matrix $\mathbf{B}_\nu(\mathbf{x}_0, \mathbf{u}_0) \in \mathbb{R}^{n_y \times n_u}$. The dependency of the system state matrix and input effectiveness matrix on the current state and control input vector $(\mathbf{x}_0, \mathbf{u}_0)$ is omitted further for better readability. Furthermore, moving the current pseudo control $\boldsymbol{\nu}_0$ to the left hand side of the Eq. (3.17) leads to the incremental formulation of the transformed system dynamics

$$\Delta \boldsymbol{\nu} = \mathbf{A}_\nu \cdot \Delta \mathbf{x} + \mathbf{B}_\nu \cdot \Delta \mathbf{u},\quad (3.18)$$

where the incremental pseudo control is $\Delta \boldsymbol{\nu} = \boldsymbol{\nu} - \boldsymbol{\nu}_0$. For further continuation of the incremental control law derivation, the following assumptions are taken

A.3.4 The sampling time of the controller is very small (of the order 10^{-2} s).

A.3.5 The control effector actuators of the system are instantaneously fast.

Owing to these assumptions, the effect of the state perturbation denoted by the term $\mathbf{A}_\nu \cdot \Delta \mathbf{x}$ in the incremental dynamics specified by Eq. (3.18) is neglected. Reason being, the instantaneously fast actuators directly impact the pseudo controls (order of the relative degree) as compared to the system states which lie further down the integrator chain. Inherently, the effect of a control input increment $\Delta \mathbf{u}$ on the state variation is insignificant in comparison to the change in the pseudo controls within the small controller computation time step. Consideration of this simplification leads to the simplified incremental dynamics

$$\Delta \boldsymbol{\nu} = \mathbf{B}_\nu \cdot \Delta \mathbf{u}.\quad (3.19)$$

It must be noted that the neglected state dependent part of the transformed dynamics is only omitted for the INDI control law derivation. In case of stability and robustness analysis for the closed-loop system of the control law with the plant, this component is

considered. Rather than performing an incremental inversion, the classical inversion of the transformed system in Eq. (3.15) can also be performed at one derivative level higher than the pseudo controls. More details about this continuous extension of the INDI strategy is covered in the next chapter.

For a given desired pseudo control trajectory $\boldsymbol{\nu}_{des} \in \mathbb{R}^{n_y}$ the incremental control law emanates by inversion of the approximated incremental dynamics in Eq. (3.19)

$$\Delta \mathbf{u}_{cmd} = \mathbf{B}_\nu^{-1} \cdot (\boldsymbol{\nu}_{des} - \hat{\boldsymbol{\nu}}). \quad (3.20)$$

The computation of the incremental control input command $\Delta \mathbf{u}_{cmd} \in \mathbb{R}^{n_u}$ in Eq. (3.20) also employs the feedback of the measured or estimated pseudo control $\hat{\boldsymbol{\nu}} \in \mathbb{R}^{n_y}$. Information about the neglected state perturbation effects is implicitly incorporated in the incremental control strategy through the pseudo control feedback [167]. Sensitivity to uncertainties in the aircraft weight and balance parameters such as the moment of inertia and the position of the center of gravity is also reduced [59]. The steady state effects produced by the deviations in these parameters are also accommodated by inclusion of the measured pseudo control in the control law computation.

The term $\mathbf{B}_\nu^{-1} \in \mathbb{R}^{n_y \times n_u}$ represents the generalized inverse of the local control input effectiveness at the point $(\mathbf{x}_0, \mathbf{u}_0)$. A large number of aircraft configurations designed to operate in the UAM domain comprise of redundant control effectors, which implies that the control input effectiveness matrix contains more columns than rows. Consequently, determination of a viable control input increment in accordance with the control law of Eq. (3.20) emerges as an algebraic problem with higher number of dependent variables (control inputs in this case) than the equations i.e. an infinite number of solutions can be found. In order to deal with such cases, a considerable number of Moore-Penrose pseudo inverse based control allocation strategies [168–170] have been proposed in the literature.

In the incremental control law of Eq. (3.20), the intended response of the system to either a pilot input or an external disturbance is specified through the desired pseudo control $\boldsymbol{\nu}_{des}$. This is equivalent to the desired pseudo control definition in a NDI control architecture. The desired pseudo control is constituted by two components – the feedforward and the error pseudo control. The feedforward component is generated based on the control variable commands. The purpose of the feedforward is to induce a direct command to the control effectors based on the pilot input, thereby initiating an aircraft response in the direction intended by the pilot without any substantial delay. Conversely, the error constituent of the desired pseudo control is computed based on the deviation of the real plant states from the corresponding reference state trajectories. The module that computes the error pseudo control is referred to as a stabilizing error controller in literature [51, 68, 76, 82, 88, 90, 171]. The function of the stabilizing error controller is to pull the plant back to the reference behavior.

The feedforward pseudo control along with the reference state trajectories are specified by a reference model. Explicit reference models have been utilized in several model-following flight control applications [51, 78, 79, 171] to establish the reference behavior of an aircraft. The upcoming section elaborates the basic concepts pertaining to the reference models.

3.1.2 Reference Model

Within the framework of flight control, the function of a reference model is to create smooth desired state trajectories, which conform to the physical limitations of the real aircraft. The simplest form of reference models are the linear reference models, which are also referred to as command filters [45, 74, 75]. As the name implies, the linear RMs filter the pilot commands, thereby generating the desired trajectories intended to be followed. The goal of a model following control approach is to enforce the tracking of the reference trajectory specified by the reference model

$$\begin{bmatrix} \mathbf{y}(t) \\ \mathbf{y}_1(t) \\ \mathbf{y}_2(t) \\ \vdots \\ \mathbf{y}_{n_y}(t) \end{bmatrix} \stackrel{!}{=} \begin{bmatrix} \mathbf{y}_R(t) \\ \mathbf{y}_{1,R}(t) \\ \mathbf{y}_{2,R}(t) \\ \vdots \\ \mathbf{y}_{n_y,R}(t) \end{bmatrix} \quad (3.21)$$

However, for systems such as the generic nonlinear system given in Eq. (3.1), only the r_i -th derivative of each output channel y_i i.e. the pseudo control ν_i can be affected by the control input. This statement is intuitively validated by the structure of the transformed system dynamics in Eq. (3.15), which express the pseudo control dynamics for each output channel. In essence, the pseudo controls ν can be manipulated through the control inputs to bring about a change in the lower order derivatives of that channel.

Alternatively, if a pseudo control demand that enables the system to follow a reference external state trajectory is known, then the desired effect can be generated in the real system by mapping this pseudo control demand to a control input command \mathbf{u}_{cmd} . From this perspective, the reference trajectory of any output channel delivered by the RM must be continuous and smooth enough such that derivatives until the order of the channel's relative degree r_i exist. The reference model is said to be perfectly tracked when

$$\begin{bmatrix} \xi^i \\ y_i(t) \\ \dot{y}_i(t) \\ \vdots \\ y_i^{(r_i)}(t) \end{bmatrix} \stackrel{!}{=} \begin{bmatrix} \xi_R^i \\ y_{i,R}(t) \\ \dot{y}_{i,R}(t) \\ \vdots \\ y_{i,R}^{(r_i)}(t) \end{bmatrix} \quad \forall \quad i = 1, 2, \dots, n_y \quad (3.22)$$

the derivatives of each plant output till their relative degrees r_i are equal to the corresponding reference signals. Figure 3.2 exhibits the structure of a linear reference model for the i -th output of a system having n_y output channels with relative degrees $[r_1, r_2, \dots, r_{n_y}]$. The exhibited framework is employed to determine the reference pseudo

controls $\nu_R \in \mathbb{R}^{n_y}$

$$\nu_R = \begin{bmatrix} \nu_{1,R} \\ \nu_{2,R} \\ \vdots \\ \nu_{n_y,R} \end{bmatrix} = \begin{bmatrix} y_{1,R}^{(r_1)} \\ y_{2,R}^{(r_2)} \\ \vdots \\ y_{n_y,R}^{(r_{n_y})} \end{bmatrix} \quad (3.23)$$

and reference external state trajectories for all outputs $\xi_R \in \mathbb{R}^r$

$$\xi_R = \begin{bmatrix} \xi_R^1 \\ \xi_R^2 \\ \vdots \\ \xi_R^{n_y} \end{bmatrix}, \text{ where } \xi_R^i = \begin{bmatrix} y_{i,R} \\ \dot{y}_{i,R} \\ \vdots \\ y_{i,R}^{(r_i-1)} \end{bmatrix} \text{ and } i = 1, 2, \dots, n_y. \quad (3.24)$$

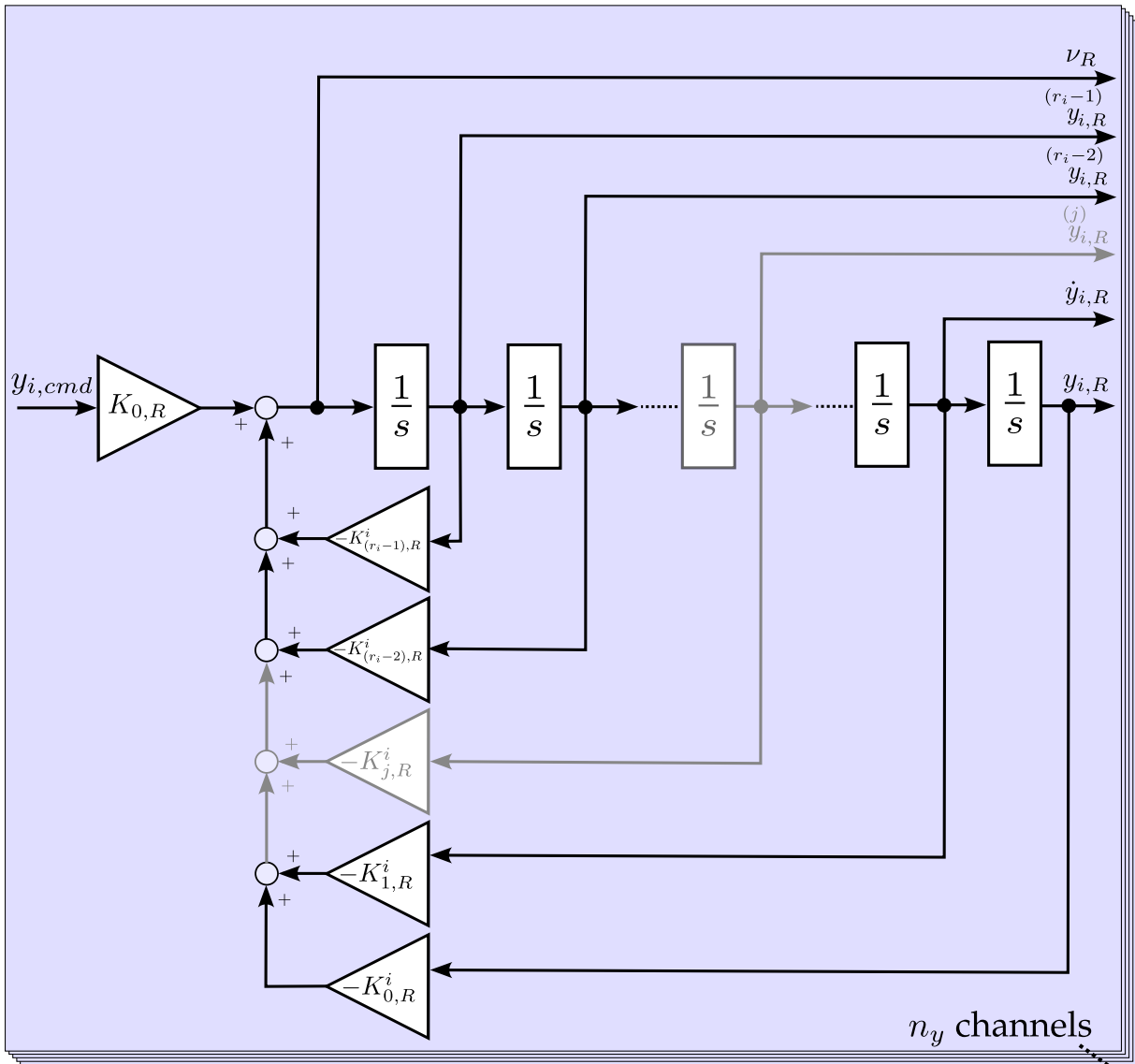


Figure 3.2: Generalized Linear Reference Model structure for a MIMO system

The coefficients $\mathbf{K}_R \in \mathbb{R}^{n_y \times r}$ are chosen in a manner such that the generated reference trajectories stay within the physical capabilities to the aircraft

$$\mathbf{K}_R = \begin{bmatrix} \mathbf{K}_R^1 & 0 & \dots & 0 \\ 0 & \mathbf{K}_R^2 & \dots & 0 \\ \vdots & & \ddots & 0 \\ 0 & 0 & 0 & \mathbf{K}_R^{n_y} \end{bmatrix}, \text{ where } \mathbf{K}_R^i = \begin{bmatrix} K_{0,R}^i & K_{1,R}^i & \dots & K_{r_i-1,R}^i \end{bmatrix}. \quad (3.25)$$

Additionally, desired aircraft response to the commanded control variables can also be specified by varying these coefficients. Subsequently, the given linear reference model structure yields the following resultant MIMO reference dynamics

$$\begin{bmatrix} {}^{(r_1)} y_{1,R} \\ {}^{(r_2)} y_{2,R} \\ \vdots \\ {}^{(r_{n_y})} y_{n_y,R} \end{bmatrix} = \underbrace{\begin{bmatrix} K_{0,R}^1 & 0 & \dots & 0 \\ 0 & K_{0,R}^2 & \dots & 0 \\ \vdots & & \ddots & 0 \\ 0 & 0 & 0 & K_{0,R}^{n_y} \end{bmatrix}}_{\mathbf{K}_{0,R}} \cdot \underbrace{\begin{bmatrix} y_{1,c} \\ y_{2,c} \\ \vdots \\ y_{n_y,c} \end{bmatrix}}_{\mathbf{y}_{cmd}} - \underbrace{\begin{bmatrix} \mathbf{K}_R^1 & 0 & \dots & 0 \\ 0 & \mathbf{K}_R^2 & \dots & 0 \\ \vdots & & \ddots & 0 \\ 0 & 0 & 0 & \mathbf{K}_R^{n_y} \end{bmatrix}}_{\mathbf{K}_R} \cdot \underbrace{\begin{bmatrix} \xi_R^1 \\ \xi_R^2 \\ \vdots \\ \xi_R^{n_y} \end{bmatrix}}_{\xi_R}. \quad (3.26)$$

The command scaling factor matrix $\mathbf{K}_{0,R} \in \mathbb{R}^{n_y \times n_y}$ and the reference state feedback gains denoted by $\mathbf{K}_R \in \mathbb{R}^{n_y \times r}$ specify amplitude independent desired response behavior to the control variable commands. However, attainable maximum magnitudes of the control variables are restricted in a real aircraft depending on the control effector limitations (absolute and rate saturations of the actuators) and inherent aircraft dynamics. In order to specify physically attainable reference dynamics, it is vital to incorporate these limitations in the reference model. Consideration of the physical aircraft limits is implemented in the RM using envelope protections.

3.1.2.1 Envelope Protection

An advantageous feature of the reference models is the ability to incorporate flight envelope protections in the definition of the reference aircraft behavior. Through the envelope protections, any pilot commands and the resultant reference states are confined within the aircraft operational limits to avoid flight envelope violations. Absolute command value limitation [172, 173], dynamic output limiting [153] and rate limitations [174, 175] have been widely employed in flight control design to facilitate envelope protection. Limitations, based on these mechanisms, are applied to the reference signals in order to restrict them within the flight envelope boundaries. However, incorrect order/method of the implementation of these limits can lead to unwanted phase delays and inconsistent responses in the generated reference trajectories [153].

Linear phase plane based approach has been proposed [176] to maintain consistent reference response to the pilot inputs even when a saturation is active. Moreover, this technique enables a smooth transition of the reference signal to its limit value as opposed to a discontinuous response, which normally occurs if the protected signal hits its saturation. To avoid this discontinuity, higher orders of the reference signals are also protected based on the **limit margin** [173]. The limit margin is defined as the difference between the limit parameter and its boundary

$$\begin{aligned}\bar{\Delta}y_{i,R} &\triangleq y_{i,up} - y_{i,R}, \\ \underline{\Delta}y_{i,R} &\triangleq y_{i,lo} - y_{i,R},\end{aligned}\quad (3.27)$$

where $y_{i,up}$ and $y_{i,lo}$ denote the maximum and minimum magnitude of the reference output $y_{i,R}$ respectively. Likewise, $\bar{\Delta}y_{i,R}$ and $\underline{\Delta}y_{i,R}$ represent the limit margins from the upper and lower boundaries respectively. Based on the limit margin of lower order reference trajectories, consecutive higher order limits are computed

$$\begin{aligned}\mathbf{y}_{i,up} &= \begin{bmatrix} y_{i,up} \\ \dot{y}_{i,up} \\ \vdots \\ y_{i,up}^{(r_i-1)} \\ y_{i,up}^{(r_i)} \end{bmatrix} = \begin{bmatrix} y_{i,up} \\ c_1 \cdot (y_{i,up} - y_{i,R}) \\ \vdots \\ c_{r_i-1} \cdot \begin{pmatrix} (r_i-2) & (r_i-2) \\ y_{i,up} & -y_{i,R} \end{pmatrix} \\ c_{r_i} \cdot \begin{pmatrix} (r_i-1) & (r_i-1) \\ y_{i,up} & -y_{i,R} \end{pmatrix} \end{bmatrix}, \\ \mathbf{y}_{i,lo} &= \begin{bmatrix} y_{i,lo} \\ \dot{y}_{i,lo} \\ \vdots \\ y_{i,lo}^{(r_i-1)} \\ y_{i,lo}^{(r_i)} \end{bmatrix} = \begin{bmatrix} y_{i,lo} \\ c_1 \cdot (y_{i,lo} - y_{i,R}) \\ \vdots \\ c_{r_i-1} \cdot \begin{pmatrix} (r_i-2) & (r_i-2) \\ y_{i,lo} & -y_{i,R} \end{pmatrix} \\ c_{r_i} \cdot \begin{pmatrix} (r_i-1) & (r_i-1) \\ y_{i,lo} & -y_{i,R} \end{pmatrix} \end{bmatrix},\end{aligned}\quad (3.28)$$

where coefficients c_1, c_2, \dots, c_{r_i} denote the rate of transition of any reference trajectory and its derivatives to their limit values. These parameters are defined such that the reference trajectories remain continuous during the approach to their boundaries. Additionally, the derivatives until the r_i -th order of any reference trajectory also exist.

The procedure, outlined by Eq. (3.28), for the computation of the limits for the higher order derivatives based on the bounds of the lower order trajectories is known as back-propagation. It also serves as an anti-windup strategy. When a state's value nears its saturation, the corresponding bound of the upstream derivative approaches zero, thereby preventing integrator wind-up. Figure 3.3 illustrates the implementation of the protection strategy for a second order reference model. **Important to note that the reference trajectories used in the calculation of the limit margins in Eq. (3.27) are the unsaturated values of the integrator for each reference state i.e. the signal lying upstream of the limitation.** When the saturated signals are used in the calculation of the limit margins for higher order trajectories, the integrators of the corresponding higher order trajectories stay fixed at non-zero values in the steady state. While transitioning from such a steady state condition the higher order state integrator values wind down to

zero (if the transition occurs in the opposite direction than the current value) before an effect in the downstream states is observed. This phenomenon can lead to undesirable phase delays in the control variable reference trajectories.

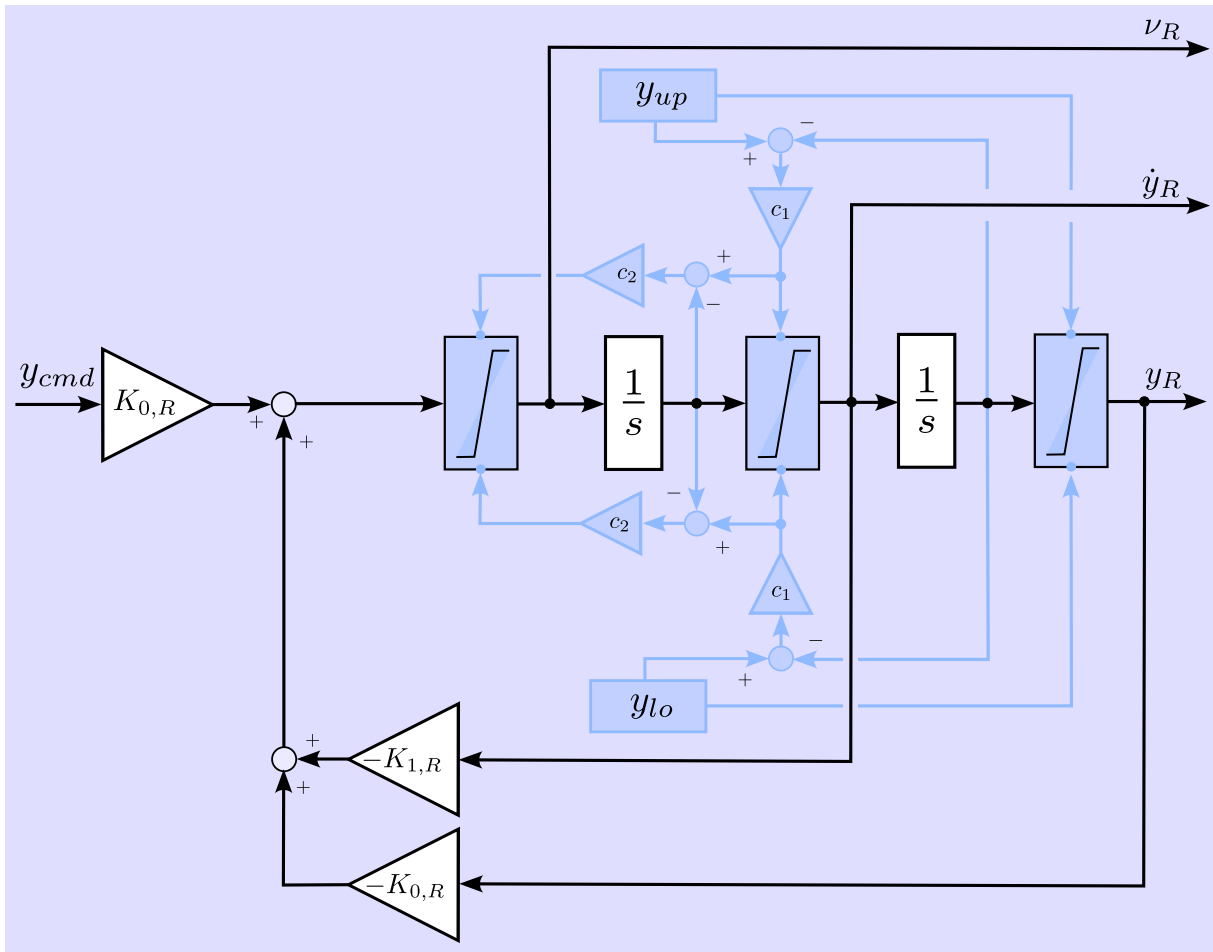


Figure 3.3: Linear phase plane based envelope protection in a second order linear RM

The phase delay induced by back-propagation of saturated lower order reference trajectories is illustrated in Fig. 3.4 by the reference control variable trajectory. The control variable command value y_{cmd} mapped from the pilot inceptor command is higher than the allowed bounds specified by y_{up} and y_{lo} . It can be observed that the reference control variable trajectory in the case where the saturated signals are propagated back to calculate the higher order variable's bounds exhibits a time delay (rounded areas) before

Parameter	Magnitude	Parameter	Magnitude
$K_{0,R}$	36	$K_{1,R}$	12
c_1	3.5	c_2	1.2
y_{up}	10	y_{lo}	-10

Table 3.1: Magnitude of parameters for simulations of the second order linear reference model

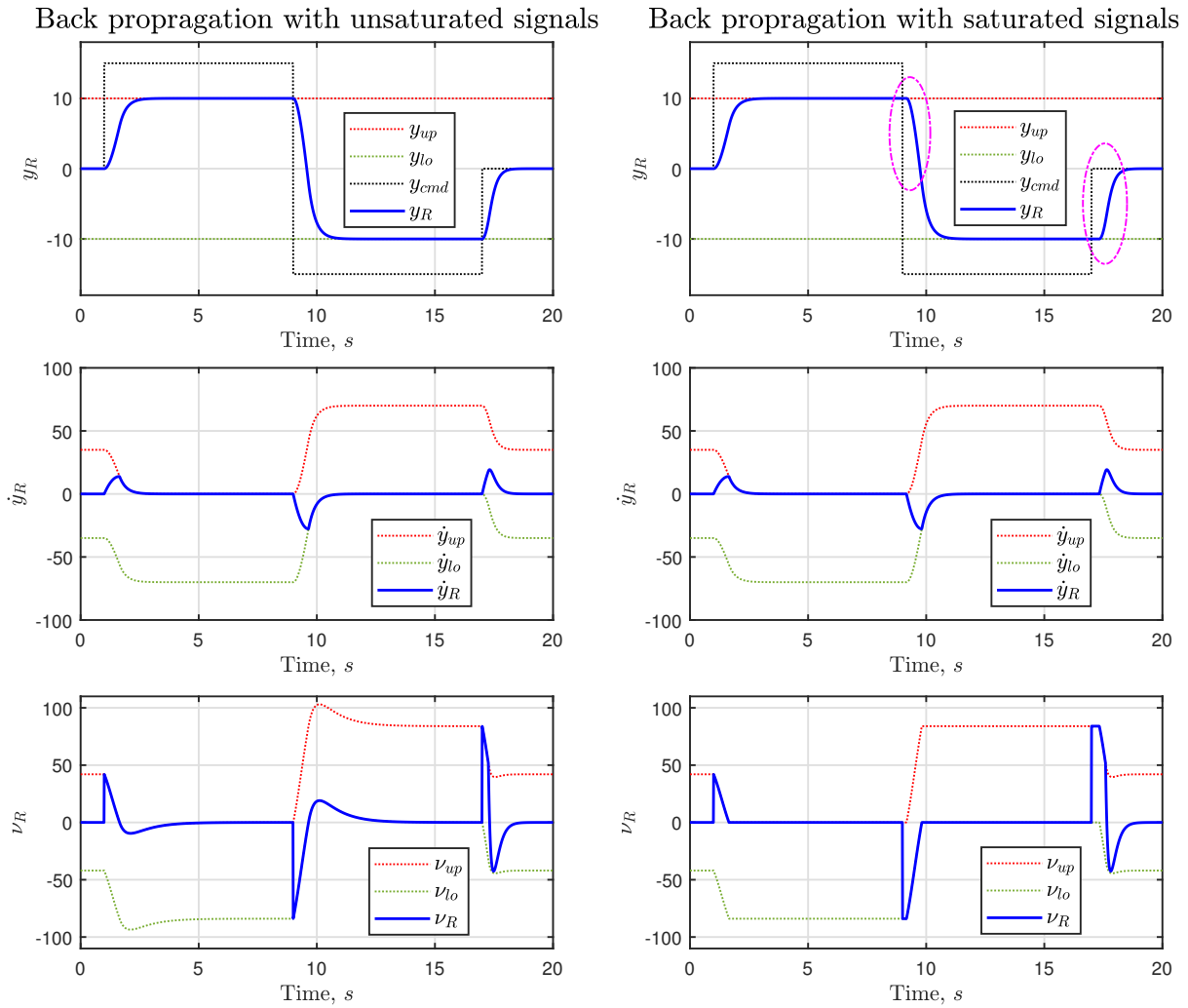


Figure 3.4: Comparison of limitation mechanism in a linear second order RM

moving towards the next set-point. These results correspond to a second order reference model having a similar structure as demonstrated in the Fig. 3.3. The parameters used in the simulation results are listed in Table 3.1.

For the simulation results represented in Fig. 3.4, the control variable bounds are specified as constant values. However, these bounds can also be defined as functions of current aircraft states to facilitate control margin awareness for the pilot.

An alternative technique to enforce bounds on the reference control variable trajectory y_R is command value limiting. Fundamentally, it involves imposing limits on the control variable command y_{cmd} to the reference model. Although, the reference control variable trajectory can be restricted through command value limiting, the higher order derivatives of the desired trajectory are not protected. For that purpose, the phase plane based protection offers the benefit of limiting derivatives until the order of the relative degree. In addition to the limits computed in the Eq. (3.28), absolute allowed bounds $y_{i,up,alw}$ and $y_{i,lo,alw}$ available to the control designer through aircraft configuration data are also

incorporated to derive the limits for each output and its derivatives [82]

$$\begin{aligned} \mathbf{y}_{i,max} &= \min(\mathbf{y}_{i,up,abs}, \mathbf{y}_{i,up}) \\ \mathbf{y}_{i,min} &= \max(\mathbf{y}_{i,lo,abs}, \mathbf{y}_{i,lo}) \quad \text{for } i = 1, 2, \dots, n_y. \end{aligned} \quad (3.29)$$

This allows for consideration of the most conservative bounds in the definition of the desired behavior by the reference model.

Thus far, concepts pertaining to linear reference models have been addressed. As already stated, these reference models establish the desired response intended to be followed by the aircraft. However, aircraft possess inherent nonlinear dynamics. Linear reference models could enforce contradictory transient behavior on an aircraft, which does not match with its nonlinear attributes. Specifically in relation to aircraft designed for UAM, substantial nonlinearities can be encountered owing to the multiple flight phases and the operating environment. Therefore, an integrated nonlinear reference model is developed for the control of a VTOL transition aircraft. Physically motivated emulation of the aircraft nonlinearities by the RM contribute to reduction in the control effort and improvement in tracking performance. The basic concepts presented in this section are built upon to achieve a modular RM architecture.

Prior to presentation of the integrated reference model, the research environment comprising of the aircraft configuration employed for testing of the developed algorithm along with the controller framework housing the reference model are introduced.

3.2 Research Environment

This section demonstrates the unmanned tilt-rotor VTOL transition aircraft used for validation of the integrated reference model architecture. Although, the presented configuration is very unique, modularity of the proposed RM structure is also emphasized during the development process. Furthermore, incremental nonlinear dynamic inversion based unified controller framework for the given aircraft configuration is elucidated. Functional description of each controller module and the nature of their interaction with the integrated reference model is also covered.

3.2.1 Aircraft Configuration

Figure 3.5 displays the illustration of the tilt-rotor VTOL transition UAV along with the sketch views, which exhibit the available control effectors (enlisted in Table 3.2). The aircraft possesses four lift thrust units (LTUs). Two main LTUs are fixed on the fuselage at the front and aft positions from the wing mounting. The rotational rates of the fixed pitch propellers attached to the front and aft main LTU are denoted by ω_F and ω_A . The two remaining thrust units are of tilt-rotor type additionally featuring aerodynamic control surfaces, which act as ailerons in high dynamic pressure flight phase. The tilt angles of the left and right tilt rotors are represented by δ_L and δ_R respectively. Likewise, the rotational rates of the propellers on the left and right tilt thrust units are given by ω_L and ω_R . Additionally, the aircraft comprises of an all-moving tail whose deflection is denoted as η .

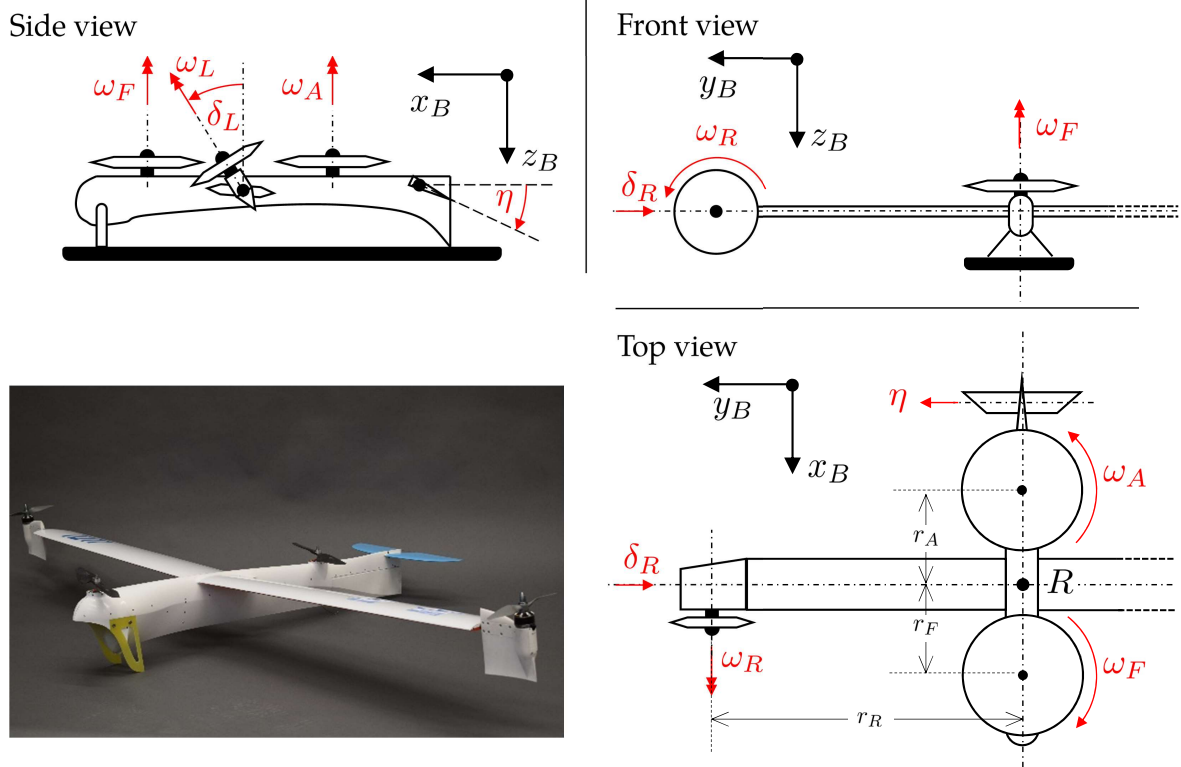


Figure 3.5: Tilt-rotor VTOL transition aircraft configuration

Control Effectors of the reference aircraft configuration	
η	Elevator Deflection
δ_L	Deflection tilt servo left
δ_R	Deflection tilt servo right
ω_L	Rotational rate tilt propeller left
ω_R	Rotational rate tilt propeller right
ω_F	Rotational rate main propeller front
ω_A	Rotational rate main propeller aft

Table 3.2: Control Effectors of the tilt-rotor VTOL transition aircraft

The dynamics of the given configuration are modeled according to the conservation of linear and angular momentum governed by Newton's second law. The translation and rotational equations of motion elaborated in Eqs. (2.89) and (2.73) describe the rigid body dynamics denoted in the body fixed frame. Total forces and moments specified in the rigid body dynamics are build up of the sum of gravitational, propulsion and

aerodynamic components

$$\begin{aligned} (\vec{\mathbf{F}}_T^R)_B &= (\vec{\mathbf{F}}_G^R)_B + (\vec{\mathbf{F}}_P^R)_B + (\vec{\mathbf{F}}_A^R)_B, \\ (\vec{\mathbf{M}}_T^R)_B &= (\vec{\mathbf{M}}_G^R)_B + (\vec{\mathbf{M}}_P^R)_B + (\vec{\mathbf{M}}_A^R)_B. \end{aligned} \quad (3.30)$$

A brief description about the generation of these forces and moments is covered next. Assuming that the propulsive forces and moments produced within the propeller plane are negligible, the forces and moments produced by each propeller of the corresponding LTUs perpendicular to their plane of rotation is modeled [46, 177–181] according to

$$\begin{aligned} F_P(t) &= k_T \cdot \omega_P^2(t), \\ N_P(t) &= \text{sgn}[\omega_P(t)] \cdot k_N \cdot \omega_P^2(t). \end{aligned} \quad (3.31)$$

Here $F_P(t) \in \mathbb{R}$ represents the force produced by the propeller along its rotational axis, $k_T \in \mathbb{R}$ and $k_N \in \mathbb{R}$ are the thrust and drag coefficients of the propeller correspondingly. Moreover, $\omega_P(t) \in \mathbb{R}$ indicate the angular velocity of the propeller. The second expression signifies the drag moment $N_P(t) \in \mathbb{R}$ resulting from the drag force of the propeller. Dependency on time is not shown hereafter for ease of reading.

Utilizing the expressions from Eq. (3.31), the powered lift produced by the main LTUs is determined

$$(\vec{\mathbf{F}}_{P,\text{main}}^R)_B = \begin{bmatrix} 0 \\ 0 \\ (F_{z,F})_B + (F_{z,A})_B \end{bmatrix} = \begin{bmatrix} 0 \\ 0 \\ -(F_z)_{M_F} - (F_z)_{M_A} \end{bmatrix}, \quad (3.32)$$

where $(F_z)_{M_F} \in \mathbb{R}$ and $(F_z)_{M_A} \in \mathbb{R}$ are the forces produced by the front and aft main thrust units in accordance with the expression in Eq. (3.31). These forces are defined in the reference frames M_F and M_A having origin on the centers of rotation for the main front and aft propellers respectively. The vertical axes z_{M_F} , z_{M_A} of the main propulsion unit frames are defined positive upwards as compared to that of the body fixed frame, which is positive downwards. Hence, the propulsive forces produced by the front main LTU $(F_{z,F})_B \in \mathbb{R}$ and aft main LTU $(F_{z,A})_B \in \mathbb{R}$ denoted in the body fixed frame are of the opposite sign.

The propulsive forces generated by the tilt thrust units are resolved in to the longitudinal x_B body fixed axis and the vertical z_B body fixed axis based on the tilt deflection angles $\delta_L \in \mathbb{R}$ and $\delta_R \in \mathbb{R}$

$$(\vec{\mathbf{F}}_{P,\text{tilt}}^R)_B = \begin{bmatrix} (F_z)_{T_L} \cdot \sin \delta_L + (F_z)_{T_R} \cdot \sin \delta_R \\ 0 \\ -(F_z)_{T_L} \cdot \cos \delta_L - (F_z)_{T_R} \cdot \cos \delta_R \end{bmatrix}, \quad (3.33)$$

where $(F_z)_{T_L} \in \mathbb{R}$ and $(F_z)_{T_R} \in \mathbb{R}$ represent the propulsive force produced by the left and right tilt propulsion units respectively. The tilt propulsion frame $T_L \in \mathbb{R}$ and $T_R \in \mathbb{R}$ are fixed to the tilt LTUs having origin at the centers of rotation of the tilt propellers. At 0 tilt deflection angles, the vertical z_T -axes of the tilt thrust units are defined as positive outward in the direction of the produced force. The lateral y_T -axis is anti-parallel to the body fixed lateral axis while the forward tilt rotor frame axes are parallel to the body fixed x_B -axis.

The moments produced by the main rotors comprise of the pitch moment due to differential thrust through the moment arms $r_F \in \mathbb{R}$ and $r_A \in \mathbb{R}$ for the front and aft main thrust units. In addition to the pitch moment, the yaw moment resulting entirely from the drag moment due to propeller rotation as expressed in Eq. (3.31) is also produced by the main LTUs. The sign of the produced yaw moment depends on the rotation direction of each propeller. Figure 3.5 shows that the front propeller rotates in clockwise direction, hence the drag moment produced by it acts in the opposite direction, which in the body-fixed B -frame is a negative yaw moment and vice-versa for the aft propeller

$$\left(\vec{M}_{P,\text{main}}^R\right)_B = \begin{bmatrix} 0 \\ -(F_{z,F})_B \cdot r_F + (F_{z,A})_B \cdot r_A \\ -(N_{P,F})_B + (N_{P,A})_B \end{bmatrix}. \quad (3.34)$$

In contrast, the tilt rotors can produce additional yaw moment owing to the tilt-able thrust vectors. The drag moment produced by the tilt propellers is very small as compared to the yaw moment generated by tilting the thrust produced by them. Hence, this aspect is neglected in the formulation of moments produced by the tilt LTUs. Additionally, perfect alignment of the tilt thrust units with respect to the Center of Gravity (CG) is assumed, therefore they do not generate any pitch moment. Moreover, the tilt LTUs produce roll moments by generating dissimilar thrust, which acts over the left $r_L \in \mathbb{R}$ and right $r_R \in \mathbb{R}$ rotor moment arms

$$\left(\vec{M}_{P,\text{tilt}}^R\right)_B = \begin{bmatrix} (F_z)_{T_L} \cdot \cos \delta_L \cdot r_L - (F_z)_{T_R} \cdot \cos \delta_R \cdot r_R \\ 0 \\ (F_z)_{T_L} \cdot \sin \delta_L \cdot r_L - (F_z)_{T_R} \cdot \sin \delta_R \cdot r_R \end{bmatrix}. \quad (3.35)$$

Thereupon, the total propulsive forces producible in the aircraft body-fixed frame are obtained by the summation of the expressions in Eqs. (3.32) and (3.33)

$$\left(\vec{F}_P^R\right)_B = \left(\vec{F}_{P,\text{main}}^R\right)_B + \left(\vec{F}_{P,\text{tilt}}^R\right)_B \quad (3.36)$$

and likewise the total propulsive moments are yielded by addition of moments produced by main thrust units (Eq. (3.34)) and tilt thrust units (Eq. (3.35))

$$\left(\vec{M}_P^R\right)_B = \left(\vec{M}_{P,\text{main}}^R\right)_B + \left(\vec{M}_{P,\text{tilt}}^R\right)_B. \quad (3.37)$$

For the aircraft shown in Fig. 3.5, the mathematical modeling of the aircraft aerodynamics is categorized in to four main components – wing body (containing tilt surfaces), full-moving elevator, vertical tail and body drag forces generated by the airframe. Firstly, the forces and moments generated by each aerodynamic surface acting on their aerodynamic reference point A are calculated. The resulting forces are directly applicable to the aircraft reference point R

$$\left(\vec{F}_A^R\right) = \left(\vec{F}_A^A\right) \quad (3.38)$$

whereas the moments need to be translated depending on the relative position of the aerodynamic reference from the aircraft reference point

$$\left(\vec{M}_A^R\right) = \left(\vec{M}_A^A\right) + \left(\vec{r}^{RA}\right) \times \left(\vec{F}_A^A\right). \quad (3.39)$$

Subsequently, the force and moment vector are rotated to the body-fixed frame. Non-dimensional force and moment coefficients are employed to specify the aerodynamic forces and moments. For the purpose of modeling the aerodynamics of this aircraft, the aerodynamic coefficients are defined in the local aerodynamic frame for each aerodynamic surface. A generalized formulation of the aerodynamic forces and moments acting at the aerodynamic center (A) denoted in the aerodynamic (A) frame (Fig. A.2) is

$$\left(\vec{\mathbf{F}}_A^A\right)_A = \begin{bmatrix} X_A^A \\ Y_A^A \\ Z_A^A \end{bmatrix}_A = \bar{q} \cdot S \cdot \begin{bmatrix} -C_D \\ C_Q \\ C_L \end{bmatrix} \quad \left(\vec{\mathbf{M}}_A^A\right)_A = \begin{bmatrix} L_A^A \\ M_A^A \\ N_A^A \end{bmatrix}_A = \bar{q} \cdot S \cdot \begin{bmatrix} s \cdot C_l \\ \bar{c} \cdot C_m \\ s \cdot C_n \end{bmatrix}, \quad (3.40)$$

where $\bar{q} \in \mathbb{R}$ represents the dynamic pressure, $S \in \mathbb{R}$, $\bar{c} \in \mathbb{R}$ and $s \in \mathbb{R}$ are the surface area, chord and semi-span of the lifting surfaces respectively. The aerodynamic drag, side and lift force coefficients $C_D \in \mathbb{R}$, $C_Q \in \mathbb{R}$, $C_L \in \mathbb{R}$ along with the aerodynamic roll, pitch and yaw moment coefficients $C_l \in \mathbb{R}$, $C_m \in \mathbb{R}$, $C_n \in \mathbb{R}$ are specified in the aerodynamic frame. Using this formulation, the forces and moments produced by each aerodynamic surface for the configuration in Fig. 3.5 are emulated.

The aerodynamics of the wing and the tilt surfaces are modeled together as a single wing body unit. The aerodynamic coefficients pertaining to the wing body are defined as functions of the aerodynamic angle of attack at the wing $\alpha_{A,w}$, body rotational rates $(\vec{\omega}_K^{OB})_B$ and tilt deflection angles δ_L, δ_R

$$C_{i,w} = C_{i,w} \left(\alpha_{A,w}, \left(\vec{\omega}_K^{OB} \right)_B, \delta_L, \delta_R \right), \quad (3.41)$$

where i denotes a common identifier for the forces D, Q, L and moments l, m, n . The functions specified in Eq. (3.41) are used to create a numeric database. The values of the force and moment coefficients are extracted from the database subject to the magnitudes of the dependent variables Eq. (3.41) through a Lookup table. Henceforth, the aerodynamic forces and moments pertaining to the wing body at the wing reference point W denoted in the local wing frame W are obtained

$$\left(\vec{\mathbf{F}}_A^W\right)_W = \bar{q} \cdot S_w \cdot \begin{bmatrix} -C_{D,w} \\ C_{Q,w} \\ C_{L,w} \end{bmatrix} \quad \left(\vec{\mathbf{M}}_A^W\right)_W = \bar{q} \cdot S_w \cdot \begin{bmatrix} s_w \cdot C_{l,w} \\ \bar{c}_w \cdot C_{m,w} \\ s_w \cdot C_{n,w} \end{bmatrix}. \quad (3.42)$$

The aerodynamic forces and moments generated by the wing are translated to the aircraft reference point and expressed in the B -frame according to the Eqs. (3.38) and (3.39)

$$\begin{aligned} \left(\vec{\mathbf{F}}_{A,w}^R\right)_B &= \mathbf{M}_{BW} \cdot \left(\vec{\mathbf{F}}_A^W\right)_W, \\ \left(\vec{\mathbf{M}}_{A,w}^R\right)_B &= \mathbf{M}_{BW} \cdot \left(\vec{\mathbf{M}}_A^W\right)_W + \left(\vec{\mathbf{r}}^{RW}\right)_B \times \left(\vec{\mathbf{F}}_{A,w}^R\right)_B. \end{aligned} \quad (3.43)$$

Here $\mathbf{M}_{BW} \in \mathbb{R}^{3 \times 3}$, elaborated in Eq. (A.3), represents the frame rotation matrix from the wing frame to the body-fixed frame using the wing angle of incidence i_w . Identically, the forces and moments produced by the elevator are modeled

$$\left(\vec{\mathbf{F}}_A^H\right)_H = \bar{q} \cdot S_\eta \cdot \begin{bmatrix} -C_{D,\eta} \\ C_{Q,\eta} \\ C_{L,\eta} \end{bmatrix} \quad \left(\vec{\mathbf{M}}_A^H\right)_H = \bar{q} \cdot S_\eta \cdot \begin{bmatrix} s_\eta \cdot C_{l,\eta} \\ \bar{c}_\eta \cdot C_{m,\eta} \\ s_\eta \cdot C_{n,\eta} \end{bmatrix}. \quad (3.44)$$

The terms $(\vec{\mathbf{F}}_A^H)_H \in \mathbb{R}^3$ and $(\vec{\mathbf{M}}_A^H)_H \in \mathbb{R}^3$ denote the aerodynamic forces and moments respectively, acting on the reference point of the elevator H indicated in a local reference frame H of the full moving horizontal tail. Similar to the transformations in Eq. (3.43), the elevator forces and moments are transformed to be expressed in the aircraft body-fixed frame at the reference point R using the frame rotation matrix $\mathbf{M}_{BH} \in \mathbb{R}^{3 \times 3}$ (Eq. (A.4)), which utilizes the horizontal tail angle of incidence i_h

$$\begin{aligned} (\vec{\mathbf{F}}_{A,\eta}^R)_B &= \mathbf{M}_{BH} \cdot (\vec{\mathbf{F}}_A^H)_H, \\ (\vec{\mathbf{M}}_{A,\eta}^R)_B &= \mathbf{M}_{BH} \cdot (\vec{\mathbf{M}}_A^H)_H + (\vec{\mathbf{r}}^{RH})_B \times (\vec{\mathbf{F}}_{A,\eta}^R)_B. \end{aligned} \quad (3.45)$$

Similarly, the forces and moments generated by the non-moving vertical tail are modeled

$$\begin{aligned} (\vec{\mathbf{F}}_{A,V}^R)_B &= \mathbf{M}_{BV} \cdot (\vec{\mathbf{F}}_A^V)_V, \\ (\vec{\mathbf{M}}_{A,V}^R)_B &= \mathbf{M}_{BV} \cdot (\vec{\mathbf{M}}_A^V)_V + (\vec{\mathbf{r}}^{RV})_B \times (\vec{\mathbf{F}}_{A,V}^R)_B, \end{aligned} \quad (3.46)$$

where $(\vec{\mathbf{F}}_A^V)_V \in \mathbb{R}^3$ and $(\vec{\mathbf{M}}_A^V)_V \in \mathbb{R}^3$ denote the aerodynamic forces and moments respectively, acting on the reference point of the vertical tail V indicated in a local reference frame V of the non-moving vertical tail. Like the transformations in Eqs. (3.43) and (3.45), the forces and moments due to the vertical tail denoted in the body frame $(\vec{\mathbf{F}}_{A,V}^R)_B \in \mathbb{R}^3$ and $(\vec{\mathbf{M}}_{A,V}^R)_B \in \mathbb{R}^3$ are computed. The frame rotation matrix $\mathbf{M}_{BV} \in \mathbb{R}^{3 \times 3}$ is an identity matrix since the vertical tail is mounted symmetric along the aircraft's longitudinal plane of symmetry, and therefore the coordinate axes of the vertical tail's local frame are parallel to the body fixed frame axes.

The aerodynamic drag force is simulated as a point mass drag model. Using the body drag coefficients and the projected surface areas perpendicular to the body-fixed axes, the body drag force $(\vec{\mathbf{F}}_{A,D}^A)_B \in \mathbb{R}^3$ at the aircraft's aerodynamic center A is given, which is equivalent to the body drag force $(\vec{\mathbf{F}}_{A,D}^R)_B \in \mathbb{R}^3$ at the aircraft reference point R

$$(\vec{\mathbf{F}}_{A,D}^R)_B = (\vec{\mathbf{F}}_A^A)_B = -\bar{q} \cdot \begin{bmatrix} S_x \cdot C_{D,x} \\ S_y \cdot C_{D,y} \\ S_z \cdot C_{D,z} \end{bmatrix}. \quad (3.47)$$

A drag moment is induced from the body drag force in Eq. (3.47) since the aerodynamic center is not at the same position as the aircraft reference point

$$(\vec{\mathbf{M}}_{A,D}^R)_B = (\vec{\mathbf{r}}^{RA})_B \times (\vec{\mathbf{F}}_{A,D}^R)_B. \quad (3.48)$$

Here $(\vec{\mathbf{r}}^{RA})_B \in \mathbb{R}^3$ signifies the position of the aircraft reference point R with respect to the aerodynamic center A . Finally, the total aerodynamic forces $(\vec{\mathbf{F}}_A^R)_B \in \mathbb{R}^3$ and moments $(\vec{\mathbf{M}}_A^R)_B \in \mathbb{R}^3$ ensue from the components in Eqs. (3.43) and (3.45) to (3.48)

$$(\vec{\mathbf{F}}_A^R)_B = (\vec{\mathbf{F}}_{A,w}^R)_B + (\vec{\mathbf{F}}_{A,\eta}^R)_B + (\vec{\mathbf{F}}_{A,V}^R)_B + (\vec{\mathbf{F}}_{A,D}^R)_B, \quad (3.49)$$

$$(\vec{\mathbf{M}}_A^R)_B = (\vec{\mathbf{M}}_{A,w}^R)_B + (\vec{\mathbf{M}}_{A,\eta}^R)_B + (\vec{\mathbf{M}}_{A,V}^R)_B + (\vec{\mathbf{M}}_{A,D}^R)_B. \quad (3.50)$$

Gravitational force is specified as a constant force field

$$\left(\vec{\mathbf{F}}_G^G\right)_O = m \cdot \left(\vec{\mathbf{g}}^G\right)_O = m \cdot \begin{bmatrix} 0 \\ 0 \\ g \end{bmatrix}. \quad (3.51)$$

The gravitational vector, presented by $\left(\vec{\mathbf{g}}^G\right)_O \in \mathbb{R}^3$ is denoted in the NED-frame (O) and $g \in \mathbb{R}$ is the constant acceleration due to gravity. The gravitational force $\left(\vec{\mathbf{F}}_G^G\right)_O \in \mathbb{R}^3$ acting at the center of gravity G is equal to the force acting at the reference point R . Hence, force due to gravity at point R indicated in the body-fixed frame is directly achieved through the frame rotation matrix \mathbf{M}_{BO} described in Eq. (A.2)

$$\left(\vec{\mathbf{F}}_G^R\right)_B = \mathbf{M}_{BO} \cdot \left(\vec{\mathbf{F}}_G^G\right)_O. \quad (3.52)$$

Emanating from the relative position $\left(\vec{\mathbf{r}}^{RG}\right)_B \in \mathbb{R}^3$ of the center of gravity G in comparison to the aircraft reference point R , the moment generated due to the gravitational force yields

$$\left(\vec{\mathbf{M}}_G^R\right)_B = \left(\vec{\mathbf{r}}^{RG}\right)_B \times \left(\vec{\mathbf{F}}_G^R\right)_B. \quad (3.53)$$

This accomplishes the specification of the forces and moments in the plant model utilized for Model-in-the-Loop (MIL) simulation of the unified INDI controller framework housing the integrated reference model. Prerequisite knowledge about the controller architecture is presented before advancing to the description of the RM.

3.2.2 Controller Structure

The controller structure, illustrated in Fig. 3.6 comprises of five main components - Integrated Reference Model (IRM), Estimation module (EST), Error Controller (EC), On-board Plant Model (OBPM) and Control Allocation (CA). The pilot inceptor commands denoted by δ_{cmd} , and the virtual control input commands $\mathbf{y}_{\nu,cmd}$ are mapped to the physical control variable commands within the integrated reference model. One of the functions encompassed in the IRM include flight phase contingent interpretation of the pilot stick deflection commands to sustain a consistent aircraft response. Moreover, the reference model facilitates generation of physically meaningful desired reference trajectories ν_R, ξ_R in addition to enforcing compliance between different reference variables for the full flight envelope of the VTOL transition aircraft. The external reference states ξ_R denote reference control variables response and their higher order derivatives up to one order less than the relative degree as shown in Eq. (3.24), and the ν_R represent the reference pseudo controls. Likewise, variables ξ and ν represent the external states and pseudo controls of the real system upon which the reference response tracking is enforced by the controller. Furthermore, the reference model incorporates RM core module, which produces the same set of reference pseudo controls and external states over the full flight envelope of a VTOL transition aircraft, thereby facilitating the design of a unified control strategy. Wind disturbance rejection behavior is explicitly accounted for in the reference model definition. Detailed information about all the aspects of the

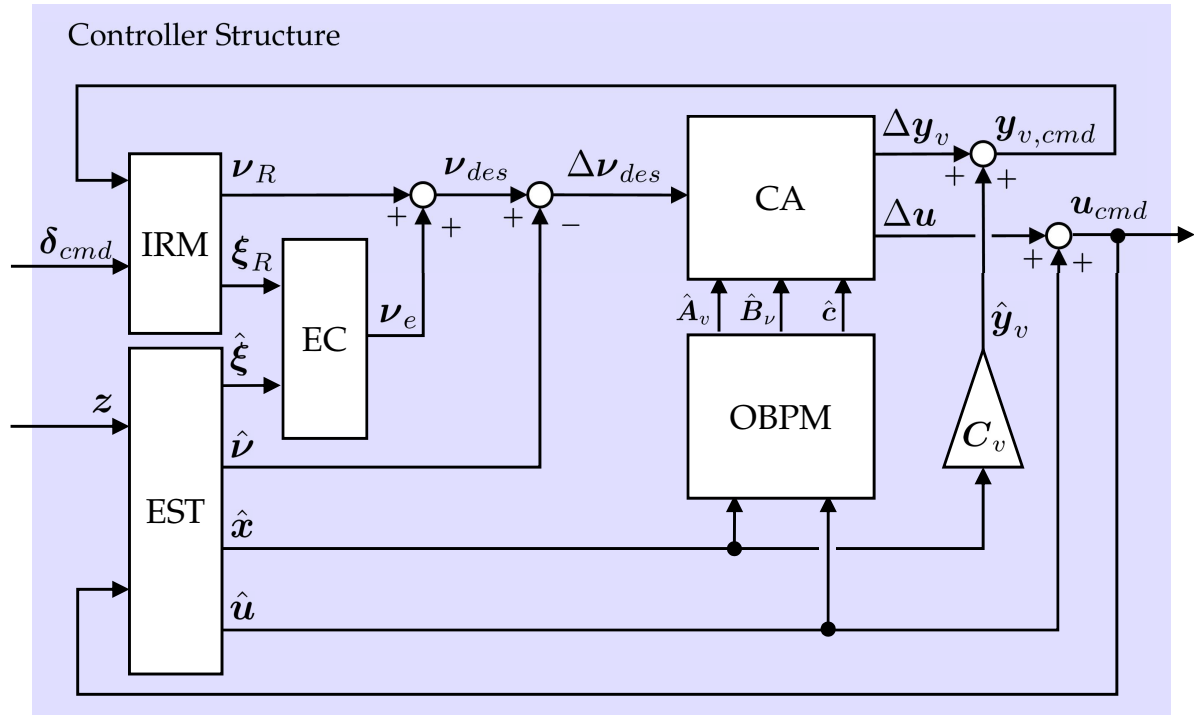


Figure 3.6: Incremental Nonlinear Dynamic Inversion controller structure

reference model are presented in the Section 3.3. Before continuing with the presentation of the integrated reference model concepts, the remaining modules of the INDI controller structure are described briefly.

3.2.2.1 Estimation

As the name suggests, the estimation module performs the task of estimating current pseudo controls $\hat{\nu}$, external states $\hat{\xi}$ and current effector position \hat{u} based on the sensor measurements z comprising of the full state feedback and the control input commands u_{cmd} . Complementary filtering [62, 182–184] is employed to assimilate the benefits of the measured data with a corresponding high-pass component obtained through a relevant system model. Body-fixed specific forces $(\hat{\mathbf{f}}_K^R)_B \in \mathbb{R}^3$ and rotational accelerations $(\hat{\omega}_K^{OB})_B \in \mathbb{R}^3$ are estimated using the complementary filters

$$\begin{aligned} \left(\hat{\mathbf{f}}_K^R\right)_B(s) &= \mathbf{G}_{Lf}(s) \cdot \left(\vec{\mathbf{f}}_{K,meas}^R\right)_B(s) + [\mathcal{I}_{3 \times 3} - \mathbf{G}_{Lf}(s)] \cdot \left(\vec{\mathbf{f}}_{K,M}^R\right)_B, \\ \left(\hat{\omega}_K^{OB}\right)_B(s) &= s \cdot \mathbf{G}_{L\dot{\omega}}(s) \cdot \left(\vec{\omega}_{K,meas}^{OB}\right)_B(s) + [\mathcal{I}_{3 \times 3} - \mathbf{G}_{L\dot{\omega}}(s)] \cdot \left(\vec{\omega}_{K,M}^{OB}\right)_B, \end{aligned} \quad (3.54)$$

where $(\vec{\mathbf{f}}_{K,M}^R)_B \in \mathbb{R}^3$ and $(\vec{\omega}_{K,M}^{OB})_B \in \mathbb{R}^3$ are the specific forces and rotational accelerations computed by the on-board plant model, detailed in the section 3.2.2.3, based on the estimated control inputs \hat{u} and the state vector \hat{x} . The term \mathbf{G}_{Lf} is a 3×3 diagonal matrix containing strictly-proper stable transfer functions with unit DC gains intended for the specific forces in the three coordinate axes of the body-fixed frame. Likewise, $\mathbf{G}_{L\dot{\omega}}$ contains transfer functions for the body angular accelerations. Second-order low pass

filters are employed in the aforementioned transfer matrices, which can be expressed in the Laplace domain as

$$G_{LP}(s) = \frac{\omega_0^2}{s^2 + 2 \cdot \zeta \cdot \omega \cdot s + \omega_0^2}. \quad (3.55)$$

Here $\omega_0 \in \mathbb{R}$ and $\zeta \in \mathbb{R}$ denote the corner frequency and the damping ratio of the roll-off filters. The complementary filter structure in Eq. (3.54) removes the high frequency noise content from the measurements $(\vec{f}_{K,meas}^R)_B$ and $(\vec{\omega}_{K,meas}^{OB})_B$ and simultaneously incorporates the high frequency system response estimates based on the model used in the OBPM. Additionally, the use of complementary filter enables to diminish the phase loss that occurs due to the low-pass filtering of the measured sensor data.

Important to note that the code flashed on the FCC employs discrete forms of the continuous filter representations shown in Eqs. (3.54) and (3.55). Besides the estimation of the pseudo controls, all measured signals are filtered using second-order low pass filters such as the one stated in Eq. (3.55) to remove the noise manifesting in the measured signals due to vibrations, analog to digital conversion and electronic noise occurring in the sensor interface circuits [185]. Additionally, the *Estimation* contains effector models which evaluate the current effector state based on the control input u_{cmd} . The actuators of the control surfaces i.e. the full moving elevator η and the tilt propeller surfaces δ_L, δ_R are emulated by second order elements, each of which can be represented as a state-space model

$$\begin{bmatrix} \dot{\hat{u}} \\ \ddot{\hat{u}} \end{bmatrix} = \begin{bmatrix} 0 & 1 \\ -\omega_a^2 & -2 \cdot \zeta_a \cdot \omega_a \end{bmatrix} \cdot \begin{bmatrix} \hat{u} \\ \dot{\hat{u}} \end{bmatrix} + \begin{bmatrix} 0 \\ \omega_a^2 \end{bmatrix} \cdot u_{cmd}. \quad (3.56)$$

The natural frequency and the damping of the actuator is denoted by $\omega_a \in \mathbb{R}$ and $\zeta_a \in \mathbb{R}$ respectively. The variables u_{cmd} and \hat{u} represent the effector command and effector estimated position for each of the control surfaces. Furthermore, the thrust units (main and tilt) are modeled as having first order dynamic behavior. In Laplace domain, the dynamics for every thrust unit are given by

$$\hat{u}(s) = \frac{\omega_P}{s + \omega_P} \cdot u_{cmd}(s), \quad (3.57)$$

where $\omega_P \in \mathbb{R}$ is the cut-off frequency of the corresponding LTU's first order dynamics. In addition to the first and second order dynamics for the thrust units and the control surface actuators, rate and absolute saturations are also incorporated in the actuator estimation models.

3.2.2.2 Error Controller

In an ideal case, the inversion cancels out the plant dynamics exactly, yielding a system that is given by a chain of integrators from the reference pseudo control ν_R to the true system output y . However, some elements like

1. external disturbances,
2. model uncertainties in the effector models along with the control input matrix \hat{B} used for control allocation,

3. errors in the estimation of the pseudo control $\hat{\nu}$,
4. delays in measurements from inherent sensor delay, transport delay and delay caused by estimation filters

can occur in practical applications such that a perfect inversion cannot be realized. As a consequence, the plant pseudo control ν drifts away from the reference pseudo control. This deviation accumulates over the r_i -integrator chain for each output channel causing the the true external states ξ to diverge from the reference external states ξ_R .

A stabilizing error controller (EC) is employed to mitigate the deviation of the real plant outputs from the corresponding reference states, which is known as the control error

$$\mathbf{e} = \begin{bmatrix} e_1 \\ e_2 \\ \vdots \\ e_{n_y} \end{bmatrix} = \begin{bmatrix} y_{1,R} - y_1 \\ y_{2,R} - y_2 \\ \vdots \\ y_{n_y,R} - y_{n_y} \end{bmatrix}. \quad (3.58)$$

Together with the control error, its derivatives until the order $r_i - 1$, which is essentially the error between the reference and true external states

$$\begin{aligned} e^{(r_i-1)} &= y_{i,R}^{(r_i-1)} - y_i^{(r_i-1)}, \\ e^{(r_i-2)} &= y_{i,R}^{(r_i-2)} - y_i^{(r_i-2)}, \\ &\vdots \\ \ddot{e} &= \ddot{y}_{i,R} - \ddot{y}_i, \\ \dot{e} &= \dot{y}_{i,R} - \dot{y}_i, \end{aligned} \quad (3.59)$$

are multiplied with the error gain matrix to yield the pseudo control error ν_e

$$\begin{aligned} \nu_e &= \mathbf{C}_{e_{r-1}} \cdot \left(\mathbf{y}_R^{(r-1)} - \mathbf{y}^{(r-1)} \right) + \mathbf{C}_{e_{r-2}} \cdot \left(\mathbf{y}_R^{(r-2)} - \mathbf{y}^{(r-2)} \right) \dots + \mathbf{C}_{e_0} \cdot (\mathbf{y}_R - \mathbf{y}) \\ \nu_e &= \underbrace{\begin{bmatrix} \mathbf{C}_{e_{r-1}} & \mathbf{C}_{e_{r-2}} & \dots & \mathbf{C}_{e_0} \end{bmatrix}}_{\mathbf{C}_e} \cdot \underbrace{\begin{bmatrix} \mathbf{y}_R^{(r-1)} - \mathbf{y}^{(r-1)} \\ \mathbf{y}_R^{(r-2)} - \mathbf{y}^{(r-2)} \\ \vdots \\ \mathbf{y}_R - \mathbf{y} \end{bmatrix}}_e = \mathbf{C}_e \cdot \mathbf{e}. \end{aligned} \quad (3.60)$$

In case of a perfect inversion, the poles of the resulting closed loop system lie in the origin of the complex plane. Since, perfect inversion is not feasible in practical applications, the gain set $\mathbf{C}_e \in \mathbb{R}^{n_y \times (r \cdot n_y)}$ specified in the error controller is chosen such that the poles of the feedback controlled system lie in the left half of the complex plane. Furthermore, the choice of the gains is also driven by constraints from the physical capabilities of the plant, control effector dynamics, sensor dynamics and time-delay characteristics of the closed loop system.

3.2.2.3 On-board Plant Model

On-board Plant Model (OBPM) utilizes an assumed plant model $\hat{F}(\hat{x}, \hat{u})$ to evaluate the Jacobian matrices \hat{B}_v and \hat{A}_v required by the control allocation function. The Jacobian matrices \hat{B}_v and \hat{A}_v specify effectiveness of the pseudo controls with reference to the control inputs u and the virtual control inputs y_v [62, 88] respectively.

Definition 3.2.1 (Virtual Control Input (VCI)). Virtual Control Input denotes a state of any system, which can directly produce a change in another physical variable of the same system, thereby providing the possibility of regulating the aforementioned variable of interest by serving as its manipulator.

For example, Eq. (2.70) specifying the bank angle command generation in the C -frame lateral motion description shows that a demand in the lateral acceleration in the control frame $(f_y)_C$ can be fulfilled by producing a bank angle Φ . Although, the bank angle is not a physical control input of any aircraft, yet within the context of the lateral acceleration and bank angle pair, the latter is a pseudo control input for the acceleration command.

The formation of the virtual control effectiveness matrix A_v is discussed next. The outputs y for the given aircraft are divided to form a distinct unit for treatment of the virtual control inputs

$$\begin{matrix} y \\ \left[\begin{array}{c} y_v \\ y_c \end{array} \right] \end{matrix} \triangleq \begin{matrix} C \\ \left[\begin{array}{c} C_v \\ C_c \end{array} \right] \end{matrix} \cdot x, \quad (3.61)$$

where the output matrix $C \in \mathbb{R}^{n_y \times n_x}$ is a unitary matrix, $C_v \in \mathbb{R}^{n_v \times n_x}$ denotes the selection matrix for the virtual control inputs and the matrix $C_c \in \mathbb{R}^{n_{y_c} \times n_x}$ is the remaining complementary part from the output matrix C . Consider an incremental form of the output equation (3.61) $\Delta y = C \cdot \Delta x$. Since C is a unitary matrix, it can be resorted to get the inverse of the incremental output equation $\Delta x = E_C \cdot \Delta y$, where $E_C = [E_v \ E_c]$. Subsequently, this inverse relation is substituted for the incremental state vector in the transformed system dynamics given in Eq. (3.19) yielding

$$\begin{aligned} \Delta \nu &= A_v \cdot E_C \cdot \begin{bmatrix} \Delta y_v \\ \Delta y_c \end{bmatrix} + B_v \cdot \Delta u \\ \Delta \nu &= \begin{bmatrix} A_v & A_c \end{bmatrix} \cdot \begin{bmatrix} \Delta y_v \\ \Delta y_c \end{bmatrix} + B_v \cdot \Delta u. \end{aligned} \quad (3.62)$$

In the preceding equation, the state matrices are given by $A_v = A_v \cdot E_v$ and $A_c = A_v \cdot E_c$. The incremental output term Δy_c is replaced with $C_c \cdot \Delta x$ (based on Eq. (3.61)) yields the incremental state dependent term, which is neglected based on the assumptions

A.3.4 and A.3.5 used for INDI control law derivation

$$\begin{aligned} \Delta \nu &= \mathbf{A}_v \cdot \Delta \mathbf{y}_v + \mathbf{A}_e \cdot \mathbf{C}_c \cdot \Delta \mathbf{x} + \mathbf{B}_\nu \cdot \Delta \mathbf{u} \\ \Delta \nu &\approx \begin{bmatrix} \mathbf{A}_v & \mathbf{B}_\nu \end{bmatrix} \cdot \begin{bmatrix} \Delta \mathbf{y}_v \\ \Delta \mathbf{u} \end{bmatrix}. \end{aligned} \quad (3.63)$$

As stated earlier, the state dependent term is always considered for stability analysis and only neglected for the control law derivation. Furthermore, given a desired pseudo control command, the combined matrix of \mathbf{A}_v and \mathbf{B}_ν can be inverted to compute incremental virtual and physical control input commands. Based on the estimated state vector $\hat{\mathbf{x}}$ and control inputs $\hat{\mathbf{u}}$, the effectiveness matrices are determined in the OBPM

$$\hat{\mathbf{B}}_\nu = \left. \frac{\partial \hat{\mathbf{F}}(\hat{\mathbf{x}}, \hat{\mathbf{u}})}{\partial \hat{\mathbf{u}}} \right|_{(\hat{\mathbf{x}}_0, \hat{\mathbf{u}}_0)} \quad \hat{\mathbf{A}}_v = \left. \frac{\partial \hat{\mathbf{F}}(\hat{\mathbf{x}}, \hat{\mathbf{u}})}{\partial \hat{\mathbf{y}}_v} \right|_{(\hat{\mathbf{x}}_0, \hat{\mathbf{u}}_0)} \quad (3.64)$$

using a single sided numeric perturbation process, whose details are presented in [88]. In addition to the effectiveness matrices, some secondary constraints $\hat{\mathbf{c}}$ are also computed in the OBPM. These constraints include cost functions on control effector utilization and flight phase specific effector positioning to facilitate smooth transition maneuvers. The constraints are formulated as a generic function $\hat{\mathbf{c}} = \hat{\mathbf{F}}_c(\hat{\mathbf{x}}, \hat{\mathbf{u}})$, $\hat{\mathbf{c}} \in \mathbb{R}^{n_c}$ where n_c specifies the number of constraints, which are limited to the surplus of effector commands i.e. $n_\nu + n_c \leq n_u$. If lesser number of secondary objectives are defined than the number which equalizes the total count of objectives to the number of effectors, it would imply that the matrix inversion problem in the CA is not exactly determined. This could result in an undesirable control effector commands from the infinitely many solutions possible for such cases [170]. The sensitivity matrices of the secondary constraints to control inputs and VCIs is estimated similar to the Jacobian matrices in Eq. (3.64). These matrices are provided to the control allocation function, however this is not illustrated in Fig. 3.6.

3.2.2.4 Control Allocation

Control Allocation (CA) deals with computation of the incremental control input as well as the virtual control input commands by solving the linear algebraic expression specified in Eq. (3.63). Besides solving a system of linear equations, redundancy in control effectors and actuator saturations are considered by the control allocation module. Keeping in mind the supplementary constraints affiliated with the problem, the control allocation is described as an optimization of a cost function \mathbf{J} under constraint of a perfect allocation [186–190]

$$\begin{aligned} \min \mathbf{J}(\Delta \mathbf{x}, \Delta \mathbf{u}) \quad \text{subject to} \quad & \Delta \nu_{des} - \begin{bmatrix} \mathbf{A}_v & \mathbf{B}_\nu \end{bmatrix} \cdot \begin{bmatrix} \Delta \mathbf{y}_v \\ \Delta \mathbf{u} \end{bmatrix} = 0, \\ & \Delta \mathbf{u} \in \mathbb{U}, \\ & \Delta \mathbf{y}_v \in \mathbb{V}. \end{aligned}$$

In this optimization representation, the equality constraint signifies the perfect allocation which implies that the goal of achieving the desired pseudo controls is the primary objective of the control allocation problem. The cost function $\mathbf{J}(\Delta \mathbf{x}, \Delta \mathbf{u})$ comprises of

some secondary objectives such as minimization of the control effector/VCI utilization, or drive effector/VCI to preferred values $[\Delta \mathbf{y}_{v,p}, \Delta \mathbf{u}_p]^T$ [190] that can result in goals such as minimization of the drag forces, maintain constant angle of attack during transition, etc. formulated by Eqs.(3.65) and (3.66) respectively

$$\mathbf{J} = \frac{1}{2} \cdot \begin{bmatrix} \Delta \mathbf{y}_v \\ \Delta \mathbf{u} \end{bmatrix}^T \cdot \begin{bmatrix} \Delta \mathbf{y}_v \\ \Delta \mathbf{u} \end{bmatrix} \quad (3.65)$$

$$\mathbf{J} = \frac{1}{2} \cdot \begin{bmatrix} \Delta \mathbf{y}_v - \Delta \mathbf{y}_{v,p} \\ \Delta \mathbf{u} - \Delta \mathbf{u}_p \end{bmatrix}^T \cdot \begin{bmatrix} \Delta \mathbf{y}_v - \Delta \mathbf{y}_{v,p} \\ \Delta \mathbf{u} - \Delta \mathbf{u}_p \end{bmatrix}. \quad (3.66)$$

The definition of secondary objectives is not restricted to the ones defined here. The control subset is given by \mathbb{U} , which includes absolute and rate limits of the effectors

$$\begin{aligned} \mathbb{U} &= \{ \Delta \mathbf{u} \in \mathbb{R}^{n_u} \mid \underline{\Delta \mathbf{u}} \leq \Delta \mathbf{u} \leq \overline{\Delta \mathbf{u}} \} \\ \overline{\Delta \mathbf{u}} &= \min \{ \bar{\mathbf{u}} - \mathbf{u}_0, \quad \bar{\dot{\mathbf{u}}} \cdot \Delta t \} \\ \underline{\Delta \mathbf{u}} &= \max \{ \mathbf{u} - \mathbf{u}_0, \quad \dot{\mathbf{u}} \cdot \Delta t \}. \end{aligned} \quad (3.67)$$

The control subset is defined by the maximum and minimum control input increments represented by $\overline{\Delta \mathbf{u}}$ and $\underline{\Delta \mathbf{u}}$ respectively. These limit magnitudes are specified based on the worst case between the available control input margins ($\bar{\mathbf{u}} - \mathbf{u}_0$ or $\mathbf{u} - \mathbf{u}_0$) and the corresponding effector rate limits ($\bar{\dot{\mathbf{u}}}$ or $\dot{\mathbf{u}}$) (available from actuator characteristics) within the controller sampling time interval Δt . Similarly, the virtual control subset \mathbb{V} is also defined based on the absolute and rate saturations of the variables used as virtual controls

$$\begin{aligned} \mathbb{V} &= \{ \Delta \mathbf{y}_\nu \in \mathbb{R}^{n_{y_\nu}} \mid \underline{\Delta \mathbf{y}_\nu} \leq \Delta \mathbf{y}_\nu \leq \overline{\Delta \mathbf{y}_\nu} \} \\ \overline{\Delta \mathbf{y}_\nu} &= \min \{ \bar{\mathbf{y}}_\nu - \mathbf{y}_{\nu_0}, \quad \bar{\dot{\mathbf{y}}}_\nu \cdot \Delta t \} \\ \underline{\Delta \mathbf{y}_\nu} &= \max \{ \mathbf{y}_\nu - \mathbf{y}_{\nu_0}, \quad \dot{\mathbf{y}}_\nu \cdot \Delta t \}. \end{aligned} \quad (3.68)$$

Since the number of control effectors are often greater than the number of pseudo controls, infinite many solutions are possible to the control allocation problem. Using Moore-Penrose pseudo inverse [191–194] of the combined control input matrix from Eq. (3.63) to get the control input (virtual and physical) increments from the desired pseudo control increments $\boldsymbol{\nu}_{des}$

$$\begin{bmatrix} \Delta \mathbf{y}_{v_{cmd}} \\ \Delta \mathbf{u}_{cmd} \end{bmatrix} = \begin{bmatrix} \mathbf{A}_v & \mathbf{B}_\nu \end{bmatrix}^\dagger \cdot \Delta \boldsymbol{\nu}_{des} \quad (3.69)$$

is the simplest allocation strategy. Moore-Penrose pseudo inverse results in a minimum norm solution, thereby minimizing the allocated control effector increments in the case an exact solution exists. If there is no exact solution, then the Euclidean norm of the allocation error $\|\Delta \boldsymbol{\nu}_{des} - [\mathbf{A}_v \ \mathbf{B}_\nu] \cdot [\Delta \mathbf{u} \ \Delta \mathbf{y}_v]^T\|_2$ is minimized. However, the pseudo inverse solution is invalid if it lies outside of the subsets \mathbb{U} and \mathbb{V} . Treatment of cases in which the pseudo inverse solution lies outside the control subset [168, 169] are presented in [195, 196] by making use of an iterative redistribution of the pseudo inverse

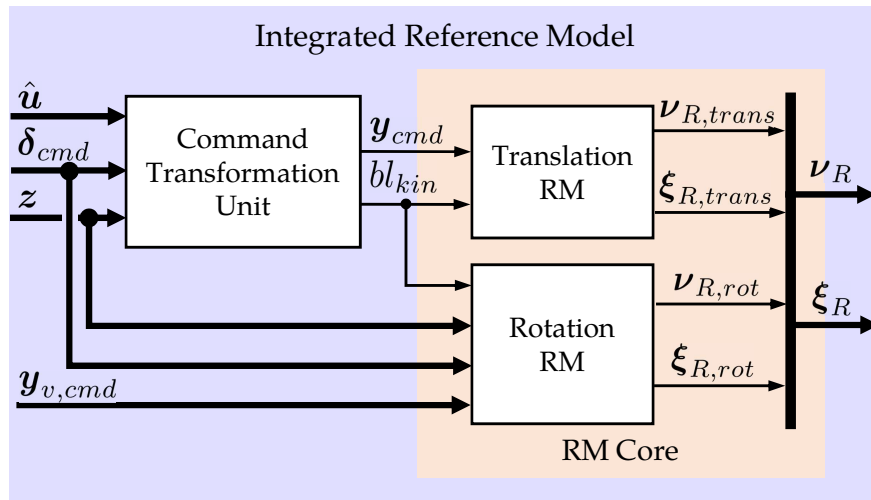


Figure 3.7: *Integrated Reference Model architecture*

solution, with an aim to minimize the allocation error norm. Further improvements to the redistribution algorithm and their application to the VTOL transition aircraft configuration given in section 3.2.1 were published in [189, 190]. Details about the allocation strategy will not be discussed here since it does not lie within the scope of this dissertation. Finally, the presentation of the controller modules employed in the INDI controller framework is concluded. The modular integrated reference model framework will be elucidated next.

3.3 Modular Integrated Reference Model architecture

The Modular Integrated Reference Model architecture, illustrated in Fig. 3.7, is constructed from two main components – Command Transformation and the Reference Model Core module. The purpose of the commands transformation module is to convert the pilot inceptor deflection to a uniform set of Control Variable (CV) commands independent of the current flight phase. The mapped CV commands serve as inputs to the RM core. Even though the inceptor deflections are ultimately transformed to the same set of variables, aircraft response to inceptor inputs evolves over the flight envelope, thereby sustaining an intuitive perception for the pilot over the complete envelope.

The Reference Model Core incorporates the translation and rotation reference models, also known as the outer and inner loop reference models. The outer loop reference models specify the desired translation dynamics through the load factors (translation pseudo controls) and kinematic velocities denoted in the C -frame. Inner loop dynamics are accounted for in the reference plant dynamics of the outer loop RM to generate desired trajectories that are closer to the real aircraft behavior. Reference body angular acceleration (rotation pseudo controls), body angular rates and Euler attitude angle

trajectories are defined by the inner loop reference model. Furthermore, the wind disturbance rejection behavior is explicitly defined through the inner loop RM of the core framework.

Other features of the proposed framework include approaches to keep consistency among all the reference variables during transition to different flight phases. Blending of CVs, flight phase specific body rotation rate command definition along with flight phase dependent slaving of reference states are the strategies engaged to achieve conformance. Subsequently, in order to assist in accurate mapping of the control variables especially in flight conditions with high wind gradients, plant state feedback is used.

Forthcoming section presents the pilot inceptor design aimed at simplifying the flying experience for a VTOL transition aircraft along with the control variables allocated to each inceptor. Design constraints that justify the proposed inceptor-control variable mapping are also provided.

3.3.1 Pilot Inceptor – Control Variables

For manual flight operation of the given configuration, the Human Machine Interface (HMI) comprises of a dual inceptor design concept illustrated by the Fig. 3.8 [87, 148]. The two inceptors are designated as the Throttle stick δ_T and the Climb stick δ_c . The Throttle stick features hybrid haptic characteristics by combining spring-centered and spring-free regions along the longitudinal deflection range of the inceptor. The forward (up) deflection of the Throttle stick is denoted as $\delta_{T,up}$ and the backward (low) deflection is given by $\delta_{T,lo}$. Furthermore, one detent and three indents have been included in the Throttle stick design to enhance situational awareness of the pilot. These haptic elements correspond to

1. Beginning of the transition phase
2. Command to power down the main LTUs and enter wingborne flight phase
3. Thrust lever position for maximum endurance
4. Thrust lever position for maximum range.

In the lateral deflection range, the Throttle stick retains a spring-centered behavior at all positions. The right and left deflections of the Throttle stick are described by $\delta_{T,r}$ and $\delta_{T,l}$ respectively.

Contrary to the hybrid design of the Throttle stick, the Climb stick possesses a spring-centered behavior for deflections in any direction. The nomenclature of the Climb stick deflections are consistent to that of the Throttle stick. The forward and backward Climb stick travel is represented by $\delta_{c,up}$ and $\delta_{c,lo}$ respectively. Moreover, the right and left deflections are expressed as $\delta_{c,r}$ and $\delta_{c,l}$. Comprehensive information about the design of the control inceptors is recorded in [148].

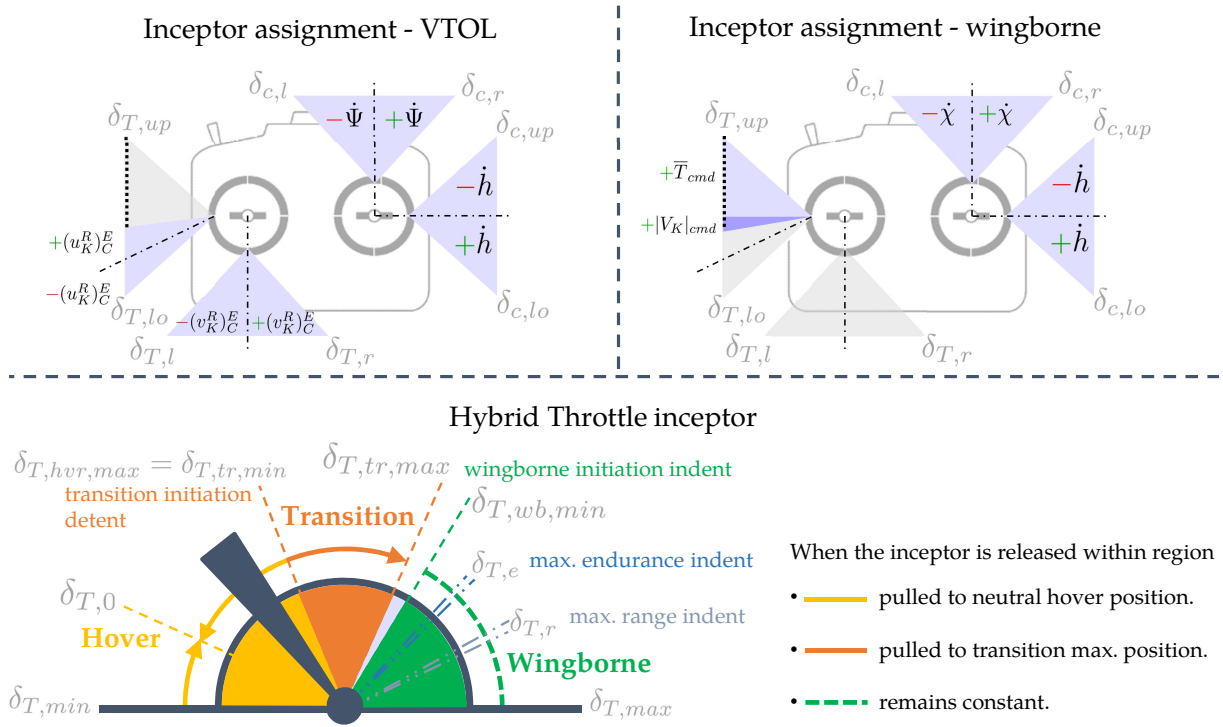


Figure 3.8: Inceptor assignment in all flight phases of the VTOL transition aircraft [87, 148]

The allocation of the control variable commands to each of the pilot inceptor deflection is performed based on three degrees of freedom.

1. **Intuitive perception for the pilot** is a factor of utmost importance, which drives the selection of the control variables and their allocation to suitable inceptor commands. Accordingly, the chosen commands in each flight phase must closely conform with the corresponding conventional command variables for single phase configurations such as fixed-wing aircraft or VTOL aircraft like multicopters.
2. Secondly, existence of a **unique mapping between each set of control variables for every flight phase** is a prerequisite for the decision on the CV choice. The chosen variables for any flight phase must allow a direct physical conversion, based on aircraft dynamics, to the control variables in the other phases, such that a smooth blending of the CVs can be ensured in the transition phases.
3. The chosen set of commands must lead to the **same set of pseudo control and reference external states** over the complete flight envelope, thereby facilitating a unified controller architecture for the flight control of the VTOL transition aircraft.

Adhering to the presented constraints, control variables for manual flight operation of the considered tilt-rotor VTOL transition aircraft configuration are defined in Table 3.3.

In the hover flight phase, the pilot stick commands relate to kinematic velocities $[(u_K^R)^E_C, (v_K^R)^E_C, (w_K^R)^E_C]^T$ denoted in the control frame along with the heading angle rate $\dot{\Psi}$. The forward $(u_K^R)^E_C$ and lateral kinematic velocities $(v_K^R)^E_C$ are commanded through the spring centered deflections of the Throttle stick. The up-down stick travel relates to the forward kinematic velocity command while the lateral kinematic velocity is commanded by the left-right deflection. Consequently, the spring centered region of the Throttle stick determines the motion of the aircraft in the horizontal plane such that the direction

Inceptor Deflection	Control Variables	
	Hover	Forward-flight
Throttle Stick up-down $\delta_{T,up,lo}$ (spring-centered)	$(u_K^R)_C^E$	–
Throttle Stick up-down $\delta_{T,up,lo}$ (spring-free)	–	$ V _K, \bar{T}$
Throttle Stick left-right $\delta_{T,l,r}$	$(v_K^R)_C^E$	–
Climb Stick up-down $\delta_{c,up,lo}$	$(w_K^R)_C^E$	$(w_K^R)_C^E$
Climb Stick left-right $\delta_{c,l,r}$	$\dot{\Psi}$	$\dot{\chi}$

Table 3.3: Flight phase specific Control Variables set intended for manual flight operation of the tilt-rotor VTOL transition aircraft

of the stick deflection corresponds to the intended command direction of the aircraft's kinematic motion by the pilot. By deflecting the Climb stick to the right or left, the pilot can command a positive or negative heading angle rate thereby rotating the nose of the aircraft to any desired heading. Moreover, pulling the Climb stick leads to a positive height rate and vice-versa command is generated by pushing it forward. Overall, there are two major differences in the inceptor behavior as compared to conventional dual stick inceptor configuration for multicopters. Firstly, the up-down deflection interpretation of the Climb stick is chosen such that it resembles the pull-up and push-down behavior of the inceptor for a fixed-wing aircraft. This makes sure that the vertical channel inceptor perception remains constant over the complete flight envelope. Secondly, the Throttle stick has a relatively small spring centered range in order to incorporate a high resolution for the wingborne region.

The command variables in forward flight phases – transition and wingborne are assigned with an aim to facilitate active flight path control. Thereupon, absolute kinematic velocity, forward thrust, height rate and side-force free coordinated course angle rate are employed as control variables in this flight regime. For forward translation, the region at the end of the spring centered region in the Throttle inceptor (labeled by end of hover phase in Fig. 3.8) marks the beginning of the transition phase commands. Absolute kinematic velocity is assigned as the command variable to the stick deflection in this region until the indent for the wingborne phase. Once the pilot places the stick at this indent, a thrust level sufficient to maintain $1.2 \cdot V_{stall}$ is commanded to the tilt propellers. Alongside, indents that indicate maximum endurance and range thrust levels are integrated in the spring-free region. The pilot has to actively push the thrust lever over these indents to command higher thrust levels. Therefore, these elements also offer a haptic feedback to the pilot. The intuitive factor pertaining to the piloted flight missions is enhanced by the interplay between the inceptor haptics and the changing command variables.

Conversely, the aircraft response to the Climb stick commands in the forward-velocity phases remains consistent to that in the hover flight. However, the physical means of generation for the desired responses varies. While in the hover flight, the height rate change is regulated through the powered-lift from the main and tilt LTUs, the commanded height rate is achieved by varying aerodynamic lift through the aerodynamic Angle-of-Attack (AoA) in the wingborne phase. The transition flight is a mixed-lift flight phase in which the powered-lift is commanded complementary to the available aerodynamic lift at a constant aerodynamic AoA. The sideways deflection of the Climb stick results in a course angle change through a coordinated bank-to-turn maneuver. Nonetheless, the ultimate effect of deflecting the Climb stick sideways is to turn the nose of the aircraft, which is equivalent to the heading angle rate response in hover flight. Overall, the Climb stick response behavior remains compatible with the side stick response in a fixed-wing aircraft.

An intuitive set of control variables for each flight phase of the VTOL transition aircraft have been proposed in this segment. The proposed control variables are agnostic of the aircraft configuration. The second constraint in control variable choice is to have a unique mapping between each set of control variables, which is carried out by the *Command Transformation* unit of the integrated reference model.

3.3.2 Command Transformation

The command transformation unit forms the link between the HMI and the reference model core, and by extension to the unified flight control law. Three main functions are carried out in this module

1. Mapping of the inceptor deflection read-outs to physical control variable commands for each flight phase.
2. Transformation of each flight phase specific CV-set to a uniform set of commands provided to the RM core.
3. Calculation of interim quantities essential for implementing a consistent control variable transformation.

As stated in the previous section, the inceptor commands are assigned to physical variables based on the current flight phase in order to establish a consistent aircraft response throughout the flight envelope. For the dual inceptor concept illustrated in Fig. 3.8, the control variables for the three major flight phases of transition vehicles are proposed

$$\begin{array}{ccc}
 \text{Hover} & \text{Transition} & \text{Wingborne} \\
 \mathbf{y}_{cmd,hvr} = \begin{bmatrix} (u_K^R)_C^E \\ (v_K^R)_C^E \\ (w_K^R)_C^E \\ \dot{\Psi} \end{bmatrix} & \mathbf{y}_{cmd,tr} = \begin{bmatrix} |V|_K \\ 0 \\ (w_K^R)_C^E \\ \dot{\chi} \end{bmatrix} & \mathbf{y}_{cmd,wb} = \begin{bmatrix} \bar{T} \\ 0 \\ (w_K^R)_C^E \\ \dot{\chi} \end{bmatrix} \cdot \quad (3.70)
 \end{array}$$

The final objective of the transformation module is to convert the three command sets enlisted in Eq. (3.70) to one unique command vector for the core component of the reference model. Since the absolute kinematic velocity $|V|_K$ can be transformed to the C -frame velocity vector $(\vec{V}_K^R)_C^E$, owing to the kinematic relation specified later in the Eq. (3.74), the hover control variables from Eq. (3.70) are chosen as the command set into which the remaining control variables are transformed. Figure 3.9 demonstrates the diagrammatic view for the transformation of the transition and wingborne control variable sets to the hover control variables.

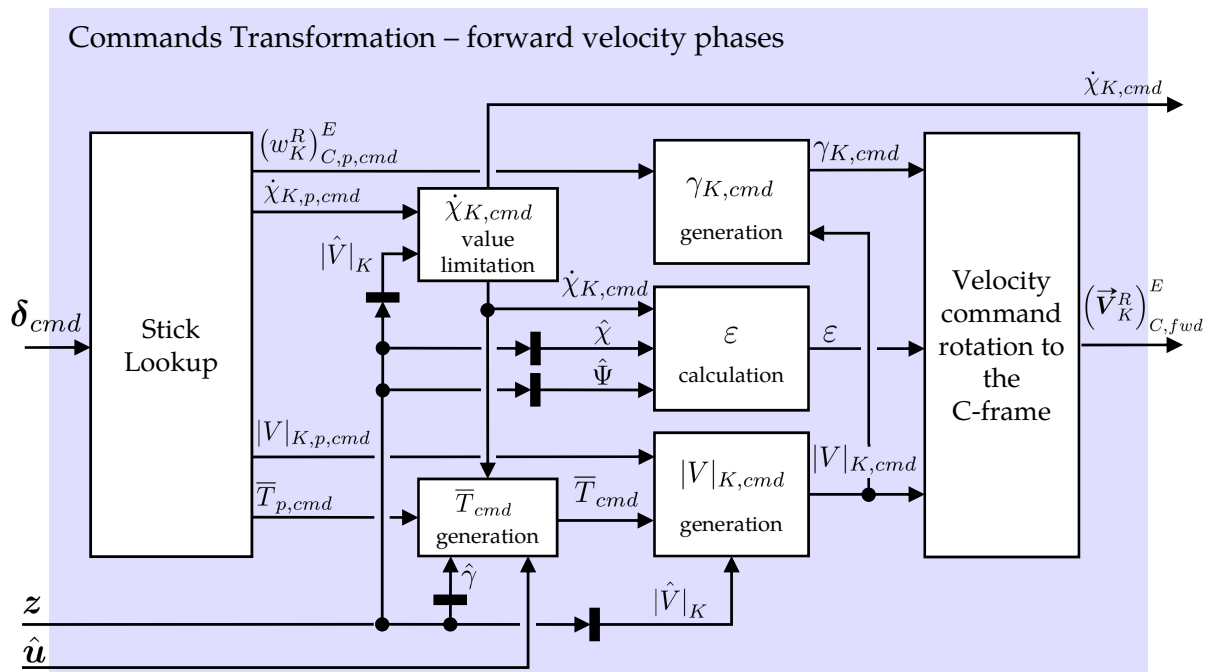


Figure 3.9: Transformation of forward-velocity flight phases control variables to RM core commands [82]

Stick Lookup Mapping

The first step is the conversion of the stick deflections to the intended variables, which is performed by the *Stick Lookup* block in the Fig. 3.9. This functional block contains one dimensional look-up tables for each stick deflection channel. Every lookup-table outputs a control variable magnitude corresponding to a stick deflection magnitude. The output of the *Stick Lookup* comprises of the thrust level command $\bar{T}_{p,cmd}$, absolute kinematic velocity $|V|_{K,p,cmd}$, course angle rate $\dot{\chi}_{K,p,cmd}$ and the vertical velocity command denoted in the control frame $(w_K^R)_C,p,cmd$. The C -frame vertical velocity is equal to the negative of the height rate perpendicular to the ground. The subscript p refers to the command variable value mapped directly from the stick deflection. The generalized conversion from stick to command variable employed in this implementation can be described

through a saturated linear element

$$CV = \begin{cases} K_{\delta \rightarrow CV} \cdot \delta & , \text{ if } \delta_{min} \leq \delta \leq \delta_{max} \\ K_{\delta \rightarrow CV} \cdot \delta_{min} & , \text{ if } \delta < \delta_{min} \\ K_{\delta \rightarrow CV} \cdot \delta_{max} & , \text{ if } \delta > \delta_{max} . \end{cases} \quad (3.71)$$

Here $CV \in \mathbb{R}$ denotes the magnitude of the mapped control variable, $\delta \in \mathbb{R}$ corresponds to the inceptor deflection commanded by the pilot and $K_{\delta \rightarrow CV} \in \mathbb{R}$ is the linear conversion factor from the stick deflection to the command magnitude. All the mapped commands are clipped to their lower and upper limits in the lookup conversion to avoid absurd output values in case the stick read-out is erroneous or out of bounds. The generalized mapping provided in Eq. (3.71) conforms with the mappings for spring-centered inceptors. However, the hybrid Throttle inceptor is interpreted through a piecewise-linear function meant for each of the three regions complementing the concept illustrated in Fig. 3.8.

Figure 3.10 shows the Throttle stick to corresponding command variable mapping for the full flight envelope of the considered aircraft configuration. When the Throttle stick lies in its spring-centered (hover phase) region, the inceptor deflection value is specified linearly between the maximum $(u_K^R)^E_{C,hvr,max}$ and the minimum $(u_K^R)^E_{C,hvr,min}$ forward velocities in the control frame. If the pilot stops applying force on the inceptor, it is pulled to its neutral position denoted by $\delta_{T,0}$ (also see Fig. 3.8). The most backward stick deflection is specified through $\delta_{T,min}$. When the pilot wants to accelerate to the transition phase, they need to actively push the inceptor over the detent at $\delta_{T,hvr,max}$. This detent position is also equal to the stick value $\delta_{T,tr,min}$, which signifies the pilot command to commence the transition. The interpreted control variable after this point is the absolute kinematic velocity $|V|_K$ whose minimum and maximum magnitudes are given as $|V|_{K,tr,min}$ and $|V|_{K,tr,max}$ respectively.

Beyond the transition-start detent, the Throttle inceptor is automatically pulled towards the indent between the positions $\delta_{T,tr,max}$ and $\delta_{T,wb,min}$ if the pilot does not exert any force on the stick. Once the inceptor is placed in this indent, a minimum value of traction thrust level capable of sustaining wingborne flight is commanded to the tilt thrust units. The pilot can further increase the traction thrust and place the stick in the maximum endurance $\delta_{T,e}$ or maximum range $\delta_{T,r}$ indents. Here the thrust levels for maximum endurance or range are commanded. In the inceptor range that corresponds to the wingborne flight, the inceptor behaves like a conventional fixed-wing aircraft's Throttle stick.

The sole difference between the transition phase and the wingborne commands is the forward translation control variable. Thrust level of the tilting thrust units is commanded in wingborne flight due to a variety of reasons that are configuration specific. The tilt-rotor transition aircraft presented in section 3.2.1 does not possess an airspeed sensor. Besides, the maximum cruise airspeed of the aircraft is just 5 m/s greater than the stall airspeed. Consequently, controlling kinematic velocity in wingborne flight brings high susceptibility to stall in tailwinds. However, if the airspeed measurement is available,

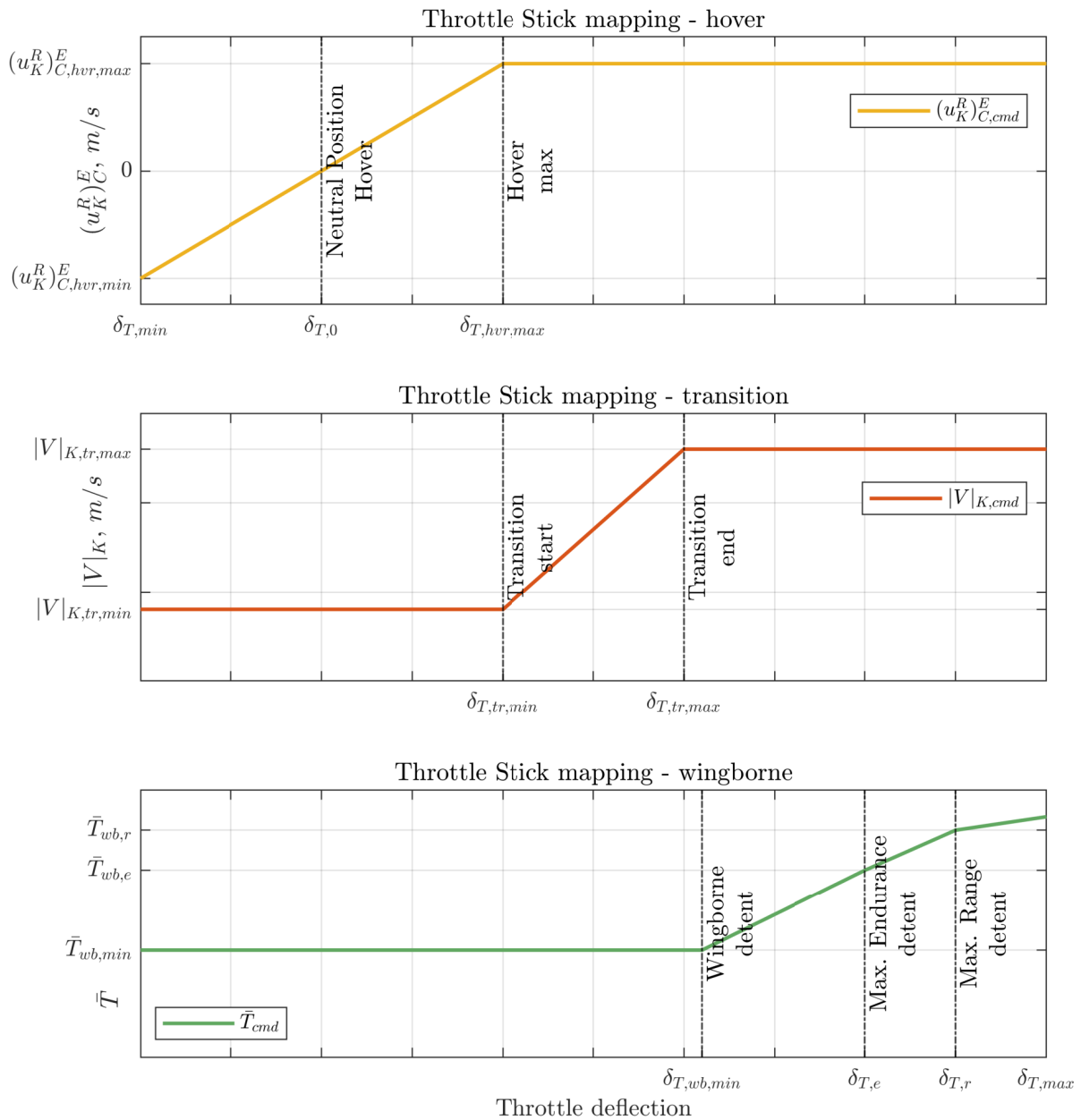


Figure 3.10: Hybrid Throttle inceptor command variable mapping

the thrust level command can be replaced by an airspeed command in the wingborne flight phase. Next the commands transformation algorithm is detailed starting from the last element *Velocity commands rotation to the C-frame* and then move to the elements upstream in Fig. 3.9.

Velocity commands rotation to the C-frame

As stated earlier, the absolute kinematic velocity

$$\begin{pmatrix} \vec{V}_K^R \end{pmatrix}_K^E = \begin{bmatrix} |V|_K \\ 0 \\ 0 \end{bmatrix}, \quad (3.72)$$

when specified as a vector quantity can be transformed to the velocity vector denoted in the control frame through the frame rotation from the kinematic K frame to the control C frame. Ergo, the next step is the calculation of the angles that form the frame rotation matrix $\mathbf{M}_{CK} \in \mathbb{R}^{3 \times 3}$

$$\mathbf{M}_{CK} = \begin{bmatrix} \cos \gamma_K \cdot \cos (\chi_K - \Psi) & -\sin (\chi_K - \Psi) & \sin \gamma_K \cdot \cos (\chi_K - \Psi) \\ \cos \gamma_K \cdot \sin (\chi_K - \Psi) & \cos (\chi_K - \Psi) & \sin \gamma_K \cdot \sin (\chi_K - \Psi) \\ -\sin \gamma_K & 0 & \cos \gamma_K \end{bmatrix}. \quad (3.73)$$

The rotation matrix presented in Eq. (3.73) can transform a three dimensional vector specified in the kinematic frame to an equivalent vector denoted in the control frame by utilizing the kinematic climb angle $\gamma_K \in \mathbb{R}$ along with the difference between the kinematic course angle $\chi_K \in \mathbb{R}$ and the heading angle $\Psi \in \mathbb{R}$. In the description of the lateral motion in the control frame (section 2.3.4), the horizontal kinematic side slip angle $\varepsilon \in \mathbb{R}$ was defined as the difference between the course angle and the heading angle in Eq. (2.55). Emanating from this concept, the term $\chi_K - \Psi$ is replaced by the horizontal kinematic angle ε in the rotation matrix from Eq. (3.73). Subsequently, the computation of the velocity vector command denoted in the C -frame is simplified as the multiplication of the first column of the frame rotation matrix \mathbf{M}_{CK} with the absolute kinematic velocity command

$$\left(\vec{\mathbf{V}}_K^R\right)_{C, fwd}^E = \begin{bmatrix} \cos \gamma_{K, cmd} \cdot \cos \varepsilon \\ \cos \gamma_{K, cmd} \cdot \sin \varepsilon \\ -\sin \gamma_{K, cmd} \end{bmatrix} \cdot |V|_{K, cmd}, \quad (3.74)$$

where $\left(\vec{\mathbf{V}}_K^R\right)_{C, fwd}^E \in \mathbb{R}^3$ represents the mapped velocity vector written in the control frame for the forward-velocity phases. Climb angle command $\gamma_{K, cmd} \in \mathbb{R}$ and the horizontal kinematic side-slip angle $\varepsilon \in \mathbb{R}$ are employed in the calculation exhibited by Eq. (3.74). The computation of these angles is described further.

Angle calculations for Command Transformation

The commanded climb angle $\gamma_{K, cmd} \in \mathbb{R}$ is calculated from the vertical velocity command $(w_K^R)_{C, p, cmd}^E \in \mathbb{R}$, which is mapped from the Climb stick up-down deflection (see Fig. 3.9), and the absolute kinematic velocity command $|V|_{K, cmd} \in \mathbb{R}$

$$\gamma_{K, cmd} = \arctan \left(\frac{-(w_K^G)_{C, cmd}^E}{\sqrt{|V|_{K, cmd}^2 - [(w_K^G)_{C, cmd}^E]^2}} \right). \quad (3.75)$$

The horizontal kinematic side slip angle ε is computed as

$$\varepsilon = \chi_{K, pred} - \hat{\Psi}. \quad (3.76)$$

Here $\hat{\Psi} \in \mathbb{R}$ indicates the feedback of the heading angle and $\chi_{K, pred} \in \mathbb{R}$ is the predicted course angle in accordance with the course angle rate command $\dot{\chi}_{K, cmd} \in \mathbb{R}$ and the course angle feedback $\hat{\chi}_K$. Within the scope of the course angle prediction,

firstly the course angle rate command is synchronized by use of the lower order equivalent representation of the bank angle dynamics denoted by the transfer characteristics $G_{\phi_{cmd} \rightarrow \dot{\phi}}$

$$\dot{\chi}_{K,comp} = G_{\phi_{cmd} \rightarrow \dot{\phi}}(s) \cdot \dot{\chi}_{K,cmd}. \quad (3.77)$$

As pointed out in section 2.3.4, the course angle rate builds up through the bank angle in forward-velocity phases, therefore the bank angle dynamics are employed to aid in a physically reasonable prediction of the true course angle rate represented by the compensated course angle rate $\dot{\chi}_{K,comp} \in \mathbb{R}$. In Eq. (3.77), the bank angle transfer characteristics $G_{\phi_{cmd} \rightarrow \dot{\phi}}$ are simply the bank angle reference dynamics specified in the reference model core. However, it is clear that the reference dynamics are not exactly followed at all times in a flight mission. Any external disturbances can lead to diversion from the course angle rate response computed in Eq. (3.77). Subsequently, deviation between the estimated course angle $\hat{\chi}_K \in \mathbb{R}$ obtained through sensor measurements and the predicted course angle $\chi_{K,pred} \in \mathbb{R}$ is incorporated through a Luenberger gain $L_{\chi,pred} \in \mathbb{R}$ in order to mitigate this divergence

$$\dot{\chi}_{K,pred} = \dot{\chi}_{comp} + L_{\chi,pred} \cdot (\hat{\chi} - \chi_{K,pred}), \quad (3.78)$$

where the predicted course angle $\chi_{K,pred} \in \mathbb{R}$ is simply obtained through integration of the predicted course angle rate $\dot{\chi}_{K,pred} \in \mathbb{R}$. Linear phase plane based protections for the external reference states and pseudo controls are incorporated in the reference model (see section 3.1.2.1), which employed back propagation of the lower order derivatives to compute the higher order limits. In that case, the limits corresponding to every reference state are not a function of any other variable. However, limits for course angle rate can vary depending on the kinematic ground speed. In the *command value limitation function for the course angle rate* (Fig. 3.9), the course angle pilot command $\dot{\chi}_{K,p,cmd}$ is limited based on the measured absolute kinematic velocity $|\hat{V}|_K$. For this purpose, the given kinematic relation for a coordinated turn [197–199] is employed

$$\tan \mu_K = \frac{|V|_K \cdot \dot{\chi}_K}{g}, \quad (3.79)$$

Here $\mu_K \in \mathbb{R}$ denotes the kinematic bank angle and $g \in \mathbb{R}$ represents the acceleration due to gravity. According to the relation in Eq. (3.79) the turn rate $\dot{\chi}_K$ varies proportionally with the kinematic bank angle. This implies that the turn rate is limited by the maximum available bank angle in any forward flight condition. Given the maximum available lift force, the maximum achievable kinematic bank angle can be calculated

$$k \cdot m \cdot g = \frac{1}{2} \cdot \rho_A \cdot V_{A,still}^2 \cdot S \cdot C_{L,max} \cdot \cos \mu_K, \quad (3.80)$$

$$\mu_{K,max} = \arccos \left[\frac{2 \cdot k \cdot m \cdot g}{\rho_A \cdot V_{A,still}^2 \cdot S \cdot C_{L,max}} \right], \quad (3.81)$$

where $k \in \mathbb{R}$ is a factor of safety meant to maintain a buffer against stall, $m \in \mathbb{R}$ represents the mass of the aircraft, $\rho_A \in \mathbb{R}$ symbolizes the air density, $V_{A,still} \in \mathbb{R}$ is the stall airspeed and $S \in \mathbb{R}$ denotes the surface area. The maximum lift coefficient $C_{L,max}$ at any airspeed

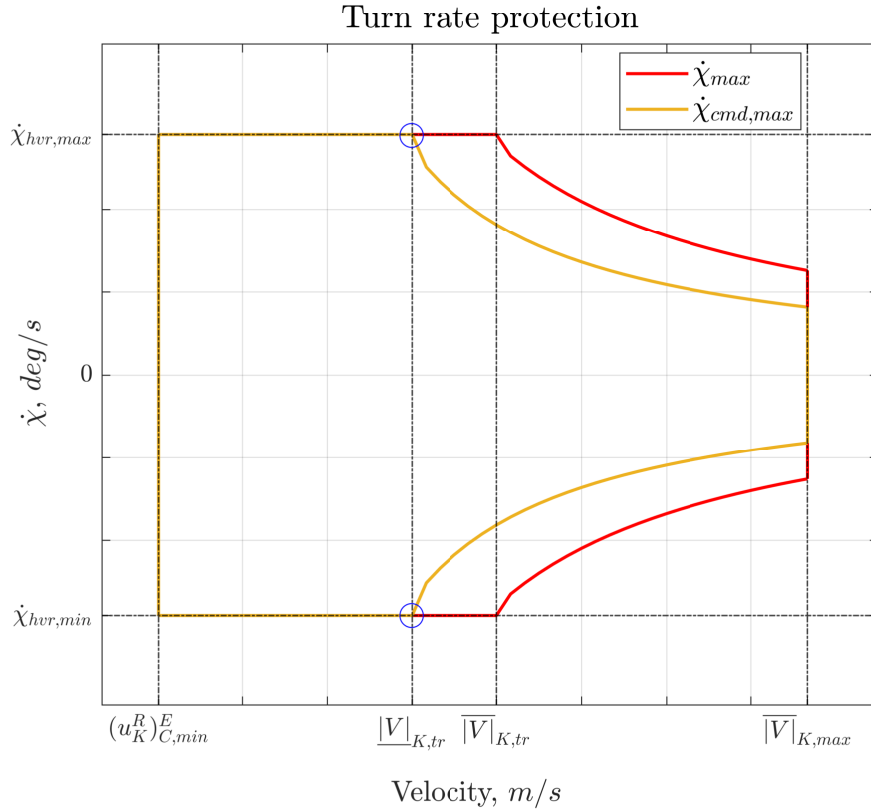


Figure 3.11: Kinematic velocity dependent phase-plane envelope protection for turn rate

occurs at the stall angle of attack for a given airspeed. The stall airspeed is utilized to remain conservative in the calculation of the maximum kinematic bank angle. The resultant kinematic bank angle limitation in Eq. (3.80) is built up from two elements – the maximum command-able bank angle $\mu_{K,cmd,max}$ and the maximum bank angle buffer retained for disturbance rejection $\mu_{K,\Delta,max}$. Certainly, the command value bounds of the turn rate $\dot{\chi}_{K,cmd,max}$ are obtained through the former limit values of the kinematic bank angle through use of the relation in Eq. (3.79)

$$\dot{\chi}_{K,cmd,max} = \frac{g \cdot \tan \mu_{K,cmd,max}}{|V|_K}. \quad (3.82)$$

Figure 3.11 demonstrates the variation of the turn rate limits with respect to the kinematic velocity. In the hover flight phase region, which is represented from minimum hover velocity $(u_K^R)_C,min^E$ to the minimum kinematic velocity $|V|_{K,tr}$ marking the start of the transition phase, the turn rate limits stay constant. In practice the course angle rate is not defined for zero kinematic velocities in the hover phase. Therefore, the illustrated constant turn rate limits are in essence the heading angle rate bounds for the command values in the hover phase. The relation derived in Eq. (3.80) is employed to yield the turn rate limits above the minimum absolute kinematic velocity for transition $|V|_{K,tr}$. The maximum course angle rate command $\dot{\chi}_{K,cmd,max}$ limits denoted by $\dot{\chi}_{hvr,max}$ and $\dot{\chi}_{hvr,min}$ at the minimum transition velocity $|V|_{K,tr}$ imply that the maximum magnitude of the kinematic bank angle $\mu_{K,cmd,max}$ has to be actively selected in order to lead to $\dot{\chi}_{K,max}$ at $|V|_{K,tr}$. Beyond the minimum transition velocity $|V|_{K,tr}$, the difference between the bounds $\dot{\chi}_{max}$ and $\dot{\chi}_{cmd,max}$ is that the latter only refers to the bounds enforced on the

command values and they are directly derived from the maximum allowable command limit for the kinematic bank angle. The absolute turn rate limit $\dot{\chi}_{max}$ incorporates the margin that is preserved for disturbance rejection.

Absolute velocity command generation

The absolute velocity command is built up from one of the two sources depending on the aircraft's current flight phase. In the transition phase, the command value is directly provided by the magnitude mapped in the *Stick Lookup* function. As previously exhibited through Fig. 3.10, the mapped pilot kinematic velocity command $|V|_{K,p,cmd}$ is given by the Throttle inceptor range within the positions $[\delta_{T,tr,min}, \delta_{T,tr,max}]$ for the transition phase. Additionally, a thrust level of the tilt thrust units are commanded during the wingborne flight depending on the deflection in the Throttle inceptor range $[\delta_{T,wb,min}, \delta_{T,max}]$. Consequently, to sustain a consistent command interface in the wingborne phase, an absolute velocity command needs to be produced from a given thrust level command. In this respect, first the estimated thrust level generated by the tilting thrust units is calculated

$$\bar{T}_{est} = \frac{\hat{\omega}_L^2 \cdot \sin \hat{\delta}_L + \hat{\omega}_R^2 \cdot \sin \hat{\delta}_R}{\omega_{L,max}^2 + \omega_{R,max}^2}, \quad (3.83)$$

where the angular rates of the left and right tilt propulsors $\hat{\omega}_L \in \mathbb{R}$, $\hat{\omega}_R \in \mathbb{R}$ are estimated by the first order LTU models given by Eq. (3.57) in the description of the *Estimation* module (section 3.2.2.1). Likewise, the estimators of the left and right tilt deflection angles $\hat{\delta}_L \in \mathbb{R}$, $\hat{\delta}_R \in \mathbb{R}$ are also incorporated in the *Estimation* module. However, second order elements mentioned in Eq. (3.56) are employed to model the tilt actuators. Following the estimated thrust level computation, an absolute velocity increment command is obtained based on the difference between the commanded and the estimated thrust level

$$\Delta|V|_{K,cmd} = K_{V,cmd} \cdot (\bar{T}_{cmd} - \bar{T}_{est}). \quad (3.84)$$

The gain $K_{V,cmd} \in \mathbb{R}$ is chosen based on the aircraft mass and the desired kinematic velocity response required in the wingborne flight. The absolute velocity command increment computed in Eq. (3.84) is then added to the measured/estimated absolute kinematic velocity $\hat{V}|_K$ to finally result in the kinematic velocity command derived from the thrust level command

$$|V|_{K,\bar{T},cmd} = \hat{V}|_K + \Delta|V|_{K,cmd}. \quad (3.85)$$

Depending on which flight phase is active, either the absolute velocity command mapped from the *Stick Lookup* function $|V|_{K,p,cmd} \in \mathbb{R}$ or the command generated through the thrust level $|V|_{K,\bar{T},cmd} \in \mathbb{R}$ is selected. The information of the active flight phase is determined by the *System Automation* functionality through consideration of pilot stick position, state feedback and control input commands for the main LTUs produced by the INDI controller. Generation of flight phase activation flags relating to transition and re-transition procedures are implemented through a state machine framework

presented in [200, 201]. The thrust level command is enabled when the pilot has placed the hybrid thrust inceptor at or beyond the wingborne indent $\delta_{T,wb,min}$. Since the velocity command is calculated through the desired thrust level increment and the feedback of the true ground speed, no discontinuous behavior is observed in the kinematic velocity response at the instant of change from pilot stick based velocity command to the velocity command calculated from the thrust level command in Eq. (3.85). Figure 3.27 verifies the continuous forward velocity response behavior in transition to wingborne and re-transition to hover flight phases.

Thrust level command generation

Instead of absolute thrust, a normalized thrust level command is employed to reduce the dependency on model knowledge. Model parameters in terms of thrust coefficients would be required to estimate the current thrust if absolute thrust was used as the control variable. Therefore, normalized thrust produced by the combination of the two tilt thrust units, as exhibited in Eq. (3.83), is defined as the control variable for the forward translation channel in wingborne flight. However, a full deflection of the thrust inceptor by the pilot does not correspond to a command equal to the maximum limit of the tilt thrust unit propellers. A reserve is saved for maintaining the climb performance because the impact of the climb angle command (Eq. (3.75)) is not accounted for in the calculation of the kinematic velocity command increment $\Delta|V|_K$. Performing a climb maneuver at a constant thrust setting leads to a deceleration in the longitudinal channel as the aircraft's kinetic energy is used to gain altitude, and this phenomenon is called bleeding.

In order to prevent this phenomenon, a total energy conservation approach [202] is employed to design a compensation for the climb angle command. The first step is to define the total energy of the aircraft which is the sum of the aircraft kinetic $E_{kin} \in \mathbb{R}$ and potential energy $E_{pot} \in \mathbb{R}$

$$E_{total} = E_{pot} + E_{kin} = m \cdot g \cdot h + \frac{1}{2} \cdot m \cdot |V|_K^2. \quad (3.86)$$

Here $h \in \mathbb{R}$ denotes the height above ground level. Deriving Eq. (3.86) yields the energy rate

$$\dot{E}_{total} = m \cdot g \cdot \dot{h} + m \cdot |V|_K \cdot \dot{|V|}_K. \quad (3.87)$$

The first term in the total energy derivative from Eq. (3.87) corresponds to the rate of change of the aircraft potential energy, which depends on the aircraft height rate $\dot{h} \in \mathbb{R}$. The height rate is related to the climb angle $\gamma_K \in \mathbb{R}$ according to

$$\dot{h} = |V|_K \cdot \sin \gamma_K. \quad (3.88)$$

Substitution of the height rate from Eq. (3.88) in the total energy rate (Eq. (3.87)), and further division by the aircraft mass $m \in \mathbb{R}$ on both sides results in the specific energy rate of the aircraft in terms of the climb angle

$$\frac{\dot{E}_{total}}{m} = (g \cdot \sin \gamma_K + \dot{|V|}_K) \cdot |V|_K. \quad (3.89)$$

The rate at which the energy enters the system is also equal to the specific excess power generated by the tilt LTUs

$$\frac{\dot{E}_{total}}{m} = \frac{(T - D) \cdot |V|_K}{m}. \quad (3.90)$$

Subsequently, comparison of the Eqs. (3.89) and (3.90) returns the excess thrust T_{ex} incorporating the effect of the climb angle

$$T_{ex} = (T - D) = m \cdot |\dot{V}|_K + m \cdot g \cdot \sin \gamma_K. \quad (3.91)$$

Since, a thrust command level is used as the control variable, the excess thrust described in Eq. (3.91) is normalized with respect to the maximum thrust of the tilt propulsion units $T_{max} = \omega_L^2 + \omega_R^2$

$$\frac{T_{ex}}{T_{max}} = \frac{\bar{T}_V}{\frac{m \cdot |\dot{V}|_K}{T_{max}}} + \frac{\bar{T}_\gamma}{\frac{m \cdot g \cdot \sin \gamma_K}{T_{max}}}, \quad (3.92)$$

where the compensation necessary to avoid bleeding of the horizontal velocity is provided by the term \bar{T}_γ . Consequently, the thrust level command compensated for the climb angle command is provided by

$$\bar{T}_{cmd,comp} = \bar{T}_{cmd} + \frac{m \cdot g \cdot \sin \gamma_{K,cmd}}{T_{max}}. \quad (3.93)$$

Important to note that the compensated thrust level command $\bar{T}_{cmd,comp}$ is ultimately employed in Eq. (3.84) to produce the absolute kinematic velocity command increment. Through this chain, it is ensured that the cumulative reduction in forward thrust due to the upcoming build-up of the real flight path angle γ_K is already considered in the command generation. Consequently, the feedforward reference pseudo controls and the reference external states are also defined accordingly in the *Reference Model Core*.

Herewith, the generation of three set of control variables each for the hover, transition and wingborne phases of the VTOL transition aircraft, as defined in Eq. (3.70), is completed. Through the *Commands Transformation - forward velocity phases*, control variable sets of the transition and wingborne phases are converted to a group matching the hover control variables. This CV group generated for the transition and wingborne phases will further be addressed as the forward velocity CV set. Remember that the variables in the commands interface to the reference model core for all flight phases maintain the same definition as the hover phase control variables. Accordingly, the hover and forward velocity control variables need to be merged appropriately such that they conform with the active flight phase. The enforcement of a flight phase dependent compliance not only applies to the commands but also to the internal variables of the reference model core. Therefore, the *Reference Model Core* is presented in the next section before detailing the strategies used for enforcing compliance among all reference variables.

Flight-phase reliant pilot inceptor interpretation demonstrated in the section 3.3.1 along with the *Commands Transformation - forward velocity phases* module proposed in this section provide the realization of the contribution **C.2.1 Flight phase dependent mappings for pilot command variables contained within the reference model**.

3.3.3 Reference Model Core

The reference model core architecture comprises of decoupled translation (outer loop) and rotation (inner loop) reference models. As the name suggests, the translation reference model generates the desired trajectories pertaining to the translation states. The reference pseudo controls produced by the outer loop RM are the load factors expressed in the C -frame and the translation reference external states include the velocity vector denoted in the control frame. Collectively, they compose the desired behavior for the velocity commands constituted from the control variable sets defined in Eq. (3.70).

Likewise, the rotation reference model defines the reference external state trajectories for Euler attitude angles, Euler attitude angle rates, and body angular rates along with the body angular accelerations as the reference pseudo controls. Virtual Control Inputs (VCI) (see section 3.2.2.3) comprising of bank and pitch angle commands along with the heading angle rate command mapped from pilot inceptor deflections serve as inputs to the rotation reference model. Through the VCIs, the rotation reference model specifies the rotational accelerations required to achieve the desired load factors by changing the direction of the available control forces.

The Euler angle commands in the virtual control inputs are calculated by the summation of an attitude angle increment command to the feedback of the corresponding attitude angle

$$\begin{aligned}\Phi_{cmd} &= \hat{\Phi} + \Delta\Phi_{cmd}, \\ \Theta_{cmd} &= \hat{\Theta} + \Delta\Theta_{cmd},\end{aligned}\tag{3.94}$$

where the bank and pitch angle command increments $\Delta\Phi_{cmd} \in \mathbb{R}$, $\Delta\Theta_{cmd} \in \mathbb{R}$ are computed by the control allocation module based on the desired load factor increments. Figure 3.12 presents a schematic of the VCI allocation loop. The lateral load factor $(n_y^R)_C$ is generated by tilting the vertical lift (powered or aerodynamic) through a bank angle according to Eq. (2.63). Therefore, given a desired increment in the lateral load factor $\Delta(n_y^R)_{C,des}$, an increment for the bank angle is computed in the control allocation. Subsequently, upon addition of the computed increment to the current bank angle measurement $\hat{\Phi}$, the bank angle command for the rotation reference model is generated. The reference roll acceleration along with the desired trajectories for the roll rate and bank angle are then specified by the inner loop RM.

Similarly, the C -frame longitudinal and vertical load factors $(n_x^R)_C$, $(n_z^R)_C$ are regulated through the pitch angle in the hover and wingborne phase respectively. Note that in the hover phase, only positive pitch angles are commanded to build up a negative longitudinal load factor while for accelerating forward the tilt propulsion units are employed. In the wingborne phase, the aerodynamic lift is regulated through the pitch angle command while taking the reference bank angle state in to account. Details about the body rotation rate command generation will be presented later in the subsection 3.3.3.3 pertaining to the rotation reference model.

Consequently, the use of VCIs with the decoupled loops in the reference model yields the advantage of having a cascaded structure for the unified INDI controller while having a combined control allocation [189] of the desired pseudo controls. The given strategy maintains the causal chain of force generation in a manner that the desired

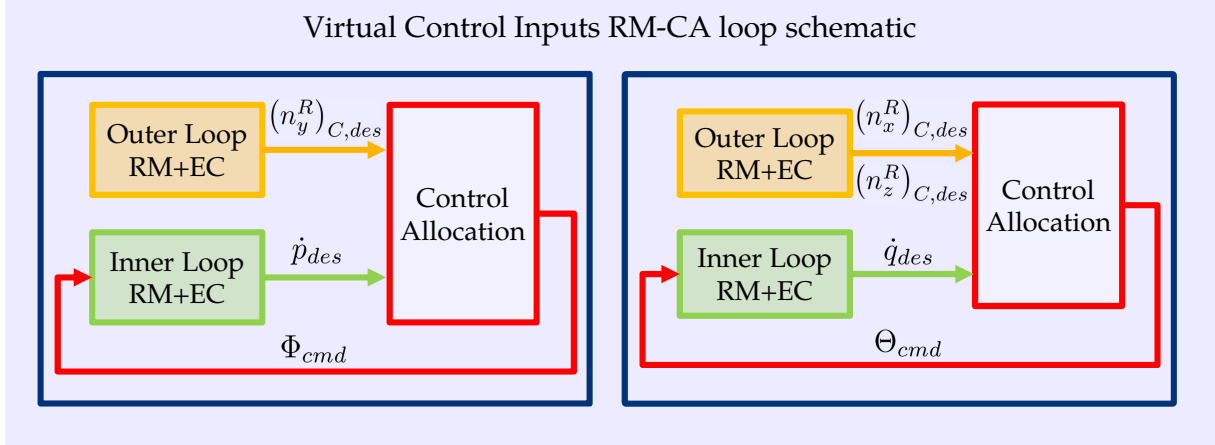


Figure 3.12: Virtual Control Inputs concept diagram

body rotational accelerations cannot influence the nominal feedforward of the load factors. Moreover, the proposed strategy eliminates the requisite of incorporating any configuration-specific aerodynamics knowledge in the reference model to specify the desired behavior either for aerodynamic lift regulation or wind disturbance rejection. Contrarily, sensor data feedback is employed to explicitly define the wind disturbance rejection behavior within the reference model, as explained in the section 3.3.3.4.

3.3.3.1 Reference Model Core Interfaces

The full overview pertaining to the input and output interfaces of the inner and outer loop RM in the reference model core is listed in the Table 3.4 and illustrated in the Fig. 3.13. As noted earlier, the outer loop RM creates reference trajectories for the translation motion. Inherently, the inputs to the translation RM contain the velocity commands. Additionally, the heading angle rate command $\dot{\Psi}_{cmd}$ is applied to generate the inter-axis coupling term $(u_K^R)_C^E \cdot \dot{\Psi}$ for computation of the reference lateral load factor in accordance with Eq. (2.61). The outputs of the translation RM consist of the translation reference pseudo controls i.e. the load factors expressed in the C -frame $(\vec{n}^R)_{C,R}$ and the corresponding kinematic velocities $(\vec{V}_K^R)_{C,R}^E$ as the translation reference external states.

The rotation RM takes the Euler attitude angle commands from the VCIs along with the heading angle rate command. In addition to the the commands, feedback of the body-frame lateral load factor is also passed to the inner loop RM. The outputs include the body angular accelerations $(\vec{\omega}_K^{OB})_B^B$ as the rotational reference pseudo controls along with the desired external state trajectories of body angular rates $(\vec{\omega}_K^{OB})_B$, Euler attitude angle rates $\dot{\Phi}$ and attitude angles Φ . Additionally, the two loops of the RM core require the blend kinematics bus bl_{kin} that incorporates all the variables related to compliance enforcement among the reference variables depending on the aircraft flight phase. Computation of these variables is covered in the section 3.3.4.

Following the interface definition of the RM core, the functional structure of the translation and rotation reference models is described in the upcoming sections.

RM core components	Inputs	Outputs
Translation RM	$\begin{bmatrix} (u_K^R)^E_C \\ (v_K^R)^E_C \\ (w_K^R)^E_C \\ \dot{\Psi} \end{bmatrix}_{cmd}, bl_{kin}$	$\begin{bmatrix} (\vec{n}^R)_{C,R} \\ (\vec{V}_K^R)^E_{C,R} \end{bmatrix}$
Rotation RM	$\begin{bmatrix} \Phi_{cmd} \\ \Theta_{cmd} \\ \dot{\Psi}_{cmd} \\ (\hat{n}_y^R)_B \end{bmatrix}, bl_{kin}$	$\begin{bmatrix} (\vec{\omega}_K^{OB})^B_{B,R} \\ (\vec{\omega}_K^{OB})^B_{B,R} \\ \dot{\Phi}_R \\ \Phi_R \end{bmatrix}$

Table 3.4: Interface definition for the Reference Model Core components

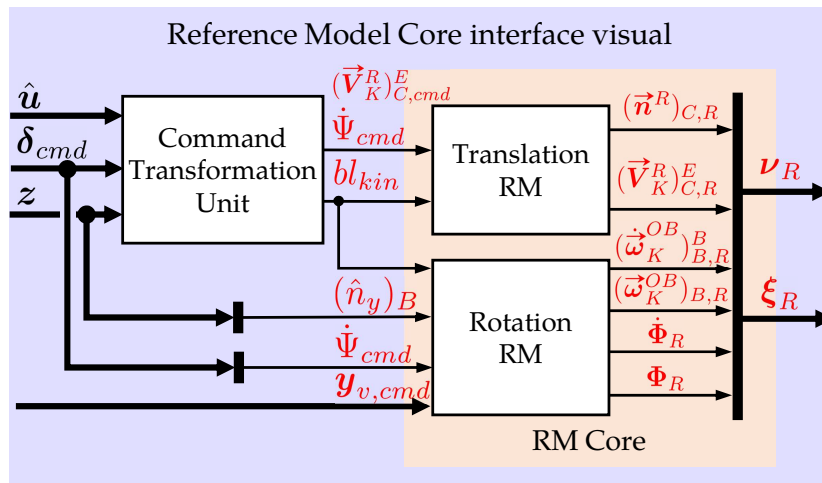


Figure 3.13: Reference Model Core interface definition

3.3.3.2 Translation Reference Model

The translation or the outer loop reference model, as exhibited in Fig. 3.14, is constituted by three units – reference translation error controller, reference acceleration inversion and reference plant dynamics. Apart from defining the desired response characteristics to the pilot commands, the translation reference model also incorporates envelope protections for the reference variables associated to all the flight phases.

Reference Translation Error Controller

The first unit, called the reference translation error controller, compares the velocity command set-point $(\vec{V}_K^R)^E_{C,cmd} \in \mathbb{R}^3$ with current value of the corresponding reference variable $(\vec{V}_K^R)^E_{C,R} \in \mathbb{R}^3$ (represented as external states $\xi_{o,R}$) to determine the required acceleration command $(\vec{V}_K^R)^{EC}_{C,cmd} \in \mathbb{R}^3$. In addition to the calculation of the acceleration

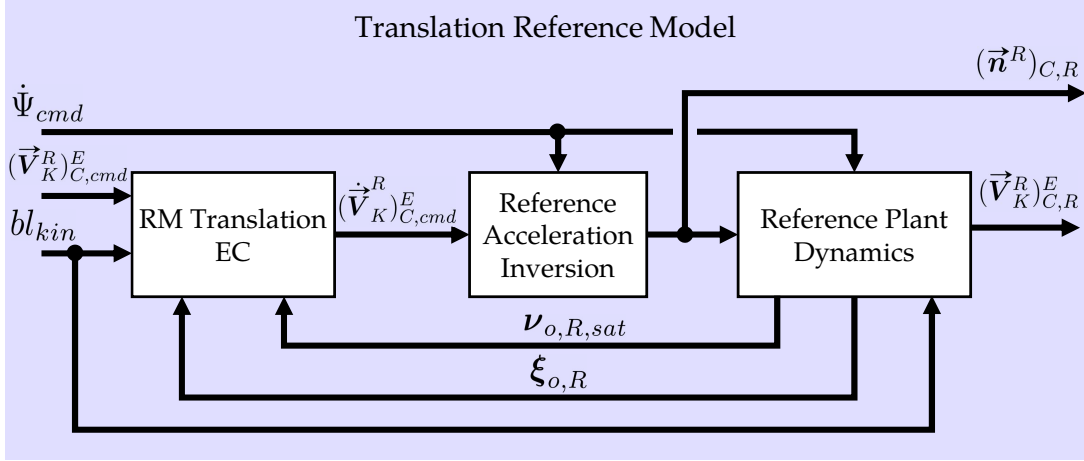


Figure 3.14: Translation Reference Model

command, the magnitude of the generated command is also limited within the bounds $\nu_{o,R,sat}$, which comprises the maximum and minimum acceleration limits specified as $\nu_{o,R,max}$ and $\nu_{o,R,min}$ from Eqs. (3.117) and (3.118) respectively

$$U = K_{V,R} \cdot \left[(\vec{V}_K^R)^E_{C,cmd} - (\vec{V}_K^R)^E_{C,R} \right],$$

$$(\dot{\vec{V}}_K^R)^{EC}_{C,cmd} = \begin{cases} U, & \text{if } (\dot{\vec{V}}_K^R)^{EC}_{C,min} \leq U \leq (\dot{\vec{V}}_K^R)^{EC}_{C,max}, \\ (\dot{\vec{V}}_K^R)^{EC}_{C,min}, & \text{if } U < (\dot{\vec{V}}_K^R)^{EC}_{C,min}, \\ (\dot{\vec{V}}_K^R)^{EC}_{C,max}, & \text{if } U > (\dot{\vec{V}}_K^R)^{EC}_{C,max}, \end{cases} \quad (3.95)$$

where $(\dot{\vec{V}}_K^R)^{EC}_{C,max} \in \mathbb{R}^3$ and $(\dot{\vec{V}}_K^R)^{EC}_{C,min} \in \mathbb{R}^3$ are the maximum and minimum allowed kinematic accelerations denoted in the control frame. Calculation of limit magnitudes for all the reference variables of the translation RM is discussed later within the scope of the reference plant dynamics. The gain matrix $K_{V,R}$ defines the amplitude independent time constant of the desired kinematic velocity response for all axes in different flight phases. Section 3.3.4 will demonstrate the mechanism and order of changing the gains (according to flight phases) defined in the matrix $K_{V,R}$ to maintain a consistent response of the aircraft.

Reference Acceleration Inversion

The next step is to determine the reference load factors by dynamically inverting the C -frame translation equations of motion given in Eq. (2.53). However, the terms pertaining to round and rotating earth along with the difference between the aircraft reference point and center of gravity are neglected on the basis of assumptions A.2.4–A.2.6. The load factor computation employs feedback of the reference velocity vector along with the heading angle rate command, which is incorporated in the angular rate vector $(\vec{\omega}_K^{OC})_{C,cmd} \in \mathbb{R}^3$

$$(\vec{n}^R)_{C,R} = \frac{1}{g} \left[(\dot{\vec{V}}_K^R)^{EC}_{C,cmd} - \mathbf{M}_{CO} \cdot (\vec{g})_O + (\vec{\omega}_K^{OC})_{C,cmd} \times (\vec{V}_K^G)^E_{C,R} \right]. \quad (3.96)$$

In the reference acceleration inversion from Eq. (3.96), $(\vec{n}^R)_{C,R} \in \mathbb{R}^3$ represents the reference load factor vector fed forward to the INDI controller as the reference translation pseudo control as well as to the reference plant dynamics. The frame rotation matrix $\mathbf{M}_{CO} \in \mathbb{R}^{3 \times 3}$ (Eq. (2.1)) is used to rotate the gravitational acceleration vector $(\vec{g})_O \in \mathbb{R}^3$ from the NED-frame to the control frame. The angular rate vector $(\vec{\omega}_K^{OC})_{C,cmd} \in \mathbb{R}^3$ describes the rotational rate of the control frame relative to the O -frame specified in the C -frame, and constituted according to Eq. (2.9).

The construction of the inter-axis coupling term $(\vec{\omega}_K^{OC})_{C,cmd} \times (\vec{V}_K^R)_{C,R}^E$ is very significant in order to facilitate bank-to-turn maneuver for the course angle rate command. The angular rate vector $(\vec{\omega}_K^{OC})_{C,cmd} = [0 \ 0 \ \dot{\Psi}_{cmd}]^T$ is composed of the heading angle rate command instead of the reference heading rate. Remember that in no-wind conditions the course angle rate and the heading rate are equal and since no aerodynamic effects are considered in the purely kinematic outer loop RM, the course angle rate command can be treated as a heading rate command in the forward-velocity flight phases. As a direct consequence, the reference lateral load factor $(n_y^R)_{C,R}$ generated through Eq. (3.96) contains the heading rate command

$$(n_y^R)_{C,R} = \frac{1}{g} \left[(\dot{v}_K^R)_{C,cmd}^{EC} + (u_K^R)_{C,R}^E \cdot \dot{\Psi}_{cmd} \right] \quad (3.97)$$

and is fed-forward to the control allocation. It was stated in the description of VCI generation that the lateral load factor is allocated to a bank angle command Φ_{cmd} . Hence, in summation a course angle rate command from the pilot is directly translated to a bank angle command, which is provided to the inner loop RM, thereby enabling bank-to-turn capability for turn rate commands.

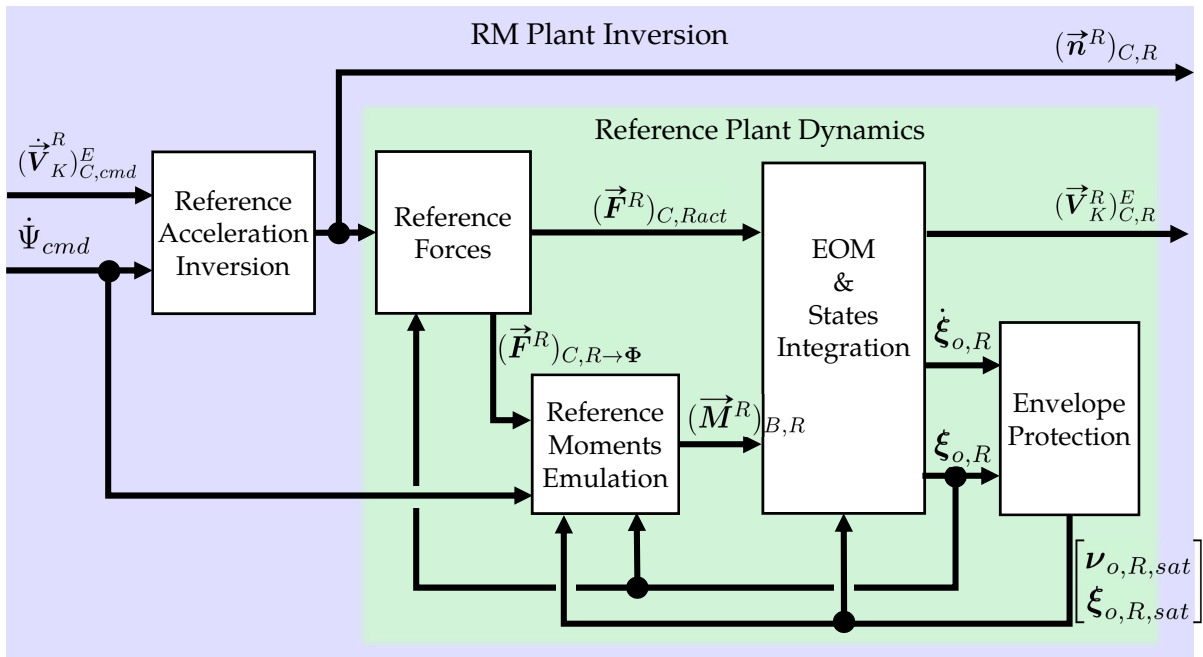


Figure 3.15: Reference Dynamics inversion in the Translation Reference Model

Reference Plant Dynamics

The reference load factors are commanded to the reference plant dynamics, whose structure is exhibited in the Fig. 3.15. The reference plant dynamics incorporate a *reference forces* calculation module, *moment emulation* unit specifically for the outer loop, *rigid body equations of motion* and the *reference states integration* along with computation of *envelope protection* bounds. Figure 3.15 illustrates the signal flow between the individual units of the reference plant dynamics. Firstly, the reference load factors produced in the acceleration inversion (Eq. (3.96)) are transmitted to the *Reference Forces* unit. The reference forces unit performs two functions

1. Specify the source of generation of the control forces. The control force production in different axes can either be performed through a control effector or through an attitude angle. The *reference forces* unit defines which alternative is used for the force build up in each axis.
 2. Emulate the dynamics of the control force buildup using pseudo-force actuators
- An overview of the control force generation mechanism in each axis of the considered VTOL transition aircraft configuration is presented in the Table 3.5.

Control Forces denoted in the C -frame	Sources of control force generation		
	Hover	Transition	Wingborne
Longitudinal force $(X^R)_C$	$\delta_{L,R}, \omega_{L,R}, \Theta$	$\delta_{L,R}, \omega_{L,R}$	$\omega_{L,R}$
Lateral force $(Y^R)_C$	$\omega_{L,R}$	Φ	Φ
Vertical force $(Z^R)_C$	$\omega_{A,F}$	$\omega_{A,F}$	Θ

Table 3.5: Sources of control force generation in all flight phases of the tilt-rotor VTOL transition aircraft

Reference Forces

The reference load factors yield the control force magnitudes simply through

$$\left(\vec{F}^R\right)_{C,R} = m \cdot g \cdot \left(\vec{n}^R\right)_{C,R}, \quad (3.98)$$

where $m \in \mathbb{R}$ denotes the mass of the aircraft and $g \in \mathbb{R}$ represents the acceleration due to gravity. In order to accelerate in the direction of positive x_C -axis, the longitudinal force is produced through the tilt thrust units, however to move along the negative x_C -axis, the pitch angle is used. This does not imply that a positive demand in the forward force $(X^R)_C$ is always produced through the tilt propulsors. However, the sign of the reference forward kinematic velocity $(u_K^R)_{C,R}^E$ is considered. In order to brake while moving backwards requires generation of a positive longitudinal force. In this case, use of pitch angle is more efficient and provides higher acceleration as compared to the tilt propellers. Therefore, based on the sign of the velocity $(u_K^R)_{C,R}^E$, the reference

longitudinal force from Eq. (3.98) is divided into two parts

$$\begin{aligned} (X^R)_{C,R \rightarrow act} &= (X^R)_{C,R} \quad , \text{if } (u_K^R)^E \geq 0, \\ (X^R)_{C,R \rightarrow \Theta} &= (X^R)_{C,R} \quad , \text{if } (u_K^R)^E < 0. \end{aligned} \quad (3.99)$$

The term $(X^R)_{C,R \rightarrow act}$ represents the longitudinal force commanded to the force actuators while $(X^R)_{C,R \rightarrow \Theta}$ denotes the force intended to be produced by the pitch angle.

The lateral force is always produced through the bank angle, therefore it is forwarded to the moment emulation module. The generation of vertical forces changes from powered lift to aerodynamic lift as the aircraft transitions from hover to wingborne flight. Since no aerodynamic effects are considered in the translation reference model, the vertical control force from Eq. (3.98) is directly transferred to the force actuators. Regulation of aerodynamic lift (when available) occurs through the incremental pitch angle command produced by the CA. With the exception of longitudinal force generation, the pitch angle command is not used for any other purpose in the outer loop RM.

As stated earlier, the lateral force $(Y^R)_{C,R}$ is generated completely through the bank angle, however the longitudinal and vertical forces can be commanded directly. Consequently, the reference forces vector commanded to the force actuators $(\vec{F}^R)_{C,R \rightarrow act} \in \mathbb{R}^3$ is expressed as

$$(\vec{F}^R)_{C,R \rightarrow act} = \begin{bmatrix} (X^R)_{C,R \rightarrow act} \\ 0 \\ (Z^R)_{C,R \rightarrow act} \end{bmatrix}. \quad (3.100)$$

The reference control forces to be produced directly by the effectors $(\vec{F}^R)_{C,Ract} \in \mathbb{R}^3$ are obtained after multiplication of the force vector output from Eq. (3.100) with the force actuator matrix \mathbf{G}_{Fact}

$$(\vec{F}^R)_{C,Ract} = \begin{bmatrix} (X^R)_{C,Ract} \\ 0 \\ (Z^R)_{C,Ract} \end{bmatrix} = \begin{matrix} \mathbf{G}_{Fact} \\ \left[\begin{array}{ccc} G_{X_R \rightarrow X_{Ract}}(s) & 0 & 0 \\ 0 & 0 & 0 \\ 0 & 0 & G_{Z_R \rightarrow Z_{Ract}}(s) \end{array} \right] \end{matrix} \cdot (\vec{F}^R)_{C,R \rightarrow act}, \quad (3.101)$$

where the transfer functions $G_{X_R \rightarrow X_{Ract}}(s)$ and $G_{Z_R \rightarrow Z_{Ract}}(s)$ represent the second order force actuators for the forward and vertical control forces respectively, which can be exhibited in the Laplace domain as

$$G_A(s) = \frac{\omega_A^2}{s^2 + 2 \cdot \zeta_A \cdot \omega_A \cdot s + \omega_A^2}. \quad (3.102)$$

Likewise, the reference forces vector $(\vec{F}^R)_{C,R \rightarrow \Phi} \in \mathbb{R}^3$ to be produced through the attitude angles $\Phi \in \mathbb{R}^3$ is specified as

$$(\vec{F}^R)_{C,R \rightarrow \Phi} = \begin{bmatrix} (X^R)_{C,R \rightarrow \Theta} \\ (Y^R)_{C,R} \\ (Z^R)_{C,Ract} \end{bmatrix} \quad \text{with} \quad \Phi = \begin{bmatrix} \Phi \\ \Theta \\ \Psi \end{bmatrix}. \quad (3.103)$$

As stated before that the vertical force $(Z^R)_{C,Ract} \in \mathbb{R}$ generation assumes direct lift control for all flight phases in the translation RM, yet it is forwarded to the forces commands intended to be produced through attitude angles $(\vec{F}^R)_{C,R \rightarrow \Phi} \in \mathbb{R}^3$, since the vertical force is essential for the computation of the attitude angle commands in the moments emulation unit.

Reference Moments emulation

The bank angle command is produced in accordance with the relation presented in Eq. (2.65)

$$\Phi_{cmd} = \arctan \left[\frac{(Y^R)_{C,R} \cdot \cos \Theta}{-(Z^R)_{C,Ract}} \right]. \quad (3.104)$$

In order to derive the expression for the pitch angle command pertaining to the generation of the longitudinal force, the equations equivalent to the first and third row of the frame rotation for the specific forces denoted in the body-fixed to the control frame, as provided by Eq. (2.62) are considered

$$\begin{aligned} (X^R)_C &= (Z^R)_B \cdot \cos \Phi \cdot \sin \Theta, \\ (Z^R)_C &= (Z^R)_B \cdot \cos \Phi \cdot \cos \Theta, \end{aligned} \quad (3.105)$$

with the conditions that direct control force cannot be produced along the body-fixed x_B . Remember that this pitch angle command is intended for movement along the negative x_C direction and the tilt thrust units are not used for this purpose. Subsequently, dividing the two expressions from Eq. (3.105) and solving for the pitch angle results in

$$\Theta_{cmd} = \arctan \left[\frac{(X^R)_{C,R \rightarrow \Theta}}{(Z^R)_{C,Ract}} \right]. \quad (3.106)$$

Bank and pitch angle commands are now available through Eqs. (3.104) and (3.106) respectively, along with the heading rate command, which is mapped from the pilot inceptor commands in the *Command Transformation Unit*. Using the feedback of the outer loop reference states $\Phi_{o,R} \in \mathbb{R}$, $\dot{\Phi}_{o,R} \in \mathbb{R}$, $\Theta_{o,R} \in \mathbb{R}$, $\dot{\Theta}_{o,R} \in \mathbb{R}$, $\Psi_{o,R} \in \mathbb{R}$, the Euler attitude angle accelerations are obtained

$$\begin{aligned} \ddot{\Phi} &= K_{D,\Phi} \left[K_{P,\Phi} \cdot (\Phi_{cmd} - \Phi_{o,R}) - \dot{\Phi}_{o,R} \right], \\ \ddot{\Theta} &= K_{D,\Theta} \left[K_{P,\Theta} \cdot (\Theta_{cmd} - \Theta_{o,R}) - \dot{\Theta}_{o,R} \right], \\ \ddot{\Psi} &= K_{P,\dot{\Psi}} \cdot (\dot{\Psi}_{cmd} - \dot{\Psi}_{o,R}), \end{aligned} \quad (3.107)$$

where the gains $K_{P,\Phi} \in \mathbb{R}$ and $K_{D,\Phi} \in \mathbb{R}$ are the proportional and derivative gains specifying the bank angle reference dynamics. Likewise, $K_{P,\Theta} \in \mathbb{R}$ and $K_{D,\Theta} \in \mathbb{R}$ determine the pitch angle reference dynamics. The heading rate desired dynamics are specified by $K_{P,\dot{\Psi}} \in \mathbb{R}$. For the bank and pitch angle reference dynamics, the proportional

and the derivatives gains are derived from the corner frequency ω_{des} and damping ratio ζ_{des} of their corresponding desired second order transfer characteristics

$$\begin{aligned} G_{des}(s) &= \frac{\omega_{des}^2}{s^2 + 2 \cdot \zeta_{des} \cdot \omega_{des} \cdot s + \omega_{des}^2}, \\ K_{P,des} &= \frac{\omega_{des}}{2 \cdot \zeta_{des}}, \\ K_{D,des} &= 2 \cdot \zeta_{des} \cdot \omega_{des}, \end{aligned} \quad (3.108)$$

whereas for the heading rate dynamics the $K_{P,\dot{\Psi}}$ is equal to the corner frequency of a first order transfer function.

The moments can be computed according to the angular momentum dynamics described in Eq. (2.73). For that purpose, body angular acceleration $(\dot{\vec{\omega}}_K^{OB})_B^B$ need to be derived from the reference Euler angle accelerations. Consider the relation between body angular rates and the Euler attitude rates $\dot{\Phi} \in \mathbb{R}^3$ given by the strapdown equation from Eq. (2.74)

$$\dot{\Phi} = \mathbf{M}(\Phi) \cdot (\vec{\omega}_K^{OB})_B. \quad (3.109)$$

Here $\mathbf{M}(\Phi) \in \mathbb{R}^{3 \times 3}$ represents the strapdown matrix (see Eq. (2.74)), which is the function of the Euler angle vector $\Phi \in \mathbb{R}^3$. Upon differentiation, the strapdown equation yields

$$\ddot{\Phi} = \dot{\mathbf{M}}(\Phi, \dot{\Phi}) \cdot (\vec{\omega}_K^{OB})_B + \mathbf{M}(\Phi) \cdot (\dot{\vec{\omega}}_K^{OB})_B^B. \quad (3.110)$$

Inverting the final expression derived in Eq. (3.110) and employing reference states from the translation RM yield the reference body angular acceleration commands

$$(\dot{\vec{\omega}}_K^{OB})_{B_o,cmd}^B = \mathbf{M}^{-1}(\Phi_{o,R}) \cdot \left[\ddot{\Phi}_{o,R} - \dot{\mathbf{M}}(\Phi_{o,R}, \dot{\Phi}_{o,R}) \cdot (\vec{\omega}_K^{OB})_{B_o,R} \right]. \quad (3.111)$$

Ultimately, the reference control moments $(\vec{M}^R)_{B,R} \in \mathbb{R}^3$ are computed from the angular momentum dynamics using the assumptions **A.2.4–A.2.6** that were also employed in the load factor computation

$$(\vec{M}^R)_{B,R} = (\mathbf{I}_{BB}^R) \cdot (\dot{\vec{\omega}}_K^{OB})_{B_o,cmd}^B + (\vec{\omega}_K^{OB})_{B_o,R} \times \mathbf{I}_{BB}^R \cdot (\vec{\omega}_K^{OB})_{B_o,R}. \quad (3.112)$$

Analogous to the force actuators defined in Eq. (3.102), consideration of the actuator dynamics is also made in the moment channels through second order elements

$$(\vec{M}^R)_{B,Ract} = \begin{matrix} \mathbf{G}_{Mact} \\ \left[\begin{array}{ccc} G_{L_R \rightarrow L_{Ract}}(s) & 0 & 0 \\ 0 & G_{M_R \rightarrow M_{Ract}}(s) & 0 \\ 0 & 0 & G_{N_R \rightarrow N_{Ract}}(s) \end{array} \right] \end{matrix} \cdot (\vec{M}^R)_{B,R}. \quad (3.113)$$

The objective of incorporating the *reference moments emulation* for the translation reference model is to anticipate the effect of the moment dynamics for force generation and account for them in the feedforward pseudo controls. Similar results can also be achieved with other alternatives like

1. Inclusion of the moment emulation as additional effectors in the force channel. The desired dynamics for the moment channels, as described by the second order elements in Eq. (3.108), can be specified as additional effectors for the force generation within the Eq. (3.101).
2. Hedging of the reference moment commands calculated in Eq. (3.112) by the reference moments specified in the inner loop RM.

However, an explicit *reference moments emulation* is performed in the translation reference model because it is not only employed to define reference trajectories for the INDI control law but also used as a tool to validate the customer requirements at the initial stages of the design phase. For that purpose, having a six degree of freedom desired behavior representation through the translation reference model is more appropriate.

Reference equations of motion and states integration

Lastly, the reference forces $(\vec{F}^R)_{C,Ract} \in \mathbb{R}^3$ and moments $(\vec{M}^R)_{B,Ract} \in \mathbb{R}^3$ are used in the rigid body equations of motion to calculate the reference linear and body angular accelerations respectively. The body rotational accelerations $(\vec{\omega}_K^{OB})_{B,o,R}^B \in \mathbb{R}^3$ are given by

$$(\vec{\omega}_K^{OB})_{B,o,R}^B = (\mathbf{I}_{BB}^R)^{-1} \cdot \left[(\vec{M}^R)_{B,Ract} - (\vec{\omega}_K^{OB})_{B,o,R} \times \mathbf{I}_{BB}^R \cdot (\vec{\omega}_K^{OB})_{B,o,R} \right], \quad (3.114)$$

which are integrated to obtain the outer loop reference body angular rates $(\vec{\omega}_K^{OB})_{B,o,R} \in \mathbb{R}^3$. The outer loop reference Euler attitude rates $\dot{\Phi}_{o,R} \in \mathbb{R}^3$ are computed through the strapdown Eq. (2.74), which are further integrated to get the corresponding Euler attitude angles $\Phi_{o,R} \in \mathbb{R}^3$. The reference kinematic acceleration defined in the C -frame $(\vec{V}_K^R)^{EC} \in \mathbb{R}^3$ is yielded by

$$\left(\vec{V}_K^R \right)_{C,R}^{EC} = \frac{1}{m} \cdot (\vec{F}^R)_{C,Ract} + \mathbf{M}_{CO} \cdot (\vec{g})_O - (\vec{\omega}_K^{OC})_{C,o,R} \times (\vec{V}_K^R)_{C,R}^E, \quad (3.115)$$

where the angular rate $(\vec{\omega}_K^{OC})_{C,o,R} \in \mathbb{R}^3$ (Eq. (2.9)) uses the reference heading rate $\dot{\Psi}_{o,R} \in \mathbb{R}$ to specify the inter-axis coupling in the lateral and forward velocity channels of the control frame. The reference trajectory of the velocity vector in the control frame is yielded upon integration of the acceleration resulting from Eq. (3.115). The integrals for all reference states are limited according to the absolute bounds of the states

$$\bar{\xi}_{o,R} = \begin{bmatrix} (\vec{V}_K^R)_{C,max}^E \\ (\vec{\omega}_K^{OB})_{B,max} \\ \dot{\Phi}_{max} \\ \Phi_{max} \end{bmatrix} \quad \underline{\xi}_{o,R} = \begin{bmatrix} (\vec{V}_K^R)_{C,min}^E \\ (\vec{\omega}_K^{OB})_{B,min} \\ \dot{\Phi}_{min} \\ \Phi_{min} \end{bmatrix}. \quad (3.116)$$

Here $\bar{\xi}_{o,R} \in \mathbb{R}^{12}$ and $\underline{\xi}_{o,R} \in \mathbb{R}^{12}$ are the maximum and minimum values to which the reference states in the outer loop RM are limited. The concept of linear phase plane protections employed for limiting the reference external states was presented in the section 3.1.2.1. In a similar manner, the bounds for the accelerations and rates are specified based on the more conservative values of either the limit margins (Eqs. (3.27)

and (3.28)) derived from the bounds of the corresponding lower order external states or the absolute value of the observed variable as demonstrated in Eq. (3.29). Consequently, the maximum limits of the pseudo controls in terms of translation accelerations and reference external states are obtained

$$\begin{aligned} \boldsymbol{\nu}_{o,R,max} &= \left[\begin{array}{c} \min \left(\left(\dot{\vec{\mathbf{V}}}_K^R \right)_{C,max}^{EC}, \mathbf{C}_{V_K} \cdot \left[\left(\vec{\mathbf{V}}_K^R \right)_{C,max}^E - \left(\vec{\mathbf{V}}_K^R \right)_{C,R}^E \right] \right) \\ \left(\vec{\mathbf{V}}_K^R \right)_{C,max}^E \\ \min \left(\left(\dot{\vec{\omega}}_K^{OB} \right)_{B,max}^B, \mathbf{C}_{\dot{\omega}} \cdot \left[\left(\vec{\omega}_K^{OB} \right)_{B,max} - \left(\vec{\omega}_K^{OB} \right)_{B,o,R} \right] \right) \\ \left(\vec{\omega}_K^{OB} \right)_{B,max} \\ \min \left(\dot{\Phi}_{max}, \mathbf{C}_{\dot{\Phi}} \cdot \left[\Phi_{max} - \Phi_{o,R} \right] \right) \\ \Phi_{max} \end{array} \right], \\ \boldsymbol{\xi}_{o,R,max} &= \left[\begin{array}{c} \left(\vec{\mathbf{V}}_K^R \right)_{C,max}^E \\ \min \left(\left(\dot{\vec{\omega}}_K^{OB} \right)_{B,max}^B, \mathbf{C}_{\dot{\omega}} \cdot \left[\left(\vec{\omega}_K^{OB} \right)_{B,max} - \left(\vec{\omega}_K^{OB} \right)_{B,o,R} \right] \right) \\ \left(\vec{\omega}_K^{OB} \right)_{B,max} \\ \min \left(\dot{\Phi}_{max}, \mathbf{C}_{\dot{\Phi}} \cdot \left[\Phi_{max} - \Phi_{o,R} \right] \right) \\ \Phi_{max} \end{array} \right], \end{aligned} \quad (3.117)$$

and likewise the minimum limits are also computed

$$\begin{aligned} \boldsymbol{\nu}_{o,R,min} &= \left[\begin{array}{c} \max \left(\left(\dot{\vec{\mathbf{V}}}_K^R \right)_{C,min}^{EC}, \mathbf{C}_{V_K} \cdot \left[\left(\vec{\mathbf{V}}_K^R \right)_{C,min}^E - \left(\vec{\mathbf{V}}_K^R \right)_{C,R}^E \right] \right) \\ \left(\vec{\mathbf{V}}_K^R \right)_{C,min}^E \\ \max \left(\left(\dot{\vec{\omega}}_K^{OB} \right)_{B,min}^B, \mathbf{C}_{\dot{\omega}} \cdot \left[\left(\vec{\omega}_K^{OB} \right)_{B,min} - \left(\vec{\omega}_K^{OB} \right)_{B,o,R} \right] \right) \\ \left(\vec{\omega}_K^{OB} \right)_{B,min} \\ \max \left(\dot{\Phi}_{min}, \mathbf{C}_{\dot{\Phi}} \cdot \left[\Phi_{min} - \Phi_{o,R} \right] \right) \\ \Phi_{min} \end{array} \right], \\ \boldsymbol{\xi}_{o,R,min} &= \left[\begin{array}{c} \left(\vec{\mathbf{V}}_K^R \right)_{C,min}^E \\ \max \left(\left(\dot{\vec{\omega}}_K^{OB} \right)_{B,min}^B, \mathbf{C}_{\dot{\omega}} \cdot \left[\left(\vec{\omega}_K^{OB} \right)_{B,min} - \left(\vec{\omega}_K^{OB} \right)_{B,o,R} \right] \right) \\ \left(\vec{\omega}_K^{OB} \right)_{B,min} \\ \max \left(\dot{\Phi}_{min}, \mathbf{C}_{\dot{\Phi}} \cdot \left[\Phi_{min} - \Phi_{o,R} \right] \right) \\ \Phi_{min} \end{array} \right]. \end{aligned} \quad (3.118)$$

Here the gain matrix $\mathbf{C}_{V_K} \in \mathbb{R}^{3 \times 3}$ contains the parameters that determine the rate at which the velocities hit their absolute saturations $\left(\vec{\mathbf{V}}_K^R \right)_{C,max}^E \in \mathbb{R}^3$, $\left(\vec{\mathbf{V}}_K^R \right)_{C,min}^E \in \mathbb{R}^3$ by varying the limits for the kinematic acceleration $\left(\dot{\vec{\mathbf{V}}}_K^R \right)_{C,max}^{EC} \in \mathbb{R}^3$ based on the current velocity limit margin $\left(\vec{\mathbf{V}}_K^R \right)_{C,min/max}^E - \left(\vec{\mathbf{V}}_K^R \right)_{C,R}^E$. Higher values of \mathbf{C}_{V_K} imply that the reference velocities approach their bounds at a high rate, which can lead to a discontinuity in the acceleration trajectory at the instant when the velocity hits its boundary. Fig. 3.16 demonstrates the difference in the behavior of the reference forward velocity upon increasing the magnitude of the C_{V_K} in calculation of the forward acceleration limits according to Eqs. (3.117) and (3.118). As compared to the first plot, it can be observed in the second plot that the reference velocity trajectory stops abruptly at the limit boundary. Although, the velocity commands can be limited through command value limitation, the linear phase plane based protections are employed to facilitate smooth desired trajectory generation by the integrated RM since the absolute velocity limits $\left(\vec{\mathbf{V}}_K^R \right)_{C,max}^E$, $\left(\vec{\mathbf{V}}_K^R \right)_{C,min}^E$ vary over the flight envelope of the VTOL transition aircraft mentioned here.

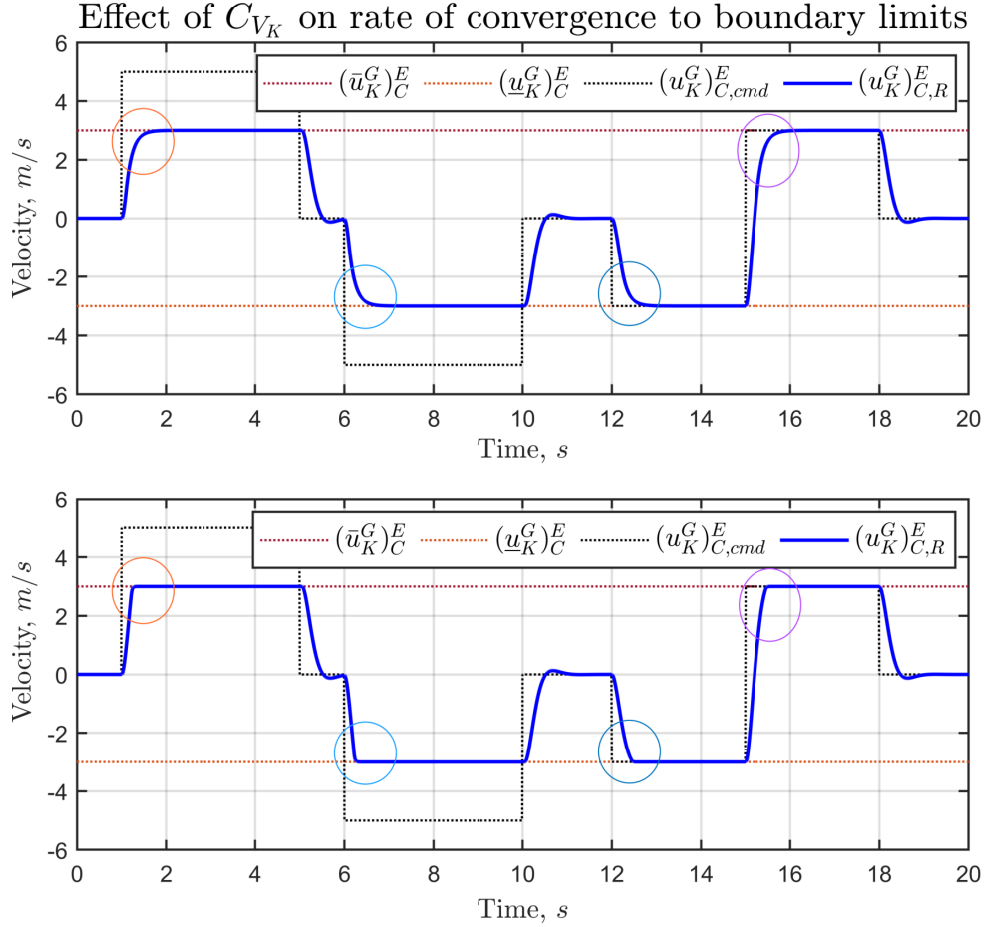


Figure 3.16: Effect of C_{V_K} on rate of convergence to boundary limits

Similarly, gain matrices $C_{\dot{\omega}} \in \mathbb{R}^{3 \times 3}$ and $C_{\dot{\phi}} \in \mathbb{R}^{3 \times 3}$ are defined to compute limit values for the body rotational acceleration and the Euler attitude rates respectively. It must be noted that the limit values calculated in Eqs. (3.117) and (3.118) are only meant to be used for the reference variables in the translation loop RM. Use of the rotation channel limits calculated here do not comply with the reference variables of the inner loop RM, since the commands to the rotation reference model is computed based on sensor feedback to include effect of aerodynamic characteristics of the aircraft along with the external disturbances that are encountered in a flight environment.

The limit values of the reference pseudo controls and external states in the translation RM, computed in Eqs. (3.117) and (3.118), are collectively represented as $\nu_{o,R,sat}$ and $\xi_{o,R,sat}$ respectively, which is also illustrated in Fig. 3.15.

Hereby, the structure of the translation reference model is completed. Physically motivated feedforward reference load factors along with the kinematic velocities are transmitted to the INDI controller. For the generation of these reference signals, force effector dynamics along with the dynamics involved in moment production are also considered. The necessary Euler attitude angle commands required to achieve the desired load factor commands are sent to the rotation reference model through the control allocation module. Subsequently, the rotational RM generates desired trajectories for the rotation acceleration, rates and Euler attitude angles, which is covered next.

3.3.3.3 Rotation Reference Model

The reference model defining the desired rotational motion behavior of the VTOL transition aircraft comprises of three main functions – *sequential desired rotation rate generation*, *rotational acceleration command calculation unit* and the *rotational reference plant dynamics* (shown in Fig. 3.17). As the nomenclature for each function implies, the sequential rotation rate command generation deals with the computation of body angular rate commands $(\vec{\omega}_K^{OB})_{B,cmd}$ for hover and forward flight phases based on the inputs derived from the translation channel. The body rate commands for all phases are propagated further for calculation of the reference rotational acceleration command $(\vec{\omega}_K^{OB})_{B,R}^B$, which are the rotational feedforward pseudo controls to the unified INDI controller. Subsequently, emulation of the effector dynamics, rigid body rotational EOM and computation of linear phase plane based limits for the reference states are incorporated in the rotational reference plant dynamics.

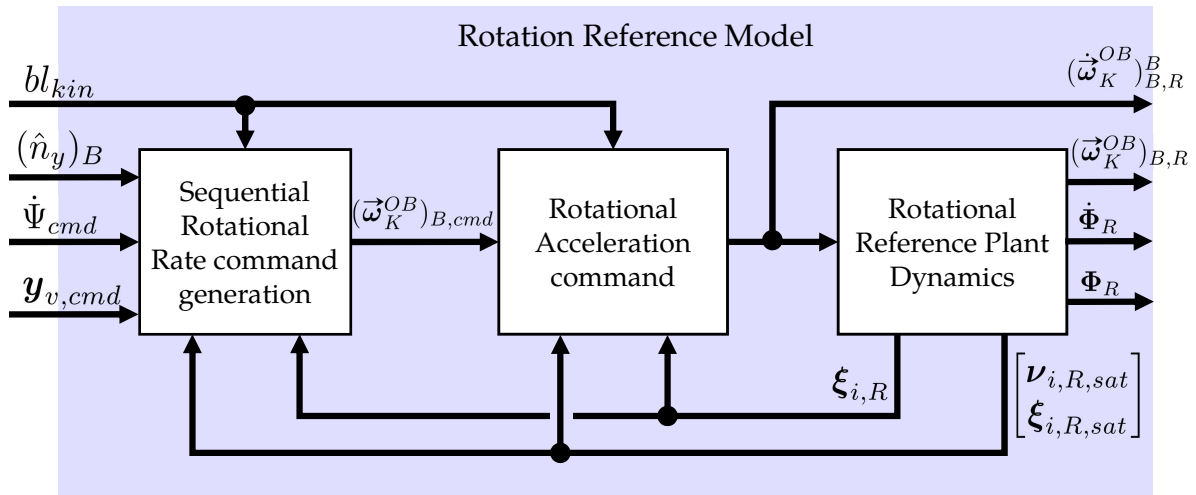


Figure 3.17: Rotation Reference Model

Sequential Desired Rotation Rate

As presented before, the virtual control inputs comprise of the bank and pitch angle command calculated in the control allocation module based on the desired increment in the load factors. Together with the heading rate command obtained from the pilot inceptor command mapping, these attitude angle commands are employed to determine the desired body rotation rates. In a nutshell, the desired rotation rate specification originates from the load factor demand, and hence the name sequential desired rotation rate. The sequential body angular rate computation fulfills the load factor requirement, which arises from the commanded maneuvers by the pilot as well as from the control effort needed to mitigate any deviations from the translation reference trajectories in presence of external disturbances.

To begin with, the rates of the Euler angles are obtained using a proportional error controller based on the reference angle values of the bank and pitch angle. Moreover, a command filter for the heading angle rate is included to filter out any high frequency content from the inceptor read out

$$\begin{bmatrix} \dot{\Phi} \\ \dot{\Theta} \\ \dot{\Psi}_f \end{bmatrix}_{cmd} = \begin{bmatrix} K_{\Phi,R} \cdot (\Phi_{cmd} - \Phi_R) \\ K_{\Theta,R} \cdot (\Theta_{cmd} - \Theta_R) \\ G_{\dot{\Psi}_{cmd}}(s) \cdot \dot{\Psi}_{cmd} \end{bmatrix}. \quad (3.119)$$

The transfer function $G_{\dot{\Psi}_{cmd}}(s)$ denotes a first order transfer function having a structure similar to the function described in Eq. (3.57) and $\dot{\Psi}_{cmd} \in \mathbb{R}$ represents the filtered heading rate command. The gains $K_{\Phi,R} \in \mathbb{R}$ and $K_{\Theta,R} \in \mathbb{R}$ define the desired response behavior to the Euler attitude angle commands. The calculation of the Euler attitude rates remains consistent to the relations described in Eq. (3.119) over the full flight envelope.

Following the calculation of the Euler angle rate commands, the body angular rate commands are generated. Similar to the method followed in Eq. (2.91) pertaining to the DRM kinematics and control, the hover phase body rotation rate commands $(\vec{\omega}_K^{OB})_{B_{cmd,hvr}}$ for the considered tilt-rotor aircraft configuration are also computed by inversion of the Euler strapdown equation introduced in Eq. (2.74)

$$\begin{bmatrix} p_{cmd} \\ q_{cmd} \\ r_{cmd} \end{bmatrix}_{hvr} = \begin{bmatrix} 1 & 0 & -\sin \Theta \\ 0 & \cos \Phi & \sin \Phi \cdot \cos \Theta \\ 0 & -\sin \Phi & \cos \Phi \cdot \cos \Theta \end{bmatrix} \cdot \begin{bmatrix} \dot{\Phi} \\ \dot{\Theta} \\ \dot{\Psi}_f \end{bmatrix}_{cmd}. \quad (3.120)$$

However, the calculation of body rotational rate commands for forward-velocity phases $(\vec{\omega}_K^{OB})_{B_{cmd,fwd}}$ are driven by the requirement of performing a steady-state coordinated turn in addition to the relations emanating from the strapdown equation. The conditions required to achieve a steady state coordinated turn are that

$$\left(\dot{v}_K^G\right)_B^{EB} = 0 \quad \left(f_y^G\right)_B = 0 \quad (3.121)$$

the lateral acceleration $(\dot{v}_K^G)_B^{EB} \in \mathbb{R}$ along with the lateral specific force denoted in the body-fixed frame $(f_y^G)_B \in \mathbb{R}$ do not manifest during a turn maneuver. In addition to the conditions listed in Eq. (3.121), the following constraints also apply

$$\dot{\Phi} = 0 \quad \dot{\Theta} = 0. \quad (3.122)$$

Applying the conditions from Eq. (3.121) to the lateral axis equation of motion in the body-fixed frame

$$\left(\dot{v}_K^G\right)_B^{EB} = \left(f_y^G\right)_B + g \cdot \sin \Phi \cdot \cos \Theta - r \cdot \left(u_K^G\right)_B^E + p \cdot \left(w_K^G\right)_B^E \quad (3.123)$$

yields

$$0 = g \cdot \sin \Phi \cdot \cos \Theta - r \cdot \left(u_K^G\right)_B^E + p \cdot \left(w_K^G\right)_B^E. \quad (3.124)$$

The resultant expression in Eq. (3.124) is simplified through the approximations

$$\begin{aligned}\cos \Theta &\approx 1 \\ \left(w_K^G\right)_B^E &\approx 0 \\ \left(u_K^G\right)_B^E &\approx |V|_K\end{aligned}\quad (3.125)$$

to obtain the trim yaw rate for a steady state bank angle Φ at a constant kinematic velocity $|V|_K$

$$r_{trim} = \frac{g}{|V|_K} \cdot \sin \Phi. \quad (3.126)$$

Proceeding from the constraint of constant pitch angle $\dot{\Theta} = 0$ in Eq. (3.122) and the approximation of small pitch angle $\cos \Theta \approx 1$ from Eq. (3.125), the relation for yaw rate from the inverse strap down equation (3.120) returns

$$r = \dot{\Psi} \cdot \cos \Phi. \quad (3.127)$$

Comparison of Eq. (3.128) with the yaw rate trim in Eq. (3.126) delivers

$$\frac{g}{|V|_K} \cdot \sin \Phi = \dot{\Psi} \cdot \cos \Phi. \quad (3.128)$$

Accordingly, a bank angle command $\Phi_{\dot{\Psi},cmd} \in \mathbb{R}$ corresponding to the filtered heading angle rate command from Eq. (3.119) is determined

$$\Phi_{\dot{\Psi},cmd} = \arctan \left(\frac{|V|_{K,R} \cdot \dot{\Psi}_{fcmd}}{g} \right), \quad (3.129)$$

which is utilized to determine a yaw rate trim command $r_{trim,cmd} \in \mathbb{R}$ based on the Eq. (3.126)

$$r_{trim,cmd} = \frac{g}{|V|_{K,R}} \cdot \sin \Phi_{\dot{\Psi},cmd} \quad (3.130)$$

Similarly, the equations pertaining to the bank and pitch rate in the inverse strapdown equation (3.120) together with the constraints, and approximations from Eqs.(3.122), and (3.125) respectively, yield the trim body rotational rate commands

$$\begin{aligned}p_{trim,cmd} &= -\frac{g}{|V|_{K,R}} \cdot \tan \Phi_{\dot{\Psi},cmd} \cdot \sin \Theta_R = -r_{trim,cmd} \cdot \frac{\sin \Theta_R}{\cos \Phi_{\dot{\Psi},cmd}}, \\ q_{trim,cmd} &= \frac{g}{|V|_{K,R}} \cdot \sin \Phi_{\dot{\Psi},cmd} \cdot \tan \Phi_{\dot{\Psi},cmd} = r_{trim,cmd} \cdot \tan \Phi_{\dot{\Psi},cmd},\end{aligned}\quad (3.131)$$

which are further stated in terms of the yaw rate trim command to reduce the number of floating point operations required in the computation of reference trajectories.

Another important reason for calculating the yaw rate command independent of the strapdown formulation in the forward-velocity phase is to avoid allocation of the pitch angle rate command $\dot{\Theta}_{cmd}$ to the yaw rate. Upon observation of the yaw rate relation in Eq. (3.120)

$$r_{cmd} = -\sin \Phi_R \cdot \dot{\Theta}_{cmd} + \cos \Phi_R \cos \Theta_R \cdot \dot{\Psi}_{fcmd} \quad (3.132)$$

it can be seen that at non-zero bank angles, the pitch angle rate command is mapped to a yaw rate command with an opposite sign as compared to the trim yaw rate required for a given bank angle in Eq. (3.130). This implies that during a constant turn maneuver, a change in the pitch angle command will reflect as a yaw rate command through the sine component of the bank angle. The magnitude of this component increases with higher magnitude of bank angle. However, this is not the intention of the pitch angle rate command generated from the pitch angle command specified in the VCI. In the forward-velocity phases, the incremental pitch angle is primarily used to regulate the aerodynamic lift. Allocation of this increment (usually positive in turn flights) through the inverse strapdown mapping would lead to a negative yaw rate, which in turn leads to an aerodynamic side-slip, thereby generating lateral body acceleration. Hence, the yaw rate command for forward-velocity phases (Eq. (3.130)) is derived through the conditions in Eqs. (3.121) and (3.122) that facilitate a coordinated turn.

Subsequently, the body rotation rate commands for the forward flight phases, denoted by $(\vec{\omega}_K^{OB})_{B, fwd} \in \mathbb{R}^3$, are constructed from two components. The first part originates from the force demand in the translation motion. This demand is mapped to the rotation rate commands (only roll and pitch rates) through the Euler rate commands by means of the inverse strapdown equation (3.120)

$$\begin{bmatrix} p_{cmd} \\ q_{cmd} \end{bmatrix} = \begin{bmatrix} 1 & 0 \\ 0 & \cos \Phi_R \end{bmatrix} \cdot \begin{bmatrix} \dot{\Phi} \\ \dot{\Theta} \end{bmatrix}_{cmd}. \quad (3.133)$$

Important to note that this component is only constituted by the bank and pitch attitude rate commands calculated from the angle commands defined by the VCI. The second component of the rotation rate commands comprise of the trim rotation rate commands, which are calculated from the bank angle command $\Phi_{\dot{\psi}, cmd}$ (Eq. (3.129)) using the filtered heading rate command. The trim rotation rate commands are presented in Eqs. (3.130) and (3.131). The yaw rate command is only composed of the trim component. An additional element of the yaw rate required to provide robust wind disturbance rejection will be specified later. Ultimately, the fusion of these two components results in

$$\begin{matrix} (\vec{\omega}_K^{OB})_{B_{cmd, fwd}} \\ \begin{bmatrix} p_{cmd} \\ q_{cmd} \\ r_{cmd} \end{bmatrix}_{fwd} \end{matrix} = \begin{bmatrix} 1 & 0 & \frac{\sin \Theta_R}{\cos \Phi_{\dot{\psi}, cmd}} \\ 0 & \cos \Phi_R & \tan \Phi_{\dot{\psi}, cmd} \\ 0 & 0 & 1 \end{bmatrix} \cdot \begin{bmatrix} \dot{\Phi}_{cmd} \\ \dot{\Theta}_{cmd} \\ r_{trim, cmd} \end{bmatrix}. \quad (3.134)$$

Rotational Acceleration Command

Dependent on the flight phase of the aircraft, appropriate body rotation rate commands among $(\vec{\omega}_K^{OB})_{B_{cmd, hvr}}$ or $(\vec{\omega}_K^{OB})_{B_{cmd, fwd}}$ are chosen to create the reference rotational acceleration commands, which are the pseudo control inputs for the rotational motion

control. The selection of the valid rotation rate commands is coupled with some factors in the translation RM as well, therefore they are elaborated in a separate section later. The final output of the body rate command selection unit is denoted as the $(\vec{\omega}_K^{OB})_{B_{cmd}}$.

Based on the angular body rate command $(\vec{\omega}_K^{OB})_{B_{cmd}} \in \mathbb{R}^3$ and the feedback of the reference body rate $(\vec{\omega}_K^{OB})_{B,R} \in \mathbb{R}^3$, the reference rotational acceleration is obtained

$$U = \mathbf{K}_{\dot{\omega}} \cdot \left[(\vec{\omega}_K^{OB})_{B_{cmd}} - (\vec{\omega}_K^{OB})_{B,R} \right],$$

$$(\vec{\omega}_K^{OB})_{B,R}^B = \begin{cases} U, & \text{if } (\vec{\omega}_K^{OB})_{B,min}^B \leq U \leq (\vec{\omega}_K^{OB})_{B,max}^B, \\ (\vec{\omega}_K^{OB})_{B,min}^B, & \text{if } U < (\vec{\omega}_K^{OB})_{B,min}^B, \\ (\vec{\omega}_K^{OB})_{B,max}^B, & \text{if } U > (\vec{\omega}_K^{OB})_{B,max}^B, \end{cases} \quad (3.135)$$

where $\mathbf{K}_{\dot{\omega}} \in \mathbb{R}^{3 \times 3}$ represents a diagonal gain matrix comprising of the proportional gains for each rotational axis. Inverse of each proportional gain defines the amplitude-independent time interval within which the reference body rate reaches 63% of the step command. The maximum and minimum magnitudes of the rotational accelerations $(\vec{\omega}_K^{OB})_{B,max}^B \in \mathbb{R}^3$, $(\vec{\omega}_K^{OB})_{B,min}^B \in \mathbb{R}^3$ are computed in the same manner as described in Eqs. (3.117) and (3.118) for the translation RM. The limit magnitude computations for the inner loop RM are performed in the rotational reference plant dynamics.

The resultant angular accelerations from Eq. (3.135) act as the feedforward to the INDI controller as well as inputs to the rotational plant dynamics presented next.

Rotational Reference Plant Dynamics

The rotational reference plant dynamics incorporate the actuator dynamics emulation in order to define a physical build-up of the rotational acceleration. Moreover, the nonlinear kinematics describing the relation between the body rate accelerations and the Euler attitude accelerations are also included in the reference plant.

The reference control rotational accelerations $(\vec{\omega}_K^{OB})_{B,Ract}^B \in \mathbb{R}^3$, imitating the accelerations to be generated by the control effectors in real aircraft are specified through the multiplication of the resultant rotational acceleration from Eq. (3.135) with the actuator matrix $\mathbf{G}_{\dot{\omega}_{act}}$

$$(\vec{\omega}_K^{OB})_{B,Ract}^B = \mathbf{G}_{\dot{\omega}_{act}} \cdot (\vec{\omega}_K^{OB})_{B,R}^B. \quad (3.136)$$

$$\mathbf{G}_{\dot{\omega}_{act}} = \begin{bmatrix} G_{\dot{\omega}_{x,R} \rightarrow \dot{\omega}_{x,Ract}}(s) & 0 & 0 \\ 0 & G_{\dot{\omega}_{y,R} \rightarrow \dot{\omega}_{y,Ract}}(s) & 0 \\ 0 & 0 & G_{\dot{\omega}_{z,R} \rightarrow \dot{\omega}_{z,Ract}}(s) \end{bmatrix}$$

Here transfer functions $G_{\dot{\omega}_{x,R} \rightarrow \dot{\omega}_{x,Ract}}(s)$, $G_{\dot{\omega}_{y,R} \rightarrow \dot{\omega}_{y,Ract}}(s)$ and $G_{\dot{\omega}_{z,R} \rightarrow \dot{\omega}_{z,Ract}}(s)$ denote the second order rotational acceleration actuators having a structure like the actuator dynamics described in Eq. (3.102). The output of the Eq. (3.136) $(\vec{\omega}_K^{OB})_{B,Ract}^B \in \mathbb{R}^3$ is the reference control rotational acceleration compensated for the effector dynamics, which is further employed for the nonlinear attitude kinematics calculation.

The next step is the calculation of the Euler attitude acceleration from the reference control rotational acceleration $(\vec{\omega}_K^{OB})_{B,Ract}^B \in \mathbb{R}^3$ using the strapdown equation derivative from Eq. (3.110)

$$\ddot{\Phi}_R = \dot{M}(\Phi_R, \dot{\Phi}_R) \cdot (\vec{\omega}_K^{OB})_{B,R}^B + M(\Phi_R) \cdot (\vec{\omega}_K^{OB})_{B,Ract}^B, \quad (3.137)$$

where $\ddot{\Phi}_R \in \mathbb{R}^3$ denote the reference Euler attitude acceleration, $M(\Phi_R) \in \mathbb{R}^{3 \times 3}$ is the Euler strapdown matrix constructed from the reference Euler attitude angles of the rotational RM and $\dot{M}(\Phi_R, \dot{\Phi}_R) \in \mathbb{R}^{3 \times 3}$ is the derivative of the Euler strapdown matrix of the attitude kinematics described in Eq. (2.74)

$$\dot{M} = \begin{bmatrix} 0 & \frac{\dot{\Theta}_R \cdot \sin \Phi_R + \dot{\Phi}_R \cdot \cos \Phi_R \cdot \cos \Theta_R \cdot \sin \Theta_R}{(\cos \Theta_R)^2} & \frac{\dot{\Theta}_R \cdot \cos \Phi_R - \dot{\Phi}_R \cdot \cos \Theta_R \cdot \sin \Phi_R \cdot \sin \Theta_R}{(\cos \Theta_R)^2} \\ 0 & -\dot{\Phi}_R \cdot \sin \Phi_R & -\dot{\Phi}_R \cdot \cos \Phi_R \\ 0 & \frac{\dot{\Phi}_R \cdot \cos \Phi_R \cdot \cos \Theta_R + \dot{\Theta}_R \cdot \sin \Phi_R \cdot \sin \Theta_R}{(\cos \Theta_R)^2} & -\frac{\dot{\Phi}_R \cdot \cos \Theta_R \cdot \sin \Phi_R - \dot{\Theta}_R \cdot \cos \Phi_R \cdot \sin \Theta_R}{(\cos \Theta_R)^2} \end{bmatrix}. \quad (3.138)$$

Subsequently, the reference trajectories for the body angular rates $(\vec{\omega}_K^{OB})_{B,R} \in \mathbb{R}^3$ are generated by integration of the rotational accelerations $(\vec{\omega}_K^{OB})_{B,Ract}^B \in \mathbb{R}^3$. Furthermore, the Euler angles Φ_R and their rates $\dot{\Phi}_R$ are obtained upon integrations of the Euler angle accelerations provided by Eq. (3.137). Although, the body rotational rates and Euler angle rates lie at the same dynamic level, both the vectors are included in the reference external states to facilitate freedom of designing the rotational error controller in the INDI. The error rotational accelerations can then be estimated based on the errors in either the body angular rates or the Euler angle rates. However, if Euler angle rates are employed for this purpose, the nonlinearities in the attitude kinematics must be taken in account.

Analogous to the reference external states in the translation RM, the integrals for all reference states in the inner loop reference model are limited as well, according to the absolute bounds of the states

$$\bar{\xi}_{i,R} = \begin{bmatrix} (\vec{\omega}_K^{OB})_{B,max} \\ \dot{\Phi}_{max} \\ \Phi_{max} \end{bmatrix}, \quad \underline{\xi}_{i,R} = \begin{bmatrix} (\vec{\omega}_K^{OB})_{B,min} \\ \dot{\Phi}_{min} \\ \Phi_{min} \end{bmatrix}, \quad (3.139)$$

where $\bar{\xi}_{i,R} \in \mathbb{R}^9$ and $\underline{\xi}_{i,R} \in \mathbb{R}^9$ are the maximum and minimum values to which the reference states in the rotational (inner loop) RM are limited. In this case as well, the concept of linear phase plane protections is employed for limiting the reference external states. The bounds for the rotational accelerations and rates are derived based from either the limit margins of the corresponding lower order external states or the absolute

value of the observed variable, whichever is more conservative

$$\begin{aligned} \nu_{i,R,max} &= \left[\min \left(\left(\vec{\omega}_K^{OB} \right)_{B,max}^B, \mathbf{C}_{\dot{\omega}} \cdot \left[\left(\vec{\omega}_K^{OB} \right)_{B,max} - \left(\vec{\omega}_K^{OB} \right)_{B,R} \right] \right) \right], \\ \xi_{i,R,max} &= \left[\begin{array}{c} \min \left(\left(\vec{\omega}_K^{OB} \right)_{B,max}^B, \mathbf{C}_{\dot{\omega}} \cdot \left[\left(\vec{\omega}_K^{OB} \right)_{B,max} - \left(\vec{\omega}_K^{OB} \right)_{B,R} \right] \right) \\ \left(\vec{\omega}_K^{OB} \right)_{B,max} \\ \min \left(\dot{\Phi}_{max}, \mathbf{C}_{\dot{\Phi}} \cdot \left[\Phi_{max} - \Phi_R \right] \right) \\ \Phi_{max} \end{array} \right], \end{aligned} \quad (3.140)$$

$$\begin{aligned} \nu_{i,R,min} &= \left[\max \left(\left(\vec{\omega}_K^{OB} \right)_{B,min}^B, \mathbf{C}_{\dot{\omega}} \cdot \left[\left(\vec{\omega}_K^{OB} \right)_{B,min} - \left(\vec{\omega}_K^{OB} \right)_{B,R} \right] \right) \right], \\ \xi_{i,R,min} &= \left[\begin{array}{c} \max \left(\left(\vec{\omega}_K^{OB} \right)_{B,min}^B, \mathbf{C}_{\dot{\omega}} \cdot \left[\left(\vec{\omega}_K^{OB} \right)_{B,min} - \left(\vec{\omega}_K^{OB} \right)_{B,R} \right] \right) \\ \left(\vec{\omega}_K^{OB} \right)_{B,min} \\ \max \left(\dot{\Phi}_{min}, \mathbf{C}_{\dot{\Phi}} \cdot \left[\Phi_{min} - \Phi_R \right] \right) \\ \Phi_{min} \end{array} \right]. \end{aligned} \quad (3.141)$$

Here the gain matrices $\mathbf{C}_{\dot{\omega}} \in \mathbb{R}^{3 \times 3}$ and $\mathbf{C}_{\dot{\Phi}} \in \mathbb{R}^{3 \times 3}$ are utilized to compute limit values for the body rotational acceleration and the Euler attitude rates respectively. The saturation limits calculated in Eqs. (3.140) and (3.141) are specifically intended to be used for limiting the reference variables in the rotation loop RM only.

Hereby, the full structure of the rotation reference model specifying the reference trajectories and feedforward for the variables defining the angular motion of the aircraft is presented. A sequential technique of producing rotation rate commands from the Euler attitude angle commands, which are derived from the desired load factor demand, for all flight phases of the VTOL transition aircraft is presented. The Euler attitude angle commands serve as virtual control inputs for the translation motion in the unified INDI control strategy. Therefore, the proposed rotation rate command calculation mechanism in tandem with the aircraft physics-oriented rotation reference model delivers the realization of the contribution **C.2.2 Sequential desired rotation rate calculation in a unified control structure** for this thesis.

In addition to the completion of the rotation reference model description, the presentation for the core element of the modular integrated reference model is also accomplished. As stated explicitly before, the core unit of the reference model architecture enables a uniform interface definition to the HMI related functions on one side and to the flight control function on the other side over the complete flight envelope of the considered tilt-rotor VTOL transition aircraft. *Reference Model core* framework comprising of the Translation and the Rotation reference models are the elements pertinent to the contribution **C.2.3 Reference Model core design to facilitate use of same set of variables for the whole flight envelope** of this dissertation. Additionally, the RM core structure proposed here is sufficiently modular for generating the reference state trajectories specific to any UAM related aircraft configuration with minor parametric changes.

3.3.3.4 Explicit Wind Disturbance Rejection Definition

Wind disturbance rejection response behavior is explicitly defined for all flight phases through this reference model framework. In hover flight, wind is countered by tilting the powered-lift vector through attitude angles against it except in case of head wind, where the tilt thrust units are tilted forward to produce thrust in the positive body-fixed x_B axis. The cross-winds are resisted by banking the vertical powered lift against the incoming direction of the wind flow. Likewise, tail winds are counteracted by pitching up, thereby balancing out the wind disturbance through the sine component of the powered lift. The aforementioned mechanism describes the actions taken to reject wind disturbance from any direction in hover flight. These counter measures are facilitated by the deviation of the reference states from the corresponding plant states in presence of the wind. The disturbance due to wind flow excites the control error which is incorporated to the desired pseudo control through the error controller described in section 3.2.2.2.

The behavior specification in presence of wind during hover flight is defined through the magnitude of the reference translation states namely velocities. For example, in a stationary hover state the magnitude of reference C -frame lateral velocity $(v_K^R)^E_{C,R}$ is zero. Upon action of a wind flow along the y_C axis of aircraft, the aircraft build up a positive acceleration and hence a positive $(v_K^R)^E_{C,R}$ velocity, although the corresponding reference state is defined to be zero. Consequently, the tracking error yields an incremental desired lateral pseudo control

$$\begin{aligned} (n_y^R)_{C,des} &= C_{ev} \cdot (0 - (v_K^R)^E_{C,R}) + (n_y^R)_{C,R}, \\ \Delta (n_y^R)_{C,des} &= (n_y^R)_{C,des} - (\hat{n}_y^R)_C, \quad \triangleq 0 \end{aligned} \quad (3.142)$$

where $(\hat{n}_y^R)_C \in \mathbb{R}$ is estimated from the body fixed acceleration measurements provided by the Inertial Measurement Unit (IMU) and the reference lateral load factor in the control frame $(\hat{n}_y^R)_{C,R} \in \mathbb{R}$ is zero in the stationary hover state being considered for this explanation. The incremental desired lateral pseudo control $\Delta (n_y^R)_{C,des} \in \mathbb{R}$ is used by the control allocation to generate an incremental negative bank angle command $\Delta \Phi_{cmd}$ ultimately used to create the bank angle command for the rotation reference model. Subsequently, a negative bank angle is then built up in order to mitigate the positive kinematic velocity generated by the wind disturbance. Similarly, tail winds lead to a positive forward kinematic velocity $(u_K^R)^E_{C,R}$, which yields corrective negative desired load factor denoted in the control frame $(n_x^R)_{C,des}$. Negative load factors in the x_C axis are produced through positive pitch angles, thereby reducing the forward velocity to zero.

In the forward-velocity phases, it is desirable to minimize the aerodynamic side-slip angle β_A for increased efficiency when flying through a cross-wind field. Nevertheless, measurement of the aerodynamic side-slip angle is not available. As an alternative, at small angles the approximation

$$(n_y)_B = \frac{\bar{q} \cdot S \cdot C_{Y\beta} \cdot \beta_A}{m \cdot g} \quad (3.143)$$

relating the lateral load factor in the body-fixed frame $(n_y^R)_B \in \mathbb{R}$ to the aerodynamic side-slip angle $\beta_A \in \mathbb{R}$ is used. Here $\bar{q} \in \mathbb{R}$ represents the dynamic pressure, $S \in \mathbb{R}$ is the surface area and $C_{Y\beta} \in \mathbb{R}$ denotes the dimensionless constant describing the gradient of the lateral force in the body-fixed frame over the aerodynamic side-slip angle. Based on the expression in Eq. (3.143), the body lateral load factor is minimized to create the same effect as that of reducing the side-slip angle, rather than the explicitly minimizing the aerodynamic side-slip angle. A pictorial representation of the difference in cross-wind disturbance rejection behavior between hover and forward flight is demonstrated by the Fig. 3.18.

The estimation of the lateral body load factor $(\hat{n}_y^R)_B \in \mathbb{R}$ is further added to the yaw rate trim command from Eq. (3.130), thereby generating the yaw rate command

$$r_{cmd} = \frac{g}{|V|_{K,R}} \cdot \sin \Phi_{\dot{\psi},cmd} + K_{n_y} \cdot (\hat{n}_y^R)_B, \quad (3.144)$$

where $K_{n_y} \in \mathbb{R}$ is a negative gain on the load factor feedback. The yaw rate command in Eq. (3.144) is finally used in the rotation rate commands vector for the forward-velocity phases in Eq. (3.134). Consequently, the yaw rate command not only enables the trim component for a steady state coordinated term but also facilitates minimization of the body lateral load factor in presence of cross-wind during forward flight. It is important to emphasize that the C -frame lateral velocity is implicitly defined through the yaw rate required to achieve zero lateral body load factor. Therefore, it is essential that the lateral velocity command in forward-velocity flight phases $(v_K^G)_C^{E,fd}$ as computed through Eq. (3.74) in the *Commands Transformation* module estimates the true kinematic lateral velocity $(v_K^G)_C^E$. If these two velocities are not equal, the desired lateral load factor in the control frame would additionally comprise of an error component computed by the stabilizing error controller in the forward-velocity phases

$$(n_y^R)_{C,des} = C_{ev} \cdot ((v_K^G)_C^{E,fd} - (v_K^G)_C^E) + (n_y^R)_{C,R} \quad (3.145)$$

leading to bank angle command, which would fight against the desired lateral velocity indirectly specified through the body lateral load factor feedback. More strategies to avoid this scenario are also presented in the upcoming sections.

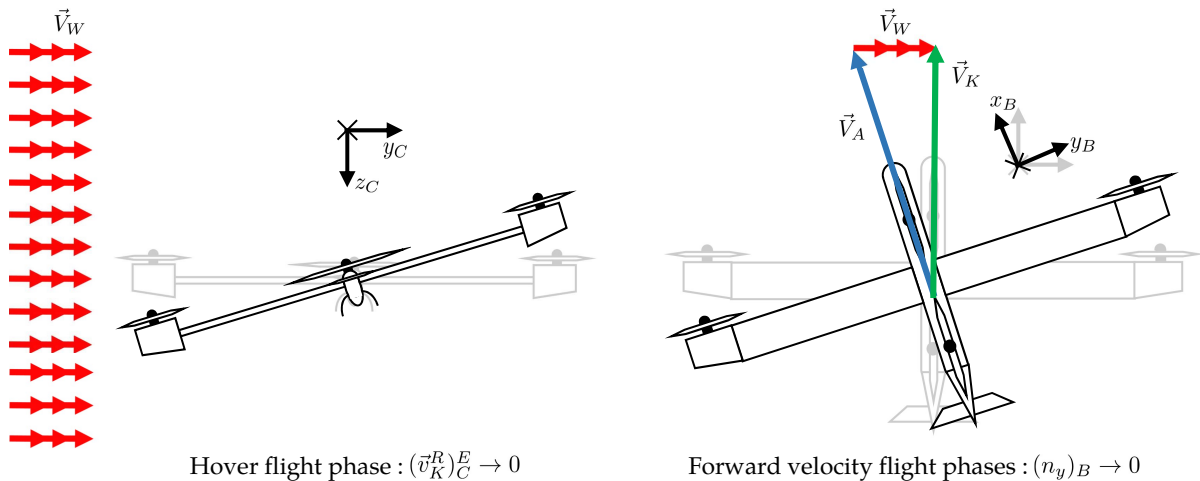


Figure 3.18: Cross-wind disturbance rejection for all flight phases

As already stated in the section 3.3.2, a thrust level of the tilt thrust units is commanded in the forward-velocity phases. Therefore, the airspeed stays constant in presence of headwind, although the ground speed reduces at a constant thrust level setting. Similarly, the airspeed stays constant in case tailwinds, thereby providing robustness against stall.

Overall, the definition of the desired behavior in presence of wind during hover flight specified by the reference model is to retain zero kinematic velocities. Furthermore, this behavior definition is incorporated in the control strategy through the kinematic velocity tracking errors, which form a component of the desired load factors. The desired load factors are achieved by tilting the powered lift through attitude angles. In the forward-velocity flight phases, the cross-wind disturbance rejection behavior is explicitly defined by employing a feedback of lateral body load factor for the generation of the yaw rate command. Susceptibility against stall due to tail wind is prevented by commanding the thrust level of the tilt rotors instead of ground speed. This section along with the thrust level command concepts described in the *Commands Transformation* section 3.3.2 provide the functionality pertaining to the contribution **C.2.4 Definition of an explicit wind disturbance rejection behavior over the complete flight envelope within the Reference Model core design** of this work.

3.3.4 Compliance Enforcement between Reference Variables

In the RM modules discussed so far, reference trajectories are computed to accommodate changing relative degrees for lift generation along with varying pilot inceptor interpretation for maintaining an intuitive aircraft response in every flight phase. The *Command Transformation* module generates three unique sets of control variables for hover, transition and wingborne phases as given in Eq. (3.70) based on the pilot inceptor commands. The *Translation RM* in the reference model core generates reference load factors as well as reference kinematic velocity trajectories for the full flight envelope. The reference variables pertaining to the translation motion must conform with the intended behavior in each flight phase. For example, the lateral velocity $(v_K^R)_C^E$ must not be controlled explicitly in the forward-velocity phases, however it is constrained through the minimization of the body lateral load factor. Therefore, in the forward-velocity phases the reference lateral velocity $(v_K^R)_{C,R}^E$ must be equal to the real velocity such that the velocity tracking error is not allocated to a bank angle like in the hover phase. Moreover, the *Rotation RM* generates different body angular rate commands for hover and forward flight. All these flight phase dependent variables generated by different reference model components must be merged in a manner that they conform with each other, thereby producing a consistent reference behavior at every point in the flight envelope.

3.3.4.1 Kinematic Velocity Commands Blending

The variables that govern the selection of reference variables in order to enforce compliance among them are specified in the *Blending Kinematics* module. This module is encompassed within the *Command Transformation Unit* (see Fig. 3.13) of the integrated

reference model. As the name implies, the *Blending Kinematics* module is responsible for the generation of the blending variables, which facilitate blending between same set of reference variables but belonging to different flight phases.

The first matter in blending of reference variables pertains to the conformity of kinematic velocity commands in different flight phases. In the *Commands Transformation – forward velocity phases* (shown by Fig. 3.9), a set of control variables comprising of the kinematic velocities in the control frame was constructed for the forward-velocity phases as given in Eq. (3.74). The absolute kinematic velocity command $|V|_{K,cmd}$ used for obtaining the velocity command vector in Eq. (3.74) was either generated through the thrust level command Eq. (3.85) or directly mapped from the *Stick Lookup* function. Selection of the source of absolute kinematic velocity command is made on the basis of *thrust_active_flg*, which is determined by the *System Automation* functionality through consideration of pilot stick position, state feedback and control input commands for the main LTUs produced by the INDI controller [200, 201]. Although, the origin of absolute velocity command changes based on the activation flag, in the end one final command value is used in the forward-velocity phases to compute the control-frame velocity command vector $(\vec{V}_K^R)_C^E, fwd$.

While the velocity command vector for forward-velocity flight phases is available through Eq. (3.74), its counterpart for the hover flight can be directly obtained through a stick lookup function based on the spring-centered deflections of all inceptors as inputs, like the stick to command variable conversion defined by Eq. (3.71)

$$(\vec{V}_K^R)_C^E, hvr = \begin{bmatrix} (u_K^R)_C^E \\ (v_K^R)_C^E \\ (w_K^R)_C^E \end{bmatrix}_{hvr}. \quad (3.146)$$

In order to generate relevant kinematic velocity commands for the *Reference Model Core*, the hover and forward-velocity phase set of command vectors from Eq. (3.146) and (3.74) respectively, are merged using a blending parameter, which is constructed from a combination of two sigmoid functions, each having a structure defined by

$$\sigma(k_\sigma, |V|_K, |V|_{K,mean}) = \frac{1}{1 + e^{-k_\sigma \cdot (|V|_K - |V|_{K,mean})}} \quad (3.147)$$

where $\sigma \in \mathbb{R}$ is the value of the sigmoid function that lies in $[0, 1]$ based on the absolute kinematic velocity $|V|_K \in \mathbb{R}$, $k_\sigma \in \mathbb{R}$ determines the rise rate of the sigmoid curve and $|V|_{K,mean}$ represents the mean value of the absolute kinematic velocity, which specifies the magnitude by which the sigmoid curve is offset from the origin.

As mentioned earlier, the blending parameter $\lambda_{vel,cmd} \in \mathbb{R}$ is built up from two sigmoid functions having the structure like the function presented in Eq. (3.147). The first sigmoid function describes the variation of the blending parameter during transition from hover to wingborne, whereas the second function relays the magnitude of the blending variable during re-transition from wingborne to hover

$$\lambda_{vel,cmd} = \begin{cases} \sigma_{fwd}(k_\sigma, |V|_K, |V|_{K,m,fwd}), & \text{for transition} \\ \sigma_{bck}(k_\sigma, |V|_K, |V|_{K,m,bck}), & \text{for re-transition} \end{cases} \quad (3.148)$$

Here the magnitude of the mean velocity parameter for the first function $|V|_{K,m, fwd}$ is defined higher than the function for re-transition $|V|_{K,m, bck}$, which results in a hysteresis blending behavior as shown in Fig. 3.19.

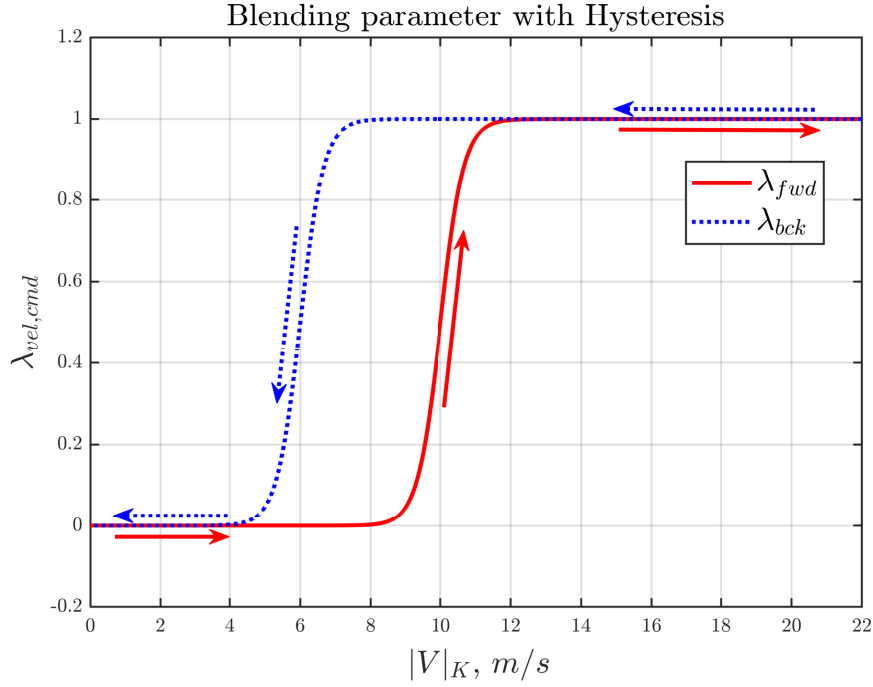


Figure 3.19: Blending parameter hysteresis over absolute kinematic velocity

Employing the $\lambda_{vel,cmd}$ variable, the two velocity command vectors from the *Commands Transformation – forward velocity phases* and the *Stick Lookup Hover Phase* are blended together in the *Commands Blending*, thereby providing the *C*-frame kinematic velocity command to the RM core. Figure 3.20 illustrates the signal flow among the different components of the *Command Transformation Unit*. Mathematically, the blending of the velocity commands can be represented as

$$\left(\vec{\mathbf{V}}_K^R \right)_{C,cmd}^E = \begin{bmatrix} \lambda \cdot \left(u_K^R \right)_{C,fwd}^E + (1 - \lambda) \cdot \left(u_K^R \right)_{C,hvr}^E \\ \lambda \cdot \left(v_K^R \right)_{C,fwd}^E + (1 - \lambda) \cdot \left(v_K^R \right)_{C,hvr}^E \\ \lambda \cdot \left(w_K^R \right)_{C,fwd}^E + (1 - \lambda) \cdot \left(w_K^R \right)_{C,hvr}^E \end{bmatrix}_{cmd}, \quad (3.149)$$

where the blending parameter $\lambda_{vel,cmd}$ is denoted by λ for ease of reading. It is clear from Eq. (3.149) that the RM core velocity command $\left(\vec{\mathbf{V}}_K^R \right)_{C,cmd}^E$ comprise of the transformed velocity command vector $\left(\vec{\mathbf{V}}_K^R \right)_{C,fwd}^E$ from Eq. (3.74) when the blending parameter λ has a value of 1 while at a magnitude of 0, the velocity commands transmitted to the RM core contain only the hover velocity command vector from Eq. (3.146). The blending parameters are encompassed within the *bl_kin*, which is the output of the *Blending Kinematics* function illustrated in the Fig. 3.20.

The hysteresis blending behavior is chosen to facilitate forward-velocity phase commands over larger range during the re-transition to the hover phase. In doing so, the pilot can change the course angle of the aircraft through the left-right deflection of the

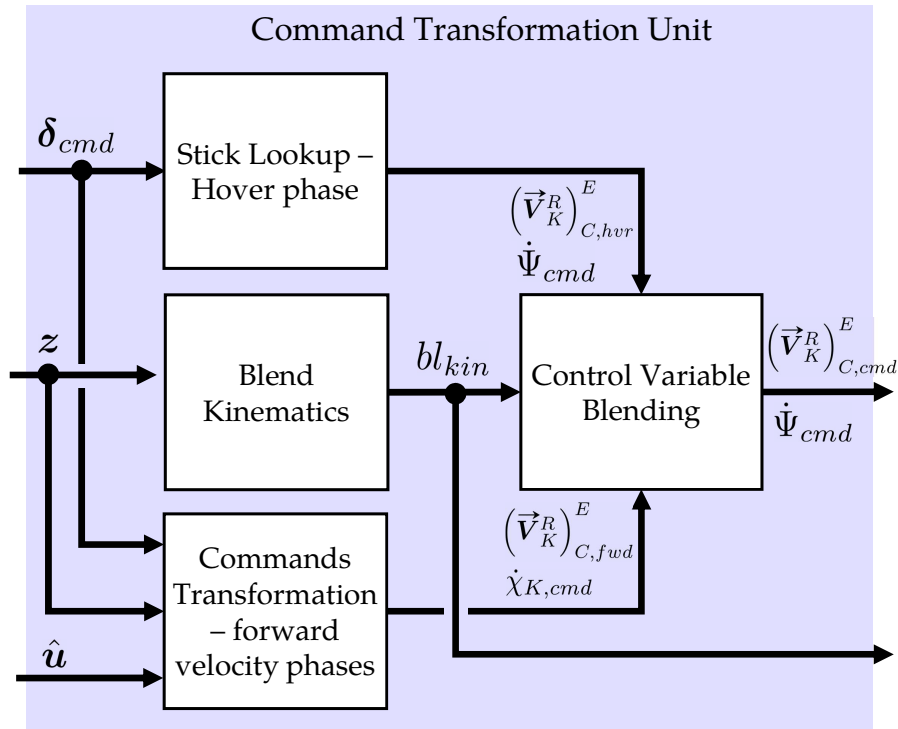


Figure 3.20: Command Transformation unit

Climb stick leading to a bank-to-turn maneuver at a lower forward kinematic velocity corresponding to the λ_{bck} represented by the blue line in the blending hysteresis plot from Fig. 3.19. This approach allows the pilot to continue operating with the same stick interpretation as for the wingborne flight. On the other hand, if the inceptor interpretation is changed to that of the hover phase in accordance with the red line (λ_{fwd}) during re-transition, the pilot has to use the left-right deflection of the Throttle stick in tandem with the left-right deflection of the Climb stick to maintain/change course using the lateral velocity command in the C -frame $(v_K^R)^E_{C,cmd}$ and heading angle rate $\dot{\Psi}_{cmd}$ respectively. This problem is not perceived during transition to wingborne because the acceleration due to tilt thrust units is higher as compared to the deceleration during re-transition, which only occurs on account of the aircraft body drag. Moreover, inadvertent pilot commands due to mode confusion are also avoided by offsetting the transit back to hover inceptor interpretation to lower kinematic velocities. It is also ensured that there is no jump from one blend curve to another during the blending phase. The curve exchange occurs only after the aircraft reaches wingborne phase after transition or hover phase after re-transition.

Ideally, the forward-velocity phase must be defined as the flight with velocity higher than the minimum control speed V_{MCA} . However, the VTOL transition configuration from section 3.2.1 is not limited by a minimum speed criteria since the availability of tilt thrust units implies that roll/yaw control can be performed by a combination of differential tilt position and thrust in all phases of the flight envelope. Therefore, the choice of mean velocity parameters for the calculation of the blending parameter in Eq. (3.148) is driven by pilot's perception.

3.3.4.2 Reference Rotation Rate Commands Blending

As specified in the description of the *Rotation RM*, two sets of rotation rate commands are computed for hover and forward-velocity flight phases in Eqs. (3.120) and (3.134) respectively. While in the hover phase, the body rotation rate commands are produced simply through inversion of the Euler strapdown equations, in forward-velocity phases the body angular rate commands are derived by addition of trim compensation rates with the body rotation rates calculated from the Euler angle rates generated to fulfill the desired load factor commands of the translation channel. In addition to the given parts, the feedback of body lateral load factor is also considered in the computation of yaw rate command r_{cmd} as shown in Eq. (3.144).

Consider the lateral rigid body translation equation (2.61) of motion denoted in the control frame

$$\left(\dot{v}_K^R\right)_C^{EC} = \left(f_y^R\right)_C - \left(u_K^R\right)_C^E \cdot \dot{\Psi}, \quad (3.150)$$

which on substituting the Euler strapdown relation from Eq. (2.74) for $\dot{\Psi}$ provides

$$\left(\dot{v}_K^R\right)_C^{EC} = \left(f_y^R\right)_C - \left(u_K^R\right)_C^E \cdot \left(\frac{\sin \Phi}{\cos \Theta} \cdot q_K + \frac{\cos \Phi}{\cos \Theta} \cdot r_K \right). \quad (3.151)$$

Remember that the yaw rate command is built up from the feedback of the side body-fixed load factor. Hence, given that the yaw rate tracking behavior is good, the desired value of the lateral kinematic velocity is implicitly governed by the lateral body load factor in the forward-velocity phases, additionally also accounting for the wind disturbance rejection. Hence, the command mapping performed in Eq. (3.74)

$$\left(v_K^R\right)_{C,cmd}^E = \cos \gamma_{K,cmd} \cdot \sin \varepsilon \cdot |V|_{K,cmd} \quad (3.152)$$

is simply a pseudo-estimation of the real velocity using simplified trigonometric relations using the climb angle command $\gamma_{K,cmd} \in \mathbb{R}$ from Eq. (3.75) and the horizontal kinematic side slip angle $\varepsilon \in \mathbb{R}$ computed as the difference between the predicted kinematic course angle $\chi_{K,pred} \in \mathbb{R}$ (integration of predicted kinematic course angle rate from Eq. (3.78)) and the measured heading angle $\hat{\Psi} \in \mathbb{R}$

$$\varepsilon = \chi_{K,pred} - \hat{\Psi}. \quad (3.153)$$

Since the lateral velocity $\left(v_K^R\right)_C^E$ is not explicitly controlled in the forward-velocity phases, the objective of the mapping in Eq. (3.152) is to match the commanded lateral velocity value to the real magnitude as close as possible in order to avoid conflict with the implicit generation of the lateral velocity due to yaw rate command in cross-wind disturbances. It is clear that this simplified trigonometric mapping would be violated under high wind and wind gradient conditions since the C -frame lateral velocity builds up according to the rigid body dynamics indicated by Eq. (3.151). Methods to overcome such situations are covered in the next subsection.

Meanwhile, through the mechanism of the desired yaw rate computation (Eq. (3.144)) and its impact on the lateral kinematic velocity in Eq. (3.151), it becomes evident that the rotation rate and velocity commands corresponding to the forward-velocity phases must

be activated/blended simultaneously such that the reference translation and rotation channel states conform with each other. Therefore, the rotation rate commands for the hover and forward-velocity phases from Eqs. (3.120) and (3.134) respectively, are blended in the *Sequential Desired Rotation Rate* unit of the Rotation RM using the velocity command blend parameter $\lambda_{vel,cmd}$ denoted as λ in the following

$$\left(\vec{\omega}_K^{OB}\right)_{B,cmd} = \begin{bmatrix} \lambda \cdot p_{cmd,fwd} + (1 - \lambda) \cdot p_{cmd,hvr} \\ \lambda \cdot q_{cmd,fwd} + (1 - \lambda) \cdot q_{cmd,hvr} \\ \lambda \cdot r_{cmd,fwd} + (1 - \lambda) \cdot r_{cmd,hvr} \end{bmatrix}_{cmd} \quad (3.154)$$

Additionally, the effect of the body lateral load factor in the generation of the yaw rate command is also weighed according to the blend parameter $\lambda_{vel,cmd}$

$$r_{cmd} = \frac{g}{|V|_{K,R}} \cdot \sin \Phi \dot{\psi}_{\dot{\psi},cmd} + \lambda_{vel,cmd} \cdot K_{n_y} \cdot \left(\hat{n}_y^R\right)_B \quad (3.155)$$

in order to have a smooth transition to and from forward-velocity phases during high cross-wind situations.

3.3.4.3 Reference Gains Blending and Flight Phase dependent Slaving

For the considered aircraft configuration, the source of lift and moment generation changes from propulsion units to aerodynamic control surfaces when transitioning from hover to wingborne flight or vice-versa in re-transition. Naturally, the transformation of the flying configuration impacts the controllability of the aircraft, since the dynamics of the control effectors corresponding to each phase differ substantially. Therefore, the reference dynamics must also be modified to account for the in-flight re-configuration such that a physically-feasible desired behavior can be defined for the full flight envelope.

Flight phase dependent adaptation of the desired behavior is performed by blending the reference error controller gains for the translation as well as the rotation RM. The reference velocity error gain matrix $\mathbf{K}_{V,R}$ introduced in Eq. (3.95)

$$\mathbf{K}_{V,R} = \begin{bmatrix} K_{uC,R} & 0 & 0 \\ 0 & K_{vC,R} & 0 \\ 0 & 0 & K_{wC,R} \end{bmatrix} \quad (3.156)$$

contains proportional gains for forward, lateral and vertical velocities in the C -frame given by $K_{uC,R} \in \mathbb{R}$, $K_{vC,R} \in \mathbb{R}$ and $K_{wC,R} \in \mathbb{R}$ respectively. The gains are altered according to the the velocity command blend parameter $\lambda_{vel,cmd}$ and the wingborne blend parameter $\lambda_{wb,active}$. The wingborne blend parameter is determined through a sigmoid function (similar to the function described in Eq. (3.147)), whose magnitude changes from 0 to 1 when the wingborne state active flag's status becomes true. The wingborne state active flag is generated by the *System Automation* functionality as described in [203].

Subsequently, the reference velocity error gains are defined contingent upon the blending parameters $\lambda_{vel,cmd}$ and $\lambda_{wb,active}$

$$\begin{aligned} K_{uC,R} &= \lambda_{vel,cmd} \cdot K_{uC,R,fwd} + (1 - \lambda_{vel,cmd}) \cdot K_{uC,R,hvr} \\ K_{vC,R} &= \lambda_{vel,cmd} \cdot K_{vC,R,fwd} + (1 - \lambda_{vel,cmd}) \cdot K_{vC,R,hvr} \\ K_{wC,R} &= \lambda_{wb,active} \cdot K_{wC,R,wb} + \\ &\quad (1 - \lambda_{wb,active}) \cdot [\lambda_{vel,cmd} \cdot K_{wC,R,tr} + (1 - \lambda_{vel,cmd}) \cdot K_{wC,R,hvr}]. \end{aligned} \quad (3.157)$$

The forward velocity gain $K_{uC,R,hvr} \in \mathbb{R}$ specifies the desired dynamics for the reference trajectory of the velocity along the x_C direction $(u_K^R)_{C,R}^E$ in hover flight. Thereafter, the corresponding reference dynamics in the forward-velocity phases are specified through $K_{uC,R,fwd} \in \mathbb{R}$. Although, the physical control variable in the forward-velocity phases changes from absolute kinematic velocity during transition to tilt rotor thrust in wingborne flight, the desired behavior can still be specified in terms of the C -frame velocity owing to the CV conversions performed in the *Commands Transformation* unit.

Likewise, the reference gains for the lateral velocity in hover and forward-velocity phases are specified by $K_{vC,R,hvr} \in \mathbb{R}$ and $K_{vC,R,fwd} \in \mathbb{R}$ respectively. As stated earlier, the lateral kinematic velocity $(v_K^R)_{C,R}^E$ is not explicitly controlled in the forward-velocity phases, but implicitly governed by the minimization of lateral body load factor through the yaw rate (Eq. (3.151)).

Unlike the reference gains for the horizontal plane velocities where only one gain was defined in the forward-velocity phases for each channel, separate gains in each of the hover, transition and wingborne phases are specified for the kinematic velocity along the vertical z_C axis $(w_K^R)_{C,R}^E$. The reference error gain $K_{wC,R,tr} \in \mathbb{R}$ for the transition phase is defined considering the variable dynamics of the effectors involved in the mixed lift generation. Although, direct lift generation by the LTUs is possible, it is not advisable to perform dynamic maneuvers in the vertical channel to avoid slip stream effects and high aerodynamic moments imposed by the flapping motion of the propellers while operating in the transition phase. Consequently, significantly higher time constant is specified for the vertical velocity which implies slow reference dynamics for the highly nonlinear transition phase. Contrarily, faster dynamics in the vertical channel are established through $K_{wC,R,hvr} \in \mathbb{R}$ and $K_{wC,R,wb} \in \mathbb{R}$ for the hover and wingborne phases respectively. Since the vertical specific force demand is regulated through the pitch channel in the wingborne flight, the pitch angle reference gain $K_{\Theta,R}$, used to compute the pitch angle rate command in the Eq. (3.119), is also blended to a higher value taking into account the reference dynamics of the vertical velocity specified by the gain $K_{wC,R,wb}$.

An important point to consider is that these proportional reference error gains only define the amplitude independent rise time for a given velocity command. The complete reference dynamics are obtained through a combined effect of the reference error gains along with the reference actuator emulation as given in Eq. (3.102).

Flight Phase dependent Reference Variable Slaving

Figures 3.21 and 3.22 indicate that the kinematic mapping used for velocity transformation in Eq. (3.74) does not hold under the impact of high wind and high wind gradient

in the forward-velocity phases. High gradient change in wind direction is simulated by performing a constant turn rate maneuver corresponding to a maximum side-wards positive deflection of the Climb stick at maximum forward thrust level in a constant unidirectional wind field. Figure 3.21 corroborates the variation in the ground speed during the turn maneuver and the corresponding bank angle for a coordinated turn.

As described earlier, the lateral velocity command mapped from the kinematic velocity command in the forward-velocity phases according to Eq. (3.74) is meant to emulate the real lateral velocity generated as a result of the minimization of the body lateral load factor. Figure 3.22 elaborates the lateral velocity command estimation for a constant turn flight in wingborne phase at different magnitudes of a wind field. This maneuver makes the aircraft experience high wind gradients since the direction of the simulated wind field is kept constant while the aircraft performs a constant turn rate maneuver. It is observed from the plots that the error between the lateral velocity command $(v_K^R)_C^{E, fwd}$ and the true lateral velocity $(v_K^R)_C^E$ increases with the wind magnitude. In this case, the reference trajectory for the lateral velocity $(v_K^R)_C^{E, R}$ generated by the translation RM will follow the erroneously defined lateral velocity command, which is not desired.

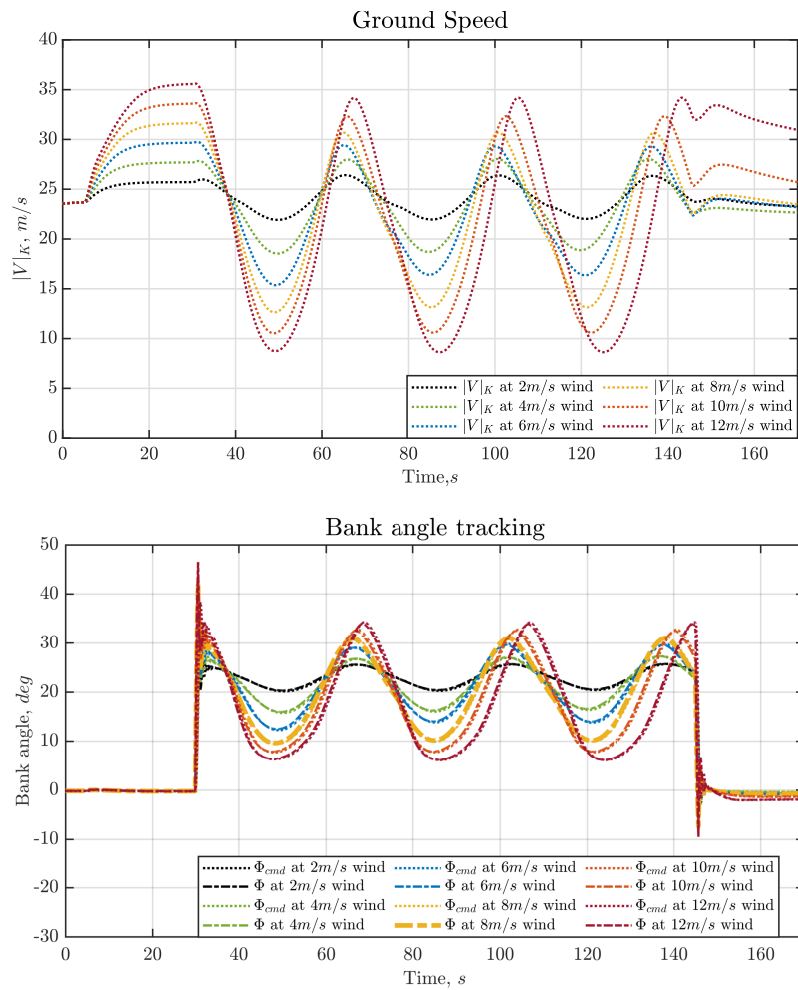


Figure 3.21: Kinematic Velocity and bank angle tracking during turn flight in a constant wind field

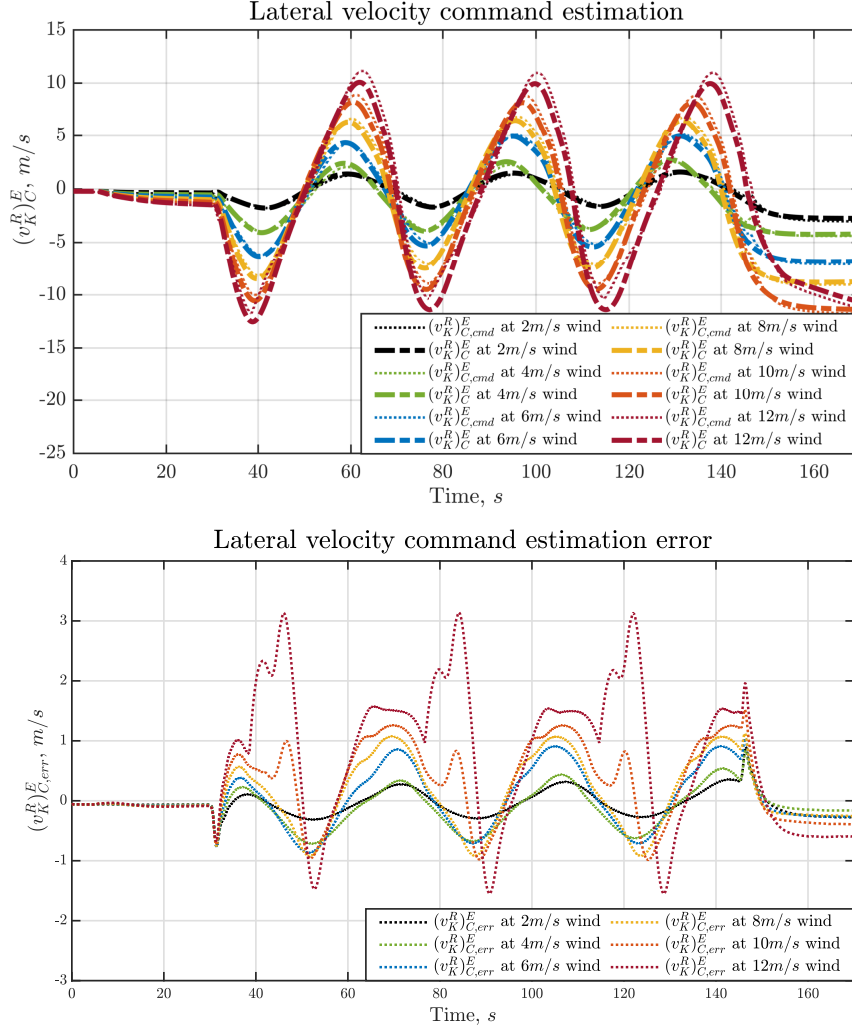


Figure 3.22: Lateral Velocity command response and tracking error during turn flight in a constant wind field

The increasing deviation of the lateral velocity command from the true velocity with increasing wind magnitudes proves that the kinematic simplifications employed for the velocity command mapping (Eq. (3.74)) in the *Commands Transformation* unit are violated in high wind gradient flight conditions. It was stated before that the true lateral velocity is implicitly controlled through minimization of the body lateral load factor. As the mapped lateral velocity command moves farther away from the real velocity, this deviation leads to generation of a reference lateral load factor $(n_y^R)_{C,R}$ which is allocated to a bank angle command. This bank angle command acts against the lateral velocity generated to minimize body lateral load factor. One way to mitigate the allocation of the lateral velocity error to the bank angle is to specify the reference gain for the lateral velocity in the forward-velocity phases $K_{v_{C,R},fwd}$ as zero. Therefore, the reference gain $K_{v_{C,R}}$ blends to zero as the aircraft accelerates to higher kinematic velocities.

However, if the proportional error gain $K_{v_{C,R},fwd}$ is specified to be zero, the reference velocity trajectory $(v_K^R)_{C,R}^E$ would stay at its last reference state value before the gain $K_{v_{C,R}}$ is completely blended to zero. This is not acceptable since the error between the reference velocity and the true velocity is transmitted to the reference pseudo control

$(n_y)_{C,R} \in \mathbb{R}$ for construction of the desired pseudo control $(n_y)_{C,des} \in \mathbb{R}$

$$(n_y)_{C,des} = (n_y)_{C,R} + K_{e,v} \cdot \left((v_K^R)_{C,R}^E - (v_K^R)_C^E \right), \quad (3.158)$$

where $(v_K^R)_C^E \in \mathbb{R}$ is the lateral velocity denoted in the control frame estimated through the sensor measurements. It is important to note that although full state measurement feedback is available, the variables used in the controller feedback architecture are still called estimated variables since the sensor measurements are processed to filter out any noise in the *Estimation* module. Equation (3.158) exhibits that the lateral velocity error forms a part of the desired lateral load factor in the control frame. Therefore, if the reference lateral velocity differs from the real velocity in the forward-velocity phases, a non-zero velocity error will be transformed to an incremental bank angle command through the CA. As it was explained before, this is not intended because the desired lateral velocity is implicitly specified through the constraint of body lateral load factor minimization (Eq. (3.155)) in the forward-velocity flight regimes.

Consequently, the requirement for the reference lateral kinematic velocity $(v_K^R)_{C,R}^E$ being equal to the real velocity in the forward-velocity flight phases originates. This equivalence requirement is fulfilled by slaving the reference variable to the estimated velocity. The reference velocity state-integrator in the Translation RM is reset to the magnitude of the real velocity when the blending parameter $\lambda_{vel,cmd}$ reaches 1 during acceleration to the transition phase as demonstrated by the velocity blending parameter plot in Fig. 3.30. This ensures that the error term in Eq. (3.158) does not produce any impact on the generation of the desired pseudo control $(n_y)_{C,des}$, hence only the reference pseudo control $(n_y)_{C,R}$ is commanded to the control allocation. Emanating from Eq. (3.97), the $(\dot{v}_K^R)_{C,cmd}^{EC}$ used for the production of the reference pseudo control $(n_y)_{C,R}$ also vanishes since the reference proportional error gain $K_{vC,R}$ is defined to be zero in the forward-velocity phases, thereby yielding

$$(n_y)_{C,R} = \frac{1}{g} \left[(u_K^R)_{C,R}^E \cdot \dot{\Psi}_{cmd} \right]. \quad (3.159)$$

Ultimately, the bank angle generation is only driven by the desired incremental pseudo control containing the commanded heading rate and is not affected by the error in the command estimation of the C -frame lateral velocity

$$\begin{aligned} (n_y)_{C,des} &= \frac{1}{g} \left[(u_K^R)_{C,R}^E \cdot \dot{\Psi}_{cmd} \right] \\ \Delta (n_y)_{C,des} &= \frac{1}{g} \left[(u_K^R)_{C,R}^E \cdot \dot{\Psi}_{cmd} \right] - (\hat{n}_y)_C^R. \end{aligned} \quad (3.160)$$

Here $(\hat{n}_y)_C^R \in \mathbb{R}$ is estimated from the body fixed acceleration measurements provided by the IMU. Thus, by slaving the reference model kinematic velocity state $(v_K^R)_{C,R}^E$ to the estimated velocity $(v_K^R)_C^E$ from sensor measurements, not only the bank-to-turn constraint is enforced in the forward-velocity phases, the cross-wind disturbance rejection strategy is also decoupled from the roll channel. Cross-winds are only dealt by turning the nose towards the direction of the wind by making use of the lateral body load factor feedback in the yaw rate command specification for the forward-velocity flight phases.

Therewith, the compliance enforcement among different reference variables to produce a consistent desired behavior specification through the integrated reference model is accomplished. Blending of flight-phase specific kinematic velocity commands, rotation rate commands and reference gains along with reference states slaving is employed to obtain conformity between all channels of the reference dynamics for each phase of the VTOL transition configuration. The proposed strategies in this section relate to the contribution **C.2.5 Approaches to enforce compliance between different reference variables** of this dissertation.

3.4 Verification

This section presents the verification results for the integrated reference model used in tandem with the INDI controller framework for the VTOL transition aircraft configuration presented in the section 3.2.1. Simulation verification results are exhibited first, and further the results from the flight test experiment are also provided.

3.4.1 Simulation Results

In order to verify the proposed strategies in this chapter, simulations are performed separately for the control variables corresponding to each motion axis in every flight phase of the full envelope. Later aircraft response is also demonstrated for coupled maneuver commands in more than one motion axes.

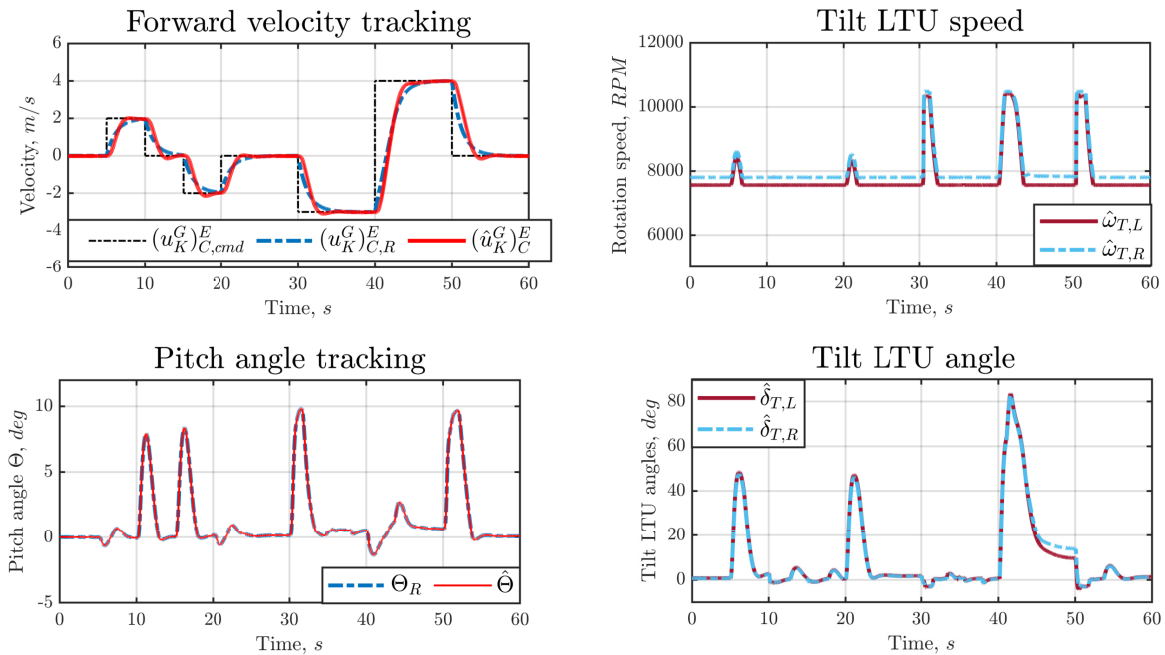


Figure 3.23: Forward velocity tracking in hover flight phase

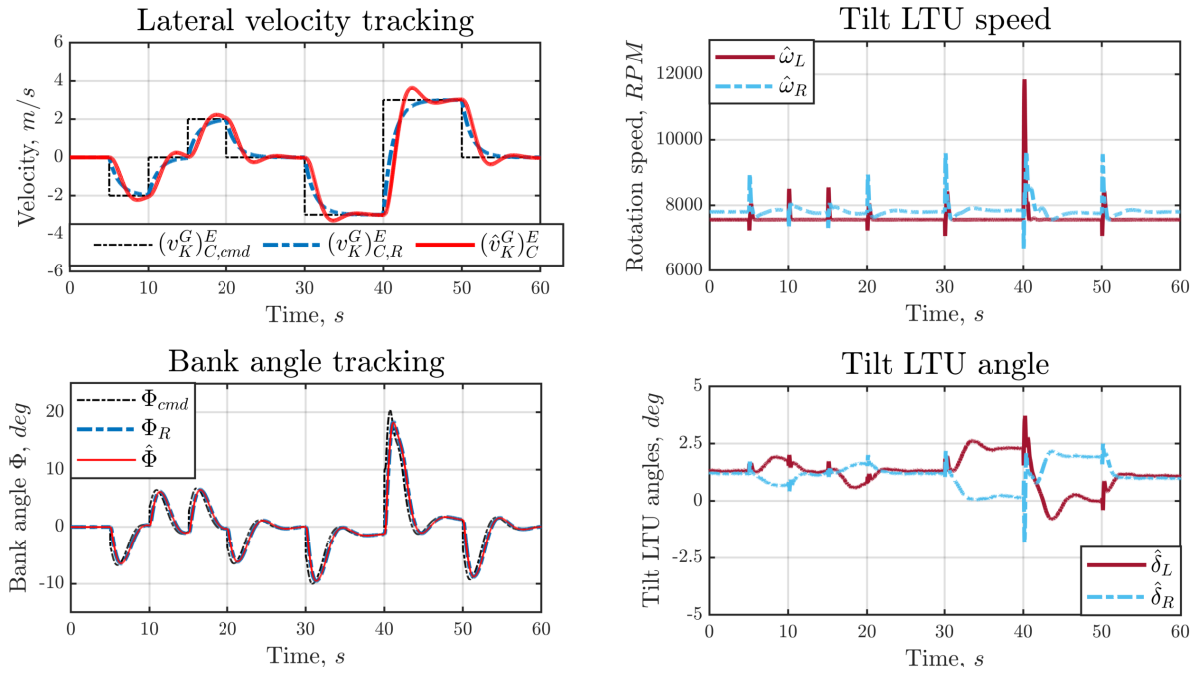


Figure 3.24: Lateral velocity tracking in hover flight phase

Firstly, single axis maneuvers in the hover flight phase are commanded. Figure 3.23 illustrates doublet maneuvers for the forward velocity in the C -frame $(u_K^G)_C^E$. It is observed in the plots that positive velocity is generated by rotating the tilt LTUs in the forward direction and negative velocity in the x_C axis is produced by tilting the powered lift through the pitch angle. Moreover, braking while moving with a positive velocity is also attained using the pitch angle in order to maintain similar transient response during acceleration and deceleration.

Contrary to the forward velocity, the lateral velocity in the control frame can only be produced by tilting the powered lift through the bank angle for hover flight. Figure 3.24 demonstrates the aircraft response to lateral velocity doublet commands. It can be seen that the difference in the rotational rates of the left $\hat{\omega}_L$ and right tilt LTUs $\hat{\omega}_R$ facilitates generation of the roll moment, which further results in the bank angle. Consequently, the lateral velocity builds up. The tilt angles of the LTUs stay close to zero. Minimal deviations in the tilt angles are commanded to counteract any disturbances or inter-axis coupling effects in the yaw channel.

The vertical velocity in hover flight can only be produced through the powered lift majorly from the main LTUs. The two plots on the left side of the Fig. 3.25 present the aircraft response to vertical velocity commands in the C -frame. It can be observed that for command values of ± 1 m/s the transient tracking follows the reference trajectory better as compared to the transient tracking for higher command values of ± 3 m/s. The reason for the deterioration in tracking response is associated with the rate saturations in the dynamics of the main LTUs. Especially, the rate saturation during deceleration of the propeller rotational speed is higher as compared to the increase in the propeller rotational speed because there is no active braking and the braking of the propeller

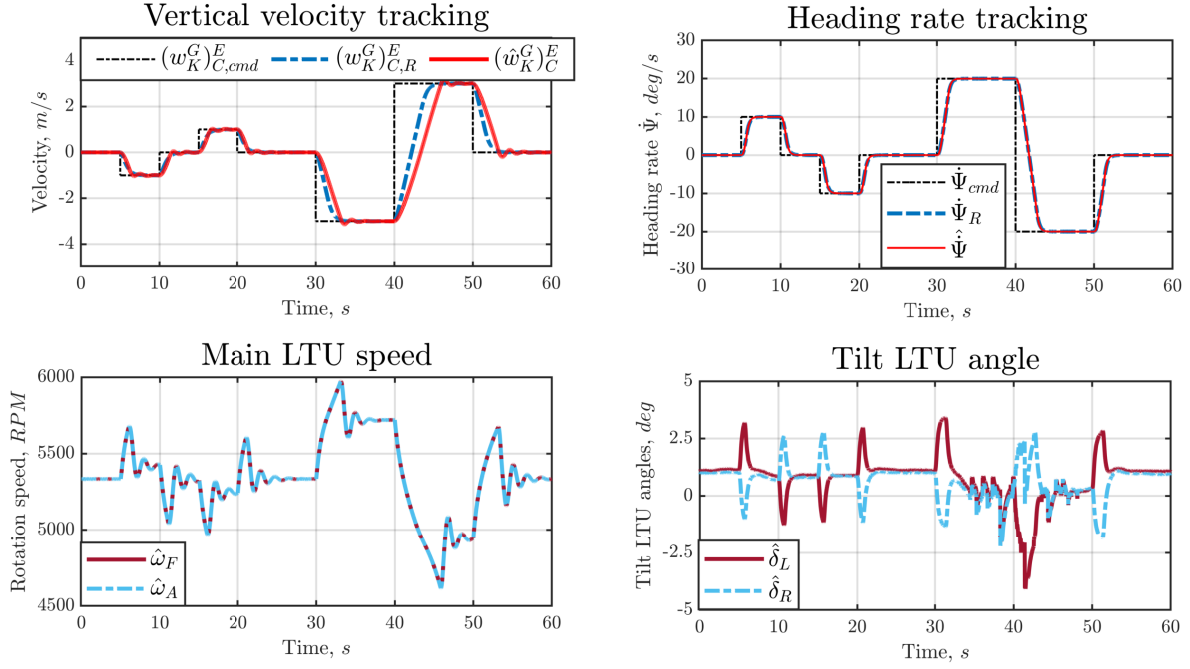


Figure 3.25: Vertical velocity and Heading angle rate tracking in hover flight phase

rotational speed only occurs through the aerodynamic drag of the propellers. The mismatch in reference tracking for higher magnitudes of positive and negative vertical velocity commands is attributed to the fact that direction dependent saturations are not specified in the reference vertical force actuator dynamics described by Eq. (3.101).

Additionally, the plots on the right side of the Fig. 3.25 demonstrate the aircraft response to the heading rate commands. The demand in the yaw angular rate corresponding to the reference heading rate trajectories is allocated to the left and right deflection angles $\hat{\delta}_L$ and $\hat{\delta}_R$ of the tilt LTUs. It can be seen that the higher bandwidth of the heading rate response is achievable owing to the large moment arm with respect to the tilt LTUs.

In order to assess the effect of inter-axis couplings in the aircraft response, a MIL simulation test with commands specified for all the control variables within the hover phase is performed. Figure 3.26 illustrates the response to velocity commands in the control frame along with the tracking of the Euler attitude (Φ , Θ) and heading rate ($\dot{\Psi}$) commands. Clearly, the reference trajectory tracking for all command variables is adequate. Although minor, the inter-axis coupling between the vertical and the longitudinal channel is visible through the vertical velocity response at time stamps of 15, 40 and 70 seconds. As deceleration along the x_C axis is commanded, a corresponding pitch angle is generated to tilt the powered lift in the negative x_C direction in order to fulfill the demand in the negative longitudinal specific force, thereby tracking the reference velocity set-point. The tilting of the powered lift implies that the main LTUs need to produce more thrust in order to maintain the altitude. However, the pitch angle builds up faster through the feedforward path before a disturbance in the vertical channel is sensed, which is then counteracted through the feedback loop. Although, the

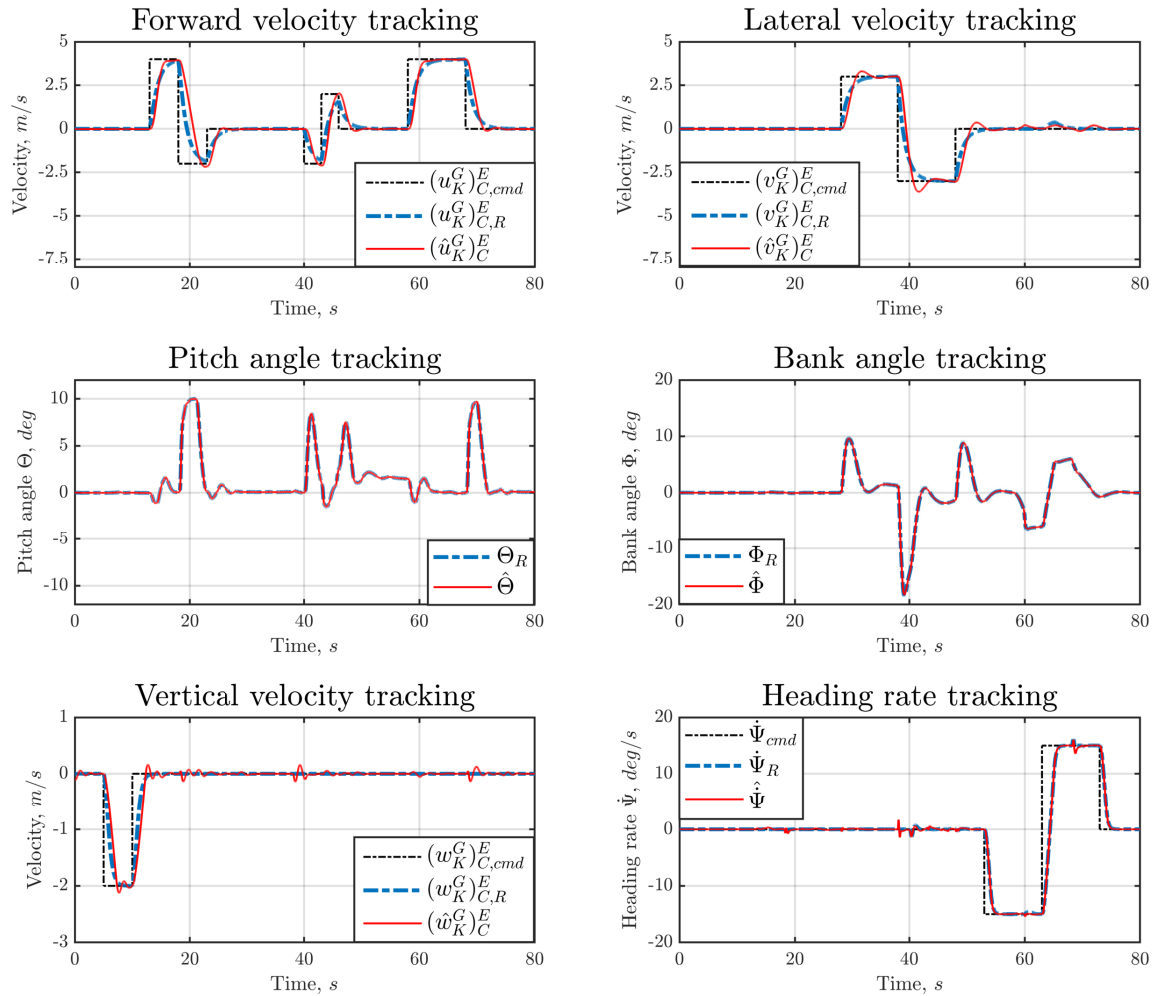


Figure 3.26: Coupled velocity and heading angle rate maneuvers in hover flight phase

effect of this coupling is incorporated through the moments emulation in the translation reference model, yet the true pitch angle command computed through the feedback of the pitch angle is also affected by the sensor dynamics and transport delays in the closed loop system. These dirt effects add to the coupling effect between the two axes and result in the minor deviations from vertical velocity reference trajectory as illustrated by the plot in Fig. 3.26.

Doublets for forward and lateral velocities in the control frame are commanded between the time intervals 30 and 50 seconds for the simulation test demonstrated in the Fig. 3.26. Accordingly, reference pitch and bank angle trajectories are specified dependent on the VCIs. It can be observed that the desired trajectories of the velocities and angles are followed without significant deterioration when compared to the aircraft response in single-axis maneuvers from Figs. 3.23 and 3.24.

Moreover, the inter-axis coupling between the longitudinal and lateral translation channel originating due to the heading rate (Eq. (2.60)) is also examined. A doublet in heading rate is commanded at the time instance of 50 second in the simulation run. Shortly after the heading rate is commanded, a forward velocity command is given. It can be seen from the bank angle response that as the forward velocity starts building

up while the heading rate remains at the commanded set-point, a reference bank angle is specified to facilitate a bank-to-turn maneuver. Importantly, the reference and true lateral velocity in the C -frame are not affected by the inter-axis coupling during the simultaneous forward velocity and heading rate maneuvers.

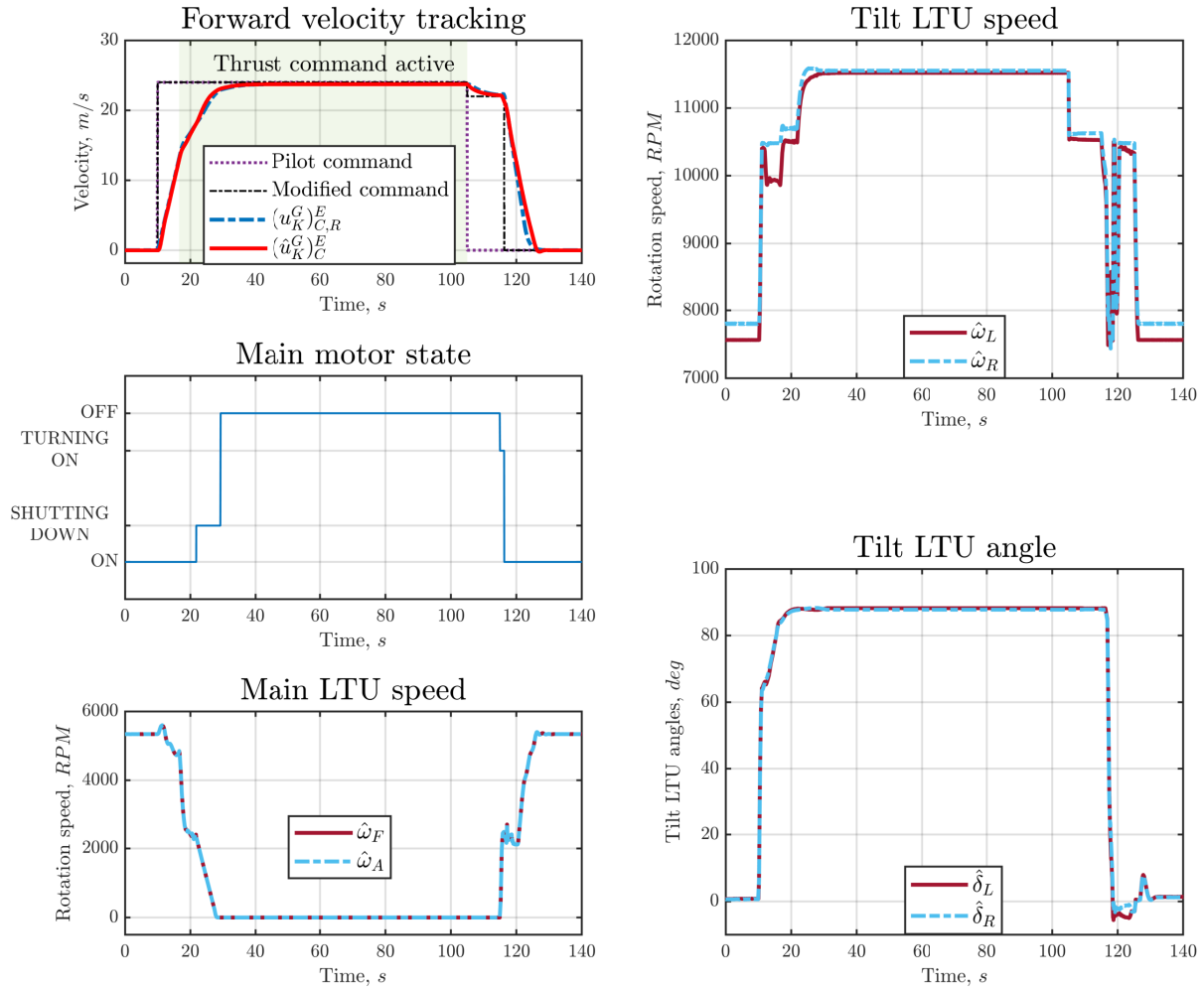


Figure 3.27: Forward velocity commands and tracking in Transition/re-transition

Aircraft response to longitudinal velocity/traction thrust command along with corresponding effector trajectories during a straight transition to wingborne flight is exhibited in the Fig. 3.27. The highlighted region in the forward velocity tracking plot shows the instant of change in interpretation of the pilot command from velocity to traction thrust as the aircraft accelerates beyond 12 m/s. Further, as the aircraft accelerates beyond the aerodynamic stall speed, the main motor state changes from SHUTTING DOWN to OFF implying that the aircraft is then in wingborne phase. This is also corroborated by the RPMs of the main LTUs. In order to produce forward acceleration, the tilt LTUs not only increase their rotational speeds, but their deflection angles are also pointed forward, where they ultimately align with the body-fixed x_B axis. Important to observe that during the entire transition procedure, the integrated reference model produces a continuous, smooth and intuitively correct desired forward velocity trajectory independent of the flight phase and the changing pilot inceptor command interpretation. When the pilot

moves the thrust inceptor to the neutral position in the spring-centered region at 105 seconds intending to command a velocity of 0 m/s and initiate a re-transition to hover phase, the main LTUs are not immediately powered on. However, the pilot command is overwritten to a lower inceptor deflection value in the spring-free region in order to reduce the airspeed to a safe value where the main propellers can start rotating without bringing about any structural damage to the aircraft. Once the safe airspeed is reached the main LTUs move to the TURNING ON state and the tilt LTUs are commanded to zero position, further decelerating the forward velocity. More details on the functions of the *System Automation* module, such as the calculation of the main motor state and the overwriting of the pilot inceptor command are described in [200].

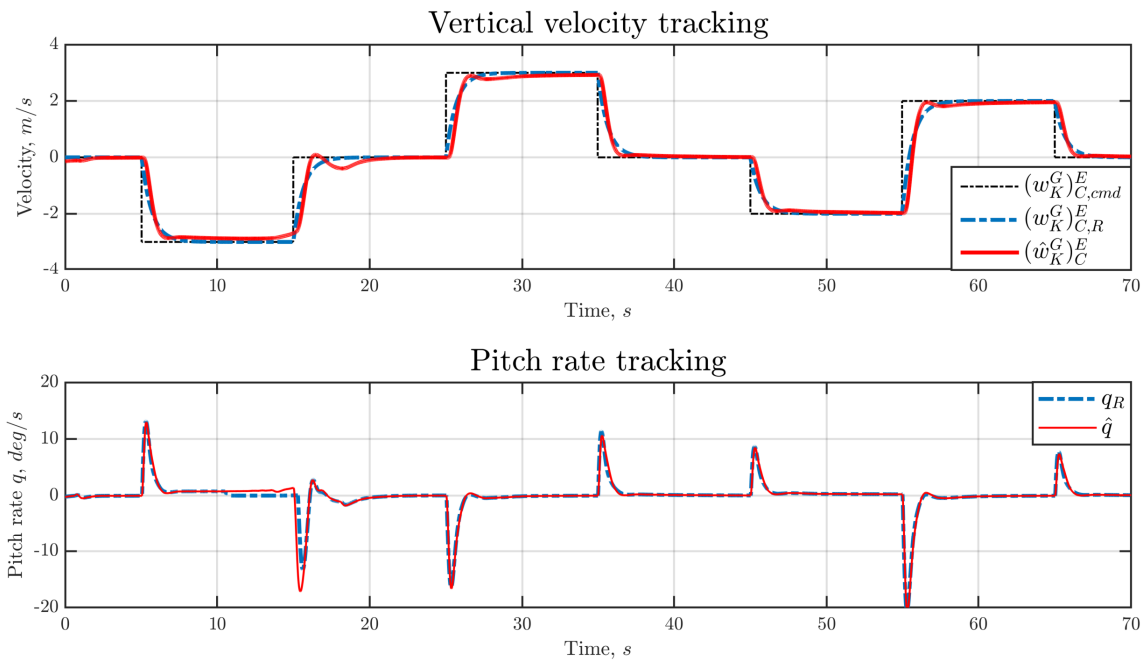


Figure 3.28: Vertical channel tracking in wingborne flight

Bi-directional steps along with doublets in the vertical velocity are simulated during wingborne flight. Figure 3.28 shows the reference tracking of the vertical velocity $(w_K^G)_C^E$ and the tracking response of the reference pitch rate q_R generated from pitch rate command for the forward-velocity phases derived in Eq. (3.134). Results demonstrate precise tracking of high bandwidth reference trajectories of pitch rate and vertical velocity in transient as well as steady-state phases. Similar test cases were performed for turning flight in the wingborne phase. Figure 3.29 illustrates the reference bank angle trajectory computed from the heading rate command, as in Eq. (3.129), to perform a steady state coordinated turn. Additionally, reference body angular rates p_R , q_R and r_R were also defined, which incorporate the trim commands derived in Eqs. (3.130) and (3.131). The computed reference angular rates satisfy the constraints of a coordinated turn given in Eqs. (3.121) and (3.122). Accurate tracking of the reference trajectories in this simulation test case results from the tilt control surface deflections $\hat{\delta}_L$ and $\hat{\delta}_R$, which act as ailerons during flight in the wingborne phase.

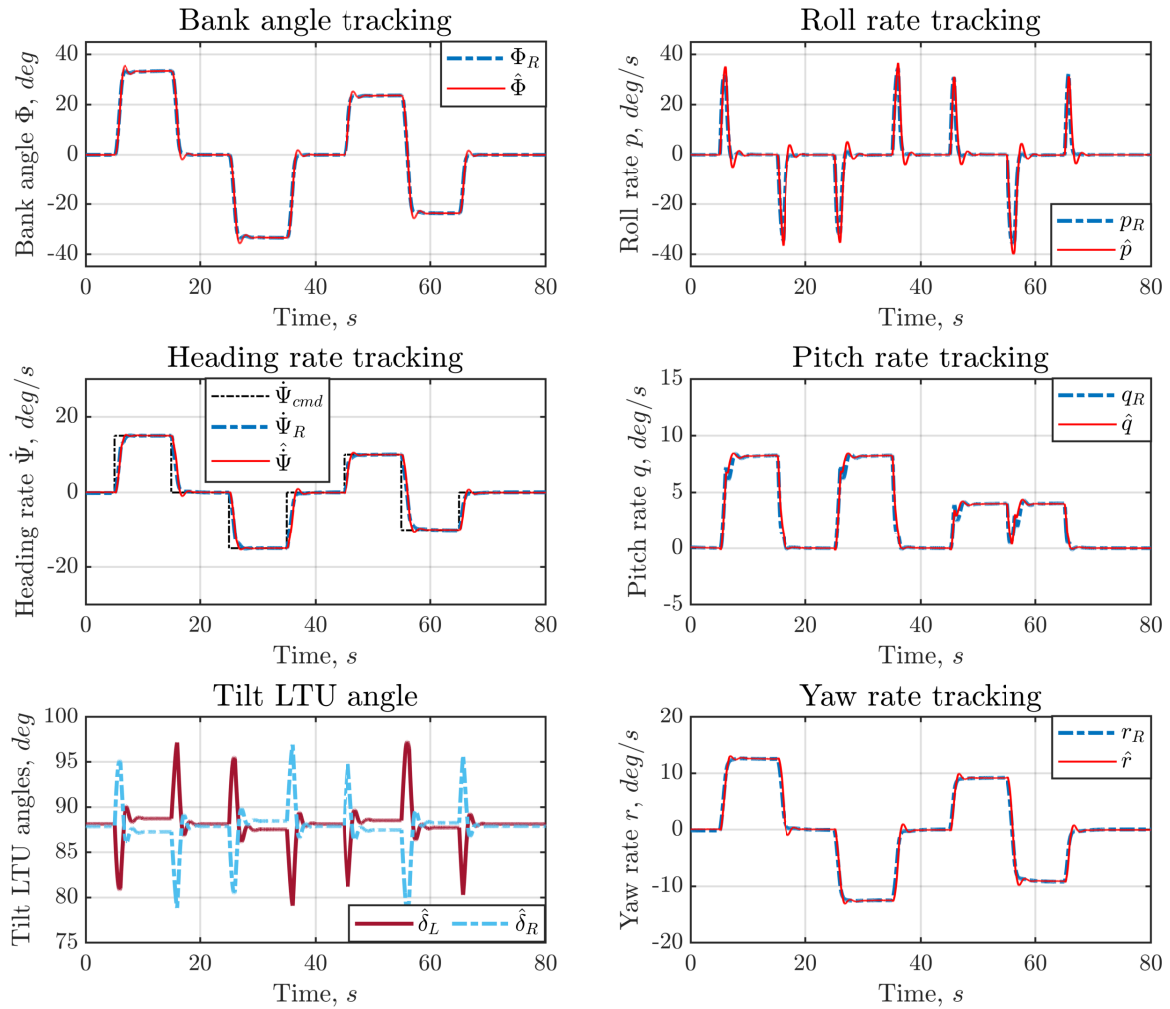


Figure 3.29: Lateral channel tracking in wingborne flight

An important feature of the proposed reference model structure is the explicit specification of the wind disturbance behavior especially in cross-wind flight situations. It was explained in the section 3.3.3.4 that the cross wind is countered in hover flight phase by tilting the powered lift through a bank angle. This bank angle is produced as a consequence of the error between the reference lateral velocity (specified as zero in this case) and the non-zero real lateral velocity caused by the external disturbance. On the other hand, cross wind is dealt with by turning the aircraft nose in the direction of the wind by employing the body lateral load factor feedback in order to bring this load factor to zero. Simultaneously, it must be ensured that the mapped lateral velocity command in Eq. (3.74) is equal to the true lateral velocity to avoid any conflict with the desired behavior resulting from the lateral load factor feedback. In order to illustrate that the intended aircraft behavior is followed, simulation test is performed for transition to wingborne from hover flight phase. The test case is performed with the aircraft flying to the north i.e. with a heading of 0° . The simulated wind disturbance had a magnitude of 6 m/s blowing towards east i.e. heading of 90° .

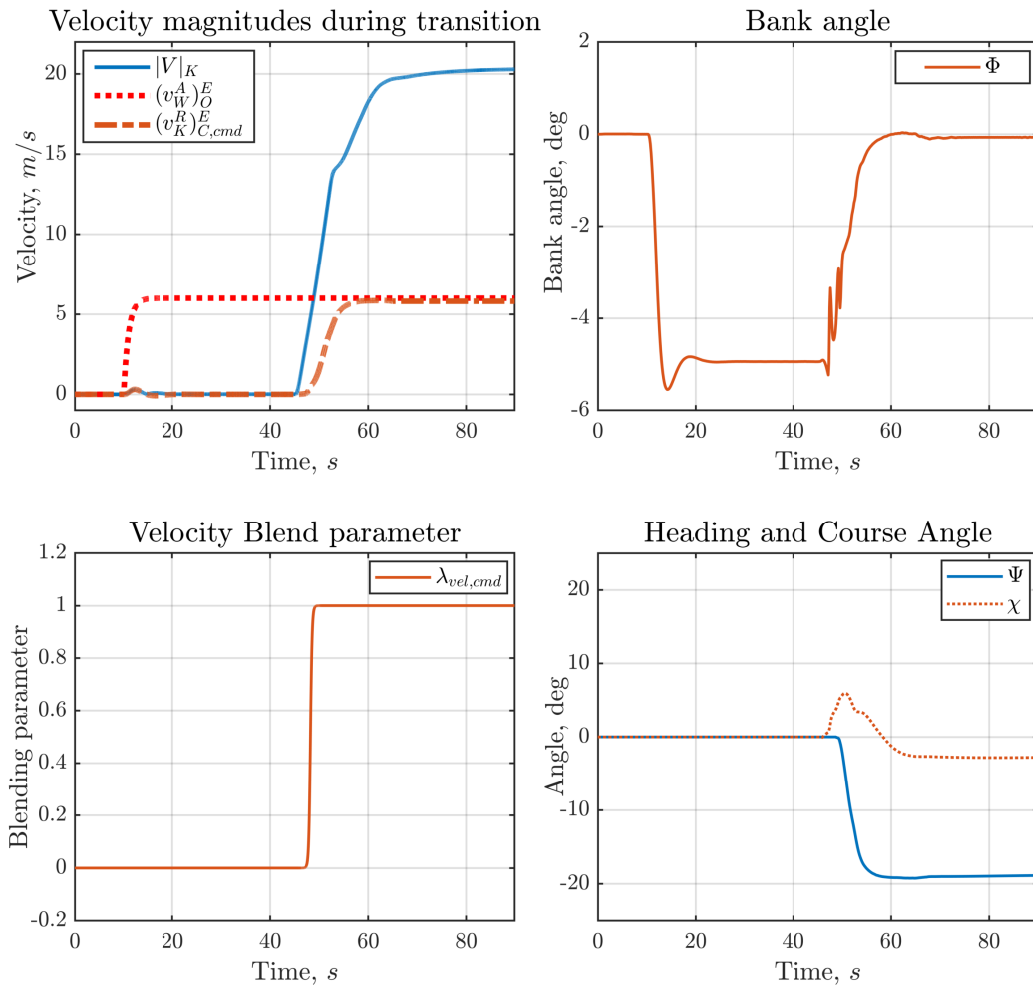


Figure 3.30: Transition to wingborne flight phase in a cross-wind field

Figure 3.30 demonstrates the transition to wingborne in the cross-wind field having the parameters specified before. As soon as the wind field simulation is initiated, a negative bank angle is built up in order to counteract the disturbance. The bank angle stays constant until the aircraft starts accelerating, and the C -frame lateral velocity command $(v_K^G)^E_{C,cmd}$ to the RM core stays at zero. When the aircraft accelerates beyond 8 m/s, the velocity blend parameter $\lambda_{vel,cmd}$ employed to blend the velocity commands in Eq. (3.149) goes to 1. Synchronously, the bank angle starts reducing to zero and the cross-wind rejection is thereafter performed by turning the aircraft nose into the direction of the wind. It can also be observed that the magnitude of the lateral velocity kinematic command $(v_K^G)^E_{C,cmd}$ computed in the *Commands Transformation* module according to Eq. (3.152), converges to the wind velocity magnitude. The convergence only occurs due to this specific simulation case where the wind velocity has been simulated at a right angle to the direction of the aircraft velocity. Another important observation is that the course angle does not show a high variation during the acceleration phase even though track hold function is not active.

Aircraft response in high wind gradient conditions in the wingborne phase has already been covered in the section 3.3.4.3. By synchronously blending the reference gains for lateral velocity and slaving the reference velocity state to the true velocity, it was ensured that any inadvertent bank angle incremental command is not generated to counteract the cross-wind in forward speed flight phases, and only the yaw rate command is employed to minimize the body lateral load factor in cross-wind conditions. Herewith, the Model-in-the-Loop (MIL) verification of the integrated reference model has been accomplished. In the next section, the reference variable tracking in an experimental flight test comprising of an automated flight mission is displayed to substantiate the feasibility of the proposed algorithms in real application.

3.4.2 Experimental Results

Automated flight test of the aircraft configuration described in the section 3.2.1 was performed using the INDI control algorithm along with the integrated reference model proposed in this work. A planned trajectory, illustrated by the Fig. 3.31, was flown during

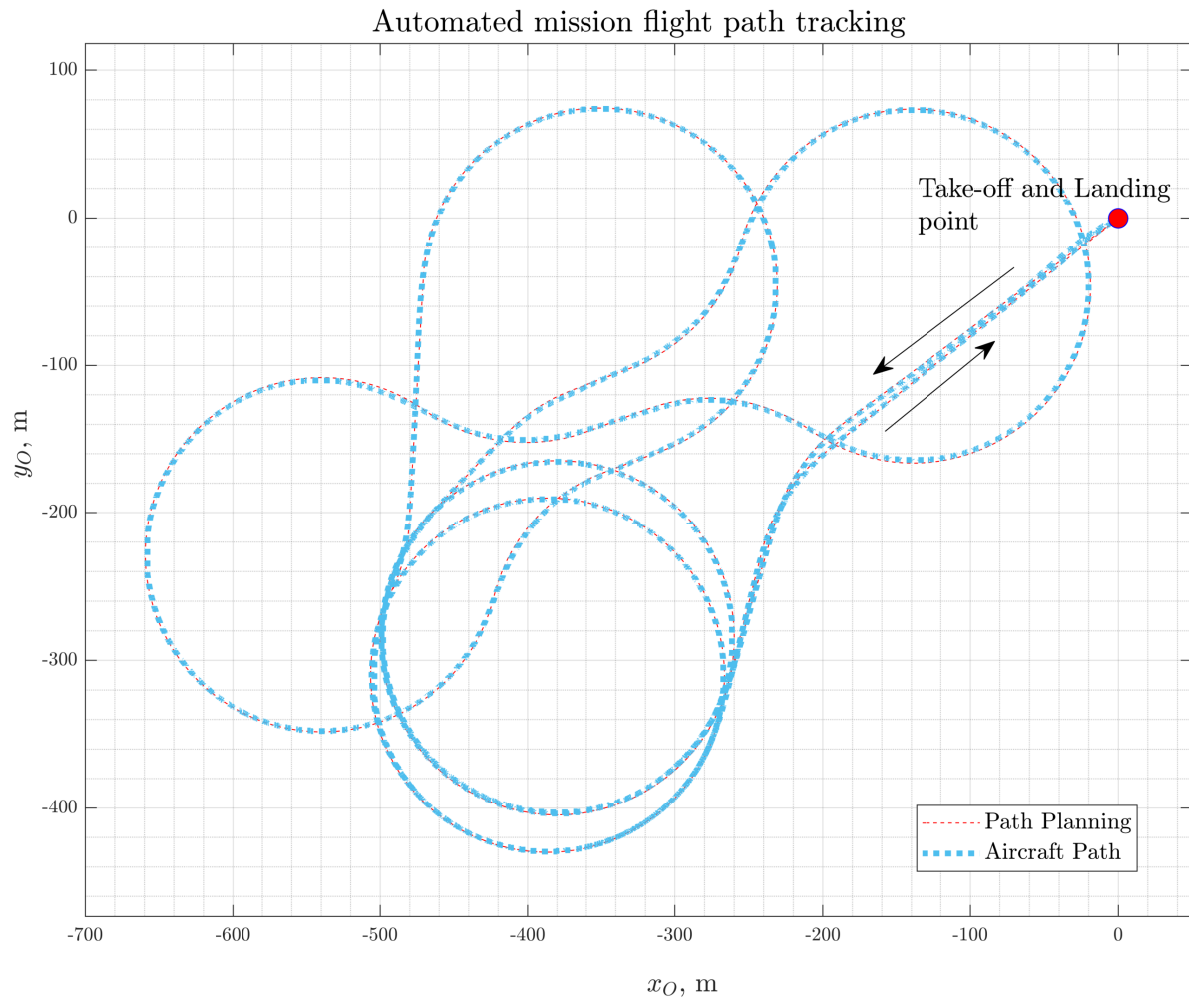


Figure 3.31: Flight path visualization during automated mission

the flight test mission. In order to follow the planned trajectory, a guidance module generated the control frame lateral velocity, course angle rate along with the height rate commands to the integrated reference model. The forward channel velocity command set point is specified in the definition of the flight mission, and is interpreted as forward velocity in the control frame, absolute kinematic velocity or thrust command based on the flight phase of the aircraft according to the description given in the section 3.3.2. Important to note that if the flight mission definition specifies a velocity of beyond 12 m/s , it is interpreted as a thrust level command equivalent of the maximum endurance thrust level $\delta_{T,e}$ (Fig. 3.8), only in the case of the automated mission. The weather conditions during the time of the flight test indicated a wind velocity of 7 kts in the south-west direction at an altitude of 160 ft above ground level. The flight mission initiates with a vertical take-off maneuver represented by the vertical velocity maneuver from 20 to 60 s demonstrated by the vertical velocity tracking plot in the Fig. 3.32. After the vertical maneuver is accomplished, the transition to wingborne flight commenced. The plot of the forward velocity tracking in the C -frame shows the reference and true

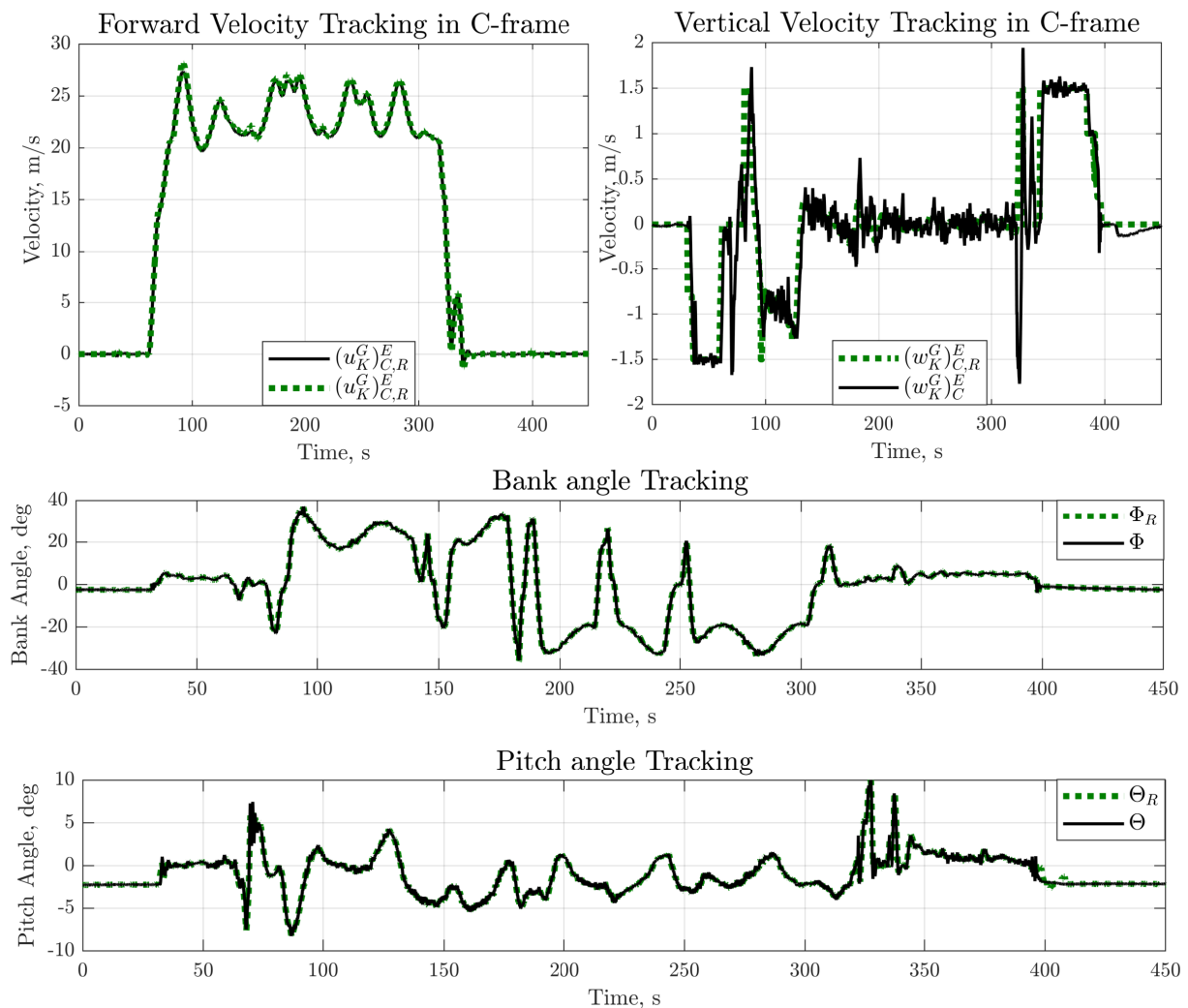


Figure 3.32: Reference velocity and attitude angle tracking in automated flight mission

forward velocity during the flight mission. It can be observed that the kinematic speed varies between 20-27 m/s depending on the relative heading of the aircraft with respect to the wind flow. The course angle rate tracking in order to follow the planned flight trajectory during the flight mission is attained through the bank angle. For this purpose, the reference bank angle is calculated according to Eq. (3.129), which is demonstrated in the bank angle tracking plot of the Fig. 3.32.

In the wingborne flight, the vertical channel is regulated through the pitch channel. Pitch angle command derived through the virtual control inputs is employed to compute the reference pitch angle trajectory which is illustrated by the pitch angle tracking plot. Moreover, during the re-transition to hover phase, the pitch angle is also used to decelerate as shown by the pitch angle plot between the time stamps 300-350 seconds. Finally, the mission ends with the vertical landing maneuver as demonstrated by the positive C -frame vertical velocity maneuver between the timestamps 350-400 seconds in the vertical velocity tracking plot of the Fig. 3.32. The lateral and vertical position deviation from the desired trajectory in the wingborne phase is demonstrated by the Fig. 3.33. It can be observed that there is a steady state positive deviation error in the vertical channel, which is explained by the fact that there is no integral error controller employed on the vertical channel position. Although the mean of the vertical deviation stays at 1.24 meters, the standard deviation is only 0.272 meters. The mean and standard deviation of the lateral position deviation is 0.133 meters and 0.998 meters respectively.

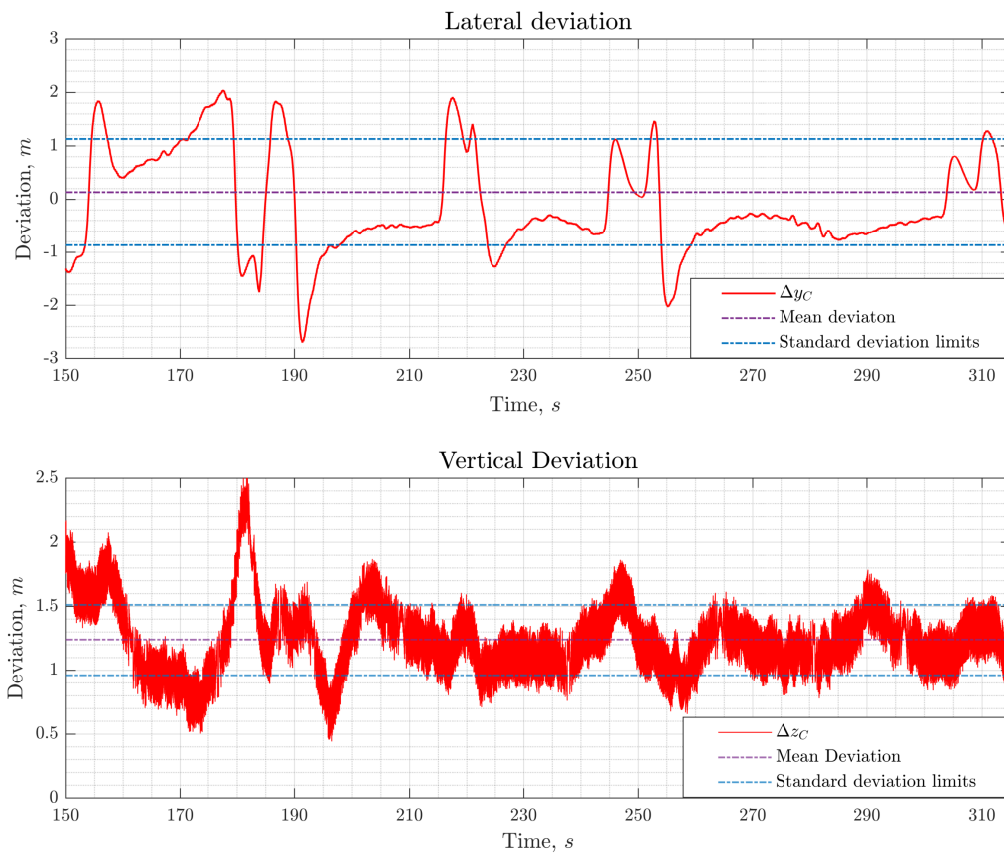


Figure 3.33: Lateral and vertical position deviation in automated flight mission

Hence, the verification of the proposed integrated reference model architecture working in tandem with the INDI controller is accomplished through the MIL simulations and flight test experiments. Upcoming section summarizes the important aspects covered in this chapter.

3.5 Summary

This chapter described the framework of a modular, aircraft configuration-independent reference model for vertical take-off and landing transition aircraft. The reference model structure proposed here enabled the application of a unified INDI control strategy over the complete flight envelope of a transition aircraft, thereby preventing the necessity of switching between flight phase specific controllers. Three sets of control variables pertaining to each of the three flight phases of the VTOL transition aircraft – hover, transition and wingborne were specified. The choice of these control variable sets was governed by the following constraints.

1. Firstly, the control variable set for each phase must match the conventional CV choice for single phase configurations such as multicopters or fixed-wing aircraft. Furthermore, the control variable to pilot inceptor mapping should be performed in a manner that the aircraft response to pilot commands remains consistent over the complete envelope.
2. The chosen control variable sets should have a direct kinematic relation to one CV set, which acts as the input interface for the RM core module.
3. Lastly, the control variable choices should lead to a uniform set of reference pseudo controls as well as reference external states for the purpose of maintaining a unified interface to the INDI controller.

The mapping of the pilot inceptor commands to the chosen control variable sets was performed in the *Command Transformation* module of the RM based on current flight phase. Moreover, the transformation of the mapped control variable sets to the reference model core's input interfaces was also carried out in this unit.

Structure of the Reference Model core, which is the flight phase agnostic unit of the integrated RM, was also elaborated. It comprises of the translation (outer loop) and rotation (inner loop) reference models. Translation RM specifies the reference trajectories for load factors and kinematic velocities denoted in the control frame. Composition of the forward-lateral inter-axis coupling term along with moments emulation and pseudo force-moment actuators in the reference plant dynamics form a part of the translation reference model. The rotation RM comprises of the sequential rotation rate command generation based on the desired load factors from the translation channels. Explicit cross-wind disturbance rejection is provided by using the body-lateral load factor feedback for the yaw rate command generation in high dynamic pressure regime. Moreover, nonlinear attitude kinematics are also considered in generation of the reference body rotational acceleration, rates and Euler attitude angle trajectories.

Techniques such as flight phase dependent blending of control variables, reference gains and rotation rate commands were applied to maintain conformity among the reference variables. Additionally, feedback of true course angle is employed to establish accurate mappings between the control variable sets specifically for flight in high wind gradient conditions. Slaving of the reference states to the true plant states was also employed to enforce consistency between all reference trajectories.

The effectiveness of the developed RM along with the INDI controller is verified through model-in-the-loop simulations and flight test experiments. The modularity of the proposed RM framework is evident through its application by other researchers in their works [204–206].

Chapter 4

Jerk-Level Physical Reference Model

This chapter introduces the design methodology for a jerk-level reference model that generates reference trajectories for a controller based on a continuous extension of the incremental nonlinear dynamic inversion. The proposed reference model design assimilates the influence of the identifiable disturbances like the state dependent damping effects as a part of a design plant. Essentially, the design plant incorporates aircraft parameters known with some level of confidence. Nonlinear dynamic inversion of the design plant is employed to produce an aircraft model based feedforward to the extended INDI framework. This technique differs from the classical NDI approach in which a system model is inverted to generate control effector commands. Contrarily, in the presented approach the model knowledge is only employed to compute the feedforward signal, which is dynamically one derivative level higher than the relative degree of the controlled system. The overall control scheme integrates the advantages of feedback linearization based on the design plant in the feedforward channel while conserving the robustness properties of the extended incremental approach in the feedback architecture. Besides the inclusion of the physical plant parameters, the jerk-level physical reference model framework incorporates effects of noise-reduction/estimation filters, input/output channel dynamics and high order effector dynamics to produce an appropriate feedforward and reference trajectories not only in terms of aircraft physics but the control system architecture as well.

The advantage of having an effective feedforward strategy is simply stated in the fact that it is independent of the feedback loop design. The feedback architecture is driven by a set-point tracking error, hence a control algorithm based solely on feedback reacts only after the error builds up. However, a feedforward can anticipate and facilitate the required proactive control action even before the tracking error emanates. Simply put, the feedforward channel can act before the feedback controller has a chance to react in many cases. This brings out the motivation for generating an effective feedforward derived through model knowledge embedded in the reference model. Important to note that the purpose of the proposed feedforward architecture is not intended to counteract

against disturbances induced by external environment. This is even causally infeasible. However, the feedforward strategy targets to preemptively account for the physical effects of the controlled system, which manifest as a result of a motion command. One of the examples of such an effect is a system state induced damping which is commonly referred to as the "A-part" of any linear time invariant system [90].

In accordance with the description in section 3.1.1 and an elaborate literature review, it has been established that the INDI control strategy lowers the dependency on an explicit aircraft model for inversion in comparison to nonlinear dynamic inversion. The INDI technique employs inversion of a linearized control effectiveness matrix as shown in Eq. (3.20). The state dependency ("A-part") is neglected owing to the assumptions A.3.4, A.3.5 of high controller refresh rate and instantaneously fast actuators respectively. Consideration of these assumptions additionally renders the linearization error trivial. However, actuators used for practical applications are not instantaneously fast. An extension to the INDI strategy was proposed in [86], which is derived by inverting the direct time derivative of the nonlinear system. This inversion leads to a control input derivative computation law. The computation of the control input increment from its derivative allows for the consideration of the effector dynamics.

Besides, the state reliant dynamics of the linearized system were also omitted in the derivation of the extended INDI law. The state induced damping terms are non-trivial for systems like fixed-wing aircraft comprising of slow actuators and relatively high controller sampling time (order of 10^{-2} s). Resulting from the omission of these dynamics, tracking errors accumulate over the integrator chain of the feedback linearized system, even if the plant is perfectly known and there are no external disturbances. Therefore, by neglecting the state dependent term, any leverage to be gained by the known plant dynamics is completely abandoned. Commonly, the neglected terms are treated through a stabilizing error controller employing proportional tracking error feedback [51, 66, 82, 88].

This chapter proposes to include the effect of these identifiable disturbances–state dependent damping terms in the feedforward from the jerk-level reference model. In the integrated reference model from Chapter 3, the reference plant dynamics are constructed using the rigid-body equations of motion only. Therefore, only the kinematic nonlinearities are considered in the reference model design. Moreover, the calculated feedforward pseudo controls are simply high-pass filtered elements of the control variables, which subsequently leads to a preemptive command of the control effector in the correct direction. However, the control effector command due to the feedforward component vanishes with the reference pseudo control, similar to the illustration in Fig. 3.4, because the state variant component is not accounted for explicitly. Contrarily, the jerk-level reference model structure introduced here employs feedback linearization of any known model dynamics to generate a feedforward, which is one derivative level higher than the relative degree of the system. The reference model assimilates additional system knowledge as a part of a design plant. These model parameters are not used in the control strategy's feedback architecture.

Some of the important aspects covered in the scope of the jerk-level physical reference model include

- 1 **Feedforward pseudo control derivative** generation, which accounts for the "A-part" omitted in the derivation of the extended INDI control law. The goal of using this model information is to reduce the impact of the neglected terms by means of the feedforward. Although, the feedforward can never absolutely compensate for the approximations made for the control law derivation, it can certainly be effective in producing a proactive control input command before the feedback controller kicks in.
- 2 In the continuous extension of the INDI, effector dynamics were accounted for in the control law. However, consideration of higher than first order actuator dynamics required use of a non-causal filter and hence the second order actuators were also approximated as first order elements [86]. The **residual higher order components of the effector dynamics** are incorporated in the higher order reference model.
- 3 Thirdly, **measurement/estimation filter effects** are also integrated in the reference model design to facilitate a phase conformity between the external reference and plant states. Inclusion of these effects delivers the advantage of faster disturbance rejection, since relatively high feedback gains can be used without inducing oscillations in the system due to phase mismatch.
- 4 Similarly, influence of **input/output channel dynamics** in terms of pure time delays is incorporated in the jerk-level reference model with the aim of maintaining phase match between the reference and plant variables.

Initial results pertaining to the jerk-level reference model were presented by the author in [90]. This chapter extracts the features of the already published work and further builds up the jerk-level RM architecture by including the aspects mentioned in points 2, 3 and 4 above. In the upcoming sections, a synopsis of the extended INDI control approach for a group of nonlinear systems is presented. Thereafter, the rationale to utilize a model based feedforward pseudo control derivative is described along with the mechanism for the generation of the feedforward command in the jerk level reference model.

4.1 Extended Incremental Nonlinear Dynamic Inversion

For deriving the control law based on the continuous extension of INDI, a generic nonlinear system like the one defined in Eq. (3.1) is considered

$$\begin{aligned}\dot{\mathbf{x}}(t) &= \mathbf{f}(\mathbf{x}(t), \mathbf{u}(t)), \\ \mathbf{y}(t) &= \mathbf{h}(\mathbf{x}(t)),\end{aligned}\tag{4.1}$$

where $\mathbf{x}(t) = [x_1(t), x_2(t), \dots, x_{n_x}(t)] \in \mathbb{R}^{n_x}$ denotes the states of the system, $\mathbf{u}(t) = [u_1(t), u_2(t), \dots, u_{n_u}(t)] \in \mathbb{R}^{n_u}$ represents the control input, $\mathbf{y}(t) = [y_1(t), y_2(t), \dots, y_{n_y}(t)] \in \mathbb{R}^{n_y}$ presents the system output, $\mathbf{f}_{n_x \times 1} : D_{x,u} \rightarrow \mathbb{R}^{n_x}$ represents the plant dynamics

and the function $\mathbf{h}_{n_y \times 1} : D_x \rightarrow \mathbb{R}^{n_y}$ signifies the output dynamics of the given system. Henceforth, the dependence of the states, control inputs and system outputs on time is not shown for better readability.

Through the nonlinear state transformation $\mathbf{z} = \Phi(\mathbf{x})$ described in section 3.1.1, the general nonlinear input non-affine system in Eq. (4.1) yields the **MIMO normal form** as illustrated in Eq. (3.10). Subsequently, the terms corresponding to the r_i -th derivative of each output channel are collected from the normal form in Eq. (3.10), resulting in a new transformed system

$$\begin{aligned} \nu_i &= F_i(\mathbf{x}, \mathbf{u}) = \xi_{r_i}^i = y_i^{(r_i)} \quad \text{where} \quad i = 1, 2, \dots, n_y \\ \boldsymbol{\nu} &= \mathbf{F}(\mathbf{x}, \mathbf{u}), \end{aligned} \quad (4.2)$$

where $\boldsymbol{\nu}(t) \in \mathbb{R}^{n_y}$ represents the pseudo controls of the system and the vector field $\mathbf{F} : D_{\mathbf{x}, \mathbf{u}} \rightarrow \mathbb{R}^{n_y}$ denotes the transformed system dynamics. The MIMO transformation of the nonlinear system in (4.1) to the pseudo control dynamics from Eq. (4.2) is demonstrated in Fig. 3.1.

Control input commands required to achieve a desired set of pseudo controls can be calculated by solving the transformed system in Eq. (4.2). Nonetheless, it might not be possible to directly solve the pseudo control dynamics function \mathbf{F} if it is not affine in the control input \mathbf{u} . Even if the system is control input -affine, an assumed system model would be used for the inversion, which makes the control strategy susceptible to model uncertainties. Additionally, a direct solution for the transformed system in Eq. (4.2) is not feasible in case the system comprises of redundant control effectors.

In order to overcome the mentioned restrictions, the INDI control strategy has been applied in many applications [56, 57, 59, 88]. The incremental control law is derived by the inversion of a linearized system obtained from Taylor's expansion of the transformed system as in Eq. (3.16). The state dependent dynamics of the linear system are neglected in the incremental control law's derivation. Furthermore, the incremental approach replaces the requirement of model information availability (state dependent dynamics) with state derivative feedback. In [86], a continuous extension of the INDI control law was proposed that not only retains the advantages of the incremental approach but also incorporates effector dynamics within the control law.

In contrast to deriving the control law by linearization of the transformed system from Eq. (4.2) as in the normal INDI, the extended incremental control law is derived by performing an exact time differentiation of the system

$$\begin{aligned} \dot{\boldsymbol{\nu}} &= \overset{A_\nu(\mathbf{x})}{\frac{\partial \mathbf{F}}{\partial \mathbf{x}}} \cdot \dot{\mathbf{x}} + \overset{B_\nu(\mathbf{x}, \mathbf{u})}{\frac{\partial \mathbf{F}}{\partial \mathbf{u}}} \cdot \dot{\mathbf{u}}, \\ \dot{\boldsymbol{\nu}} &= \overset{\dot{\nu}_x}{\mathbf{A}_\nu(\mathbf{x}) \cdot \dot{\mathbf{x}}} + \overset{\dot{\nu}_u}{\mathbf{B}_\nu(\mathbf{x}, \mathbf{u}) \cdot \dot{\mathbf{u}}}, \end{aligned} \quad (4.3)$$

where $\mathbf{A}_\nu \in \mathbb{R}^{n_y \times n_x}$ and $\mathbf{B}_\nu \in \mathbb{R}^{n_y \times n_u}$ are the Jacobian matrices with respect to the states \mathbf{x} and controls \mathbf{u} . Dependencies of the Jacobian matrices are omitted hereafter for better readability. The impact of pseudo control rate produced due to state derivative $\dot{\nu}_x \in \mathbb{R}^{n_y}$ is neglected as compared to the effect of pseudo control derivative due to control input derivative $\dot{\nu}_u \in \mathbb{R}^{n_y}$ owing to the assumptions **A.3.4**, **A.3.5** of small controller sampling time (order of $10^{-2}s$) and instantaneously fast actuators respectively similar to the procedure in the normal INDI control law derivation from section 3.1.1. The state dependent term is neglected for the extended INDI control law derivation, however it is accounted in the stability analysis of the closed loop system. Subsequently, the approximate system dynamics

$$\dot{\nu} = \mathbf{B}_\nu \cdot \dot{\mathbf{u}} \quad (4.4)$$

are employed to derive the inversion control law

$$\dot{\mathbf{u}}_{cmd} = \mathbf{B}_\nu^{-1} \cdot \dot{\nu}_{u,cmd}, \quad (4.5)$$

where $\dot{\nu}_{u,cmd} \in \mathbb{R}^{n_y}$ denotes the pseudo control derivative command generated by the controller, $\dot{\mathbf{u}}_{cmd} \in \mathbb{R}^{n_u}$ represents the control input rate command and \mathbf{B}_ν^{-1} specifies a generalized inverse of the control effectiveness matrix \mathbf{B}_ν . Control allocation techniques such as the ones defined in [168, 169, 189, 190] can directly be used for the allocation of the pseudo control derivative command to the control effector rate commands. However, the interface from the FCC to the actuator input is commonly defined at the level of absolute effector position rather than its derivative. Computation of the control input commands from the derivative command specified by the control law in Eq. (4.5) whilst accounting for the effector dynamics is presented next. The calculation for the first and second order actuator dynamics is covered here since the actuators used in practical applications are commonly estimated through first or second order transfer characteristics [27, 51, 156] when operating in nominal ranges. Important to note that nonlinear elements of real actuators like absolute and rate saturations are not considered in the following computations.

Control input command for effectors with first order actuators

A first order actuator G_A having a natural frequency $\omega_A \in \mathbb{R}$ can be represented in the Laplace domain as

$$G_A(s) = \frac{\omega_A}{s + \omega_A}. \quad (4.6)$$

The relation between the control input command and the achieved control input is shown by

$$u(s) = \frac{\omega_A}{s + \omega_A} \cdot u_{cmd}(s). \quad (4.7)$$

By taking the transfer function to the other side

$$\left(\frac{s}{\omega_A} + 1\right) \cdot u(s) = u_{cmd}(s) \quad (4.8)$$

the relation between the command increment and the absolute command is specified in Laplace domain

$$s \cdot u(s) = \frac{K_A}{\omega_A} \cdot \Delta u_{cmd}(s) - u(s), \quad (4.9)$$

which delivers the following expression in the time domain

$$\dot{u} = K_A \cdot \Delta u_{cmd}. \quad (4.10)$$

Given a control input rate command \dot{u}_{cmd} generated through the extended INDI control law in Eq. (4.5), the incremental effector command is generated by inversion of the relation from Eq. (4.10)

$$\Delta u_{cmd} = K_A^{-1} \cdot \dot{u}_{cmd}. \quad (4.11)$$

Additionally, it is also possible to combine the effector dynamics consideration from Eq. (4.11) with the control allocation technique employed to invert the effectiveness matrix B_ν for all control inputs of a MIMO system

$$\Delta \mathbf{u}_{cmd} = (\mathbf{B}_\nu \cdot \mathbf{K}_A)^{-1} \cdot \dot{\mathbf{v}}_{u,cmd}, \quad (4.12)$$

such that the effector position and rate protections in the allocation algorithm [190] are not violated by post multiplication of the inverse bandwidth matrix \mathbf{K}_A^{-1} later in the chain.

Figure 4.1a illustrates the control input command u_{cmd} generation employing the first order effector dynamics consideration along with the feedback of the control input. In this scenario, the transfer characteristics from an incremental command Δu_{cmd} to the corresponding actuator output u , denoted as $G_{\Delta u_{cmd} \rightarrow u}$, are given by

$$G_{\Delta u_{cmd} \rightarrow u}(s) = \frac{G_A}{1 - G_A} = \frac{K_A}{s} \quad (4.13)$$

Hence, the combined characteristics from control input rate command to the actuator state $G_{\dot{u}_{cmd} \rightarrow u}$ are rendered as an integrator by combining the first order effector dynamics consideration K_A^{-1} with the transfer function in Eq. (4.13)

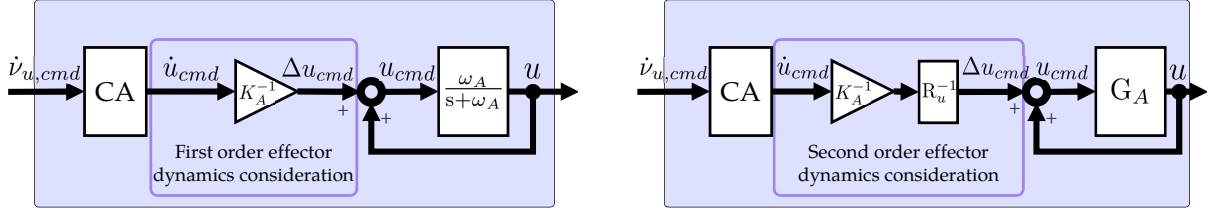
$$G_{\dot{u}_{cmd} \rightarrow u}(s) = K_A^{-1} \cdot G_{\Delta u_{cmd} \rightarrow u}(s) = \frac{1}{s}, \quad (4.14)$$

under the assumption

A.4.1 The natural frequency of the first order actuator is perfectly known.

Following the assumption **A.4.1** and the relation in Eq. (4.14) straightforwardly yields

$$G_{\dot{u}_{cmd} \rightarrow \dot{u}}(s) = s \cdot G_{\dot{u}_{cmd} \rightarrow u}(s) = 1. \quad (4.15)$$



(a) First-order effector dynamics consideration

(b) Second-order effector dynamics consideration

Figure 4.1: Effector Dynamics consideration in the continuous extension of INDI

Control input command for effectors with second order actuators

In case of a second order actuator G_A having a damping ratio $\zeta_A \in \mathbb{R}$ and natural frequency $\omega_A \in \mathbb{R}$

$$G_A(s) = \frac{\omega_A^2}{s^2 + 2 \cdot \zeta_A \cdot \omega_A \cdot s + \omega_A^2}, \quad (4.16)$$

the effector position is determined by

$$u(s) = \frac{\omega_A^2}{s^2 + 2 \cdot \zeta_A \cdot \omega_A \cdot s + \omega_A^2} \cdot u_{cmd}(s). \quad (4.17)$$

Similar to the first order case, the transfer dynamics are moved to the LHS

$$\left(\frac{s^2 + 2 \cdot \zeta_A \cdot \omega_A \cdot s}{\omega_A^2} + 1 \right) \cdot u(s) = u_{cmd}(s), \quad (4.18)$$

and the terms from the transfer element are expanded

$$\left(\frac{s + 2 \cdot \zeta_A \cdot \omega_A}{\omega_A^2} \right) \cdot s \cdot u(s) = \boxed{u_{cmd}(s) - u(s)}, \quad (4.19)$$

$$s \cdot u(s) = \left(\frac{\omega_A^2}{s + 2 \cdot \zeta_A \cdot \omega_A} \right) \cdot \Delta u_{cmd}(s), \quad (4.20)$$

where the RHS is multiplied and divided by $2 \cdot \zeta_A$ to deliver the relation between the incremental control input command Δu_{cmd} and the rate of a second order actuator \dot{u}

$$\dot{u} = \boxed{\left(\frac{2 \cdot \zeta_A \cdot \omega_A}{s + 2 \cdot \zeta_A \cdot \omega_A} \right)} \cdot \boxed{\left(\frac{\omega_A}{2 \cdot \zeta_A} \right)} \cdot \Delta u_{cmd} \quad (4.21)$$

Employing a control input rate command \dot{u}_{cmd} generated by allocation of the related pseudo control rate command $\dot{v}_{u,cmd}$, the effector increment command is produced by inversion of the expression derived in Eq. (4.21)

$$\begin{aligned} \Delta u_{cmd} &= K_A^{-1} \cdot R_u^{-1}(s) \cdot \dot{u}_{cmd}, \\ G_{\dot{u}_{cmd} \rightarrow \Delta u_{cmd}}(s) &= K_A^{-1} \cdot R_u^{-1}(s), \end{aligned} \quad (4.22)$$

which is depicted in Fig. 4.1b as well. Consider the transfer function $G_{\Delta u_{cmd} \rightarrow u}$ from effector increment command Δu_{cmd} to the effector state u for the second order case

$$G_{\Delta u_{cmd} \rightarrow u}(s) = \frac{G_A}{1 - G_A} = \overset{R_u(s)}{\left(\frac{2 \cdot \zeta_A \cdot \omega_A}{s + 2 \cdot \zeta_A \cdot \omega_A} \right)} \cdot \overset{K_A}{\left(\frac{\omega_A}{2 \cdot \zeta_A} \right)} \cdot \frac{1}{s}. \quad (4.23)$$

Clearly, the combined transfer characteristics from Eq. (4.22) and Eq. (4.23) deliver an integral relation between the effector rate command to the effector state

$$G_{\dot{u}_{cmd} \rightarrow u}(s) = G_{\dot{u}_{cmd} \rightarrow \Delta u_{cmd}}(s) \cdot G_{\Delta u_{cmd} \rightarrow u}(s) = \frac{1}{s}, \quad (4.24)$$

given that the following assumption is valid.

A.4.2 The natural frequency and the damping ratio of the second order actuator is perfectly known.

Moreover, to obtain the integral transfer characteristic mentioned in Eq. (4.24), the inverse of the transfer function $R_u(s)$ needs to be computed in the transfer function $G_{\dot{u}_{cmd} \rightarrow \Delta u_{cmd}}(s)$ as given in Eq. (4.22). This implies that the effector dynamics consideration involves calculation of a derivative because of the presence of the complex variable s in the numerator of $R_u^{-1}(s)$, which makes it non-causal. One option is to approximate the time derivative through discrete methods, which is possible in a practical application as the the control algorithm is run on a FCC. However, this could lead to noise amplification and cause jittering in the control effector commands. An alternative to tackle the residual effector dynamics $R_u(s)$, without needing to calculate a time derivative, is presented in the jerk-level reference model later.

Analogous to the first order actuator case, the actuator bandwidth scaling can be combined with the control effectiveness matrix, to avoid violation of effector command protection algorithm [190] included in the control allocation function. Hence, for a MIMO system the incremental effector command is given by

$$\begin{aligned} \Delta \mathbf{u}_{R,cmd} &= (\mathbf{B}_\nu \cdot \mathbf{K}_A)^{-1} \cdot \dot{\boldsymbol{\nu}}_{u,cmd}, \\ \Delta \mathbf{u}_{cmd} &= \mathbf{R}_u^{-1}(s) \cdot \Delta \mathbf{u}_{R,cmd}, \end{aligned} \quad (4.25)$$

where $\Delta \mathbf{u}_{R,cmd} \in \mathbb{R}^{n_u}$ represented the control input increment command not compensated for the residual effector dynamics $\mathbf{R}_u(s)$ and $\mathbf{R}_u^{-1}(s)$ is a diagonal transfer matrix containing the inverse residual effector transfer function for each control effector.

Closed-loop System Dynamics

Upon substitution of the extended INDI control law from Eq. (4.5) in the differentiated transformed system dynamics given by Eq. (4.3) the closed loop dynamics are yielded

$$\begin{aligned} \dot{\boldsymbol{\nu}} &= \mathbf{A}_\nu \cdot \dot{\mathbf{x}} + \mathbf{B}_\nu \cdot \mathbf{B}_\nu^{-1} \cdot \dot{\boldsymbol{\nu}}_{u,cmd}, \\ \dot{\boldsymbol{\nu}} - \dot{\boldsymbol{\nu}}_{u,cmd} &= \overset{\Delta_x = \dot{\boldsymbol{\nu}}_x}{\mathbf{A}_\nu \cdot \dot{\mathbf{x}}}. \end{aligned} \quad (4.26)$$

The aforementioned derivation of the closed loop dynamics is valid under the assumption

A.4.3 The control input matrix B_v is perfectly known.

It is observed through the resulting closed loop system dynamics that the neglected state dependent component of the pseudo control derivative $\dot{\nu}_x$ remains as an error Δ_x . The outputs \mathbf{y} result from $(r + 1)$ integrations of the pseudo control derivative $\dot{\nu}$. Consequently, the residual error in the pseudo control rate would proliferate with each integration even if the plant dynamics are known precisely in an ideal case scenario. Neglecting $\dot{\nu}_x$ for deriving the extended INDI control law in Eq. (4.5) could be justified citing the assumptions **A.3.4** and **A.3.5**. Nonetheless, these approximations do not hold for systems that possess high damping characteristics like fixed wing aircraft with slow actuators. Additionally, low refresh rate (≈ 50 Hz) of the flight control computer would also violate the approximation made due to these assumptions.

Normally, an error controller [51, 62, 86–88] is used to pull the plant states towards the reference states, thereby compensating for the disparity created by neglecting $\dot{\nu}_x$. This solution does not take any profit from known plant information. The author proposes to incorporate the effect of the state dependent pseudo control rate in the feedforward command from the reference model by utilizing model knowledge. The effect of the model parameter uncertainties used within the reference model is also quantified through a simplified linear analysis of the closed loop system. Furthermore, uncertainty bounds for the model parameters with respect to the actual plant parameters is derived within which the proposed feedforward improves set point tracking. A detailed overview of the feedforward generation is given in the next section.

4.2 Jerk-level Reference Model

The extended INDI control law employs the pseudo control derivative command $\dot{\nu}_{u,cmd}$ to specify the demand needed to track the pilot command variables \mathbf{y}_{cmd} . The pseudo control derivative command is comprised of a feedback and a feedforward component. The feedback component of the pseudo control rate command is produced based on the error between the command variable reference trajectories and the corresponding system outputs. The feedforward element is generated by the jerk-level reference model, which contains a design plant using nominal model parameters. The resultant physically feasible feedforward command attempts to compensate for the state variant terms neglected in the extended INDI control law derivation. Additionally, appropriate control variable reference trajectories are also specified by the reference model. Since the design plant is an imitation of the real plant, a reference system based on the transformed system dynamics in Eq. (4.3) is considered

$$\boldsymbol{\nu}_R = \mathbf{F}_R(\mathbf{x}_R, \mathbf{u}_R). \quad (4.27)$$

Identical to the differentiation of the real system, direct time derivative of the reference system is also computed

$$\dot{\boldsymbol{\nu}}_R = \overset{\mathbf{A}_{\nu,R}(\mathbf{x}_R)}{\boxed{\frac{\partial \mathbf{F}_R}{\partial \mathbf{x}_R}}} \cdot \dot{\mathbf{x}}_R + \overset{\mathbf{B}_{\nu,R}(\mathbf{x}_R, \mathbf{u}_R)}{\boxed{\frac{\partial \mathbf{F}_R}{\partial \mathbf{u}_R}}} \cdot \dot{\mathbf{u}}_R, \quad (4.28)$$

$$\dot{\boldsymbol{\nu}}_R = \mathbf{A}_{\nu,R}(\mathbf{x}_R) \cdot \dot{\mathbf{x}}_R + \mathbf{B}_{\nu,R}(\mathbf{x}_R, \mathbf{u}_R) \cdot \dot{\mathbf{u}}_R,$$

thereby obtaining a system that is affine in the reference control input rate $\dot{\mathbf{u}}_R \in \mathbb{R}^{n_u}$. In the reference model, this system constitutes the design plant. The design plant incorporates information about the effects of the state dependence, namely the term $\mathbf{A}_{\nu,R} \cdot \dot{\mathbf{x}}_R$, on the reference pseudo control rate $\dot{\boldsymbol{\nu}}_R \in \mathbb{R}^{n_y}$. The reference state matrix $\mathbf{A}_{\nu,R} \in \mathbb{R}^{n_y \times n_x}$ is chosen based on the available data about the true system matrix \mathbf{A}_{ν} . For example, the roll damping L_p is a parameter that can be used in the reference state matrix while designing a roll rate or a bank angle command controller for a fixed wing aircraft. It is clear that perfect knowledge of the plant system matrix parameters is not available in real life applications. However, it would be shown later that as long as the parameters in the reference state matrix lie within a bound of the parameters in the true state matrix, it leads to an improvement in terms of set-point tracking. These bounds are also derived through classical linear analysis in further sections.

The compensation for the neglected pseudo control rate $\dot{\boldsymbol{\nu}}_x$ in the closed loop dynamics of Eq. (4.26) is achieved through a feedforward pseudo control rate command produced by the reference model. The first step is to calculate the reference control rate $\dot{\mathbf{u}}_R \in \mathbb{R}^{n_u}$ for a given $\dot{\boldsymbol{\nu}}_{R,cmd} \in \mathbb{R}^{n_y}$ by dynamically inverting the design plant described in Eq. (4.28)

$$\begin{aligned} \dot{\boldsymbol{\nu}}_{R,cmd} &= \mathbf{A}_{\nu,R} \cdot \dot{\mathbf{x}}_R + \mathbf{B}_{\nu,R} \cdot \dot{\mathbf{u}}_R, \\ \dot{\mathbf{u}}_{R,cmd} &= \mathbf{B}_{\nu,R}^{-1} \cdot \left(\dot{\boldsymbol{\nu}}_{R,cmd} - \overset{\dot{\boldsymbol{\nu}}_{x,R}}{\boxed{\mathbf{A}_{\nu,R} \cdot \dot{\mathbf{x}}_R}} \right), \end{aligned} \quad (4.29)$$

and then the feedforward pseudo control derivative $\dot{\boldsymbol{\nu}}_{ff} \in \mathbb{R}^{n_y}$, which can also be denoted as the control input rate dependent pseudo control derivative command $\dot{\boldsymbol{\nu}}_{u,R,cmd} \in \mathbb{R}^{n_y}$, is simply the product of the reference control input rate command $\dot{\mathbf{u}}_{R,cmd}$ with the reference input matrix

$$\begin{aligned} \dot{\boldsymbol{\nu}}_{ff} &= \dot{\boldsymbol{\nu}}_{u,R,cmd} = \mathbf{B}_{\nu,R} \cdot \mathbf{B}_{\nu,R}^{-1} \cdot (\dot{\boldsymbol{\nu}}_{R,cmd} - \mathbf{A}_{\nu,R} \cdot \dot{\mathbf{x}}_R), \\ \dot{\boldsymbol{\nu}}_{ff} &= \dot{\boldsymbol{\nu}}_{u,R,cmd} = \dot{\boldsymbol{\nu}}_{R,cmd} - \mathbf{A}_{\nu,R} \cdot \dot{\mathbf{x}}_R. \end{aligned} \quad (4.30)$$

It is clear from the resulting relation that the feedforward rate $\dot{\boldsymbol{\nu}}_{ff}$ is generated from the given pseudo control rate command by actively accounting for the effect of the state variant term. The feedforward is propagated to the control allocation. Since the state reliant damping effect is already anticipated in the feedforward pseudo control rate based on the design plant feedback $\mathbf{A}_{\nu,R} \cdot \dot{\mathbf{x}}_R$, the allocated effector command counteracts against the modeled effect without using any real system feedback. Incorporation of the

reference damping element $\dot{\nu}_{x,R}$ in the feedforward channel facilitates to counter the residual component Δ_x in the closed-loop system dynamics delivered by continuous dynamic inversion strategy in Eq. (4.26). Certainly, the true plant could be different from the design plant, yet the proposed concept improves reference tracking as long as the model deviation stays within the bounds specified in the section 4.4.1.

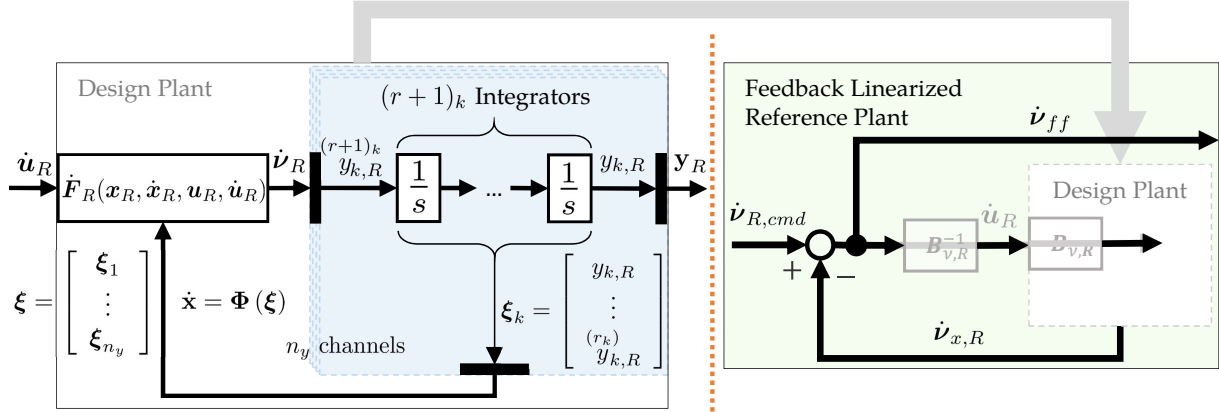


Figure 4.2: Feedforward generation in the Jerk-level reference model for a MIMO system

Although, the assumption **A.4.3** states that the control input matrix is perfectly known, its reference counterpart $B_{\nu,R} \in \mathbb{R}^{n_y \times n_u}$ is not even required in the reference model dynamics. As observed in Eq. (4.30), the $B_{\nu,R}$ cancels out in feedforward command generation. Therefore, the input to the design plant is made in terms of the pseudo control rate rather than a control input derivative as reflected in Fig. 4.2, while the control input matrix and its inverse are commented out. Hence, the need of explicitly implementing a control allocation algorithm within the RM is avoided. For sake of completion, the closed loop reference dynamics are obtained by substituting the reference control input rate from Eq. (4.29) in the higher order reference dynamics from Eq. (4.28)

$$\dot{\nu}_R = A_{\nu,R} \cdot \dot{x}_R + B_{\nu,R} \cdot B_{\nu,R}^{-1} \cdot (\dot{\nu}_{R,cmd} - A_{\nu,R} \cdot \dot{x}_R) \quad (4.31)$$

$$\dot{\nu}_R = \underbrace{A_{\nu,R} \cdot \dot{x}_R}_{\dot{\nu}_{x,R}} + \underbrace{(\dot{\nu}_{R,cmd} - A_{\nu,R} \cdot \dot{x}_R)}_{\dot{\nu}_{ff}}, \quad (4.32)$$

which trivially simplifies to

$$\dot{\nu}_R = \dot{\nu}_{R,cmd}$$

So far the expression derived for the feedforward generation stems from the mathematical structure of the given system. Nevertheless, rather than adhering to the theoretical framework more advantages are gained by following a physics-centric approach to the control problem, which results in a physically motivated reference model structure. Moreover, flight-dynamics as well as system architecture specific components can be employed to compose the RM structure. Following this design methodology provides the advantage of defining reference parameters based on aircraft dynamics and control

system architecture knowledge. In order to explain the jerk level reference model's design systemically, the RM structure for a Single Input Single Output (SISO) system is presented before demonstrating the same for the MIMO case.

4.2.1 Jerk-level Reference Model Structure: SISO system

Consider a scalar equivalent of the generic nonlinear reference system given in Eq. (4.27)

$$\nu_R = F_R(x_R, u_R), \quad (4.33)$$

where $F_R \in \mathbb{R}$ denotes the SISO reference system dynamics dependent on the reference state $x_R \in \mathbb{R}$ and the control input $u_R \in \mathbb{R}$. The system in the Eq. (4.33) is defined to have a relative degree of 1, thereby $\nu_R = \dot{y}_R$. The term y_R represents the reference external state/output of the reference system, which is defined in relation to the reference state x_R according to $y_R = C_R \cdot x_R$, where $C_R \in \mathbb{R}$ is a scalar value. Similar to the direct time derivation of the MIMO reference system in Eq. (4.28), the scalar reference system from Eq. (4.33) is also derived

$$\begin{aligned} \dot{\nu}_R &= \frac{\overset{A_{\nu,R}}{\partial F_R}}{\partial x_R} \cdot \dot{x}_R + \frac{\overset{B_{\nu,R}}{\partial F_R}}{\partial u_R} \cdot \dot{u}_R, \\ \dot{\nu}_R &= A_{\nu,R} \cdot \dot{x}_R + B_{\nu,R} \cdot \dot{u}_R. \end{aligned} \quad (4.34)$$

Here $A_{\nu,R} \in \mathbb{R}$ and $B_{\nu,R} \in \mathbb{R}$ define the state dependency parameter and the control effectiveness and Eq. (4.34) denote the design plant dynamics to be used in the reference model. As said before, no explicit control allocation is performed in the reference model, and therefore the input to the design plant is the control input rate dependent pseudo control derivative $\dot{\nu}_{u,R} = B_{\nu,R} \cdot \dot{u}_R$ which renders Eq. (4.34) to

$$\dot{\nu}_R = A_{\nu,R} \cdot \dot{x}_R + \dot{\nu}_{u,R}. \quad (4.35)$$

For the illustration provided in the Fig. 4.3, the control input rate dependent pseudo control derivative $\dot{\nu}_{u,R} = \dot{\nu}_{ff}$ is equal to the feedforward pseudo control derivative if the saturation limits are not violated. Accordingly, the feedforward pseudo control derivative $\dot{\nu}_{ff} \in \mathbb{R}$ is also known as the control input related pseudo control derivative command $\dot{\nu}_{u,R,cmd} \in \mathbb{R}$. Rather than calculating the feedforward pseudo control derivative, as per the theoretical derivation in Eq. (4.30) i.e. by inverting the design plant dynamics for a given reference pseudo control rate command $\dot{\nu}_{R,cmd}$

$$\begin{aligned} \dot{u}_{R,cmd} &= \frac{1}{B_{\nu,R}} (\dot{\nu}_{R,cmd} - A_{\nu,R} \cdot \dot{x}_R), \\ \boxed{B_{\nu,R} \cdot \dot{u}_{R,cmd}} &= (\dot{\nu}_{R,cmd} - A_{\nu,R} \cdot \dot{x}_R), \\ \dot{\nu}_{u,R,cmd} &= \dot{\nu}_{ff} \end{aligned} \quad (4.36)$$

the feedforward in the implemented reference model architecture displayed by the Fig. 4.3 is calculated in the reference actuator according to

$$\dot{\nu}_{ff} = \dot{\nu}_{u,R,cmd} = K_{R,u} \cdot (\nu_{u,R,cmd} - \nu_{u,R,act}). \quad (4.37)$$

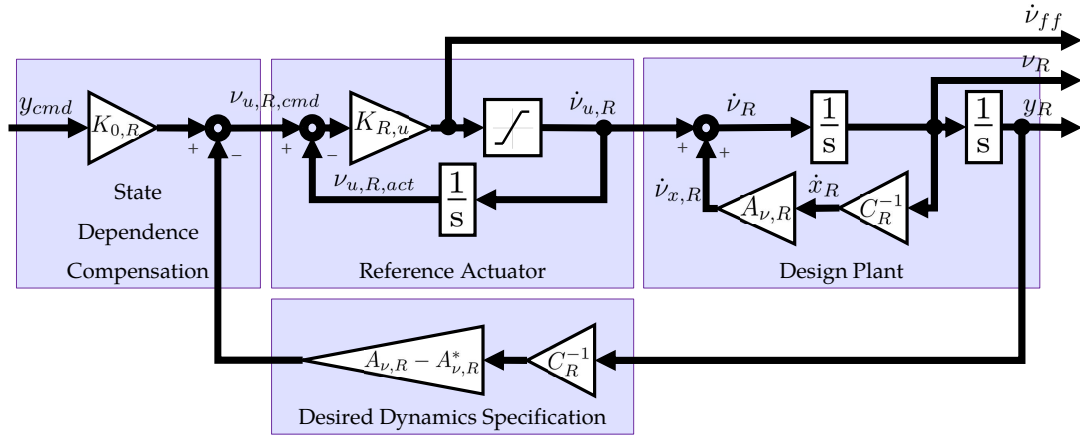


Figure 4.3: Jerk-level reference model structure for a SISO system

Here $K_{R,u} \in \mathbb{R}$ is the reference actuator gain, $\nu_{u,R,cmd} \in \mathbb{R}$ is the pseudo control command intended to be produced by the control input, and $\nu_{u,R,act} \in \mathbb{R}$ is the state of the reference actuator. The calculation of the feedforward is done through the reference actuator rather than the direct inversion at the jerk level as described in Eq. (4.36) in order to facilitate inclusion of the residual effector dynamics from higher order effectors such as the ones presented in Eq. (4.21) as well as dynamics of the estimation/noise attenuation filters. The mechanism of incorporating these elements will be detailed later. In the feedforward calculation demonstrated by Eq. (4.37), the state dependent effect is contained in the control input related pseudo control command $\nu_{u,R,cmd}$, which is determined as

$$\nu_{u,R,cmd} = \boxed{\nu_{R,cmd}} - \boxed{\nu_x}, \quad (4.38)$$

where the terms $\nu_{R,cmd} \in \mathbb{R}$ for a system with relative degree 1 is calculated according to $K_{0,R} \cdot (y_{cmd} - y_R)$ and $\nu_x = A_{\nu,R} \cdot x_R$, which on substituting back in Eq. (4.38) yields

$$\begin{aligned} \nu_{u,R,cmd} &= \boxed{K_{0,R} \cdot (y_{cmd} - y_R)} - \boxed{A_{\nu,R} \cdot x_R}, \\ \nu_{u,R,cmd} &= K_{0,R} \cdot y_{cmd} - K_{0,R} \cdot \boxed{y_R} - A_{\nu,R} \cdot x_R, \\ \nu_{u,R,cmd} &= K_{0,R} \cdot y_{cmd} - K_{0,R} \cdot \boxed{C_R \cdot x_R} - A_{\nu,R} \cdot x_R, \quad \because y_R = C_R \cdot x_R \\ \nu_{u,R,cmd} &= K_{0,R} \cdot y_{cmd} - A_{\nu,R}^* \cdot x_R - A_{\nu,R} \cdot x_R, \quad \because A_{\nu,R}^* \triangleq -K_{0,R} \cdot C_R \\ \nu_{u,R,cmd} &= K_{0,R} \cdot y_{cmd} - (A_{\nu,R} - A_{\nu,R}^*) \cdot x_R. \end{aligned} \quad (4.39)$$

In the structure demonstrated until now, only the state damping effect is incorporated in the reference model. From an aircraft dynamics point of view not only the state dependency effect is considered in the reference model design, but the actuator dynamics are also incorporated. Although, the effector dynamics consideration is easily merged into the control allocation for effectors having a first order behavior (Eq. (4.12)), consideration of dynamics for effectors exhibiting second order behavior required use of

a non-causal transfer function (Eq. (4.25)) [86]. Such an implementation can be avoided by dealing with the actuator dynamics of higher than the first order within the reference model.

In terms of the control system architecture, input/output channel dynamics are considered in the reference model. One significant component of these dynamics is the dead time delay occurring in a flight control system. Transport delay, sensor delay [92] and time synchronization delays constitute the cumulative time delay in the input/output channel dynamics of a control system architecture. The sensor delay comprises of delay due to anti-aliasing filters [93] and analog to digital conversion [94]. Transport delay and sensor delays are constant for a given system architecture, whereas the time synchronization delays vary depending on the arbitration of the data packets in to communication protocols being employed. The reference model includes consideration of only constant delays in the closed loop system. Apart from the pure time delay, the reference model incorporates higher order effects of measurement/estimation filters used for pseudo control estimation (high-pass) and noise cancellation (low-pass) in the extended INDI controller.

The residual effector dynamics $R_u(s)$ (given in Eq. (4.21)) along with the estimation/noise attenuation filter $G_{LP}(s)$ like the low-pass filter described in Eq. (3.55) are accounted in the higher order effect emulation $G_L(s)$, which is embedded in the reference actuator as demonstrated by the Fig. 4.4. Moreover, the feedforward pseudo control

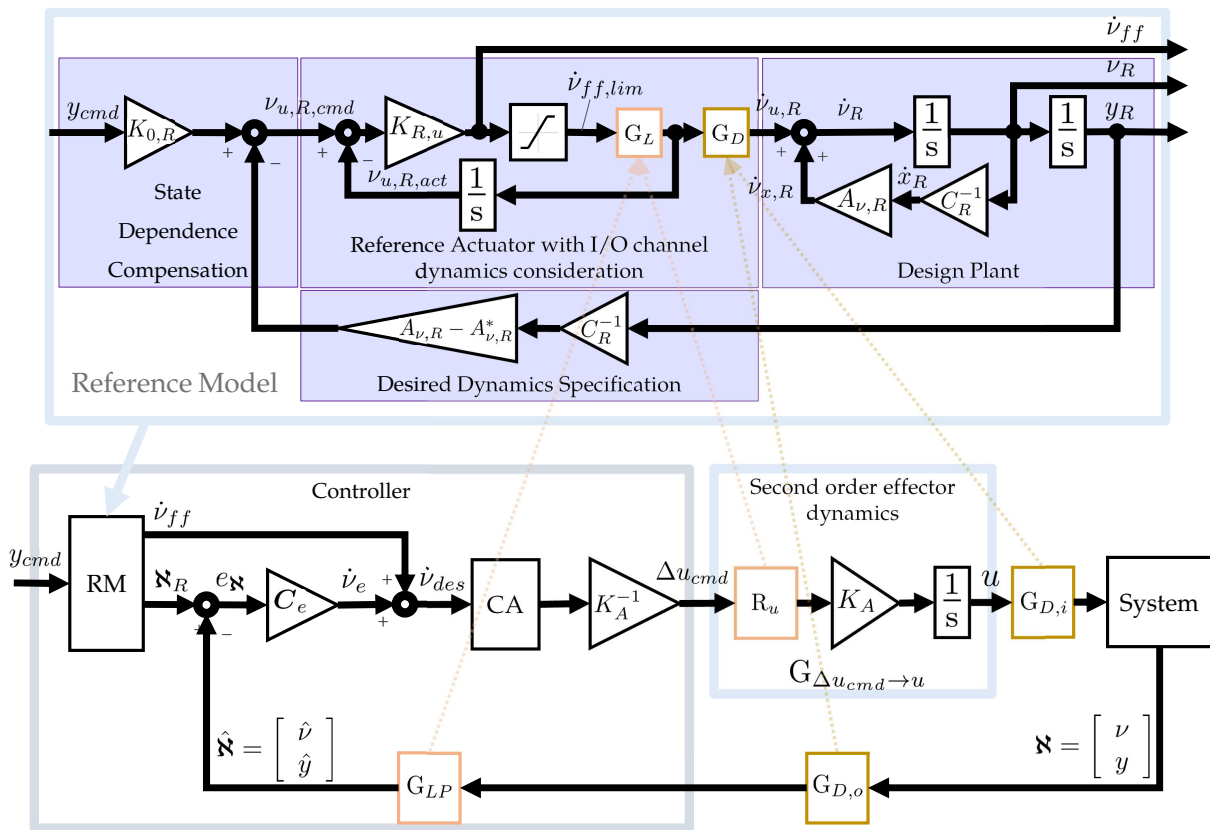


Figure 4.4: Delay and Higher order effects inclusion in the jerk-level reference model structure for a SISO system

derivative as computed in the Eq. (4.37) is given by

$$\begin{aligned} \dot{\nu}_{ff} &= K_{R,u} \cdot (\nu_{u,R,cmd} - \nu_{u,R,act}), \quad \text{where} \\ \nu_{u,R,act} &= \frac{1}{s} \cdot [G_L(s) \cdot \dot{\nu}_{ff,lim}]. \end{aligned} \quad (4.40)$$

Here $\dot{\nu}_{ff,lim}$ is the feedforward commanded limited according to its absolute limits and the higher order effect emulation $G_L(s)$ is composed from the components mentioned earlier, according to

$$G_L(s) = R_u(s) \cdot G_{LP}(s). \quad (4.41)$$

Additionally, the input to the design plant $\dot{\nu}_{u,R}$, as shown in Eq. (4.35), is calculated further considering the input and output channel delays denoted by $G_{D,i}(s)$ and $G_{D,o}(s)$ respectively within the delay emulation $G_D(s)$ as presented in the Fig. 4.4. The delay emulation element is specified to be

$$G_D(s) = G_{D,i}(s) \cdot G_{D,o}(s). \quad (4.42)$$

Subsequently, the design plant input pseudo control derivative $\dot{\nu}_{u,R}$ specified by

$$\dot{\nu}_{u,R} = G_D(s) \cdot G_L(s) \cdot \dot{\nu}_{ff,lim}. \quad (4.43)$$

With this, the basic architecture of the jerk-level reference model is established. In the upcoming section, this structure is extended to a MIMO system.

4.2.2 Jerk-level Reference Model Structure: MIMO system

Given the physical structure of the jerk-level reference model presented for the SISO case, the major components constituting the reference model are defined as the *desired dynamics specification unit*, *state dependence compensation*, *reference actuator with input/output channel dynamics consideration* and the *design plant* for a MIMO system such as the one presented in Eq. (4.2). The structure of the corresponding jerk-level reference model is illustrated by the Fig. 4.5. With an aim of maintaining physical correspondence to the reference model structure, the compensation of the state dependent term is performed at the pseudo control level rather than the jerk level. This is feasible even for a control input non-affine system since no explicit control allocation is performed in the reference model. Furthermore, the control engineer maintains a "god mode" within the reference model where information about all the reference states is perfectly known, therefore treating the state reliance at one integration level above the pseudo control derivative/jerk level does not produce any inadvertent effects.

As stated before in Eq. (4.28), the design plant dynamics obtained by performing a direct time derivative of the nonlinear reference system from Eq. (4.28) is given as

$$\begin{aligned} \dot{\nu}_R &= \mathbf{A}_{\nu,R} \cdot \dot{\mathbf{x}}_R + \mathbf{B}_{\nu,R} \cdot \dot{\mathbf{u}}_R, \\ \dot{\nu}_R &= \mathbf{A}_{\nu,R} \cdot \dot{\mathbf{x}}_R + \dot{\nu}_{u,R}, \end{aligned} \quad (4.44)$$

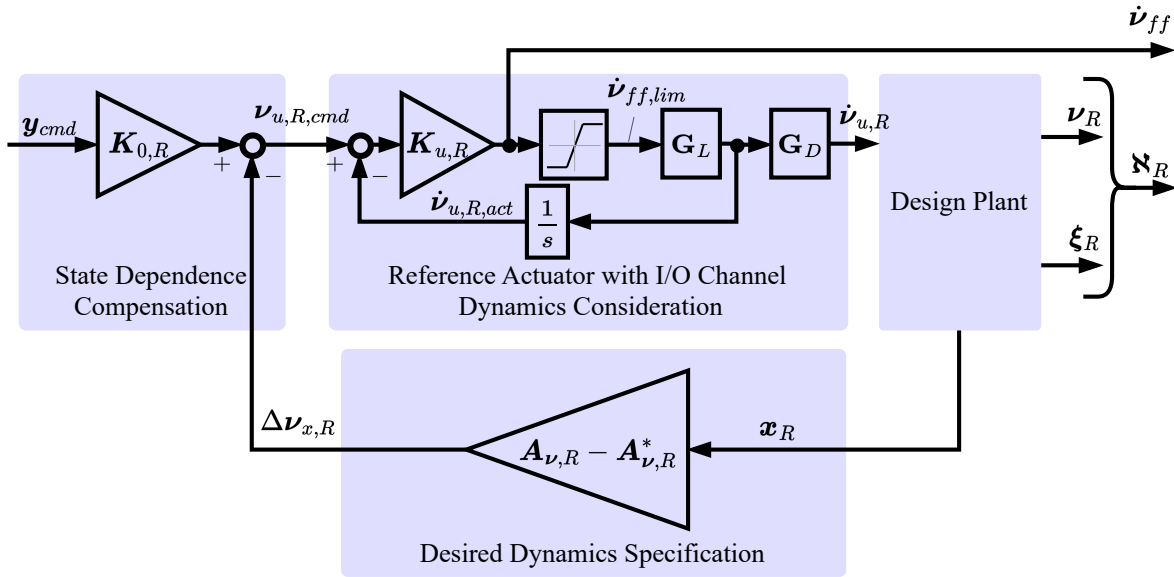


Figure 4.5: Jerk level reference model for a MIMO system

whose input is the control rate dependent pseudo control derivative $\dot{\nu}_{u,R} \in \mathbb{R}^{n_y}$. This input to the design plant encompasses effects of the higher than first order actuator dynamics, estimation dynamics and input/output delays. The first step in its calculation is to obtain a pseudo control command $\nu_{cmd} \in \mathbb{R}^{n_y}$ from a given control variable command $\mathbf{y}_{cmd} \in \mathbb{R}^{n_y}$ based on certain desired dynamics. As the name suggests, the desired dynamics specification unit establishes the reference dynamics using the coefficients $\mathbf{K}_R \in \mathbb{R}^{n_y \times r}$

$$\mathbf{K}_R = \begin{bmatrix} \mathbf{K}_R^1 & 0 & \dots & 0 \\ 0 & \mathbf{K}_R^2 & \dots & 0 \\ \vdots & & \ddots & 0 \\ 0 & 0 & \dots & \mathbf{K}_R^{n_y} \end{bmatrix} \in \mathbb{R}^{n_y \times r}, \text{ where} \quad (4.45)$$

$$\mathbf{K}_R^i := \begin{bmatrix} K_{0,R}^i \\ K_{1,R}^i \\ \vdots \\ K_{r_i,R}^i \end{bmatrix}^T \in \mathbb{R}^{1 \times r_i} : \forall i = \{1, 2, \dots, n_y\}, n_y \in \mathbb{N}.$$

Here $\mathbf{K}_R^i \in \mathbb{R}^{1 \times r_i}$ represents a vector of positive definite gain parameters which define the desired amplitude-independent gradient of the reference external states response to the corresponding control variable command $y_{i,cmd} \in \mathbb{R}$.

Thereafter, employing the reference coefficients presented in Eq. (4.45), the pseudo control command $\boldsymbol{\nu}_{R,cmd} \in \mathbb{R}^{n_y}$ (not explicitly demonstrated in Fig. 4.5) can be computed

$$\begin{aligned}
 \boldsymbol{\nu}_{R,cmd} = \begin{bmatrix} (r_1) \\ y_{1,R} \\ (r_2) \\ y_{2,R} \\ \vdots \\ (r_{n_y}) \\ y_{n_y,R} \end{bmatrix} &= \begin{matrix} \mathbf{K}_{0,R} \\ \begin{bmatrix} K_{0,R}^1 & 0 & \dots & 0 \\ 0 & K_{0,R}^2 & \dots & 0 \\ \vdots & & \ddots & 0 \\ 0 & 0 & 0 & K_{0,R}^{n_y} \end{bmatrix} \end{matrix} \cdot \begin{matrix} \mathbf{y}_{cmd} \\ \begin{bmatrix} y_{1,cmd} \\ y_{2,cmd} \\ \vdots \\ y_{n_y,cmd} \end{bmatrix} \end{matrix} - \\
 & \begin{matrix} \mathbf{K}_R \\ \begin{bmatrix} \mathbf{K}_R^1 & 0 & \dots & 0 \\ 0 & \mathbf{K}_R^2 & \dots & 0 \\ \vdots & & \ddots & 0 \\ 0 & 0 & 0 & \mathbf{K}_R^{n_y} \end{bmatrix} \end{matrix} \cdot \begin{matrix} \boldsymbol{\xi}_R \\ \begin{bmatrix} \boldsymbol{\xi}_R^1 \\ \boldsymbol{\xi}_R^2 \\ \vdots \\ \boldsymbol{\xi}_R^{n_y} \end{bmatrix} \end{matrix}, \quad (4.46)
 \end{aligned}$$

where $\boldsymbol{\xi}_R^i \in \mathbb{R}^{r_i}$ for $i = 1, 2, \dots, n_y$ comprise of the reference external states for each output channel similar to the vectors described by Eq. (3.24). As mentioned earlier, the compensation of the state dependent terms can be performed at the pseudo control level in the reference model without dealing with the non-affine control inputs. Accordingly, the reference pseudo control command from Eq. (4.46) is employed to compute the control input dependent component of the reference pseudo control command $\boldsymbol{\nu}_{u,R,cmd} \in \mathbb{R}^{n_y}$

$$\boldsymbol{\nu}_{u,R,cmd} = \boldsymbol{\nu}_{R,cmd} - \begin{matrix} \boldsymbol{\nu}_{x,R} \\ \mathbf{A}_{\nu,R} \cdot \mathbf{x}_R \end{matrix}, \quad (4.47)$$

by using the reference state associated reference pseudo control feedback $\boldsymbol{\nu}_{x,R} \in \mathbb{R}^{n_y}$ from the design plant. Important to note that Eq. (4.47) exclusively demonstrates the mathematics involved in the creation of the reference pseudo control component $\boldsymbol{\nu}_{u,R,cmd}$. However, the implementation is oriented to assist in an intuitive design of the reference model and remain a close analogue to aircraft physics as far as possible. From this perspective, the relations in Eqs. (4.46) and (4.47) are combined to yield

$$\boldsymbol{\nu}_{u,R,cmd} = \mathbf{K}_{0,R} \cdot \mathbf{y}_{cmd} - \mathbf{K}_R \cdot \boldsymbol{\xi}_R - \mathbf{A}_{\nu,R} \cdot \mathbf{x}_R, \quad (4.48)$$

which calculates the reference pseudo control command intended to be generated by the control input only. Since the reference transformed system dynamics in Eq. (4.27) are derived to deliver a linear system of one order higher than the relative degrees of every output channel, the reference pseudo controls as well as the reference external states $\boldsymbol{\xi}_R$ are the result of r integrations of the pseudo control rates. By lieu of the linearized system, the reference external states $\boldsymbol{\xi}_R$ can be substituted with a term constituting the reference states \mathbf{x}_R through the relation $\boldsymbol{\xi}_R = \mathbf{C}_{\nu,R} \cdot \mathbf{x}_R$ to yield

$$\begin{aligned}
 \boldsymbol{\nu}_{u,R,cmd} &= \mathbf{K}_{0,R} \cdot \mathbf{y}_{cmd} - \overset{\mathbf{A}_{\nu,R}^*}{\mathbf{K}_R \cdot \mathbf{C}_{\nu,R}} \cdot \mathbf{x}_R - \mathbf{A}_{\nu,R} \cdot \mathbf{x}_R, \\
 \boldsymbol{\nu}_{u,R,cmd} &= \mathbf{K}_{0,R} \cdot \mathbf{y}_{cmd} - \overset{\Delta \boldsymbol{\nu}_{x,R}}{\left(\mathbf{A}_{\nu,R} - \mathbf{A}_{\nu,R}^* \right) \cdot \mathbf{x}_R},
 \end{aligned} \tag{4.49}$$

where the coefficient matrix $\mathbf{A}_{\nu,R}^* \in \mathbb{R}^{n_y \times n_x}$ denotes the desired state matrix, which provides the desired dynamics specification. The difference $\mathbf{A}_{\nu,R} - \mathbf{A}_{\nu,R}^*$ can be perceived as replacement of the design plant system matrix $\mathbf{A}_{\nu,R}$ with the desired dynamics $\mathbf{A}_{\nu,R}^*$. Meanwhile, the gain matrix $\mathbf{K}_{0,R} \in \mathbb{R}^{n_y \times n_y}$ denotes the feedforward gain for the control variable commands. Subsequently, the final relation in Eq. (4.49) exhibits the generation of the reference pseudo control command $\boldsymbol{\nu}_{u,R,cmd}$ implemented in the jerk-level RM as shown in Fig. 4.5.

The feedforward pseudo control derivative command is then computed through a reference actuator that additionally accommodates input/output channel dynamics. The feedforward command is calculated as

$$\dot{\boldsymbol{\nu}}_{ff} = \mathbf{K}_{u,R} \cdot (\boldsymbol{\nu}_{u,R,cmd} - \boldsymbol{\nu}_{u,R,act}), \tag{4.50}$$

where $\dot{\boldsymbol{\nu}}_{ff} \in \mathbb{R}^{n_y}$ is the feedforward pseudo control rate, $\mathbf{K}_{u,R} \in \mathbb{R}^{n_y \times n_y}$ denotes the reference actuator gain matrix and $\boldsymbol{\nu}_{u,R,act} \in \mathbb{R}^{n_y}$ is the pseudo control associated with the reference actuator. The latter originates by applying the higher order emulation element $\mathbf{G}_L(s)$ on the feedforward limited according to its absolute values $\dot{\boldsymbol{\nu}}_{ff,lim}$, and integrating thereafter

$$\boldsymbol{\nu}_{u,R,act}(s) = \frac{1}{s} \cdot [\mathbf{G}_L(s) \cdot \dot{\boldsymbol{\nu}}_{ff,lim}(s)]. \tag{4.51}$$

The higher order emulation element $\mathbf{G}_L(s)$ denotes a transfer matrix comprising of strictly stable proper transfer functions with a unit DC gain. These transfer functions emulate effects from three sources

- 1 The residual transfer function $R_u(s)$ from the second order effector dynamics consideration in Eq. (4.23). Exact cancellation of the effector dynamics in the computation of the incremental control inputs requires inversion of these residual dynamics as derived in Eq. (4.22). Instead, these residual dynamics are encompassed in the higher order emulation element $\mathbf{G}_L(s)$ of the RM, thereby accounting for these dynamics through the pseudo control rate feedforward rather than performing a discrete time derivative computation for the inversion of the residual.
- 2 The effect of noise attenuation filters $G_{LP}(s)$ such as the ones described in Eq. (3.55) from section 3.2.2.1 and their high-pass components employed to estimate state derivatives (such as in the complementary filters for angular acceleration estimation in Eq. (3.54)) is also incorporated within the transfer matrix $\mathbf{G}_L(s)$. Since the states of the same roll-off filter deliver the noise attenuated signal and state derivative estimation, the higher order emulation in the RM employs the corresponding low pass filter for the relevant pseudo control channel.

3 Lastly, transfer characteristics due to the internal filtering $G_{sens}(s)$ employed in the COTS sensors also forms a part of the input-output channel dynamics, and is added to the higher order emulation element $G_L(s)$ if it is known.

For every channel of the MIMO system, the corresponding transfer element $G_{L,i}(s)$ for $i = 1, 2, \dots, n_y$ in the higher order effect emulation $G_L(s)$ is built up in accordance with the respective transfer functions for the given three sources

$$\begin{aligned} R_{u,i}(s) &= \frac{2 \cdot \zeta_{A,i} \cdot \omega_{A,i}}{s + 2 \cdot \zeta_{A,i} \cdot \omega_{A,i}}, \\ G_{LP,i}(s) &= \frac{\omega_{LP,i}^2}{s^2 + 2 \cdot \zeta_{LP,i} \cdot \omega_{LP,i} \cdot s + \omega_{LP,i}^2}, \\ G_{sens,i}(s) &= \frac{\omega_{sens,i}^2}{s^2 + 2 \cdot \zeta_{sens,i} \cdot \omega_{sens,i} \cdot s + \omega_{sens,i}^2}, \\ G_{L,i}(s) &= R_{u,i}(s) \cdot G_{LP,i}(s) \cdot G_{sens,i}(s). \end{aligned} \quad (4.52)$$

Thereafter, the higher order effect emulation $G_L(s)$ is generated as a transfer function matrix for the n_y pseudo control derivatives

$$\mathbf{G}_L(s) = \begin{bmatrix} G_{L,1}(s) & 0 & \dots & 0 \\ 0 & G_{L,2}(s) & \dots & 0 \\ \vdots & & \ddots & 0 \\ 0 & 0 & \dots & G_{L,n_y}(s) \end{bmatrix}. \quad (4.53)$$

Furthermore, the sum of confidently known time-delays in the input/output transmission channels of the closed loop system is reflected by the delay element $G_D(s)$ in the reference model framework from Fig. 4.5. The time-delay element is represented in the Laplace domain continuous form as

$$\mathbf{G}_D(s) = \begin{bmatrix} e^{-sT_1} & 0 & \dots & 0 \\ 0 & e^{-sT_2} & \dots & 0 \\ \vdots & & \ddots & 0 \\ 0 & 0 & \dots & e^{-sT_{n_y}} \end{bmatrix}, \quad (4.54)$$

where T_1, T_2, \dots, T_{n_y} represent the time delays in the n_y pseudo control channels of the closed loop system dynamics. Important to note that these time-delays are implemented as discrete multiples of the FCC refresh rate for the actual control algorithm implementation. Ultimately, the input to the design plant emanates using the input/output channel dynamics consideration

$$\dot{\boldsymbol{\nu}}_{u,R} = \mathbf{G}_D(s) \cdot \mathbf{G}_L(s) \cdot \dot{\boldsymbol{\nu}}_{ff,lim}. \quad (4.55)$$

The design plant computes reference pseudo control rate according to the dynamics in Eq. (4.28). Further integrals of $\dot{\boldsymbol{\nu}}_R$ result in desired trajectories for the reference pseudo controls $\boldsymbol{\nu}_R$ and the external states $\boldsymbol{\xi}_R$ which are united

$$\boldsymbol{\mathfrak{N}}_R = \begin{bmatrix} \boldsymbol{\nu}_R \\ \boldsymbol{\xi}_R \end{bmatrix} \quad (4.56)$$

to denote the reference trajectories $\mathfrak{N}_R \in \mathbb{R}^{n_\nu+r}$, which are to be tracked by the extended INDI control law. This section elucidates the concepts pertaining to the contribution **C.3.1 Feedforward pseudo control derivative generation for input non-affine systems** of this thesis. Integration of the jerk-level RM by interfacing the pseudo control rate feedforward $\dot{\nu}_{ff}$ and the reference trajectories \mathfrak{N}_R with the continuous dynamic inversion controller is elaborated in the next section.

4.3 Jerk level Reference Model in an Extended INDI Control Architecture

A generic controller architecture pertaining to the continuous extension of the incremental nonlinear dynamic inversion is exhibited by Fig. 4.6. Like any model following control strategy, the control objective of the illustrated framework

$$\lim_{t \rightarrow \infty} \left\| \begin{bmatrix} \dot{\nu} \\ \nu \\ \xi \end{bmatrix} - \begin{bmatrix} \dot{\nu} \\ \nu \\ \xi \end{bmatrix}_R \right\| = 0, \quad (4.57)$$

is to enforce zero tracking error between the system of interest and the corresponding higher order reference model in terms of pseudo control rates $\dot{\nu}$, $\dot{\nu}_R$ along with their lower order derivatives $[\nu, \xi]^T$, $[\nu_R, \xi_R]^T$. Essential to point out that the feedforward pseudo control derivative $\dot{\nu}_{ff}$ is not equivalent to the reference pseudo control rate $\dot{\nu}_R$ as observed in Eqs. (4.27)-(4.30). The feedforward command is created in a manner that if the design plant in the jerk-level RM exactly imitates the real system, then the true plant achieves the reference trajectories $[\dot{\nu}_R, \mathfrak{N}_R]^T$ without any feedback. Verification of this assertion is easily provided through the closed loop system dynamics derived by substituting the reference control input rate $\dot{u}_{R,cmd}$ from Eq. (4.29) in the total derivative of the transformed system dynamics from Eq. (4.3), under the assumptions that the design plant parameters $[A_{\nu,R}, B_{\nu,R}]$ are equal to the respective true system parameters $[A_\nu, B_\nu]$ and the RM states are initialized equal to the system states

$$\dot{\nu} = \cancel{A_\nu \cdot \vec{x}} + B_\nu \cdot [B_{\nu,R}^{-1} \cdot (\dot{\nu}_{R,cmd} - \cancel{A_{\nu,R} \cdot \vec{x}_R})] = \dot{\nu}_{R,cmd} = \dot{\nu}_R. \quad (4.58)$$

Instead of the reference control input rate command $\dot{u}_{R,cmd}$, the feedforward comprises of the pseudo control derivative. Allocation of the feedforward (denoted by the matrix inversion $B_{\nu,R}^{-1}$ in Eq. (4.58)) to the real control input commands is then performed by a combination of the control allocation function and effector dynamics consideration as exhibited in Fig. 4.6. As described in the section 4.1, the exact effector dynamics cancellation is directly feasible for the first-order actuators while consideration of the second order dynamics requires inversion of a proper transfer function. In order to avoid doing a discrete inversion, the residual dynamics $R_u(s)$ (Eq. (4.23)) are incorporated within the higher order effects emulation $G_L(s)$ in the RM. Therefore, effector consideration only for the first order dynamics is performed in the extended INDI controller shown by the Fig. 4.6.

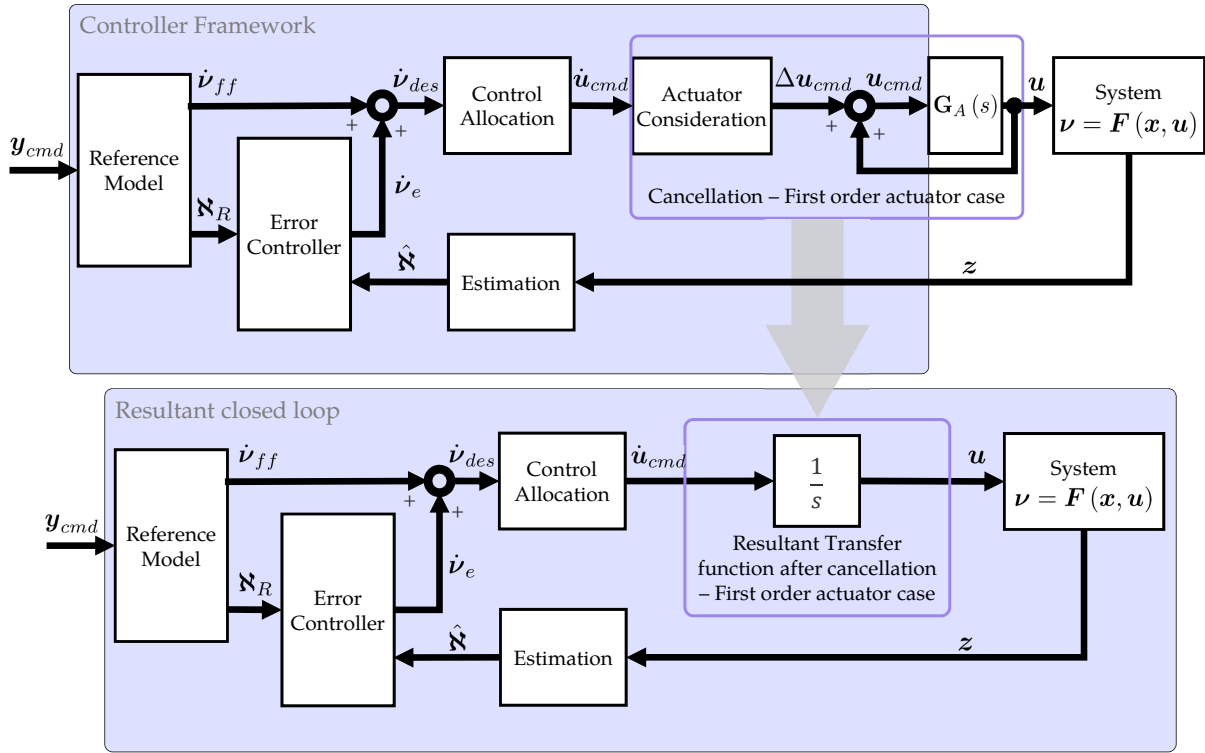


Figure 4.6: Extended INDI control architecture with jerk-level reference model [90]

The closed loop system dynamics yielded solely by the feedforward channel in Eq. (4.58) are only valid for an ideal case of perfect plant knowledge, however it is irrelevant for practical applications. In a real scenario, the true aircraft's pseudo control rate can easily deviate from its reference counterpart due to factors such as unmodeled dynamics, presence of external disturbances along with model uncertainties. Consequently, the plant pseudo controls ν and external states ξ diverge from the reference trajectories $[\nu_R, \xi_R]^T$ upon propagation through the $(r_i + 1)$ integrator chain.

Similar to the stabilizing error controller described in the section 3.2.2.2, a proportional error controller is employed to counteract the deviation of the plant states from the reference trajectories. In addition to using the tracking errors of the external states as in Eq. (3.60), the error controller in the extended INDI controller framework also incorporates the errors in pseudo control tracking, hence yielding the pseudo control error rate $\dot{\nu}_e \in \mathbb{R}^{n_y}$

$$\dot{\nu}_e = C_{e_r} \cdot \begin{pmatrix} (r_{n_y}) \\ \mathbf{y}_R - \mathbf{y} \end{pmatrix} + C_{e_{r-1}} \cdot \begin{pmatrix} (r_{n_y}-1) \\ \mathbf{y}_R - \mathbf{y} \end{pmatrix} \dots + C_{e_0} \cdot (\mathbf{y}_R - \mathbf{y}),$$

$$\dot{\nu}_e = \begin{bmatrix} C_{e_r} & C_{e_{r-1}} & \dots & C_{e_0} \end{bmatrix} \cdot \begin{bmatrix} \mathbf{y}_R - \mathbf{y} \\ \mathbf{y}_R - \mathbf{y} \\ \vdots \\ \mathbf{y}_R - \mathbf{y} \end{bmatrix} = C_e \cdot e, \quad (4.59)$$

where the gains in the matrix $C_e \in \mathbb{R}^{n_y \times [(r+1) \cdot n_y]}$ are chosen such that the poles of the closed-loop system lie in the left-half plane. The feedforward $\dot{\nu}_{ff}$ accomplishes set point tracking task without any feedback for the ideal case depicted in Eq. (4.58) by rendering $\dot{\nu} = \dot{\nu}_R$. Ergo, the tracking error $e \in \mathbb{R}^{(r+1) \cdot n_y}$ comprising of the error in the pseudo controls and the external states does not manifest since the reference trajectories are tracked perfectly, thereby maintaining $\dot{\nu}_e = 0$. The error pseudo control rate $\dot{\nu}_e$ only reacts when the true plant deviates from the nominal design plant. In the general INDI controller structure presented in section 3.2.2, the estimated pseudo control $\hat{\nu}$ is employed to generate the desired incremental pseudo control, which is input to the control allocation module. However, in the continuous extension the pseudo control feedback is merged in the error controller through the first term in Eq. (4.59). Therefore, the desired pseudo control derivative command to the control allocation

$$\dot{\nu}_{des} = \dot{\nu}_{ff} + \dot{\nu}_e \quad (4.60)$$

is the summation of the feedforward and the error pseudo control derivative. Subsequently, the control input rate command \dot{u}_{cmd} is produced by the control allocation module using the same algorithms employed by the unified controller framework described in the section 3.2.2.4. However, the solution produced by the control allocation algorithm is constrained within the control subset derived from control input rate limits rather than incremental limits as given in Eq.(3.67). In the case where the effector consideration is merged with the control allocation, as described by Eq. (4.12), the allocated solution is constrained in the bounds of the control subset as derived in Eq. (3.67). Thereupon, the extended INDI control law for the computation of the effector rate commands emanates

$$\dot{u}_{cmd} = B_\nu^{-1} \cdot \dot{\nu}_{des} = B_\nu^{-1} \cdot (\dot{\nu}_{ff} + \dot{\nu}_e). \quad (4.61)$$

Based on the effector dynamics consideration described in the section 4.1, the effector rate command is equal to the effector rate $\dot{u}_{cmd} = \dot{u}$ given that the assumptions **A.4.1**, **A.4.2** pertaining to the perfect knowledge of the actuators are valid. Together with the equality relation and substitution of the control law Eq. (4.61) in the derived system dynamics from Eq. (4.3), the closed loop system dynamics involving the pseudo control rate feedforward arise

$$\dot{\nu} = A_\nu \cdot x + \cancel{B_\nu} B_\nu^{-T} (\dot{\nu}_{ff} + \dot{\nu}_e). \quad (4.62)$$

Here it is assumed that the control effectiveness matrix employed in the control allocation is perfectly known. Subsequently, upon subtracting the closed loop dynamics derived in Eq. (4.62) from the reference closed loop dynamics in Eq. (4.31) the error dynamics originate

$$\begin{aligned} \overset{e_{\dot{\nu}}}{\dot{\nu}_R - \dot{\nu}} &= A_{\nu,R} \cdot \dot{x}_R + \cancel{\dot{\nu}_{ff}} - A_\nu \cdot \dot{x} - \cancel{\dot{\nu}_{ff}} - C_e \cdot e, \\ e_{\dot{\nu}} + C_e \cdot e &= \overset{\dot{\nu}_{x,R}}{A_{\nu,R} \cdot \dot{x}_R} - \overset{\dot{\nu}_x}{A_\nu \cdot \dot{x}}. \end{aligned} \quad (4.63)$$

The consequent error dynamics indicate that the tracking error is excited by the difference in the magnitude of the state dependent pseudo control rate between the design plant and real system under the considered assumptions and in the absence of any external disturbances. It can be observed from the error dynamics that the presence of the reference component $\mathbf{A}_{\nu,R} \cdot \dot{\mathbf{x}}_R$ mitigates the magnitude of excitation of the tracking error. However, if the reference term is omitted then the control error dynamics are excited by the complete state reliant pseudo control dynamics $\mathbf{A}_\nu \cdot \dot{\mathbf{x}}$ neglected in the continuous INDI control strategy derivation. The reduction in the control error excitation takes place even if the assumed plant parameters $\mathbf{A}_{\nu,R}$ utilized in the design plant do not perfectly match the real parameters. Nonetheless, mitigation of the tracking error excitation occurs in a range of the reference state matrix relative to the corresponding real plant matrix \mathbf{A}_ν , which will be derived in the upcoming section.

Alternative formulation of the error dynamics in Eq. (4.63) can also be presented by adding and subtracting $\mathbf{A}_{\nu,R} \cdot \dot{\mathbf{x}}$ on the RHS of the equation to visualize the effect of the model uncertainty $\tilde{\mathbf{A}} = \mathbf{A}_{\nu,R} - \mathbf{A}_\nu$

$$\begin{aligned}
 e_{\dot{\nu}} + \mathbf{C}_e \cdot e &= \mathbf{A}_{\nu,R} \cdot \dot{\mathbf{x}}_R - \mathbf{A}_{\nu,R} \cdot \dot{\mathbf{x}} + \mathbf{A}_{\nu,R} \cdot \dot{\mathbf{x}} - \mathbf{A}_\nu \cdot \dot{\mathbf{x}}, \\
 e_{\dot{\nu}} + \mathbf{C}_e \cdot e &= \mathbf{A}_{\nu,R} \cdot (\dot{\mathbf{x}}_R - \dot{\mathbf{x}}) + \underbrace{(\mathbf{A}_{\nu,R} - \mathbf{A}_\nu)}_{\tilde{\mathbf{A}}} \cdot \dot{\mathbf{x}}, \\
 e_{\dot{\nu}} + \mathbf{C}_e \cdot e &= \mathbf{A}_{\nu,R} \cdot (\dot{\mathbf{x}}_R - \dot{\mathbf{x}}) + \tilde{\mathbf{A}} \cdot \dot{\mathbf{x}}.
 \end{aligned} \tag{4.64}$$

In [207] (attached in Appendix D), the author presented a predictor based model reference adaptive control framework to estimate the model uncertainty $\tilde{\mathbf{A}}$ and use it to adapt the design plant in the jerk-level reference model, thereby increasing the effectiveness of the feedforward in reducing the excitation of the error dynamics.

4.4 Analysis and Verification

Based on the extended INDI controller architecture containing the jerk-level reference model, linear analysis is performed in this section emphasizing the advantages of the design plant based feedforward and inclusion of higher order effects from actuator dynamics, estimation filters as well as time delays in the RM design. Furthermore, the proposed concept is verified through time domain simulations.

4.4.1 Linear Analysis - SISO case

Linear analysis of the controller framework proposed in the section 4.3 is performed for a SISO system in order to assess the closed loop dynamics in a simplified manner. Effect of the inclusion of noise reduction filters in the RM and uncertainty in the design plant parameters on the closed loop system performance is also analyzed. Analogous to the MIMO transformed dynamics in Eq (4.2), a nonlinear SISO system described by the following transformed dynamics is considered

$$\nu = F(x, u) \tag{4.65}$$

having relative degree 1, thereby $\nu = \dot{y}$. In order to simplify the analysis, the system's output y is defined to be the system state x , which also implies that $\nu = \dot{y} = \dot{x}$. The total time derivative of the SISO system yields

$$\begin{aligned} \dot{\nu} &= \boxed{\frac{\partial F}{\partial x}} \cdot \dot{x} + \boxed{\frac{\partial F}{\partial u}} \cdot \dot{u}, \\ \dot{\nu} &= A_\nu \cdot \nu + B_\nu \cdot \dot{u}, \quad \because \boxed{\nu = \dot{x}}, \end{aligned} \quad (4.66)$$

where $A_\nu \in \mathbb{R}$ and $B_\nu \in \mathbb{R}$ are the scalars describing the Jacobian with respect to the system state x and control u respectively. **As said before the output y of the system is the state x itself, therefore in the upcoming analyses the state dependent term at the pseudo control ν level in the RM is directly visualized as $A_{\nu,R} \cdot y_R$ as compared to $A_{\nu,R} \cdot x_R$. This nomenclature is driven by the aim of simplifying the analysis through omission of the terms pertaining to conversion between the system output and the state, without loss of generality, as they are not relevant to the current investigation.**

The design plant dynamics are also chosen according to the system dynamics in Eq. (4.66)

$$\dot{\nu}_R = A_{\nu,R} \cdot \nu_R + \boxed{B_{\nu,R} \cdot \dot{u}_R}, \quad (4.67)$$

and incorporated in the reference model for the SISO case analysis as illustrated in Fig. 4.7. As already stated during the description of the jerk-level RM in section 4.2, no control allocation is performed in the reference model, hence $B_{\nu,R} \cdot \dot{u}_R \in \mathbb{R}$ is substituted by the pseudo control rate produced by the effector rates $\dot{\nu}_{u,R} \in \mathbb{R}$. Within the context of the linear analysis, the following quantities are assumed to be known exactly

- 1 The control input matrix $B_\nu \in \mathbb{R}$.
- 2 The natural frequency $\omega_A \in \mathbb{R}$ of the actuators, and in addition the damping ratio $\zeta_A \in \mathbb{R}$ for the second order actuators wherever applicable.
- 3 Roll-off filter $G_{LP}(s)$ used for noise attenuation of the sensor feedback.

In this sub-section, the higher order emulation element $G_L(s)$ is utilized to take into account the effects of noise-attenuation filter $G_{LP}(s)$ during generation of the reference trajectories. The noise attenuation filter $G_{LP}(s)$ is modeled as a first order element

$$G_{LP}(s) = \frac{\omega_{LP}}{s + \omega_{LP}}, \quad (4.68)$$

and the higher order emulation unit is specified as equal to the noise attenuation filter $G_L(s) = G_{LP}(s)$.

The analysis starts with the calculation of the transfer characteristics of the jerk-level reference model. As demonstrated in the Fig. 4.7, the reference model comprises of two components – the **reference transfer characteristics $G_R(s)$**

$$\mathbf{G}_R(s) = \begin{bmatrix} G_{y_{cmd} \rightarrow \nu_R}(s) \\ G_{y_{cmd} \rightarrow y_R}(s) \end{bmatrix} = \begin{bmatrix} \frac{\nu_R(s)}{y_{cmd}(s)} \\ \frac{y_R(s)}{y_{cmd}(s)} \end{bmatrix} \quad (4.69)$$

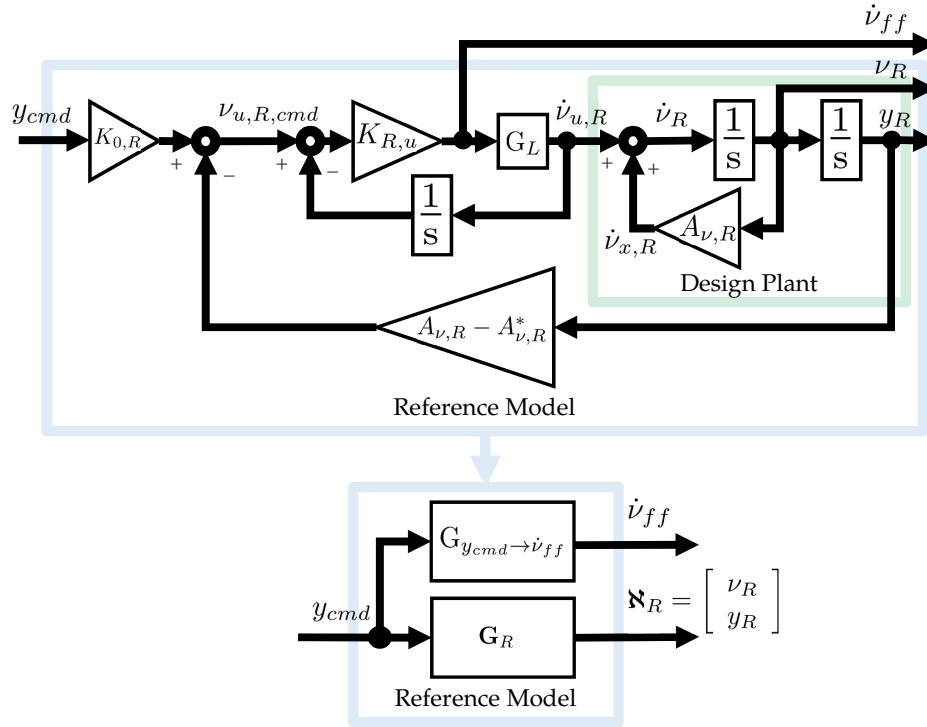


Figure 4.7: Jerk level reference model - transfer functions in a SISO case

and the feedforward transfer function $G_{y_{cmd} \rightarrow \dot{v}_{ff}}(s)$

$$G_{y_{cmd} \rightarrow \dot{v}_{ff}}(s) = \frac{\dot{v}_{ff}(s)}{y_{cmd}(s)}. \quad (4.70)$$

The first step in deriving these transfer functions is to obtain the transfer characteristics from the pseudo derivative feedforward \dot{v}_{ff} to the reference pseudo control ν_R and reference external state y_R . In order to achieve this, the control input dependent pseudo control derivative $\dot{v}_{u,R}$ is substituted with $G_L(s) \cdot \dot{v}_{ff}$ (according to Fig. 4.7) in the design plant dynamics

$$\begin{aligned} \dot{\nu}_R &= A_{\nu,R} \cdot \nu_R + \dot{v}_{u,R}, \\ s \cdot \nu_R &= A_{\nu,R} \cdot \nu_R + G_L(s) \cdot \dot{v}_{ff}, \end{aligned} \quad (4.71)$$

to obtain the transfer functions

$$\begin{aligned} G_{\dot{v}_{ff} \rightarrow \nu_R}(s) &= \frac{\nu_R(s)}{\dot{v}_{ff}(s)} = \frac{G_L(s)}{(s - A_{\nu,R})}, \\ G_{\dot{v}_{ff} \rightarrow y_R}(s) &= \frac{y_R(s)}{\dot{v}_{ff}(s)} = \frac{G_L(s)}{s \cdot (s - A_{\nu,R})}, \end{aligned} \quad \because \boxed{y_R = \frac{1}{s} \cdot \nu_R}. \quad (4.72)$$

It directly follows that the transfer function from the reference pseudo control to the reference state $G_{\nu_R \rightarrow y_R}$ is just an integrator

$$G_{\nu_R \rightarrow y_R}(s) = \frac{1}{s}. \quad (4.73)$$

The next step is to obtain the transfer function from reference control input dependent pseudo control command $\nu_{u,R,cmd}$ to the feedforward pseudo control derivative \dot{v}_{ff} . For this purpose, consider the feedforward calculation performed by using the reference

actuator gain $K_{R,u} \in \mathbb{R}$ and the pseudo control command intended to be generated by the system effector $\nu_{u,R,cmd}$

$$\dot{\nu}_{ff} = K_{R,u} \cdot \left(\nu_{u,R,cmd} - \frac{1}{s} \cdot G_L(s) \cdot \dot{\nu}_{ff} \right), \quad (4.74)$$

Collecting the terms pertaining to $\dot{\nu}_{ff}$, the transfer function from the control input dependent pseudo control command to the feedforward $G_{\nu_{u,R,cmd} \rightarrow \dot{\nu}_{ff}}$ is obtained

$$\begin{aligned} (s + K_{R,u} \cdot G_L(s)) \cdot \dot{\nu}_{ff} &= s \cdot K_{R,u} \cdot \nu_{u,R,cmd}, \\ G_{\nu_{u,R,cmd} \rightarrow \dot{\nu}_{ff}}(s) &= \frac{\dot{\nu}_{ff}(s)}{\nu_{u,R,cmd}(s)} = \frac{s \cdot K_{R,u}}{(s + K_{R,u} \cdot G_L(s))}. \end{aligned} \quad (4.75)$$

Merging the results from Eqs. (4.72) and (4.75), the transfer characteristics from the control input dependent pseudo control command $\nu_{u,R,cmd}$ to the reference external state y_R emanate

$$G_{\nu_{u,R,cmd} \rightarrow y_R}(s) = G_{\nu_{u,R,cmd} \rightarrow \dot{\nu}_{ff}} \cdot G_{\dot{\nu}_{ff} \rightarrow y_R} = \frac{y_R(s)}{\nu_{u,R,cmd}(s)}, \quad (4.76)$$

$$G_{\nu_{u,R,cmd} \rightarrow y_R}(s) = \frac{K_{R,u} \cdot G_L(s)}{s^2 + (K_{R,u} \cdot G_L(s) - A_{\nu,R}) \cdot s - K_{R,u} \cdot G_L(s) \cdot A_{\nu,R}}.$$

The missing piece in the reference transfer function $G_{y_{cmd} \rightarrow y_R}(s)$ are the dynamics from control variable command y_{cmd} to the pseudo control command $\nu_{u,R,cmd}$. In order to derive this transfer function, the relation for computation of pseudo control command $\nu_{u,R,cmd}$, given in Eq. (4.39) is employed

$$\nu_{u,R,cmd} = K_{0,R} \cdot y_{cmd} - \left(A_{\nu,R} - A_{\nu,R}^* \right) \boxed{y_R}, \quad (4.77)$$

$G_{\nu_{u,R,cmd} \rightarrow y_R}(s) \cdot \nu_{u,R,cmd}$

where $A_{\nu,R}^* = -K_{0,R}$ specify the desired reference dynamics for the control variable command response. Consider the relation in Eq. (4.77) in the Laplace domain. Upon substitution of the reference state y_R with the term $G_{\nu_{u,R,cmd} \rightarrow y_R}(s) \cdot \nu_{u,R,cmd}$, and further expanding the transfer function $G_{\nu_{u,R,cmd} \rightarrow y_R}(s)$ as derived in Eq. (4.76), the relation between the control variable command y_{cmd} and the pseudo control command $\nu_{u,R,cmd}$ is acquired

$$\begin{aligned} \nu_{u,R,cmd} &= K_{0,R} \cdot y_{cmd} - \\ &\left(A_{\nu,R} - A_{\nu,R}^* \right) \cdot \frac{K_{R,u} \cdot G_L(s)}{s^2 + (K_{R,u} \cdot G_L(s) - A_{\nu,R}) \cdot s - K_{R,u} \cdot G_L(s) \cdot A_{\nu,R}} \cdot \nu_{u,R,cmd}. \end{aligned} \quad (4.78)$$

Utilizing the expression in Eq. (4.78), the transfer dynamics from control variable command y_{cmd} to the pseudo control command $\nu_{u,R,cmd}$, denoted by $G_{y_{cmd} \rightarrow \nu_{u,R,cmd}}(s)$, are derived

$$\begin{aligned} G_{y_{cmd} \rightarrow \nu_{u,R,cmd}}(s) &= \frac{\nu_{u,R,cmd}(s)}{y_{cmd}(s)} \\ G_{y_{cmd} \rightarrow \nu_{u,R,cmd}}(s) &= K_{0,R} \cdot \frac{s^2 + (K_{R,u} \cdot G_L(s) - A_{\nu,R}) \cdot s - K_{R,u} \cdot G_L(s) \cdot A_{\nu,R}}{s^2 + (K_{R,u} \cdot G_L(s) - A_{\nu,R}) \cdot s - K_{R,u} \cdot G_L(s) \cdot A_{\nu,R}^*}. \end{aligned} \quad (4.79)$$

Subsequently, the resulting transfer functions from Eqs. (4.79) and (4.76) along with the relation in Eq. (4.73) lead to the reference transfer characteristics

$$\mathbf{G}_R(s) = \begin{cases} G_{y_{cmd} \rightarrow y_R}(s) = \frac{K_{R,u} \cdot G_L(s) \cdot K_{0,R}}{s^2 + (K_{R,u} \cdot G_L(s) - A_{\nu,R}) \cdot s - K_{R,u} \cdot G_L(s) \cdot A_{\nu,R}^*} \\ G_{y_{cmd} \rightarrow \nu_R}(s) = \frac{K_{R,u} \cdot G_L(s) \cdot K_{0,R} \cdot s}{s^2 + (K_{R,u} \cdot G_L(s) - A_{\nu,R}) \cdot s - K_{R,u} \cdot G_L(s) \cdot A_{\nu,R}^*} \end{cases}. \quad (4.80)$$

It was mentioned earlier that the relation between the desired state dynamics and the command scaling is given as $A_{\nu,R}^* = -K_{0,R}$, which implies that $K_{R,u} \cdot G_L(s) \cdot K_{0,R} = -K_{R,u} \cdot G_L(s) \cdot A_{\nu,R}^*$. Hence, it verifies that the command variable response transfer function $G_{y_{cmd} \rightarrow y_R}(s)$ has a unit DC gain. Ultimately, the second component of the reference dynamics from Fig. 4.7 – the feedforward transfer function $G_{y_{cmd} \rightarrow \dot{\nu}_{ff}}(s)$ is derived using the combination of transfer functions from Eqs. (4.79) and (4.76)

$$\begin{aligned} G_{y_{cmd} \rightarrow \dot{\nu}_{ff}}(s) &= G_{y_{cmd} \rightarrow \nu_{u,R,cmd}}(s) \cdot G_{\nu_{u,R,cmd} \rightarrow \dot{\nu}_{ff}}(s), \\ G_{y_{cmd} \rightarrow \dot{\nu}_{ff}}(s) &= \frac{\dot{\nu}_{ff}(s)}{y_{cmd}(s)} = \frac{s \cdot K_{R,u} \cdot K_{0,R} \cdot (s - A_{\nu,R})}{s^2 + (K_{R,u} \cdot G_L(s) - A_{\nu,R}) \cdot s - K_{R,u} \cdot G_L(s) \cdot A_{\nu,R}^*}. \end{aligned} \quad (4.81)$$

Following the computation of the reference transfer dynamics, the transfer function $G_{y_R \rightarrow y}(s)$ pertaining to the closed loop exhibited in Fig. 4.8 is derived. The SISO closed loop transfer function from the reference external state y_R to the plant output y is also affected by the feedforward pseudo control derivative. First, the function $G_{y_R \rightarrow \dot{\nu}_{ff}}(s)$ specifying the transfer characteristics from the reference external state to the feedforward command (shown by Fig. 4.8) needs to be calculated. Rather than taking the transfer function $G_{y_{cmd} \rightarrow \dot{\nu}_{ff}}(s)$ from the command variable y_{cmd} to the feedforward $\dot{\nu}_{ff}$, the transfer characteristics from the reference external state y_R to the feedforward are used because goal of this analysis is to establish the effect of employing the design plant in the RM on the tracking error $(y_R - \hat{y})$, which is computed with respect to the reference external state y_R instead of the command variable y_{cmd} . Subsequently, the transfer function $G_{y_R \rightarrow \dot{\nu}_{ff}}(s)$ is delivered by using the transfer functions from Eqs. (4.81) and (4.80)

$$G_{y_R \rightarrow \dot{\nu}_{ff}}(s) = \frac{G_{y_{cmd} \rightarrow \dot{\nu}_{ff}}(s)}{G_{y_{cmd} \rightarrow y_R}(s)} = \frac{s \cdot (s - A_{\nu,R})}{G_L(s)}, \quad (4.82)$$

which is essentially the inverse of the characteristics $G_{\dot{\nu}_{ff} \rightarrow y_R}(s)$ defined in Eq. (4.72). Crucial to mention that the transfer function derived in Eq. (4.82) is not meant for any real software implementation on account that it is non-causal, but only used for the purpose of analysis.

As stated before, it is assumed that the parameters of the actuator dynamics are known perfectly. For the current analysis, the system is assumed to have a first order effector. Therefore, in accordance with Eq. (4.15), $\dot{u}_{cmd} = \dot{u}$, and the effector rate input to the plant is given by

$$\dot{u} = K_B \cdot G_{y_R \rightarrow \dot{\nu}_{ff}}(s) \cdot y_R + K_B \cdot \mathbf{C}_e \left(\mathbf{x}_R - \hat{\mathbf{x}} \right), \quad (4.83)$$

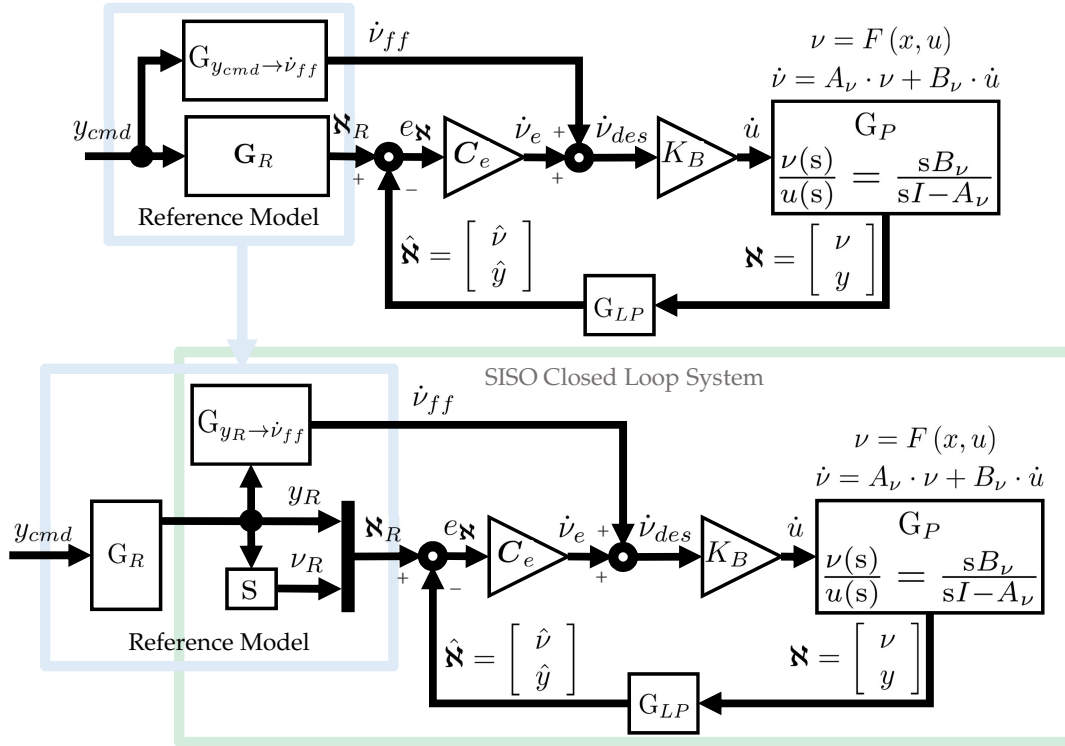


Figure 4.8: Jerk-level RM in a closed Loop system for a SISO case

where $K_B = B_\nu^{-1}$ is the inverse of the control effectiveness, and $\hat{\mathbf{n}} = [\hat{\nu}, \hat{y}]^T$ comprises of the estimated pseudo control $\hat{\nu}$ as well as the filtered output \hat{y} . The pseudo control ν and output y are available as measurements, and the variables $[\hat{\nu}, \hat{y}]^T$ are obtained by filtering the measurements through the low-pass filter $G_{LP}(s)$ described by Eq. (4.68). The term \mathbf{n}_R contains the reference trajectories $[\nu_R, y_R]^T$. The gain variable $C_e = [C_{ey}, C_{e\nu}]$ is a row vector of error controller gains $C_{ey} \in \mathbb{R}$ and $C_{e\nu} \in \mathbb{R}$ for the tracking errors in output and pseudo control respectively. As stated before, the considered system has a relative degree of 1, hence the reference and true pseudo controls can be specified in the Laplace domain in terms of the corresponding outputs $s \cdot y_R$ and $s \cdot y$ respectively. Consequently, the error term in Eq. (4.83) is transformed

$$\begin{aligned}
 C_e (\mathbf{n}_R - \hat{\mathbf{n}}) &= \underbrace{(C_{ey} + C_{e\nu} \cdot s)}_{G_e(s)} \cdot y_R - \underbrace{(C_{ey} + C_{e\nu} \cdot s)}_{G_e(s)} \cdot \hat{y}, \\
 C_e (\mathbf{n}_R - \hat{\mathbf{n}}) &= G_e(s) \cdot y_R - G_e(s) \cdot G_{LP}(s) \cdot y, \quad \because \hat{y} = G_{LP}(s) \cdot y. \quad (4.84)
 \end{aligned}$$

The result is substituted back to the control input rate expression from Eq. (4.83)

$$\dot{u} = K_B \cdot G_{y_R \rightarrow \dot{\nu}_{ff}}(s) \cdot y_R + K_B \cdot G_e(s) \cdot y_R - K_B \cdot G_e(s) \cdot G_{LP}(s) \cdot y. \quad (4.85)$$

In the frequency domain, the SISO system dynamics from Eq. (4.66) can be shown as

$$\begin{aligned}
 \dot{\nu} &= A_\nu \cdot \nu + B_\nu \cdot \dot{u}, \\
 s \cdot \nu &= A_\nu \cdot \nu + B_\nu \cdot \dot{u}, \\
 (s - A_\nu) \cdot \nu &= B_\nu \cdot \dot{u}, \\
 \nu &= \frac{B_\nu}{s - A_\nu} \cdot \dot{u} = G_P(s) \cdot \dot{u}.
 \end{aligned} \tag{4.86}$$

Dependence on the complex variable s is not shown in the equations hereafter for ease of reading. To acquire the closed loop transfer dynamics, control input rate from Eq. (4.85) along with the relation $\nu = s \cdot y$ are substituted in the SISO system dynamics from Eq. (4.86)

$$\begin{aligned}
 s \cdot y &= G_P \cdot \left[K_B \cdot G_{y_R \rightarrow \dot{\nu}_{ff}} \cdot y_R + K_B \cdot G_e \cdot y_R - K_B \cdot G_e \cdot G_{LP} \cdot y \right], \\
 y &= \frac{G_P}{s} \cdot \left[K_B \cdot G_{y_R \rightarrow \dot{\nu}_{ff}} \cdot y_R + K_B \cdot G_e \cdot y_R - K_B \cdot G_e \cdot G_{LP} \cdot y \right], \\
 y &= \left[G_{\bar{P}} \cdot K_B \cdot G_{y_R \rightarrow \dot{\nu}_{ff}} + G_{\bar{P}} \cdot K_B \cdot G_e \right] \cdot y_R - \underbrace{G_{\bar{P}} \cdot K_B \cdot G_e \cdot G_{LP}}_{L(s)} \cdot y,
 \end{aligned} \tag{4.87}$$

where $L(s)$ denotes the open loop transfer function of the SISO closed loop system from Fig. 4.8 in the absence of any feedforward element. Further, by collecting the terms pertaining to output y on one side

$$[1 + L] \cdot y = \left[G_{\bar{P}} \cdot K_B \cdot G_{y_R \rightarrow \dot{\nu}_{ff}} + G_{\bar{P}} \cdot K_B \cdot G_e \right] \cdot y_R \tag{4.88}$$

the transfer characteristics from the reference external state y_R to the plant output y emanate

$$G_{y_R \rightarrow y}(s) = \frac{y(s)}{y_R(s)} = \frac{G_{\bar{P}} \cdot K_B \cdot G_{y_R \rightarrow \dot{\nu}_{ff}} + G_{\bar{P}} \cdot K_B \cdot G_e}{1 + L}. \tag{4.89}$$

Equation (4.89) depicts the response of the real plant in terms of the output y to a given set-point of the reference external state y_R . However, the control loop does not receive information about the true plant output, but an estimated/filtered value \hat{y} . For this analysis, it is presumed that output and pseudo control feedback is available and no model based state estimation algorithms are used. Only a first-order low-pass filter $G_{LP}(s)$ (given in Eq. (4.68)) is employed for processing the raw sensor measurements of the output y and pseudo control ν . Consequently, the transfer function from the reference signal y_R to the estimated output \hat{y} is obtained by the product of the transfer relation $G_{y_R \rightarrow y}(s)$ from Eq. (4.89) and the noise attenuation filter $G_{LP}(s)$

$$\begin{aligned}
 G_{y_R \rightarrow \hat{y}}(s) &= G_{y_R \rightarrow y}(s) \cdot G_{LP}(s), \\
 G_{y_R \rightarrow \hat{y}}(s) &= \frac{\hat{y}(s)}{y_R(s)} = \frac{G_{\bar{P}} \cdot K_B \cdot G_{y_R \rightarrow \dot{\nu}_{ff}} \cdot G_{LP} + \underbrace{G_{\bar{P}} \cdot K_B \cdot G_e \cdot G_{LP}}_{L(s)}}{1 + L}, \\
 G_{y_R \rightarrow \hat{y}}(s) &= \frac{\hat{y}(s)}{y_R(s)} = \frac{G_{\bar{P}} \cdot K_B \cdot G_{y_R \rightarrow \dot{\nu}_{ff}} \cdot G_{LP} + L}{1 + L}.
 \end{aligned} \tag{4.90}$$

Finally, the closed loop transfer function in Eq. (4.90) is utilized to derive the transfer characteristics from the reference external state y_R to the perceived tracking error $e_{\hat{y}}$

$$e_{\hat{y}} = y_R - \hat{y} = [1 - G_{y_R \rightarrow \hat{y}}] \cdot y_R, \quad (4.91)$$

$$G_{y_R \rightarrow e_{\hat{y}}}(s) = \frac{e_{\hat{y}}(s)}{y_R(s)} = \frac{1 - G_{\bar{P}} \cdot K_B \cdot G_{y_R \rightarrow \dot{v}_{ff}} \cdot G_{LP}}{1 + L},$$

which characterizes the tracking performance of the extended INDI controller incorporating the jerk-level reference model for the considered SISO case. As stated at the beginning of this analysis, the control effectiveness B_ν and the transfer characteristics of the noise attenuation filter $G_{LP}(s)$ are known perfectly. For the relation in Eq. (4.91), the higher order effects emulation $G_L(s)$, encompassed in the feed forward transfer function $G_{y_R \rightarrow \dot{v}_{ff}}(s)$ (see Eq. (4.82)), is substituted equal to the roll-off filter $G_{LP}(s)$. Additionally, upon expanding the system dynamics $G_{\bar{P}}(s)$, the open loop transfer function $L(s)$, and using the relation $K_B = B_\nu^{-1}$ in the tracking error transfer dynamics from Eq. (4.91), the transfer function describing the effect of the difference between the true system parameter A_ν and the design plant parameter $A_{\nu,R}$ on the tracking error $e_{\hat{y}}$ is yielded

$$G_{y_R \rightarrow e_{\hat{y}}}(s) = \frac{(A_{\nu,R} - A_\nu) \cdot s}{s^2 - A_\nu \cdot s + G_e \cdot G_{LP}}. \quad (4.92)$$

Since the difference between the true and design plant parameter ($A_{\nu,R} - A_\nu$) emanates in the transfer function from Eq. (4.92), it is a good candidate to perform a sensitivity analysis of the model uncertainty between the design and true system on the tracking performance the extended INDI strategy employing the proposed jerk level RM.

The current analysis considers only stable systems, while the treatment of unstable systems is covered later in the section 4.4.6. Accordingly, the system state parameter A_ν for the SISO transformed dynamics in Eq. (4.66) is given in the Table 4.1. Simultaneously, an appropriate value of the control effectiveness B_ν is also defined. The control effectiveness is assumed to be known exactly, therefore $K_B = B_\nu^{-1}$. The magnitudes of the plant parameters along with the controller feedback gains $C_{ey}, C_{e\nu}$ are listed in Table 4.1. Additionally the reference gains $K_{0,R}, K_{R,u}$ are also given. The noise attenuation filter $G_{LP}(s)$ with the roll-off frequency ω_{LP} having a structure similar to the first order element in Eq. (4.68) is considered. The effect of this filter is incorporated in the higher order effects emulation $G_L(s)$ of the RM. Other sensor effects are not included yet to simplify the analysis.

Results pertaining to the sensitivity analysis are demonstrated in Fig. 4.9. The top left gain plot illustrates the effect of decreasing design plant uncertainty $\Delta A = A_{\nu,R} - A_\nu$. Each line represents the gain variation of the transfer function $G_{y_R \rightarrow e_{\hat{y}}}(s)$ at a given value of the design plant parameter $A_{\nu,R}$. The value of the design parameter is increased from zero to $0.9 \cdot A_\nu$ and the transfer function magnitude is drawn for each iteration. Noticeably, when the magnitude of $A_{\nu,R}$ lies in $[0, A_\nu]$, use of the pseudo control derivative feedforward from the RM facilitates deamplification of the tracking error $e_{\hat{y}}$ because the gain of the transfer function $G_{y_R \rightarrow e_{\hat{y}}}(s)$ offsets to a more negative value as $A_{\nu,R}$

Parameter	Magnitude	Parameter	Magnitude
$K_{0,R}$	3	A_ν	-2
$A_{\nu,R}^*$	-3	B_ν	1.5
$K_{u,R}$	12	C_{ex}	6
ω_{LP}	20	C_{ev}	18

Table 4.1: Magnitude of parameters used in the linear analysis of the jerk-level RM with the extended INDI controller

approaches the true plant A_ν . The gain of $G_{y_R \rightarrow e_{\dot{y}}}(s)$ in the limit case $A_{\nu,R} = A_\nu$ is zero, which indicates that the closed loop system runs only on the feedforward command without any control tracking error.

Likewise, in the case where the design parameter lies in the range $[A_\nu, 2 \cdot A_\nu]$, the design model dependent feedforward also reduces the gain of the tracking error transfer characteristics $G_{y_R \rightarrow e_{\dot{y}}}(s)$. The top right subplot shows the transfer function's gain plots while increasing the design parameter $A_{\nu,R}$ value from $1.1 \cdot A_\nu$ to $2.5 \cdot A_\nu$. For every step increase of the $A_{\nu,R}$ value in the range $[A_\nu, 2 \cdot A_\nu]$, the magnitude of the transfer function offsets to a higher value. However, the gain plots for each of these cases lie below the gain plot in the situation when $A_{\nu,R} = 2 \cdot A_\nu$, which exactly matches the gain plot in the case of $A_{\nu,R} = 0$ as verified by the bottom left plot in the Fig. 4.9. Needless to say,

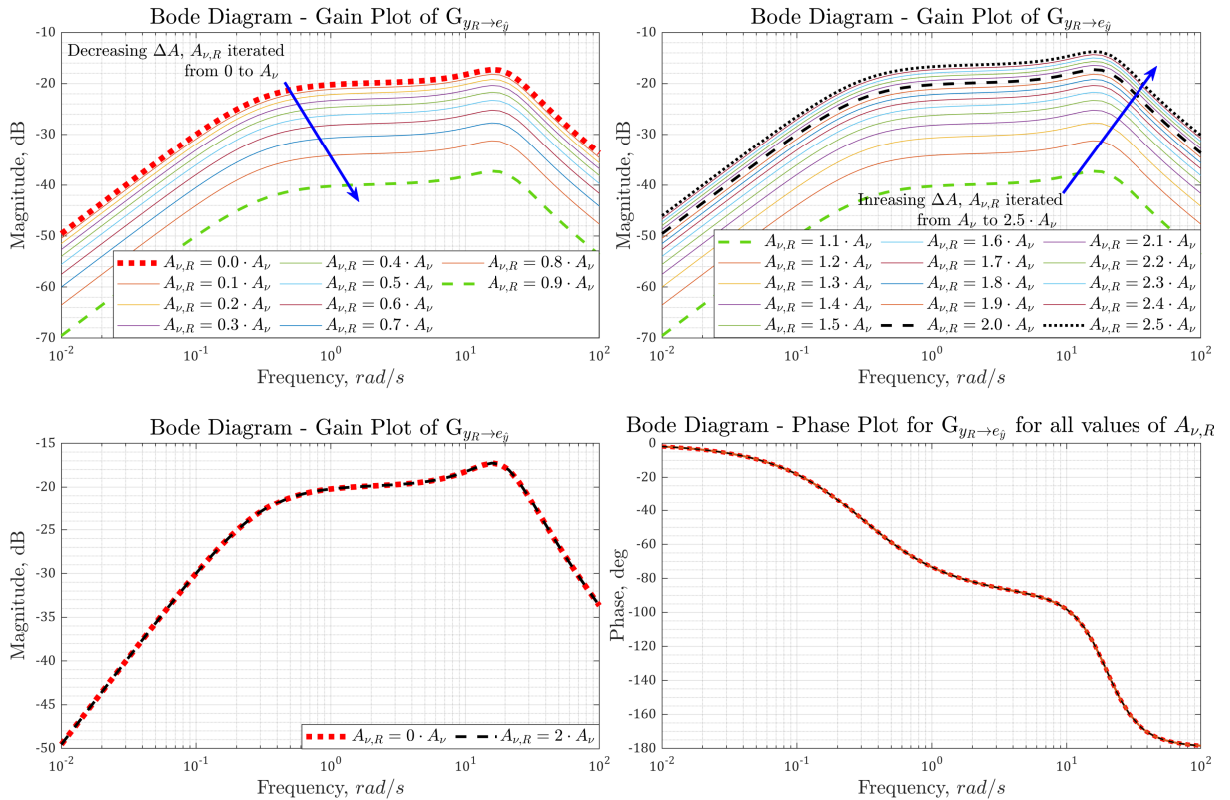


Figure 4.9: Frequency domain illustration of the effect of model uncertainty in A_ν on tracking error

the phase characteristics of the transfer function from the reference external state to the control error $G_{y_R \rightarrow e_{\dot{y}}}(s)$ are not influenced by the feedforward as demonstrated by the phase plot for all cases in the bottom right of the Fig. 4.9.

Thereupon, through the above-mentioned analysis it is demonstrated that the set point tracking of the closed loop system is improved by employing model knowledge $A_{\nu,R}$ in the design plant given that $A_{\nu,R}$ lies within $[0, 2 \cdot A_{\nu}]$, which is proven by reduction in the gain of the tracking error transfer characteristics $G_{y_R \rightarrow e_{\dot{y}}}(s)$.

The desired trajectory of the reference external state y_R as well as the feedforward pseudo control derivative \dot{v}_{ff} is dependent on the control variable scaling $K_{0,R}$, reference actuator gain $K_{R,u}$, the design plant parameter $A_{\nu,R}$, the desired state dynamics specification parameters $A_{\nu,R}^*$ and the higher order effect element $G_L(s)$. Important to note that the control variable scaling $K_{0,R}$ is always defined as negative of the desired state dynamics specification parameters $A_{\nu,R}^*$. The design plant parameter $A_{\nu,R}$ as well as the higher order effect element $G_L(s)$ are the essential elements for generating an effective feedforward command, which brings about the deamplification of the tracking error $e_{\dot{y}}$.

4.4.2 MUAD Analysis

Primarily, the design of the reference response is conducted based on the handling quality requirements such as the ones specified in the Tables 2.4 and 2.5. For the considered SISO case, the reference transfer characteristics $G_{y_{cmd} \rightarrow y_R}(s)$ from Eq. (4.80) describe the desired handling qualities by defining the reference external state response trajectory y_R for a command variable set point y_{cmd} specified by a pilot or a remote operator. Upon substituting the reference external state y_R with $G_{y_{cmd} \rightarrow y_R}(s) \cdot y_{cmd}$ in the closed loop transfer function $G_{y_R \rightarrow y}(s)$ from Eq. (4.89), the transfer function from the command variable to the plant output $G_{y_{cmd} \rightarrow y}(s)$ is obtained

$$\begin{aligned} \frac{y(s)}{y_R(s)} &= \frac{G_{\bar{P}} \cdot K_B \cdot G_{y_R \rightarrow \dot{v}_{ff}} + G_{\bar{P}} \cdot K_B \cdot G_e}{1 + L}, \\ y(s) &= \frac{G_{\bar{P}} \cdot K_B \cdot G_{y_R \rightarrow \dot{v}_{ff}} + G_{\bar{P}} \cdot K_B \cdot G_e}{1 + L} \cdot y_R(s), \\ y(s) &= \frac{G_{\bar{P}} \cdot K_B \cdot G_{y_R \rightarrow \dot{v}_{ff}} + G_{\bar{P}} \cdot K_B \cdot G_e}{1 + L} \cdot G_{y_{cmd} \rightarrow y_R} \cdot y_{cmd}(s), \\ G_{y_{cmd} \rightarrow y}(s) &= \frac{G_{\bar{P}} \cdot K_B \cdot G_{y_R \rightarrow \dot{v}_{ff}} \cdot G_{LP} \cdot G_{y_{cmd} \rightarrow y_R} + G_{\bar{P}} \cdot K_B \cdot G_e \cdot G_{y_{cmd} \rightarrow y_R}}{1 + L}. \end{aligned} \tag{4.93}$$

Here $L(s)$ represents the loop transfer function as derived in the previous section

$$L(s) = G_{\bar{P}} \cdot K_B \cdot G_e \cdot G_{LP}. \tag{4.94}$$

The derived transfer function in Eq. (4.93) is used to study the added dynamics introduced in the controlled system due to difference in magnitude of the design plant parameter $A_{\nu,R}$ from the true plant A_{ν} .

The Maximum Unnoticeable Added Dynamics (MUAD) [208, 209] envelopes define the frequency domain regions within which any change in the dynamic characteristics of an augmented system are indistinguishable to the pilot, thereby yielding similar handling quality ratings as the desired behavior. These boundaries are derived based on the qualitative ratings of pilots during manual mission task elements in presence of added dynamics [210]. Therefore, the aim of a control designer is to ensure that any kind of additional dynamics do not violate the derived envelope boundaries. The MUAD bounds recorded in [208] are enlisted in the Table 4.2.

Envelope	Transfer Function
Upper Gain Envelope	$\frac{3.16 \cdot s^2 + 31.61 \cdot s + 22.79}{s^2 + 27.14 \cdot s + 1.84}$
Lower Gain Envelope	$\frac{0.0955 \cdot s^2 + 9.92 \cdot s + 2.15}{s^2 + 11.60 \cdot s + 4.95}$
Upper Phase Envelope	$\frac{68.89 \cdot s^2 + 1100.12 \cdot s - 275.22}{s^2 + 39.94 \cdot s + 9.99} \cdot e^{0.0059 \cdot s}$
Lower Phase Envelope	$\frac{475.32 \cdot s^2 + 184100 \cdot s + 29456.1}{s^2 + 11.66 \cdot s + 0.0389} \cdot e^{-0.0072 \cdot s}$

Table 4.2: Transfer functions for envelopes of Maximum Unnoticeable Added Dynamics[208]

The impact of added dynamics due to the variation between the design and true plant state damping parameter ($A_{\nu,R} - A_{\nu}$) is assessed. The difference of the gain/phase characteristics between values in the uncertain range $A_{\nu,R} \in [0, 2 \cdot A_{\nu}]$ and the nominal value $A_{\nu,R} = A_{\nu}$ for the closed loop transfer function $G_{y_{cmd} \rightarrow y}(s)$ (Eq. (4.93)) are plotted against the MUAD bounds in Fig. 4.10. The gain and phase variation due the added dynamics (uncertainty in $A_{\nu,R}$) are obtained according to

$$\begin{aligned} \Delta|G_{y_{cmd} \rightarrow y}(s)| &= |\Delta G_{y_{cmd} \rightarrow y}(s)| : A_{\nu,R} \in [0, 2 \cdot A_{\nu}] - |G_{y_{cmd} \rightarrow y}(s)| : A_{\nu,R} = A_{\nu}, \\ \Delta \angle G_{y_{cmd} \rightarrow y}(s) &= \angle G_{y_{cmd} \rightarrow y}(s) : A_{\nu,R} \in [0, 2 \cdot A_{\nu}] - \angle G_{y_{cmd} \rightarrow y}(s) : A_{\nu,R} = A_{\nu}. \end{aligned} \quad (4.95)$$

Fig. 4.10 demonstrates the magnitude and phase difference generated in the loop transfer function $G_{y_{cmd} \rightarrow y}(s)$ while iterating the value of the design plant parameter $A_{\nu,R}$ from zero to twice of the true plant parameter A_{ν} . As already stated, the plant exactly follows the desired dynamics specified in the reference model through the ideal feedforward in case of perfect plant knowledge without evoking any tracking error. Any deviation from the ideal case does not change the reference dynamics, however it impacts the closed loop system response since the feedforward command is no longer ideal and the induced tracking error is mitigated in accordance with the dynamics specified in the feedback error controller. It can be deduced from the resulting magnitude and phase plots in Fig. 4.10 that as long as the value of the design plant parameter $A_{\nu,R}$ lies within $\pm 100\%$ of the true plant parameter for the considered case, the transfer characteristics of the loop transfer function do not violate the MUAD bounds.

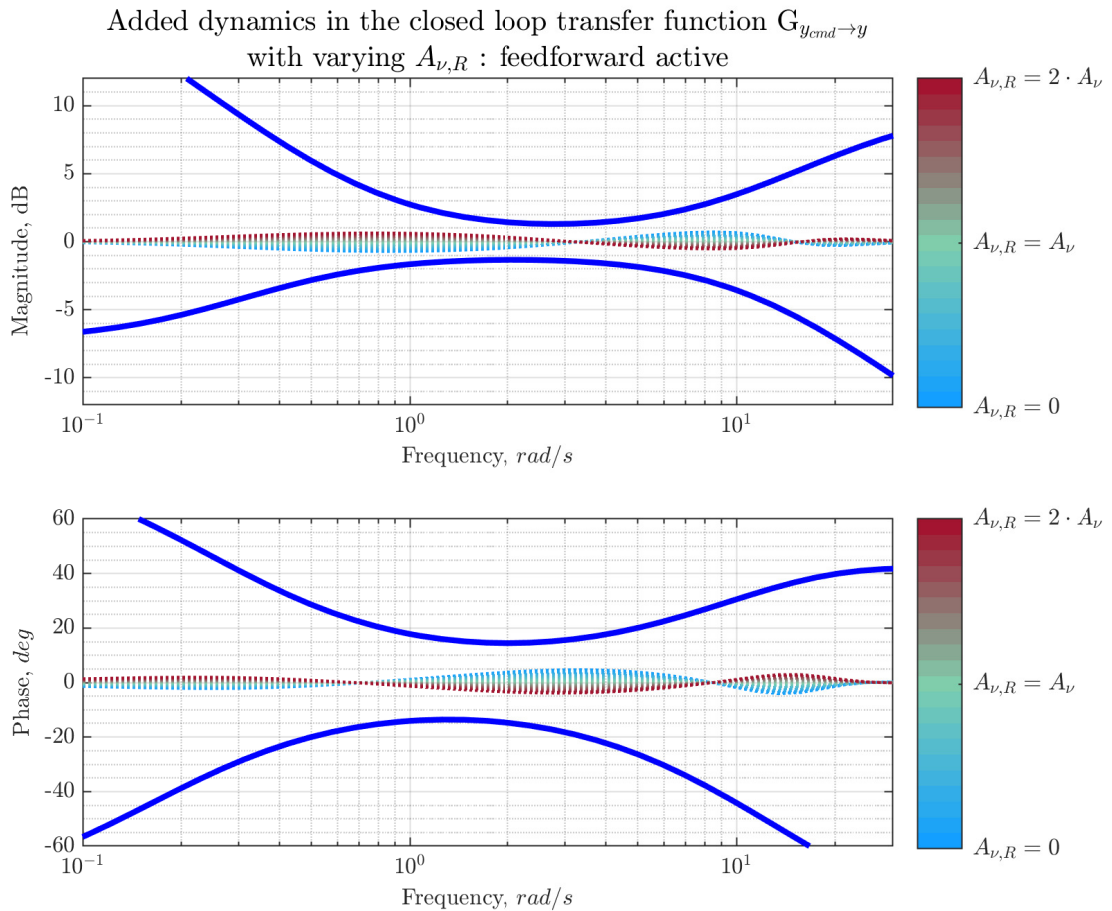


Figure 4.10: Added dynamics by the model uncertainty A_{ν} on the loop transfer characteristics $G_{y_{cmd} \rightarrow y}(s)$ with feedforward

In order to demonstrate the effectiveness of the feedforward, the MUAD analysis demonstrated by the Fig. 4.10 is performed again under the same conditions, while removing the feedforward signal from the RM to the extended INDI controller. It can be observed in the Fig. 4.11 that for the considered SISO case, removal of the feedforward to the controller leads to violation of the phase MUAD bounds considering the closed loop transfer function $G_{y_{cmd} \rightarrow y}(s)$ for any value of the design plant parameter at higher frequencies.

From the analyses performed so far, it is observed that inclusion of the "A-part" for the feedforward generation in the considered case improves set-point tracking while having indistinguishable effects on handling qualities given that the deviation of the design plant parameter does not exceed $\pm 100\%$ as compared to the corresponding parameter of the real system.

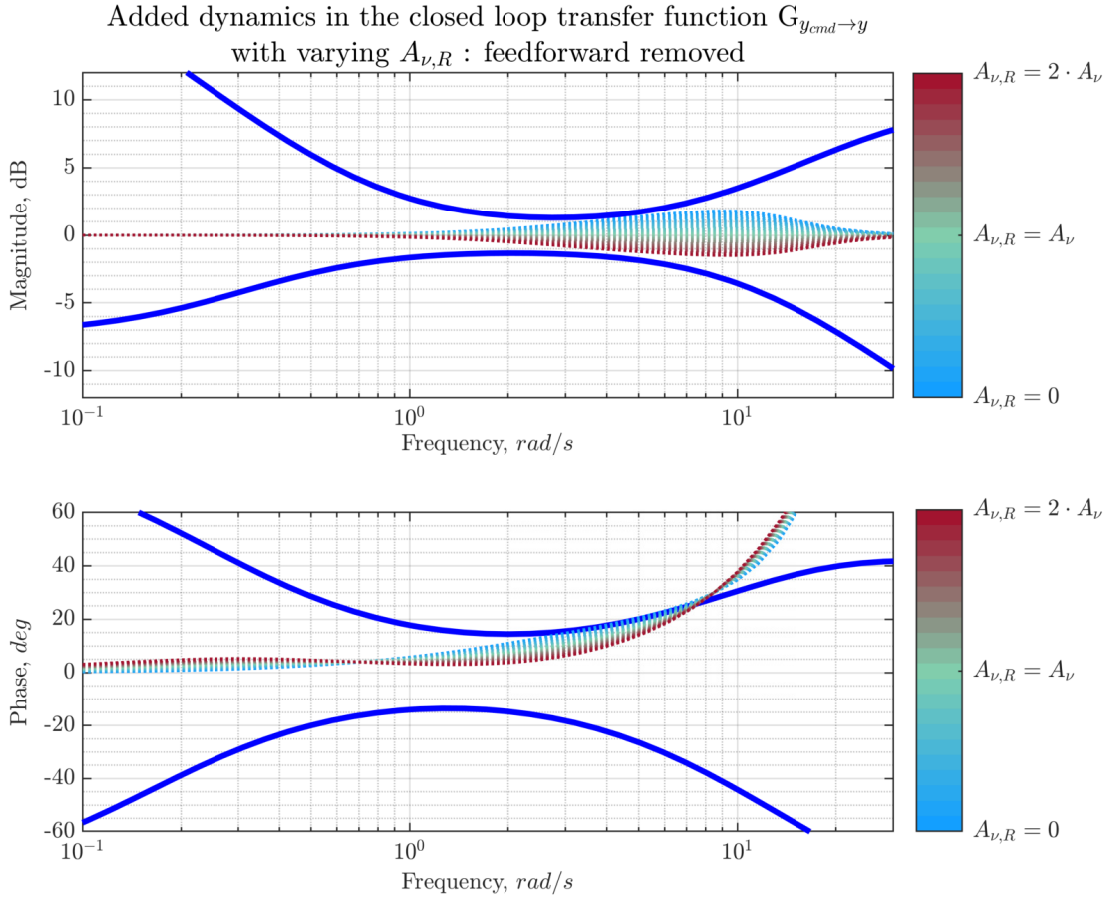


Figure 4.11: Added dynamics by the model uncertainty A_{ν} on the loop transfer characteristics $G_{y_{cmd} \rightarrow y}(s)$ without feedforward

4.4.3 Consideration of High-pass/Estimation filter

In the previous section, the pseudo control feedback was considered to be available. However, in the common flight controls application, the pseudo controls for the regulation of the rigid body rotational motion are the state derivatives i.e. body angular accelerations whose measurements are generally not directly available [211]. One way to obtain the state derivative is to combine the measurement data and a model data through a prediction algorithm [59, 212] or a complementary filter [213] (also shown in Eq. (3.54)). The other method is to compute the time derivative of the state measurement through discrete methods as the control algorithm is run on a FCC, however it is prone to noise amplification. A common alternative is to use a higher order filter in order to not only filter the state measurement but also to obtain a filtered state derivative estimation [60, 61]. In the current analysis for the SISO case, a second order roll-off filter represented by the state-space model

$$\begin{bmatrix} \dot{\hat{y}} \\ \ddot{\hat{y}} \end{bmatrix} = \begin{bmatrix} 0 & 1 \\ -\omega_{LP}^2 & -2 \cdot \zeta_{LP} \cdot \omega_{LP} \end{bmatrix} \cdot \begin{bmatrix} \hat{y} \\ \dot{\hat{y}} \end{bmatrix} + \begin{bmatrix} 0 \\ \omega_{LP}^2 \end{bmatrix} \cdot y, \quad (4.96)$$

is used. Here the filter state $\hat{y} \in \mathbb{R}$ serves as an estimation of the pseudo control $\nu = \dot{\hat{y}}$, $\omega_{LP} \in \mathbb{R}$ denotes the roll-off frequency of the second order filter and $\zeta_{LP} \in \mathbb{R}$ represents the damping ratio of the second-order element shown in Eq. (4.96). The estimation of the state and the pseudo control through the second order filter can be represented in the Laplace domain as

$$\hat{y} = \frac{G_{LP}}{\omega_{LP}^2} \cdot y = G_{LP} \cdot y, \quad (4.97)$$

$$\hat{\nu} = \dot{\hat{y}} = s \cdot \frac{G_{LP}}{\omega_{LP}^2} \cdot y = s \cdot G_{LP} \cdot y.$$

Clearly, the pseudo control estimation in the case described here is a filtered high-pass of the plant output y . Since the filter structure is known perfectly to the control designer, the dynamics of this estimation filter are directly included in the higher order effect emulation unit $G_L(s)$ of the RM as

$$G_L = \frac{\omega_{LP}^2}{s^2 + 2 \cdot \zeta_{LP} \cdot \omega_{LP} \cdot s + \omega_{LP}^2}. \quad (4.98)$$

In order to study the impact of including the estimation filter dynamics through $G_L(s)$ in the RM, consider the transfer characteristics between the reference state and the true state from Eq. (4.89)

$$G_{y_R \rightarrow y}(s) = \frac{y(s)}{y_R(s)} = \frac{G_{\bar{P}} \cdot K_B \cdot G_{y_R \rightarrow \dot{\nu}_{ff}} + G_{\bar{P}} \cdot K_B \cdot G_e}{1 + L}, \quad (4.99)$$

where the plant dynamics $G_{\bar{P}}(s)$ from Eq. (4.87) and the reference feedforward characteristics $G_{y_R \rightarrow \dot{\nu}_{ff}}(s)$ from Eq. (4.82) are substituted in the first term of the numerator for the ideal case $A_{\nu,R} = A_\nu$

$$G_{\bar{P}} \cdot K_B \cdot G_{y_R \rightarrow \dot{\nu}_{ff}} = \frac{\cancel{B_\nu}}{s \cdot (s - A_\nu)} \cdot \cancel{B_\nu} \cdot \frac{s \cdot (s - A_{\nu,R})}{G_L} = \frac{1}{G_L} \quad (4.100)$$

to yield

$$\frac{y(s)}{y_R(s)} = \frac{1 + G_{\bar{P}} \cdot K_B \cdot G_e \cdot G_L}{G_L \cdot (1 + L)}, \quad (4.101)$$

The definition of the loop transfer function $L(s)$ from Eq. (4.94)

$$L(s) = G_{\bar{P}} \cdot K_B \cdot G_e \cdot G_{LP} \quad (4.102)$$

is employed in the preceding equation

$$\frac{y(s)}{y_R(s)} = \frac{1 + G_{\bar{P}} \cdot K_B \cdot G_e \cdot G_L}{G_L \cdot (1 + G_{\bar{P}} \cdot K_B \cdot G_e \cdot G_{LP})}, \quad (4.103)$$

demonstrating that if the high order effect emulation element $G_L(s)$ in the RM perfectly matches the estimation filter $G_{LP}(s)$ used in the feedback control loop, the transfer characteristics from the reference external state y_R to the true output y are rendered to

$$\frac{y(s)}{y_R(s)} = \frac{1}{G_L} \implies G_L \cdot y(s) = y_R(s), \quad (4.104)$$

$$\hat{y}(s) = y_R(s) \quad \because G_L = G_{LP}.$$

Hence, the estimated output \hat{y} perfectly follows the reference trajectory y_R in the given ideal scenario. However, as stated before that the true plant parameter is not perfectly known in most practical applications. On the other hand, the parameters of the estimation filters such as the ones given in Eq. (4.97) are known since they are defined by the control designer. Assuming this case, the transfer characteristics from the reference external state to the estimated plant output $G_{y_R \rightarrow \hat{y}}(s)$ derived in Eq. (4.90) are investigated for the range of the design plant parameter $A_{\nu,R} \in [0, A_\nu]$ with and without using the higher order effect emulation $G_L(s)$ in the reference model.

Figure 4.12 exhibits the transfer characteristics for the two events of inclusion and omission of $G_L(s)$ in the RM. Clearly, the inclusion of the estimation filter dynamics within the reference model prevents a substantial gain amplification in the frequency range from 3 to 15 rad/sec and a gain drop beyond 15 rad/sec as compared to the case

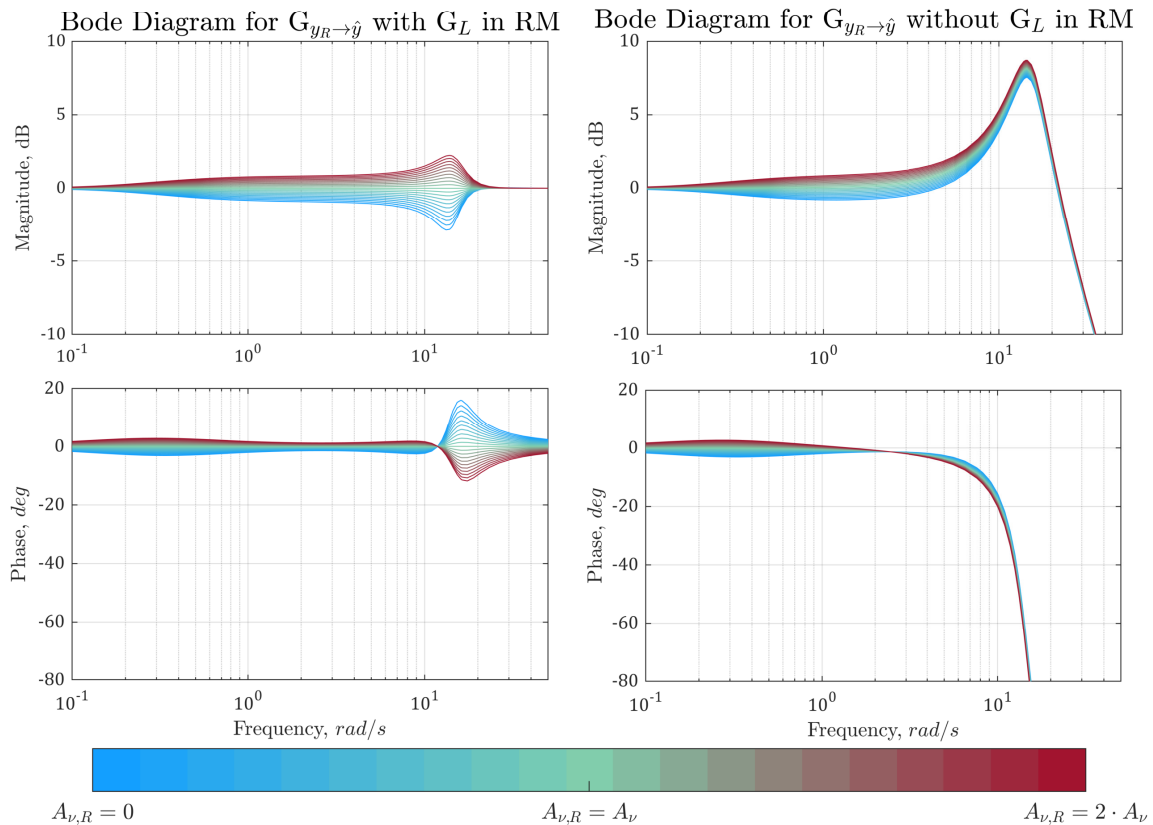


Figure 4.12: Effect of the inclusion of G_L in RM on the transfer characteristics $G_{y_R \rightarrow \hat{y}}$

when they are not considered in the reference dynamics. The frequency range $[3, 15]$ rad/sec is of interest because the desired dynamics listed in Table 4.1 lie in it. **This phenomenon of gain variation for the transfer function $G_{y_R \rightarrow \hat{y}}(s)$ occurs in the full range of the reference parameter $A_{\nu,R} \in [0, 2 \cdot A_\nu]$ considered for this analysis if the reference model does not explicitly account for the estimation filter dynamics, even when $A_{\nu,R}$ is exactly equal to the real system parameter A_ν .**

The noise attenuation/estimation filter such as the one employed in Eq. (4.97) causes a phase drop between the true output y and its filtered counterpart \hat{y} . Consequently, the phase difference is also manifests between the reference and the filtered output. It is verifiable from the results in Eq. (4.104) that the inclusion of the estimation filter dynamics in $G_L(s)$ of the RM provides not only a magnitude equivalence but also delivers a phase conformity between the estimated output \hat{y} and the reference external state y_R . **Figure 4.12 (bottom plots) illustrate the effectiveness of the noise attenuation/estimation filter consideration in the RM to bring phase conformity between the reference external state and the true output when the design plant state parameter $A_{\nu,R}$ lies within $\pm 100\%$ of the true state parameter A_ν .** When the filter is not accounted for in the specification of the reference dynamics considerable phase drop can be observed in the frequency range $[3, 15]$ rad/sec (bottom right in Fig. 4.12) in comparison to the case where the higher order effect emulation $G_L(s)$ in RM encompasses the roll-off filter dynamics (bottom left in Fig. 4.12). In this case, the variation in phase is significantly minimized, thereby facilitating phase conformance between the reference state and the estimated state.

The advantage of including the estimation dynamics through the element $G_L(s)$ in the reference model is depicted through the tracking response to a $3 - 2 - 1 - 1$ maneuver for the considered SISO model in Fig. 4.13. The design plant uncertainty is not considered for this simulation in order to study the effect of the estimation dynamics in isolation. **It can be observed from the results in Fig. 4.13 that the reference external state as well as pseudo control tracking deteriorate when the estimation filter is not considered in the specification of the reference trajectories.** Important to note that the feedback loop gains remain unchanged across both the simulation cases. The sole change between the two simulation tests is the incorporation and omission of the second order estimation filter in the higher order effect emulation component $G_L(s)$ of the reference model. The reference trajectories also vary in the two cases because of this modification. When the $G_L(s)$ includes the estimation dynamics, the generated reference trajectories comply with the phase of the estimated system response, thereby facilitating precise tracking. On the other hand, when the estimation filter transfer characteristics are not accounted in the RM, same set of error controller gains $[C_{ey}, C_{ev}]$ introduce an oscillatory component in the pseudo control tracking response owing to the mismatch between the phase of the reference trajectories $[y_R, \nu_R]$ and the estimated plant variables $[\hat{y}, \hat{\nu}]$. Without having to include the estimation dynamics in the RM, the alternative to mitigate these oscillations is to reduce the magnitude of the error gains, however it would also decrease the disturbance rejection capability of the control strategy. Evidently, phase

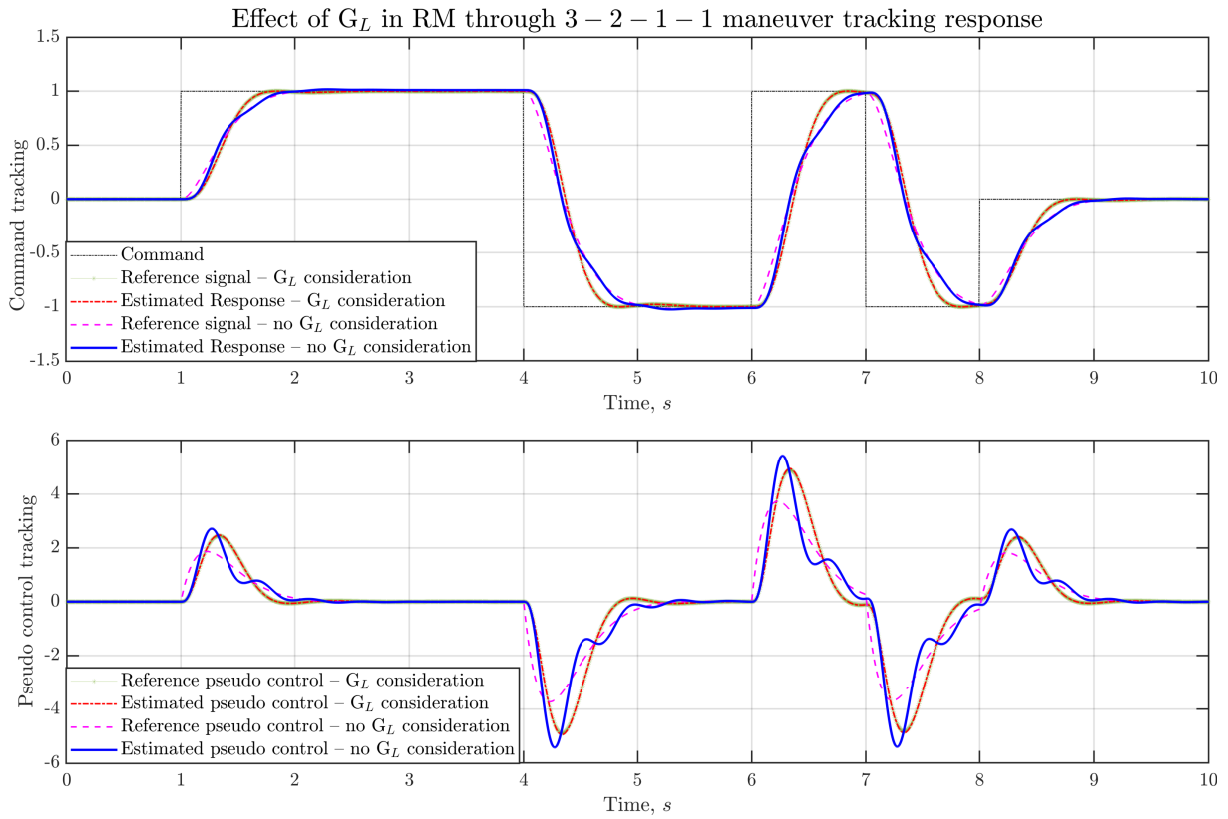


Figure 4.13: 3 – 2 – 1 – 1 maneuver simulation to illustrate effect of the inclusion of G_L in RM

conformance of the reference trajectories produced by the jerk-level reference model with the estimated variables from sensor measurements is significant to the performance of the controller.

The analysis pertaining to the consideration of the noise attenuation/estimation filter in this sub-section along with the inclusion of the higher order effects emulation unit in the structure of the jerk-level reference model described by section 4.2 provides the realization of the contribution **C.3.2 Inclusion of measurement/estimation filter effects in the reference model design to achieve phase conformity between external reference and estimated plant states.**

4.4.4 Consideration of Time Delays

In addition to the estimation filters, another element that leads to a phase mismatch between the reference set-point and measured/estimated output is the time-delay in the input/output channel dynamics. Transport, sensor and time synchronization delays are the major contributors to the cumulative time delay in a flight control system. While transport and sensor delay are constant for a system architecture, synchronization delays vary depending on the arbitration of the data packets in the employed communication protocols e.g. CAN, UART, SPI, and others.

Within the context of the linear analysis in this section, constant time delays emanating from different components in the input and the output channels of the closed loop system are assumed to be known exactly.

The delay unit $\mathbf{G}_D(s)$ (Eq. (4.54)) incorporated in the jerk-level reference model architecture (Fig. 4.5) is proposed to take the constant known time delays in to account while specifying reference variable trajectories. The total sum of time delays in the input $\mathbf{G}_{D,i}(s)$ as well as output channels $\mathbf{G}_{D,o}(s)$ are combined and incorporated as one component in the delay unit of the reference model

$$\mathbf{G}_D(s) = \mathbf{G}_{D,i}(s) \cdot \mathbf{G}_{D,o}(s)$$

$$\begin{bmatrix} e^{-sT_1} & 0 & \dots & 0 \\ 0 & e^{-sT_2} & \dots & 0 \\ \vdots & & \ddots & \\ 0 & 0 & \dots & e^{-sT_{n_y}} \end{bmatrix} = \begin{bmatrix} e^{-sT_{1,i}} & 0 & \dots & 0 \\ 0 & e^{-sT_{2,i}} & \dots & 0 \\ \vdots & & \ddots & \\ 0 & 0 & \dots & e^{-sT_{n_y,i}} \end{bmatrix} \cdot \begin{bmatrix} e^{-sT_{1,o}} & 0 & \dots & 0 \\ 0 & e^{-sT_{2,o}} & \dots & 0 \\ \vdots & & \ddots & \\ 0 & 0 & \dots & e^{-sT_{n_y,o}} \end{bmatrix} \quad (4.105)$$

where $T_{1,i}, T_{2,i}, \dots, T_{n_y,i}$ and $T_{1,o}, T_{2,o}, \dots, T_{n_y,o}$ represent the time delays (unit: seconds) in the input and the output channels respectively, for each of the n_y pseudo controls in the closed loop system dynamics for a MIMO system. For illustration purposes the reader can refer to Fig. 4.14, which demonstrates the delay emulation unit $\mathbf{G}_D(s)$ included in the reference model compensating for the input $\mathbf{G}_{D,i}(s)$ and output $\mathbf{G}_{D,o}(s)$ delays occurring in a controlled SISO system. Therefore, the delay unit is defined as $\mathbf{G}_D = \mathbf{G}_{D,i} \cdot \mathbf{G}_{D,o}$. Moreover, the SISO system similar to the plant used in the section 4.4.1 is considered to analyze the impact of including the delay emulation in the RM on the tracking performance. Following the steps used in Eq. (4.72), the transfer characteristic from the pseudo control derivative feedforward $\dot{\nu}_{ff}$ to the reference external state y_R incorporating the effect of the delay emulation $\mathbf{G}_D(s)$ is derived

$$\mathbf{G}_{\dot{\nu}_{ff} \rightarrow y_R}(s) = \frac{y_R(s)}{\dot{\nu}_{ff}(s)} = \frac{\mathbf{G}_L \cdot \mathbf{G}_D}{s \cdot (s - A_{\nu,R})}. \quad (4.106)$$

Furthermore, tracing the steps from Eqs. (4.73) to (4.76) the reference transfer functions involving the consideration of the delay emulation unit $\mathbf{G}_D(s)$ are obtained

$$\mathbf{G}_{y_{cmd} \rightarrow y_R}(s) = \frac{K_{R,u} \cdot \mathbf{G}_L \cdot K_{0,R} \cdot \mathbf{G}_D}{D(s)}, \quad (4.107)$$

$$\mathbf{G}_{y_{cmd} \rightarrow \nu_R}(s) = \frac{K_{R,u} \cdot \mathbf{G}_L \cdot K_{0,R} \cdot \mathbf{G}_D \cdot s}{D(s)},$$

where the transfer function in the denominator $D(s)$ is

$$D(s) = s^2 + (K_{R,u} \cdot \mathbf{G}_L - A_{\nu,R}) \cdot s - K_{R,u} \cdot \mathbf{G}_L \cdot \mathbf{G}_D \cdot A_{\nu,R}^* + K_{R,u} \cdot \mathbf{G}_L \cdot A_{\nu,R} \cdot (\mathbf{G}_D - 1). \quad (4.108)$$

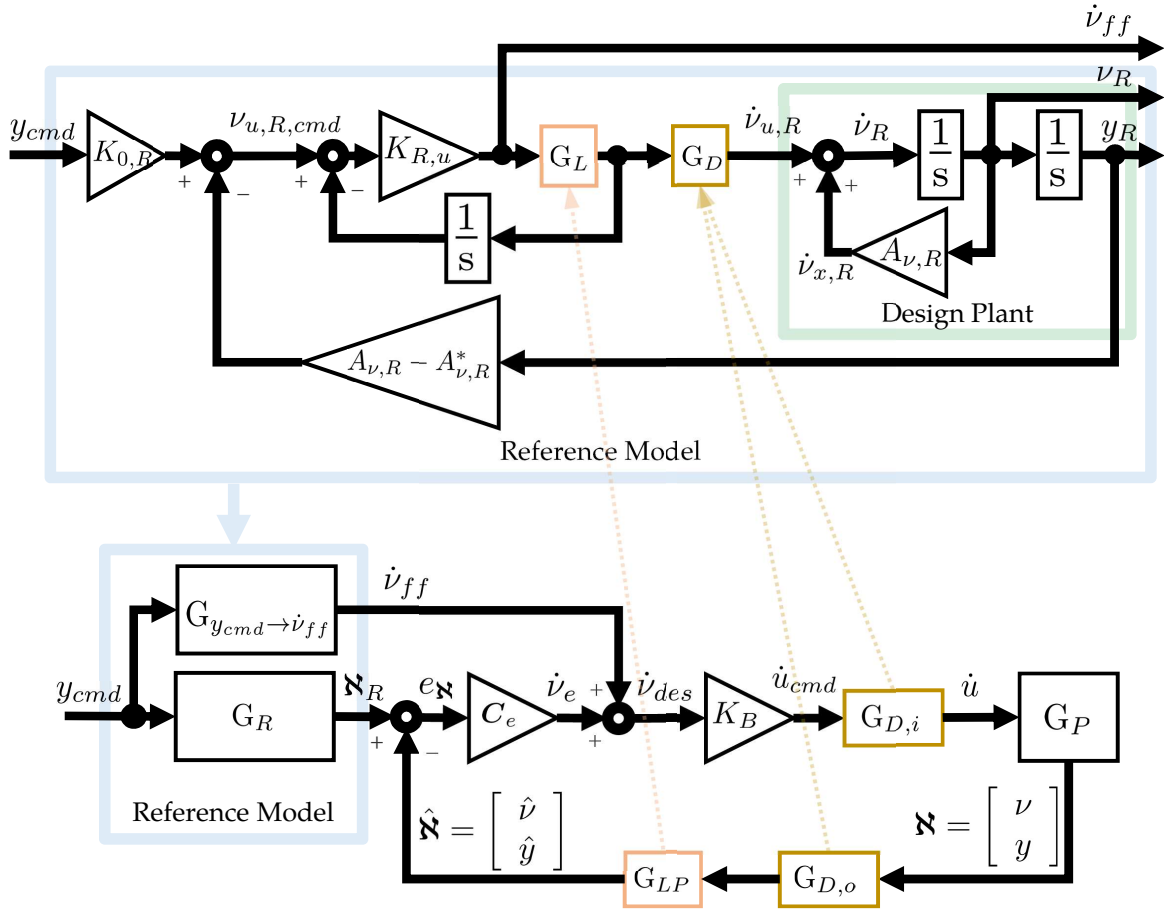


Figure 4.14: Delay emulation in the Jerk level reference model for a SISO system

Likewise, the closed loop SISO transfer dynamics from the reference external state y_R to the true plant output y : $G_{y_R \rightarrow y}(s)$ are obtained by following the procedure as in the Eqs. (4.83) to (4.89) for the analysis performed in the section 4.4.1. Consequently, by following these steps, the closed loop transfer dynamics including the input/output channel delays $G_{D,i}$ and $G_{D,o}$, as demonstrated in Fig. 4.14, can be observed

$$G_{y_R \rightarrow y}(s) = \frac{y(s)}{y_R(s)} = \frac{G_{\bar{P}} \cdot K_B \cdot G_{y_R \rightarrow \dot{v}_{ff}} \cdot G_{D,i} + G_{\bar{P}} \cdot G_{D,i} \cdot K_B \cdot G_e}{1 + L}. \quad (4.109)$$

Here the loop transfer function $L(s)$ is defined as

$$L(s) = G_{\bar{P}} \cdot G_{D,i} \cdot K_B \cdot G_e \cdot G_{D,o} \cdot G_{LP}. \quad (4.110)$$

The current investigation builds up on the analysis carried out in section 4.4.3 where the estimation dynamics were incorporated within the reference model. The filtered output and the estimated pseudo control are obtained using a second order estimation filter $G_{LP}(s)$ described in Eq. (4.97). Additionally, the measured variables are delayed by the sensor and transport delay cumulatively denoted by $G_{D,o}(s)$. Subsequently, the transfer characteristics from the reference state to the filtered state $G_{y_R \rightarrow \hat{y}}(s)$ are derived by utilizing the estimation filter dynamics $G_{LP}(s)$, the output channel delay $G_{D,o}(s)$ and

the closed loop transfer dynamics $G_{y_R \rightarrow y}(s)$ derived in Eq. (4.109)

$$\begin{aligned} G_{y_R \rightarrow \hat{y}}(s) &= G_{y_R \rightarrow y}(s) \cdot G_{D,o}(s) \cdot G_{LP}(s), \\ G_{y_R \rightarrow \hat{y}}(s) &= \frac{\hat{y}(s)}{y_R(s)} = \frac{G_{\bar{P}} \cdot G_{D,i} \cdot K_B \cdot G_{y_R \rightarrow \dot{v}_{ff}} \cdot G_{D,o} \cdot G_{LP} + L}{1 + L}. \end{aligned} \quad (4.111)$$

Consider the transfer dynamics obtained in Eq. (4.111) for the ideal case $A_{\nu,R} = A_{\nu}$, and $K_B = B_{\nu}^{-1}$. Additionally, it has already been established that the estimation dynamics denoted by $G_{LP}(s)$ and the input/output delays are also known exactly for the current analysis. Therefore, the higher order effect emulation in the RM can be defined as $G_L(s) = G_{LP}(s)$, and the delay unit can be specified to fulfill $G_D(s) = G_{D,i}(s) \cdot G_{D,o}(s)$. Subsequently, utilizing these equalities in the inverse feedforward to reference external state transfer function $G_{y_R \rightarrow \dot{v}_{ff}}(s)$ obtained from Eq. (4.106), render the first term of the numerator from Eq. (4.111) to 1

$$\begin{aligned} G_{\bar{P}} \cdot G_{D,i} \cdot K_B \cdot G_{y_R \rightarrow \dot{v}_{ff}} \cdot G_{D,o} \cdot G_{LP} &= \frac{\cancel{B_{\nu}}}{s \cdot (s - A_{\nu})} \cdot \cancel{G_{D,i}} \cdot \cancel{B_{\nu}^{-1}} \cdot \frac{s \cdot (s - A_{\nu,R})}{\cancel{G_L} \cdot \cancel{G_D}} \cdot \cancel{G_{D,o}} \cdot \cancel{G_{LP}}, \\ G_{\bar{P}} \cdot G_{D,i} \cdot K_B \cdot G_{y_R \rightarrow \dot{v}_{ff}} \cdot G_{D,o} \cdot G_{LP} &= 1. \end{aligned} \quad (4.112)$$

which upon substitution in the relation from Eq. (4.111) proves the equivalence of the reference external state y_R and the filtered output \hat{y} under the conditions state above

$$\begin{aligned} \frac{\hat{y}(s)}{y_R(s)} &= \frac{1 + L}{1 + L}, \\ \hat{y} &= y_R. \end{aligned} \quad (4.113)$$

Among the perfectly known parameters considered to sustain equivalence between the reference and filtered output in Eq. (4.113), the state damping parameter $A_{\nu,R}$ used in the design plant of the reference model remains most uncertain during the control design process. The impact of this uncertainty manifests through the feedforward transfer function $G_{y_R \rightarrow \dot{v}_{ff}}$ in the closed loop transfer dynamics $G_{y_R \rightarrow \hat{y}}(s)$ of the SISO system. To quantify the effect of the deviation of $A_{\nu,R}$ from its true value on the SISO system's transfer dynamics, the bode plots of the function derived in Eq. (4.111) are illustrated in Fig. 4.15 for values of the design parameter $A_{\nu,R}$ iterating in the range $[0, 2 \cdot A_{\nu}]$ as performed in the previous analyses as well. Two cases with inclusion and omission of the delay emulation $G_D(s)$ in the RM are compared. The parameters utilized for the linear analysis of the SISO system including the time delays are enlisted in Table 4.3.

The gain plots of the closed loop transfer characteristics in Fig. 4.15 indicate that the use of the delay emulation unit $G_D(s)$ in the reference model reduces the magnitude variation between the reference external state and the estimated output in the frequency range of 1 to 12 rad/sec for all iterations of the design plant parameter's $A_{\nu,R}$ magnitude. For the parameters specified in Table 4.3, the reference response frequency for a given command is illustrated by the bode plot of the transfer function $G_{y_{cmd} \rightarrow y_R}$ (Eq. (4.107)) in Fig. 4.16. The -180° phase crossover frequency is determined to be 6.35 rad/sec, which lies in the effective frequency range where the use of the delay emulation in the reference model mitigates magnitude variation for the closed loop transfer characteristics $G_{y_R \rightarrow \hat{y}}$.

Parameter	Magnitude	Parameter	Magnitude
$K_{0,R}$	3	A_ν	-2
$A_{\nu,R}^*$	-3	B_ν	1.5
$K_{u,R}$	6	C_{ey}	2
ω_{LP}	20	C_{ev}	8
ζ_{LP}	1	T_i, T_o	0.05, 0.05

Table 4.3: Magnitude of parameters used in the linear analysis of the jerk-level RM including delay emulation with the extended INDI controller

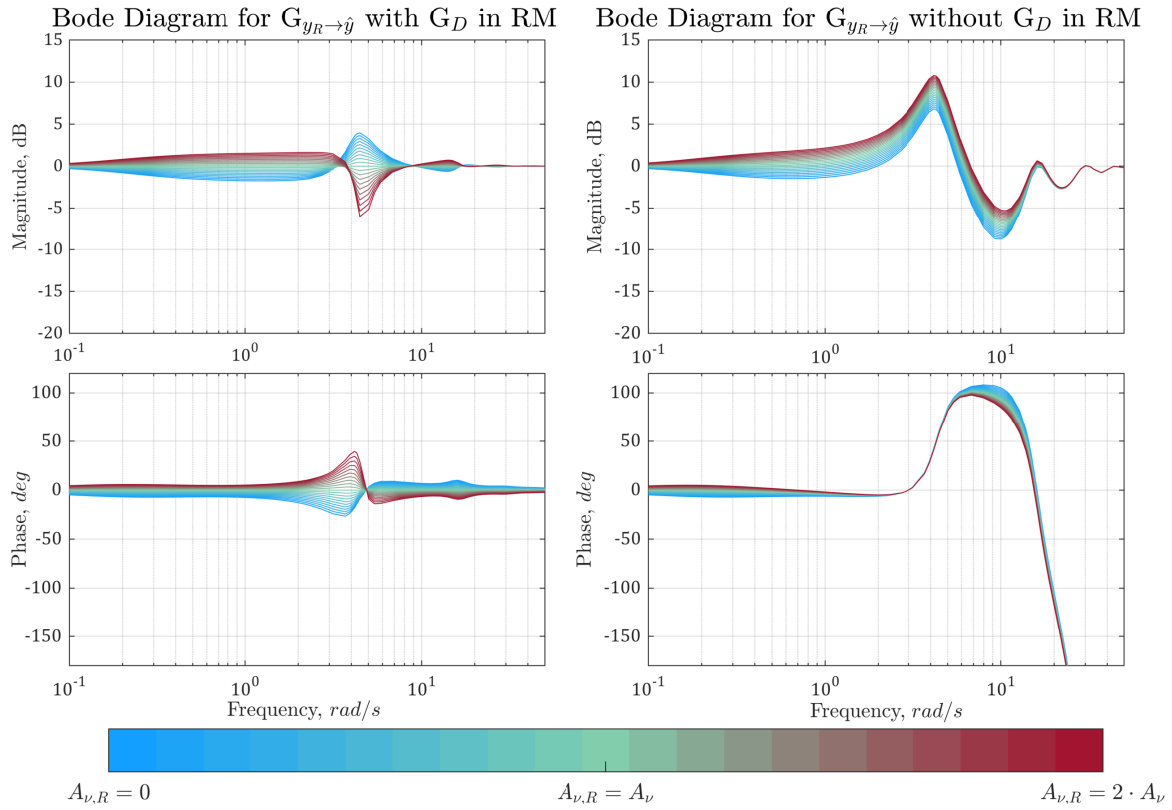


Figure 4.15: Effect of the inclusion of G_D in RM on the transfer characteristics $G_{y_R \rightarrow \hat{y}}$

One of the important motives behind accounting for the time delays in the input/output channel dynamics is to facilitate phase match between the reference model and the estimated plant outputs. Figure 4.15 shows that in the considered range of uncertainty for $A_{\nu,R}$, accounting for time delay in the RM drastically reduces phase variation between the reference external state's set point and the estimated state across the frequency range $[4, 12]$ rad/sec.

Furthermore, a time domain simulation result for the considered SISO case is presented in Fig. 4.17 for which the time delay magnitude within the delay emulation unit G_D is varied from 0 ms to 200 ms in the ideal case of design plant knowledge i.e. $A_{\nu,R} = A_\nu$. The purpose of this simulation is to study the impact that accurate knowledge of the input/output time delay has on the system response. The sum of the system communication time delays T_i, T_o as mentioned in Table 4.3 is kept at 0.1 s or

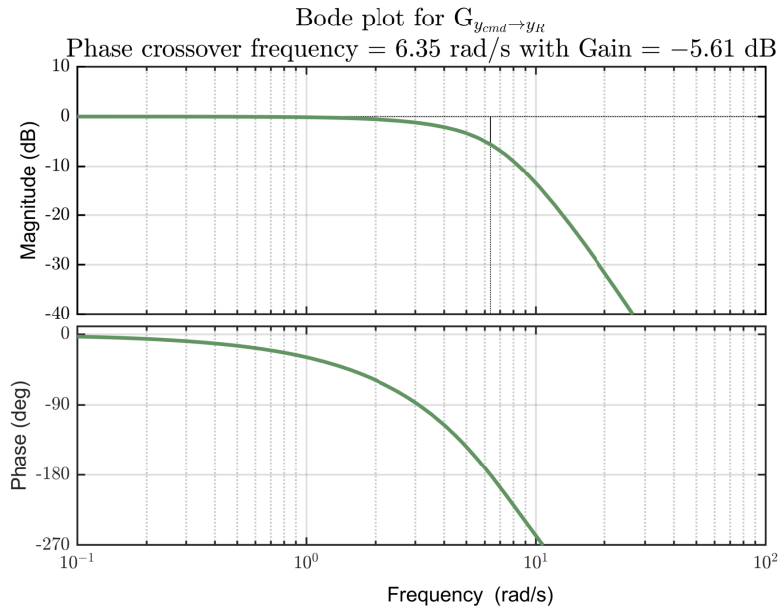


Figure 4.16: Reference response characteristics based on the transfer function $G_{y_{cmd} \rightarrow y_R}$

100 ms. The results in Fig. 4.17 depict the change in the filtered output response \hat{y} to a unit step control variable command as the time delay considered by the reference model varies from 0 to twice of the real system delay. Evidently, as the accuracy of the delay considered in the RM improves with respect to the real system's time delay,

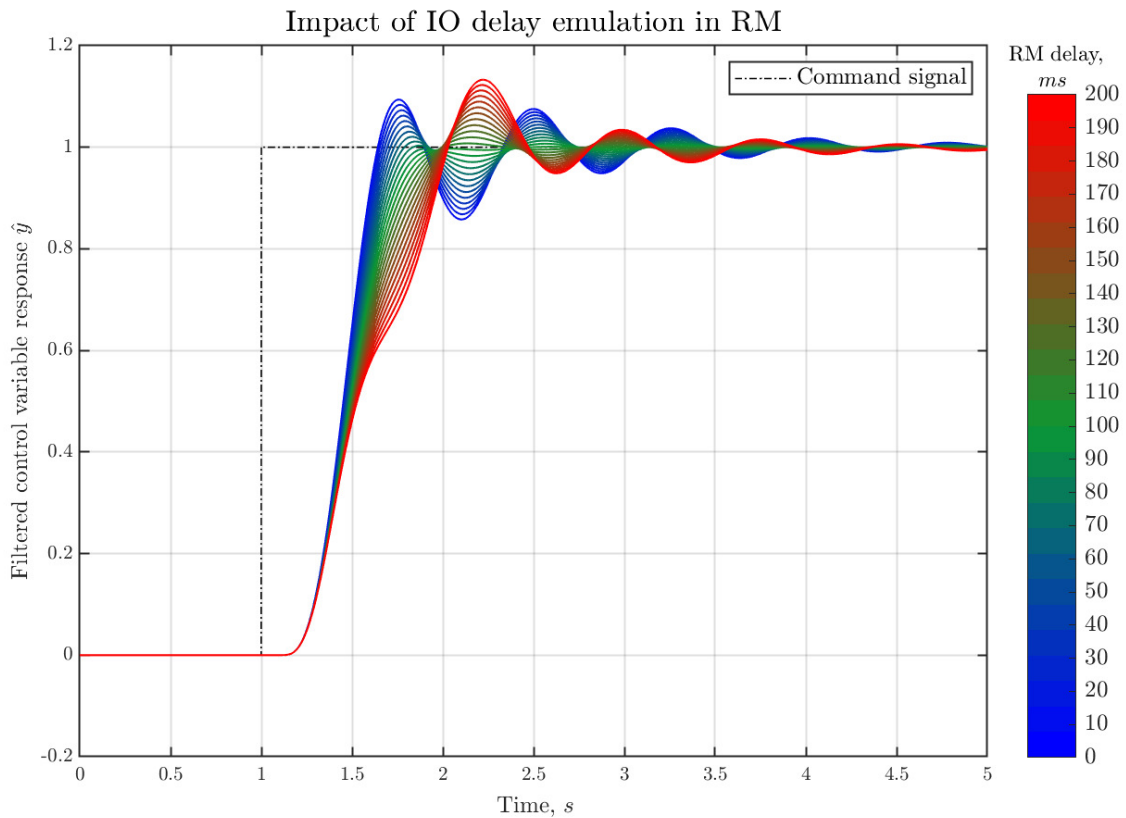


Figure 4.17: Impact of the delay magnitude in Input Output delay emulation G_D of the RM on unit step response of the controlled SISO system

the set-point tracking performance of the controlled system improves with the same feedback error gains. The improvement in the tracking performance is owed to the mitigation of the gain and phase variation between the external reference state y_R and filtered plant output \hat{y} by accounting for the time delays occurring in the input/output channel dynamics of the controlled system.

The analyses performed on the consideration of the input/output time delays in this sub-section along with the inclusion of the delay emulation unit in the architecture of the jerk-level reference model described by section 4.2 provides the realization of the contribution **C.3.3 Integration of time-delays from the input/output channel dynamics within reference model design to facilitate phase match between external reference and estimated plant states.**

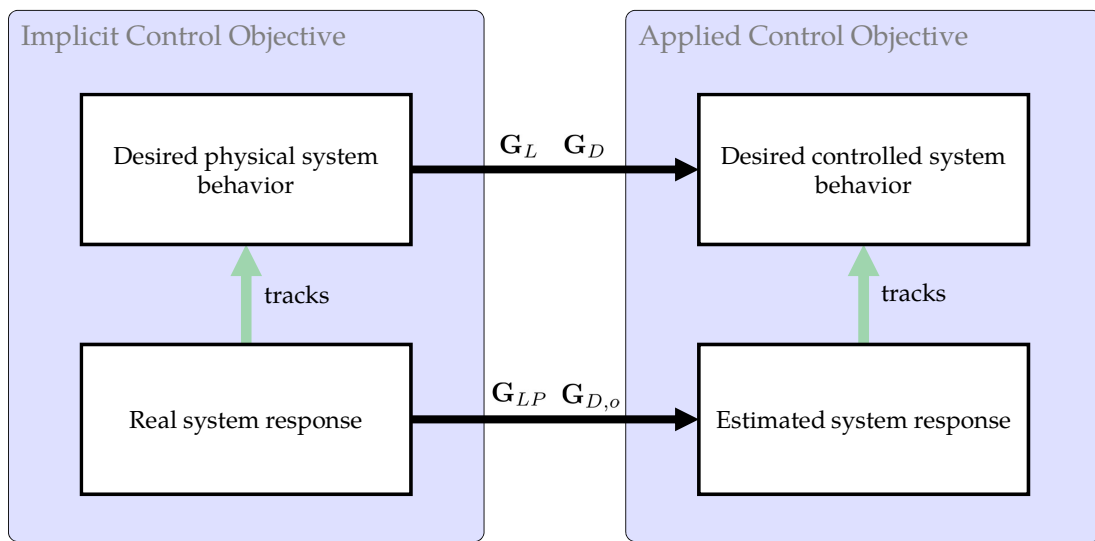


Figure 4.18: *Bi-level control design objective in the Jerk level reference model*

Incorporation of the higher order dynamics from state estimation and time delays from the output channel dynamics brings out a bi-level control objective in the proposed extended INDI strategy with the jerk level reference model. Contrary to the control objective defined in Eq. (4.57), the control objective pursued by the implemented strategy is to make the estimated system response $\hat{\mathbf{N}}$ follow the desired controlled system behavior \mathbf{N}_R specified by the reference model. Simultaneously, as demonstrated in Fig. 4.18, the real system response \mathbf{N} tracks the desired physical system behavior \mathbf{N}_R which is implicitly defined in the reference model. The estimation dynamics emulation and the inclusion of time delays constitute the difference between the desired physical system and the desired controlled system specification.

Figure 4.19 compares the response of the real system with the estimated system through a time domain simulation. This simulation test considers an ideal case of perfect plant knowledge with the controller parameters defined in Table 4.3. The purpose of this simulation is to visualize the tracking behavior of the real system with respect to the reference behavior defined for the estimated system. As it can be observed, the estimated output follows the reference signal, however the true system leads desired controlled state response specified by the reference signal. The reason for this phenomenon is that

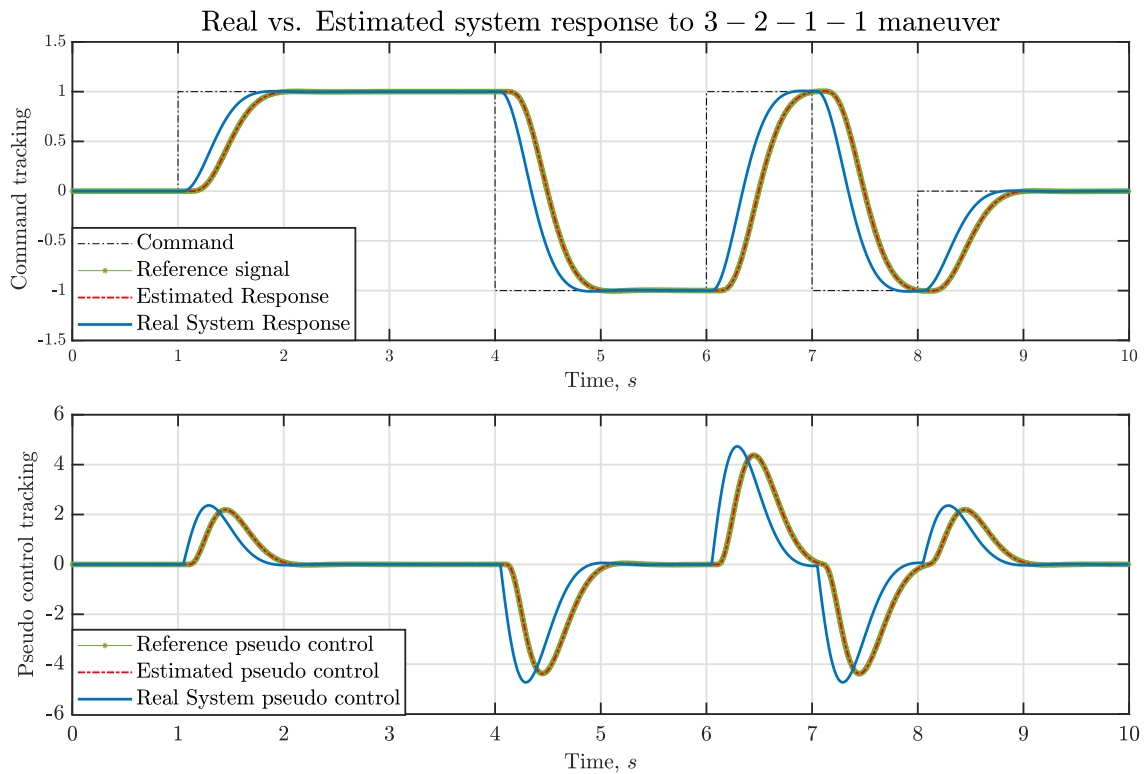


Figure 4.19: Real vs. Estimated system response corresponding to bi-level control objectives

the reference model specifies the reference external state trajectory for the estimated output rather than the true output. By defining the desired behavior for the estimated system rather than the true system, only the deviations of the estimated output from the reference external state trajectory occurring due to external disturbances result in a corrective command generated by the error controller (Eq. (4.84)). Most importantly, the deviation resulting from the phase shift due to the estimation and output channel dynamics is hidden from the error dynamics since the error is calculated as the difference between the reference trajectories for the estimated system \mathfrak{N}_R and the estimated system response $\hat{\mathfrak{N}}$. The error pseudo control derivative along with the feedforward produce the control input rate command intended for the true plant (Eq. (4.83)). The control input rate command is equivalent to the real control input rate because the first order actuator dynamics considered in this case are canceled exactly. Subsequently, the generated effector rate makes the real system follow the desired physical system behavior implicit in the applied reference model.

4.4.5 Consideration of Residual Effector Dynamics

Thus far the analysis and simulations considered first order effector dynamics, which are accounted according to the first order effector dynamics consideration described by Eqs. (4.13) - (4.15), thereby resulting in the equivalence of the effector rate command and real effector rate $\dot{u}_{cmd} = \dot{u}$. However, as specified earlier in the section 4.1, exact cancellation for second order effector dynamics is not possible without calculating an inverse of the residual effector dynamics $\mathbf{R}_u(s)$ (Eq. (4.25)). The inverse computation

requires calculation of a discrete time derivative which could lead to noise amplification and inject high frequency content in the control effector commands. Alternatively, the author proposes to take the residual effector dynamics into account within the higher order effect emulation $G_L(s)$ of the jerk level reference model. In doing so, the effector gain inverse K_A^{-1} can still be incorporated in the control allocation as specified in Eq. (4.25) but it eliminates the need of performing an inverse of the residual dynamics $R_u^{-1}(s)$.

For the sake of simplification, the effect of the residual effector dynamics and its consideration in the RM is presented through the SISO system being used until now in other analyses. Figure 4.20 illustrates a schematic for the resultant SISO closed loop constituted by the extended INDI controller containing the jerk level reference model and the transformed plant dynamics $G_P(s)$ as given in Eq. (4.86). **The given diagram only contains the main elements affecting the transfer characteristics of the closed loop system and does not demonstrate the real implementation of the flight control software. The implementation of the extended INDI flight control strategy to be flashed on a FCC is exhibited by Fig. 4.6.** Equation (4.23) describes the transfer characteristics from an incremental effector command computed by the controller to an absolute effector position $G_{\Delta u_{cmd} \rightarrow u}(s)$ for an effector comprising of second order actuator dynamics. Using the relation in Eq. (4.23), the transfer function from the incremental

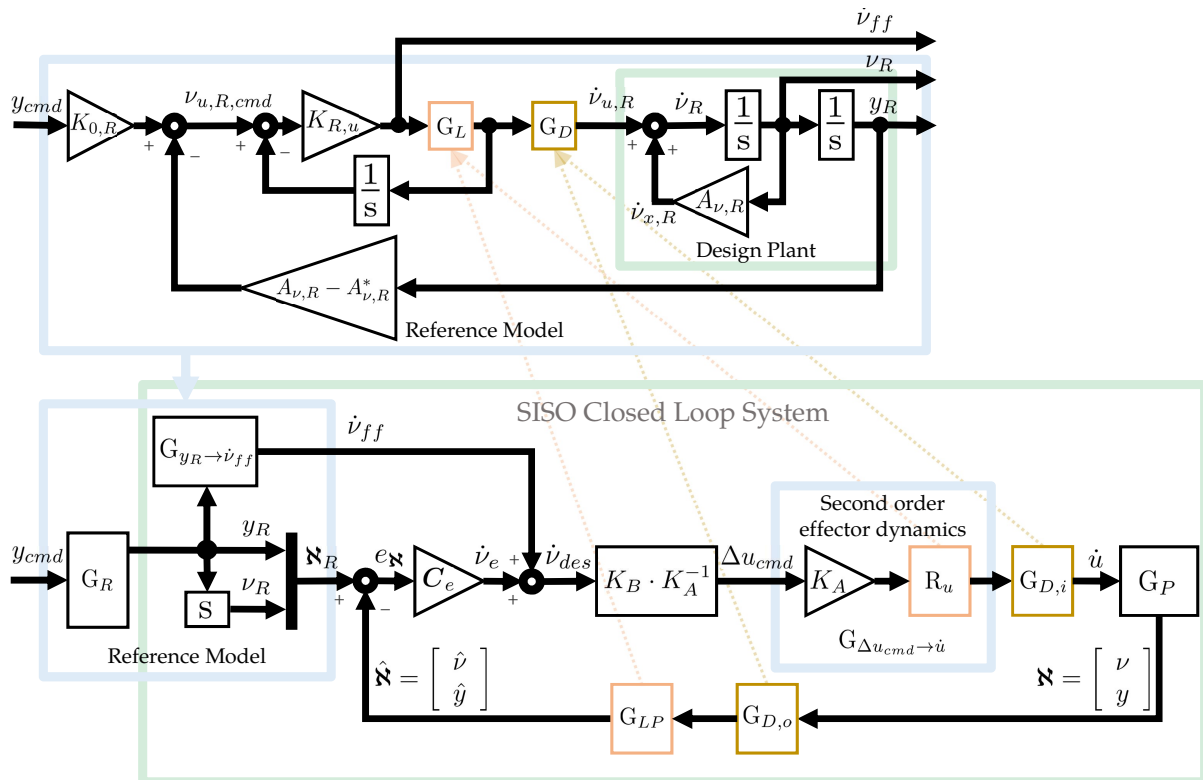


Figure 4.20: Jerk level reference model in a closed loop SISO system with second order effector dynamics

effector command to the effector rate $G_{\Delta u_{cmd} \rightarrow \dot{u}}$ emanates

$$G_{\Delta u_{cmd} \rightarrow \dot{u}}(s) = \boxed{\left(\frac{2 \cdot \zeta_A \cdot \omega_A}{s + 2 \cdot \zeta_A \cdot \omega_A} \right)} \cdot \boxed{\left(\frac{\omega_A}{2 \cdot \zeta_A} \right)}, \quad (4.114)$$

which is used to present the effector dynamics in the SISO closed loop illustration in Fig. 4.20. The effector gain $K_A \in \mathbb{R}$ is nullified by its inverse incorporated in the control allocation described by the product $K_B \cdot K_A^{-1}$, where $K_B = B_\nu^{-1}$. Therefore, only the residual dynamics $R_u(s)$ remain to be accounted for in the presented closed loop dynamics.

Following the feedforward transfer relation derived in Eq. (4.106), the inclusion of the residual effector dynamics in the higher order effect emulation unit $G_L(s)$ of the reference model can be described

$$\begin{aligned} G_{\dot{v}_{ff} \rightarrow y_R}(s) &= \frac{y_R(s)}{\dot{v}_{ff}(s)} = \frac{G_L \cdot G_D}{s \cdot (s - A_{\nu,R})}, \\ G_{\dot{v}_{ff} \rightarrow y_R}(s) &= \frac{y_R(s)}{\dot{v}_{ff}(s)} = \frac{G_{LP} \cdot R_u \cdot G_D}{s \cdot (s - A_{\nu,R})} \quad \because \boxed{G_L = G_{LP} \cdot R_u}. \end{aligned} \quad (4.115)$$

Here the noise-attenuation filter is defined like the second order filter given in Eq. (4.97)

$$G_{LP} = \frac{\omega_{LP}^2}{s^2 + 2 \cdot \zeta_{LP} \cdot \omega_{LP} \cdot s + \omega_{LP}^2}. \quad (4.116)$$

Furthermore, the closed loop SISO transfer dynamics from the reference external state y_R to the true plant output y : $G_{y_R \rightarrow y}(s)$ are obtained by pursuing the steps taken from Eqs. (4.83) to (4.89). Additionally, the residual dynamics $R_u(s)$ remaining after the cancellation of the effector gain K_A for the second order effector dynamics are encompassed in the forenamed steps to deliver the closed loop transfer dynamics

$$G_{y_R \rightarrow y}(s) = \frac{y(s)}{y_R(s)} = \frac{G_{\bar{P}} \cdot R_u \cdot K_B \cdot G_{y_R \rightarrow \dot{v}_{ff}} \cdot G_{D,i} + G_{\bar{P}} \cdot G_{D,i} \cdot R_u \cdot K_B \cdot G_e}{1 + L}, \quad (4.117)$$

where the loop transfer function $L(s)$ is

$$L(s) = G_{\bar{P}} \cdot G_{D,i} \cdot R_u \cdot K_B \cdot G_e \cdot G_{D,o} \cdot G_{LP}. \quad (4.118)$$

As stated before, the estimated variables are delayed by the sensor and transport delay cumulatively as well as the estimation filters. Therefore, the transfer characteristics from the reference state to the estimated state $G_{y_R \rightarrow \hat{y}}(s)$ emanate after consideration of the estimation filter dynamics $G_{LP}(s)$ and the output channel dynamics $G_{D,o}(s)$ along with the transfer function $G_{y_R \rightarrow y}(s)$

$$G_{y_R \rightarrow \hat{y}}(s) = G_{y_R \rightarrow y}(s) \cdot G_{D,o}(s) \cdot G_{LP}(s). \quad (4.119)$$

By substituting the transfer function $G_{y_R \rightarrow y}(s)$ from Eq. (4.117) in the expression from Eq. (4.119), the loop transfer function $L(s)$, given by Eq. (4.118), appears as the second term in the numerator

$$G_{y_R \rightarrow \hat{y}}(s) = \frac{\hat{y}(s)}{y_R(s)} = \frac{G_{\bar{P}} \cdot G_{D,i} \cdot R_u \cdot K_B \cdot G_{y_R \rightarrow \dot{v}_{ff}} \cdot G_{D,o} \cdot G_{LP} + L}{1 + L}. \quad (4.120)$$

The current investigation builds up on the analysis carried out in the sections 4.4.3 and 4.4.4, where the estimation dynamics and output channel delays were incorporated within the reference model. Here the residual effector dynamics from the second order effectors are incorporated additionally.

In order to bring out the advantage of including the residual dynamics in the higher order effect emulation unit $G_L(s)$ of the RM, the transfer dynamics from Eq. (4.120) are simplified for the ideal case $A_{\nu,R} = A_\nu$ as performed in Eqs. (4.112) - (4.113) for the consideration of delays in the input/output channel dynamics. Firstly, inverse of the feedforward to reference state transfer function from Eq. (4.115) is substituted in the first term of the numerator from Eq. (4.120) to yield

$$G_{\bar{P}} \cdot G_{D,i} \cdot R_u \cdot K_B \cdot G_{y_R \rightarrow \dot{v}_{ff}} \cdot G_{D,o} \cdot G_{LP} = \frac{\cancel{B_\nu}}{s \cdot (s - A_\nu)} \cdot \cancel{G_{D,i}} \cdot \cancel{R_u} \cdot \cancel{B_\nu} \cdot \frac{s \cdot (s - A_{\nu,R})}{\cancel{G_{LP}} \cdot \cancel{R_u} \cdot \cancel{G_D}} \cdot \cancel{G_{D,o}} \cdot \cancel{G_{LP}},$$

$$G_{\bar{P}} \cdot G_{D,i} \cdot R_u \cdot K_B \cdot G_{y_R \rightarrow \dot{v}_{ff}} \cdot G_{D,o} \cdot G_{LP} = 1. \quad (4.121)$$

which renders the relation from Eq. (4.120) to

$$\frac{\hat{y}(s)}{y_R(s)} = \frac{1 + L}{1 + L},$$

$$\hat{y} = y_R,$$
(4.122)

thereby proving the equivalence of the reference external state and the estimated output brought about by the proposed feedforward from the jerk level RM under the conditions of perfect system knowledge being included in the design plant.

Similar to the procedure in previous analyses, effectiveness of the inclusion of the residual effector dynamics is quantified in presence of uncertainty in the state damping parameter $A_{\nu,R}$ employed in the reference model design plant. Magnitude and phase characteristics of the closed loop dynamics in Eq. (4.120) are plotted in Fig. 4.21 for values of the design parameter $A_{\nu,R}$ in the range $[0, 2 \cdot A_\nu]$. Additionally, comparative plots for the closed loop transfer characteristics without the residual dynamics but including the previously mentioned considerations in the reference model are demonstrated on the right side. For the second order effector dynamics values of natural frequency ω_A and the damping ratio ζ_A are 10 rad/s and 1 respectively. Remaining values of the parameters utilized for the linear analysis of the SISO system are enlisted in Table 4.3.

It is evident from the magnitude characteristics of the closed loop transfer function that the gain is not significantly affected by the inclusion of the residual dynamics apart from the improvement observed in the range of $[4, 12]$ rad/s, in which the reference response frequency (shown by Fig. 4.16) also lies. The phase variation in the closed loop transfer dynamics notably reduces beyond the frequency range of 5 rad/sec upon

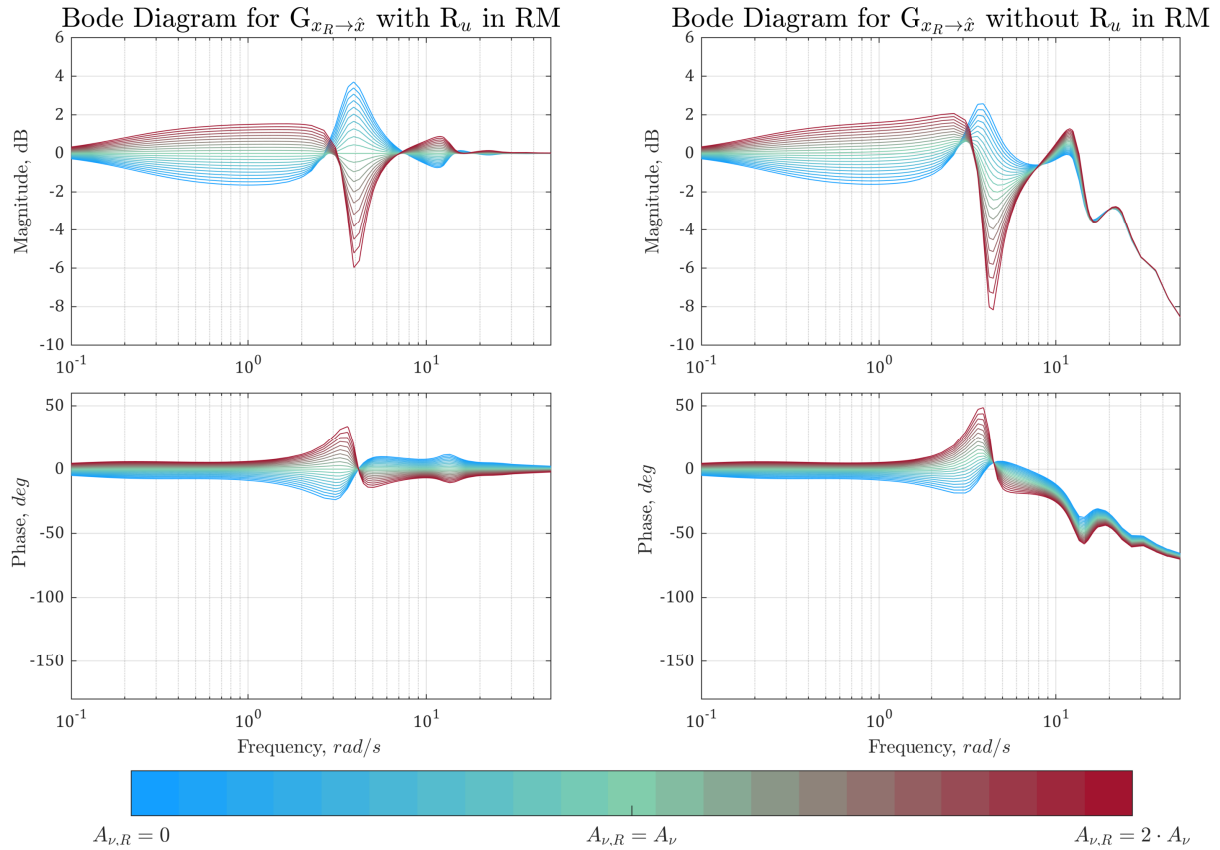


Figure 4.21: Effect of the inclusion of R_u in RM on the transfer characteristics $G_{y_R \rightarrow \hat{y}}$

inclusion of the residual dynamics in the RM for the parameters utilized in this analysis. Similarly, any order of effector dynamics higher than the first order can be incorporated within the reference model, thereby accounting for those components of the effector dynamics that can not be readily compensated in the extended INDI strategy such as the residual dynamics $R_u(s)$ for the second order dynamics described in this work.

The analyses performed on the consideration of the residual dynamics from the second order effector dynamics in this sub-section along with their inclusion in the higher order emulation unit of the jerk-level reference model whose architecture was described in the section 4.2 provides the realization of the contribution **C.3.4 Consideration of higher than first order effector dynamics in the generation of external reference states and feedforward pseudo control rate.**

In addition to the analyses performed to verify the effectiveness of the feedforward command emanating from the design plant based reference model given that the reference state derivative dependent parameter stays within $\pm 100\%$ of the true parameter, the author also proposed adaptation of the design plant parameters to bring them as close to the real system values as possible. The strategy and results related to **design plant adaptation in the jerk-level RM** were presented in a research article [207] and it is added in the Appendix D for the reader's reference.

4.4.6 Treatment of Unstable Systems

The analyses presented so far considered stable SISO systems. However, many aircraft configurations being developed within the scope of UAM are multicopter configurations or VTOL transition aircraft, which are inherently unstable in the hover flight phase. Therefore, the current section presents the treatment of unstable systems or at least flight phases in which a system is unstable.

As proven through the analyses before, the feedforward pseudo control derivative command produced by the reference model remains effective in improving the tracking performance as long as the design plant parameter $A_{\nu,R}$ lies within $\pm 100\%$ of the true plant parameter A_{ν} . Therefore for an unstable system the design plant parameter can safely be chosen as zero rather than basing the generation of the reference trajectories on an unstable design plant. This implies that without the other elements like higher order effect and delay emulation units proposed to be incorporated in the reference model, the reference model with a design plant parameter equal to zero would be equivalent to a higher order linear reference model. However, as discussed before that apart from the state dependent dynamics, inclusion of higher order effector dynamics, transport delays and estimation dynamics has a significant impact in producing a feasible feedforward command, which delivers better tracking performance without having to alter the feedback error gain set. So even though the knowledge of the state dependent parameter cannot be effectively utilized in the feedforward generation for an unstable system, information about estimation dynamics, higher order effector dynamics and time delays can still be employed.

From this perspective, an unstable SISO system controlled by an extended INDI controller having a jerk level reference model with the parameters defined in the Table 4.4 is considered. In order to display the effectiveness of using the feedforward command from the jerk-level RM even though the design plant's state damping parameter $A_{\nu,R}$ was chosen as zero, the bode plot of the closed loop transfer function $G_{y_R \rightarrow \hat{y}}(s)$ from Eq. (4.120) is considered in the Fig. 4.22. Two cases with the design plant parameter kept at 0 are analyzed. Both the cases differ by inclusion and omission of the higher order effect emulation $G_L(s)$ and the time delay emulation $G_D(s)$ in the reference model. The higher order effect emulation $G_L(s)$ is built up from the residual effector dynamics of a

Parameter	Magnitude	Parameter	Magnitude
$K_{0,R}$	0.8	ζ_A	1
$A_{\nu,R}^*$	-0.8	A_{ν}	0.5
$K_{u,R}$	2	B_{ν}	1.5
$A_{\nu,R}$	0	C_{ey}	2
ω_{LP}	20	C_{ev}	6
ζ_{LP}	1	T_i	0.05 s
ω_A	10	T_o	0.05 s

Table 4.4: Magnitude of parameters used in the linear analysis of the jerk-level RM with the extended INDI controller for an unstable system

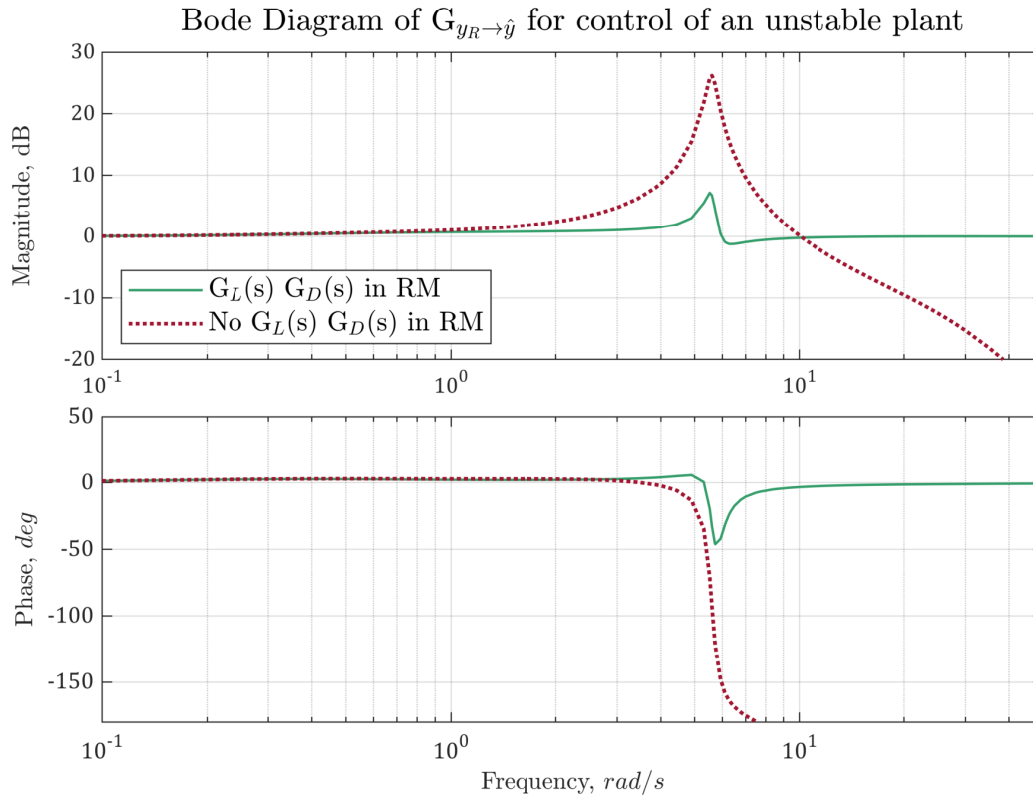


Figure 4.22: Effect of inclusion of Input/Output delay emulation G_D and higher order effect emulation G_L in the RM on the transfer characteristics $G_{y_R \rightarrow \hat{y}}$ for control of an unstable SISO system

second order effector having natural frequency and damping of 10 and 1 respectively. Additionally, the estimation filter dynamics from a second order filter, as described in Eq. (4.97), are also included in $G_L(s)$. The time delay emulation $G_D(s)$ incorporates the effect of input and output channel delays of 0.05 seconds each. Figure 4.22 demonstrates that consideration of the higher order effects and pure time delay in the reference model mitigates the resonant peak in the gain plot of the closed loop transfer function $G_{y_R \rightarrow \hat{y}}(s)$, and it facilitates a phase match between the reference external state and the filtered output \hat{y} .

Furthermore, the effectiveness of using the proposed jerk-level RM structure including information about the higher order effects $G_L(s)$ and time delays $G_D(s)$ is also visible through the results of the time domain simulations illustrated by the Fig. 4.23. Similar to the linear analysis performed earlier in this section, two cases of inclusion and omission of $G_L(s)$ and $G_D(s)$ were compared for these simulations. It was observed from the results that for control of the considered unstable system, steady state tracking remained similar for the two cases, however the transient tracking performance improved when the effects $G_L(s)$, $G_D(s)$ are accounted by the RM. In the absence of these elements from the RM, the pseudo control tracking exhibited oscillatory behavior during transients for the same set of feedback error controller gains.

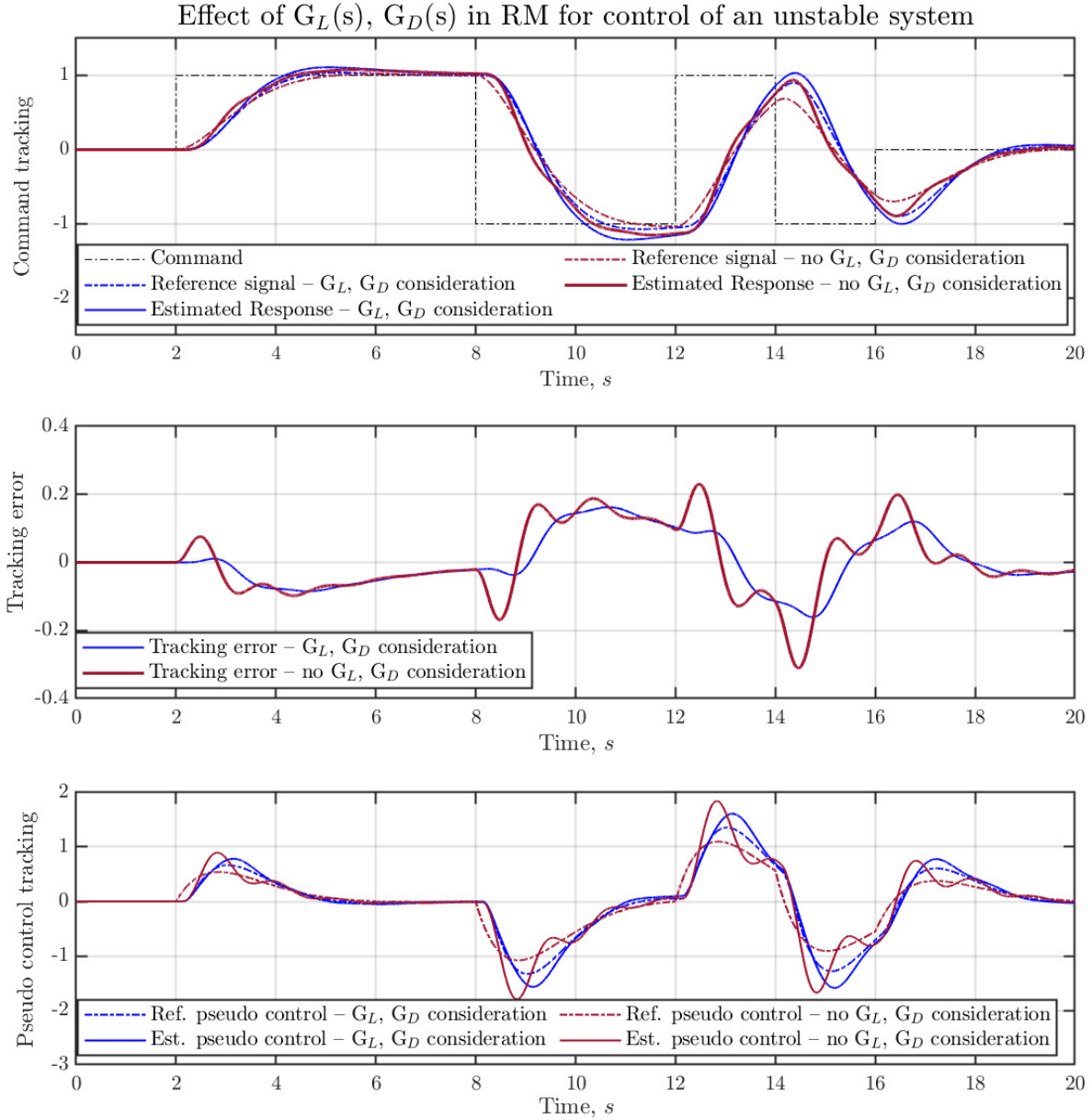


Figure 4.23: Impact of the consideration of Input/Output delay emulation G_D and higher order effect emulation G_L in the RM on the tracking performance for control of an unstable SISO system

4.4.7 Experimental Verification

The concept of employing a design plant in a reference model is verified in an experimental setup used to control the rotational rate of a LTU. The block diagram of the experimental setup is demonstrated in Fig. 4.24. The setup comprises of an Engine Interface Unit (EIU), which receives the propeller rotational rate command $\omega_{cmd} \in \mathbb{R}$ and calculates a desired torque command $T_{M,des} \in \mathbb{R}$ based on the LTU's rotational rate feedback $\omega \in \mathbb{R}$.

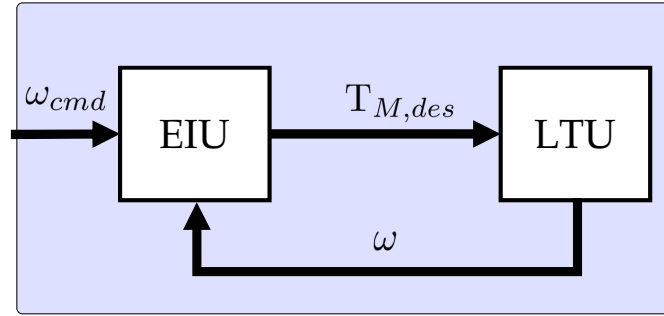


Figure 4.24: System view for RPM control system of the Lift Thrust Unit

In order to specify the construction of the feedforward from the reference model and the structure of the LTU rotational rate controller, first the equation of motion for the LTU comprising of a Direct Current (DC) motor with a fixed-pitch propeller is given

$$I_{LTU} \cdot \dot{\omega} = k_N \cdot \omega^2 + T_M. \quad (4.123)$$

Here $I_{LTU} \in \mathbb{R}$ denotes the combined moment of inertia of the DC motor and the propeller, $k_N \in \mathbb{R}$ comprises of the drag moment coefficient of the propeller as well as the friction coefficient of the motor and T_M describes the motor torque. The term $k_N \cdot \omega^2$ constitutes the load torque originating from the drag produced by the rotating propeller. This state dependent effect is a good candidate to be included in the design plant of the RM for generating an effective feedforward command. Considering the dynamics specified in Eq. (4.123) in terms of a classical linear system $\dot{x} = a \cdot x + b \cdot u$

$$\dot{\omega} = I_{LTU}^{-1} \cdot k_N \cdot \omega^2 + I_{LTU}^{-1} \cdot T_M, \quad (4.124)$$

$I_{LTU}^{-1} \cdot k_N$ is the system state parameter, I_{LTU}^{-1} originates as the control effectiveness parameter and T_M is the control input to the system. The LTU used in this experiment accepts desired motor torque as an input, therefore the dynamics presented in Eq. (4.124) can directly be used as a basis for the controller design.

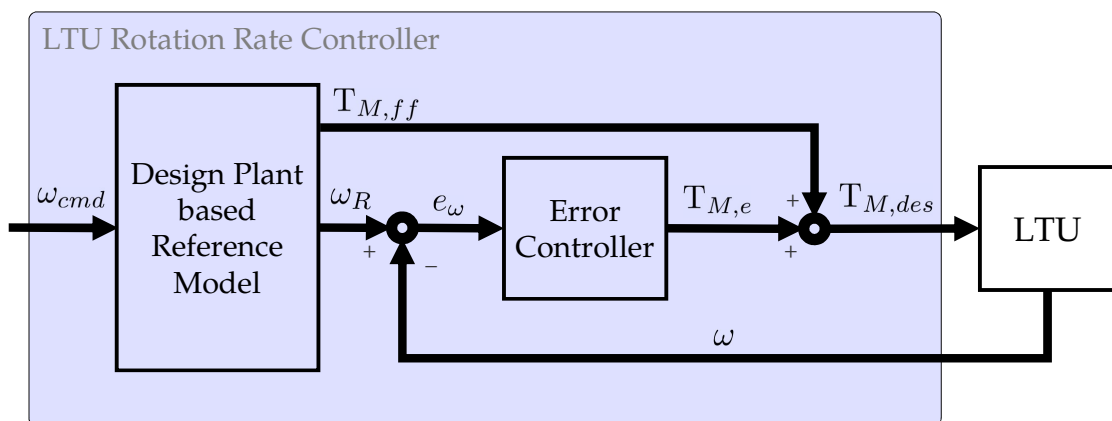


Figure 4.25: RPM controller of the LTU

Figure 4.25 illustrates the architecture of the LTU Rotation Rate Controller. The reference model comprising of the design plant computes the feedforward motor torque command $T_{M,ff} \in \mathbb{R}$ and the reference LTU rotational rate. The feedforward torque $T_{M,ff}$ is computed similar to the relation derived in Eq. (4.39)

$$T_{M,ff} = K_{0,R} \cdot \omega_{cmd}^2 + (k_{N,R} - k_{N,R}^*) \cdot \omega_R^2, \quad (4.125)$$

where $K_{0,R} \in \mathbb{R}$ is the command scaling for the square of the LTU rotation rate command $\omega_{cmd}^2 \in \mathbb{R}$, which provides the steady state feedforward command, $k_{N,R}^* \in \mathbb{R}$ specifies the desired dynamics corresponding to the design plant parameter $k_{N,R} \in \mathbb{R}$. The design plant of the reference model takes the feedforward torque as input, thereby generating the reference rotational rate trajectories

$$\dot{\omega}_R = I_{LTU,R} \cdot (k_{N,R} \cdot \omega_R^2 + T_{M,ff}). \quad (4.126)$$

The parameter $I_{LTU,R} \in \mathbb{R}$ represents the best estimate for the combined moment of inertia for the motor and propeller to be used in the design plant of the reference model. Similarly, $k_{N,R} \in \mathbb{R}$ is the estimate of the propeller drag coefficient used in the design plant. Since the current dynamics in the electric motor used by the lift thrust unit are instantaneously fast, higher order dynamics than the torque level are not pursued in this experiment.

Furthermore, the feedback error based motor torque $T_{M,e} \in \mathbb{R}$ is computed in the error controller

$$T_{M,e} = I_{LTU,R} \cdot \left(K_P \cdot e_\omega + K_I \cdot \int e_\omega \cdot dt \right), \quad (4.127)$$

where $K_P \in \mathbb{R}$ and $K_I \in \mathbb{R}$ define the proportional and integral gains for the tracking error $e_\omega = \omega_R - \omega$. Finally, the desired motor torque $T_{M,des}$ command to the lift thrust unit is computed

$$T_{M,des} = T_{M,ff} + T_{M,e}. \quad (4.128)$$

In order to verify the effectiveness of the feedforward motor torque generated by the reference model, two experimental runs are carried out. In the first case, depicted by the left plot in Fig. 4.26, only the feedforward command is sent to the lift thrust unit according to the rotational rate commands from 1200 to 1800 RPM in steps of 100 RPM. It can be observed that even without using the feedback loop, the rotation rate of the lift thrust unit moves in the direction of the commanded value and sustains a steady state rotation rate, although with a constant error. Naturally, when used along with the feedback loop, the described rotation rate controller achieves the commanded setpoint of the LTU rotation rate. As already stated before, the design plant based feedforward presented in this chapter is only intended to alleviate the control effort from the feedback loop by anticipating the known disturbances in the system, thereby enhancing the command response. Accordingly, the utilized feedforward motor torque command provides an immediate response of the LTU's rotation rate in the commanded direction, and the residual tracking error is compensated by the error controller.

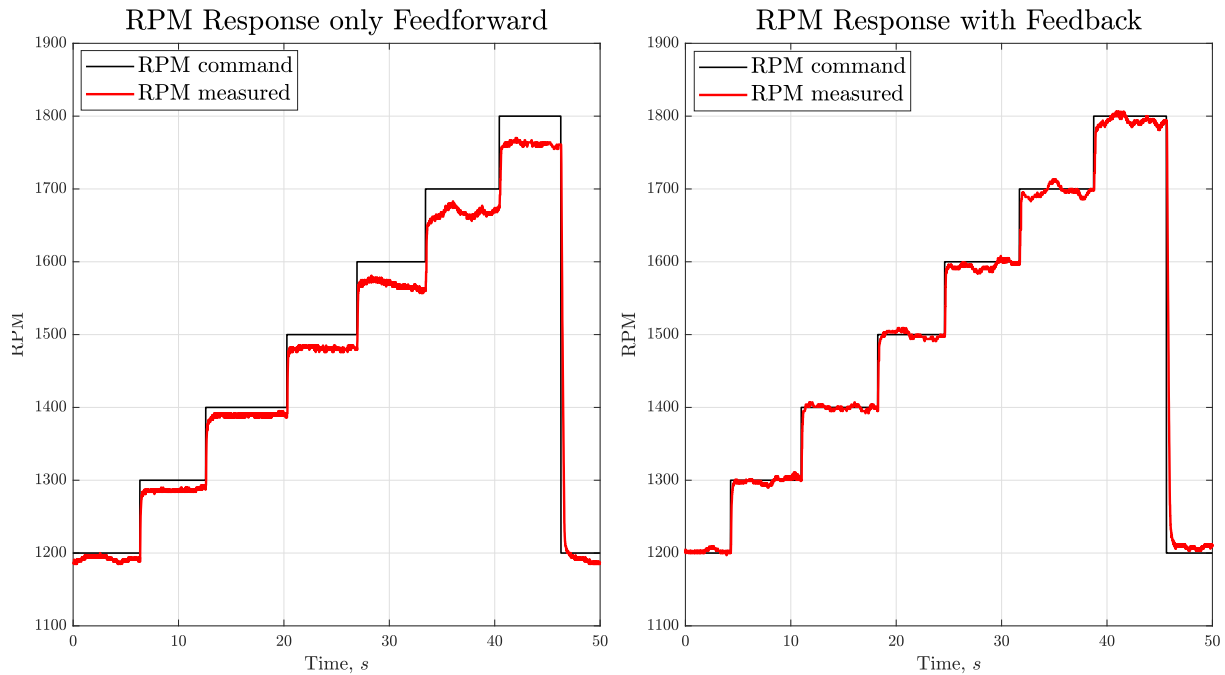


Figure 4.26: Comparison of RPM control in case of only feedforward against the case with both feedforward and feedback active

4.5 Summary

This chapter described the framework of the jerk-level reference model employed with a continuous extension of the INDI control strategy. The main feature of the proposed reference model is the incorporation of state dependent damping terms in the generation of reference external state trajectories and the feedforward command. The consideration of the state dependent terms allowed to anticipate the effect of such identifiable disturbances and act on them through the feedforward command, even before the control error develops. The state dependent terms also known as the "*A*-part" were included in the design plant of the reference model.

Feedback linearization of the design plant was performed within the jerk-level RM to produce the feedforward to the extended INDI controller. Rather than the classical INDI approach where a system model is inverted to produce control effector commands, dynamic inversion was only utilized to produce a pseudo control derivative feedforward command in the jerk-level RM. Consequently, the jerk level reference model produced a physically meaningful feedforward command which results in an effector command not only in the right direction but also provides a steady state magnitude based on the aircraft knowledge added in the design plant. Evidently, the feedforward produced by the jerk-level RM is more effective than the feedforward pseudo control commands produced by linear reference models, which are simply high-pass filtered components of the control variable command.

The jerk level reference model was built up from four functional units, namely – *desired dynamics specification unit*, *state dependence compensation unit*, *reference actuator with input/output channel dynamics consideration* and the *design plant*. As the name suggests, the *desired dynamics specification unit* was used to define the reference dynamics for each control variable channel, while the *state dependence compensation unit* was used to compute the control effector relevant pseudo control command $\nu_{u,R,cmd}$ for the reference actuators based on the feedback from the design plant. The *reference actuator with input/output channel dynamics consideration* combined effects of the noise attenuation/estimation filters, pure time delays in the closed loop system and higher than first order actuator dynamics. The *design plant* incorporated the system knowledge relevant to each of the pseudo control channels.

Furthermore, the controller structure embedding the jerk-level reference model in the extended INDI framework was elaborated. Derivation of resultant error dynamics for the closed loop system revealed that the presence of the aircraft knowledge in the design plant mitigated the magnitude of excitation of the tracking error. However, the mitigation of tracking error excitation only occurred as long as the design plant parameters stayed within a range of the true plant parameters.

This effective parameter range for the design plant was established through linear analysis for a SISO case. For the considered case, it was found out that as long as the design plant parameter is defined to be within a range of $\pm 100\%$ of the true plant parameter, the use of the proposed jerk-level RM reduced the magnitude of the set-point tracking error with the same set of feedback controller gains. This analysis was further elaborated by reviewing the impact of the design plant uncertainty within the effective parameter range against the MUAD bounds. Results displayed that the MUAD bounds are not violated as long as the design plant parameter stayed within the effective range i.e. $\pm 100\%$ of the real system parameter and the feedforward command from the RM was utilized by the controller. Omission of the feedforward command in computation of the desired pseudo control derivative led to violation of the MUAD bounds pertaining to the phase. Moreover, the facilitation of phase conformity between the reference trajectories and the estimated variables by incorporating noise attenuation/estimation filters in the reference model design was also demonstrated through linear analysis and time domain simulations. Inclusion of the estimation dynamics did not only reduce phase mismatch between the reference external states and the estimated outputs, but also mitigated the gain variation between the two, thereby allowing the possibility of using higher feedback gains and enhancing external disturbance rejection.

Similarly, time-delays of the input/output channel dynamics were added in the RM to enforce phase match between external reference and estimated plant states. Resulting bode plots showed that the gain and phase difference between the reference external state y_R and the filtered output \hat{y} reduced significantly within the effective design parameter range for the considered SISO case. Addition of the estimation dynamics and the time delays brings out the bi-level control objective resulting from the inclusion of the jerk level reference model in the extended INDI strategy. The jerk level RM specifies the

desired behavior for the estimated system while the true plant is enforced to follow the implicit reference behavior embedded in the RM, which is equal to the applied reference behavior without the time delays and the dynamics of the noise attenuation filters.

Higher than first order effector dynamics were not completely accounted by the actuator dynamics consideration of the extended INDI architecture. It was proposed that the unaccounted residual dynamics be encompassed in the higher order delay emulation unit of the reference model. In order to demonstrate this aspect, the effect of including the residual dynamics for a second order actuator within the jerk-level RM was provided through linear analysis for a scalar system. The inclusion of these residual dynamics also facilitated reduction in phase difference between the reference external state and the estimated output.

Finally, experimental verification for the design plant based reference model structure was provided through a control strategy used for RPM control of a lift thrust unit. Results showed that even without using the feedback of the current rotational rate, the feedforward path was able to effectively guide the lift thrust unit in the commanded direction and maintain a steady state rotational rate, though with a steady state error. The remaining errors were mitigated by the feedback error controller.

Chapter 5

Unified Trajectory Control for VTOL Transition Aircraft

This chapter proposes a configuration agnostic unified trajectory control strategy for VTOL transition aircraft. As mentioned in the state of the art section 1.2.3, nonlinear control strategies deliver the benefit of utilizing the full control authority of the aircraft by considering their physical capabilities. Furthermore, it was also established through the literature survey that jerk control for path-following delivers advantages in improving tracking accuracy, consideration of effector dynamics, enhancing passenger comfort as well as reducing efficiency-loss in actuators. Therefore, rigid-body kinematic translation jerk dynamics denoted in the C -frame are derived, which are used to obtain the position jerk error dynamics and define the terms required in the feedforward path of the unified trajectory control strategy. In addition to the feedforward terms, feedback of position, velocity and acceleration errors is employed in the trajectory controller to compute specific force rate commands, which are allocated to Euler attitude rate commands through an interfacing module. Consequently, the commands generated by the trajectory controller can interface with any kind of configuration dependent inner loop controller irrespective of the applied control strategy. Ultimately, the unified trajectory controller along with the trajectory generation modules provide a configuration agnostic guidance system framework that operates in the full flight envelope of a VTOL transition aircraft.

With the emergence of Urban Air Mobility, the demand of strategies yielding high precision trajectory following in urban airspace has also risen. Urban topology comprise of high-rise structures, which generate atmospheric disturbances due to boundary layer effects and unsteady wind-fields [95]. Even in presence of these dynamic environmental conditions coupled with a limited operating volume and high traffic expectancy in the urban airspace, stringent bounds on the deviation from the desired path still need to be enforced at all times during a flight mission. With this aim, a unified controller capable of providing high accuracy for trajectory tracking is developed in this dissertation. In addition to being aircraft configuration agnostic, the proposed design yields a flight

phase independent feedback control architecture without having to switch control laws during transition between hover and forward velocity flight phases for trajectory control of a VTOL transition aircraft.

Before commencing the theory of the proposed strategy, the nomenclature pertaining to the trajectory control is recapped. As mentioned in section 1.2.3, the term *trajectory* refers to the time history of any state of the system under examination. Since the term *trajectory* is used in the context of geometric guidance and control in this chapter, hence it refers to the time history of the geometric path of an aircraft. Accordingly, the objective of *trajectory control* is to track a desired position in space under a time constraint. Contrarily, in *path-following control* the time constraint is disregarded, and the control objective is reduced to following the desired geometric path without any time limitations. In order to bring out a clear distinction, Table 1.2 displayed the functions incorporated in trajectory and path-following control.

In this chapter, the derivation of the control law is performed for trajectory control i.e. the forward translation channel is also included to take the time constraint into consideration. However, the resulting control law can be easily reduced to path-following control functionality by neglecting the trajectory controller's output related to regulation of the forward translation. Henceforth, trajectory controller and path following will be used synonymously in this chapter.

The trajectory control technique presented in this work is capable of functioning in the full flight envelope of a VTOL transition aircraft. One of the important factors that allow to design this approach is the choice of a valid frame of operation for the control law in the complete flight envelope. Additionally, employment of kinematic error dynamics for generation of subsequent commands to the inner loops give freedom from the requirement of any aircraft model knowledge. Hence, this trajectory/path-following controller can be applied to any aircraft with marginal effort.

The utility of the *C*-frame in deriving a unified control law for all flight phases of a VTOL transition aircraft has already been detailed in the section 2.1. Therefore, this chapter starts with the derivation of the jerk level translation dynamics in the control frame. Thereafter, an order analysis for the terms arising in the jerk translation dynamics is performed to ascertain their impact given the parameter ranges of the control problem. Depending on the outcome of the order analysis, terms with negligible effects are removed to obtain the jerk translation equations of motion to be employed for derivation of nonlinear jerk error dynamics. It is also shown that the derived jerk error dynamics are linear in the trajectory error states. Subsequently, the unified control law is derived by dynamic inversion of the nonlinear jerk error dynamics. A modular framework for the software implementation of the unified controller is elaborated. Additionally, an interface module, which generates attitude/attitude-rate commands for inner loop control of any multicopter configuration is also presented. Ultimately, verification of the proposed unified trajectory control strategy is performed through MIL simulation tests employing a multicopter aircraft and a simplified INDI based inner loop controller.

5.1 Jerk-level Translation Dynamics in the Control Frame

In this section, the jerk level translation dynamics are derived using the translation equations of motion denoted in the control frame presented by the Eq. (2.53)

$$\left(\ddot{\vec{V}}_K^R\right)_C^{EC} + \left(\vec{\omega}_K^{OC}\right)_C \times \left(\vec{V}_K^R\right)_C^E + \boxed{\left(\vec{a}_{tr}^R\right)_C + \left(\vec{a}_{e,rot}^R\right)_C + \left(\vec{a}_{b,rot}^{RG}\right)_C} = \left(\vec{f}_T^R\right)_C, \quad (5.1)$$

where the acceleration emanating from transport rate $\left(\vec{a}_{tr}^R\right)_C \in \mathbb{R}^3$ as given in Eq. (2.33), earth's rotation $\left(\vec{a}_{e,rot}^R\right)_C \in \mathbb{R}^3$ derived in Eq. (2.34) as well as rigid body rotation $\left(\vec{a}_{b,rot}^{RG}\right)_C \in \mathbb{R}^3$ as shown in Eq. (2.35) are combined in to one term denoting them as other accelerations $\left(\vec{a}_{oth}\right)_C \in \mathbb{R}^3$. The resulting translation equations of motion are differentiated with respect to time in reference to the inertial frame I

$$\left(\ddot{\vec{V}}_K^R\right)_C^{ECI} + \left(\vec{\omega}_K^{OC}\right)_C^I \times \left(\vec{V}_K^R\right)_C^E + \left(\vec{\omega}_K^{OC}\right)_C \times \left(\ddot{\vec{V}}_K^R\right)_C^{EI} + \left(\dot{\vec{a}}_{oth}\right)_C^I = \left(\dot{\vec{f}}^R\right)_C^I, \quad (5.2)$$

and the colored terms are transformed to their corresponding counterparts of the control frame using the Euler differentiation rule

$$\left(\dot{\vec{X}}\right)_B^{AA} = \left(\dot{\vec{X}}\right)_B^{AB} + \left(\vec{\omega}_K^{AB}\right)_B \times \left(\vec{X}\right)_B^A \quad (5.3)$$

to obtain jerk-level dynamics denoted in the C -frame

$$\begin{aligned} & \left(\ddot{\vec{V}}_K^R\right)_C^{ECC} + \left(\vec{\omega}_K^{IC}\right)_C \times \left(\dot{\vec{V}}_K^R\right)_C^{EC} + \left[\left(\vec{\omega}_K^{OC}\right)_C + \left(\vec{\omega}_K^{IC}\right)_C \times \left(\vec{\omega}_K^{OC}\right)_C\right] \times \left(\vec{V}_K^R\right)_C^E + \\ & \left(\vec{\omega}_K^{OC}\right)_C \times \left[\left(\dot{\vec{V}}_K^R\right)_C^{EC} + \left(\vec{\omega}_K^{IC}\right)_C \times \left(\vec{V}_K^R\right)_C^E\right] + \left(\dot{\vec{a}}_{oth}\right)_C^C + \left(\vec{\omega}_K^{IC}\right)_C \times \left(\vec{a}_{oth}\right)_C \\ & = \left(\dot{\vec{f}}^R\right)_C^C + \left(\vec{\omega}_K^{IC}\right)_C \times \left(\vec{f}^R\right)_C. \end{aligned} \quad (5.4)$$

The rotational rate $\left(\vec{\omega}_K^{IC}\right)_C \in \mathbb{R}^3$ is made up of three components denoted in the control frame – earth's rotation rate $\left(\vec{\omega}_K^{IE}\right)_C \in \mathbb{R}^3$, transport rate $\left(\vec{\omega}_K^{EO}\right)_C \in \mathbb{R}^3$ and the rotation of the control frame with respect to the NED-frame $\left(\vec{\omega}_K^{OC}\right)_C \in \mathbb{R}^3$

$$\left(\vec{\omega}_K^{IC}\right)_C = \boxed{\left(\vec{\omega}_K^{IE}\right)_C + \left(\vec{\omega}_K^{EO}\right)_C} + \left(\vec{\omega}_K^{OC}\right)_C \quad (5.5)$$

$\left(\vec{\omega}_K^{IO}\right)_C$

among which the earth's rotation rate and transport rate are combined

$$\left(\vec{\omega}_K^{IC}\right)_C = \left(\vec{\omega}_K^{IO}\right)_C + \left(\vec{\omega}_K^{OC}\right)_C \quad (5.6)$$

and then substituted in Eq. (5.4) to yield

$$\begin{aligned}
 & \left(\ddot{\vec{V}}_K^R \right)_C^{ECC} + \left[\left(\vec{\omega}_K^{IO} \right)_C + \left(\vec{\omega}_K^{OC} \right)_C \right] \times \left(\dot{\vec{V}}_K^R \right)_C^{EC} + \\
 & \left[\left(\vec{\omega}_K^{OC} \right)_C^C + \left[\left(\vec{\omega}_K^{IO} \right)_C + \left(\vec{\omega}_K^{OC} \right)_C \right] \times \left(\vec{\omega}_K^{OC} \right)_C \right] \times \left(\vec{V}_K^R \right)_C^E + \\
 & \left(\vec{\omega}_K^{OC} \right)_C \times \left[\left(\dot{\vec{V}}_K^R \right)_C^{EC} + \left[\left(\vec{\omega}_K^{IO} \right)_C + \left(\vec{\omega}_K^{OC} \right)_C \right] \times \left(\vec{V}_K^R \right)_C^E \right] + \left(\vec{a}_{oth} \right)_C^C + \\
 & \left[\left(\vec{\omega}_K^{IO} \right)_C + \left(\vec{\omega}_K^{OC} \right)_C \right] \times \left(\vec{a}_{oth} \right)_C = \left(\dot{\vec{f}}^R \right)_C^C + \left[\left(\vec{\omega}_K^{IO} \right)_C + \left(\vec{\omega}_K^{OC} \right)_C \right] \times \left(\vec{f}^R \right)_C.
 \end{aligned} \tag{5.7}$$

In the second row of the above equation, the cross product of the rotational rate $(\vec{\omega}_K^{OC})_C \in \mathbb{R}^3$ with itself emerges, which is evaluated as zero

$$\begin{aligned}
 & \left(\ddot{\vec{V}}_K^R \right)_C^{ECC} + \left(\vec{\omega}_K^{IO} \right)_C \times \left(\dot{\vec{V}}_K^R \right)_C^{EC} + \left(\vec{\omega}_K^{OC} \right)_C \times \left(\dot{\vec{V}}_K^R \right)_C^{EC} + \\
 & \left[\left(\vec{\omega}_K^{OC} \right)_C^C + \left(\vec{\omega}_K^{IO} \right)_C \times \left(\vec{\omega}_K^{OC} \right)_C + \underbrace{\left(\vec{\omega}_K^{OC} \right)_C \times \left(\vec{\omega}_K^{OC} \right)_C}_{=0} \right] \times \left(\vec{V}_K^R \right)_C^E + \\
 & \left(\vec{\omega}_K^{OC} \right)_C \times \left[\left(\dot{\vec{V}}_K^R \right)_C^{EC} + \left(\vec{\omega}_K^{IO} \right)_C \times \left(\vec{V}_K^R \right)_C^E + \left(\vec{\omega}_K^{OC} \right)_C \times \left(\vec{V}_K^R \right)_C^E \right] + \\
 & \left(\vec{a}_{oth} \right)_C^C + \left(\vec{\omega}_K^{IO} \right)_C \times \left(\vec{a}_{oth} \right)_C + \left(\vec{\omega}_K^{OC} \right)_C \times \left(\vec{a}_{oth} \right)_C = \left(\dot{\vec{f}}^R \right)_C^C + \left(\vec{\omega}_K^{IC} \right)_C \times \left(\vec{f}^R \right)_C.
 \end{aligned} \tag{5.8}$$

Furthermore, the cross product terms with the two rotational rates $(\vec{\omega}_K^{IO})_C$ and $(\vec{\omega}_K^{OC})_C$ are collected separately to provide the translation jerk dynamics defined in the C -frame

$$\begin{aligned}
 & \text{Linear jerk} \quad \text{Centripetal jerk} \quad \text{Coriolis jerk due to } (\vec{\omega}_K^{OC})_C \\
 & \left(\ddot{\vec{V}}_K^R \right)_C^{ECC} + \left(\vec{\omega}_K^{OC} \right)_C^C \times \left(\vec{V}_K^R \right)_C^E + \left(\vec{\omega}_K^{OC} \right)_C \times \left[2 \cdot \left(\dot{\vec{V}}_K^R \right)_C^{EC} + \left(\vec{a}_{oth} \right)_C \right] + \\
 & \text{Centrifugal jerk due to } (\vec{\omega}_K^{OC})_C \quad \text{Coriolis jerk due to } (\vec{\omega}_K^{IO})_C \\
 & \left(\vec{\omega}_K^{OC} \right)_C \times \left[\left(\vec{\omega}_K^{OC} \right)_C \times \left(\vec{V}_K^R \right)_C^E \right] + \left(\vec{\omega}_K^{IO} \right)_C \times \left[\left(\dot{\vec{V}}_K^R \right)_C^{EC} + \left(\vec{a}_{oth} \right)_C \right] + \\
 & \text{Triple cross product terms} \quad \text{Improper Jerk} \\
 & \left[\left(\vec{\omega}_K^{IO} \right)_C \times \left(\vec{\omega}_K^{OC} \right)_C \right] \times \left(\vec{V}_K^R \right)_C^E + \left(\vec{\omega}_K^{OC} \right)_C \times \left[\left(\vec{\omega}_K^{IO} \right)_C \times \left(\vec{V}_K^R \right)_C^E \right] + \left(\vec{a}_{oth} \right)_C^C \\
 & = \left(\dot{\vec{f}}^R \right)_C^C + \left(\vec{\omega}_K^{IO} \right)_C \times \left(\vec{f}^R \right)_C + \left(\vec{\omega}_K^{OC} \right)_C \times \left(\vec{f}^R \right)_C.
 \end{aligned} \tag{5.9}$$

The first row in Eq. (5.9) constitutes the linear jerk, centripetal jerk and the jerk emanating from the Coriolis effect due to the rotational rate $(\vec{\omega}_K^{OC})_C$. Additionally, the centrifugal jerk due to $(\vec{\omega}_K^{OC})_C$ is presented in the second row along with the Coriolis jerk due to the rotational rate $(\vec{\omega}_K^{IO})_C$. The terms pertaining to the triple cross products of the rotational rates and velocity along with the derivative of the other accelerations $(\vec{a}_{oth})_C^C$ are written in the third row. Subsequently, the last row consists of the terms emanating from the differentiation of specific forces.

5.1.1 Improper Jerk

The vector cross product term $(\vec{\omega}_K^{IC})_C \times (\vec{a}_{oth})_C$ appears in Eq. (5.4) when the jerk with respect to the inertial frame $(\vec{a}_{oth})_C^I$ is transformed according to the Euler differentiation rule (Eq. (5.31)) such that it is specified with respect to the control frame $(\vec{a}_{oth})_C^C$. This cross product term $(\vec{\omega}_K^{IC})_C \times (\vec{a}_{oth})_C$ is divided into two components each corresponding to the angular rates $(\vec{\omega}_K^{IO})_C$ and $(\vec{\omega}_K^{OC})_C$, which are denoted as the Coriolis jerk terms in Eq. (5.9). Hence, only the improper jerk $(\vec{a}_{oth})_C^C \in \mathbb{R}^3$ remains which originates due to the rate of change of *other accelerations* $(\vec{a}_{oth})_C$ specified in Eq. (5.1), namely accelerations due to transport rate, earth's rotation and rigid body rotation. Likewise, the improper jerk term can also be represented as a sum of its sources

$$(\vec{a}_{oth})_C^C = (\vec{a}_{tr}^R)_C^C + (\vec{a}_{e,rot}^R)_C^C + (\vec{a}_{b,rot}^{RG})_C^C. \quad (5.10)$$

Although the jerk terms specified in the equation above do not affect the calculation of the outputs generated by the trajectory control law, the constituents that form these jerk terms are derived for the sake of completion.

Jerk due to Transport rate

The acceleration due to transport rate from Eq. (2.37) is derived in the C -frame to compute the jerk due to transport rate

$$(\vec{a}_{tr}^R)_C^C = (\dot{\Omega}^{EO})_{CC}^C \cdot (\vec{V}_K^R)_C^E + (\Omega^{EO})_{CC} \cdot (\vec{V}_K^R)_C^{EC}, \quad (5.11)$$

where $(\vec{V}_K^R)_C^{EC} \in \mathbb{R}^3$ and $(\vec{V}_K^R)_C^E \in \mathbb{R}^3$ are the rigid body acceleration and velocity specified in the control frame. Furthermore, the jerk due to transport rate in Eq. (5.11) encompasses the skew symmetric matrix $(\Omega^{EO})_{CC} \in \mathbb{R}^{3 \times 3}$, presented in Eq. (2.39), as well as its time derivative

$$\begin{aligned} (\dot{\Omega}^{EO})_{CC}^C[:, 1] &= \begin{bmatrix} 0 \\ -\ddot{\lambda} \cdot \sin \phi - \dot{\lambda} \cdot \dot{\phi} \cdot \cos \phi \\ \ddot{\phi} \cdot \cos \Psi + \ddot{\lambda} \cdot \sin \Psi \cdot \cos \phi - \dot{\Psi} \cdot \dot{\phi} \cdot \sin \Psi + \\ \dot{\Psi} \cdot \dot{\lambda} \cdot \cos \Psi \cdot \cos \phi - \dot{\lambda} \cdot \dot{\phi} \cdot \sin \Psi \cdot \sin \phi \end{bmatrix}_{CC}^C \\ (\dot{\Omega}^{EO})_{CC}^C[:, 2] &= \begin{bmatrix} \ddot{\lambda} \cdot \sin \phi + \dot{\lambda} \cdot \dot{\phi} \cdot \cos \phi \\ 0 \\ \ddot{\lambda} \cdot \cos \Psi \cdot \cos \phi - \ddot{\phi} \cdot \sin \Psi - \dot{\Psi} \cdot \dot{\phi} \cdot \cos \Psi - \\ \dot{\Psi} \cdot \dot{\lambda} \cdot \sin \Psi \cdot \cos \phi - \dot{\lambda} \cdot \dot{\phi} \cdot \cos \Psi \cdot \sin \phi \end{bmatrix}_{CC}^C \\ (\dot{\Omega}^{EO})_{CC}^C[:, 3] &= \begin{bmatrix} \dot{\Psi} \cdot \dot{\phi} \cdot \sin \Psi - \ddot{\lambda} \cdot \sin \Psi \cdot \cos \phi - \ddot{\phi} \cdot \cos \Psi - \\ \dot{\Psi} \cdot \dot{\lambda} \cdot \cos \Psi \cdot \cos \phi + \dot{\lambda} \cdot \dot{\phi} \cdot \sin \Psi \cdot \sin \phi \\ \ddot{\phi} \cdot \sin \Psi - \ddot{\lambda} \cdot \cos \Psi \cdot \cos \phi + \dot{\Psi} \cdot \dot{\phi} \cdot \cos \Psi + \\ \dot{\Psi} \cdot \dot{\lambda} \cdot \sin \Psi \cdot \cos \phi + \dot{\lambda} \cdot \dot{\phi} \cdot \cos \Psi \cdot \sin \phi \\ 0 \end{bmatrix}_{CC}^C, \end{aligned} \quad (5.12)$$

where $(\dot{\Omega}^{EO})_{CC}^C[:, k] \in \mathbb{R}^3$ specifies the k -th column of the skew symmetric matrix derivative $(\dot{\Omega}^{EO})_{CC}^C \in \mathbb{R}^{3 \times 3}$.

Jerk due to Earth's rotation

Corresponding to the derivation of the transport jerk, the jerk induced by earth's rotation $(\dot{\vec{a}}_{e,rot}^R)_C^C$ is obtained through the differentiation of the acceleration due to earth's rotation from Eq. (2.45)

$$\begin{aligned} (\dot{\vec{a}}_{e,rot}^R)_C^C &= 2 \cdot (\dot{\Omega}^{IE})_{CC}^C \cdot (\vec{V}_K^R)_C^E + 2 \cdot (\Omega^{IE})_{CC} \cdot (\dot{\vec{V}}_K^R)_{EC}^{EC} + \\ &\quad \left[(\dot{\Omega}^{IE})_{CC}^C \cdot (\Omega^{IE})_{CC} + (\Omega^{IE})_{CC} \cdot (\dot{\Omega}^{IE})_{CC}^C \right] \cdot (\vec{r}^R)_C + \\ &\quad \left[(\Omega^{IE})_{CC} \right]^2 \cdot (\vec{V}_K^R)_C^E \end{aligned} \quad (5.13)$$

in which $(\vec{r}^R)_C \in \mathbb{R}^3$ denotes the position vector of the reference point of the aircraft in the control frame. Moreover, the skew symmetric matrix derivative $(\dot{\Omega}^{IE})_{CC}^C \in \mathbb{R}^{3 \times 3}$ also appears, which is constructed from the column vectors

$$\begin{aligned} (\dot{\Omega}^{IE})_{CC}^C[:, 1] &= \omega_E \cdot \begin{bmatrix} 0 \\ -\dot{\phi} \cdot \cos \phi \\ \dot{\Psi} \cdot \cos \Psi \cdot \cos \phi - \dot{\phi} \cdot \sin \Psi \cdot \sin \phi \end{bmatrix} \\ (\dot{\Omega}^{IE})_{CC}^C[:, 2] &= \omega_E \cdot \begin{bmatrix} \dot{\phi} \cdot \cos \phi \\ 0 \\ -\dot{\Psi} \cdot \sin \Psi \cdot \cos \phi - \dot{\phi} \cdot \cos \Psi \cdot \sin \phi \end{bmatrix} \\ (\dot{\Omega}^{IE})_{CC}^C[:, 3] &= \omega_E \cdot \begin{bmatrix} \dot{\phi} \cdot \sin \Psi \cdot \sin \phi - \dot{\Psi} \cdot \cos \Psi \cdot \cos \phi \\ \dot{\Psi} \cdot \sin \Psi \cdot \cos \phi + \dot{\phi} \cdot \cos \Psi \cdot \sin \phi \\ 0 \end{bmatrix}. \end{aligned} \quad (5.14)$$

Jerk due to rigid body rotation

Subsequently, by differentiating Eq. (2.50) in the control frame, the jerk emanating from rigid body rotation at the aircraft reference point R is obtained

$$\begin{aligned} (\dot{\vec{a}}_{b,rot}^{RG})_C &= \dot{\mathbf{M}}_{CB}^C \cdot \left\{ \left[(\dot{\Omega}^{EO})_{BB}^B + (\dot{\Omega}^{OB})_{BB}^B \right] \cdot (\vec{r}^{RG})_B + \right. \\ &\quad \left. \left[(\Omega^{IO})_{BB} + (\Omega^{OB})_{BB} \right]^2 \cdot (\vec{r}^{RG})_B \right\} + \\ &\quad \mathbf{M}_{CB} \cdot \left\{ \left[(\ddot{\Omega}^{EO})_{BB}^{BB} + (\ddot{\Omega}^{OB})_{BB}^{BB} \right] \cdot (\vec{r}^{RG})_B + \right. \\ &\quad \left. 2 \cdot \left[(\Omega^{IO})_{BB} + (\Omega^{OB})_{BB} \right] \cdot \left[(\dot{\Omega}^{IO})_{BB}^B + (\dot{\Omega}^{OB})_{BB}^B \right] \cdot (\vec{r}^{RG})_B \right\}, \end{aligned} \quad (5.15)$$

where terms containing $(\dot{\vec{r}}^{RG})_B^B \in \mathbb{R}^3$, which is the rate of change of the position of aircraft reference point R with respect to the center of gravity G are neglected owing to the rigid body assumption **A.2.1**. Furthermore, $\dot{\mathbf{M}}_{CB}^C \in \mathbb{R}^{3 \times 3}$ is the derivative of the frame rotation matrix $\mathbf{M}_{CB} \in \mathbb{R}^{3 \times 3}$ with respect to the control frame

$$\dot{\mathbf{M}}_{CB}^C = \begin{bmatrix} -\dot{\Theta} \cdot \sin \Theta & \dot{\Phi} \cdot \cos \Phi \cdot \sin \Theta + \dot{\Theta} \cdot \cos \Theta \cdot \sin \Phi & \dot{\Theta} \cdot \cos \Phi \cdot \cos \Theta - \dot{\Phi} \cdot \sin \Phi \cdot \sin \Theta \\ 0 & -\dot{\Phi} \cdot \sin \Phi & -\dot{\Phi} \cdot \cos \Phi \\ -\dot{\Theta} \cdot \cos \Theta & \dot{\Phi} \cdot \cos \Phi \cdot \cos \Theta - \dot{\Theta} \cdot \sin \Phi \cdot \sin \Theta & -\dot{\Phi} \cdot \cos \Theta \cdot \sin \Phi - \dot{\Theta} \cdot \cos \Phi \cdot \sin \Theta \end{bmatrix} \quad (5.16)$$

and $(\ddot{\Omega}^{OB})_{BB}^{BB} \in \mathbb{R}^{3 \times 3}$ is the skew symmetric matrix containing the body rotation jerk

$$(\ddot{\Omega}^{OB})_{BB}^{BB} = \begin{bmatrix} 0 & -\ddot{r}_K & \ddot{q}_K \\ \ddot{r}_K & 0 & -\ddot{p}_K \\ -\ddot{q}_K & \ddot{p}_K & 0 \end{bmatrix}_{BB}^{BB}. \quad (5.17)$$

The skew symmetric matrix derivative $(\dot{\Omega}^{EO})_{BB}^B \in \mathbb{R}^{3 \times 3}$ is constructed from the elements of the angular acceleration $(\vec{\omega}_K^{EO})_B^B \in \mathbb{R}^3$ described in Eq. (B.6) according to the generic skew symmetric matrix form given in Eq. (2.4). Rate of $(\dot{\Omega}^{EO})_{BB}^B \in \mathbb{R}^{3 \times 3}$ also appears in the Eq. (5.15), however it is not derived due to the high number of terms that appear in its calculation and it is not even used in the controller design. The skew symmetric matrices $(\Omega^{IO})_{BB} \in \mathbb{R}^{3 \times 3}$ and $(\dot{\Omega}^{IO})_{BB}^B \in \mathbb{R}^{3 \times 3}$ are built up from the elements of the angular rate $(\vec{\omega}_K^{IO})_B \in \mathbb{R}^3$ and acceleration $(\vec{\omega}_K^{IO})_B^B \in \mathbb{R}^3$ presented in Eqs. (B.4) and (B.5) respectively, according to the matrix form in Eq. (2.4).

As stated before, the improper jerk terms described in this section do not affect the calculation of the outputs generated by the trajectory control law. The constituents that form these jerk terms were derived only for the sake of completion.

5.1.2 Order Analysis of terms in Jerk-level Dynamics

It is important to quantify the impact of different terms originated from the derivation of the translation jerk dynamics described in Eq. (5.9). Hence, an order analysis of these terms is performed in this next section to determine which terms can be neglected in the control law derivation to reduce complexity.

Triple cross-products in the Jerk Dynamics

The triple cross product terms comprising of the angular rates $(\vec{\omega}_K^{IO})_C \in \mathbb{R}^3$, $(\vec{\omega}_K^{OC})_C \in \mathbb{R}^3$ and velocity $(\vec{V}_K^R)_C^E \in \mathbb{R}^3$ appear in Eq. (5.9). The magnitude ranges of these terms are assessed to determine their effect on the jerk level translation dynamics. Firstly, the two products are expanded to reveal the constituting terms

$$\begin{aligned} [(\vec{\omega}_K^{IO})_C \times (\vec{\omega}_K^{OC})_C] \times (\vec{V}_K^R)_C^E &= \begin{bmatrix} -\dot{\Psi} \cdot (w_K^R)_C^E \cdot \sigma_1 \\ \dot{\Psi} \cdot (w_K^R)_C^E \cdot \sigma_2 \\ \dot{\Psi} \cdot (u_K^R)_C^E \cdot \sigma_1 - \dot{\Psi} \cdot (v_K^R)_C^E \cdot \sigma_2 \end{bmatrix}, \quad (5.18) \\ (\vec{\omega}_K^{OC})_C \times [(\vec{\omega}_K^{IO})_C \times (\vec{V}_K^R)_C^E] &= \begin{bmatrix} \dot{\Psi} \cdot [(w_K^R)_C^E \cdot \sigma_1 + (u_K^R)_C^E \cdot (\dot{\lambda} + \omega_E) \cdot \sin \phi] \\ -\dot{\Psi} \cdot [(w_K^R)_C^E \cdot \sigma_2 - (v_K^R)_C^E \cdot (\dot{\lambda} + \omega_E) \cdot \sin \phi] \\ 0 \end{bmatrix}, \end{aligned}$$

where

$$\sigma_1 = \dot{\lambda} \cdot \cos \Psi \cdot \cos \phi - \dot{\phi} \cdot \sin \Psi + \omega_E \cdot \cos \Psi \cdot \cos \phi,$$

$$\sigma_2 = \dot{\phi} \cdot \cos \Psi + \dot{\lambda} \cdot \sin \Psi \cdot \cos \phi + \omega_E \cdot \sin \Psi \cdot \cos \phi.$$

5.1 Jerk-level Translation Dynamics in the Control Frame

It is clear from the terms in the elements (rows) of the triple cross products demonstrated in Eq. (5.18) that the C -frame velocities along with the heading angle rate $\dot{\Psi} \in \mathbb{R}$ are the major components that drive their magnitude. The WGS84 longitude and latitude rates $(\dot{\lambda}, \dot{\phi})$ appear due to the effect of the transport rate due to ellipsoid $(\vec{\omega}_K^{OE})_O \in \mathbb{R}^3$ (Eq. (2.36)), which is a part of the angular rate $(\vec{\omega}_K^{IO})_C \in \mathbb{R}^3$. Similarly, Earth's rotation denoted in the control frame $(\vec{\omega}_K^{IE})_C \in \mathbb{R}^3$ (Eq. (2.42)) accounts for the trigonometric components of the heading angle $\Psi \in \mathbb{R}$ and latitude $\phi \in \mathbb{R}$. Since the longitude and latitude rates are directly proportional to the kinematic velocities, only the heading rate and the latitude remain as the independent variables. Therefore, the magnitude of the three elements for each triple product in Eq. (5.18) are computed over the range of the heading angle rate and the absolute latitude range along with the kinematic velocity in the NED frame $(\vec{V}_K^R)_O^E \in \mathbb{R}^3$ as specified in Table 5.1. Moreover, the analysis is carried out for an aircraft flying at a bearing angle $\Psi = 45^\circ$. Consequently, kinematic velocity in the control frame $(\vec{V}_K^R)_C^E \in \mathbb{R}^3$ is also computed with the frame rotation matrix $M_{CO} \in \mathbb{R}^{3 \times 3}$ that uses the heading angle Ψ . The altitude h is chosen to be 0.

These parameter magnitudes are chosen to visualize the maximum influence that the elements of the triple products can generate in the jerk level dynamics. The left column of plots in Figure 5.1 illustrates the magnitude of the three elements for the first triple product over the specified ranges whereas the right column of plots demonstrates the elements of the second triple product in Eq. (5.18).

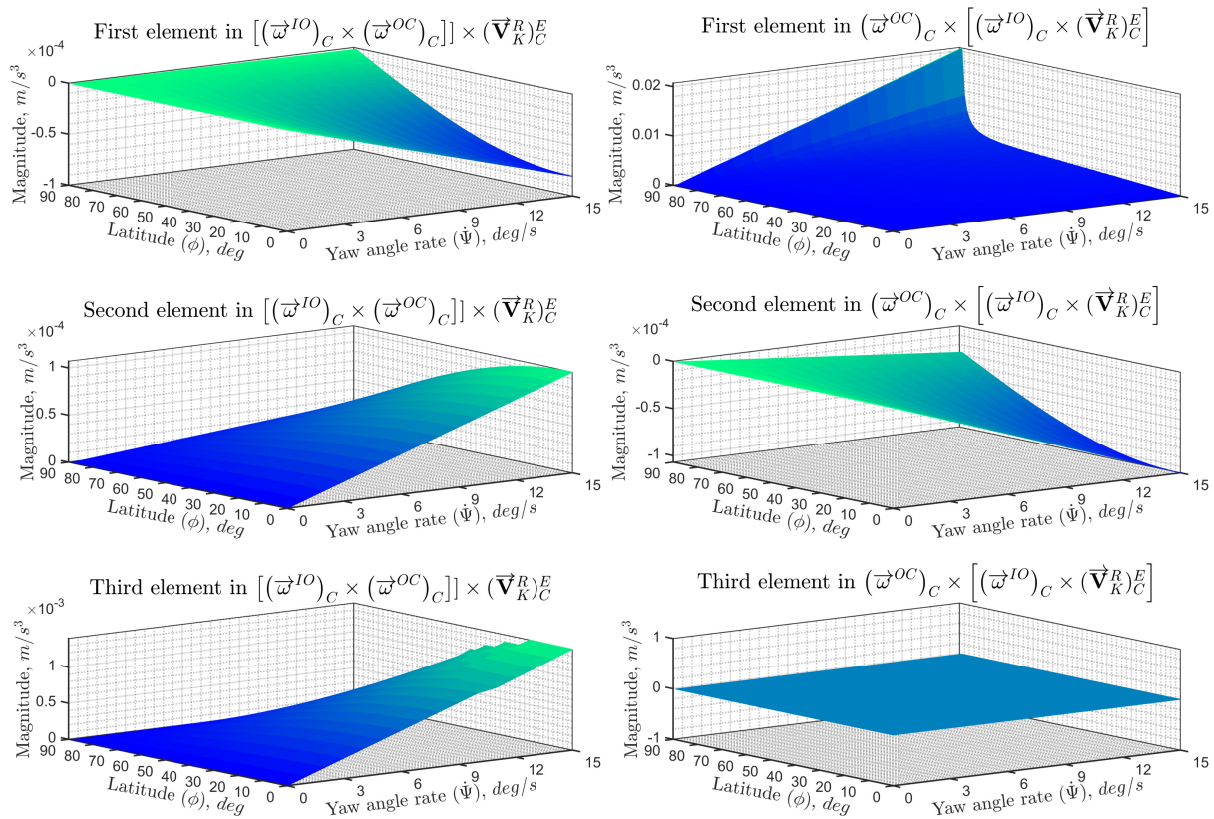


Figure 5.1: Magnitudes of the triple cross product terms in the C -frame Jerk-level translation dynamics

States	Magnitude and Range
Heading angle rate $\dot{\Psi}$ range, deg/s	[0, 15]
Absolute Latitude $ \phi $ range, deg	[0°, 89°]
NED Velocities $(\vec{V}_K^R)^E, m/s$	[75; 75; -6]
C-frame Velocities $(\vec{V}_K^R)^E, m/s$	[106.06; 0; -6]

Table 5.1: *Magnitude and Range of states for order analysis*

For the first product, the z -component (third element) indicates a maximum magnitude of 1.4×10^{-3} at a latitude of 0° . The magnitude of this term is small enough to disregard since any minimal deviations caused by it can be easily corrected through the trajectory error controller. Alternatively, the x -component (first element) in the second cross product rises abruptly to a maximum magnitude of 0.0207 as the absolute latitude of 89° is approached. This behavior results from the singularity at the latitude $|\phi| = 90^\circ$ which originates due to the trigonometric term $\cos \phi$ in the denominator of the longitude $\dot{\lambda} \in \mathbb{R}$ and latitude update $\dot{\phi} \in \mathbb{R}$ described by the position differential equation (C.1). This singularity can be avoided by using an alternative set of equations employing normal vector (n -vector) position representation [214], however it is not a part of this work. Nonetheless, at an absolute latitude of 85° , its magnitude drops down to the order of 5.7×10^{-3} . Moreover, this value represents a worst-case scenario since it results from a flight state at $106m/s \approx 206kts$ with a turn rate of $15^\circ/s$ which would require a bank angle of 70.54° for a coordinated turn. In the configurations utilized for the purpose of UAM [13–15] high velocities such as the ones used for this magnitude order calculation coupled with the turn rate and flights at latitudes near the earth's poles do not hold much practical relevance and are therefore only presented for theoretical analysis. Consequently, the second cross product term can also be neglected based on the reason that errors caused by this approximation are compensated by the error controller.

Coriolis Jerk due to $(\vec{\omega}_K^{IO})_C$

The jerk generated due to the angular rate $(\vec{\omega}_K^{IO})_C \in \mathbb{R}^3$ when an aircraft accelerates with $(\vec{V}_K^R)^{EC} \in \mathbb{R}^3$ and $(\vec{a}_{oth})_C \in \mathbb{R}^3$

$$(\vec{\omega}_K^{IO})_C \times \left[(\vec{V}_K^R)^{EC} + (\vec{a}_{oth})_C \right] \quad (5.19)$$

as presented in Eq. (5.9) is termed as the Coriolis jerk due to $(\vec{\omega}_K^{IO})_C \in \mathbb{R}^3$. The impact of this term is primarily dependent on the magnitude of the angular rate $(\vec{\omega}_K^{IO})_C \in \mathbb{R}^3$

$$(\vec{\omega}_K^{IO})_C = \begin{bmatrix} \dot{\lambda} \cdot \cos \Psi \cdot \cos \phi - \dot{\phi} \cdot \sin \Psi + \omega_E \cdot \cos \Psi \cdot \cos \phi \\ -\dot{\phi} \cdot \cos \Psi - \dot{\lambda} \cdot \sin \Psi \cdot \cos \phi - \omega_E \cdot \sin \Psi \cdot \cos \phi \\ -\dot{\lambda} \cdot \sin \phi - \omega_E \cdot \sin \phi \end{bmatrix} \quad (5.20)$$

since the sum of the two accelerations is vector multiplied with the given angular rate. Table 5.2 shows the range of linear acceleration $(\vec{V}_K^R)^{EC} \in \mathbb{R}^3$ for the aircraft configurations considered in this thesis along with the ranges for accelerations due to transport rate and the Earth's rotation in the control frame.

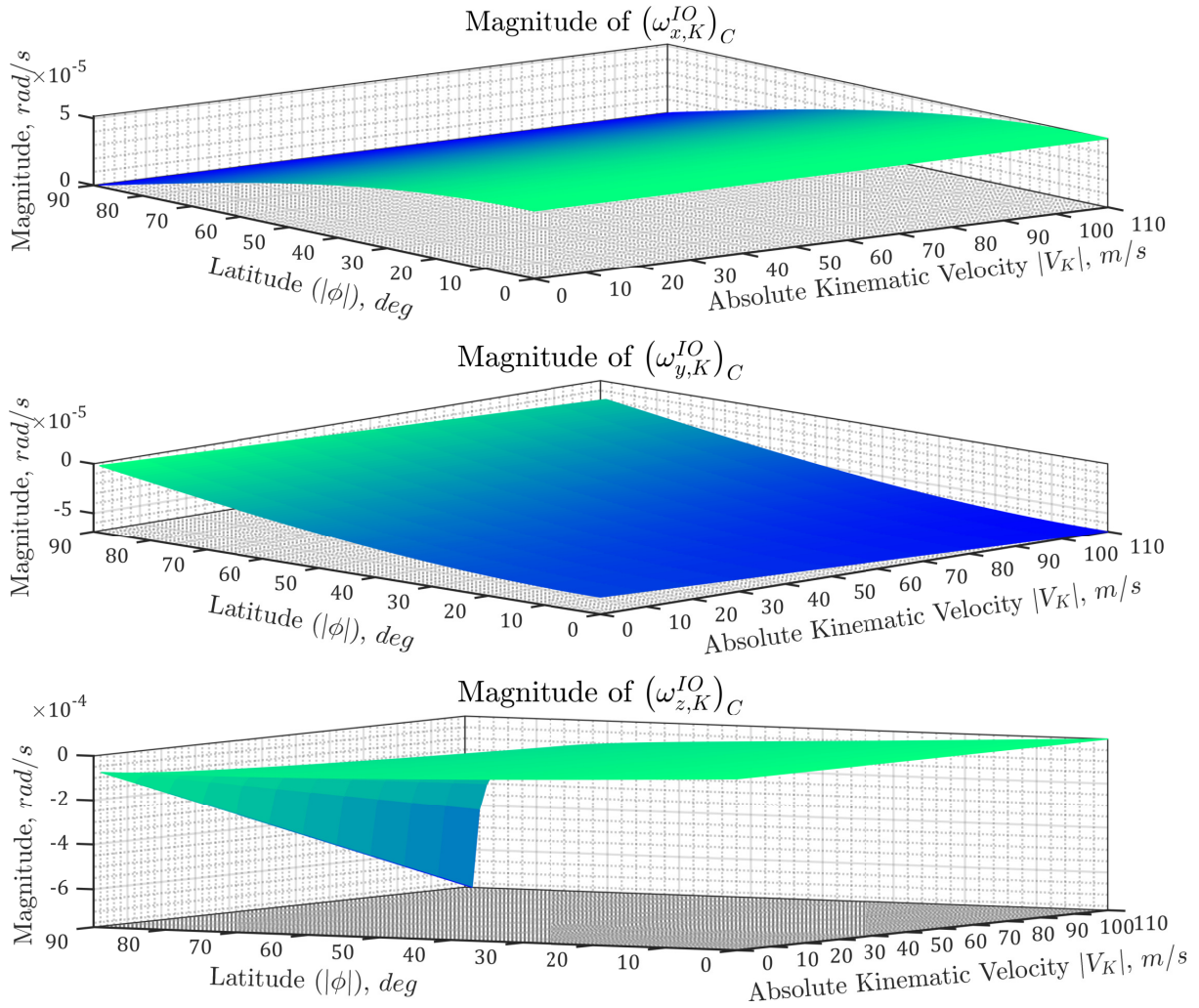
Vector Components	Acceleration Ranges			
	$(\vec{V}_K^R)^{EC}$	$(\vec{a}_{tr})_C$	$(\vec{a}_{e,rot})_C$	$(\vec{V}_K^R)^{EC} + (\vec{a}_{oth})_C$
$x, m/s^2$	$[-3, 3]$	$[-0.016, 0.017]$	$[-3.25, 3.25] \times 10^{-3}$	$[-3.0192, 3.0202]$
$y, m/s^2$	$[-10, 10]$	$[-0.091, 0.091]$	$[-0.016, 0.016]$	$[-10.1070, 10.1070]$
$z, m/s^2$	$[-6, 6]$	$[0, 2] \times 10^{-3}$	$[-0.016, 0.016]$	$[-6.016, 6.0180]$

Table 5.2: Ranges of accelerations contributing to Coriolis jerk due to $(\vec{\omega}_K^{IO})_C$

The control frame longitudinal $(\dot{u}_K^R)^{EC} \in \mathbb{R}$ and vertical $(\dot{w}_K^R)^{EC} \in \mathbb{R}$ accelerations lie in the ranges $[-3, 3] m/s^2$ and $[-6, 6] m/s^2$ respectively. The lateral acceleration span over the range $[10, -10] m/s^2$. Additionally, the order of the accelerations due to transport rate and earth's rotation included in the term $(\vec{a}_{oth})_C \in \mathbb{R}^3$ as calculated in the appendix C.1 are also presented in Table 5.2. However, the acceleration due to rigid body rotation is considered trivial based on the assumption that the reference point R is located very close to the center of gravity G .

The order analysis of the angular rate $(\vec{\omega}_K^{IO})_C \in \mathbb{R}^3$ is carried out for a flight at a fixed bearing angle $\Psi = 45^\circ$ and the absolute latitude range as listed in Table 5.1. The variation in magnitudes of the components of the angular rate vector $(\vec{\omega}_K^{IO})_C \in \mathbb{R}^3$ over the given latitude range and an absolute kinematic velocity range $[0, 110] m/s$ is illustrated in the Fig. 5.2. The x and y components of the angular rate exhibit a magnitude of the order of 10^{-5} and the z component remains within the order of 10^{-4} until the singularity at the absolute latitude of 90° is approached. However, a flight mission in the polar geographical region is not a use-case related to this work. Therefore, the maximum magnitude of the order of 10^{-4} is considered for the z -component. Using the negative range of the latitudes $[-89^\circ, 0^\circ]$ only changes the sign of the magnitude of $(\omega_{K,z}^{IO})_C \in \mathbb{R}$ since it is composed of the sine component of the latitude $\phi \in \mathbb{R}$.

The maximum magnitudes for each vector component of the angular rate $(\vec{\omega}_K^{IO})_C \in \mathbb{R}^3$ along with the maximum values of the acceleration ranges from Table 5.2 are utilized to compute the range of magnitude for the Coriolis jerk term in Eq. (5.19). The results are compiled in Table 5.3. It is observed that the x and y vector components of the Coriolis jerk term lie in the magnitude range of the order 10^{-3} and the vertical component's magnitude has the order of 10^{-4} for the range of inputs considered in this order analysis. Hence, this term is also dropped on account of reducing the complexity of the upcoming trajectory control law derivation. Moreover, an approximation of this order can be easily compensated by the controller.


Figure 5.2: Magnitudes of $(\vec{\omega}_K^{IO})_C$

Range and Magnitude			
Vector Components	$(\vec{\omega}_K^{IO})_C, \text{ rad/s}$	$(\vec{V}_K^R)_C^{EC} + (\vec{a}_{oth})_C, \text{ m/s}^2$	$\max((\vec{\omega}_K^{IO})_C \times [(\vec{V}_K^R)_C^{EC} + (\vec{a}_{oth})_C]), \text{ m/s}^3$
x	$[0, 5.14] \times 10^{-5}$	$[-3.0192, 3.202]$	7.8×10^{-3}
y	$[-6.87, 0] \times 10^{-5}$	$[-10.1070, 10.1070]$	2.3×10^{-3}
z	$[-7.69, 7.69] \times 10^{-4}$	$[-6.016, 6.0180]$	5.0×10^{-4}

Table 5.3: Maximum magnitude for the vector components of Coriolis jerk due to $(\vec{\omega}_K^{IO})_C$

Similarly, the order of jerk emanating from specific forces due to angular rate $(\vec{\omega}_K^{IO})_C$

$$(\vec{\omega}_K^{IO})_C \times (\vec{f}^R)_C \quad (5.21)$$

is analyzed in Table 5.4. The range of the specific forces is physically motivated from the aircraft utilized in this research. The maximum magnitude of the jerk resulting from rotation of the specific forces is bounded within the order of magnitude of 10^{-3}

so this term can also be neglected safely. Additionally, neglecting the Coriolis jerk term of Eq. (5.19) in the left hand side (LHS) of the jerk dynamics derived in Eq. (5.9) reduces the error that would be generated by ignoring the term of Eq. (5.21) in the right hand side (RHS) of the jerk dynamics (Eq. (5.9)) since the difference between the two terms remains very small owing to the vector product with the low magnitude angular rate $(\vec{\omega}_K^{IO})_C$. Analytically, the difference between the two terms can be visualized by rearranging the control frame translation equations of motion from Eq. (5.1) as

$$(\vec{f}^R)_C - (\dot{\vec{v}}_K^R)^{EC} - (\vec{a}_{oth})_C = (\vec{\omega}_K^{OC})_C \times (\vec{v}_K^R)_C^E \quad (5.22)$$

and taking a vector product with the angular rate $(\vec{\omega}_K^{IO})_C$ on both sides

$$(\vec{\omega}_K^{IO})_C \times \left[(\vec{f}^R)_C - (\dot{\vec{v}}_K^R)^{EC} - (\vec{a}_{oth})_C \right] = (\vec{\omega}_K^{IO})_C \times \left[(\vec{\omega}_K^{OC})_C \times (\vec{v}_K^R)_C^E \right]. \quad (5.23)$$

The resulting relation shows that the difference in omitting the Coriolis jerk due to the angular rate $(\vec{\omega}_K^{IO})_C \in \mathbb{R}^3$ emanating from the accelerations and specific forces on either side of the jerk dynamics from Eq. (5.9) has a magnitude equivalent to the vector product of the angular rate $(\vec{\omega}_K^{IO})_C \in \mathbb{R}^3$ with the inter-axis coupling term $(\vec{\omega}_K^{OC})_C \times (\vec{v}_K^R)_C^E$ in the C -frame translation motion. Given the low magnitude of the angular rate $(\vec{\omega}_K^{IO})_C \in \mathbb{R}^3$, the omission of these terms has negligible effects on the jerk translation dynamics.

Vector	Range and Magnitude		
Components	$(\vec{\omega}_K^{IO})_C, \text{ rad/s}$	$(\vec{f}^R)_C, \text{ m/s}^2$	$\max((\vec{\omega}_K^{IO})_C \times (\vec{f}^R)_C), \text{ m/s}^3$
x	$[0, 5.14] \times 10^{-5}$	$[-3, 3]$	8.0×10^{-3}
y	$[-6.87, 0] \times 10^{-5}$	$[-10, 10]$	2.5×10^{-3}
z	$[-7.69, 7.69] \times 10^{-4}$	$[-15.8, -3.8]$	5.0×10^{-4}

Table 5.4: Maximum magnitude of jerk emanating from specific forces in C -frame due to $(\vec{\omega}_K^{IO})_C$

5.1.3 Jerk Translation Equations of Motion

An order analysis of the terms in the C -frame jerk translation dynamics derived in Eq. (5.9) was performed in Section 5.1.2. Deducing from the order analysis, terms pertaining to

N.1.1 Triple cross products

N.1.2 Coriolis jerk due to the angular rate $(\vec{\omega}_K^{IO})_C$

N.1.3 Jerk emanating from specific forces $(\vec{f}^R)_C$ due to the angular rate $(\vec{\omega}_K^{IO})_C$

are neglected based on the reasoning that their effect is small enough such that it is counteracted by the controller designed in the section 5.2. Moreover, the specific force rate $(\dot{\vec{f}}^R)_C \in \mathbb{R}^3$ term from Eq. (5.9) is separated into the components emanating from accelerations (proper and improper) and the gravitational effects

$$(\dot{\vec{f}}^R)_C = (\dot{\vec{f}}_a^R)_C + (\dot{\vec{f}}_g^R)_C. \quad (5.24)$$

Consequently, the jerk-level equations of motion in the control frame emerge

$$\begin{aligned}
 & \text{Linear jerk} \quad \text{Centripetal jerk} \quad \text{Coriolis jerk due to } (\vec{\omega}_K^{OC})_C \\
 & \left(\ddot{\vec{V}}_K^R \right)_C^{ECC} + \left(\dot{\vec{\omega}}_K^{OC} \right)_C \times \left(\vec{V}_K^R \right)_C^E + \left(\vec{\omega}_K^{OC} \right)_C \times \left[2 \cdot \left(\dot{\vec{V}}_K^R \right)_C^{EC} + \left(\vec{a}_{oth} \right)_C \right] + \\
 & \text{Centrifugal jerk due to } (\vec{\omega}_K^{OC})_C \quad \left(\dot{\vec{f}}_K^R \right)_C \\
 & \left(\vec{\omega}_K^{OC} \right)_C \times \left[\left(\vec{\omega}_K^{OC} \right)_C \times \left(\vec{V}_K^R \right)_C^E \right] = \left(\dot{\vec{f}}_a^R \right)_C - \left(\vec{a}_{oth} \right)_C + \quad (5.25) \\
 & \left(\dot{\vec{f}}_g^R \right)_C + \left(\vec{\omega}_K^{OC} \right)_C \times \left(\vec{f}^R \right)_C.
 \end{aligned}$$

The terms associated with the Coriolis and the centrifugal jerk due to angular rate $(\vec{\omega}_K^{OC})_C \in \mathbb{R}^3$ are rearranged such that equality with the C -frame translation equations of motion in Eq. (5.1) is realized

$$\begin{aligned}
 & \left(\ddot{\vec{V}}_K^R \right)_C^{ECC} + \left(\dot{\vec{\omega}}_K^{OC} \right)_C \times \left(\vec{V}_K^R \right)_C^E + \left(\vec{\omega}_K^{OC} \right)_C \times \left(\dot{\vec{V}}_K^R \right)_C^{EC} \\
 & \quad \text{LHS of Eq. (5.1)} \\
 & \left(\vec{\omega}_K^{OC} \right)_C \times \left[\left(\dot{\vec{V}}_K^R \right)_C^{EC} + \left(\vec{\omega}_K^{OC} \right)_C \times \left(\vec{V}_K^R \right)_C^E + \left(\vec{a}_{oth} \right)_C \right] \\
 & \quad \text{RHS of Eq. (5.1)} \\
 & = \left(\dot{\vec{f}}_K^R \right)_C + \left(\dot{\vec{f}}_g^R \right)_C + \left(\vec{\omega}_K^{OC} \right)_C \times \left(\vec{f}^R \right)_C
 \end{aligned} \quad (5.26)$$

to cancel out the highlighted components from both sides of the equation. Finally, the jerk translation equations of motion in the C -frame are denoted

$$\left(\ddot{\vec{V}}_K^R \right)_C^{ECC} + \left(\dot{\vec{\omega}}_K^{OC} \right)_C \times \left(\vec{V}_K^R \right)_C^E + \left(\vec{\omega}_K^{OC} \right)_C \times \left(\dot{\vec{V}}_K^R \right)_C^{EC} = \left(\dot{\vec{f}}_K^R \right)_C + \left(\dot{\vec{f}}_g^R \right)_C. \quad (5.27)$$

The kinematic specific force rate $(\dot{\vec{f}}_K^R)_C \in \mathbb{R}^3$ only consists of the effects originating from changes in proper accelerations. The specific force rate originating from gravity field, though negligible for the application considered in this dissertation, is denoted by $(\dot{\vec{f}}_{K,g}^R)_C \in \mathbb{R}^3$.

5.1.4 Nonlinear Jerk-level Error Dynamics

This section derives nonlinear jerk level translation error dynamics, which are employed in the design of the unified trajectory controller for all phases of a VTOL transition/VTOL aircraft using Nonlinear Dynamic Inversion (NDI). In this case, NDI is used instead of the incremental inversion because the jerk error dynamics are pure kinematics, hence analytic inversion without any uncertainties is feasible. The derived error dynamics describe the build up of the error between the current aircraft position and a desired position on the planned trajectory. The resultant dynamics are purely kinematic comprising of all the nonlinearities originating due to inter-axis couplings of the aircraft kinematic motion in the full flight envelope of any VTOL transition/VTOL aircraft.

5.1.4.1 Trajectory Tracking Error Variables

The primary objective of the trajectory control module is to mitigate the deviation between the current aircraft position and a specific point on the desired trajectory, called the trajectory footpoint F . The current aircraft position is denoted by its reference point R .

In the previous works about error dynamics based trajectory controllers for a fixed-wing aircraft [99, 136], the trajectory tracking errors were defined in the trajectory frame T . The trajectory frame has its origin at the trajectory footpoint, and is obtained through rotation of the NED (O) frame by the trajectory course angle $\chi_T \in \mathbb{R}$ and climb angle $\gamma_T \in \mathbb{R}$ along the z_O and y_O axes respectively as illustrated in Fig. 5.3. Forward velocity control was decoupled from the trajectory control problem, which implies that explicit dependency on time was not considered. Consequently, the longitudinal component of the position deviation Δx_T and its derivative Δu_T dropped out from the control problem for the wingborne phase. In this case, the trajectory footpoint F lies at the foot of the perpendicular from the aircraft reference point R to the desired trajectory.

However, the unified trajectory controller proposed in this work considers track errors in the desired path frame (D) as shown by the Fig 5.3. The desired path frame originates at the trajectory footpoint F and is defined by rotation of the local NED frame through the desired heading angle $\Psi_D^F \in \mathbb{R}$.

For the hover flight phase the desired trajectory parameters and the track errors denoted in the desired path frame are directly provided by the Auto Take-Off and Landing (ATOL) trajectory generation module [215]. Additionally, for the forward velocity phases – transition and wingborne, the trajectory generation algorithm proposed in [117, 118] provides the feedforward commands and the deviation of the aircraft reference point R from the trajectory footpoint F denoted in the trajectory frame T . The feedforward and error terms denoted in the trajectory frame are transformed to the desired path frame before utilizing them in the trajectory control law.

The derivation of the unified trajectory controller performed in this chapter considers the trajectory tracking objective along all three axes of the desired path frame, thereby providing a generic formulation for the trajectory control law including the time constraint as well. However, if required the time dependency can be removed by disregarding the feedback of the longitudinal track error Δx_D and its higher order derivatives. In case of the forward velocity flight phases, the lateral track error in the trajectory frame Δy_T constitutes of both the longitudinal Δx_D and lateral Δy_D components in the desired path frame as illustrated in the Fig 5.3. As a result, the unified trajectory controller considers this additional x-component of the error terms in the desired frame to correct for any lateral deviations from the desired trajectory in the forward velocity phases. Such an additional longitudinal error component does not manifest in the lateral tracking objective for the hover flight phase since the ATOL module provides the position, velocity and acceleration errors in the D -frame readily. Similarly, the vertical deviation errors denoted in the D -frame are provided by the ATOL module for the hover

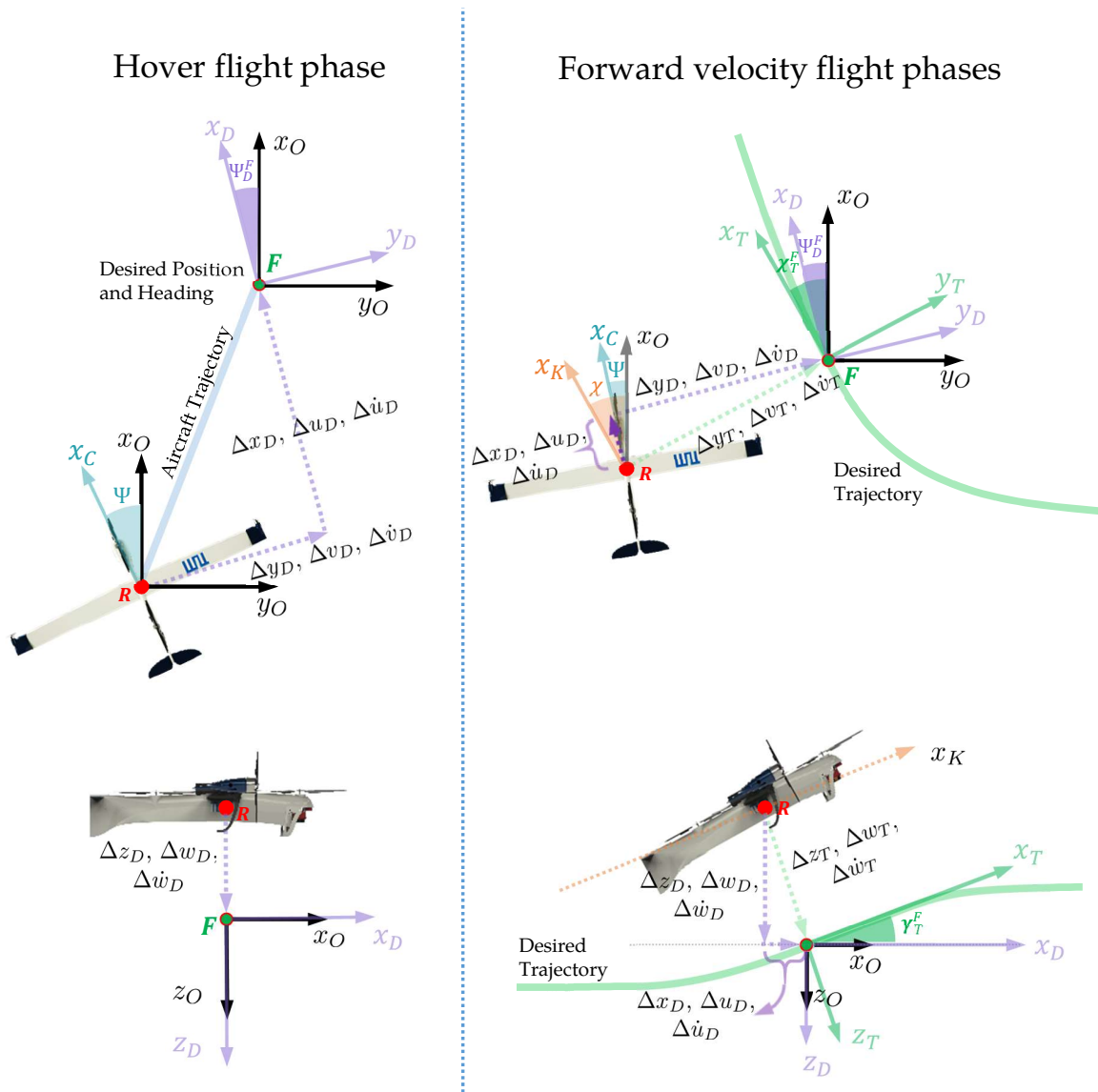


Figure 5.3: Trajectory tracking error variables

phase, whereas the trajectory generation module specifies the error and feedforward terms in the trajectory frame, which are transformed to the desired path frame. These transformations will be presented in the section 5.2.

Tracking error variables	Flight Phase		
	Hover	Transition	Wingborne
$\Delta x_D, \Delta u_D, \Delta \dot{u}_D$	✓	✓	✓
$\Delta y_D, \Delta v_D, \Delta \dot{v}_D$	✓	✓	✓
$\Delta z_D, \Delta w_D, \Delta \dot{w}_D$	✓	✓	✓
$\Delta \Psi, \Delta \dot{\Psi}$	✓	-	-

Table 5.5: Trajectory tracking error variables for each flight phase

In addition to reducing the deviation of the aircraft from the trajectory footpoint, the aircraft's heading orientation surfaces as a supplementary degree of freedom in the hover phase for the trajectory control module. Consequently, position change and hold is the predominant functionality of the trajectory control module in addition to the heading control in hover flight phase. Overall, the aim of the control strategy is to produce a command for the inner loop such the aircraft follows the trajectory footpoint. Table 5.5 summarizes all the tracking error variables utilized in each flight phase by the unified trajectory controller. Employing the feedforward along with the deviation error from the desired trajectory, the unified trajectory controller produces specific force rate commands to the inner loop controller such that the desired trajectory is followed. The attitude orientation of the aircraft is controlled by the inner loop controller based on flight dynamics constraints like turn coordination and drag minimization. The upcoming section derives the position jerk error dynamics denoted in the desired path frame to be used for designing the unified trajectory control law.

5.1.4.2 Derivation of the Position Jerk Error Dynamics in the D -Frame

The following derivation of the position jerk error dynamics does not neglect the error terms emanating from the transport rate and the curvature of the earth. To start with, consider the position of the aircraft reference point R with respect to the position on the desired trajectory represented by the desired trajectory footpoint F , which denotes the track error $(\vec{r}^{FR})_D \in \mathbb{R}^3$

$$(\vec{r}^{FR})_D = (\vec{r}^R)_D - (\vec{r}^F)_D = [\Delta x_D \quad \Delta y_D \quad \Delta z_D]^T. \quad (5.28)$$

The track error is differentiated until the third derivative to obtain the jerk level error dynamics. The first derivative of the position error in Eq. (5.28) with respect to the D -frame yields the velocity error relative to the desired path frame

$$\left(\frac{d}{dt}\right)^D \cdot (\vec{r}^{FR})_D \triangleq (\vec{V}_K^{FR})_D^D. \quad (5.29)$$

The velocity error in Eq. (5.29) is transformed to the deviation rate with respect to the Earth-Centered-Earth-Fixed ECEF frame (E)

$$\left(\frac{d}{dt}\right)^D \cdot (\vec{r}^{FR})_D = (\vec{V}_K^{FR})_D^D = (\vec{V}_K^{FR})_D^E + (\vec{\omega}_K^{DE})_D \times (\vec{r}^{FR})_D, \quad (5.30)$$

using the Euler differentiation rule for any vector \mathbf{X}

$$\left(\frac{d}{dt}\right)^B \cdot (\vec{X}^G)_B = (\dot{\vec{X}}^G)_B^B = (\dot{\vec{X}}^G)_B^A + (\vec{\omega}_K^{BA})_B \times (\vec{X}^G)_B. \quad (5.31)$$

Emanating from the velocity error in Eq. (5.30), the acceleration error is computed by differentiating further

$$\left(\dot{\vec{V}}_K^{FR}\right)_D^{DD} = \left(\dot{\vec{V}}_K^{FR}\right)_D^{ED} + (\vec{\omega}_K^{DE})_D^D \times (\vec{r}^{FR})_D + (\vec{\omega}_K^{DE})_D \times (\vec{V}_K^{FR})_D^D, \quad (5.32)$$

where the acceleration deviation $(\dot{\vec{V}}_K^{FR})_D^{ED} \in \mathbb{R}^3$ is reformulated in terms of the difference between the aircraft reference point acceleration $(\dot{\vec{V}}_K^R)_D^{ED} \in \mathbb{R}^3$ and the desired footpoint acceleration $(\dot{\vec{V}}_{des,K}^F)_D^{ED} \in \mathbb{R}^3$

$$\begin{aligned} (\dot{\vec{V}}_K^{FR})_D^{DD} &= \boxed{(\dot{\vec{V}}_K^R)_D^{ED} - (\dot{\vec{V}}_{des,K}^F)_D^{ED}} + (\vec{\omega}_K^{DE})_D^D \times (\vec{r}^{FR})_D + \\ &(\vec{\omega}_K^{DE})_D^D \times (\vec{V}_K^{FR})_D^D. \end{aligned} \quad (5.33)$$

The aircraft reference point acceleration with respect to the D -frame $(\dot{\vec{V}}_K^R)_D^{ED} \in \mathbb{R}^3$ is transformed to the acceleration relative to the control frame $(\dot{\vec{V}}_K^R)_D^{EC} \in \mathbb{R}^3$ using the Euler transformation rule described in Eq. (5.31)

$$(\dot{\vec{V}}_K^R)_D^{ED} = (\dot{\vec{V}}_K^R)_D^{EC} + (\vec{\omega}_K^{DC})_D \times (\vec{V}_K^R)_D^E \quad (5.34)$$

and substituted in the acceleration error $(\dot{\vec{V}}_K^{FR})_D^{DD} \in \mathbb{R}^3$ from Eq. (5.33) to yield

$$\begin{aligned} (\dot{\vec{V}}_K^{FR})_D^{DD} &= (\dot{\vec{V}}_K^R)_D^{EC} + (\vec{\omega}_K^{DC})_D \times (\vec{V}_K^R)_D^E - (\dot{\vec{V}}_{des,K}^F)_D^{ED} + \\ &(\vec{\omega}_K^{DE})_D^D \times (\vec{r}^{FR})_D + (\vec{\omega}_K^{DE})_D \times (\vec{V}_K^{FR})_D^D. \end{aligned} \quad (5.35)$$

Ultimately, the jerk error is derived by differentiating the acceleration error with respect to the desired path frame

$$\begin{aligned} (\ddot{\vec{V}}_K^{FR})_D^{DDD} &= (\ddot{\vec{V}}_K^R)_D^{ECD} + (\dot{\vec{\omega}}_K^{DC})_D^D \times (\vec{V}_K^R)_D^E + (\vec{\omega}_K^{DC})_D \times (\dot{\vec{V}}_K^R)_D^{ED} - \\ &(\ddot{\vec{V}}_{des,K}^F)_D^{EDD} + (\dot{\vec{\omega}}_K^{DE})_D^{DD} \times (\vec{r}^{FR})_D + (\vec{\omega}_K^{DE})_D^D \times (\dot{\vec{V}}_K^{FR})_D^D + \\ &(\dot{\vec{\omega}}_K^{DE})_D^D \times (\vec{V}_K^{FR})_D^D + (\vec{\omega}_K^{DE})_D \times (\dot{\vec{V}}_K^{FR})_D^{DD} \end{aligned} \quad (5.36)$$

and the common terms (highlighted) are added

$$\begin{aligned} (\ddot{\vec{V}}_K^{FR})_D^{DDD} &= (\ddot{\vec{V}}_K^R)_D^{ECD} + (\dot{\vec{\omega}}_K^{DC})_D^D \times (\vec{V}_K^R)_D^E + (\vec{\omega}_K^{DC})_D \times (\dot{\vec{V}}_K^R)_D^{ED} - \\ &(\ddot{\vec{V}}_{des,K}^F)_D^{EDD} + (\dot{\vec{\omega}}_K^{DE})_D^{DD} \times (\vec{r}^{FR})_D + 2 \cdot (\dot{\vec{\omega}}_K^{DE})_D^D \times (\vec{V}_K^{FR})_D^D + \\ &(\vec{\omega}_K^{DE})_D \times (\dot{\vec{V}}_K^{FR})_D^{DD}. \end{aligned} \quad (5.37)$$

Linear acceleration and jerk terms pertaining to the aircraft reference point, identified by the blue and green colors respectively, are recalculated with reference to the control frame by utilizing the Euler transformation rule from Eq. (5.31). Additionally, angular

rate and accelerations are expanded according to the relations

$$\begin{aligned}
 (\vec{\omega}_K^{DC})_D &= (\vec{\omega}_K^{DO})_D + (\vec{\omega}_K^{OC})_D, \\
 (\ddot{\vec{v}}_K^R)^{ECD} &= (\ddot{\vec{v}}_K^R)^{ECC} + (\vec{\omega}_K^{DC})_D \times (\dot{\vec{v}}_K^R)^{EC} \\
 &= (\ddot{\vec{v}}_K^R)^{ECC} + [(\vec{\omega}_K^{DO})_D + (\vec{\omega}_K^{OC})_D] \times (\dot{\vec{v}}_K^R)^{EC}, \\
 (\vec{\omega}_K^{DC})_D \times (\dot{\vec{v}}_K^R)^{ED} &= (\vec{\omega}_K^{DC})_D \times [(\dot{\vec{v}}_K^R)^{EC} + (\vec{\omega}_K^{DC})_D \times (\vec{v}_K^R)^E] \\
 &= [(\vec{\omega}_K^{DO})_D + (\vec{\omega}_K^{OC})_D] \times (\dot{\vec{v}}_K^R)^{EC} + \\
 &\quad (\vec{\omega}_K^{DC})_D \times [(\vec{\omega}_K^{DC})_D \times (\vec{v}_K^R)^E], \\
 (\vec{\omega}_K^{DC})_D &\stackrel{=0}{=} (\vec{\omega}_K^{DC})_D^C + \boxed{(\vec{\omega}_K^{DC})_D \times (\vec{\omega}_K^{DC})_D} = (\vec{\omega}_K^{DO})_D^C + (\vec{\omega}_K^{OC})_D^C.
 \end{aligned} \tag{5.38}$$

The terms resulting from the expansion specified in Eq. (5.38) are substituted back in the jerk error dynamics from Eq. (5.37)

$$\begin{aligned}
 (\ddot{\vec{v}}_K^{FR})_D^{DDD} &= (\ddot{\vec{v}}_K^R)^{ECC} + [(\vec{\omega}_K^{DO})_D^C + (\vec{\omega}_K^{OC})_D^C] \times (\vec{v}_K^R)^E + \\
 &\quad 2 \cdot [(\vec{\omega}_K^{DO})_D + (\vec{\omega}_K^{OC})_D] \times (\dot{\vec{v}}_K^R)^{EC} + \\
 &\quad (\vec{\omega}_K^{DC})_D \times [(\vec{\omega}_K^{DC})_D \times (\vec{v}_K^R)^E] - (\ddot{\vec{v}}_{des,K}^F)^{EDD} + \\
 &\quad (\vec{\omega}_K^{DE})_D^{DD} \times (\vec{r}^{FR})_D + 2 \cdot (\vec{\omega}_K^{DE})_D^D \times (\vec{v}_K^{FR})_D^D + (\vec{\omega}_K^{DE})_D \times (\dot{\vec{v}}_K^{FR})_D^{DD}.
 \end{aligned} \tag{5.39}$$

Additionally, the terms that correspond to the aircraft dynamics are assembled separately in the first row of the subsequent equation

$$\begin{aligned}
 (\ddot{\vec{v}}_K^{FR})_D^{DDD} &= (\ddot{\vec{v}}_K^R)^{ECC} + (\vec{\omega}_K^{OC})_D^C \times (\vec{v}_K^R)^E + 2 \cdot (\vec{\omega}_K^{OC})_D \times (\dot{\vec{v}}_K^R)^{EC} \\
 &\quad (\vec{\omega}_K^{DO})_D^C \times (\vec{v}_K^R)^E + 2 \cdot (\vec{\omega}_K^{DO})_D \times (\dot{\vec{v}}_K^R)^{EC} + \\
 &\quad (\vec{\omega}_K^{DC})_D \times [(\vec{\omega}_K^{DC})_D \times (\vec{v}_K^R)^E] - (\ddot{\vec{v}}_{des,K}^F)^{EDD} + \\
 &\quad \boxed{(\vec{\omega}_K^{DE})_D^{DD} \times (\vec{r}^{FR})_D + 2 \cdot (\vec{\omega}_K^{DE})_D^D \times (\vec{v}_K^{FR})_D^D + (\vec{\omega}_K^{DE})_D \times (\dot{\vec{v}}_K^{FR})_D^{DD}}.
 \end{aligned} \tag{5.40}$$

Based on the relation $(\vec{\omega}_K^{DE})_D = (\vec{\omega}_K^{DO})_D + (\vec{\omega}_K^{OE})_D$, the angular rate, acceleration and jerk terms related to $(\vec{\omega}_K^{DO})_D \in \mathbb{R}^3$ are separated from corresponding terms pertaining to the transport rate in the desired path frame $(\vec{\omega}_K^{OE})_D \in \mathbb{R}^3$ occurring in the last row of

Eq. (5.40)

$$\begin{aligned}
 \left(\ddot{\vec{V}}_K^{FR}\right)_D^{DDD} &= \left(\ddot{\vec{V}}_K^R\right)_D^{ECC} + \left(\dot{\vec{\omega}}_K^{OC}\right)_D^C \times \left(\vec{V}_K^R\right)_D^E + 2 \cdot \left(\dot{\vec{\omega}}_K^{OC}\right)_D \times \left(\dot{\vec{V}}_K^R\right)_D^{EC} \\
 &\quad \left(\dot{\vec{\omega}}_K^{DO}\right)_D^C \times \left(\vec{V}_K^R\right)_D^E + 2 \cdot \left(\dot{\vec{\omega}}_K^{DO}\right)_D \times \left(\dot{\vec{V}}_K^R\right)_D^{EC} + \\
 &\quad \left(\dot{\vec{\omega}}_K^{DC}\right)_D \times \left[\left(\dot{\vec{\omega}}_K^{DC}\right)_D \times \left(\vec{V}_K^R\right)_D^E \right] - \left(\ddot{\vec{V}}_{des,K}^F\right)_D^{EDD} + \\
 &\quad \boxed{\left(\ddot{\vec{\omega}}_K^{DO}\right)_D^{DD} \times \left(\vec{r}^{FR}\right)_D} + 2 \cdot \boxed{\left(\dot{\vec{\omega}}_K^{DO}\right)_D^D \times \left(\vec{V}_K^{FR}\right)_D^D} + \boxed{\left(\dot{\vec{\omega}}_K^{DO}\right)_D \times \left(\dot{\vec{V}}_K^{FR}\right)_D^{DD}} + \\
 &\quad \boxed{\left(\ddot{\vec{\omega}}_K^{OE}\right)_D^{DD} \times \left(\vec{r}^{FR}\right)_D} + 2 \cdot \boxed{\left(\dot{\vec{\omega}}_K^{OE}\right)_D^D \times \left(\vec{V}_K^{FR}\right)_D^D} + \boxed{\left(\dot{\vec{\omega}}_K^{OE}\right)_D \times \left(\dot{\vec{V}}_K^{FR}\right)_D^{DD}}.
 \end{aligned} \tag{5.41}$$

Furthermore, the highlighted cross products are replaced with skew-symmetric matrix multiplications, according to the transformations

$$\begin{aligned}
 \left[\left(\ddot{\vec{\omega}}_K^{DO}\right)_D^{DD} + \left(\ddot{\vec{\omega}}_K^{OE}\right)_D^{DD} \right] \times \left(\vec{r}^{FR}\right)_D &= \left[\left(\ddot{\Omega}^{DO}\right)_{DD}^{DD} + \left(\ddot{\Omega}^{OE}\right)_{DD}^{DD} \right] \cdot \left(\vec{r}^{FR}\right)_D, \\
 2 \cdot \left[\left(\dot{\vec{\omega}}_K^{DO}\right)_D^D + \left(\dot{\vec{\omega}}_K^{OE}\right)_D^D \right] \times \left(\vec{V}_K^{FR}\right)_D^D &= 2 \cdot \left[\left(\dot{\Omega}^{DO}\right)_{DD}^D + \left(\dot{\Omega}^{OE}\right)_{DD}^D \right] \cdot \left(\vec{V}_K^{FR}\right)_D^D, \\
 \left[\left(\dot{\vec{\omega}}_K^{DO}\right)_D + \left(\dot{\vec{\omega}}_K^{OD}\right)_D \right] \times \left(\dot{\vec{V}}_K^{FR}\right)_D^{DD} &= \left[\left(\Omega^{DO}\right)_{DD} + \left(\Omega^{OE}\right)_{DD} \right] \cdot \left(\dot{\vec{V}}_K^{FR}\right)_D^{DD},
 \end{aligned} \tag{5.42}$$

in the D -frame jerk level error dynamics from Eq. (5.41) to result in

$$\begin{aligned}
 \left(\ddot{\vec{V}}_K^{FR}\right)_D^{DDD} &= \left(\ddot{\vec{V}}_K^R\right)_D^{ECC} + \left(\dot{\vec{\omega}}_K^{OC}\right)_D^C \times \left(\vec{V}_K^R\right)_D^E + 2 \cdot \left(\dot{\vec{\omega}}_K^{OC}\right)_D \times \left(\dot{\vec{V}}_K^R\right)_D^{EC} \\
 &\quad \left(\dot{\vec{\omega}}_K^{DO}\right)_D^C \times \left(\vec{V}_K^R\right)_D^E + 2 \cdot \left(\dot{\vec{\omega}}_K^{DO}\right)_D \times \left(\dot{\vec{V}}_K^R\right)_D^{EC} + \\
 &\quad \left(\dot{\vec{\omega}}_K^{DC}\right)_D \times \left[\left(\dot{\vec{\omega}}_K^{DC}\right)_D \times \left(\vec{V}_K^R\right)_D^E \right] - \left(\ddot{\vec{V}}_{des,K}^F\right)_D^{EDD} + \\
 &\quad \left(\ddot{\Omega}^{DO}\right)_{DD}^{DD} \cdot \left(\vec{r}^{FR}\right)_D + 2 \cdot \left(\dot{\Omega}^{DO}\right)_{DD}^D \cdot \left(\vec{V}_K^{FR}\right)_D^D + \left(\Omega^{DO}\right)_{DD} \cdot \left(\dot{\vec{V}}_K^{FR}\right)_D^{DD} + \\
 &\quad \left(\ddot{\Omega}^{OE}\right)_{DD}^{DD} \cdot \left(\vec{r}^{FR}\right)_D + 2 \cdot \left(\dot{\Omega}^{OE}\right)_{DD}^D \cdot \left(\vec{V}_K^{FR}\right)_D^D + \left(\Omega^{OE}\right)_{DD} \cdot \left(\dot{\vec{V}}_K^{FR}\right)_D^{DD}.
 \end{aligned} \tag{5.43}$$

The resultant relation exhibits that the jerk-level position error dynamics expressed in the desired path frame are affine in deviation $\left(\vec{r}^{FR}\right)_D \in \mathbb{R}^3$, deviation rates $\left(\vec{V}_K^{FR}\right)_D^D \in \mathbb{R}^3$ as well as acceleration $\left(\dot{\vec{V}}_K^{FR}\right)_D^{DD} \in \mathbb{R}^3$. However, the nonlinearities occur in the kinematic states and the skew-symmetric matrices. The derivation of the error dynamics performed in this section delivers the contribution **C.4.1 Derivation of nonlinear jerk-level position error dynamics with respect to the desired path**.

Before commencing the derivation of the trajectory control law based on the derived jerk error dynamics, certain prerequisites are assumed to be fulfilled

- A.5.1** Smooth desired aircraft trajectory, i.e. position differentiable at least up to the fourth order and heading, course, climb angles at least until the third order, is available for all flight phases along with position, velocity and acceleration errors in the desired path frame.
- A.5.2** The inner loop controller is designed such that it can interface with the desired specific force rate outputs generated by the trajectory controller. In case, the specific force rate output interface is not available, either Euler angle rate command or Euler angle command interface shall also suffice.
- A.5.3** Wind rejection behavior is not specified by the trajectory controller (since it is purely kinematic). The behavior definition of wind disturbance must be specified by the inner loop e.g. like the wind disturbance rejection specification by the inner loop RM in section 3.3.3.4.

5.2 Unified Trajectory Control Law

Making use of the C -frame rigid body jerk dynamics derived in Eq. (5.27)

$$\left(\dot{\vec{f}}_K^R\right)_C^C + \left(\dot{\vec{f}}_g^R\right)_C^C = \left(\ddot{\vec{V}}_K^R\right)_C^{ECC} + \left(\dot{\vec{\omega}}_K^{OC}\right)_C^C \times \left(\vec{V}_K^R\right)_C^E + \left(\vec{\omega}_K^{OC}\right)_C \times \left(\dot{\vec{V}}_K^R\right)_C^{EC}, \quad (5.44)$$

the specific force jerk and gravitational jerk in the desired path frame can be obtained

$$\mathbf{M}_{DC} \cdot \left[\left(\dot{\vec{f}}_K^R\right)_C^C + \left(\dot{\vec{f}}_g^R\right)_C^C \right] = \left(\ddot{\vec{V}}_K^R\right)_D^{ECC} + \left(\dot{\vec{\omega}}_K^{OC}\right)_D^C \times \left(\vec{V}_K^R\right)_D^E + \left(\vec{\omega}_K^{OC}\right)_D \times \left(\dot{\vec{V}}_K^R\right)_D^{EC}, \quad (5.45)$$

which are substituted for the sum of the blue-colored terms in the jerk error dynamics from Eq. (5.43) resulting in

$$\begin{aligned} \left(\ddot{\vec{V}}_K^{FR}\right)_D^{DDD} &= \mathbf{M}_{DC} \cdot \left[\left(\dot{\vec{f}}_K^R\right)_C^C + \left(\dot{\vec{f}}_g^R\right)_C^C \right] \\ &= \left(\ddot{\vec{V}}_K^R\right)_D^{ECC} + \left(\dot{\vec{\omega}}_K^{OC}\right)_D^C \times \left(\vec{V}_K^R\right)_D^E + \left(\vec{\omega}_K^{OC}\right)_D \times \left(\dot{\vec{V}}_K^R\right)_D^{EC} + \\ &\quad \left(\vec{\omega}_K^{OC}\right)_D \times \left(\dot{\vec{V}}_K^R\right)_D^{EC} + \left(\dot{\vec{\omega}}_K^{DO}\right)_D^C \times \left(\vec{V}_K^R\right)_D^E + 2 \cdot \left(\vec{\omega}_K^{DO}\right)_D \times \left(\dot{\vec{V}}_K^R\right)_D^{EC} + \\ &\quad \left(\vec{\omega}_K^{DC}\right)_D \times \left[\left(\vec{\omega}_K^{DC}\right)_D \times \left(\vec{V}_K^R\right)_D^E \right] - \left(\ddot{\vec{r}}_{des,K}^F\right)_D^{EDD} + \\ &\quad \left(\ddot{\Omega}^{DO}\right)_{DD}^{DD} \cdot \left(\vec{r}^{FR}\right)_D + 2 \cdot \left(\dot{\Omega}^{DO}\right)_{DD}^D \cdot \left(\vec{V}_K^{FR}\right)_D^D + \left(\Omega^{DO}\right)_{DD} \cdot \left(\dot{\vec{V}}_K^{FR}\right)_D^{DD} + \\ &\quad \left(\ddot{\Omega}^{OE}\right)_{DD}^{DD} \cdot \left(\vec{r}^{FR}\right)_D + 2 \cdot \left(\dot{\Omega}^{OE}\right)_{DD}^D \cdot \left(\vec{V}_K^{FR}\right)_D^D + \left(\Omega^{OE}\right)_{DD} \cdot \left(\dot{\vec{V}}_K^{FR}\right)_D^{DD}. \end{aligned} \quad (5.46)$$

By specifying the trajectory deviations as the output $\mathbf{y} \in \mathbb{R}^3$ of the error dynamics

$$\mathbf{y} = \left(\vec{r}^{FR}\right)_D = \begin{bmatrix} \Delta x \\ \Delta y \\ \Delta z \end{bmatrix}_D, \quad (5.47)$$

the higher orders of the the position deviation by definition correspond to

$$\dot{\mathbf{y}} \triangleq \left(\vec{\mathbf{V}}_K^{FR} \right)_D^D, \quad \ddot{\mathbf{y}} \triangleq \left(\dot{\vec{\mathbf{V}}}_K^{FR} \right)_D^{DD}, \quad \dddot{\mathbf{y}} \triangleq \left(\ddot{\vec{\mathbf{V}}}_K^{FR} \right)_D^{DDD}. \quad (5.48)$$

Furthermore, the nonlinear terms in the rows 2 till 5 of the Eq. (5.46) are represented as $\mathbf{G}(\mathbf{x})$, thereby resulting in the trajectory tracking jerk-level error dynamics

$$\ddot{\mathbf{y}} = \mathbf{M}_{DC} \cdot \left(\dot{\vec{\mathbf{f}}}_K^R \right)_C^C + \overset{\Delta_g}{\mathbf{M}_{DC} \cdot \left(\dot{\vec{\mathbf{f}}}_{K,g}^R \right)_C^C} + \mathbf{G}(\mathbf{x}). \quad (5.49)$$

The terms in the error dynamics from Eq. (5.49) are further classified according to the definition of a generic nonlinear system. The acceleration deviation $\ddot{\mathbf{y}} \in \mathbb{R}^3$ is denoted as the pseudo control $\boldsymbol{\nu} \in \mathbb{R}^3$ which can be regulated using the specific forces $\left(\vec{\mathbf{f}}_K^R \right)_C \in \mathbb{R}^3$ generated by the aircraft effectors. Consequently, the specific forces are denoted as the control input \mathbf{u} for the derived system in Eq. (5.49). Since the error dynamics in Eq. (5.49) are specified at the jerk level, naturally the derivatives of pseudo control and control input are used. Additionally, Δ_g is the disturbance manifesting as a result of the change in the acceleration due to gravity. However, the magnitude of this disturbance term is negligible for the applications considered in this work. Therefore, this term is omitted in deriving the control law based on the premise that the error feedback controller (presented in section 5.2.4) suffices to counteract it.

Non-linear dynamic inversion (NDI) is used to compute the trajectory control law that generates the specific force rates commands in the C -frame, which are the control input rate commands $\dot{\mathbf{u}}_{cmd} \in \mathbb{R}^3$ specified by the trajectory controller to the inner loop control. The pre-requisite for the control input generation is the desired pseudo controls $\dot{\boldsymbol{\nu}}_{des} = \left(\ddot{\vec{\mathbf{V}}}_{des,K}^{FR} \right)_D^{DDD}$ that constitutes the feedforward and the feedback error jerk components required to make the aircraft follow the desired trajectory. Given a desired pseudo control derivative $\dot{\boldsymbol{\nu}}_{des} \in \mathbb{R}^3$, the control law is defined

$$\dot{\mathbf{u}}_{cmd} = \mathbf{M}_{CD} \cdot [\dot{\boldsymbol{\nu}}_{des} - \mathbf{G}(\mathbf{x})]. \quad (5.50)$$

The critical disadvantage of the reduction in the robustness of the NDI control strategy due to model uncertainties is averted in this application since the closed loop error dynamics in Eq. (5.49) contain only kinematic variables. Consequently, the aircraft modes such as the phugoid or short period mode that arise from its aerodynamic properties as well as higher order effects of actuator and sensor dynamics are deemed as inner loop characteristics, which are decoupled from the trajectory controller.

Before presenting the computation of the desired pseudo control rate, the components constituting the nonlinear function $\mathbf{G}(\mathbf{x})$

$$\begin{aligned}
 \mathbf{G}(\mathbf{x}) = & \overset{\mathbf{G}_{est}(\mathbf{x})}{\left(\vec{\omega}_K^{OC} \right)_D \times \left(\vec{v}_K^R \right)_D^{EC} + \left(\vec{\omega}_K^{DO} \right)_D^C \times \left(\vec{v}_K^R \right)_D^E + 2 \cdot \left(\vec{\omega}_K^{DO} \right)_D \times \left(\vec{v}_K^R \right)_D^{EC} +} \\
 & \overset{\mathbf{G}_{des}(\mathbf{x})}{\left(\vec{\omega}_K^{DC} \right)_D \times \left[\left(\vec{\omega}_K^{DC} \right)_D \times \left(\vec{v}_K^R \right)_D^E \right]} - \overset{\mathbf{G}_{err}(\mathbf{x})}{\left(\vec{v}_{des,K}^F \right)_D^{EDD}} + \quad (5.51) \\
 & \left(\ddot{\Omega}^{DO} \right)_{DD}^{DD} \cdot \left(\vec{r}^{FR} \right)_D + 2 \cdot \left(\dot{\Omega}^{DO} \right)_{DD}^D \cdot \left(\vec{v}_K^{FR} \right)_D^D + \left(\Omega^{DO} \right)_{DD} \cdot \left(\vec{v}_K^R \right)_D^{DD} + \\
 & \left(\ddot{\Omega}^{OE} \right)_{DD}^{DD} \cdot \left(\vec{r}^{FR} \right)_D + 2 \cdot \left(\dot{\Omega}^{OE} \right)_{DD}^D \cdot \left(\vec{v}_K^{FR} \right)_D^D + \left(\Omega^{OE} \right)_{DD} \cdot \left(\vec{v}_K^R \right)_D^{DD} .
 \end{aligned}$$

are elaborated. The nonlinear expression in Eq. (5.51) encapsulates

1. Parameters of the desired trajectory produced by the ATOL and the online trajectory generation module denoted by $\mathbf{G}_{des}(\mathbf{x})$.
 2. Kinematic states measurement and estimated variables like the horizontal side slip angle ε and its rate $\dot{\varepsilon}$ combined in $\mathbf{G}_{est}(\mathbf{x})$.
 3. Position, velocity and acceleration error states in the D frame denoted as $\left(\vec{r}^{FR} \right)_D \in \mathbb{R}^3$, $\left(\vec{v}_K^{FR} \right)_D^D \in \mathbb{R}^3$, and $\left(\vec{v}_K^R \right)_D^{DD} \in \mathbb{R}^3$ respectively, which are combined in $\mathbf{G}_{err}(\mathbf{x})$.
- In the following subsections, the constituents of the nonlinear term $\mathbf{G}(\mathbf{x})$ are elaborated.

5.2.1 Desired Trajectory Parameters in $\mathbf{G}(\mathbf{x})$

Desired Heading angle and higher order derivatives

The desired heading angle at the trajectory footpoint denoted in the desired path frame $\Psi_D^F \in \mathbb{R}$ along with its derivatives until the third order specify the direction of the planned trajectory. These desired trajectory parameters are contained within the skew symmetric matrix $\left(\Omega^{DO} \right)_{DD} \in \mathbb{R}^{3 \times 3}$ and its derivatives $\left(\dot{\Omega}^{DO} \right)_{DD}^D \in \mathbb{R}^{3 \times 3}$, $\left(\ddot{\Omega}^{DO} \right)_{DD}^{DD} \in \mathbb{R}^{3 \times 3}$ which lie in the fourth row of the jerk-level error dynamics from Eq. (5.46). These matrices are built from their corresponding angular rate $\left(\vec{\omega}_K^{DO} \right)_D \in \mathbb{R}^3$, acceleration $\left(\vec{\omega}_K^{DO} \right)_D^D \in \mathbb{R}^3$ and jerk $\left(\vec{\omega}_K^{DO} \right)_D^{DD} \in \mathbb{R}^3$

$$\left(\vec{\omega}_K^{DO} \right)_D = \begin{bmatrix} 0 \\ 0 \\ -\dot{\Psi}_D^F \end{bmatrix} \quad \left(\vec{\omega}_K^{DO} \right)_D^D = \begin{bmatrix} 0 \\ 0 \\ -\ddot{\Psi}_D^F \end{bmatrix} \quad \left(\vec{\omega}_K^{DO} \right)_D^{DD} = \begin{bmatrix} 0 \\ 0 \\ -\ddot{\Psi}_D^F \end{bmatrix} \quad (5.52)$$

according to the skew symmetric matrix structure defined in Eq. (2.4). Although, these matrices are defined in the error component $\mathbf{G}_{err}(\mathbf{x})$ of the nonlinear function in Eq. (5.51) since they are multiplied with the errors, it is important to note that they are constructed from the desired variables shown in Eq. (5.52). In addition to these

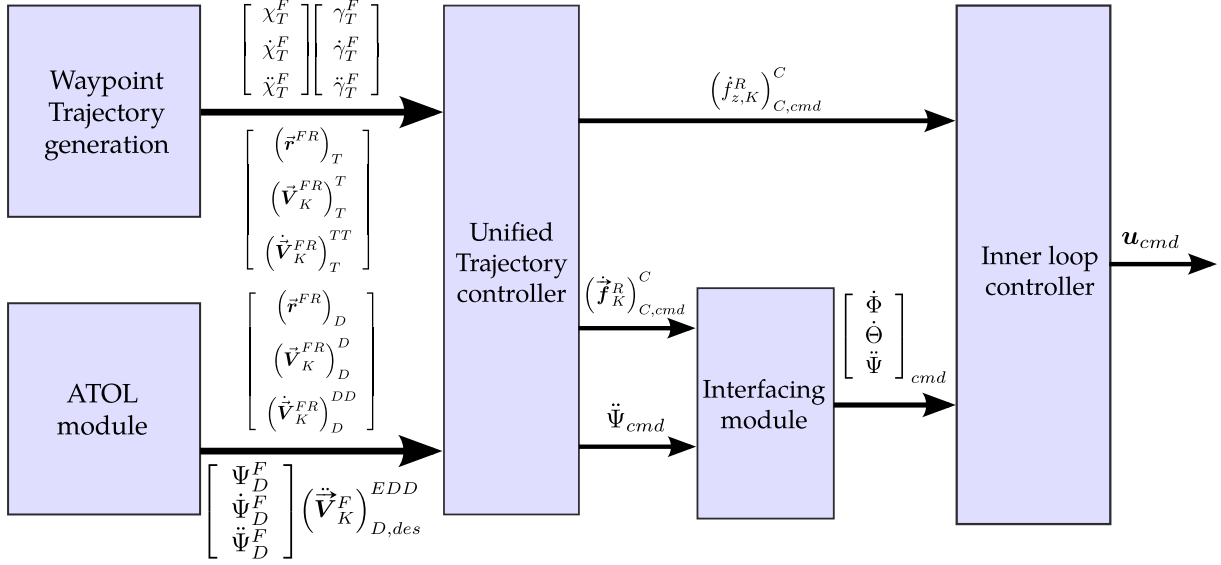


Figure 5.4: Guidance and control function framework

matrices, the desired trajectory parameters are also constituents of the angular rates $(\vec{\omega}_K^{DC})_D \in \mathbb{R}^3$ and the angular acceleration $(\vec{\omega}_K^{DO})_D^C \in \mathbb{R}^3$ that form vector products with measured velocities and accelerations in the first two rows of Eq. (5.51).

For the hover flight phase the desired heading angle rate $\dot{\Psi}_D^F \in \mathbb{R}$ and its derivatives are directly provided by the ATOL trajectory generation module [215], which are then utilized to construct the rotation rate, acceleration and jerk terms specified in Eq. (5.52). Additionally, the ATOL module provides position error $(\vec{r}^{FR})_D \in \mathbb{R}^3$, velocity error $(\vec{V}_K^{FR})_D^D \in \mathbb{R}^3$ and acceleration error $(\vec{V}_K^{FR})_D^{DD} \in \mathbb{R}^3$ denoted in the desired path frame as illustrated by Fig. 5.4. Together, these terms build up the nonlinear term $G(x)$, which is employed in the trajectory control law.

One of the major aspects of this unified trajectory control is to accommodate wind disturbance rejection behavior for all phases without affecting path following. Usually for a generic VTOL transition aircraft, cross wind disturbance rejection is achieved by banking the powered lift to counter the wind in the hover phase. This behavior is implicitly defined through the hover trajectory control's position hold function at the desired waypoint. Lateral wind disturbance leads to deviation in position which in turn produces lateral specific force rate command to the inner loop. The roll maneuver is then commanded by the inner loop in order to achieve the desired force rate command. Moreover, rejection of head or tail wind disturbance is primarily configuration dependent. The aircraft that possess traction systems can usually counteract a head wind using the horizontal propulsion units. The tail wind is resisted by tilting the vertical propulsion lift through a pitch angle to generate force in the negative x_K direction of the Kinematic frame. In case of multicopter configurations, which do not have any traction units, a negative pitch angle is also used to create the necessary force to neutralize the effect of head wind. Nonetheless, the trajectory controller remains configuration agnostic since it commands specific force rates to the inner loop which then achieves the desired force commands and fulfills the task of disturbance rejection depending on the available effectors.

However, consideration of wind disturbance rejection behavior is very critical in the forward velocity phases with high dynamic pressure, and especially for the proposed trajectory controller since it uses heading angle feedback which inherently contains wind direction information in case of a zero body lateral acceleration flight. As shown in Fig. 5.4 the trajectory generation algorithm [117, 118] used for the wingborne flight phase delivers desired trajectory course angle $\chi_T^F \in \mathbb{R}$ and its higher derivatives at the trajectory footpoint. Henceforth, the desired heading angle $\Psi_D^F \in \mathbb{R}$ and its rate, required by the unified trajectory controller are computed by utilizing the horizontal side slip angle $\varepsilon \in \mathbb{R}$ and its derivative $\dot{\varepsilon} \in \mathbb{R}$

$$\begin{aligned}\Psi_D^F &= \chi_T^F - \varepsilon, \\ \dot{\Psi}_D^F &= \dot{\chi}_T^F - \dot{\varepsilon}.\end{aligned}\tag{5.53}$$

The horizontal side slip angle $\varepsilon \in \mathbb{R}$ and rate $\dot{\varepsilon} \in \mathbb{R}$ are estimated by using C -frame velocity and acceleration measurements as demonstrated in Eqs. (2.56) and (2.58) respectively as

$$\begin{aligned}\varepsilon &= \arctan \left[\frac{(v_K^G)_C^E}{(u_K^G)_C^E} \right], \\ \dot{\varepsilon} &= \frac{(u_K^G)_C^{EC} \cdot (v_K^G)_C^E - (u_K^G)_C^E \cdot (v_K^G)_C^{EC}}{[(u_K^G)_C^E]^2 + [(v_K^G)_C^E]^2}.\end{aligned}\tag{5.54}$$

The calculation in Eq. (5.53) uses the feedback of the kinematic horizontal side-slip angle and rate in order to avoid conflict between the objectives of wind disturbance rejection and path deviation minimization. By removing the information pertaining to the real kinematic horizontal side-slip rate $\dot{\varepsilon} \in \mathbb{R}$ from the desired course angle rate $\dot{\chi}_T^F \in \mathbb{R}$, the effect of the yaw rotation rate required to achieve zero aerodynamic side slip or body lateral load factor is decoupled from the rotation rate needed for course change. As elaborated in the section 3.3.3.4, the wind disturbance rejection occurs through feedback of body lateral load factor to generate body yaw rate $r \in \mathbb{R}$ command, which is at the same dynamic level as the first derivative of the directional angles $\Psi \in \mathbb{R}$ and $\chi \in \mathbb{R}$. Consequently, subsequent higher order derivatives of the heading rate indicated in Eq. (5.52) are treated as equal to the corresponding derivatives of the desired course angle in the trajectory controller.

In addition to the derivatives of the desired heading angle until the third order, the angle itself is required for constructing the rotation matrix \mathbf{M}_{CD} for the control law in Eq. (5.50). The rotation matrix constitutes of the deviation of the true heading angle from the the desired heading angle $(\Psi_D^F - \Psi)$

$$\mathbf{M}_{CD} = \begin{bmatrix} \cos(\Psi_D^F - \Psi) & -\sin(\Psi_D^F - \Psi) & 0 \\ \sin(\Psi_D^F - \Psi) & \cos(\Psi_D^F - \Psi) & 0 \\ 0 & 0 & 1 \end{bmatrix}.\tag{5.55}$$

Transport rate and higher order derivatives in the D -frame

The skew symmetric matrix $(\boldsymbol{\Omega}^{OE})_{DD} \in \mathbb{R}^{3 \times 3}$ and its derivatives $(\dot{\boldsymbol{\Omega}}^{OE})_{DD}^D \in \mathbb{R}^{3 \times 3}$, $(\ddot{\boldsymbol{\Omega}}^{OE})_{DD}^{DD} \in \mathbb{R}^{3 \times 3}$, occurring in the last row of the closed loop error dynamics from Eq. (5.46), are constructed from the negative counterparts of transport rate, acceleration and jerk denoted in the desired path frame, which are detailed in Eqs. (5.56), (5.57) and (5.58) respectively. The transport rate and its higher order derivatives denoted in the D -frame contain the desired heading angle and its derivatives specified by the trajectory generation. Additionally, the feedback of WGS-84 latitude and longitude along with their derivatives until the third order occur in these terms. In [99], an order analysis on the individual elements of the transport rate and its derivative was performed. It was deduced from the order analysis that the effect of the cross product terms incorporating the transport rate and its derivative can be neglected because the maximum magnitude of their corresponding elements is limited to an order of 10^{-6} . Although, the order analysis was performed for the transport rate denoted in the Trajectory frame $(\vec{\omega}_K^{EO})_T$, rotation to the desired path frame together with the negative complement $(\vec{\omega}_K^{OE})_D$ does not alter the order of the terms.

The angular rate $(\vec{\omega}_K^{OE})_D \in \mathbb{R}^3$ denoted in the D -frame is given by the rotation of the negative transport rate $(\vec{\omega}_K^{OE})_O = -(\vec{\omega}_K^{EO})_O$ (Eq. (2.36)) denoted in the NED frame through the rotation matrix \mathbf{M}_{DO}

$$(\vec{\omega}_K^{OE})_D = \mathbf{M}_{DO} \cdot (\vec{\omega}_K^{OE})_O = \begin{bmatrix} \dot{\phi} \cdot \sin \Psi_D^F - \dot{\lambda} \cdot \cos \Psi_D^F \cdot \cos \phi \\ \dot{\phi} \cdot \cos \Psi_D^F + \dot{\lambda} \cdot \sin \Psi_D^F \cdot \cos \phi \\ \dot{\lambda} \cdot \sin \phi \end{bmatrix}. \quad (5.56)$$

First derivative of the angular rate $(\vec{\omega}_K^{OE})_D \in \mathbb{R}^3$ from Eq. (5.56) with respect to the desired path frame yields

$$(\dot{\vec{\omega}}_K^{OE})_D^D = \begin{bmatrix} \ddot{\phi} \cdot \sin \Psi_D^F - \ddot{\lambda} \cdot \cos \Psi_D^F \cdot \cos \phi + \dot{\Psi}_D^F \cdot \dot{\phi} \cdot \cos \Psi_D^F + \\ \dot{\lambda} \cdot \dot{\phi} \cdot \cos \Psi_D^F \cdot \sin \phi + \dot{\lambda} \cdot \dot{\phi} \cdot \sin \Psi_D^F \cdot \cos \phi \\ \ddot{\phi} \cdot \cos \Psi_D^F + \ddot{\lambda} \cdot \sin \Psi_D^F \cdot \cos \phi - \dot{\Psi}_D^F \cdot \dot{\phi} \cdot \sin \Psi_D^F + \\ \dot{\lambda} \cdot \dot{\phi} \cdot \cos \Psi_D^F \cdot \cos \phi - \dot{\lambda} \cdot \dot{\phi} \cdot \sin \Psi_D^F \cdot \sin \phi \\ \ddot{\lambda} \cdot \sin \phi + \dot{\lambda} \cdot \dot{\phi} \cdot \cos \phi \end{bmatrix}. \quad (5.57)$$

Subsequent differentiation of the angular acceleration $(\vec{\omega}_K^{OE})_D^D \in \mathbb{R}^3$ from Eq. (5.57) results in

$$(\vec{\omega}_K^{OE})_D^{DD} = \begin{bmatrix} \ddot{\phi} \cdot \sin \Psi_D^F - \dot{\Psi}_D^F \cdot \dot{\phi}^2 \cdot \sin \Psi_D^F - \ddot{\lambda} \cdot \cos \Psi_D^F \cdot \cos \phi + \\ \dot{\Psi}_D^F \cdot \ddot{\Psi}_D^F \cdot \cos \Psi_D^F + 2 \cdot \dot{\phi} \cdot \ddot{\phi} \cdot \cos \Psi_D^F + 2 \cdot \dot{\lambda} \cdot \dot{\phi}^2 \cdot \cos \Psi_D^F \cdot \cos \phi - \\ 2 \cdot \dot{\lambda} \cdot \dot{\phi}^2 \cdot \sin \Psi_D^F \cdot \sin \phi + \ddot{\Psi}_D^F \cdot \dot{\lambda} \cdot \sin \Psi_D^F \cdot \cos \phi + \\ 2 \cdot \ddot{\lambda} \cdot \dot{\phi} \cdot \cos \Psi_D^F \cdot \sin \phi + 2 \cdot \ddot{\lambda} \cdot \dot{\phi} \cdot \sin \Psi_D^F \cdot \cos \phi \\ \\ \ddot{\phi} \cdot \cos \Psi_D^F - 2 \cdot \dot{\phi} \cdot \ddot{\phi} \cdot \sin \Psi_D^F - \dot{\Psi}_D^F \cdot \dot{\phi}^2 \cdot \cos \Psi_D^F + \\ \ddot{\lambda} \cdot \sin \Psi_D^F \cdot \cos \phi - \dot{\Psi}_D^F \cdot \ddot{\Psi}_D^F \cdot \sin \Psi_D^F - 2 \cdot \dot{\lambda} \cdot \dot{\phi}^2 \cdot \cos \Psi_D^F \cdot \sin \phi - \\ 2 \cdot \dot{\lambda} \cdot \dot{\phi}^2 \cdot \sin \Psi_D^F \cdot \cos \phi + \ddot{\Psi}_D^F \cdot \dot{\lambda} \cdot \cos \Psi_D^F \cdot \cos \phi + \\ 2 \cdot \ddot{\lambda} \cdot \dot{\phi} \cdot \cos \Psi_D^F \cdot \cos \phi - 2 \cdot \ddot{\lambda} \cdot \dot{\phi} \cdot \sin \Psi_D^F \cdot \sin \phi \\ \\ -\dot{\lambda} \cdot \sin \phi \cdot \dot{\phi}^2 + 2 \cdot \ddot{\lambda} \cdot \cos \phi \cdot \dot{\phi} + \ddot{\lambda} \cdot \sin \phi \end{bmatrix}. \quad (5.58)$$

Desired Jerk

The desired jerk $(\vec{V}_{des,K}^F)_D^{EDD} \in \mathbb{R}^3$ is another important parameter of the reference trajectory. For the hover flight phase, the desired jerk constitutes the feedforward translation jerk from the ATOL module. The definition of the longitudinal jerk $(\ddot{u}_{des,K}^F)_D^{EDD} \in \mathbb{R}$ is derived either from position control to the next waypoint in the hover flight phase or from a velocity command when the transition to forward velocity phases is required. Similarly, the lateral jerk component $(\ddot{v}_{des,K}^F)_D^{EDD} \in \mathbb{R}$ is also generated using the principle of position or velocity control depending on whether displacement to a stationary waypoint or transition to the forward velocity phases is desired, respectively. The vertical desired jerk component $(\ddot{w}_{des,K}^F)_D^{EDD} \in \mathbb{R}$ is specified by the ATOL module using a reference vertical velocity command during take-off and landing. If a hover waypoint is specified with a height different than the current height, the desired vertical jerk is computed depending on the height difference between the aircraft position and the specified waypoint. Further details about the command generation by the ATOL module are covered in [215]. Therefore, in hover flight phase the desired jerk contains

$$(\vec{V}_{des,K}^F)_D^{EDD} = \begin{bmatrix} (\ddot{u}_{des,K}^F) \\ (\ddot{v}_{des,K}^F) \\ (\ddot{w}_{des,K}^F) \end{bmatrix}_D^{EDD}. \quad (5.59)$$

In the forward velocity flight, the unified trajectory controller's objective is reduced to path following, which implies that the time constraint to reach any desired waypoint is not considered. The trajectory controller only aims to reduce the deviation between the aircraft reference point and its perpendicular projection on the reference trajectory, which is denoted by the trajectory footpoint F [118]. Hence, the desired longitudinal translation jerk $(\ddot{u}_{des,K}^F)_D^{EDD}$ is dropped out. The feedforward for the lateral maneuver is implicitly included through the vector products of the planned trajectory rotational rate $(\vec{\omega}_K^{DO})_D$ and rotational acceleration $(\vec{\omega}_K^{DO})_D^C$ with the aircraft kinematic velocities and acceleration respectively. These feedforward elements for the lateral channel in the forward velocity flight phases are elaborated in the nonlinear terms constructed

using measurements or estimated variables $\mathbf{G}_{est}(\mathbf{x})$ by Eq. (5.77) and (5.78) in the next section 5.2.2. As a result, explicit feedforward in the lateral channel is also not defined through the desired translation jerk.

Nevertheless, the desired climb angle and its higher order derivatives that establish the feedforward jerk in the vertical channel do not appear in any measured or error based terms of the nonlinear function $\mathbf{G}(\mathbf{x})$. This occurs due to the coincidence of the z -axis in the C , D and NED frames. Hence, the rotation of the error and aircraft states with respect to the desired path frame do not contain any vertical axis elements. Therefore, the desired vertical jerk component $(\ddot{w}_{des,K}^F)_D^{EDD} \in \mathbb{R}$ is constructed from the trajectory footpoint's climb angle acceleration $\ddot{\gamma}_T^F \in \mathbb{R}$, climb angle rate $\dot{\gamma}_T^F \in \mathbb{R}$ and the climb angle $\gamma_T^F \in \mathbb{R}$ to incorporate these feedforward terms through the desired jerk $(\ddot{\mathbf{V}}_{des,K}^F)_D^{EDD} \in \mathbb{R}^3$ in the nonlinear function $\mathbf{G}(\mathbf{x})$ for the forward velocity flight phase. As illustrated in Fig. 5.4, the trajectory generation module specifies commands and errors in the trajectory (T) frame for the forward velocity flight phase. Subsequently, the desired jerk $(\ddot{\mathbf{V}}_{des,K}^F)_D^{EDD} \in \mathbb{R}^3$ is calculated from the components defined in the T -frame. Firstly, the acceleration with respect to the desired path frame is transformed according to the Euler rule from Eq. (5.31)

$$\left(\dot{\mathbf{V}}_K^F\right)_D^{ED} = \mathbf{M}_{DT} \cdot \left(\dot{\mathbf{V}}_K^F\right)_T^{ET} + \left(\boldsymbol{\omega}_K^{DT}\right)_D \times \left(\mathbf{V}_K^F\right)_D^E. \quad (5.60)$$

The resulting expression is differentiated relative to the desired path frame again

$$\left(\ddot{\mathbf{V}}_K^F\right)_D^{EDD} = \left(\ddot{\mathbf{V}}_K^F\right)_D^{ETD} + \left(\dot{\boldsymbol{\omega}}_K^{DT}\right)_D \times \left(\mathbf{V}_K^F\right)_D^E + \left(\boldsymbol{\omega}_K^{DT}\right)_D \times \left(\dot{\mathbf{V}}_K^F\right)_D^{ED}, \quad (5.61)$$

after which the corresponding jerk in the trajectory frame $(\ddot{\mathbf{V}}_K^F)_T^{ETT} \in \mathbb{R}^3$ is extracted

$$\left(\ddot{\mathbf{V}}_K^F\right)_D^{EDD} = \mathbf{M}_{DT} \cdot \left(\ddot{\mathbf{V}}_K^F\right)_T^{ETT} + \left(\boldsymbol{\omega}_K^{DT}\right)_D \times \left(\dot{\mathbf{V}}_K^F\right)_D^{ET} + \left(\dot{\boldsymbol{\omega}}_K^{DT}\right)_D \times \left(\mathbf{V}_K^F\right)_D^E + \left(\boldsymbol{\omega}_K^{DT}\right)_D \times \left(\dot{\mathbf{V}}_K^F\right)_D^{ED}. \quad (5.62)$$

The jerk and acceleration terms in the trajectory frame contain

$$\left(\ddot{\mathbf{V}}_K^F\right)_T^{ETT} = \begin{bmatrix} \left(\ddot{\mathbf{V}}_K^F\right)_T^{ETT} \\ 0 \\ 0 \end{bmatrix}, \quad \left(\dot{\mathbf{V}}_K^F\right)_T^{ET} = \begin{bmatrix} \left(\dot{\mathbf{V}}_K^F\right)_T^{ET} \\ 0 \\ 0 \end{bmatrix}. \quad (5.63)$$

The longitudinal jerk $(\ddot{\mathbf{V}}_K^F)_T^{ETT} \in \mathbb{R}$ and acceleration $(\dot{\mathbf{V}}_K^F)_T^{ET} \in \mathbb{R}$ component in Eq. (5.63) are nullified owing to the objective of maintaining a jerk minimal aircraft trajectory and removing the time constraint from the trajectory following problem. With this

consideration, the relation in Eq. (5.62) yields

$$\left(\ddot{\vec{V}}_K^F\right)_D^{EDD} = \left(\dot{\vec{\omega}}_K^{DT}\right)_D^D \times \left(\vec{V}_K^F\right)_D^E + \left(\vec{\omega}_K^{DT}\right)_D \times \left(\dot{\vec{V}}_K^F\right)_D^{ED}. \quad (5.64)$$

Additionally, for disregarding the time component of the trajectory following, trajectory footpoint velocity $\left(\vec{V}_K^F\right)_D^E \in \mathbb{R}^3$ and acceleration $\left(\dot{\vec{V}}_K^F\right)_D^{ED} \in \mathbb{R}^3$ are replaced in Eq. (5.64) by the estimated aircraft kinematic velocity $\left(\vec{V}_K^R\right)_D^E \in \mathbb{R}^3$ and acceleration $\left(\dot{\vec{V}}_K^R\right)_D^{ED} \in \mathbb{R}^3$ respectively, which are calculated as

$$\begin{aligned} \left(\vec{V}_K^R\right)_D^E &= \mathbf{M}_{DK} \cdot \left(\vec{V}_K^R\right)_K^E, \\ \left(\dot{\vec{V}}_K^R\right)_D^{ED} &= \mathbf{M}_{DK} \cdot \left(\dot{\vec{V}}_K^R\right)_K^{EK} + \left(\vec{\omega}_K^{DK}\right)_D \times \left[\mathbf{M}_{DK} \cdot \left(\vec{V}_K^R\right)_K^E\right], \end{aligned} \quad (5.65)$$

where $\left(\vec{V}_K^R\right)_K^E \in \mathbb{R}^3$ is the measured aircraft kinematic velocity denoted in the kinematic frame, $\left(\dot{\vec{V}}_K^R\right)_K^{EK} \in \mathbb{R}^3$ denotes the measured aircraft kinematic acceleration, $\mathbf{M}_{DK} \in \mathbb{R}^{3 \times 3}$ represents the frame rotation matrix from the kinematic frame to the desired path frame

$$\mathbf{M}_{DK} = \begin{bmatrix} \cos \gamma_K \cdot \cos \left(\Psi_D^F - \chi_K\right) & \sin \left(\Psi_D^F - \chi_K\right) & \cos \left(\Psi_D^F - \chi_K\right) \cdot \sin \gamma_K \\ -\cos \gamma_K \cdot \sin \left(\Psi_D^F - \chi_K\right) & \cos \left(\Psi_D^F - \chi_K\right) & -\sin \gamma_K \cdot \sin \left(\Psi_D^F - \chi_K\right) \\ -\sin \gamma_K & 0 & \cos \gamma_K \end{bmatrix} \quad (5.66)$$

and $\left(\vec{\omega}_K^{DK}\right)_D \in \mathbb{R}^3$ is the angular rotation rate of the kinematic frame relative to the desired path frame denoted in the D -frame

$$\left(\vec{\omega}_K^{DK}\right)_D = \begin{bmatrix} \dot{\gamma}_K \cdot \sin \left(\Psi_D^F - \chi_K\right) \\ \dot{\gamma}_K \cdot \cos \left(\Psi_D^F - \chi_K\right) \\ \dot{\chi}_K - \dot{\Psi}_D^F \end{bmatrix}_D. \quad (5.67)$$

Subsequently, the desired jerk $\left(\ddot{\vec{V}}_{des,K}^F\right)_D^{EDD} \in \mathbb{R}^3$ is defined by substituting the estimated aircraft velocity and acceleration denoted in the desired path frame from Eq. (5.65) in Eq. (5.64)

$$\begin{aligned} \left(\ddot{\vec{V}}_{des,K}^F\right)_D^{EDD} &= \left(\dot{\vec{\omega}}_K^{DT}\right)_D^D \times \left[\mathbf{M}_{DK} \cdot \left(\vec{V}_K^R\right)_K^E\right] + \\ &\left(\vec{\omega}_K^{DT}\right)_D \times \left[\mathbf{M}_{DK} \cdot \left(\dot{\vec{V}}_K^R\right)_K^{EK} + \left(\vec{\omega}_K^{DK}\right)_D \times \left[\mathbf{M}_{DK} \cdot \left(\vec{V}_K^R\right)_K^E\right]\right]. \end{aligned} \quad (5.68)$$

In the expression from Eq. (5.68), the desired climb rate $\dot{\gamma}_T^F \in \mathbb{R}$ appears in the rotation rate $\left(\vec{\omega}_K^{DT}\right)_D \in \mathbb{R}^3$

$$\left(\vec{\omega}_K^{DT}\right)_D = \begin{bmatrix} \dot{\gamma}_T^F \cdot \sin \left(\Psi_D^F - \chi_T^F\right) \\ \dot{\gamma}_T^F \cdot \cos \left(\Psi_D^F - \chi_T^F\right) \\ \dot{\chi}_T^F - \dot{\Psi}_D^F \end{bmatrix}_D. \quad (5.69)$$

Moreover, the desired climb rate $\dot{\gamma}_T^F \in \mathbb{R}$ and acceleration $\ddot{\gamma}_T^F \in \mathbb{R}$ also constitute the rotational acceleration $(\ddot{\omega}_K^{DT})_D^D$ in Eq. (5.68)

$$(\ddot{\omega}_K^{DT})_D^D = \begin{bmatrix} \ddot{\gamma}_T^F \cdot \sin(\Psi_D^F - \chi_T^F) + \dot{\gamma}_T^F \cdot \cos(\Psi_D^F - \chi_T^F) \cdot (\dot{\Psi}_D^F - \dot{\chi}_T^F) \\ \ddot{\gamma}_T^F \cdot \cos(\Psi_D^F - \chi_T^F) - \dot{\gamma}_T^F \cdot \sin(\Psi_D^F - \chi_T^F) \cdot (\dot{\Psi}_D^F - \dot{\chi}_T^F) \\ \ddot{\chi}_T^F - \ddot{\Psi}_D^F \end{bmatrix}. \quad (5.70)$$

As detailed earlier in this section, only the z -component of the desired jerk is used for construction of the nonlinear term $\mathbf{G}(x)$ in Eq. (5.51) for the forward velocity flight phase, thereby incorporating the feedforward in terms of the climb rate $\dot{\gamma}_T^F \in \mathbb{R}$ and acceleration $\ddot{\gamma}_T^F \in \mathbb{R}$ from the trajectory generation module. Subsequently, the vertical component of the desired jerk $(\ddot{w}_{des,K}^F)^{EDD}$ is elaborated with its individual elements

$$\begin{aligned} (\ddot{w}_{des,K}^F)^{EDD} &= V_K^R \cdot \dot{\gamma}_T^F \cdot (\dot{\chi}_T^F - \dot{\chi}_K) \cdot \sin(\chi_T^F - \chi_K) \cdot \cos \gamma_K + \\ &V_K^R \cdot \dot{\gamma}_T^F \cdot \dot{\gamma}_K \cdot \cos(\chi_T^F - \chi_K) \cdot \sin \gamma_K - \\ &(\dot{V}_K^R \cdot \dot{\gamma}_T^F + V_K^R \cdot \ddot{\gamma}_T^F) \cdot \cos(\chi_T^F - \chi_K) \cdot \cos \gamma_K. \end{aligned} \quad (5.71)$$

5.2.2 Measurements and Estimated Terms in $\mathbf{G}(x)$

The terms of the nonlinear function $\mathbf{G}(x)$, which are constructed from transformed sensor measurements and estimations based on sensor measurements are contained in the first two rows of the Eq. (5.51). These terms are collected together to form

$$\begin{aligned} \mathbf{G}_{est}(x) &= \begin{matrix} \text{Estimated} \\ \left(\vec{\omega}_K^{OC} \right)_D \end{matrix} \times \begin{matrix} \text{Measured} \\ \left(\vec{v}_K^R \right)_D^{EC} \end{matrix} + \begin{matrix} \text{Estimated} \\ \left(\vec{\omega}_K^{DO} \right)_D^C \end{matrix} \times \begin{matrix} \text{Measured} \\ \left(\vec{v}_K^R \right)_D^E \end{matrix} + 2 \cdot \begin{matrix} \text{Measured} \\ \left(\vec{\omega}_K^{DO} \right)_D \end{matrix} \times \begin{matrix} \text{Measured} \\ \left(\vec{v}_K^R \right)_D^{EC} \end{matrix} + \\ &\begin{matrix} \text{Estimated} \\ \left(\vec{\omega}_K^{DC} \right)_D \end{matrix} \times \left[\begin{matrix} \text{Estimated} \\ \left(\vec{\omega}_K^{DC} \right)_D \end{matrix} \times \begin{matrix} \text{Measured} \\ \left(\vec{v}_K^R \right)_D^E \end{matrix} \right]. \end{aligned} \quad (5.72)$$

Velocity $(\vec{v}_K^R)_D^E \in \mathbb{R}^3$ and acceleration $(\vec{v}_K^R)_D^{EC} \in \mathbb{R}^3$ contained in $\mathbf{G}_{est}(x)$ are denoted in the desired path frame. These terms are obtained by transforming the measurements of their C -frame counterparts using the frame rotation matrix \mathbf{M}_{DC} , which is equal to the transpose of the frame rotation matrix described in Eq. (5.55)

$$\begin{aligned} (\vec{v}_K^R)_D^E &= \mathbf{M}_{DC} \cdot (\vec{v}_K^R)_C^E, & (\vec{v}_K^R)_D^{EC} &= \mathbf{M}_{DC} \cdot (\vec{v}_K^R)_C^{EC}. \end{aligned} \quad (5.73)$$

The first term in Eq. (5.72) specifies the inter-axis coupling of the longitudinal and lateral accelerations $(\dot{u}_K^R)_C^{EC} \in \mathbb{R}$, $(\dot{v}_K^R)_C^{EC} \in \mathbb{R}$ in the C -frame due to the true heading angle rate $\dot{\Psi} \in \mathbb{R}$, which is estimated from the body rotational rate and Euler attitude angle measurements. Moreover, difference between the desired heading angle and the

measured heading angle $\Delta\Psi = \Psi_D^F - \Psi$ also affects the magnitude of the coupling

$$\left(\vec{\omega}_K^{OC}\right)_D \times \left(\vec{V}_K^R\right)_D^{EC} = \begin{bmatrix} -\dot{\Psi} \cdot \left[\left(\dot{v}_K^R\right)_C^{EC} \cdot \cos \Delta\Psi - \left(\dot{u}_K^R\right)_C^{EC} \cdot \sin \Delta\Psi \right] \\ \dot{\Psi} \cdot \left[\left(\dot{u}_K^R\right)_C^{EC} \cdot \cos \Delta\Psi + \left(\dot{v}_K^R\right)_C^{EC} \cdot \sin \Delta\Psi \right] \\ 0 \end{bmatrix}. \quad (5.74)$$

The second term in the first row of Eq. (5.72) contains the angular rotation acceleration $\left(\vec{\omega}_K^{DO}\right)_D^C \in \mathbb{R}^3$, which is extended using the Euler rule from Eq. (5.31)

$$\left(\vec{\omega}_K^{DO}\right)_D^C \times \left(\vec{V}_K^R\right)_D^E = \left[\left(\vec{\omega}_K^{DO}\right)_D^D + \left(\vec{\omega}_K^{CD}\right)_D \times \left(\vec{\omega}_K^{DO}\right)_D \right] \times \left(\vec{V}_K^R\right)_D^E. \quad (5.75)$$

The rotation acceleration $\left(\vec{\omega}_K^{DO}\right)_D^D \in \mathbb{R}^3$ and rotational rate $\left(\vec{\omega}_K^{DO}\right)_D \in \mathbb{R}^3$ used in the Eq. (5.75) were introduced in the Eq. (5.52). The rotation rate $\left(\vec{\omega}_K^{CD}\right)_D \in \mathbb{R}^3$ describes the rotation of the desired path frame with respect to the control frame denoted in the D -frame

$$\left(\vec{\omega}_K^{CD}\right)_D = \begin{bmatrix} 0 \\ 0 \\ \dot{\Psi}_D^F - \dot{\Psi} \end{bmatrix}, \quad (5.76)$$

which comprises the difference between the desired heading angle rate of the trajectory footpoint $\dot{\Psi}_D^F \in \mathbb{R}$ and the true heading angle rate $\dot{\Psi} \in \mathbb{R}$. Similar to the first term of the estimated nonlinear function $\mathbf{G}_{est}(x)$ in Eq. (5.74), the second term, which is elaborated in Eq. (5.75), also demonstrates an inter-axis coupling between the longitudinal and lateral channels through the respective velocities $\left(u_K^R\right)_C^E \in \mathbb{R}$ and $\left(v_K^R\right)_C^E \in \mathbb{R}$ denoted in the control frame. Contrarily, in this term the aircraft reference point velocity is coupled due to the desired heading angle acceleration $\ddot{\Psi}_D^F \in \mathbb{R}$

$$\left(\vec{\omega}_K^{DO}\right)_D^C \times \left(\vec{V}_K^R\right)_D^E = \begin{bmatrix} \ddot{\Psi}_D^F \cdot \left[\left(v_K^R\right)_C^E \cdot \cos \Delta\Psi - \left(u_K^R\right)_C^E \cdot \sin \Delta\Psi \right] \\ -\ddot{\Psi}_D^F \cdot \left[\left(u_K^R\right)_C^E \cdot \cos \Delta\Psi + \left(v_K^R\right)_C^E \cdot \sin \Delta\Psi \right] \\ 0 \end{bmatrix}. \quad (5.77)$$

Hence, this term constitutes a feedforward component generated from the desired heading angle acceleration $\ddot{\Psi}_D^F \in \mathbb{R}$ for all flight phases. Likewise, the third term of Eq. (5.72) specifies another inter-axis coupling feedforward component of the estimated kinematic acceleration $\left(\vec{V}_K^R\right)_D^{EC} \in \mathbb{R}^3$ due to desired heading angle rate $\dot{\Psi}_D^F \in \mathbb{R}$

$$2 \cdot \left(\vec{\omega}_K^{DO}\right)_D \times \left(\vec{V}_K^R\right)_D^{EC} = \begin{bmatrix} 2 \cdot \dot{\Psi}_D^F \cdot \left[\left(\dot{v}_K^R\right)_C^{EC} \cdot \cos \Delta\Psi - \left(\dot{u}_K^R\right)_C^{EC} \cdot \sin \Delta\Psi \right] \\ -2 \cdot \dot{\Psi}_D^F \cdot \left[\left(\dot{u}_K^R\right)_C^{EC} \cdot \cos \Delta\Psi + \left(\dot{v}_K^R\right)_C^{EC} \cdot \sin \Delta\Psi \right] \\ 0 \end{bmatrix}. \quad (5.78)$$

The last term in the Eq. (5.72) is the triple cross product, which exhibits the effect generated by the squared error in heading angle rate $\Delta\dot{\Psi}^2 = (\dot{\Psi}_D^F - \dot{\Psi})^2$ in presence of non-zero kinematic velocity on the jerk error

$$\left(\vec{\omega}_K^{DC}\right)_D \times \left[\left(\vec{\omega}_K^{DC}\right)_D \times \left(\vec{V}_K^R\right)_D^E\right] = \begin{bmatrix} -\Delta\dot{\Psi}^2 \cdot \left[\left(u_K^R\right)_C^E \cdot \cos \Delta\Psi + \left(v_K^R\right)_C^E \cdot \sin \Delta\Psi\right] \\ -\Delta\dot{\Psi}^2 \cdot \left[\left(v_K^R\right)_C^E \cdot \cos \Delta\Psi - \left(u_K^R\right)_C^E \cdot \sin \Delta\Psi\right] \\ 0 \end{bmatrix}. \quad (5.79)$$

With the aim of obtaining an expression that facilitates the software implementation of the part pertaining to the estimated variables in the nonlinear function $\mathbf{G}(\mathbf{x})$, the extended term from Eq. (5.75) is substituted in Eq. (5.72)

$$\begin{aligned} \mathbf{G}_{est}(\mathbf{x}) = & \left(\vec{\omega}_K^{OC}\right)_D \times \left(\vec{V}_K^R\right)_D^{EC} + \left[\left(\dot{\vec{\omega}}_K^{DO}\right)_D^D + \left(\vec{\omega}_K^{CD}\right)_D \times \left(\vec{\omega}_K^{DO}\right)_D\right] \times \left(\vec{V}_K^R\right)_D^E + \\ & 2 \cdot \left(\vec{\omega}_K^{DO}\right)_D \times \left(\vec{V}_K^R\right)_D^{EC} + \left(\vec{\omega}_K^{DC}\right)_D \times \left[\left(\vec{\omega}_K^{DC}\right)_D \times \left(\vec{V}_K^R\right)_D^E\right]. \end{aligned} \quad (5.80)$$

It is evident from the elements of the terms discussed in this sub-section there are no feedforward signals in this part of the nonlinear function for kinematic translation in the hover flight phase (zero kinematic velocity) and for the vertical channel in any flight phase. The feedforward terms for these channels were presented earlier in the section 5.2.1.

5.2.3 Error Terms in $\mathbf{G}(\mathbf{x})$

The error component of the nonlinear term $\mathbf{G}_{err}(\mathbf{x})$ contains the terms constituting the third row of the Eq. (5.51)

$$\begin{aligned} \mathbf{G}_{err}(\mathbf{x}) = & \left(\ddot{\Omega}^{DO}\right)_{DD}^{DD} \cdot \left(\vec{r}^{FR}\right)_D + 2 \cdot \left(\dot{\Omega}^{DO}\right)_{DD}^D \cdot \left(\vec{V}_K^{FR}\right)_D^D + \\ & \left(\Omega^{DO}\right)_{DD} \cdot \left(\dot{\vec{V}}_K^{FR}\right)_D^{DD}. \end{aligned} \quad (5.81)$$

It comprises of the angular rate, acceleration and jerk skew symmetric matrices built from their corresponding vectors defined in the Eq. (5.52) and the errors denoted in the desired path (D) frame. The ATOL module, illustrated in Fig. 5.4, relays the position, velocity and acceleration errors in the desired path frame. The unified trajectory controller can utilize the error terms in the D -frame directly to compute the error component of the nonlinear term $\mathbf{G}_{err}(\mathbf{x})$. However, the high speed waypoint trajectory generation module determines these errors in the trajectory frame. Consequently, the error terms are transformed relative to the D -frame in the framework of the unified trajectory controller

according to

$$\begin{aligned}
 (\vec{r}^{FR})_D &= \mathbf{M}_{DT} \cdot (\vec{r}^{FR})_T, \\
 (\vec{V}_K^{FR})_D^D &= \mathbf{M}_{DT} \cdot \left[(\vec{V}_K^{FR})_T^T + (\vec{\omega}_K^{DT})_T \times (\vec{r}^{FR})_T \right], \\
 (\dot{\vec{V}}_K^{FR})_D^{DD} &= \mathbf{M}_{DT} \cdot \left[(\dot{\vec{V}}_K^{FR})_T^{TT} + (\vec{\omega}_K^{DT})_T \times (\vec{V}_K^{FR})_T^T + (\dot{\vec{\omega}}_K^{DT})_T^T \times (\vec{r}^{FR})_T \right] + \\
 &\quad \mathbf{M}_{DT} \cdot (\boldsymbol{\Omega}^{DT})_{TT} \\
 &\quad \boxed{\dot{\mathbf{M}}_{DT}^D} \cdot \left[(\vec{V}_K^{FR})_T^T + (\vec{\omega}_K^{DT})_T \times (\vec{r}^{FR})_T \right].
 \end{aligned} \tag{5.82}$$

The frame rotation matrix derivative $\dot{\mathbf{M}}_{DT}^D \in \mathbb{R}^{3 \times 3}$ that appears in the acceleration error is expanded in terms of the frame rotation matrix $\mathbf{M}_{DT} \in \mathbb{R}^{3 \times 3}$ and the skew symmetric matrix $(\boldsymbol{\Omega}^{DT})_{TT} \in \mathbb{R}^{3 \times 3}$. Furthermore, the skew symmetric matrix multiplication occurring in the last term from Eq. (5.82) is reformulated using

$$(\boldsymbol{\Omega}^{AB})_{BB} \cdot (\vec{X}^G)_B = (\vec{\omega}_K^{AB})_B \times (\vec{X}^G)_B \tag{5.83}$$

to a vector product with the angular rotation rate of the trajectory frame with respect to the desired path frame $(\vec{\omega}_K^{DT})_T \in \mathbb{R}^3$

$$\begin{aligned}
 (\dot{\vec{V}}_K^{FR})_D^{DD} &= \mathbf{M}_{DT} \cdot \left[(\dot{\vec{V}}_K^{FR})_T^{TT} + (\vec{\omega}_K^{DT})_T \times (\vec{V}_K^{FR})_T^T + (\dot{\vec{\omega}}_K^{DT})_T^T \times (\vec{r}^{FR})_T \right] + \\
 &\quad \mathbf{M}_{DT} \cdot \left[(\vec{\omega}_K^{DT})_T \times \left[(\vec{V}_K^{FR})_T^T + (\vec{\omega}_K^{DT})_T \times (\vec{r}^{FR})_T \right] \right].
 \end{aligned} \tag{5.84}$$

The frame rotation matrix $\mathbf{M}_{DT} \in \mathbb{R}^{3 \times 3}$ used for the transformations in Eq. (5.84) is given by

$$\mathbf{M}_{DT} = \begin{bmatrix} \cos \gamma_T^F \cdot \cos (\Psi_D^F - \chi_T^F) & \sin (\Psi_D^F - \chi_T^F) & \sin \gamma_T^F \cdot \cos (\Psi_D^F - \chi_T^F) \\ -\cos \gamma_T^F \cdot \sin (\Psi_D^F - \chi_T^F) & \cos (\Psi_D^F - \chi_T^F) & -\sin \gamma_T^F \cdot \sin (\Psi_D^F - \chi_T^F) \\ -\sin \gamma_T^F & 0 & \cos \gamma_T^F \end{bmatrix}. \tag{5.85}$$

and the rotation rate $(\vec{\omega}_K^{DT})_T \in \mathbb{R}^3$ is denoted as

$$(\vec{\omega}_K^{DT})_T = \begin{bmatrix} (\dot{\Psi}_D^F - \dot{\chi}_T^F) \cdot \sin \gamma_T^F \\ \dot{\gamma}_T^F \\ -(\dot{\Psi}_D^F - \dot{\chi}_T^F) \cdot \cos \gamma_T^F \end{bmatrix}. \tag{5.86}$$

Finally, all the constituting terms of the nonlinear function $\mathbf{G}(\mathbf{x})$ for the full flight envelope of a VTOL transition aircraft have been detailed. It is coherent from the description of these components that the composition of the nonlinear function varies with the current flight phase of the aircraft. A summary specifying the origin of each component in the nonlinear function is elaborated in Table 5.6. The transition and wingborne flight phases have been combined into the forward velocity flight phase because the trajectory

Components of the nonlinear function $\mathbf{G}(\mathbf{x})$	Flight Phase	
	Hover	Forward velocity
Estimated Terms	Eqns. (5.74), (5.77), (5.78), (5.79) and (5.80) with desired heading angle, rate, and acceleration provided by the ATOL module	Eqns. (5.74), (5.77), (5.78), (5.79) and (5.80) with desired heading angle and rate computed using Eq. (5.53) from commands of online trajectory generation module
Desired Terms	Desired jerk in all axis from Eq. (5.59) specified by the ATOL module	Vertical desired jerk as shown in Eq. (5.71) using parameters specified by the online trajectory generation module
Error Terms	Position, velocity and acceleration errors provided by the ATOL module	Errors in D -frame calculated as per Eqns. (5.82) and (5.84)

Table 5.6: Composition of the nonlinear term $\mathbf{G}(\mathbf{x})$ for each flight phase

controller is derived by dynamic inversion of the kinematic error dynamics, and does not differentiate the flight phases based on the source of lift generation. Moreover, the structure of these error dynamics remains independent of the dynamic pressure as long as the aircraft is flying with a positive kinematic velocity. Therefore, the trajectory control problem is treated uniformly in transition and wingborne phases and similarly the composition of the nonlinear function $\mathbf{G}(\mathbf{x})$ also remains identical.

To recap the composition of the nonlinear term $\mathbf{G}(\mathbf{x})$ as summarized in the Table 5.6, the estimated terms denote the jerk deviation produced due to rotation of the measured kinematic velocity and acceleration if the true heading angle and its rate differ from the desired heading angle and rate, respectively. Moreover, these terms also provide the feedforward commands calculated from desired heading angle rate and acceleration. In the forward velocity phase, the trajectory generation module provides the desired course angle and rate, therefore the corresponding desired heading angle and rate are calculated using an estimate of the horizontal side slip variables ε and $\dot{\varepsilon}$ as shown in Eqs. (2.56) and (2.58) respectively.

The desired jerk specification is also flight phase dependent. While for the hover phase, the desired jerk is directly produced by the ATOL module, in the forward velocity phase only the vertical component of the desired jerk expressed in the desired path D frame is used. Since the waypoint trajectory generation module provides the desired

trajectory states only in the T frame, the desired vertical jerk in the D frame is computed according to Eq. (5.71) using the desired climb and course angle along with their derivatives specified by the trajectory generation module.

Similarly, rotation of the error deviation and its higher orders through the desired angular rate $(\vec{\omega}_K^{DO})_D$ acceleration $(\vec{\omega}_K^{DO})_D^D$ and jerk $(\vec{\omega}_K^{DO})_D^{DD}$ constitute the error terms, and are constructed from two sources depending on the flight phase. For the hover phase, the errors are directly specified by the ATOL module, however in the forward velocity mode the errors in the D frame are computed from the errors specified by the waypoint trajectory generation module in the trajectory frame according to the relations in Eq. (5.82).

5.2.4 Error Feedback Controller

As mentioned before, the position $(\vec{r}^{FR})_D \in \mathbb{R}^3$, velocity $(\vec{V}_K^{FR})_D^D \in \mathbb{R}^3$ and acceleration errors $(\vec{V}_K^{FR})_D^{DD} \in \mathbb{R}^3$ are either directly provided by the ATOL module or are calculated according to the Eq. (5.82) from the errors in the T -frame, which are specified by the waypoint trajectory generation module. The two sets of errors are blended based on the forward C -frame kinematic velocity $(u_K^R)_C^E$ using the sigmoid blending described in the section 3.3.4.1. As opposed to the hysteresis blending, the error states are blended using only one sigmoid element, similar to the function described in Eq. (3.147), independent of the transition direction between the hover and forward velocity phase.

Subsequently, the position, velocity, and acceleration error are combined together using a proportional error controller to generate the desired pseudo control rate $\dot{\nu}_{des} \in \mathbb{R}^3$

$$\dot{\nu}_{des} = -\mathbf{K}_r \cdot (\vec{r}^{FR})_D - \mathbf{K}_V \cdot (\vec{V}_K^{FR})_D^D - \mathbf{K}_a \cdot (\vec{V}_K^{FR})_D^{DD}. \quad (5.87)$$

Here $\mathbf{K}_r \in \mathbb{R}^{3 \times 3}$, $\mathbf{K}_V \in \mathbb{R}^{3 \times 3}$ and $\mathbf{K}_a \in \mathbb{R}^{3 \times 3}$ denote the diagonal positive definite matrices comprising of the proportional error gains for position, velocity and acceleration errors, respectively. The acceleration error gain matrix \mathbf{K}_a is chosen considering the dynamics of the inner loop controllers. For a VTOL transition aircraft, the inner loop usually the comprises of the rotational rate control loop for the lateral axis, however the force generation bandwidths in the longitudinal and vertical axes are directly limited by the bandwidth of the traction units and the LTUs respectively in hover flight. Additionally, the bandwidth for the vertical axes control varies depending on the dynamic pressure since the source of lift generation changes with it. Depending on the limiting bandwidth of the inner loop for each axis, the acceleration error gain matrix is defined using the time-scale separation principle. Similarly, the error gains matrices for lower order errors (velocity and position) are defined maintaining the time-scale separation between the control loops.

Contrarily, there is one difference when defining the error gains for a multicopter configuration. Since such aircraft operate only with powered-lift in the full flight mission, the gains for the trajectory deviations along the lateral as well as the longitudinal axis, as defined in Eq. (5.87), are always limited by the bandwidth of the corresponding rota-

tional rate control loop. The force generation bandwidth along the vertical channel does not vary substantially, therefore the choice of the gain related to the vertical trajectory error is only dependent on the dynamics of the LTUs.

Finally, employing the nonlinear term $\mathbf{G}(\mathbf{x})$ (composition in Table 5.6) along with the desired pseudo control rate $\dot{\boldsymbol{\nu}}_{des} \in \mathbb{R}^3$ delivered by the proportional error controller in the proposed law from Eq. (5.50), the unified trajectory control law encompassing all flight phases of a VTOL transition aircraft emanates

$$\left(\dot{\vec{\mathbf{f}}}_K^R\right)_{C,cmd}^C = \begin{bmatrix} \cos(\Psi_D^F - \Psi) & -\sin(\Psi_D^F - \Psi) & 0 \\ \sin(\Psi_D^F - \Psi) & \cos(\Psi_D^F - \Psi) & 0 \\ 0 & 0 & 1 \end{bmatrix} \cdot [\dot{\boldsymbol{\nu}}_{des} - \mathbf{G}(\mathbf{x})]. \quad (5.88)$$

The output of the unified trajectory control law is the specific force rate commands defined in the control frame $(\dot{\vec{\mathbf{f}}}_K^R)_{C,cmd}^C \in \mathbb{R}^3$. These specific force rate commands can either be incorporated directly in a inner loop controller based on the extended INDI strategy, which is covered in Chapter 4 or they can also be transformed to attitude angle rate commands, especially useful for multicopter VTOL aircraft, as covered later in the interfacing module of the trajectory controller. Subsequently, the concepts presented in this section provide the realization of the contribution **C.4.2 Unified trajectory control law for all flight phases of a VTOL transition aircraft**. The next section provides a linear state space formulation of the trajectory tracking jerk error dynamics combined with the unified trajectory control law defined in Eq. (5.88).

5.2.5 State-space Formulation: Jerk Error Dynamics and Unified Trajectory Control Law

A linear system formulation of the jerk error dynamics and the closed loop error dynamics obtained as a result of employing the feedback stabilizing error control law from Eq. (5.87) is presented in this section. With this aim, the jerk error dynamics derived in Eq. (5.46)

$$\begin{aligned} \left(\ddot{\vec{\mathbf{v}}}_K^{FR}\right)_D^{DDD} &= \left(\dot{\vec{\mathbf{f}}}_K^R\right)_D^C + \left(\dot{\vec{\mathbf{f}}}_g^R\right)_D^C + \left(\vec{\omega}_K^{OC}\right)_D \times \left(\dot{\vec{\mathbf{v}}}_K^R\right)_D^{EC} + \\ &\quad \left(\vec{\omega}_K^{DO}\right)_D^C \times \left(\vec{\mathbf{v}}_K^R\right)_D^E + 2 \cdot \left(\vec{\omega}_K^{DO}\right)_D \times \left(\dot{\vec{\mathbf{v}}}_K^R\right)_D^{EC} + \\ &\quad \left(\vec{\omega}_K^{DC}\right)_D \times \left[\left(\vec{\omega}_K^{DC}\right)_D \times \left(\vec{\mathbf{v}}_K^R\right)_D^E\right] - \left(\ddot{\vec{\mathbf{v}}}_{des,K}^F\right)_D^{EDD} + \\ &\quad \left(\ddot{\Omega}^{DE}\right)_{DD}^{DD} \cdot \left(\vec{\mathbf{r}}^{FR}\right)_D + 2 \cdot \left(\dot{\Omega}^{DE}\right)_{DD}^D \cdot \left(\vec{\mathbf{v}}_K^{FR}\right)_D^D + \left(\Omega^{DE}\right)_{DD} \cdot \left(\dot{\vec{\mathbf{v}}}_K^R\right)_D^{DD}. \end{aligned} \quad (5.89)$$

are formulated by transforming the cross product terms to skew-symmetric matrix multiplications

$$\begin{aligned}
 \left(\ddot{\vec{V}}_K^{FR}\right)_D^{DDD} &= \left(\dot{\vec{f}}_K^R\right)_D^C + \left(\dot{\vec{f}}_g^R\right)_D^C + [2 \cdot (\Omega^{DO})_{DD} + (\Omega^{OC})_{DD}] \cdot \left(\dot{\vec{V}}_K^R\right)_D^{EC} + \\
 &\quad [(\dot{\Omega}^{DO})_{DD}^C + [(\Omega^{DC})_{DD}]^2] \cdot \left(\vec{V}_K^R\right)_D^E - \left(\ddot{\vec{V}}_{des,K}^F\right)_D^{DDD} + \\
 &\quad \left(\ddot{\Omega}^{DE}\right)_{DD}^{DD} \cdot \left(\vec{r}^{FR}\right)_D + 2 \cdot \left(\dot{\Omega}^{DE}\right)_{DD}^D \cdot \left(\vec{V}_K^{FR}\right)_D^D + (\Omega^{DE})_{DD} \cdot \left(\dot{\vec{V}}_K^{FR}\right)_D^{DD}.
 \end{aligned} \tag{5.90}$$

In [216], the path following acceleration-level error dynamics were formulated as a Linear Time-Varying (LTV) system based on which a stability analysis of the trajectory controller from [99] was performed. Similarly, the jerk-level error dynamics from Eq. (5.90) can be represented as a linear system with the kinematic and gravity induced specific force rates combined in a total specific force derivative $\left(\dot{\vec{f}}_T^R\right)_D^C = \left(\dot{\vec{f}}_K^R\right)_D^C + \left(\dot{\vec{f}}_g^R\right)_D^C$ and considering an additional specific force rate component for control $\left(\dot{\vec{f}}_{ctrl}^R\right)_D^C \in \mathbb{R}^3$

$$\begin{aligned}
 \dot{e} &= \begin{bmatrix} \left(\dot{\vec{V}}_K^{FR}\right)_D^D \\ \left(\ddot{\vec{V}}_K^{FR}\right)_D^{DD} \\ \left(\ddot{\dot{\vec{V}}_K^{FR}}\right)_D^{DDD} \end{bmatrix} = \begin{bmatrix} \mathbf{0}_{3 \times 3} & \mathbf{I}_{3 \times 3} & \mathbf{0}_{3 \times 3} \\ \mathbf{0}_{3 \times 3} & \mathbf{0}_{3 \times 3} & \mathbf{I}_{3 \times 3} \\ \left(\ddot{\Omega}^{DE}\right)_{DD}^{DD} & 2 \cdot \left(\dot{\Omega}^{DE}\right)_{DD}^D & (\Omega^{DE})_{DD} \end{bmatrix} \cdot \begin{bmatrix} \left(\vec{r}^{FR}\right)_D^D \\ \left(\vec{V}_K^{FR}\right)_D^D \\ \left(\dot{\vec{V}}_K^{FR}\right)_D^{DD} \end{bmatrix} + \begin{bmatrix} \mathbf{0}_{3 \times 3} \\ \mathbf{0}_{3 \times 3} \\ \mathbf{I}_{3 \times 3} \end{bmatrix} \cdot \begin{bmatrix} \mathbf{r} \\ \left(\ddot{\vec{V}}_{des,K}^F\right)_D^{DDD} \end{bmatrix} + \\
 &\quad \begin{bmatrix} \mathbf{0}_{3 \times 3} & \mathbf{0}_{3 \times 3} & \mathbf{0}_{3 \times 3} \\ \mathbf{0}_{3 \times 3} & \mathbf{0}_{3 \times 3} & \mathbf{0}_{3 \times 3} \\ [(\dot{\Omega}^{DO})_{DD}^C + [(\Omega^{DC})_{DD}]^2] & [2 \cdot (\Omega^{DO})_{DD} + (\Omega^{OC})_{DD}] & \mathbf{I}_{3 \times 3} \end{bmatrix} \cdot \tag{5.91} \\
 &\quad \mathbf{g}_{ac} \\
 &\quad \begin{bmatrix} \left(\vec{V}_K^R\right)_D^E \\ \left(\dot{\vec{V}}_K^R\right)_D^{EC} \\ \left(\dot{\vec{f}}_T^R\right)_D^C + \left(\dot{\vec{f}}_{ctrl}^R\right)_D^C \end{bmatrix},
 \end{aligned}$$

where the reference input $\mathbf{r} \in \mathbb{R}^3$ is the desired jerk $\left(\ddot{\vec{V}}_{des,K}^F\right)_D^{DDD} \in \mathbb{R}^3$, $\mathbf{g}_{ac} \in \mathbb{R}^9$ represents the influence of the aircraft dynamics on the error derivative $\dot{e} \in \mathbb{R}^9$. Importantly, the error dynamics in Eq. (5.91) are linear in the error states $e \in \mathbb{R}^9$. Furthermore, the specific force rate component employed for trajectory control $\left(\dot{\vec{f}}_{ctrl}^R\right)_D^C \in \mathbb{R}^3$ in Eq. (5.91) is substituted with the stabilizing feedback error component of the control law defined in Eq. (5.87), thereby delivering the closed loop error dynamics in the form of a state

space model

$$\begin{aligned}
 \begin{bmatrix} (\vec{v}_K^{FR})_D^D \\ (\dot{\vec{v}}_K^{FR})_D^{DD} \\ (\ddot{\vec{v}}_K^{FR})_D^{DDD} \end{bmatrix} &= \begin{bmatrix} \mathbf{0}_{3 \times 3} & \mathbf{I}_{3 \times 3} & \mathbf{0}_{3 \times 3} \\ \mathbf{0}_{3 \times 3} & \mathbf{0}_{3 \times 3} & \mathbf{I}_{3 \times 3} \\ (\dot{\Omega}^{DE})_{DD}^{DD} & 2 \cdot (\dot{\Omega}^{DE})_{DD}^D & (\Omega^{DE})_{DD} \end{bmatrix} \cdot \begin{bmatrix} (\vec{r}_K^{FR})_D^D \\ (\vec{v}_K^{FR})_D^D \\ (\dot{\vec{v}}_K^{FR})_D^{DD} \end{bmatrix} + \\
 &\begin{bmatrix} \mathbf{0}_{3 \times 3} & \mathbf{0}_{3 \times 3} & \mathbf{0}_{3 \times 3} \\ \mathbf{0}_{3 \times 3} & \mathbf{0}_{3 \times 3} & \mathbf{0}_{3 \times 3} \\ -\mathbf{K}_r & -\mathbf{K}_V & -\mathbf{K}_a \end{bmatrix} \cdot \begin{bmatrix} (\vec{r}_K^{FR})_D^D \\ (\vec{v}_K^{FR})_D^D \\ (\dot{\vec{v}}_K^{FR})_D^{DD} \end{bmatrix} + \begin{bmatrix} \mathbf{0}_{3 \times 3} \\ \mathbf{0}_{3 \times 3} \\ \mathbf{I}_{3 \times 3} \end{bmatrix} \cdot \left(\ddot{\vec{v}}_{des,K}^F \right)_D^{DDD} + \\
 &\begin{bmatrix} \mathbf{0}_{3 \times 3} & \mathbf{0}_{3 \times 3} & \mathbf{0}_{3 \times 3} \\ \mathbf{0}_{3 \times 3} & \mathbf{0}_{3 \times 3} & \mathbf{0}_{3 \times 3} \\ [(\dot{\Omega}^{DO})_{DD}^C + [(\Omega^{DO})_{DD}]^2] & [2 \cdot (\Omega^{DO})_{DD} + (\Omega^{OC})_{DD}] & \mathbf{I}_{3 \times 3} \end{bmatrix} \cdot \begin{bmatrix} (\vec{v}_K^R)_D^E \\ (\dot{\vec{v}}_K^R)_D^{EC} \\ (\dot{\vec{f}}_T^R)_D^C \end{bmatrix}
 \end{aligned} \tag{5.92}$$

Like the methodology presented in [216], the closed loop linear system derived in the Eq. (5.92) can be utilized to assess stability of the unified jerk-level trajectory controller in a classical manner. The stability analysis of the proposed controller does not lie within the scope of this dissertation and will be covered in the future works.

The upcoming section briefs the framework of the trajectory control module, which focuses on being independent from any type of aircraft configuration.

5.3 Unified Trajectory Controller Framework

The unified trajectory controller framework comprises of five units, which are defined based on the type of terms that are required in the subsequent computation of the specific force derivative commands. The composition of the aforementioned terms is already covered in the section 5.2. This segment only deals with the organization of these elements in an efficient and modular software structure. As illustrated in Fig. 5.5, the units are classified as

1. Rotation matrices generator
2. Rotation rate acceleration jerk calculation
3. Translation states transformation
4. Nonlinear term composer
5. Unified trajectory control law.

Rotation Matrices Generator

As the name suggests, the *Rotation matrices generator* houses the computation of all the frame rotation matrices required in the unified trajectory controller framework. The inputs to this unit comprise of the desired as well as measured angles as reflected in the Table 5.7 along with their source of origin.

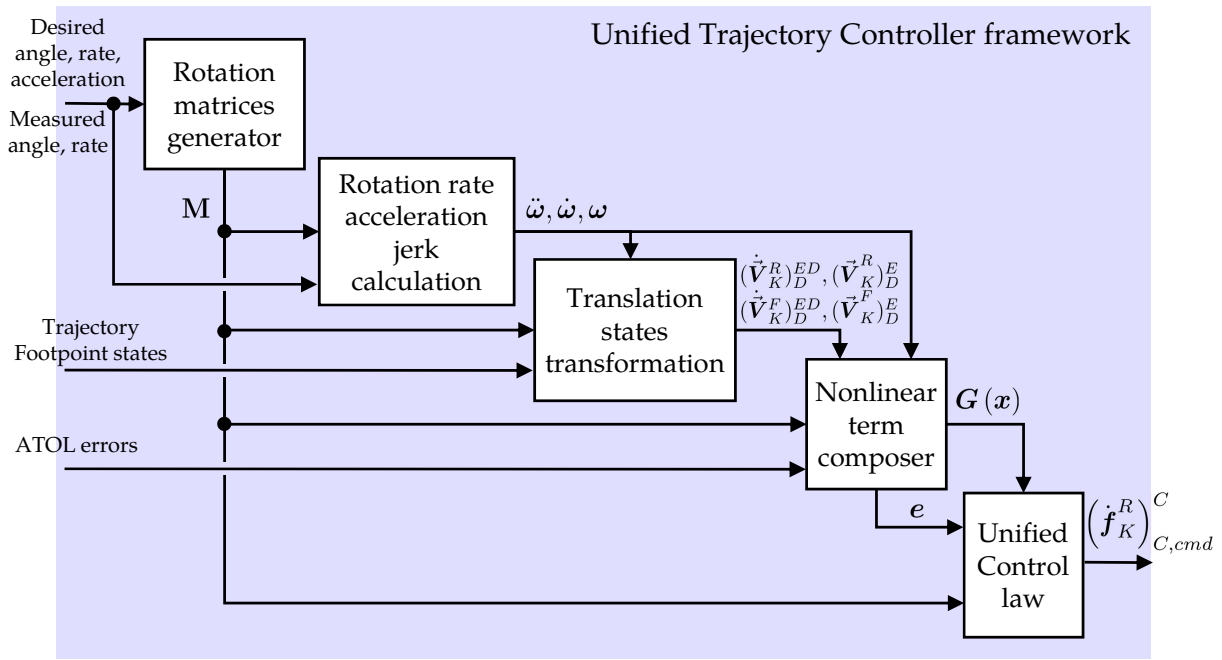


Figure 5.5: Aircraft configuration-agnostic Unified Trajectory Controller Framework

Angle	Origin source
Desired Heading Angle Ψ_D^F	ATOL module
Trajectory Course Angle χ_T^F	Waypoint trajectory generation module
Trajectory Climb Angle γ_T^F	Waypoint trajectory generation module
Kinematic Course Angle χ_K	Measurement
Kinematic Climb Angle γ_K	Measurement

Table 5.7: Inputs to the Rotation matrices generator unit

Subsequently, seven orthogonal frame rotation matrices and their inverses are calculated, through the transpose identity

$$\mathbf{M}_{BA} = \mathbf{M}_{AB}^T, \tag{5.93}$$

in this unit. The frame rotation matrices are summarized in Table 5.8. The rotation matrices computed in this module are employed by the rest of the units to compute further terms required in the unified trajectory control law.

Rotation Rate Acceleration Jerk Calculation

The *Rotation rate acceleration jerk calculation* houses the computations pertaining to the rotation rates, accelerations and jerk required by the *Translation states transformation* and *Nonlinear term $G(x)$ composer*. Inputs to the current unit comprise of desired angles and their higher order counterparts, specified by the ATOL module and the waypoint

Frame Rotation	Matrix symbol
Desired Path to NED frame	\mathbf{M}_{OD}
Desired Path to Trajectory frame	\mathbf{M}_{TD}
Desired Path to Kinematic frame	\mathbf{M}_{KD}
Control to NED frame	\mathbf{M}_{OC}
Control to Desired Path frame	\mathbf{M}_{DC}
Kinematic to NED frame	\mathbf{M}_{OK}
Trajectory to NED frame	\mathbf{M}_{OT}

Table 5.8: *Outputs of the Rotation matrices generator unit*

trajectory generation, along with the measured kinematic track angles and their rates. Moreover, frame rotation matrices \mathbf{M}_{DC} and \mathbf{M}_{TD} provided by the *Rotation matrices generator* are also employed in the calculations of the rotational variables. Table 5.9 enlists all the inputs utilized by the *Rotation rate acceleration jerk calculation unit*.

Inputs	Symbols
Desired Heading Angle until third order	$\Psi_D^F, \dot{\Psi}_D^F, \ddot{\Psi}_D^F, \dddot{\Psi}_D^F$
Trajectory Course Angle until second order	$\chi_T^F, \dot{\chi}_T^F, \ddot{\chi}_T^F$
Trajectory Climb Angle until second order	$\gamma_T^F, \dot{\gamma}_T^F, \ddot{\gamma}_T^F$
Kinematic Course Angle until first order	$\chi_K, \dot{\chi}_K$
Kinematic Climb Angle until first order	$\gamma_K, \dot{\gamma}_K$
Frame Rotation Matrices	$\mathbf{M}_{DC}, \mathbf{M}_{TD}$

Table 5.9: *Inputs to the Rotation rate acceleration jerk calculation unit*

The rotation rates calculated by the current module are summarized in the Table 5.10. Besides the rotation rates indicated in the referred Table, their inverse rotation rates are also provided simply by using the identity

$$\left(\vec{\omega}_K^{XY}\right)_Z = -\left(\vec{\omega}_K^{YX}\right)_Z. \quad (5.94)$$

In addition to the rotation rates, this unit also encompasses the computation of rotational accelerations and jerks. The rotational accelerations computed in this module include

1. Rotational acceleration of the NED frame relative to the D -frame denoted in the D -frame and derived with respect to the control frame $\left(\vec{\omega}_K^{DO}\right)_D^C$
2. Rotational acceleration of the desired path frame relative to the NED frame denoted in the D -frame and derived with respect to the desired path frame $\left(\vec{\omega}_K^{OD}\right)_D^D$
3. Rotational acceleration of the trajectory frame relative to the desired path frame denoted in the D -frame and derived with respect to the desired path frame $\left(\vec{\omega}_K^{DT}\right)_D^D$

4. Rotational acceleration of the trajectory frame relative to the desired path frame denoted in the T -frame and derived with respect to the trajectory frame $(\vec{\omega}_K^{DT})_T^T$.

Rotation Rate	Symbol
C -frame w.r.t. NED frame denoted in desired path (D) frame	$(\vec{\omega}_K^{OC})_D$
Desired path frame w.r.t. Control (C) frame denoted in D -frame	$(\vec{\omega}_K^{CD})_D$
Desired path frame w.r.t. NED frame denoted in D -frame	$(\vec{\omega}_K^{OD})_D$
D -frame w.r.t. Trajectory (T) frame denoted in D -frame	$(\vec{\omega}_K^{TD})_D$
D -frame w.r.t. Kinematic (K) frame denoted in D -frame	$(\vec{\omega}_K^{KD})_D$
Control frame w.r.t. NED frame denoted in C -frame	$(\vec{\omega}_K^{OC})_C$
Trajectory frame w.r.t. Desired path frame denoted in T -frame	$(\vec{\omega}_K^{DT})_T$

Table 5.10: Rotation rates for the unified trajectory control law

Furthermore, the rotational jerk of the desired path frame relative to the NED frame denoted in the D -frame and derived twice with respect to the desired path frame $(\vec{\omega}_K^{OD})_D^{DD}$ is also calculated.

Translation States Transformation

The purpose of the *Translation states transformation* involves

1. Transformation of the measured velocities and accelerations to the desired path frame
2. Transformation of the trajectory footpoint velocities and accelerations, provided by the waypoint trajectory generation, to the desired path frame

intended to be used in the construction of the nonlinear term $\mathbf{G}(\mathbf{x})$ by the *Nonlinear term composer*. The inputs required to perform these transformations comprise of measured kinematic velocities and accelerations along with the trajectory footpoint velocities and accelerations. Frame rotation matrices \mathbf{M}_{DC} , \mathbf{M}_{DK} and \mathbf{M}_{DT} are also employed in the

Inputs	Symbols
Measured/Estimated velocities	$(\vec{\mathbf{v}}_K^R)_C^E$
Measured/Estimated accelerations	$(\dot{\vec{\mathbf{v}}}_K^R)_C^{EC}$, $(\dot{\vec{\mathbf{v}}}_K^R)_K^{EK}$
Trajectory footpoint states	$(\vec{\mathbf{v}}_K^F)_T^E$, $(\vec{\mathbf{v}}_K^F)_T^{ET}$
Rotation rates	$(\vec{\omega}_K^{DK})_D$, $(\vec{\omega}_K^{DT})_T$
Frame rotation matrices	\mathbf{M}_{DC} , \mathbf{M}_{DK} , \mathbf{M}_{DT}

Table 5.11: Inputs to the Translation states transformation unit

transformations. Furthermore, rotation rates computed in the *Rotation rate acceleration jerk calculation* unit are also used here. Table 5.11 presents the inputs utilized by the *Translation states transformation* unit.

The transformed translation states are listed in the Table 5.12. The aircraft reference point velocity expressed in the desired path frame $(\vec{V}_K^R)_D^E$ and along with the kinematic acceleration denoted in the D -frame and derived relative to the C -frame $(\dot{\vec{V}}_K^R)_D^{EC}$ is calculated according to the Eq. (5.73). Moreover, the kinematic acceleration denoted in and derived relative to the D -frame $(\dot{\vec{V}}_K^R)_D^{ED}$ is computed using the Eq. (5.65). The trajectory footpoint velocity along the desired path frame $(\vec{V}_K^F)_D^E$ is given by rotation of the footpoint velocity specified in the trajectory frame through the rotation matrix M_{DT} , and the trajectory footpoint acceleration $(\dot{\vec{V}}_K^F)_D^{ED}$ denoted in and derived with respect to the D -frame is computed based on the Eq. (5.60). The translation states derived in this module are further used to construct the nonlinear term $G(x)$.

Transformed translation states	Symbols
Measured/Estimated velocities denoted in D -frame	$(\vec{V}_K^R)_D^E$
Measured/Estimated accelerations denoted in D -frame	$(\dot{\vec{V}}_K^R)_D^{EC}$, $(\dot{\vec{V}}_K^R)_D^{ED}$
Trajectory footpoint states denoted in D -frame	$(\vec{V}_K^F)_D^E$, $(\dot{\vec{V}}_K^F)_D^{ED}$

Table 5.12: Outputs from the Translation states transformation unit

Nonlinear Term Composer

The components of the nonlinear term $G(x)$, as elaborated in the section 5.2 are calculated in the *Nonlinear term composer* unit. The calculation of the nonlinear term is sub-divided in to three parts

1. The nonlinear jerk, which incorporates the desired terms from the ATOL module and the waypoint trajectory generation as detailed in the section 5.2.1
2. The nonlinear terms emanating from the measured/estimated aircraft states according to the definitions in the section 5.2.2
3. The error terms incorporating the deviation of the trajectory footpoint from the aircraft reference point as indicated in the section 5.2.3.

For the hover flight phase, the desired nonlinear jerk $(\ddot{\vec{V}}_{des,K}^F)_D^{EDD}$ is directly supplied by the ATOL module. However, for the forward flight phases, the desired jerk is computed according to Eq. (5.62) employing the frame rotation matrix M_{DT} , along with the rotational rate $(\vec{\omega}_K^{DT})_D$ and acceleration $(\dot{\vec{\omega}}_K^{DT})_D^D$ from the *Rotation matrices generator* and *Rotation rate acceleration jerk calculation* units respectively. Additionally, the kinematic velocity and acceleration of the trajectory footpoint denoted in the desired path frame as computed by the *Translation states transformation* unit are employed. Subsequently, the desired jerk from the ATOL module in hover flight phase and its corresponding

counterpart from the waypoint trajectory generation module in the forward flight phases are blended over aircraft kinematic velocity using a sigmoid function like the function described in Eq. (3.147).

The component of the nonlinear function $G(x)$ arising from the estimated aircraft states is agnostic of the flight phase. This component is simply computed based on the relation in the Eq. (5.80).

As stated before, the waypoint trajectory generation module specifies deviation of the aircraft reference point position, velocity and acceleration from the desired trajectory footpoint in the trajectory frame. Therefore, these errors are rotated to be specified in the D -frame according to the expressions detailed in the Eq. (5.82). Furthermore, the errors transformed from the T -frame and the errors provided by ATOL module are blended together similar to the blending carried out for the jerk component of the nonlinear function. Thereafter, the error component of the nonlinear term $G_{err}(x)$ is computed according to the Eq. (5.81). The blended errors for position, velocity and acceleration are also forwarded to the *Unified trajectory control law* unit to compute the desired pseudo control rate according to the Eq. (5.87).

Ultimately, the three components of the nonlinear term are summed up to deliver the full nonlinear term $G(x)$ for use in the trajectory control law.

Unified Control Law

Corresponding to its name, the *Unified Control law* unit implements the law defined in the Eq. (5.88). The desired pseudo control rate $\dot{\nu}_{des}$ is computed based on the position, velocity and acceleration deviation supplied by the error computation in the *Nonlinear term composer* in accordance with the Eq. (5.87). Furthermore, the nonlinear term $G(x)$ is subtracted from the desired pseudo control rate and rotated to the control frame using the frame rotation matrix M_{CD} presented by Eq. (5.55), thereby resulting in the specific force derivative commands denoted in and derived with respect to the C -frame.

As noted previously, the heading angle control appears as an additional degree of freedom in specifying the aircraft orientation in the hover flight phase. Therefore, in addition to the specific force rate commands, a heading angle acceleration command $\ddot{\Psi}_{cmd} \in \mathbb{R}$ is also calculated using the desired heading angle $\Psi_D^F \in \mathbb{R}$, rate $\dot{\Psi}_D^F \in \mathbb{R}$ and acceleration $\ddot{\Psi}_D^F \in \mathbb{R}$ (feedforward) from the ATOL module along with the heading angle Ψ and rate $\dot{\Psi} \in \mathbb{R}$ feedback through the control law

$$\ddot{\Psi}_{cmd} = \ddot{\Psi}_D^F + K_{\dot{\Psi}} \cdot (\dot{\Psi}_D^F - \dot{\Psi}) + K_{\Psi} \cdot (\Psi_D^F - \Psi). \quad (5.95)$$

An aircraft configuration agnostic structure of the unified trajectory controller is presented here. Modular units encompassing calculations of associated variables form the basis of the proposed framework. Therefore, any changes in the individual units can be carried out with relative ease without overhauling the complete architecture. The unified framework presented in this section relates to the contribution **C.4.3 Configuration-agnostic design of the unified trajectory control framework**. The next section defines an interface module for any multicopter platform having Euler attitude angle or rate based command variables for its inner loop control law.

5.4 Interface Module to Multicopter Configurations

The outputs of the unified trajectory controller framework include specific force derivative and heading angle acceleration commands. For an extended INDI (section 4.1) based inner loop control, the given trajectory controller commands can be incorporated directly if the control scheme is defined according to the works described in [86, 87]. Additionally, in this section an interface module generating commands for a generic multicopter platform having an inner loop control law with control variables as Euler attitude angle/rate and height rate is derived. The command variable set for such a platform is equivalent to that of the hover phase of the design reference model presented in the section 2.5. Common multicopter configurations [13, 33] do not possess any traction system, and therefore rely on tilting the powered lift through attitude angles to generate forces for translation in the horizontal plane. Therefore, the trajectory interface module has been developed according to the same constraints.

Two sets of control variables can be provided by the interface module depending on the structure of the inner loop being employed. The first set includes bank angle rate $\dot{\Phi}_{cmd} \in \mathbb{R}$ and pitch angle rate $\dot{\Theta}_{cmd} \in \mathbb{R}$ commands, which involves a direct transformation of the trajectory specific force rate commands $(\vec{f}_K^R)_C^C \in \mathbb{R}^3$ by making use of the specific force feedback. The second set is defined with the absolute bank angle $\Phi_{cmd} \in \mathbb{R}$ and pitch angle $\Theta_{cmd} \in \mathbb{R}$ commands, however it requires feedback of the Euler attitude angles. Corresponding to the two sets of the control variables, heading angle acceleration $\ddot{\Psi}_{cmd} \in \mathbb{R}$, calculated according to Eq. (5.95), is used as the control variable for the yaw channel in the first set or the heading angle rate command $\dot{\Psi}_{cmd} \in \mathbb{R}$ can be computed using the heading angle rate feedback and heading acceleration command for the second set of control variables. Likewise for vertical translation, either the vertical specific force rate command from the unified trajectory controller can be directly employed as in the extended INDI framework proposed by [86], or an absolute command can be specified by utilizing the vertical specific force feedback. The two control variable sets along with the required feedback signals are summarized in the Table 5.13. The mechanism for the generation of the two control variable sets is presented next.

Firstly, the generation of the Euler attitude rate commands is described. Using the expression for the tangent of the bank angle based on specific forces denoted in the C -frame by the Eq. (2.65) with the small angle assumption $\cos \Theta \approx 1$ yields

$$\Phi = \arctan \left[\frac{(f_y^R)_C}{-(f_z^R)_C} \right]. \quad (5.96)$$

The expression for bank angle rate emanates by further deriving the relation specified in the Eq. (5.96)

$$\dot{\Phi} = \frac{-(\dot{f}_y^R)_C \cdot (f_z^R)_C + (f_y^R)_C \cdot (\dot{f}_z^R)_C}{[(f_y^R)_C]^2 + [(f_z^R)_C]^2}. \quad (5.97)$$

For the implementation of the bank angle rate calculation derived in Eq. (5.97), feedback of the lateral specific force $(\hat{f}_y^R)_C \in \mathbb{R}$ and the vertical specific force $(\hat{f}_z^R)_C \in \mathbb{R}$ denoted in the C -frame are employed. The second term in the numerator containing the vertical

Control Variable sets	Required Feedback signals
$\begin{bmatrix} \dot{\Phi} \\ \dot{\Theta} \\ \dot{\Psi} \\ (f_z^R)_C^C \end{bmatrix}_{cmd}$	$\left(\hat{\mathbf{f}}_K^R \right)_C$
$\begin{bmatrix} \Phi \\ \Theta \\ \Psi \\ (f_z^R)_C \end{bmatrix}_{cmd}$	$\left(\hat{\mathbf{f}}_K^R \right)_C, \hat{\Phi}, \hat{\Theta}, \hat{\Psi}$

Table 5.13: Control variable sets produced by the Interface module for the Unified Trajectory Controller

specific force rate $(f_z^R)_C^C \in \mathbb{R}$ is omitted to avoid allocation of the vertical channel commands to the bank angle, thereby resulting in the bank angle rate command $\dot{\Phi}_{cmd} \in \mathbb{R}$ given by

$$\dot{\Phi}_{cmd} = \frac{-\left(\dot{f}_y^R\right)_{C,cmd} \cdot \left(\hat{f}_z^R\right)_C}{\left[\left(\hat{f}_y^R\right)_C\right]^2 + \left[\left(\hat{f}_z^R\right)_C\right]^2}. \quad (5.98)$$

Analogous to the relation for the bank angle given in Eq. (5.96), the pitch angle can also be specified using the longitudinal specific force along the control frame $(f_x^R)_C \in \mathbb{R}$

$$\Theta = \arctan \left[\frac{\left(f_x^R\right)_C}{\left(f_z^R\right)_C} \right]. \quad (5.99)$$

Employing the same procedure for calculation of the pitch angle rate as performed for the bank angle rate command generation in Eqs. (5.97) and (5.98), the following is obtained

$$\dot{\Theta}_{cmd} = \frac{\left(\dot{f}_x^R\right)_{C,cmd} \cdot \left(\hat{f}_z^R\right)_C}{\left[\left(\hat{f}_x^R\right)_C\right]^2 + \left[\left(\hat{f}_z^R\right)_C\right]^2}. \quad (5.100)$$

As said before, the second set of command variables for the inner loop comprise of the absolute bank and pitch angle commands. The absolute angle commands can be generated from the rate commands calculated by the Eqs. (5.98) and (5.100). An incremental angle command is computed based on the principle used in Eq. (4.11)

$$\begin{aligned} \Delta\Phi_{cmd} &= K_{\Phi}^{-1} \cdot \dot{\Phi}_{cmd}, \\ \Delta\Theta_{cmd} &= K_{\Theta}^{-1} \cdot \dot{\Theta}_{cmd}, \end{aligned} \quad (5.101)$$

where $K_\Phi \in \mathbb{R}$ and $K_\Theta \in \mathbb{R}$ represent the desired bandwidth for the bank and pitch angle response defined in the inner loop controller. Consequently, the absolute angle commands are obtained by adding the feedback of the Euler attitude angles to the incremental commands in the Eq. (5.101)

$$\begin{aligned}\Phi_{cmd} &= \hat{\Phi} + \Delta\Phi_{cmd}, \\ \Theta_{cmd} &= \hat{\Theta} + \Delta\Theta_{cmd}.\end{aligned}\tag{5.102}$$

Along the same lines, the heading angle rate command $\dot{\Psi}_{cmd} \in \mathbb{R}$ as well as the absolute vertical specific force command $(f_z^R)_{C,cmd} \in \mathbb{R}$ can also be calculated from the heading angle acceleration $\ddot{\Psi}_{cmd} \in \mathbb{R}$ and the vertical specific force rate command $(\dot{f}_z^R)_{C,cmd}^C \in \mathbb{R}$ respectively

$$\dot{\Psi}_{cmd} = \hat{\Psi} + K_{\dot{\Psi}}^{-1} \cdot \ddot{\Psi}_{cmd},\tag{5.103}$$

$$(f_z^R)_{C,cmd} = (\hat{f}_z^R)_C + K_{f_z}^{-1} \cdot (\dot{f}_z^R)_{C,cmd}^C,\tag{5.104}$$

where $K_{\dot{\Psi}} \in \mathbb{R}$ and $K_{f_z} \in \mathbb{R}$ denote the desired bandwidth of the heading angle rate and the vertical channel respectively, as specified in the inner loop control law. Hence, the given interface module can be used to connect the unified trajectory control module to any suitable inner loop controller of a multicopter aircraft having Euler attitude angle/rate command interface. This section provides the concepts pertaining to the contribution **C.4.4 Interface function for trajectory controller with inner loop control law incorporating conversion of specific force rate commands to attitude angle rate commands for a multicopter platform.**

5.5 Verification

In the context of the C2Land project at the Institute of Flight System Dynamics, Technische Universität München, the Unified Trajectory Control framework proposed in this chapter was verified using an INDI based inner loop controller for a generic multicopter configuration based on the aircraft illustrated in the Fig. 1.1c.

5.5.1 Reference Configuration

The generic multicopter configuration utilized for the verification of the unified trajectory control framework comprises of 18 LTUs having fixed-pitch propellers. The forces and moments generated by each propeller perpendicular to their plane of rotation is modeled in accordance with the relation described in Eq. (3.31)

$$\begin{aligned}F_P(t) &= k_T \cdot \omega_P^2(t), \\ N_P(t) &= -sgn[\omega_P(t)] \cdot k_N \cdot \omega_P^2(t),\end{aligned}\tag{5.105}$$

where $F_P(t) \in \mathbb{R}$ is the force produced by the propeller along its rotational axis whose positive direction is along the direction of the produced thrust, $k_T \in \mathbb{R}$ and $k_N \in \mathbb{R}$ denote the thrust and drag coefficients of the propeller respectively. Angular velocity

of the propeller is represented as $\omega_P(t) \in \mathbb{R}$, and $N_P(t) \in \mathbb{R}$ signifies the drag moment resulting from the drag force of the propeller. Dependency on time is omitted from here on for ease of reading.

Through the relation in Eq. (5.105), the propulsive lift is determined

$$\left(\vec{\mathbf{F}}_P^R\right)_B = \begin{bmatrix} 0 \\ 0 \\ \sum_{i=1}^{18} -k_{T,i} \cdot \omega_{P,i}^2 \cdot \cos \delta_{P,i} \end{bmatrix}, \quad (5.106)$$

where $k_{T,i} \in \mathbb{R}$ and $\omega_{P,i} \in \mathbb{R}$ are the thrust coefficient and rotational rate for each of the 18 LTUs. The mounting angle of each LTU with respect to their rotational axes is indicated by $\delta_{P,i}$, where $i = 1, 2, \dots, 18$. Since the body fixed vertical axis z_B is defined positive downwards and is parallel to the rotational axes of the propellers, the propulsive force is shown with a negative sign in the body fixed frame. The propulsive moments in the body frame $\left(\vec{\mathbf{M}}_P^R\right)_B \in \mathbb{R}^3$ are computed as

$$\left(\vec{\mathbf{M}}_P^R\right)_B = \begin{bmatrix} \sum_{i=1}^{18} -k_{T,i} \cdot \omega_{P,i}^2 \cdot \left(r_y^{RP_i}\right)_B \\ \sum_{i=1}^{18} k_{T,i} \cdot \omega_{P,i}^2 \cdot \left(r_x^{RP_i}\right)_B \\ \sum_{i=1}^{18} \text{sgn}[\omega_P] \cdot k_{N,i} \cdot \omega_{P,i}^2 - k_{T,i} \cdot \omega_{P,i}^2 \cdot \left| \left(r_x^{RP_i}\right)_B \right| \cdot \sin \delta_{P,i} \end{bmatrix}. \quad (5.107)$$

Here $\left(r_x^{RP_i}\right)_B \in \mathbb{R}$ and $\left(r_y^{RP_i}\right)_B \in \mathbb{R}$ indicate the x and y coordinates of the position of an LTUs with respect to the aircraft reference point R for $i = 1, 2, \dots, 18$. The drag coefficient of each LTU is denoted as $k_{N,i}$.

The aerodynamic drag force is modeled as a point mass drag model. The body drag force $\left(\vec{\mathbf{F}}_{A,D}^A\right)_B \in \mathbb{R}^3$ at the aircraft's aerodynamic center A is obtained using the body drag coefficients $C_{D,i} \in \mathbb{R}$ and the projected surface areas perpendicular to the body-fixed axes $S_i \in \mathbb{R}$ for $i = x, y, z$

$$\left(\vec{\mathbf{F}}_{A,D}^A\right)_B = -\bar{q} \cdot \begin{bmatrix} S_x \cdot C_{D,x} \\ S_y \cdot C_{D,y} \\ S_z \cdot C_{D,z} \end{bmatrix}. \quad (5.108)$$

The body drag force in Eq. (5.108) induces a drag moment because the aerodynamic center A does not coincide with the aircraft reference point R

$$\left(\vec{\mathbf{M}}_{A,D}^R\right)_B = \left(\vec{\mathbf{r}}^{RA}\right)_B \times \left(\vec{\mathbf{F}}_{A,D}^A\right)_B, \quad (5.109)$$

where $\left(\vec{\mathbf{r}}^{RA}\right)_B \in \mathbb{R}^3$ represents the position of the aircraft reference point R with respect to the aerodynamic center A . The gravitational forces and moments are modeled according to the Eqs. (3.52) and (3.53) respectively. This accomplishes the description about modeling of forces and moments performed in the plant model used for verification of the unified trajectory controller through Model-in-the-Loop (MIL) simulation.

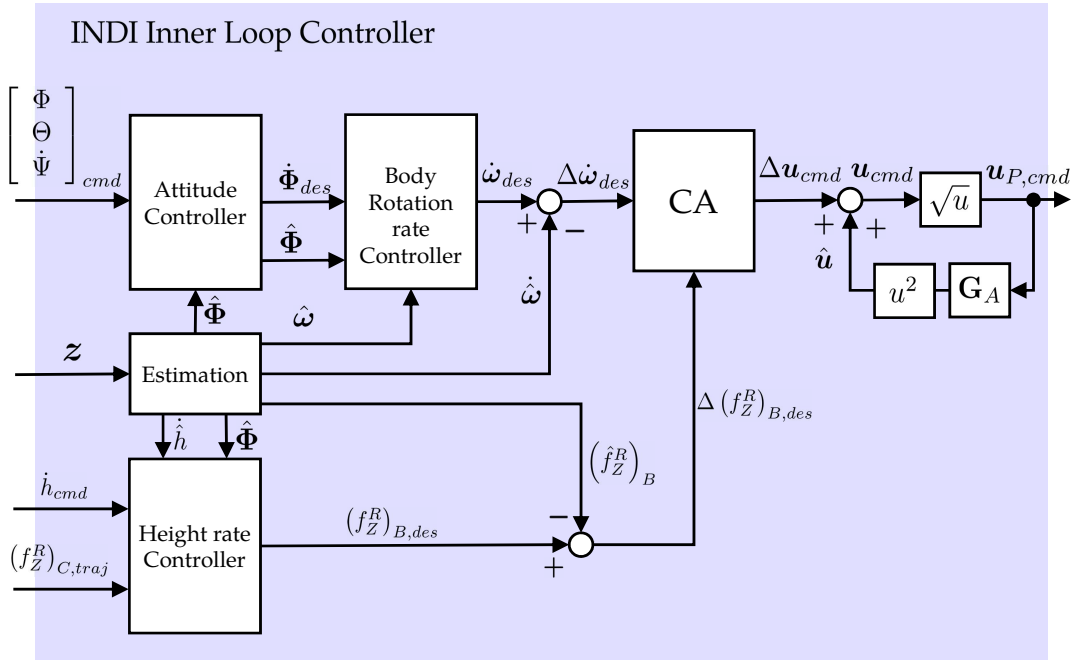


Figure 5.6: Simplified Inner Loop controller used in the verification of the Unified Trajectory controller

5.5.2 Inner Loop Controller

A simplified INDI based inner loop controller used for control of the multicopter configuration is demonstrated in the Fig. 5.6. This controller does not implement the strategies and algorithms presented in the chapter 4 pertaining to the jerk-level reference model with the extended INDI framework. However, only a simplified INDI controller is employed with the intention of specifically demonstrating the capability of the unified trajectory controller. The simplified INDI controller houses an attitude controller, which accepts bank angle $\Phi_{cmd} \in \mathbb{R}$, pitch angle $\Theta_{cmd} \in \mathbb{R}$ and heading angle rate $\dot{\Psi}_{cmd} \in \mathbb{R}$ as the command variables. For the attitude angle commands, first order linear reference models, based on the generalized structure described in the section 3.1.2, are employed to produce the reference attitude angle trajectories $\Phi_R \in \mathbb{R}$, $\Theta_R \in \mathbb{R}$ along with the attitude rate feedforward $\dot{\Phi}_R \in \mathbb{R}$, $\dot{\Theta}_R \in \mathbb{R}$. Furthermore, a stabilizing proportional error controller is employed to mitigate any deviations of the measured attitude angles $\hat{\Phi} \in \mathbb{R}$, $\hat{\Theta} \in \mathbb{R}$ with respect to the reference angles to generate the attitude error rate components

$$\begin{aligned}\dot{\Phi}_e &= K_{\Phi,e} \cdot (\Phi_R - \hat{\Phi}), \\ \dot{\Theta}_e &= K_{\Theta,e} \cdot (\Theta_R - \hat{\Theta}),\end{aligned}\tag{5.110}$$

where $K_{\Phi,e} \in \mathbb{R}$ and $K_{\Theta,e} \in \mathbb{R}$ are the proportional error gains for the bank and the pitch angle respectively. The attitude error rates from Eq. (5.110) are then added to the reference attitude rate feedforward

$$\begin{aligned}\dot{\Phi}_{des} &= \dot{\Phi}_R + \dot{\Phi}_e, \\ \dot{\Theta}_{des} &= \dot{\Theta}_R + \dot{\Theta}_e,\end{aligned}\tag{5.111}$$

thereby generating the desired attitude rate $\dot{\Phi}_{des} \in \mathbb{R}^3$

$$\dot{\Phi}_{des} = \begin{bmatrix} \dot{\Phi}_{des} \\ \dot{\Theta}_{des} \\ \dot{\Psi}_{cmd} \end{bmatrix}. \quad (5.112)$$

Here the heading angle rate command $\dot{\Psi}_{cmd} \in \mathbb{R}$ is directly fed to the desired attitude rates.

Furthermore, the desired attitude rates $\dot{\Phi}_{des} \in \mathbb{R}^3$ are commanded to the rotation rate controller. In the rotation rate controller, the first step is to compute the rotation rate commands $(\vec{\omega}_K^{OB})_{B,cmd} \in \mathbb{R}^3$ based on the desired attitude rates and the attitude feedback $\hat{\Phi} \in \mathbb{R}^3$

$$\begin{matrix} (\vec{\omega}_K^{OB})_{B,cmd} \\ \left[\begin{array}{c} p \\ q \\ r \end{array} \right]_{cmd} \end{matrix} = \begin{bmatrix} 1 & 0 & -\sin \hat{\Theta} \\ 0 & \cos \hat{\Phi} & \sin \hat{\Phi} \cdot \cos \hat{\Theta} \\ 0 & -\sin \hat{\Phi} & \cos \hat{\Phi} \cdot \cos \hat{\Theta} \end{bmatrix} \cdot \begin{bmatrix} \dot{\Phi}_{des} \\ \dot{\Theta}_{des} \\ \dot{\Psi}_{cmd} \end{bmatrix}. \quad (5.113)$$

After the calculation of the body rotation rate commands $(\vec{\omega}_K^{OB})_{B,cmd} \in \mathbb{R}^3$, the reference rotational rate trajectories $(\vec{\omega}_K^{OB})_{B,R} \in \mathbb{R}^3$ and rotational acceleration feedforward $(\dot{\vec{\omega}}_K^{OB})_{B,R}^B \in \mathbb{R}^3$ are generated from first order linear reference models. Subsequently, the desired body rotational acceleration $(\dot{\vec{\omega}}_K^{OB})_{B,des}^B \in \mathbb{R}^3$ is computed following the same process as performed in the attitude controller

$$(\dot{\vec{\omega}}_K^{OB})_{B,des}^B = (\dot{\vec{\omega}}_K^{OB})_{B,R}^B + \mathbf{K}_{\dot{\omega},e} \cdot \left((\vec{\omega}_K^{OB})_{B,R} - (\vec{\omega}_K^{OB})_B \right). \quad (5.114)$$

Here $\mathbf{K}_{\dot{\omega},e} \in \mathbb{R}^{3 \times 3}$ represents the diagonal error controller matrix for the rotation rates. Finally, the desired incremental rotational acceleration is computed

$$\Delta (\dot{\vec{\omega}}_K^{OB})_{B,des}^B = (\dot{\vec{\omega}}_K^{OB})_{B,des}^B - (\dot{\vec{\omega}}_K^{OB})_B^B. \quad (5.115)$$

The estimated angular acceleration $(\dot{\vec{\omega}}_K^{OB})_B^B \in \mathbb{R}^3$ is obtained from the derivative state of a second order roll-off filter as described in Eq. (4.97).

For the vertical channel, height rate $\dot{h}_{cmd} \in \mathbb{R}$ is the primary command variable in addition to the C -frame vertical specific force $(f_K^R)_{C,tra_j}$ as command interface for the trajectory controller. The specific force command can be activated in the height rate controller rather than switching to another controller. Firstly, the reference height rate $\dot{h}_R \in \mathbb{R}$ and reference vertical acceleration $\ddot{h}_R \in \mathbb{R}$ are specified using a first order linear reference model. The desired vertical acceleration $\ddot{h}_{des} \in \mathbb{R}$ is obtained by adding the stabilizing error controller component

$$\ddot{h}_{des} = \ddot{h}_R + K_{\dot{h},e} \cdot (\dot{h}_R - \dot{h}), \quad (5.116)$$

where $\dot{\hat{h}} \in \mathbb{R}$ is the measured height rate and $K_{\dot{h},e} \in \mathbb{R}$ is the proportional gain for the height rate error. The desired vertical specific force denoted in the C -frame can be obtained based on the desired vertical acceleration in Eq. (5.116)

$$\left(f_z^R\right)_{C,des} = -\ddot{h}_{des} - g. \quad (5.117)$$

Here $g \in \mathbb{R}$ denotes the acceleration due to gravity. When the trajectory controller is activated, the desired specific force in Eq. (5.117) is replaced with the specific force command $\left(f_z^R\right)_{C,tra} \in \mathbb{R}$ generated by the interface module described in the section 5.4. Furthermore, the desired specific force in the control frame is transformed to be denoted in the body fixed frame by using the relation in Eq. (2.64)

$$\left(f_z^R\right)_{B,des} = \frac{\left(f_z^R\right)_{C,des}}{\cos \hat{\Phi} \cdot \cos \hat{\Theta}}. \quad (5.118)$$

Ultimately, the desired incremental specific force $\left(f_z^R\right)_B \in \mathbb{R}$ is computed using a filtered measurement of the body fixed vertical specific force $\left(\hat{f}_z^R\right)_B \in \mathbb{R}$

$$\Delta \left(f_z^R\right)_{B,des} = \left(f_z^R\right)_{B,des} - \left(\hat{f}_z^R\right)_B \quad (5.119)$$

Based on the desired incremental pseudo control $\Delta \boldsymbol{\nu}_{des} \in \mathbb{R}^4$

$$\Delta \boldsymbol{\nu}_{des} = \begin{bmatrix} \Delta \left(f_z^R\right)_B \\ \Delta \left(\vec{\omega}_K^{OB}\right)_B^B \end{bmatrix}_{des} \quad (5.120)$$

the incremental control input command $\Delta \boldsymbol{u}_{cmd} \in \mathbb{R}^{18}$ is computed using the incremental control law described in the Eq. (3.20)

$$\Delta \boldsymbol{u}_{cmd} = \boldsymbol{B}^\dagger \cdot \Delta \boldsymbol{\nu}_{des}. \quad (5.121)$$

Here $\boldsymbol{B}^\dagger \in \mathbb{R}^{18 \times 4}$ represents a generalized inverse of the control effectiveness matrix $\boldsymbol{B} \in \mathbb{R}^{4 \times 18}$. The inverse of the considered over-actuated system is calculated using redistributed pseudo inverse method [195, 196]. In this control strategy, each element Δu_i of the incremental control input vector $\Delta \boldsymbol{u}_{cmd} \in \mathbb{R}^{18}$ is the increment in the square of the rotational speed of each LTU $\Delta \omega_i^2$. By doing this, the control effectiveness matrix can be estimated as a constant matrix. The absolute control input command $\boldsymbol{u} \in \mathbb{R}^{18}$ is calculated by the summation of the incremental command with the control input estimate $\hat{\boldsymbol{u}} \in \mathbb{R}^{18}$

$$\boldsymbol{u}_{cmd} = \Delta \boldsymbol{u}_{cmd} + \hat{\boldsymbol{u}} \quad (5.122)$$

The control input estimate $\hat{\boldsymbol{u}} \in \mathbb{R}^{18}$ is obtained from the actuator models displayed as \mathbf{G}_A in the Fig. 5.6. The actuators models for the LTUs contain first order elements as described in Eq. (4.6). The control input commands transmitted to the LTUs, denoted as $\boldsymbol{u}_{P,cmd} \in \mathbb{R}^{18}$, are equal to the positive square root of the corresponding element in $\boldsymbol{u}_{cmd} \in \mathbb{R}^{18}$. This accomplishes the description of the INDI based inner loop controller used for the verification of the unified trajectory controller. The MIL simulation results will be presented next.

5.5.3 Simulation Results

Figure 5.7 displays the planned and the followed aircraft trajectory in the horizontal plane during the full flight mission simulation test of the unified trajectory controller in tandem with the inner loop controller described in the section 5.5.2 for the aircraft configuration presented in the section 5.5.1. The flight mission starts with the vertical take-off maneuver during which the aircraft heading aligns with the heading of the first way point. The desired trajectory parameters and error deviations are provided to the trajectory controller by the ATOL module during this phase. Thereafter, a forward kinematic velocity of 20 m/s is commanded with a constant climb rate till the end of the straight leg. Figure 5.8 demonstrates the take-off trajectory, which corresponds to the Vertical Take-Off (VTO) mentioned in the Means of Compliance for Special Condition VTOL [135], illustrated by the Fig. 1.5. After the aircraft gains a forward kinematic velocity $(u_K^R)_C^E$ of higher than 4 m/s , the desired trajectory parameters and error deviations specified by the waypoint trajectory generation module are used by trajectory controller to generate command for the inner loop controller.

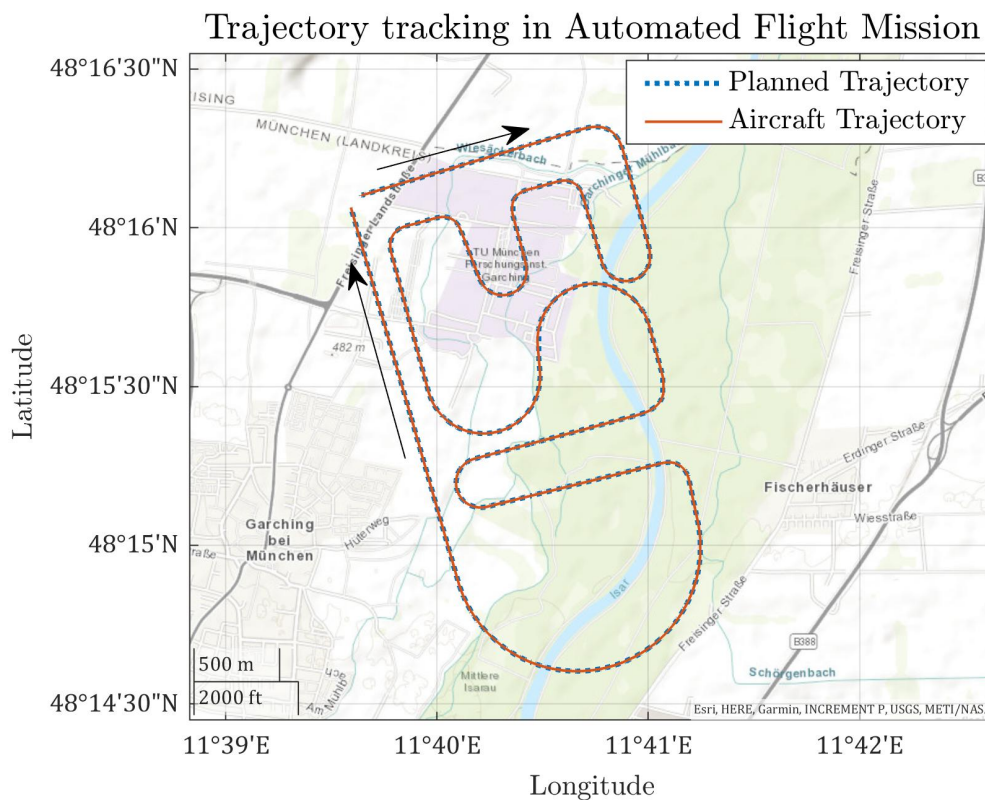
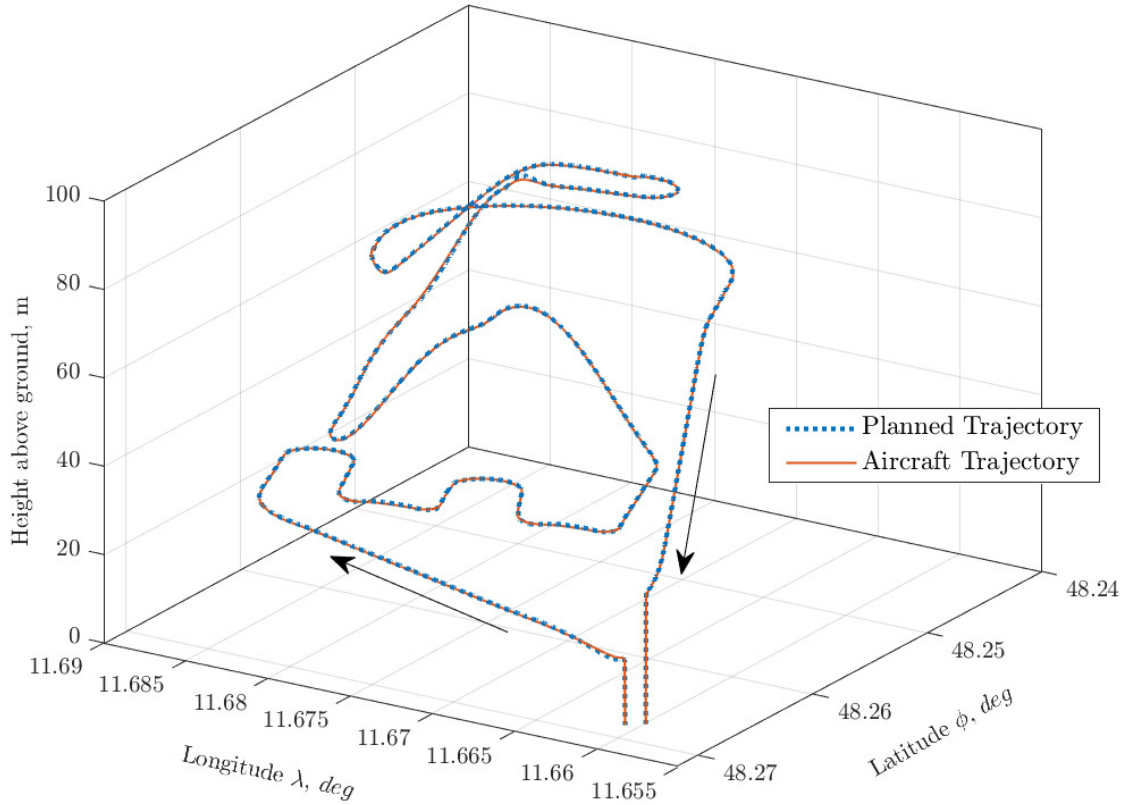


Figure 5.7: Full Mission Trajectory tracking in the horizontal plane

The next part of the flight mission involves multiple fly-by and radius-to-fix maneuvers at a constant altitude and constant forward kinematic velocity in order to assess the lateral channel tracking performance of the unified trajectory controller. Referring to the Fig. 5.9, this part of the flight mission lies within the timestamps 100 s to 300 s . It starts with a fly-by maneuver at the timestamp of 100 s , followed by two maneuvers each of which involves a radius-to-fix and two fly-by legs, thereby accomplishing the letter F in the flight plan. The magnified view of the bank angle tracking in one of the maneuvers

Three dimensional visualization for Trajectory Flight Mission

**Figure 5.8:** Three dimensional visualization of the Automated Trajectory Flight Mission

encompassing one radius-to-fix and two fly-by legs is demonstrated in Fig 5.10. The absolute bank angle command calculated by the trajectory interface module according to the Eq. (5.102) has a higher slope at the initiation of a turn maneuver in order to enforce a faster build up of the reference bank angle and subsequently the true bank angle. Similar behavior can also be observed at the instances before the bank angle command reaches a steady state value in order to impose faster transition of the true bank angle to the steady state value.

For the remaining parts of the flight mission visualized as letters *S* and *D*, vertical axis maneuvers as well as change in forward velocity are commanded along with the radius-to-fix turn legs in order to assess the lateral tracking performance in combined maneuvers. The tracking performance along with the forward velocity at which the maneuvers are performed can be visualized in Fig. 5.9. It can be observed that in the full flight mission, the lateral position error deviation denoted in the desired path frame Δy_D largely remains within a range of $[-0.5, 0.5]$ m except the deviation initial forward acceleration phase.

The tracking performance of the trajectory controller in the vertical channel is displayed through the Fig. 5.11. Single axis maneuvers for the vertical channel correspond to the vertical take-off at the beginning of the flight mission and vertical landing maneuver at the end. In both cases, the vertical position tracking error lies within $[0.6, -0.4]$ m. Additionally, the vertical channel tracking performance during the combined acceleration and climb maneuver towards the first waypoint of the flight plan as well as

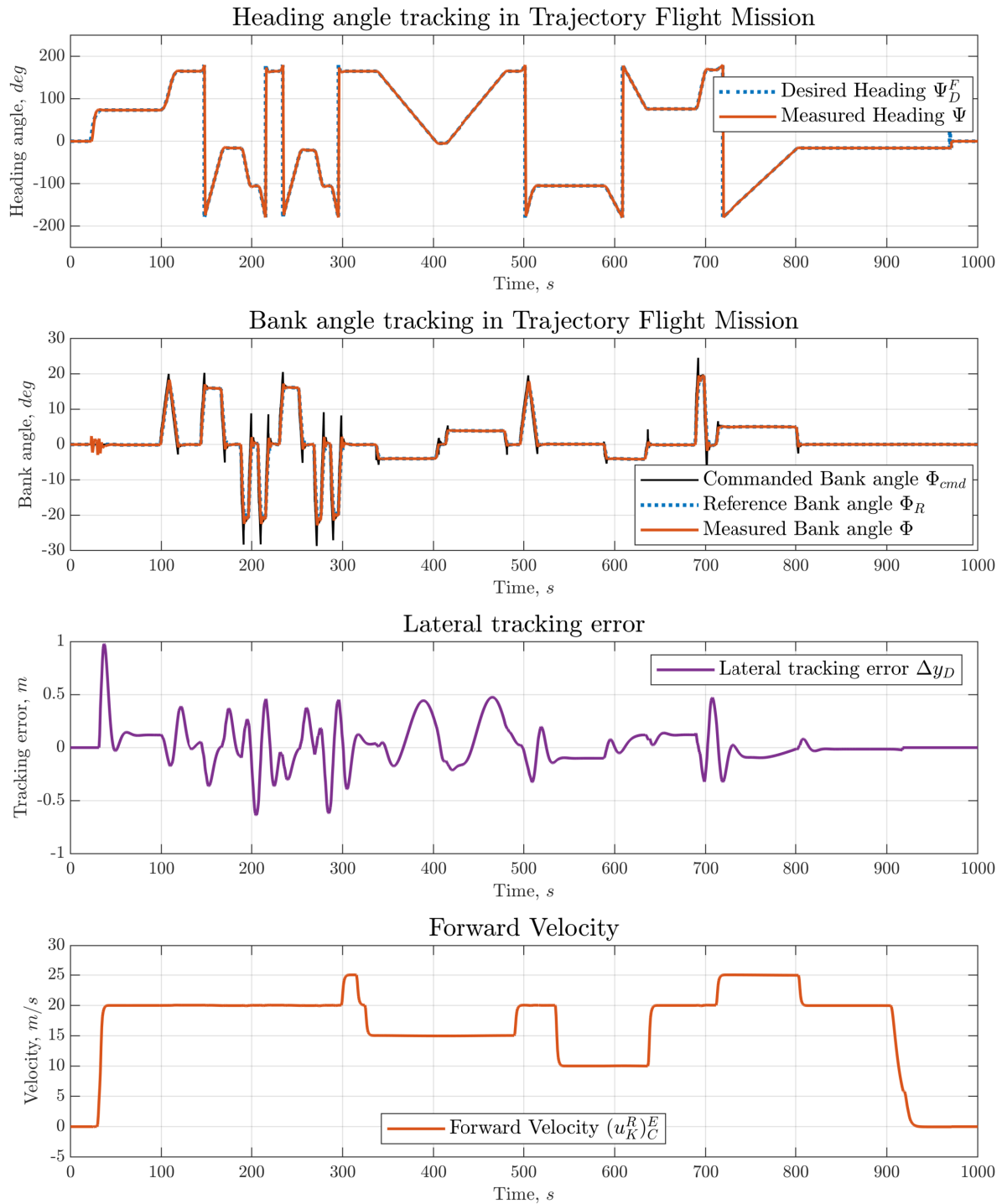


Figure 5.9: Lateral channel tracking in the Automated Trajectory Flight Mission

the combined deceleration and descent maneuver while approaching the landing point exhibit similar deviation bounds. During the multiple turn maneuvers corresponding to the letter *F* in the flight plan (between timestamps 100 s and 300 s), the change in altitude remains within $[-0.4, 0.2]$ m. Moreover, in the combined radius-to-fix and climb/descend maneuvers corresponding to the letter *S* (between timestamps 300 s and 500 s), the deviation of the true altitude from the desired altitude lies within $[-0.3, -0.1]$ m. The vertical tracking performance deteriorates slightly during the step climb maneuver in the straight legs between the letters *S* and *D* (between timestamps 500 s and

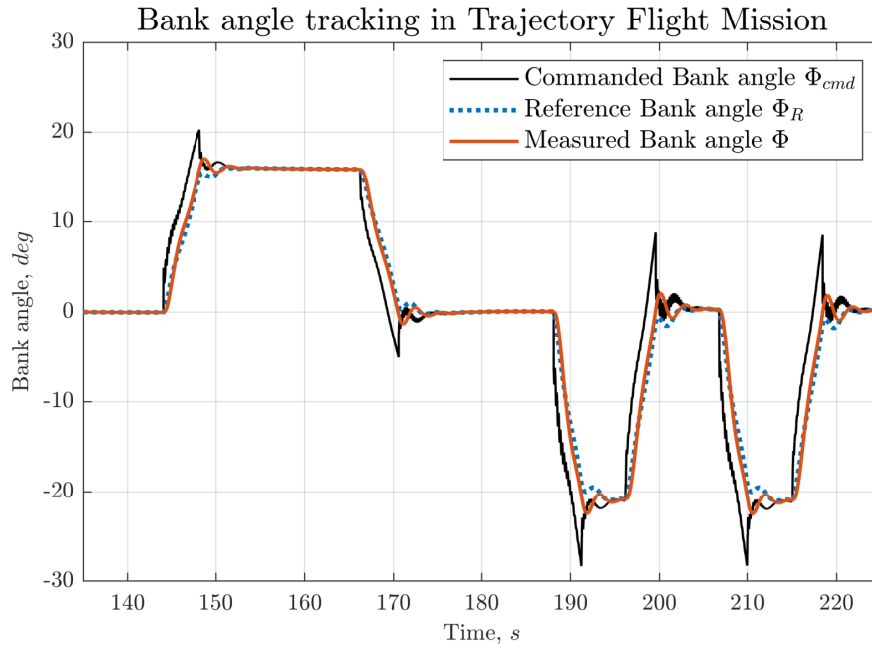


Figure 5.10: Bank angle tracking in the Automated Trajectory Flight Mission

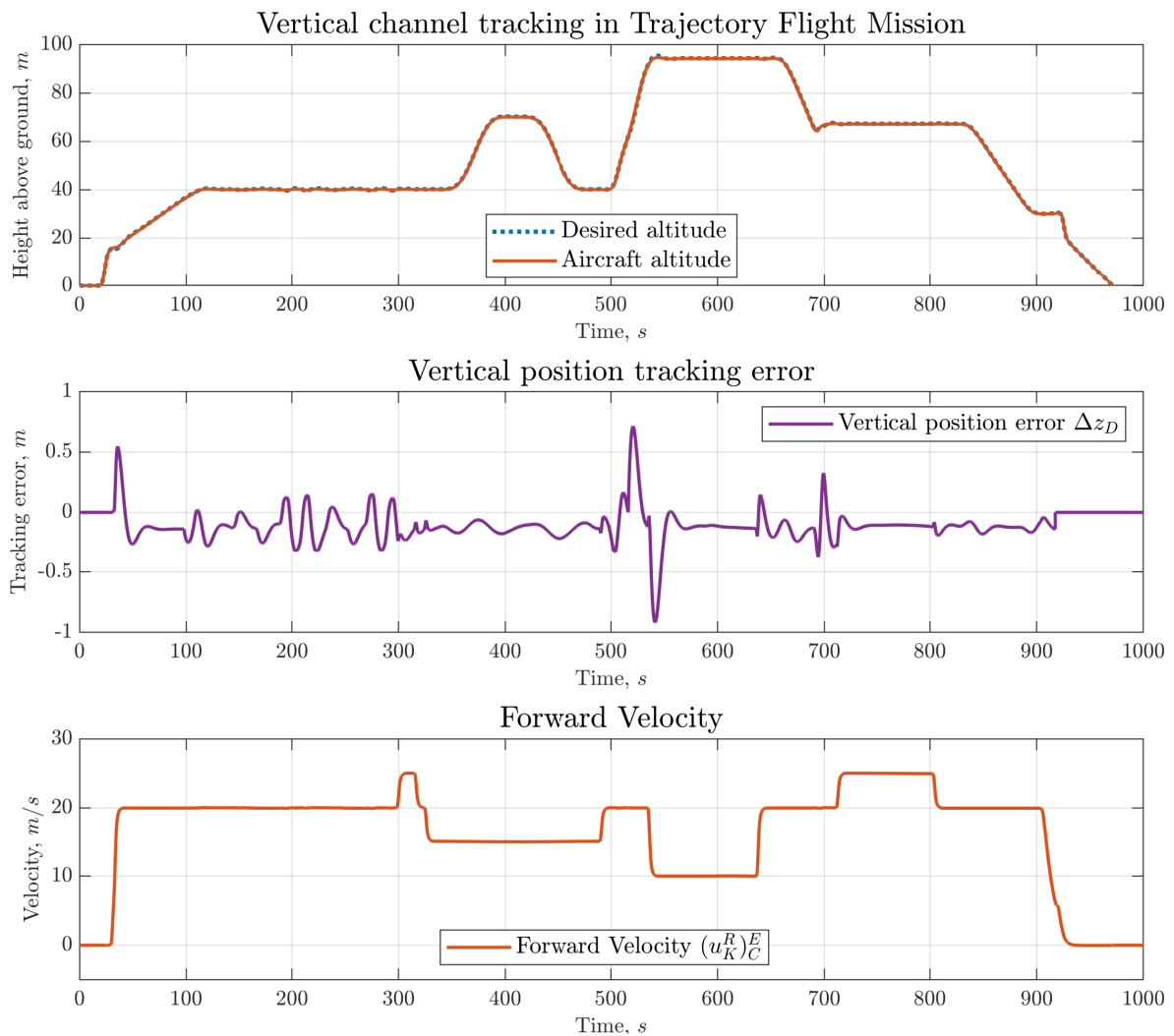


Figure 5.11: Vertical channel tracking in the Automated Trajectory Flight Mission

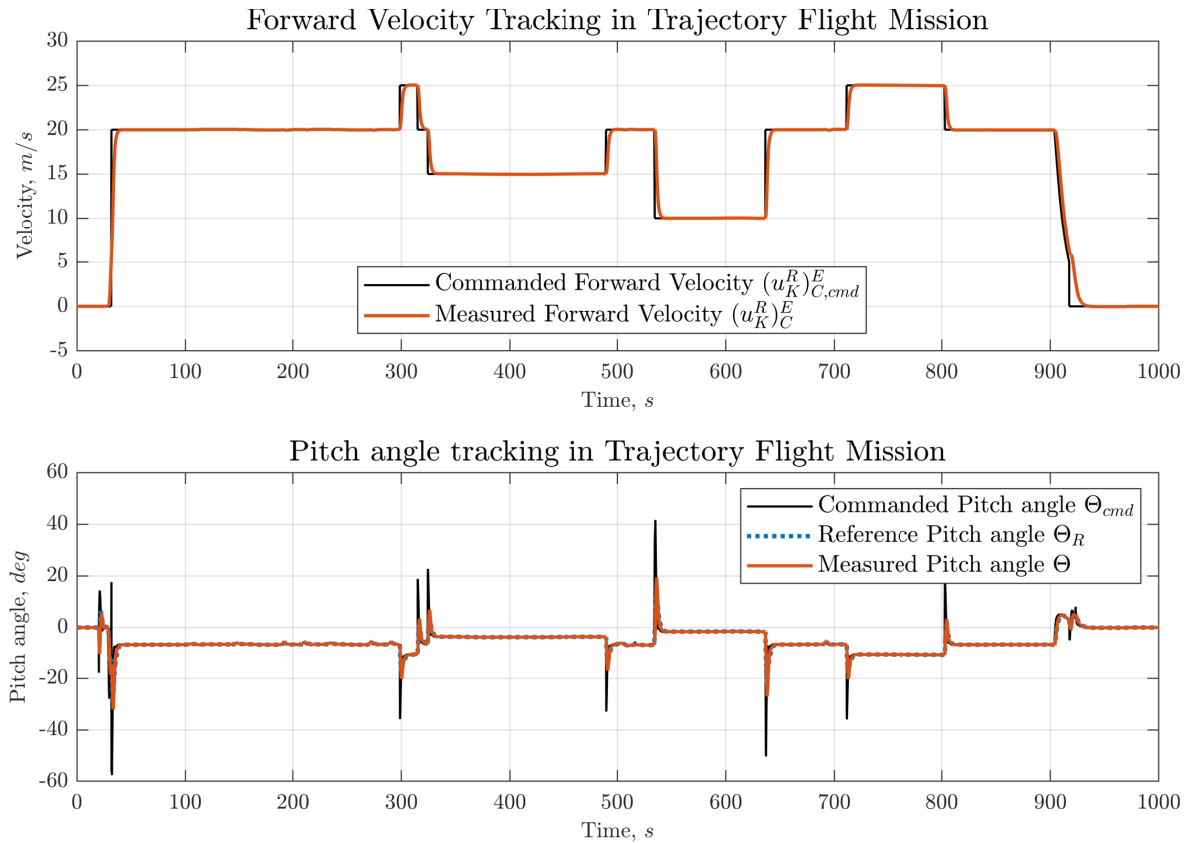


Figure 5.12: Forward channel tracking in the Automated Trajectory Flight Mission

600 s) of the flight plan as visualized in Fig. 5.11. Overall the vertical position error lie within the bounds $[-1, 0.6]$ m during the simulation of the given flight plan for the considered aircraft configuration.

Ultimately, the forward velocity tracking during the automated flight mission is presented in the Fig. 5.12. Important to note that for this simulation test, the desired longitudinal position of the trajectory footpoint was not tracked, rather only the velocity of the footpoint $(u_K^F)^E_T$ from the waypoint trajectory generation module was tracked by the trajectory controller to generate corresponding specific force rate commands and subsequently the pitch angle commands for the multicopter configuration according to Eq. (5.102). Fig. 5.12 demonstrates that acceleration and deceleration in the forward velocity is brought about by tilting the powered lift from the LTUs through the pitch angle.

Like the bank angle command generated by the interface module, it can be observed in the magnified view of the pitch angle tracking shown by Fig. 5.13, a large step in the pitch angle command is generated to bring about a rapid change in the reference pitch attitude and as result the true pitch angle. Since the strategies proposed for the jerk-level reference model in chapter 4 are not employed in the linear reference models used in the inner loop controller from the section 5.5.2, it can be observed that the measured pitch angle does not exactly follow the reference pitch angle during the transient period.

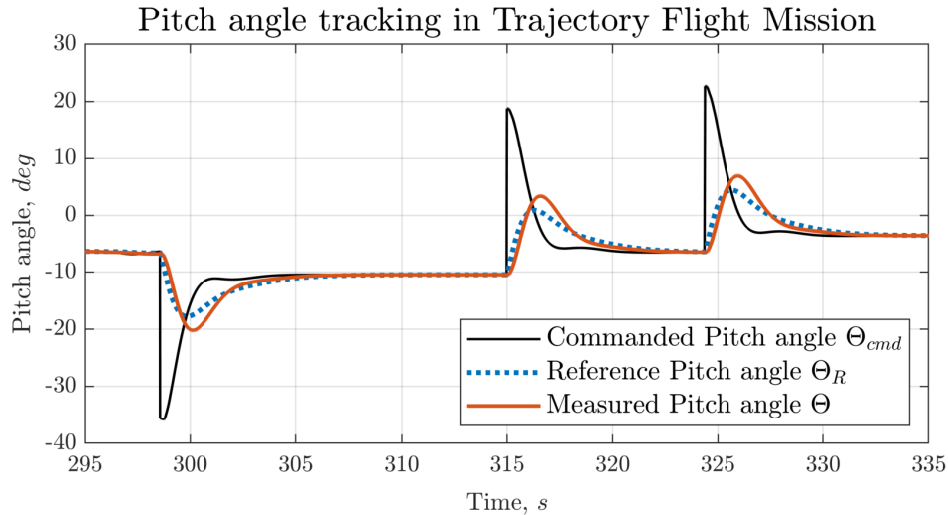


Figure 5.13: Pitch angle tracking in the Automated Trajectory Flight Mission

Hence, the verification of the proposed Unified Trajectory Controller framework was accomplished using MIL tests with the multicopter configuration presented in the section 5.5.1. Although, a multicopter configuration was utilized, functionalities corresponding to hover as well as forward velocity phases could be verified since the proposed framework is agnostic of the aircraft configuration as well as flight phase-specific control forces and moments generation mechanism.

5.6 Summary

This chapter presented a configuration agnostic unified trajectory control strategy for VTOL transition/VTOL aircraft configurations. The proposed strategy produced specific force rate commands depending on the feedforward from the reference trajectory specification along with the position, velocity and acceleration deviations. The specific force rate or the jerk control was chosen as a solution for path-following problem, since it facilitates improved tracking and possibility of effector dynamics consideration.

Rigid-body kinematic translation jerk dynamics denoted in the C -frame were derived. After performing an order analysis of the terms in the C -frame jerk-level dynamics, terms having negligible magnitudes within the bounds of the latitude, kinematic velocities and turn rates applicable for UAM were removed. The resulting jerk-level dynamics were utilized to derive position jerk error dynamics. The jerk error dynamics were affine in position, velocity and acceleration errors and further contained the nonlinear effects emanating from aircraft velocity, acceleration and specific forces. Except the jerk error and the specific force rate, the remaining terms of the jerk error dynamics were encompassed in a nonlinear term $G(x)$.

Nonlinear dynamic inversion (NDI) of the jerk error dynamics was performed which employed the desired jerk computed from the proportional trajectory track feedback error controller along with the nonlinear term. The nonlinear term was segregated in to three components – desired trajectory parameters, measurements/estimated terms and

the error terms for ease of computation of its constituent terms based on the current flight phase. Flight phase dependent composition of the nonlinear term along with a proportional trajectory track error controller yielded a unified trajectory control law, which not only covers all flight phases of a VTOL transition aircraft but can also be used for a VTOL multicopter configuration without making any structural changes. A state space formulation of the jerk error dynamics and the closed loop system employing the unified trajectory control law was also formulated, which can be employed to perform stability and robustness analysis of the closed loop system. In addition to the translation degrees of freedom, yaw channel manifests as an additional independent degree of freedom in the hover phase. Therefore, a heading angle control law, in addition to the trajectory control law, was specified which produced heading acceleration commands for the inner loop controllers.

Unified Trajectory Controller framework demonstrating a modular implementation of the proposed strategy was also described. The framework comprised of five units, namely – *rotation matrices generator*, *rotation rate acceleration jerk calculation*, *translation states transformation*, *nonlinear term composer* and the *unified trajectory control law*. Input-Output interfaces of each unit were described and details about the inter-dependencies among different units were also provided.

An interface module as an addendum to the unified trajectory controller framework was presented. The function of this module is to generate attitude rate commands along with the already calculated heading acceleration and vertical specific force rate as a possible control variable set for the inner loop controller of a generic multicopter configuration. Additionally, absolute attitude angle commands, heading angle rate and vertical specific force command can also be specified as an alternative control variable set depending on the design of the inner loop controller.

The verification of the proposed trajectory control strategy was performed through MIL simulation tests for a multicopter configuration, which utilized an INDI based inner loop controller. Test results showed that for the considered aircraft configuration and the inner loop controller, the unified trajectory control provided good tracking of the reference trajectory in cases of single axis maneuvers as well as coupled maneuvers in multiple axes as defined in the flight plan used for simulations. The position error in all axes was found to be within 1 *m* with respect to the desired trajectory.

Chapter 6

Conclusion

One of the key elements essential for the realization of Urban Air Mobility (UAM) is flight control approaches that can ensure safe operation of novel aircraft configurations in urban airspace, which is prone to external disturbances generated due to interaction of wind with buildings and wake turbulence from other entities. Accordingly, challenges in flight control for UAM originate from two factors – novel aircraft configurations driven by Distributed Electric Propulsion (DEP) and operational airspace with high external disturbances. Three main Problem Statements PSs were identified based on the aforementioned factors in the motivation (section 1.1) of this thesis

PS.1 Changing dynamics and relative degree of the system

PS.2 Uniform behavior over complete flight envelope

PS.3 Precision tracking and disturbance rejection

These problem statements stimulated the development of methods proposed in this thesis in order to deliver nonlinear flight control strategies suitable for UAM.

An extensive literature review of the techniques employed to overcome these challenges brought about the gaps that still needed to be closed. The objectives included investigation of rigid body dynamics of a VTOL transition aircraft in order to specify a physically motivated aircraft motion behavior in each flight phase and define strategies to achieve this behavior. In addition to the specification of the desired motion behavior, a uniform aircraft response to pilot commands over the full flight envelope needed to be established by selecting appropriate pilot command variables in each flight phase. Furthermore, specification of physically viable control variable reference trajectories through an integrated and configuration agnostic reference model design was aimed. By identifying precisely known higher order effects in the closed loop system architecture, it was intended that the knowledge of these unmodeled dynamics along with the aircraft model parameters can be incorporated in the reference models. Consequently, effective feedforward commands as well as reference trajectories were to be defined, which consider aircraft physics together with system architecture specific effects. Additionally, development of a unified controller delivering precise trajectory following in all phases of a VTOL transition/VTOL aircraft was targeted. In pursuit of these objectives, the common goal was to develop strategies that were modular and agnostic of the aircraft configuration.

Considering the aforementioned objectives, this dissertation proposed flight control strategies and related design methodologies to accomplish the contributions, listed in the section 1.4, which mitigate the shortcomings identified from the analysis of existing literature.

6.1 Dynamics and Control of Vertical Take-off and Landing Transition Aircraft

Chapter 2 depicted the concepts associated with dynamics of vertical take-off and landing transition aircraft. Primarily, translation dynamics were derived with the reference frame as the C -frame in order to obtain a unified formulation of the control problem across all the flight phases of a VTOL transition aircraft. The resulting C -frame translation dynamics were utilized to devise unified strategies for motion control in the lateral and vertical axes for the complete flight envelope without switching between control techniques tailored for every flight phase.

An aircraft configuration agnostic design of a Design Reference Model (DRM) was proposed. The purpose of the DRM was to provide a flyable specification of the desired aircraft behavior, which could be validated with regard to handling qualities, inceptor interpretation, flight mission requirements, and more, even before a detailed system design is available in the aircraft development process. Preliminary knowledge of aircraft-specific parameters was possible to incorporate by using a separate aircraft configuration specific module. Accordingly, effector dynamics were encompassed in the DRM at the level of control forces and moments. Interpretation of pilot commands from a dual inceptor concept, comprising of a hybrid thrust inceptor and a centered climb inceptor, for a control strategy using attitude angles and height rate as control variables was elaborated.

Contribution C.1 Derivation of required maneuverability phase planes through Design Reference Model simulations for a VTOL transition aircraft was effectively attained by employing the aforementioned DRM framework. Based on the handling quality requirements pertaining to attitude quickness from the Aeronautical Design Standard for Military Rotorcraft ADS-33E-PRF [84], maneuverability phase planes (Fig. 2.20–2.22) specifying required body rotational accelerations and jerk in the hover flight phase to achieve different handling quality levels were acquired. The resultant required maneuverability phase planes remain independent of any aircraft configuration. Notably, these phase planes provide rotational acceleration and jerk only for maneuverability. Additional margins for mitigating the effects of external disturbances and failures must be considered separately.

6.2 Integrated Nonlinear Reference Model for Vertical Take-Off and Landing Transition Aircraft

Chapter 3 presented a modular, aircraft configuration-agnostic reference model architecture for VTOL transition aircraft. A significant attribute of the proposed RM design was to include pilot inceptor command interpretation in terms of physical control variables for each flight phase – hover, transition and wingborne within a flight phase specific module named as the *Commands Transformation* module. Three sets of control variables corresponding to each flight phase of the VTOL transition aircraft were selected. The choice of the Control Variable (CV) sets was governed by constraints of providing intuitive pilot perception for flight operation in each flight phase, having a direct kinematic relation to one CV set and that all chosen CV sets lead to the same set of reference pseudo controls and external states. Furthermore, mapping of the pilot inceptor commands to the CV sets for each flight phase was performed in this module along with transformation of the mapped control variables to the inputs of the reference model core. The methodologies applied in the *Commands Transformation* module provided the realization of the contribution **C.2.1 Flight phase dependent mappings for pilot command variables contained within the reference model**.

The second module of the integrated RM, called the *Reference Model Core*, was designed to be flight phase agnostic such that it can provide same set of reference pseudo controls and external states over the complete flight envelope. To that effect, the RM core was constituted by decoupled translation and rotation reference models. Translation RM generated reference trajectories for load factors and kinematic velocities specified in the control frame, while accounting for inter-axis coupling between the forward and lateral translation axes, moment dynamics emulation as well as pseudo force-moment actuator dynamics. The rotation reference model encapsulated computation of body rotation rate commands pertaining to hover and forward velocity flight phases depending on the virtual control inputs calculated from the desired translation load factors in the control allocation module. Employing nonlinear attitude kinematics, reference trajectories for body rotational accelerations, rates and Euler attitude angles were specified by the rotation reference model that remain physically consistent with the aircraft dynamics of the current flight phase. The proposed implementation of the rotation reference model relates to the contribution **C.2.2 Sequential desired rotation rate calculation in a unified control structure**. Overall, the design of the RM core module pertains to the contribution **C.2.3 Reference Model core design to facilitate use of same set of variables for the whole flight envelope**.

Explicit wind disturbance rejection behavior was defined as a part of the integrated reference model framework. For wind disturbance rejection in hover flight, the desired behavior was specified as maintaining the commanded velocity by the pilot in all translation directions. In high dynamic pressure regime, the cross wind disturbance rejection behavior was defined such that the body lateral load factor is minimized. This was accomplished by utilizing the body lateral load factor feedback in the yaw rate command generation. Use of tilt LTU thrust command as the control variable in high dynamic pressure flight provided an implicit airspeed control and increased robustness against

stall due to tail wind. In this manner, contribution **C.2.4 Definition of an explicit wind disturbance rejection behavior over the complete flight envelope within the Reference Model core design** was achieved with the proposed RM design.

Flight phase reliant blending of the reference bandwidths, body rotation rate commands as well as control variables was performed to facilitate consistency between the reference variables. To specify accurate mappings between the different CV sets in high wind gradient environment, feedback of the true course angle was used. Moreover, reference states were slaved to the true plant states in specific flight phases to enforce conformity between all reference trajectories. These methods pertain to the contribution **C.2.5 Approaches to enforce compliance between different reference variables**.

The integrated reference model architecture proposed in this dissertation enabled the implementation of a unified INDI controller over the full flight envelope of a VTOL transition aircraft, hence avoiding the use of flight phase specific controllers and any switching procedures between them. Simulation and experimental flight test results for a tilt-rotor aircraft configuration proved the effectiveness of the proposed algorithms. The modular property of the proposed reference model can be verified based on its application by other researchers in their works [204–206]. The complete RM architecture presented in chapter 3 fulfills the contribution **C.2 Integrated Nonlinear Reference Model Structure for Vertical Take-Off and Landing transition aircraft**.

6.3 Jerk-Level Physical Reference Model

Chapter 4 presented the concepts and analyses pertaining to the contribution **C.3 Jerk-level Physical Reference Model design**. A design methodology was established for creating a jerk-level reference model, which can specify reference trajectories for controllers based on a continuous extension of the incremental nonlinear dynamic inversion strategy. The primary feature of the proposed reference model is the inclusion of identifiable disturbances like the state dependent damping effects within the RM. Consequently, the impact of these disturbances can be counteracted preemptively through the feedforward command even prior to the emergence of the control error. The aircraft parameters characterizing these state reliant damping terms, also known as the "**A**-part", were incorporated in the design plant of the reference model.

The feedforward to the extended INDI controller was produced by feedback linearization of the design plant within the jerk-level RM by using reference state feedback. Unlike the classical NDI methodology of inverting a plant model to generate control effector commands, dynamic inversion was employed for generation of a feedforward pseudo control derivative command in the jerk-level RM, hence directly applicable for input non-affine systems as well. Subsequently, the physically motivated feedforward command yielded control effector command acting in the correct direction as well as maintaining a steady state magnitude depending on the aircraft parameters included in the design plant. The magnitude of these aircraft parameters cannot be known perfectly in practical applications. Therefore, an effective range for the aircraft parameters included in the design plant was determined by means of linear analysis for a SISO case.

For the analyzed case, it was identified that employing the proposed feedforward from the jerk-level RM decreased the magnitude of the set-point tracking error without changing the feedback gains, provided that the design plant parameter lied within $\pm 100\%$ of the real aircraft parameter. This analysis was extended by evaluating the influence of the design plant uncertainty with respect to the MUAD bounds. Findings indicated that the MUAD bounds were not violated if the magnitude of the design plant parameter remains within the effective range defined as $\pm 100\%$ of the true plant parameter, and feedforward from the reference model is used by the controller. Notably, it was observed that by removing the feedforward component from the desired pseudo control rate calculation, the MUAD bounds corresponding to the phase were violated. Certainly, the proposed feedforward command generated by the jerk-level RM is more effective than the high-pass constituent of a command computed by a linear reference model. Therefore, the technique employed for the generation of the feedforward command fulfilled the contribution **C.3.1 Feedforward pseudo control derivative generation for input non-affine systems**.

With the purpose of maintaining phase conformity between the reference trajectories and the corresponding estimated variables, noise attenuation/estimation filters were incorporated in the jerk-level reference model design. Linear analysis revealed that consideration of estimation dynamics also diminishes gain variation between the reference external states and measured/estimated outputs in addition to mitigating phase difference between them for the effective range of the design plant parameter as defined before. Consequently, higher feedback gains can be employed to elevate external disturbance rejection capability. Addition of estimation dynamics in the reference model accomplished the contribution **C.3.2 Inclusion of measurement/estimation filter effects in the reference model design to achieve phase conformity between external reference and estimated plant states**.

Time delays occurring in the input/output channel dynamics are another source of causing phase mismatch between the reference and measured/estimated variables. Hence, these time delays were also included in the jerk-level RM in order to reduce the aforementioned phase difference. Linear analysis results for a SISO case verified that the addition of the information about time delays in the reference model lowered the gain and phase difference between the external reference state and the filtered output in the effective range of the design plant parameter. Assimilation of time delays in the jerk-level RM relates to the contribution **C.3.3 Integration of time-delays from the input/output channel dynamics within reference model design to facilitate phase match between external reference and estimated plant states**.

Consideration of time delays and estimation dynamics highlighted the bi-level control objective manifested by using the jerk-level reference model in the extended INDI framework. The reference model defined the reference behavior for the estimated plant while the real system follows the desired behavior implicitly specified by the reference model, which is equivalent to the implemented reference specification without the filter dynamics and the time delays.

Along the same lines as the estimation dynamics, higher than first order effector dynamics were also proposed to be included in the reference model, since the first order dynamics were already compensated in the extended INDI control law. Efficacy of the inclusion of these residual dynamics was shown through the linear analysis for a scalar case using second order effector dynamics. For the analyzed case, consideration of the residual dynamics also lowered the phase difference between the reference state trajectory and the estimated output in the effective range of the design plant parameter. Accordingly, the contribution **C.3.4 Consideration of higher than first order effector dynamics in the generation of external reference states and feedforward pseudo control rate** was achieved.

The architecture of the jerk-level reference model comprised of four functional units, called as – *desired dynamics specification unit*, *state dependence compensation unit*, *reference actuator with input/output channel dynamics consideration* and the *design plant*. Desired dynamics for each command variable channel were specified by the *desired dynamics specification unit*. The pseudo control command intended to be produced by the control effectors was computed in the *state dependence compensation unit* by using the design plant feedback. As the name implies, the *reference actuator with input/output channel dynamics consideration* was comprised of the closed loop system time delays, noise attenuation filter dynamics and effector dynamics higher than the first order. The *design plant* contained the best estimate of the system parameters corresponding to every pseudo control channel.

Experimental verification of the proposed reference model strategy employing a design plant was demonstrated by applying it for RPM control of a lift thrust unit. Findings indicated that by using the feedforward commands only, the lift thrust units were commanded in the direction of the reference set-point and sustained a steady state rotational rate, though a residual error remained. The residual error was readily diminished by the feedback error controller when both the feedforward and feedback control paths were activated simultaneously.

6.4 Unified Trajectory Control for VTOL Transition Aircraft

Chapter 5 introduced a modular unified trajectory control strategy for VTOL transition/VTOL aircraft, which is independent of aircraft configuration specific parameters. Based on the position, velocity and acceleration error with respect to the desired trajectory as well as the feedforward commands from the reference trajectory definition, specific force rate commands were generated in the proposed approach to facilitate trajectory tracking. Specific force rate control, which lies at the dynamic level of translation jerk, was preferred because it was established through literature review that it improved tracking performance in other applications. Moreover jerk control offered future potential for effector dynamics consideration by the trajectory control law.

Accordingly, C -frame rigid-body translation jerk dynamics were derived employing the translation equations of motion. Terms having very small magnitudes within the limits of latitude, turn rates, and kinematic velocities, relevant for UAM, were excluded. Subsequently, position jerk error dynamics were formulated from the jerk-level translation dynamics. Importantly, the jerk error dynamics were linear with respect to position, velocity and acceleration errors and further contained nonlinear terms originating from aircraft dynamics. The derivation of the jerk error dynamics relates to the contribution **C.4.1 Derivation of nonlinear jerk-level position error dynamics with respect to the desired path.**

The obtained jerk error dynamics did not comprise of any uncertainties since they were purely kinematic, which implied that an analytic inversion was possible. Therefore, nonlinear dynamic inversion (NDI) strategy was used to derive the control law. For this purpose, the jerk error dynamics were categorized into three components – jerk error, specific force derivative and the remaining terms combined in a nonlinear term $G(x)$. Using NDI, specific force derivative commands were computed based on the desired jerk, obtained from a stabilizing proportional error feedback controller, and the nonlinear term $G(x)$ composed of desired trajectory parameters, measured/estimated terms and error terms. Consequently, the proportional track error feedback controller along with a flight phase specific construction of the nonlinear term delivered a unified trajectory control law, which can be employed over the complete flight envelope of a VTOL transition aircraft, and even for VTOL configurations such as multicopters. The yaw channel emanates as an independent degree of freedom in the hover flight phase. Hence, heading angle control law was also specified alongside the unified trajectory control law to generate heading angle acceleration command, which was input to the inner loop controller. The derivation of the unified trajectory control law realized the contribution **C.4.2 Unified trajectory control law for all flight phases of a VTOL transition aircraft.**

The proposed approach for the unified trajectory control law along with the associated computations were implemented as a modular framework. The framework was constituted by five units – *rotation matrices generator*, *rotation rate acceleration jerk calculation*, *translation states transformation*, *nonlinear term composer* and the *unified trajectory control law*. The presented framework pertains to the contribution **C.4.3 Configuration-agnostic design of the unified trajectory control framework.**

Moreover, an interface module for the unified trajectory controller was developed. This module provided the possibility of transforming the specific force rate commands from the unified trajectory control law to bank and pitch angle rate command. Together with the heading angle acceleration and vertical force derivative command, they form a feasible control variable set for the inner loop control law of a generic multicopter configuration. Alternatively, it was also possible to generate absolute bank and pitch angle commands along with heading angle rate and vertical specific force commands as the control variables for the inner loop. The interface module provides the accomplishment of the contribution **C.4.4 Interface function for trajectory controller with inner loop control law incorporating conversion of specific force rate commands to attitude angle rate commands for a multicopter platform.**

The presented unified trajectory control approach was verified through MIL simulations using a multicopter platform, which employed a simplified INDI based inner loop controller. Test results showed that the position error from the desired trajectory lied within 1 m during all the single axis and coupled axes maneuvers performed as a part of the automated trajectory flight mission. From a the trajectory control point of view, forward velocity flight phases for multicopter or transition aircraft are similar, since the trajectory controller is not affected by the mechanism of control force and moment generation. Altogether, chapter 5 provided the realization of the contribution **C.4 Unified trajectory control module for Vertical Take-Off and Landing transition aircraft.**

6.5 Future Work

The results obtained in this dissertation give rise to further research topics that need to be inquired.

Consideration of external disturbances in the required maneuverability phase planes

The maneuverability phase planes derived in the section 2.6 did not include impact of external disturbances on the required rotational accelerations and jerk. The next part of this work would involve extending the maneuverability phase planes by quantifying the effect of external disturbances based on the operational environment.

Preliminary sizing of the Lift Thrust Units

The maneuverability phase planes map the handling quality requirements to physical variable limits according to handling quality levels. In the future work, these limits can be used in preliminary sizing of the lift thrust units and their spatial positioning during the initial aircraft design process.

Employment of state dependent dynamics in the RM for unstable systems

For the treatment of unstable systems proposed in the jerk level reference model as per the section 4.4.6, the design plant state dependency parameter was considered as zero. Although, inclusion of higher order dynamics and time delay information for the feedforward calculation improved reference tracking significantly, no benefit could be gained through the knowledge about state damping parameters. Inclusion of this component is a potential topic for further research.

Generic formulation to include any higher order effector dynamics in the reference model

Chapter 4 only covered inclusion of actuator dynamics until the second order in the jerk-level reference model. A generic formulation to include any higher order effector dynamics in the RM is lacking. This aspect can also be covered in further research attempts.

Adaptation of unmatched uncertainties in the Design plant

The design plant adaptation in the jerk-level RM proposed by the author in [207] (Appendix D) focused on identification of the matched parameters in the state derivative dependency matrix A_v . By accurate identification of the parameters in this matrix, more accurate feedforward command could be generated thereby improving reference set point tracking performance. In the future works, the design plant adaptive augmentation architecture can be extended to consider the identification of the unmatched parameters in the state dependency matrix additionally.

Jerk-level unified reference model for VTOL transition aircraft

As a part of the future development, the concepts proposed in the chapters 3 and 4 can be utilized to design a jerk-level unified reference model architecture for a VTOL transition aircraft, which incorporates state dependent damping effects, unmodeled dynamics and time delays of the closed loop system for specifying the reference behavior.

Stability robustness analysis of the unified trajectory controller

Similar to the work carried out in [216] with relation to stability analysis of an acceleration error based trajectory controller, stability robustness analysis of the closed loop system obtained by the application of the unified trajectory control law can be performed while accounting for parameters varying according to the aircraft envelope.

Consideration of unmodeled dynamics and time delays in the unified trajectory controller

Further research about the unified trajectory control law can focus on inclusion of the effector dynamics, unmodeled higher order dynamics, time delays in the generation of the specific force rate commands to improve the tracking performance of the controller.

Appendix A

Coordinate Frames and Transformations

A.1 Coordinate Frame Definitions

Subject	Description
Index	B
Utilization	To denote forces and moments
Origin	Aircraft reference point (R)
Translation	Translates with the reference point of the aircraft
Rotation	Rigid body aircraft rotation rates
Axes: x_B	Points towards the direction of the nose of the aircraft
y_B	Points to the right side of the wing forming a right angle to the x_B axis in the horizontal plane
z_B	Points downwards and orthogonal to both x_B, y_B axes according to a right hand system

Table A.1: *Body-fixed frame* [143]

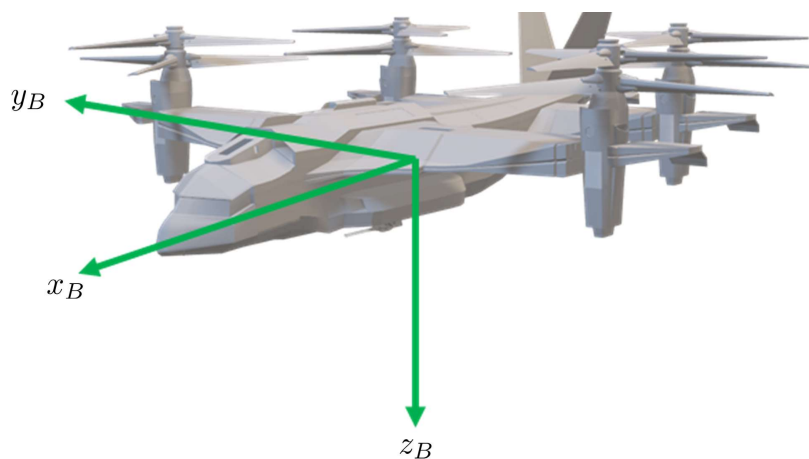


Figure A.1: *Body-fixed Frame* [141]

Subject	Description
Index	A
Utilization	To denote the aerodynamic forces and moments
Origin	Aircraft reference point (R)
Translation	Translates with the reference point of the aircraft
Rotation	Rotates with the aerodynamic flow's direction
Axes: x_A	Points towards the direction of the aerodynamic velocity
y_A	Points to the right, perpendicular to x_A, z_A axes
z_A	Points downwards perpendicular to the aerodynamic velocity

Table A.2: Aerodynamic frame [143]

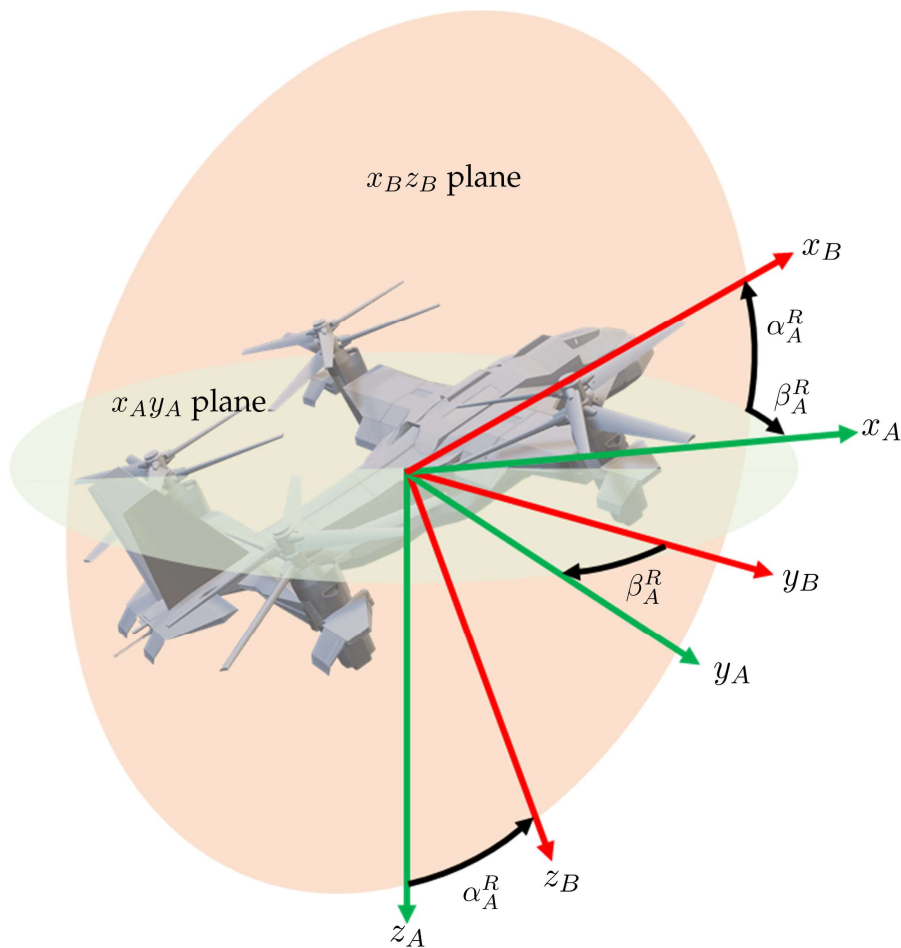
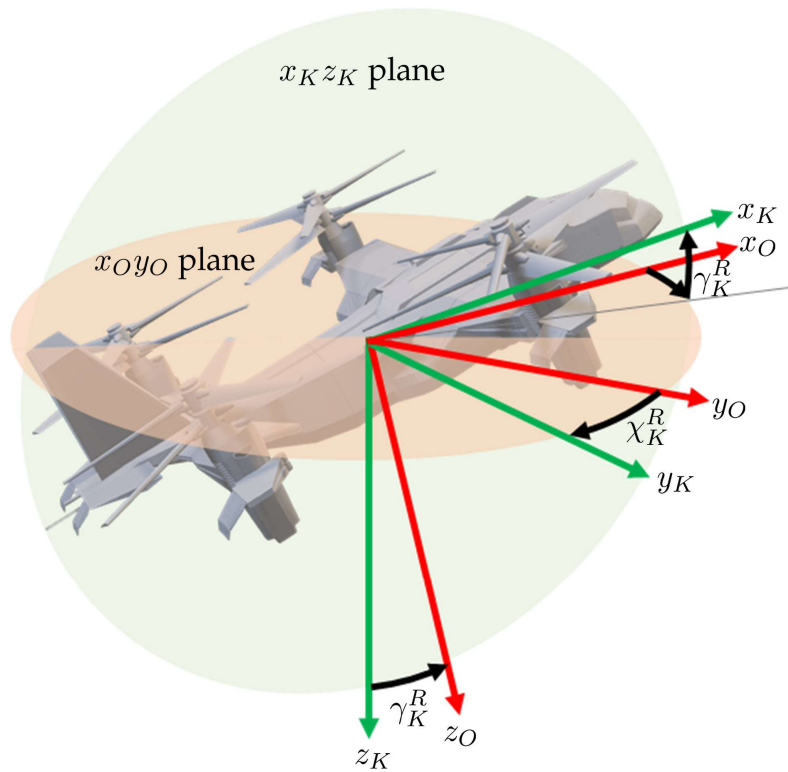


Figure A.2: Aerodynamic Frame [141]

Subject	Description
Index	K
Utilization	To denote the flight path of the aircraft
Origin	Aircraft reference point (R)
Translation	Translates with the reference point of the aircraft
Rotation	Rotates with the kinematic velocity direction
Axes: x_K	Points towards the direction of the kinematic velocity
y_K	Points to the right, perpendicular to x_K, z_K axes
z_K	Points downwards perpendicular to the kinematic velocity and parallel to the local normal's projection to the WGS-84 ellipsoid

Table A.3: Kinematic frame [143]

Figure A.3: Kinematic Frame [141]

A.2 Frame Transformations

The frame transformation matrices applicable in the derivations performed in this dissertation are presented in this section.

The frame rotation matrix \mathbf{M}_{CB} transforms a vector defined in the body-fixed frame B to the control frame C

$$\mathbf{M}_{CB} = \begin{bmatrix} \cos \Theta & \sin \Phi \cdot \sin \Theta & \cos \Phi \cdot \sin \Theta \\ 0 & \cos \Phi & -\sin \Phi \\ -\sin \Theta & \sin \Phi \cdot \cos \Theta & \cos \Phi \cdot \cos \Theta \end{bmatrix} \quad (\text{A.1})$$

The frame rotation matrix \mathbf{M}_{BO} that transforms a vector denoted in the North-East-Down frame O to the body-fixed frame B

$$\mathbf{M}_{BO} = \begin{bmatrix} \cos \Psi \cdot \cos \Theta & \sin \Psi \cdot \cos \Theta & -\sin \Theta \\ \cos \Psi \cdot \sin \Phi \cdot \sin \Theta - \sin \Psi \cdot \cos \Phi & \cos \Psi \cdot \cos \Phi + \sin \Psi \cdot \sin \Phi \cdot \sin \Theta & \cos \Theta \cdot \sin \Phi \\ \sin \Psi \cdot \sin \Phi + \cos \Psi \cdot \cos \Phi \cdot \sin \Theta & \sin \Psi \cdot \cos \Phi \cdot \sin \Theta - \cos \Psi \cdot \sin \Phi & \cos \Phi \cdot \cos \Theta \end{bmatrix} \quad (\text{A.2})$$

The frame rotation matrix \mathbf{M}_{BW} that transforms a vector denoted in the local wing-body frame W to the body-fixed frame B using the wing angle of incidence i_w

$$\mathbf{M}_{BW} = \begin{bmatrix} \cos i_w & 0 & -\sin i_w \\ 0 & 1 & 0 \\ \sin i_w & 0 & \cos i_w \end{bmatrix} \quad (\text{A.3})$$

The frame rotation matrix \mathbf{M}_{BH} that transforms a vector denoted in the local horizontal tail frame H to the body-fixed frame B using the horizontal tail angle of incidence i_h

$$\mathbf{M}_{BH} = \begin{bmatrix} \cos i_h & 0 & -\sin i_h \\ 0 & 1 & 0 \\ \sin i_h & 0 & \cos i_h \end{bmatrix} \quad (\text{A.4})$$

Appendix B

Angular Rotation Rates

The angular velocity of the Earth Centered Earth Fixed (ECEF) frame with respect to the Earth Centered Inertial (ECI) frame, specifying the rotation rate of the Earth ω_E , expressed in the control frame is denoted as $(\vec{\omega}_K^{IE})_C \in \mathbb{R}^3$ (Eq. (2.43)). The skew symmetric matrix pertaining to the angular velocity $(\vec{\omega}_K^{IE})_C$ is

$$(\Omega^{IE})_{CC} = \omega_E \cdot \begin{bmatrix} 0 & \sin \phi & -\cos \phi \cdot \sin \Psi \\ -\sin \phi & 0 & -\cos \phi \cdot \cos \Psi \\ \cos \phi \cdot \sin \Psi & \cos \phi \cdot \cos \Psi & 0 \end{bmatrix}_{CC}. \quad (\text{B.1})$$

Likewise, the angular velocity of the Earth Centered Earth Fixed (ECEF) frame with respect to the Earth Centered Inertial (ECI) frame expressed in the body fixed (B) frame is denoted by $(\vec{\omega}_K^{IE})_B \in \mathbb{R}^3$

$$(\vec{\omega}_K^{IE})_B = \omega_E \cdot \begin{bmatrix} \sin \Theta \cdot \sin \phi + \cos \Psi \cdot \cos \Theta \cdot \cos \phi \\ -\cos \phi \cdot (\cos \Phi \cdot \sin \Psi - \cos \Psi \cdot \sin \Phi \cdot \sin \Theta) - \\ \cos \Theta \cdot \sin \Phi \cdot \sin \phi \\ \cos \phi \cdot (\sin \Phi \cdot \sin \Psi + \cos \Phi \cdot \cos \Psi \cdot \sin \Theta) - \\ \cos \Phi \cdot \cos \Theta \cdot \sin \phi \end{bmatrix} \quad (\text{B.2})$$

The transport rate is expressed in the control frame as $(\vec{\omega}_K^{EO})_C$ (Eq. (2.43)). The columns of the skew symmetric matrix pertaining to the transport rate $(\vec{\omega}_K^{EO})_C$ are given by

$$\begin{aligned} (\Omega^{EO})_{CC}(:, 1) &= \begin{bmatrix} 0 \\ -\dot{\lambda} \cdot \sin \phi \\ \dot{\phi} \cdot \cos \Psi + \dot{\lambda} \cdot \cos \phi \cdot \sin \Psi \end{bmatrix}, \\ (\Omega^{EO})_{CC}(:, 2) &= \begin{bmatrix} \dot{\lambda} \cdot \sin \phi \\ 0 \\ \dot{\lambda} \cdot \cos \phi \cdot \cos \Psi - \dot{\phi} \cdot \sin \Psi \end{bmatrix}, \\ (\Omega^{EO})_{CC}(:, 3) &= \begin{bmatrix} -\dot{\phi} \cdot \cos \Psi - \dot{\lambda} \cdot \cos \phi \cdot \sin \Psi \\ -\dot{\lambda} \cdot \cos \phi \cdot \cos \Psi + \dot{\phi} \cdot \sin \Psi \\ 0 \end{bmatrix}. \end{aligned} \quad (\text{B.3})$$

The angular velocity of the NED (O) frame relative to the ECI frame denoted in the body fixed frame is given as

$$\left(\vec{\omega}_{K}^{IO} \right)_B = \begin{bmatrix} \dot{\lambda} \cdot \sin \Theta \cdot \sin \phi - \dot{\phi} \cdot \cos \Theta \cdot \sin \Psi + \omega_E \cdot \sin \Theta \cdot \sin \phi + \\ \dot{\lambda} \cdot \cos \Psi \cdot \cos \Theta \cdot \cos \phi + \omega_E \cdot \cos \Psi \cdot \cos \Theta \cdot \cos \phi \\ - \dot{\phi} \cdot (\cos \Phi \cdot \cos \Psi + \sin \Phi \cdot \sin \Psi \cdot \sin \Theta) - \\ \dot{\lambda} \cdot \cos \phi \cdot (\cos \Phi \cdot \sin \Psi - \cos \Psi \cdot \sin \Phi \cdot \sin \Theta) - \\ \omega_E \cdot \cos \phi \cdot (\cos \Phi \cdot \sin \Psi - \cos \Psi \cdot \sin \Phi \cdot \sin \Theta) - \\ \dot{\lambda} \cdot \cos \Theta \cdot \sin \Phi \cdot \sin \phi - \omega_E \cdot \cos \Theta \cdot \sin \Phi \cdot \sin \phi \\ \dot{\phi} \cdot (\cos \Psi \cdot \sin \Phi - \cos \Phi \cdot \sin \Psi \cdot \sin \Theta) + \\ \dot{\lambda} \cdot \cos \phi \cdot (\sin \Phi \cdot \sin \Psi + \cos \Phi \cdot \cos \Psi \cdot \sin \Theta) + \\ \omega_E \cdot \cos \phi \cdot (\sin \Phi \cdot \sin \Psi + \cos \Phi \cdot \cos \Psi \cdot \sin \Theta) - \\ \dot{\lambda} \cdot \cos \Phi \cdot \cos \Theta \cdot \sin \phi - \omega_E \cdot \cos \Phi \cdot \cos \Theta \cdot \sin \phi \end{bmatrix} \quad (\text{B.4})$$

The angular acceleration of the NED (O) frame relative to the ECI frame denoted in the body fixed frame and derived with respect to the body fixed frame results in

$$\begin{aligned}
 \left(\dot{\omega}_{K,x}^{IO} \right)_B &= \ddot{\lambda} \cdot \sin \Theta \cdot \sin \phi - \ddot{\phi} \cdot \cos \Theta \cdot \sin \Psi + \ddot{\lambda} \cdot \cos \Psi \cdot \cos \Theta \cdot \cos \phi - \\
 &\quad \dot{\Psi} \cdot \dot{\phi} \cdot \cos \Psi \cdot \cos \Theta + \dot{\Theta} \cdot \dot{\phi} \cdot \sin \Psi \cdot \sin \Theta + \dot{\Theta} \cdot \dot{\lambda} \cdot \cos \Theta \cdot \sin \phi + \\
 &\quad \dot{\Theta} \cdot \omega_E \cdot \cos \Theta \cdot \sin \phi + \dot{\lambda} \cdot \dot{\phi} \cdot \sin \Theta \cdot \cos \phi + \omega_E \cdot \dot{\phi} \cdot \sin \Theta \cdot \cos \phi - \\
 &\quad \dot{\Psi} \cdot \dot{\lambda} \cdot \cos \Theta \cdot \sin \Psi \cdot \cos \phi - \dot{\Psi} \cdot \omega_E \cdot \cos \Theta \cdot \sin \Psi \cdot \cos \phi - \\
 &\quad \dot{\Theta} \cdot \dot{\lambda} \cdot \cos \Psi \cdot \sin \Theta \cdot \cos \phi - \dot{\Theta} \cdot \omega_E \cdot \cos \Psi \cdot \sin \Theta \cdot \cos \phi - \\
 &\quad \dot{\lambda} \cdot \dot{\phi} \cdot \cos \Psi \cdot \cos \Theta \cdot \sin \phi - \omega_E \cdot \dot{\phi} \cdot \cos \Psi \cdot \cos \Theta \cdot \sin \phi \\
 \left(\dot{\omega}_{K,y}^{IO} \right)_B &= \dot{\Phi} \cdot \dot{\phi} \cdot \cos \Psi \cdot \sin \Phi - \ddot{\lambda} \cdot \cos \Phi \cdot \sin \Psi \cdot \cos \phi - \\
 &\quad \ddot{\phi} \cdot \sin \Phi \cdot \sin \Psi \cdot \sin \Theta - \ddot{\lambda} \cdot \cos \Theta \cdot \sin \Phi \cdot \sin \phi - \ddot{\phi} \cdot \cos \Phi \cdot \cos \Psi + \\
 &\quad \dot{\Psi} \cdot \dot{\phi} \cdot \cos \Phi \cdot \sin \Psi - \dot{\Psi} \cdot \dot{\lambda} \cdot \cos \Phi \cdot \cos \Psi \cdot \cos \phi - \\
 &\quad \dot{\Psi} \cdot \omega_E \cdot \cos \Phi \cdot \cos \Psi \cdot \cos \phi - \dot{\Phi} \cdot \dot{\phi} \cdot \cos \Phi \cdot \sin \Psi \cdot \sin \Theta - \\
 &\quad \dot{\Psi} \cdot \dot{\phi} \cdot \cos \Psi \cdot \sin \Phi \cdot \sin \Theta - \dot{\Theta} \cdot \dot{\phi} \cdot \cos \Theta \cdot \sin \Phi \cdot \sin \Psi - \\
 &\quad \dot{\Phi} \cdot \dot{\lambda} \cdot \cos \Phi \cdot \cos \Theta \cdot \sin \phi - \dot{\Phi} \cdot \omega_E \cdot \cos \Phi \cdot \cos \Theta \cdot \sin \phi + \\
 &\quad \dot{\Phi} \cdot \dot{\lambda} \cdot \sin \Phi \cdot \sin \Psi \cdot \cos \phi + \dot{\Phi} \cdot \omega_E \cdot \sin \Phi \cdot \sin \Psi \cdot \cos \phi - \\
 &\quad \dot{\lambda} \cdot \dot{\phi} \cdot \cos \Theta \cdot \sin \Phi \cdot \cos \phi - \omega_E \cdot \dot{\phi} \cdot \cos \Theta \cdot \sin \Phi \cdot \cos \phi + \\
 &\quad \dot{\Theta} \cdot \dot{\lambda} \cdot \sin \Phi \cdot \sin \Theta \cdot \sin \phi + \dot{\Theta} \cdot \omega_E \cdot \sin \Phi \cdot \sin \Theta \cdot \sin \phi + \\
 &\quad \dot{\lambda} \cdot \dot{\phi} \cdot \cos \Phi \cdot \sin \Psi \cdot \sin \phi + \omega_E \cdot \dot{\phi} \cdot \cos \Phi \cdot \sin \Psi \cdot \sin \phi + \\
 &\quad \ddot{\lambda} \cdot \cos \Psi \cdot \sin \Phi \cdot \sin \Theta \cdot \cos \phi + \dot{\Phi} \cdot \dot{\lambda} \cdot \cos \Phi \cdot \cos \Psi \cdot \sin \Theta \cdot \cos \phi + \\
 &\quad \dot{\Phi} \cdot \omega_E \cdot \cos \Phi \cdot \cos \Psi \cdot \sin \Theta \cdot \cos \phi + \dot{\Theta} \cdot \dot{\lambda} \cdot \cos \Psi \cdot \cos \Theta \cdot \sin \Phi \cdot \cos \phi + \\
 &\quad \dot{\Theta} \cdot \omega_E \cdot \cos \Psi \cdot \cos \Theta \cdot \sin \Phi \cdot \cos \phi - \dot{\Psi} \cdot \dot{\lambda} \cdot \sin \Phi \cdot \sin \Psi \cdot \sin \Theta \cdot \cos \phi - \\
 &\quad \dot{\Psi} \cdot \omega_E \cdot \sin \Phi \cdot \sin \Psi \cdot \sin \Theta \cdot \cos \phi - \dot{\lambda} \cdot \dot{\phi} \cdot \cos \Psi \cdot \sin \Phi \cdot \sin \Theta \cdot \sin \phi -
 \end{aligned} \quad (\text{B.5})$$

$$\begin{aligned}
 & \omega_E \cdot \dot{\phi} \cdot \cos \Psi \cdot \sin \Phi \cdot \sin \Theta \cdot \sin \phi \\
 \left(\dot{\omega}_{K,z}^{IO} \right)_B^B &= \ddot{\phi} \cdot \cos \Psi \cdot \sin \Phi - \ddot{\phi} \cdot \cos \Phi \cdot \sin \Psi \cdot \sin \Theta - \ddot{\lambda} \cdot \cos \Phi \cdot \cos \Theta \cdot \sin \phi + \\
 & \ddot{\lambda} \cdot \sin \Phi \cdot \sin \Psi \cdot \cos \phi + \dot{\Phi} \cdot \dot{\phi} \cdot \cos \Phi \cdot \cos \Psi - \dot{\Psi} \cdot \dot{\phi} \cdot \sin \Phi \cdot \sin \Psi - \\
 & \dot{\Psi} \cdot \dot{\phi} \cdot \cos \Phi \cdot \cos \Psi \cdot \sin \Theta - \dot{\Theta} \cdot \dot{\phi} \cdot \cos \Phi \cdot \cos \Theta \cdot \sin \Psi + \\
 & \dot{\Phi} \cdot \dot{\lambda} \cdot \cos \Phi \cdot \sin \Psi \cdot \cos \phi + \dot{\Psi} \cdot \dot{\lambda} \cdot \cos \Psi \cdot \sin \Phi \cdot \cos \phi + \\
 & \dot{\Phi} \cdot \omega_E \cdot \cos \Phi \cdot \sin \Psi \cdot \cos \phi + \dot{\Psi} \cdot \omega_E \cdot \cos \Psi \cdot \sin \Phi \cdot \cos \phi + \\
 & \dot{\Phi} \cdot \dot{\phi} \cdot \sin \Phi \cdot \sin \Psi \cdot \sin \Theta + \dot{\Phi} \cdot \dot{\lambda} \cdot \cos \Theta \cdot \sin \Phi \cdot \sin \phi - \\
 & \dot{\lambda} \cdot \dot{\phi} \cdot \cos \Phi \cdot \cos \Theta \cdot \cos \phi + \dot{\Phi} \cdot \omega_E \cdot \cos \Theta \cdot \sin \Phi \cdot \sin \phi - \\
 & \omega_E \cdot \dot{\phi} \cdot \cos \Phi \cdot \cos \Theta \cdot \cos \phi + \dot{\Theta} \cdot \dot{\lambda} \cdot \cos \Phi \cdot \sin \Theta \cdot \sin \phi + \\
 & \dot{\Theta} \cdot \omega_E \cdot \cos \Phi \cdot \sin \Theta \cdot \sin \phi - \dot{\lambda} \cdot \dot{\phi} \cdot \sin \Phi \cdot \sin \Psi \cdot \sin \phi - \\
 & \omega_E \cdot \dot{\phi} \cdot \sin \Phi \cdot \sin \Psi \cdot \sin \phi + \ddot{\lambda} \cdot \cos \Phi \cdot \cos \Psi \cdot \sin \Theta \cdot \cos \phi + \\
 & \dot{\Theta} \cdot \dot{\lambda} \cdot \cos \Phi \cdot \cos \Psi \cdot \cos \Theta \cdot \cos \phi + \dot{\Theta} \cdot \omega_E \cdot \cos \Phi \cdot \cos \Psi \cdot \cos \Theta \cdot \cos \phi - \\
 & \dot{\Phi} \cdot \dot{\lambda} \cdot \cos \Psi \cdot \sin \Phi \cdot \sin \Theta \cdot \cos \phi - \dot{\Psi} \cdot \dot{\lambda} \cdot \cos \Phi \cdot \sin \Psi \cdot \sin \Theta \cdot \cos \phi - \\
 & \dot{\Phi} \cdot \omega_E \cdot \cos \Psi \cdot \sin \Phi \cdot \sin \Theta \cdot \cos \phi - \dot{\Psi} \cdot \omega_E \cdot \cos \Phi \cdot \sin \Psi \cdot \sin \Theta \cdot \cos \phi - \\
 & \dot{\lambda} \cdot \dot{\phi} \cdot \cos \Phi \cdot \cos \Psi \cdot \sin \Theta \cdot \sin \phi - \omega_E \cdot \dot{\phi} \cdot \cos \Phi \cdot \cos \Psi \cdot \sin \Theta \cdot \sin \phi
 \end{aligned}$$

The angular acceleration of the NED (O) frame relative to the Earth Centered Earth Fixed (E) frame derived with respect to the B -frame and also denoted in the B -frame comprises of the elements

$$\begin{aligned}
 \left(\dot{\omega}_{K,x}^{EO} \right)_B^B &= \ddot{\lambda} \cdot \sin \Theta \cdot \sin \phi - \ddot{\phi} \cdot \cos \Theta \cdot \sin \Psi + \ddot{\lambda} \cdot \cos \Psi \cdot \cos \Theta \cdot \cos \phi - \\
 & \dot{\Psi} \cdot \dot{\phi} \cdot \cos \Psi \cdot \cos \Theta + \dot{\Theta} \cdot \dot{\phi} \cdot \sin \Psi \cdot \sin \Theta + \dot{\Theta} \cdot \dot{\lambda} \cdot \cos \Theta \cdot \sin \phi + \\
 & \dot{\lambda} \cdot \dot{\phi} \cdot \sin \Theta \cdot \cos \phi - \dot{\Psi} \cdot \dot{\lambda} \cdot \cos \Theta \cdot \sin \Psi \cdot \cos \phi - \\
 & \dot{\Theta} \cdot \dot{\lambda} \cdot \cos \Psi \cdot \sin \Theta \cdot \cos \phi - \dot{\lambda} \cdot \dot{\phi} \cdot \cos \Psi \cdot \cos \Theta \cdot \sin \phi \\
 \left(\dot{\omega}_{K,y}^{EO} \right)_B^B &= \dot{\lambda} \cdot \cos \phi \cdot \left(\dot{\Phi} \cdot \sin \Phi \cdot \sin \Psi - \dot{\Psi} \cdot \cos \Phi \cdot \cos \Psi + \dot{\Phi} \cdot \cos \Phi \cdot \cos \Psi \cdot \sin \Theta + \right. \\
 & \left. \dot{\Theta} \cdot \cos \Psi \cdot \cos \Theta \cdot \sin \Phi - \dot{\Psi} \cdot \sin \Phi \cdot \sin \Psi \cdot \sin \Theta \right) - \ddot{\phi} \cdot (\cos \Phi \cdot \cos \Psi + \\
 & \sin \Phi \cdot \sin \Psi \cdot \sin \Theta) - \dot{\phi} \cdot \left(\dot{\Phi} \cdot \cos \Phi \cdot \sin \Psi \cdot \sin \Theta - \dot{\Psi} \cdot \cos \Phi \cdot \sin \Psi - \right. \\
 & \left. \dot{\Phi} \cdot \cos \Psi \cdot \sin \Phi + \dot{\Psi} \cdot \cos \Psi \cdot \sin \Phi \cdot \sin \Theta + \dot{\Theta} \cdot \cos \Theta \cdot \sin \Phi \cdot \sin \Psi \right) - \quad (B.6) \\
 & \ddot{\lambda} \cdot \cos \phi \cdot (\cos \Phi \cdot \sin \Psi - \cos \Psi \cdot \sin \Phi \cdot \sin \Theta) - \ddot{\lambda} \cdot \cos \Theta \cdot \sin \Phi \cdot \sin \phi + \\
 & \dot{\lambda} \cdot \dot{\phi} \cdot \sin \phi \cdot (\cos \Phi \cdot \sin \Psi - \cos \Psi \cdot \sin \Phi \cdot \sin \Theta) - \dot{\Phi} \cdot \dot{\lambda} \cdot \cos \Phi \cdot \cos \Theta \cdot \sin \phi - \\
 & \dot{\lambda} \cdot \dot{\phi} \cdot \cos \Theta \cdot \sin \Phi \cdot \cos \phi + \dot{\Theta} \cdot \dot{\lambda} \cdot \sin \Phi \cdot \sin \Theta \cdot \sin \phi
 \end{aligned}$$

$$\begin{aligned}
 \left(\dot{\omega}_{K,z}^{EO} \right)_B^B &= \ddot{\phi} \cdot (\cos \Psi \cdot \sin \Phi - \cos \Phi \cdot \sin \Psi \cdot \sin \Theta) - \dot{\phi} \cdot \left(\dot{\Psi} \cdot \sin \Phi \cdot \sin \Psi - \right. \\
 & \left. \dot{\Phi} \cdot \cos \Phi \cdot \cos \Psi + \dot{\Psi} \cdot \cos \Phi \cdot \cos \Psi \cdot \sin \Theta + \dot{\Theta} \cdot \cos \Phi \cdot \cos \Theta \cdot \sin \Psi - \right.
 \end{aligned}$$

$$\begin{aligned}
& \dot{\Phi} \cdot \sin \Phi \cdot \sin \Psi \cdot \sin \Theta) + \dot{\lambda} \cdot \cos \phi \cdot (\dot{\Phi} \cdot \cos \Phi \cdot \sin \Psi + \dot{\Psi} \cdot \cos \Psi \cdot \sin \Phi + \\
& \dot{\Theta} \cdot \cos \Phi \cdot \cos \Psi \cdot \cos \Theta - \dot{\Phi} \cdot \cos \Psi \cdot \sin \Phi \cdot \sin \Theta - \dot{\Psi} \cdot \cos \Phi \cdot \sin \Psi \cdot \sin \Theta) + \\
& \ddot{\lambda} \cdot \cos \phi \cdot (\sin \Phi \cdot \sin \Psi + \cos \Phi \cdot \cos \Psi \cdot \sin \Theta) - \ddot{\lambda} \cdot \cos \Phi \cdot \cos \Theta \cdot \sin \phi - \\
& \dot{\lambda} \cdot \dot{\phi} \cdot \sin \phi \cdot (\sin \Phi \cdot \sin \Psi + \cos \Phi \cdot \cos \Psi \cdot \sin \Theta) + \dot{\Phi} \cdot \dot{\lambda} \cdot \cos \Theta \cdot \sin \Phi \cdot \sin \phi - \\
& \dot{\lambda} \cdot \dot{\phi} \cdot \cos \Phi \cdot \cos \Theta \cdot \cos \phi + \dot{\Theta} \cdot \dot{\lambda} \cdot \cos \Phi \cdot \sin \Theta \cdot \sin \phi
\end{aligned}$$

Appendix C

Miscellaneous

The translation motion of the aircraft relative to the earth changes the position of the aircraft. In order to describe the position propagation of the aircraft, the following position differential equations are employed

$$\begin{bmatrix} \dot{\lambda} \\ \dot{\phi} \\ \dot{h} \end{bmatrix}_O^E = \begin{bmatrix} \frac{v_K^G}{(N_\mu + h) \cdot \cos \phi} \\ \frac{u_K^G}{(M_\mu + h) \cdot \cos \phi} \\ -w_K^G \end{bmatrix}_O^E. \quad (\text{C.1})$$

The nonlinear state transformation $z = \Phi(x)$, presented in the section 3.1.1, for a generic nonlinear system defined by Eq. (3.1) is valid only if it is at least a local diffeomorphism i.e. uniquely invertible in the local region where the transformation is defined. Local diffeomorphism can be verified through the linear independence of the first r rows of the Jacobian matrix

$$\nabla \Phi(x) = \frac{\partial \Phi}{\partial x} = \begin{bmatrix} \frac{\partial \Phi_1}{\partial x_1} & \frac{\partial \Phi_1}{\partial x_2} & \frac{\partial \Phi_1}{\partial x_3} & \dots & \frac{\partial \Phi_1}{\partial x_{n_x}} \\ \frac{\partial \Phi_2}{\partial x_1} & \frac{\partial \Phi_2}{\partial x_2} & \dots & \dots & \frac{\partial \Phi_2}{\partial x_{n_x}} \\ \vdots & \vdots & \ddots & \ddots & \vdots \\ \vdots & \vdots & \ddots & \ddots & \frac{\partial \Phi_{r-1}}{\partial x_{n_x}} \\ \frac{\partial \Phi_r}{\partial x_1} & \frac{\partial \Phi_r}{\partial x_2} & \frac{\partial \Phi_r}{\partial x_3} & \dots & \frac{\partial \Phi_r}{\partial x_{n_x}} \end{bmatrix}. \quad (\text{C.2})$$

C.1 Order Analysis of Improper Accelerations

C.1.1 Acceleration due to Transport Rate

The resulting magnitude from the order analysis of acceleration due to transport rate in Eq. (2.40) is presented over absolute latitude $|\phi|$ and control frame forward velocity in Figure C.1. The magnitudes of the acceleration's vector components are computed based on the values and ranges of the states listed in Table C.1.

States	Magnitude
Forward Velocity in C -frame $(u_K^R)_C^E, m/s$	[0, 110]
Lateral Velocity in C -frame $(v_K^R)_C^E, m/s$	20
Vertical Velocity in C -frame $(w_K^R)_C^E, m/s$	-10
Absolute Latitude $ \phi , deg$	[0, 89]
Yaw angle Ψ, deg	45

Table C.1: Magnitude of states for order analysis of acceleration due to transport rate

Due to the presence of the singularity in $\dot{\lambda}$ at a latitude of 90° , the x -component of $(\vec{a}_{tr}^R)_C$ increases to a magnitude of $0.017 m/s^2$ at 89° from $1.8 \times 10^{-3} m/s^2$ at 80° while the control frame velocity is constant at $110 m/s$. Upon opposing the signs of lateral and vertical velocities in Table C.1, the resultant magnitude of $(a_{x,tr}^R)_C$ for same forward velocity are $-0.012 m/s^2$ at 89° and $-2.4 \times 10^{-3} m/s^2$ at 80° latitude.

Similarly, the lateral component of $(\vec{a}_{tr}^R)_C$ rises drastically to $-0.0905 m/s^2$ at a latitude of 89° owing to the singularity in $\dot{\lambda}$. Until the latitude of 80° , the maximum value of $(a_{y,tr}^R)_C$ is observed to be $-8.9 \times 10^{-3} m/s^2$. Alternatively, the vertical component $(a_{z,tr}^R)_C$ does not consist of any singularity and it reaches a maximum magnitude of $2 \times 10^{-3} m/s^2$.

If the latitudes of the southern hemisphere $[0^\circ, -89^\circ]$ are considered, the x and y components of the acceleration flip their signs. Table C.2 summarizes the resultant ranges of magnitude for all components of $(\vec{a}_{tr}^R)_C$ in this analysis.

Vector	$(\vec{a}_{tr}^R)_C$ at (Latitude $^\circ, (u_K^R)_C^E m/s$)		
	$(\pm 89, 110)$	$(\pm 80, 110)$	$(\pm 65, 110)$
$x, m/s^2$	$[-0.016, 0.017]$	$[-1.3, 1.8] \times 10^{-3}$	$[-5.9, 7.8] \times 10^{-4}$
$y, m/s^2$	$[-0.091, 0.091]$	$[-8.9, 8.9] \times 10^{-3}$	$[-3.4, 3.4] \times 10^{-3}$
$z, m/s^2$	$[0, 2] \times 10^{-3}$	$[0, 2] \times 10^{-3}$	$[0, 2] \times 10^{-3}$

Table C.2: Range of components of acceleration due to transport rate in C -frame

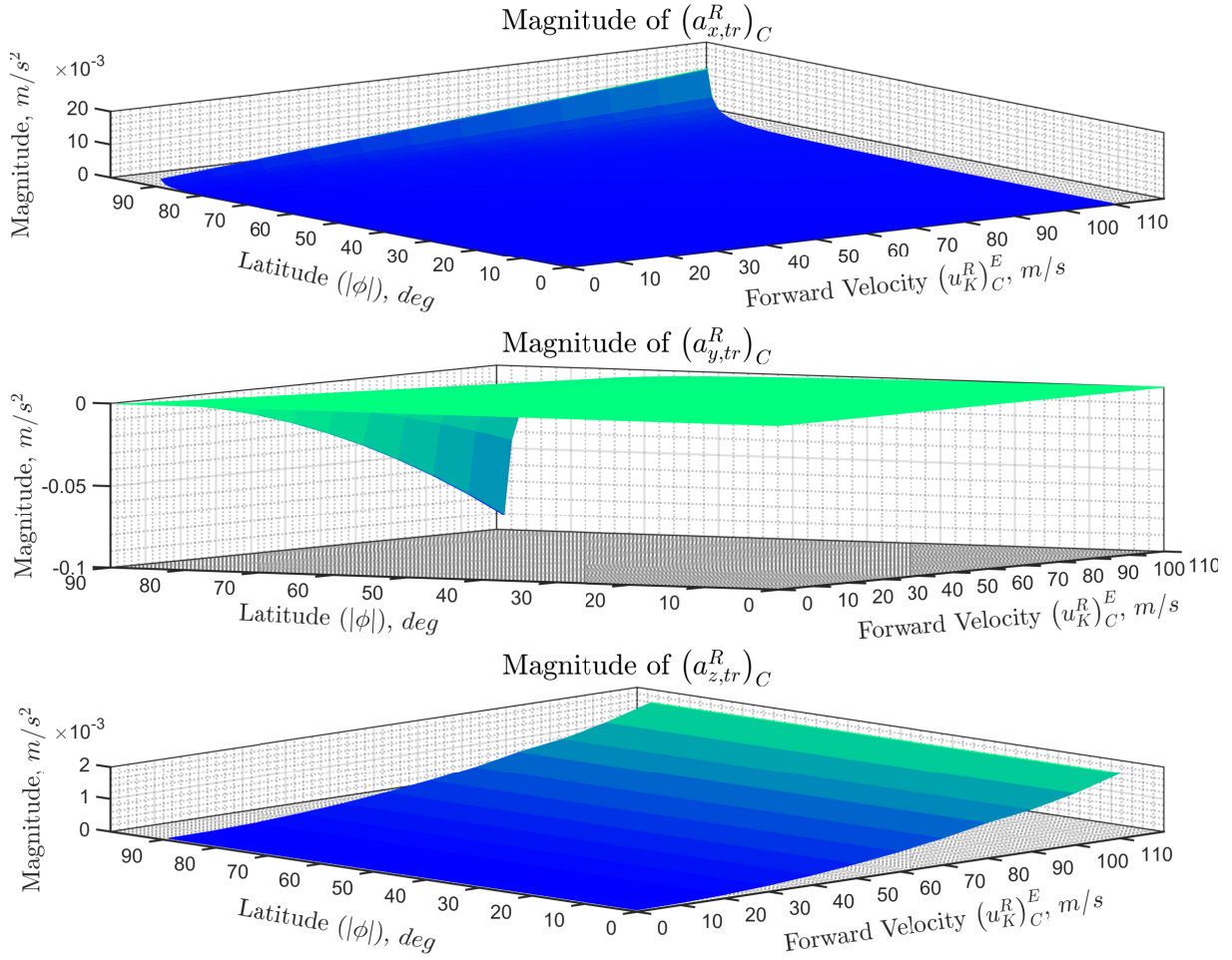


Figure C.1: Magnitudes of $(\vec{a}_{tr}^R)_C$

C.1.2 Acceleration due to Earth's Rotation

The effect pertaining to the centrifugal acceleration due to Earth's rotation in Eq. (2.46) has the square of the rotational rate of Earth ω_E^2 as a multiplier which amounts to 5.2885×10^{-9} . Other terms of notice in this component are the local position coordinates in the control frame. Since the maximum range of the configurations considered in this work lie within $300 \text{ km} = 3 \times 10^5 \text{ m}$, the centrifugal acceleration generated by Earth's rotation is neglected. Only the Coriolis acceleration produced by rotation of the Earth is used in the subsequent analysis.

The magnitudes of the vector components of $(\vec{a}_{e,rot}^R)_C$ are illustrated in Figure C.2 over a range of absolute latitude and forward velocity in the C -frame similar to the ranges specified in Table C.1. The lateral and vertical velocities are set to zero for the generation of the plots in Figure C.2. Therefore, the x -component of this acceleration remains at zero because it is only affected by the lateral and vertical velocity in the control frame. However, a maximum value for x -component

$$(a_{x,e,rot}^R)_C = 2 \cdot \omega_E \cdot \left((v_K^R)_C^E \cdot \sin \phi - (w_K^R)_C^E \cdot \sin \Psi \cdot \cos \phi \right) \quad (\text{C.3})$$

is calculated by using the values in Table C.3. The velocities mentioned in this table lie outside the physical envelope of any aircraft considered in this thesis. These values are chosen to maximize the magnitude of $(a_{x_{e,rot}}^R)_C$ so that a quantitative justification is available for neglecting this term in the control law derivation. The resultant magnitude of the vector component in Eq. C.3 is 3.25×10^{-3} . If the signs of the velocities in Table C.3 are opposed, the resulting magnitude is -3.25×10^{-3} . Hence, $(a_{x_{e,rot}}^R)_C$ lies in the range $[-3.25, 3.25] \times 10^{-3}$.

States	Magnitude
Lateral Velocity in C -frame $(v_K^R)_C^E, m/s$	20
Vertical Velocity in C -frame $(w_K^R)_C^E, m/s$	-10
Latitude $\phi, deg,$	63
Yaw angle $\Psi, deg,$	90

Table C.3: Magnitude of states for order analysis of the x -component of acceleration due to transport rate and Earth's rotation

As stated earlier, the lateral and vertical velocities are not considered in the order calculation for the remaining vector components since these velocity ranges are small as compared to the forward velocity range therefore no major effects are neglected. As the earth's north pole is approached at the velocity of $110 m/s$, the y -component approaches a maximum negative magnitude of $-0.016 m/s^2$. If the full latitude range $[-89^\circ, 89^\circ]$ is considered instead of the absolute latitude, the y -component would lie in the range $[-0.016, 0.016]$. Although, this acceleration does not contain any singularity at the poles, their latitudes $\pm 90^\circ$ are not considered here to remain consistent with the analysis done earlier. This component's magnitude reduces to a range of $[-9.5, 9.5] \times 10^{-3}$ within the maximum kinematic velocity $65 m/s = 126.35 kts$ which is a realistic upper limit of kinematic velocity for an urban aviation purposes. Furthermore, the z -component reaches the maximum magnitude of $0.016 m/s^2$ at the velocity of $110 m/s$ at the 0° latitude with a bearing of 90° . Nonetheless, within the operating velocity range of $65 m/s$, it is also reduced to a magnitude of 9.5×10^{-3} . Table C.4 summarizes some of the ranges of the acceleration due to Earth's rotation at different latitudes and velocities that are of importance for some derivations in this work.

Vector	$(\vec{a}_{e,rot}^R)_C$ at (Latitude $^\circ$, $(u_K^R)_C^E$ m/s)	
Components ($\pm 89, 110$)	($\pm 89, 65$)	
$x, m/s^2$	$[-3.25, 3.25] \times 10^{-3}$	$[-3.25, 3.25] \times 10^{-3}$
$y, m/s^2$	$[-0.016, 0.016]$	$[-9.5, 9.5] \times 10^{-3}$
$z, m/s^2$	$[-0.016, 0.016]$	$[-9.5, 9.5] \times 10^{-3}$

Table C.4: Range of components of acceleration due to Earth's rotation in C-frame

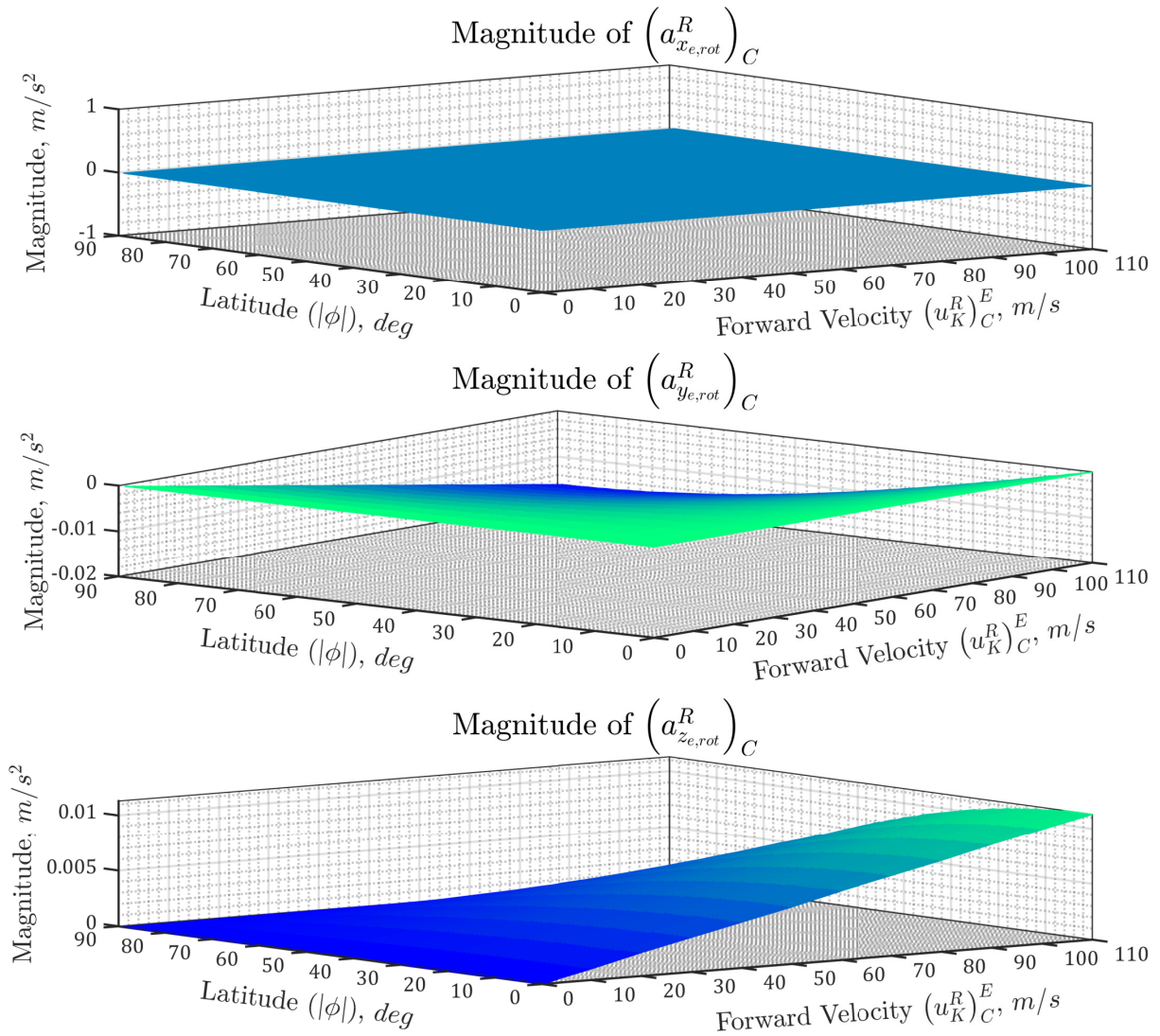


Figure C.2: Magnitudes of $(\vec{a}_{e,rot}^R)_C$

Appendix D

Design Plant Adaptation in Jerk-level Reference Model

Pranav Bhardwaj ^{*}, Philipp Müller [†], Florian Holzapfel [‡]

Institute of Flight System Dynamics, Technische Universität München, Garching, 85748, Germany

Parameters of the state dependent damping terms incorporated in the design plant of a higher order reference model are adapted. Accurate identification of these parameters augments the feedforward pseudo control derivative generation, which improves the set point tracking performance of an extended incremental nonlinear dynamic inversion controller. A state predictor based adaptive control architecture is employed for the parameter identification task. This strategy is different from the predictor based model reference adaptive control approach in which the identified difference between real plant and desired dynamics is used to compute an adaptive control input. Contrarily, in the proposed framework, the estimated deviation between the design plant and the true plant parameters is utilized to produce an augmented feedforward command. Additionally, physically meaningful bounds of the adapted parameters available using classical linear analysis of the closed loop system are used to restrict the adaptation of the parameters, thereby retaining the robustness of the extended incremental strategy.

I. Nomenclature

x	=	State vector
u	=	Control input vector
y	=	Output vector
r	=	Relative Degree
v	=	Pseudo control vector
A_v	=	System matrix of the transformed system
B_v	=	Control input matrix of the transformed system
G	=	Transfer function
a	=	Internal reference model coefficients
C	=	Gain vector
K	=	Diagonal gain matrix
e	=	Error vector
Θ_v^*	=	Ideal state deviation matrix
$\hat{\Theta}_v$	=	State deviation matrix estimate
X_{iR}	=	Internal reference signal X
X_R	=	Reference variable/signal X
X_{ff}	=	Feedforward signal X
X_{cmd}	=	Command signal X
X_e	=	Error signal X
X_P	=	Plant signal X
$X^{(r)}$	=	r -th derivative of variable X

II. Introduction

INCREMENTAL nonlinear dynamic inversion (INDI) has been proposed as a robust alternative to nonlinear dynamic inversion (NDI) in recent times [1–6]. The increased robustness of the INDI strategy is credited to substituting a full

^{*}Research Assistant, E-Mail: pranav.bhardwaj@tum.de.

[†]Graduate Student, E-Mail: philippjulius.mueller@tum.de.

[‡]Professor, E-Mail: Florian.Holzapfel@tum.de, Associate Fellow AIAA.

plant model inversion (as in NDI) by the inversion of a linearized control input matrix facilitated through use of state derivative measurements or estimates. Therefore, use of INDI disposes the need of having an accurate plant model while still providing high control performance. In the derivation of the INDI control law, it is assumed that the actuators are instantaneously fast and the controller is operated at a high refresh rate. Following these assumptions, the state dependent component of the linearized plant dynamics was neglected in the control law derivation.

Assumption of instantaneously fast actuators is not practical. Therefore, in order to consider actuator dynamics within the control law, continuous dynamic inversion was proposed in [7, 8]. The continuous strategy eliminated the need of the linearization approximation by utilizing direct time derivatives of the nonlinear system. No additional plant feedback was required in the continuous extension to the incremental strategy. However, the state variant term was still disregarded in the control law derivation. For systems with considerable state dependent damping such as a fixed wing aircraft, and flight control architectures having a low controller sampling frequency, this assumption is invalid. In such cases, application of this assumption would generate errors which further enhance on traversing across the integrators of the feedback-linearized system even in absence of any model uncertainties and external disturbances. Usually these errors are compensated by using a proportional feedback error controller [9]. Nonetheless, an error controller does not provide a benefit in terms of improving controller performance which can otherwise be gained by using any knowledge of the plant dynamics.

A higher order reference model (HORM) structure was proposed in [10], which uses dynamic inversion of the design plant in the reference model (RM) to generate a feedforward command that can compensate for the state dependent damping terms. This was made possible by incorporating estimates of real plant parameters in the design plant. Moreover, it was demonstrated that the use of plant parameter estimates in the design plant of the HORM reduced the feedback control effort even when the parameter estimates were uncertain. Closed loop frequency domain analysis was performed to derive the range of this uncertainty in the design plant parameters as compared to the true parameters. It was shown that within this range of parameters, applying the HORM lowered the feedback control effort and significantly improved set point tracking.

Precise knowledge of true plant dynamics is not always available during practical applications. Therefore, in this article, the uncertain parameters related to the state dependent damping terms are estimated. The estimates are then incorporated in the design plant of the HORM. By identifying the real plant parameters accurately, the design plant can be brought closer to the true plant. Consequently, the feedforward pseudo control derivative generated by using the adapted design plant improves the set point tracking performance of an extended incremental nonlinear dynamic inversion controller. A state predictor based adaptive control architecture is employed for the parameter identification task. Usually, a predictor based model reference adaptive control (MRAC) is used to compute an adaptive control input by identification of the plant dynamics [6, 11]. However, the proposed approach is different since in this method the estimated deviation between the design plant and the true plant parameters is utilized to produce an augmented feedforward command. One of the advantage of using the MRAC architecture in this framework is that the parameters to be identified can be limited using meaningful bounds. For the purpose of this application, the bounds are dependent on the allowed uncertainty ranges derived in [10] through classical linear analysis. Therefore, the robustness of the extended incremental strategy is not degraded by restricting the adaptive parameters within the derived bounds.

III. Preliminaries

This section presents the theory of the continuous extension to the incremental nonlinear dynamic inversion (INDI) [7] for a general nonlinear system. Furthermore, the theory behind utilization of the state dependent terms for generation of the feedforward signal is detailed. The architecture of the nominal jerk-level reference models emanates from the philosophy of the feedforward command generation. The design plant of the reference model uses parameters which can differ from the true plant parameters. A predictor based model reference adaptive control approach is proposed to identify the true plant parameters for use in the design plant of the jerk level reference model, thereby aiding in the computation of an ideal feedforward command which produces the desired response in the plant without using the stabilizing error controller in case of no external disturbances.

A. System Description

A general nonlinear, input non-affine and time invariant system is considered for which the extended INDI control strategy will be derived later

$$\begin{aligned}\dot{\mathbf{x}}(t) &= \mathbf{f}(\mathbf{x}(t), \mathbf{u}(t)), \\ \mathbf{y}(t) &= \mathbf{h}(\mathbf{x}(t)),\end{aligned}\quad (1)$$

where $\mathbf{x}(t) \in \mathbb{R}^{n_x}$ denotes the state vector, the control input vector is represented by $\mathbf{u}(t) \in \mathbb{R}^{n_u}$ and $\mathbf{y}(t) \in \mathbb{R}^{n_y}$ stands for the plant output vector. The nonlinear function $\mathbf{f}_{n_x \times 1} : D_{\mathbf{x}} \rightarrow \mathbb{R}^{n_x}$ specifies the plant dynamics and $\mathbf{h}_{n_y \times 1} : D_{\mathbf{x}} \rightarrow \mathbb{R}^{n_y}$ indicates the output dynamics of the generic, nonlinear system. The dependency on time for the components of the nonlinear system $\mathbf{x}, \mathbf{u}, \mathbf{y}$ in Eq. (1) is not shown further in this article for improving readability. Every output y_i of the system in Eq. (1) is differentiated repeatedly with respect to the control input \mathbf{u}

$$\frac{\partial y_i^{(k)}}{\partial \mathbf{u}} = \mathbf{0}^T, \dots, \quad \frac{\partial y_i^{(r_i)}}{\partial \mathbf{u}} \neq \mathbf{0}^T \quad \forall k \in [0, 1, \dots, r_i - 1]. \quad (2)$$

until a non-zero derivative $y_i^{(r_i)}$ occurs. The order r_i of this non-zero derivative is the relative degree of the output channel y_i for the nonlinear system in Eq. (1). It is assumed that the sum of the relative degrees for all outputs is equal to the number of states \mathbf{x} of the nonlinear system, thereby asserting that the system has no internal states. Results for every output from Eq. (2)

$$\mathbf{v}_i = F_i(\mathbf{x}, \mathbf{u}) = y_i^{(r_i)}, \quad (3)$$

are collected together to show the transformed system in terms of the pseudo control vector $\mathbf{v}(t)$ which contains the derivatives $y_i^{(r_i)}$ for all output channels

$$\mathbf{v} = \mathbf{F}(\mathbf{x}, \mathbf{u}). \quad (4)$$

Here, the reformulated plant dynamics are denoted by the function $\mathbf{F}_{n_x \times 1} : D_{\mathbf{x}} \rightarrow \mathbb{R}^{n_x}$. The transformation of the general nonlinear system to the reformulated system in Eq. (4) is depicted in Fig. 1. This transformed system is significant since it provides a straight forward path to derive the extended incremental nonlinear dynamic inversion law in the next section.

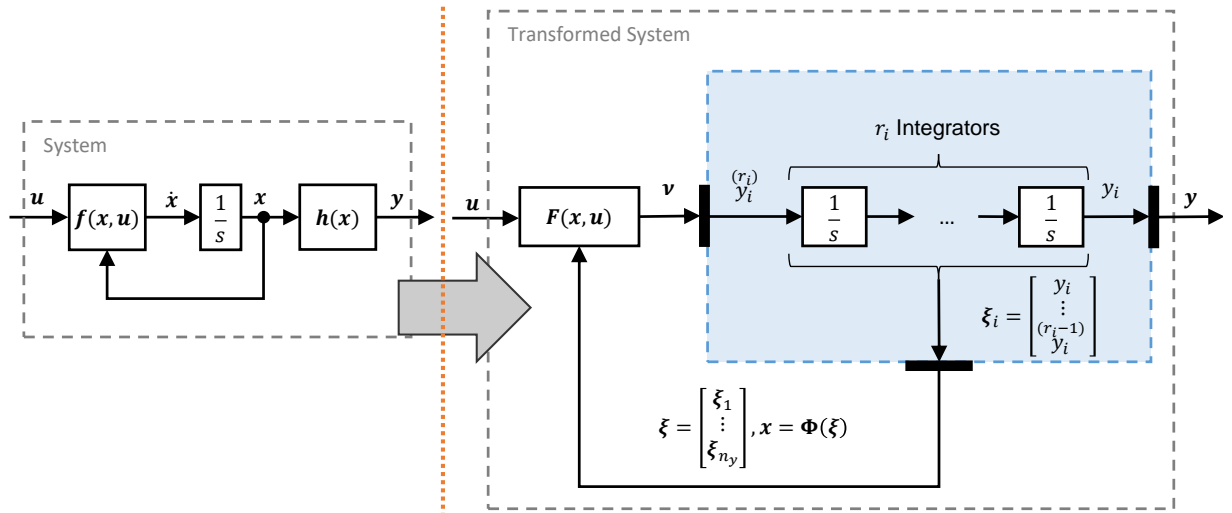


Fig. 1 System Transformation [10]

B. Extended Incremental Nonlinear Dynamic Inversion

The derivation of the INDI control law in [1–5] uses a Taylor series approximation of nonlinear system dynamics given by Eq. (4). Consequently, the derived control strategy delivers the advantage of inverting linearized aircraft dynamics based on current state \mathbf{x}_0 and control input \mathbf{u}_0 feedback instead of full aircraft dynamics. Additionally, state derivative

feedback is needed for the online linearization of the aircraft dynamics. As a result, INDI provides increased robustness against model uncertainties as compared to nonlinear dynamic inversion (NDI) control strategy by utilizing model information inherent in the state derivative feedback. Nevertheless, in [7] a new method was proposed which, along with retaining the advantages of INDI, also provides the possibility of accounting for actuator dynamics within the control law.

For deriving the extended INDI control law, the reformulated system defined in Eq. (4) is considered. Computing the first order time derivative of the pseudo control \mathbf{v} results in

$$\begin{aligned}\dot{\mathbf{v}} &= \underbrace{\frac{\partial \mathbf{F}}{\partial \mathbf{x}}}_{\mathbf{A}_v} \cdot \dot{\mathbf{x}} + \underbrace{\frac{\partial \mathbf{F}}{\partial \mathbf{u}}}_{\mathbf{B}_v} \cdot \dot{\mathbf{u}}, \\ \dot{\mathbf{v}} &= \underbrace{\mathbf{A}_v \cdot \dot{\mathbf{x}}}_{\dot{\mathbf{v}}_x} + \underbrace{\mathbf{B}_v \cdot \dot{\mathbf{u}}}_{\dot{\mathbf{v}}_u}.\end{aligned}\tag{5}$$

It is assumed that the controller sampling time is small (order of $10e^{-3}s$). Additionally, it is assumed that the actuators are faster than the state dynamics. Therefore, the effect of $\dot{\mathbf{v}}_x$ on $\dot{\mathbf{v}}$ is negligible when compared to the effect of $\dot{\mathbf{v}}_u$ within the small controller sampling time such that approximately

$$\dot{\mathbf{v}} = \mathbf{B}_v \cdot \dot{\mathbf{u}}.\tag{6}$$

Given a pseudo control rate command $\dot{\mathbf{v}}_{u,cmd}$ to be produced by the control input rate, the inversion law is computed from Eq. (6)

$$\dot{\mathbf{u}}_{cmd} = \mathbf{B}_v^{-1} \cdot \dot{\mathbf{v}}_{u,cmd}.\tag{7}$$

Detailed information on the generation of the effector control input command \mathbf{u}_{cmd} from the control input rate command $\dot{\mathbf{u}}_{cmd}$ is given in [7]. Closed loop dynamics of the controller with the nonlinear system are derived by substituting the control law from Eq. (7) in the transformed system from Eq. (5) to gain more insight

$$\begin{aligned}\dot{\mathbf{v}} &= \mathbf{A}_v \cdot \dot{\mathbf{x}} + \mathbf{B}_v \cdot \mathbf{B}_v^{-1} \cdot \dot{\mathbf{v}}_{u,cmd}, \\ \dot{\mathbf{v}} - \dot{\mathbf{v}}_{u,cmd} &= \underbrace{\mathbf{A}_v \cdot \dot{\mathbf{x}}}_{\Delta_x}.\end{aligned}\tag{8}$$

The residual pseudo control rate error Δ_x , emanating from the neglected state dependent part in the closed loop dynamics, would generate an error in the outputs \mathbf{y} by propagating through a chain of $r + 1$ integrators. The error propagation occurs even in the ideal case where the plant dynamics are known exactly. Generally, a stabilizing output error controller is used [5, 7, 8] to subside the error propagation. Nevertheless, no system parameter knowledge is leveraged.

It was proposed in the previous work [10] to include the effect of the state dependent term in the feedforward command. The resulting strategy improved the set point tracking of the closed loop system as long as the design plant parameters in the reference model stayed within the derived bounds [10] compared to the real plant parameters. However, true plant parameters are not always known. To overcome this issue, predictor based model reference adaptive control (PMRAC) is used in the RM to identify the real plant parameters and further update the design plant parameters, thereby generating a perfect feedforward pseudo control rate command. Before introducing the incorporation of predictor based MRAC in the RM, the structure of the jerk-level RM using ideal parameters is briefly presented.

C. Jerk-level Higher Order Reference Model

The reference model consists of a design plant model that incorporates known plant knowledge. The effect of the design plant dynamics, especially the reference state variant term $\mathbf{A}_{v,R} \cdot \dot{\mathbf{x}}_R$ is accounted in the generation of external reference state trajectories ξ_R and the feedforward pseudo control derivative $\dot{\mathbf{v}}_{ff}$. In this section, the structure of the higher order reference model is derived assuming that the real plant is known exactly.

The design plant in the jerk level reference model is derived from a nonlinear, time-invariant and input non-affine reference system, which is based on the structure of the reformulated system in Eq. (4)

$$\mathbf{v}_R = \mathbf{F}_R(\mathbf{x}_R, \mathbf{u}_R),\tag{9}$$

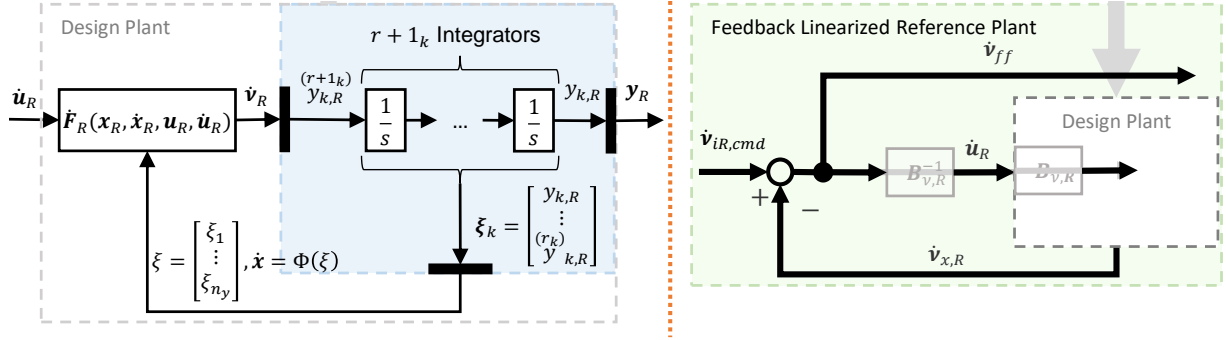


Fig. 2 \dot{v}_{ff} Generation in the Reference Model [10]

whose direct time derivative yields the design plant model in Fig. 2, which is utilized in the higher order reference model

$$\dot{\mathbf{v}}_R = \underbrace{\frac{\partial \mathbf{F}_R}{\partial \mathbf{x}_R}}_{\mathbf{A}_{v,R}} \cdot \dot{\mathbf{x}}_R + \underbrace{\frac{\partial \mathbf{F}_R}{\partial \mathbf{u}_R}}_{\mathbf{B}_{v,R}} \cdot \dot{\mathbf{u}}_R, \quad (10)$$

$$\dot{\mathbf{v}}_R = \mathbf{A}_{v,R} \cdot \dot{\mathbf{x}}_R + \mathbf{B}_{v,R} \cdot \dot{\mathbf{u}}_R.$$

It is assumed throughout this article that the reference input matrix $\mathbf{B}_{v,R}$ is equal to the real control input matrix \mathbf{B}_v . This assumption is practical since the input matrix constitutes the control effectiveness of all control effectors which are known or estimated early in the controller design phase. The reference state dependent term $\mathbf{A}_{v,R} \cdot \dot{\mathbf{x}}_R$ includes the reference state matrix $\mathbf{A}_{v,R}$. The ideal feedforward pseudo control derivative command is generated if the reference state matrix is equal to the real plant state matrix \mathbf{A}_v . The estimation of the state matrix using a state predictor and its inclusion in the reference model is presented in the next section.

The feedforward generated by the RM constitutes a part of the pseudo control rate command $\dot{\mathbf{v}}_{u,cmd}$ in Eq. (7) which is then allocated to a control effector rate command. Similarly, using a given internal reference pseudo control rate command $\dot{\mathbf{v}}_{iR,cmd}$, the reference effector rate command $\dot{\mathbf{u}}_{Rcmd}$ can be calculated by inverting Eq. (10)

$$\dot{\mathbf{v}}_{iR,cmd} = \mathbf{A}_{v,R} \cdot \dot{\mathbf{x}}_R + \mathbf{B}_{v,R} \cdot \dot{\mathbf{u}}_R, \quad (11)$$

$$\dot{\mathbf{u}}_{Rcmd} = \mathbf{B}_{v,R}^{-1} (\dot{\mathbf{v}}_{iR,cmd} - \mathbf{A}_{v,R} \cdot \dot{\mathbf{x}}_R).$$

The internal reference pseudo control rate command $\dot{\mathbf{v}}_{iR,cmd}$ is generated by using a linear command filter [10] that incorporates handling qualities consideration and accommodates time-domain response requirements like rise time, maximum overshoot and settling time in the design of the jerk-level RM. Furthermore, the design plant response is assessed through the closed loop reference dynamics, which are obtained by substituting the reference control input rate from Eq. (11) in Eq. (10)

$$\dot{\mathbf{v}}_R = \mathbf{A}_{v,R} \cdot \dot{\mathbf{x}}_R + \mathbf{B}_{v,R} \cdot \mathbf{B}_{v,R}^{-1} (\dot{\mathbf{v}}_{iR,cmd} - \mathbf{A}_{v,R} \cdot \dot{\mathbf{x}}_R),$$

$$\dot{\mathbf{v}}_R = \underbrace{\mathbf{A}_{v,R} \cdot \dot{\mathbf{x}}_R}_{\dot{\mathbf{v}}_{x,R}} + \underbrace{(\dot{\mathbf{v}}_{iR,cmd} - \mathbf{A}_{v,R} \cdot \dot{\mathbf{x}}_R)}_{\dot{\mathbf{v}}_{ff}}, \quad (12)$$

which consequentially shows that the design plant exactly follows the internal reference pseudo control rate command

$$\dot{\mathbf{v}}_R = \dot{\mathbf{v}}_{iR,cmd}. \quad (13)$$

It can be observed from the relation in Eq. (12) that the feedforward pseudo control derivative $\dot{\mathbf{v}}_{ff}$ includes the effect of the state damping component $\dot{\mathbf{v}}_{x,R}$, thereby facilitating cancellation of the effect of the neglected term Δ_x in the control law from Eq. (7). However, exact cancellation of the neglected term is only possible in an ideal case where the ideal reference state matrix $\mathbf{A}_{v,R}^*$, equal to the true state matrix \mathbf{A}_v , is known. This leads to the ideal feedforward command

$$\dot{\mathbf{v}}_{ff,id} = \dot{\mathbf{v}}_R - \mathbf{A}_{v,R}^* \cdot \dot{\mathbf{x}}_R. \quad (14)$$

Here the term $A_{v,R}^* \cdot \dot{x}_R$ represents the ideal state dependent pseudo control rate. If the ideal feedforward from Eq. (14) is used as $\dot{v}_{u,cmd}$ in the closed loop system dynamics from Eq. (8)

$$\begin{aligned} \dot{v} - \dot{v}_R + A_{v,R}^* \dot{x}_R &= A_{v,R}^* \dot{x}_R, \\ \dot{v} &= \dot{v}_R \end{aligned} \quad (15)$$

it follows that the real plant tracks the desired reference trajectories without any feedback, provided that the initial conditions of the reference and the plant states are also equal. Moreover, it is evident from Eq. (12) that any control allocation is not needed in the RM since the reference control input matrix $B_{v,R}$ cancels out. This aspect is also shown in Fig. 2 which exhibits the generation of feedforward pseudo control derivative by dynamic inversion of the reference system in Eq. (10).

The feedback linearized design plant takes the internal pseudo control rate command as the input. This internal command is computed by summation of the feedforward part $\dot{v}_{iR,ref}$ from the internal reference model and the feedback error component $\dot{v}_{iR,ec}$ from the RM error controller

$$\dot{v}_{iR,cmd} = \dot{v}_{iR,ref} + \begin{bmatrix} C_{R_{n_y}} & C_{R_{n_y-1}} & \dots & C_{R_0} \end{bmatrix} \cdot \begin{bmatrix} {}^{(n_y)} y_{iR} - {}^{(n_y)} y_R \\ {}^{(n_y-1)} y_{iR} - {}^{(n_y-1)} y_R \\ \vdots \\ y_{iR} - y_R \end{bmatrix}, \quad (16)$$

where $C_{R_k} \in \mathbb{R}^{n_y}$ denotes the reference error gain vector for the k -th derivative of the reference error $y_{iR}^{(k)} - y_R^{(k)}$. Here k represents the order of the derivative of the reference command variable response y_R . Together, the three modules – internal reference model, RM error controller and the feedback linearized design plant, constitute the jerk-level reference model architecture which is depicted in Fig. 3. Details about the modules of the higher order RM are available in [10].

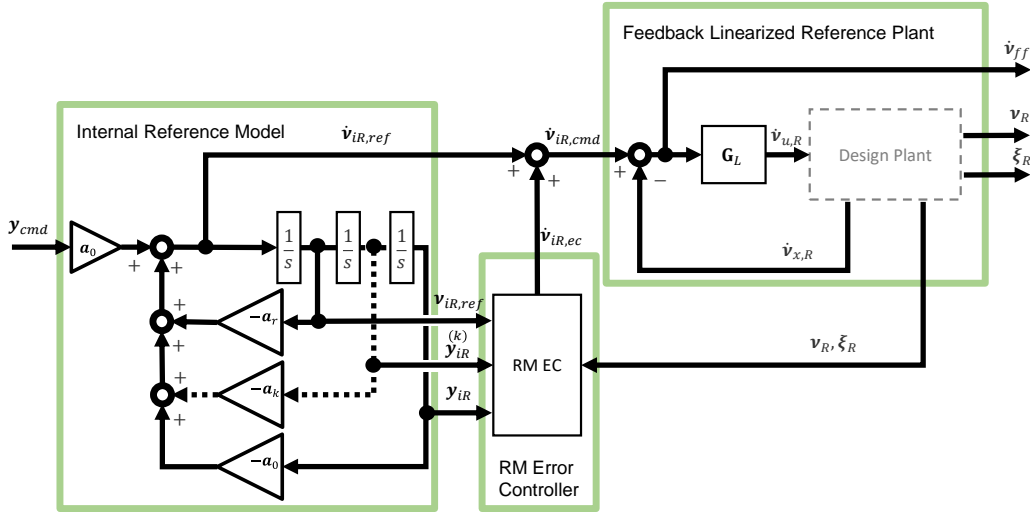


Fig. 3 Higher Order Reference Model [10]

The transfer function G_L used in the feedback linearized plant is meant to include higher order effects of actuator and sensor dynamics in the reference model. Without inclusion of such dynamics, the dynamic inversion in the RM is perfect and there is no need for an error controller. So far only the generation of an ideal feedforward command has been discussed which requires accurate information about the true state matrix A_v . However, this is usually not the case in real applications. Therefore, the plant state matrix is identified using a predictor based MRAC strategy, using which the reference state matrix $A_{v,R}$ is updated to make the feedforward command approach the ideal feedforward command.

D. Design Plant Adaptation in Jerk-level Reference Model

If the reference state matrix $A_{v,R}$ is equal to the true state matrix A_v , the generated feedforward pseudo control derivative, as shown in Eq. (12), is the ideal feedforward command on which the closed loop system could run without using any state feedback. Uncertainties in $A_{v,R}$ lead to the generation of a feedforward command that is different from the ideal feedforward command. Assuming that the difference between the reference state matrix and the true plant matrix, which is equal to the ideal state matrix $A_{v,R}^*$, lies within the span of the control input matrix B_v , the following parameterization is realized

$$\begin{aligned} \overbrace{A_{v,R}^* - A_{v,R}}^{A_v} &= B_v \cdot \Theta_v^* \\ A_v &= A_{v,R} + B_v \cdot \Theta_v^* \end{aligned} \quad (17)$$

where Θ_v^* denotes the ideal values of the estimated parameter matrix $\hat{\Theta}_v$, obtained through the adaptive update law contained in the PMRAC. The parameterization in Eq. (17) is generally known as the matching condition in literature [11, 12], and it indicates that the difference between the ideal and the assumed reference matrix is a matched uncertainty. In other words, this uncertainty can be compensated directly through an appropriate input to the control effectors. Since the plant state matrix A_v is unknown, it is divided into the known reference state matrix of the design plant and the unknown ideal part $B_v \cdot \Theta_v^*$ by employing the matching condition in the real plant dynamics defined in Eq. (5)

$$\dot{v} = [A_{v,R} + B_v \cdot \Theta_v^*] \cdot \dot{x} + B_v \cdot \dot{u}. \quad (18)$$

Hence, if the ideal state matrix deviation parameter Θ_v^* is known, then these parameterized plant dynamics will exactly mimic the true plant dynamics. In order to estimate the state deviation matrix Θ_v^* , a predictor based model reference adaptive control strategy is utilized. Using the estimated value $\hat{\Theta}_v$ of the ideal parameter in the parameterized plant dynamics of Eq. (18), the predictor dynamics are defined as

$$\begin{aligned} \hat{v} &= [A_{v,R} + B_v \cdot \hat{\Theta}_v] \cdot \dot{x} + B_v \cdot \dot{u} - K_P \cdot e_P, \\ \hat{v} &= A_{v,R} \cdot \dot{x} + B_v \cdot [\dot{u} + \hat{\Theta}_v \cdot \dot{x}] - K_P \cdot e_P. \end{aligned} \quad (19)$$

where $K_P \in \mathbb{R}^{n_y \times n_y}$ is a positive definite gain matrix using which the effect of the pseudo control prediction error $e_P \in \mathbb{R}^{n_y}$

$$e_P = \hat{v} - v \quad (20)$$

is included in the predictor dynamics. The gain matrix K_P is chosen such that $-K_P$ is stable according to the Lyapunov equation [13]

$$-K_P^T \cdot P - P \cdot K_P = -Q_0, \quad (21)$$

in which P and Q_0 are positive definite, symmetric matrices. The derivation of the update law for the estimated parameter $\hat{\Theta}_v$ using the prediction error dynamics is detailed later. First, the inclusion of the predictor and the adaptive update algorithm in the reference design plant is demonstrated as a block diagram in Fig. 4.

It can be observed from the block diagram and also the predictor dynamics in Eq. (19), that the state predictor requires the estimated plant state derivative \dot{x} , the estimated matrix $\hat{\Theta}_v$ and the effector command derivative \dot{u} as inputs. The prediction error e_P is used by the adaptive update law in addition to a regressor, which is the state derivative estimate. Finally, the estimated state deviation matrix $\hat{\Theta}_v$ is used to compute the uncertainty estimate $B_{v,R} \cdot \hat{\Theta}_v$ and add it to the reference state matrix, yielding the adapted design plant dynamics

$$\dot{v}_R = \underbrace{[A_{v,R} + B_{v,R} \cdot \hat{\Theta}_v]}_{\dot{v}_{x,ad}} \cdot \dot{x}_R + B_{v,R} \cdot \dot{u}_R. \quad (22)$$

The ideal state dependent pseudo control rate from Eq. (14) is replaced by the adapted pseudo control rate due to the state dependency $\dot{v}_{x,ad}$, thereby generating the adaptive feedforward pseudo control derivative command

$$\dot{v}_{ff} = \dot{v}_{iR,cmd} - [A_{v,R} + B_v \cdot \hat{\Theta}_v] \cdot \dot{x}_R. \quad (23)$$

Note that the adaptive feedforward uses the real input matrix B_v in place of the reference input matrix $B_{v,R}$ because it is assumed throughout this article that the plant input matrix is known. It was proved using linear analysis in [10] that using the proposed higher order reference model structure led to improvement in set-point tracking given that $A_{v,R}$ lies in the range $[0, 2 \cdot A_v]$. Consequently, this derived range of allowable uncertainty can be used to specify conservative bounds on the adapted parameter $\hat{\Theta}_v$ without degrading the reference tracking of the closed loop system.

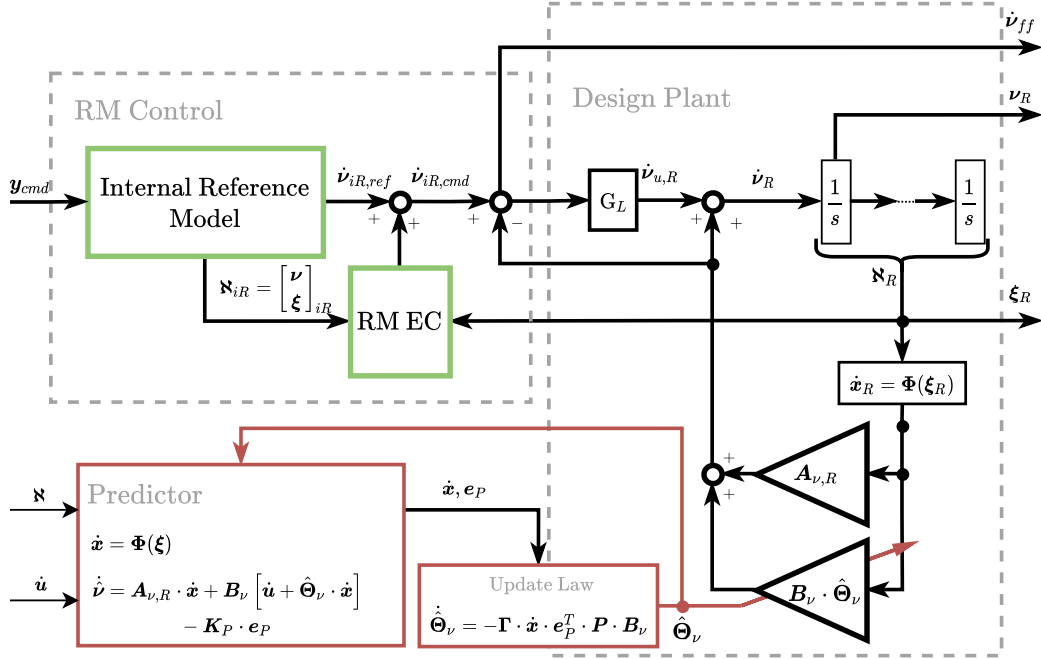


Fig. 4 Design Plant Adaptation in Jerk-level Reference Model

E. Parameter Update Laws

In this subsection, the parameter update law for the state deviation matrix $\hat{\Theta}_\nu$ is derived. Firstly, the prediction error dynamics are calculated. Based on the states that occur in the error dynamics, a Lyapunov function candidate is derived. Using the condition of stability from the Lyapunov stability theorem, the parameter update law is obtained. Detailed Lyapunov's analysis is not covered in this article since it has already been extensively covered in literature [11–14].

The purpose of the predictor defined in Eq. (19) is to accurately imitate the plant response given that the ideal value of the estimated deviation matrix has been identified. Subsequently, the control input rate to the predictor is modified through the adaptive feedforward from Eq. (23) to make the predictor follow the desired dynamics [6, 11, 15]. Since, the predictor behaves like the true plant and the modified control input rate makes it follow the desired dynamics, providing the same control input rate to the real plant makes it behave like the reference model.

The first step is to compute the prediction error dynamics, which is accomplished by subtracting the parameterized true plant dynamics given in Eq. (18) from the predictor dynamics of Eq. (19)

$$\dot{e}_P = -K_P \cdot e_P + B_\nu \cdot \tilde{\Theta}_\nu \cdot \dot{x}, \quad (24)$$

where $\tilde{\Theta}_\nu$ represents the error in the state matrix deviation parameters

$$\tilde{\Theta}_\nu = \hat{\Theta}_\nu - \Theta_\nu^*. \quad (25)$$

The Lyapunov candidate function, incorporating the squares of the error states of the predictor dynamics, is chosen

$$V = \frac{1}{2} \cdot e_P^T \cdot P \cdot e_P + \frac{1}{2} \cdot \text{Tr} \left[\tilde{\Theta}_\nu \cdot \Gamma^{-1} \cdot \tilde{\Theta}_\nu^T \right] \quad (26)$$

where Γ specifies the learning rate of adaptation and Tr denotes the trace of a matrix. Differentiation of the Lyapunov candidate function with respect to time and substitution of the predictor dynamics along with the Lyapunov equation (21) in the resulting expression [9, 13] yields

$$\dot{V} = -\frac{1}{2} \cdot e_P^T \cdot Q_0 \cdot e_P + \text{Tr} \left[\tilde{\Theta}_\nu \cdot \left(\dot{x} \cdot e_P^T \cdot P \cdot B_\nu + \Gamma^{-1} \cdot \tilde{\Theta}_\nu^T \right) \right] \quad (27)$$

In the Lyapunov function derivative, the positive definite matrix Q_0 occurs with a negative sign which implies that the first term stays negative thereby satisfying the stability criterion in the sense of Lyapunov. However, no statement can

be made about the second term, since its sign is unknown. Therefore, by equating this term to zero, the state matrix deviation estimate update law is derived

$$\hat{\Theta}_v^T = -\Gamma \cdot \dot{\mathbf{x}} \cdot \mathbf{e}_P^T \cdot \mathbf{P} \cdot \mathbf{B}_v. \quad (28)$$

Global stability and boundedness [14] of the errors \mathbf{e}_P and $\tilde{\Theta}_v$ is proven by Lyapunov's stability analysis. Additionally, asymptotic convergence of the errors is proven through Barbalat's Lemma [13, 16]. Thus, the estimate of the state deviation matrix is computed with the update law in Eq. (28), which is then further used to generate the adaptive feedforward command from Eq. (23).

In addition to Eq. (28), which uses only instantaneous error data to update the adaptive parameters, concurrent learning can be used to store data points in a buffer and update $\hat{\Theta}_v$, even when the system states are not persistently exciting. Background on concurrent learning, its definition and benefits can be found in [17, 18]. The extended update reads

$$\hat{\Theta}_v^T = -\Gamma_1 \cdot \dot{\mathbf{x}} \cdot \mathbf{e}_P^T \cdot \mathbf{P} \cdot \mathbf{B}_v - \Gamma_2 \sum_{j=1}^{P_{max}} \dot{\mathbf{x}}_j \mathbf{e}_j^T. \quad (29)$$

Next, the application of the adaptive jerk-level RM in an extended INDI controller framework is presented.

IV. Extended INDI Controller Framework with Adaptive Jerk-level Reference Model

This section presents the incorporation of the adaptive jerk-level reference model in a controller framework that employs the extended INDI strategy. Firstly, the controller architecture is explained. Furthermore, the effect of the adaptive feedforward is analyzed by deriving the closed loop error dynamics of the given controller and the generic nonlinear system from Eq. (1).

A. Controller Framework

Figure 5 exhibits a controller structure that uses the adaptive jerk-level RM. The adaptive reference model constitutes of the nominal higher order RM functionality along with the adaptive update for the design plant in the reference model. It gets the pilot commands \mathbf{y}_{cmd} as inputs which serve as the control variables. The adaptive update consists of the predictor model that estimates the state deviation matrix $\hat{\Theta}_v$. This estimate is used to update the design plant state matrix $\mathbf{A}_{v,R}$. Ultimately, the adaptive HORM produces the feedforward command given in Eq. (23) along with its lower order derivatives $\mathfrak{N}_R = [\nu_R, \xi_R]^T$ that contain the reference pseudo control and external states.

The control objective is to track $\dot{\nu}_R$ and consequently the lower derivatives \mathfrak{N}_R , which constitute the control variable reference trajectories. The reference pseudo control rate $\dot{\nu}_R$ is exactly tracked if the ideal feedforward $\dot{\nu}_{ff,id}$ from

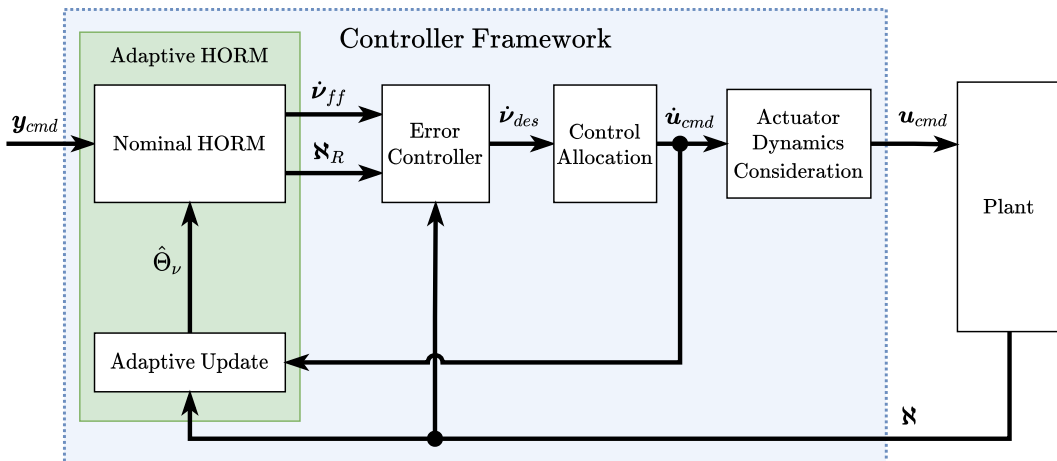


Fig. 5 Controller Framework

Eq. (14) is produced by the RM. This statement further highlights the concept covered earlier through Eqs. (10) and (12) that $\dot{v}_{ff} \neq \dot{v}_R$. The feedforward command only contains the component of the pseudo control rate that would be produced by the control input while excluding the effect of state dependent damping terms from the reference pseudo control rate. However, feedforward alone cannot provide robustness against model uncertainties and external disturbances which are abundantly encountered in practical applications.

Therefore, a stabilizing error controller [5, 6, 19] is used in the presented controller architecture. It computes a proportional feedback pseudo control rate \dot{v}_e based on the tracking error, which is defined as the deviation of the plant variables \mathbf{N} from their corresponding reference variables \mathbf{N}_R

$$\dot{v}_e = \mathbf{C}_e \cdot [\mathbf{N}_R - \mathbf{N}] = \mathbf{C}_e \cdot \mathbf{e} = \underbrace{\begin{bmatrix} C_{e_r} & C_{e_{r-1}} & \dots & C_{e_0} \end{bmatrix}}_{\mathbf{C}_e} \cdot \underbrace{\begin{bmatrix} \begin{matrix} (r_{n_y}) & (r_{n_y}) \\ \mathbf{y}_R & - \mathbf{y} \end{matrix} \\ \begin{matrix} (r_{n_y}-1) & (r_{n_y}-1) \\ \dot{\mathbf{y}}_R & - \dot{\mathbf{y}} \end{matrix} \\ \vdots \\ \mathbf{y}_R - \mathbf{y} \end{bmatrix}}_{\mathbf{e}} \quad (30)$$

$$\dot{v}_e = C_{e_r} \cdot \left(\begin{matrix} (r_{n_y}) & (r_{n_y}) \\ \mathbf{y}_R & - \mathbf{y} \end{matrix} \right) + C_{e_{r-1}} \cdot \left(\begin{matrix} (r_{n_y}-1) & (r_{n_y}-1) \\ \dot{\mathbf{y}}_R & - \dot{\mathbf{y}} \end{matrix} \right) \dots + C_{e_0} \cdot (\mathbf{y}_R - \mathbf{y})$$

The error controller gains specified in the gain vector are chosen such that the poles of the resulting closed loop system lie in the left-half plane and hence facilitate in directing the real plant outputs to their desired trajectories when any deviation occurs. If the ideal feedforward pseudo control derivative $\dot{v}_{ff,id}$ from Eq. (14) is known, the tracking error and hence, the error pseudo control derivative \dot{v}_e is zero. Therefore, the feedback error based correction \dot{v}_e from Eq. (30) generated to counteract the deviations only manifests when the nominal reference system deviates from the true plant dynamics. Subsequently, the desired command to the control allocation module is calculated by addition of the feedforward pseudo control derivative and the error correction

$$\dot{v}_{des} = \dot{v}_{ff} + \dot{v}_e. \quad (31)$$

Next, the control allocation module converts the desired pseudo control rate \dot{v}_{des} to control effector command rates $\dot{\mathbf{u}}_{cmd}$ through a generalized inverse of the control input matrix \mathbf{B}_v

$$\dot{\mathbf{u}}_{cmd} = \mathbf{B}_v^{-1} \cdot \dot{v}_{des} = \mathbf{B}_v^{-1} \cdot (\dot{v}_{ff} + \dot{v}_e), \quad (32)$$

which yields the control law for the given extended INDI control structure. Several control allocation techniques described in the literature [20] for INDI controllers are also compatible with this controller framework. Finally, actuator dynamics consideration is used to calculate the absolute control input command \mathbf{u}_{cmd} to the plant, which is extensively covered in [7, 10].

In order to assess the effect of the adaptive feedforward on the controlled system, the error dynamics need to be evaluated. For that reason, first the closed loop system dynamics are obtained by substituting the control law from Eq. (32) in the total derivative of the transformed nonlinear system from Eq. (5)

$$\dot{\mathbf{v}} = \mathbf{A}_v \cdot \dot{\mathbf{x}} + \mathbf{B}_v \cdot \mathbf{B}_v^{-1} \cdot (\dot{v}_{ff} + \dot{v}_e) \quad (33)$$

in which the adaptive feedforward command using the estimate of the state deviation matrix $\hat{\Theta}_v$ from Eq. (23) is applied

$$\dot{\mathbf{v}} = \mathbf{A}_v \cdot \dot{\mathbf{x}} + \dot{v}_R - [\mathbf{A}_{v,R} + \mathbf{B}_v \cdot \hat{\Theta}_v] \cdot \dot{\mathbf{x}}_R + \dot{v}_e. \quad (34)$$

Following from the parameterization specified by Eq. (17) in section III.D, the true state matrix \mathbf{A}_v is replaced using the nominal design plant state matrix $\mathbf{A}_{v,R}$ and the ideal parameter Θ_v^*

$$\dot{\mathbf{v}} = [\mathbf{A}_{v,R} + \mathbf{B}_v \cdot \Theta_v^*] \cdot \dot{\mathbf{x}} + \dot{v}_R - [\mathbf{A}_{v,R} + \mathbf{B}_v \cdot \hat{\Theta}_v] \cdot \dot{\mathbf{x}}_R + \dot{v}_e \quad (35)$$

to bring about the error dynamics of the closed loop system with adaptation

$$\dot{v}_R - \dot{\mathbf{v}} + \dot{v}_e = \mathbf{A}_{v,R} \cdot \mathbf{e}_{\dot{\mathbf{x}}} - \mathbf{B}_v \cdot \Theta_v^* \cdot \dot{\mathbf{x}} + \mathbf{B}_v \cdot \hat{\Theta}_v \cdot \dot{\mathbf{x}}_R. \quad (36)$$

The error between the reference and true pseudo control derivatives $\dot{v}_R - \dot{v}$ is further denoted as the error derivative \dot{e} while the error pseudo control derivative \dot{v}_e is substituted by the expression in Eq. (30). Moreover, by adding and subtracting $B_v \cdot \hat{\Theta}_v \cdot \dot{x}$, the closed loop error dynamics are transformed

$$\begin{aligned}\dot{e} + C_e \cdot e &= A_{v,R} \cdot e_{\dot{x}} + B_v \cdot \hat{\Theta}_v \cdot \dot{x} - B_v \cdot \Theta_v^* \cdot \dot{x} + B_v \cdot \hat{\Theta}_v \cdot \dot{x}_R - B_v \cdot \hat{\Theta}_v \cdot \dot{x}, \\ \dot{e} + C_e \cdot e &= A_{v,R} \cdot e_{\dot{x}} + B_v \cdot \hat{\Theta}_v \cdot e_{\dot{x}} + B_v \cdot \tilde{\Theta}_v \cdot \dot{x}, \\ \dot{e} + C_e \cdot e &= [A_{v,R} + B_v \cdot \hat{\Theta}_v] \cdot e_{\dot{x}} + B_v \cdot \tilde{\Theta}_v \cdot \dot{x}.\end{aligned}\quad (37)$$

The components that excite the closed loop error dynamics can be analyzed from the resulting relation in Eq. (37). The coefficient for the error in state derivative $e_{\dot{x}}$ has a stabilizing effect since the reference state matrix $A_{v,R}$ is chosen as Hurwitz. Additionally, taking the control input matrix B_v into account, the state deviation matrix estimate $\hat{\Theta}_v$ is limited such that the sum $[A_{v,R} + B_v \cdot \hat{\Theta}_v]$ also stays Hurwitz. It is already proven through Lyapunov analysis in section III.E that the estimated state deviation matrix is driven to its ideal value by the parameter update laws in Eq. (28). Hence, the second term tends to null, thereby establishing the stability of the closed loop error dynamics of the controlled nonlinear system.

V. Results

The proposed controller framework in section IV was tested for the short period approximation model of a stable aircraft. The simulation environment describes the parameterization of the reference dynamics used for a pitch rate q command controller. Further, the adapted state variation term is derived which is used to calculate the adaptive feedforward command. After defining the plant and controller systems, results of the numerical simulations are discussed.

A. Simulation Environment

The short period dynamics of an aircraft, linearized around a steady-state trim condition, are defined as in [21]

$$\underbrace{\begin{bmatrix} \dot{\alpha} \\ \dot{q} \end{bmatrix}}_{\dot{x}} = \underbrace{\begin{bmatrix} Z_\alpha & 1 + Z_q \\ M_\alpha & M_q \end{bmatrix}}_A \underbrace{\begin{bmatrix} \alpha \\ q \end{bmatrix}}_x + \underbrace{\begin{bmatrix} Z_\eta \\ M_\eta \end{bmatrix}}_B \underbrace{\eta}_{u}.\quad (38)$$

For further simplification, it is assumed that $Z_\eta \approx 0$. Next, the output to be tracked is defined as the pitch-rate, thus, the pseudo control and its rate becomes

$$\begin{aligned}y &= q, \\ v &= \dot{y} = \dot{q} = M_\alpha \alpha + M_q q + M_\eta \eta, \\ \dot{v} &= \ddot{y} = M_\alpha \dot{\alpha} + M_q \dot{q} + M_\eta \dot{\eta},\end{aligned}\quad (39)$$

in which Eq. (39) is similar in structure to Eq. (5) and the angle-of-attack α acts as an internal state with the dynamics

$$\dot{\alpha} = Z_\alpha \alpha + (1 + Z_q) q.\quad (40)$$

Consequently, the nominal design plant is defined using the same structure, but reference parameters as

$$\dot{v}_R = M_{\alpha,R} \dot{\alpha}_R + M_{q,R} \dot{q}_R + M_{\eta,R} \dot{\eta}_R,\quad (41)$$

$$\dot{\alpha}_R = Z_{\alpha,R} \alpha_R + (1 + Z_{q,R}) q_R.\quad (42)$$

Since in general $M_{\alpha,R} \neq M_\alpha$ and $M_{q,R} \neq M_q$, the adaptive augmentation as proposed in section III.D is introduced. Following the outlined methods, it is assumed that the input gain is perfectly known, thus $M_{\eta,R} = M_\eta$. Due to the input matrix being $B_v = [0 \ M_\eta]^T$, a deviation in M_α and M_q is matched, while Z_α and Z_q are unmatched parameters. Consequently, two adaptive parameters are required, giving

$$\hat{\Theta}_v = [\hat{\Theta}_\alpha, \hat{\Theta}_q]^T.\quad (43)$$

The auxiliary Eq. (42) thereby stays constant while the design plant pseudo control rate Eq. (41) with adaptation becomes

$$\dot{\nu}_R = \left(M_{\alpha,R} + M_{\eta} \cdot \hat{\Theta}_{\alpha} \right) \cdot \dot{\alpha}_R + \left(M_{q,R} + M_{\eta} \cdot \hat{\Theta}_q \right) \cdot \dot{q}_R + M_{\eta} \cdot \dot{\eta}_R. \quad (44)$$

The state predictor that utilizes state variation matrix estimate $\hat{\Theta}_v$ is defined according to section III.D. Using the state derivative estimate $\dot{x} = [\dot{\alpha}, \dot{q}]^T$, the update law is given by Eq. (28) or Eq.(29) depending on whether the concurrent learning update is used or not. Finally, the state dependent damping term is extracted as

$$\dot{\nu}_{x,ad} = \left(M_{\alpha,R} + M_{\eta} \cdot \hat{\Theta}_{\alpha} \right) \cdot \dot{\alpha}_R + \left(M_{q,R} + M_{\eta} \cdot \hat{\Theta}_q \right) \cdot \dot{q}_R \quad (45)$$

and used in the feedforward pseudo command rate (see Eq. (23)).

B. Test Results

The simulation results for an uncertain case in which the design plant adaptation was active is presented in Fig. 6. Uncertainties of 80% were defined in the matched parameters by setting $M_{\alpha,R} = 1.8M_{\alpha}$ and $M_{q,R} = 0.2M_q$. The predictor and adaptation parameters were

$$\Gamma = \begin{bmatrix} 75 & 0 \\ 0 & 75 \end{bmatrix}, \quad \mathcal{Q}_0 = \begin{bmatrix} 1 & 0 \\ 0 & 1 \end{bmatrix}, \quad \mathbf{K}_P = \begin{bmatrix} -3 & 0 \\ 0 & -9 \end{bmatrix} \quad (46)$$

Only the instantaneous parameter update law Eq. (28) is used at this point. The results show that the uncertainties in the reference state matrix $A_{v,R}$ are estimated accurately using the adaptive RM architecture. The parameters $\hat{\Theta}_v$ used in the

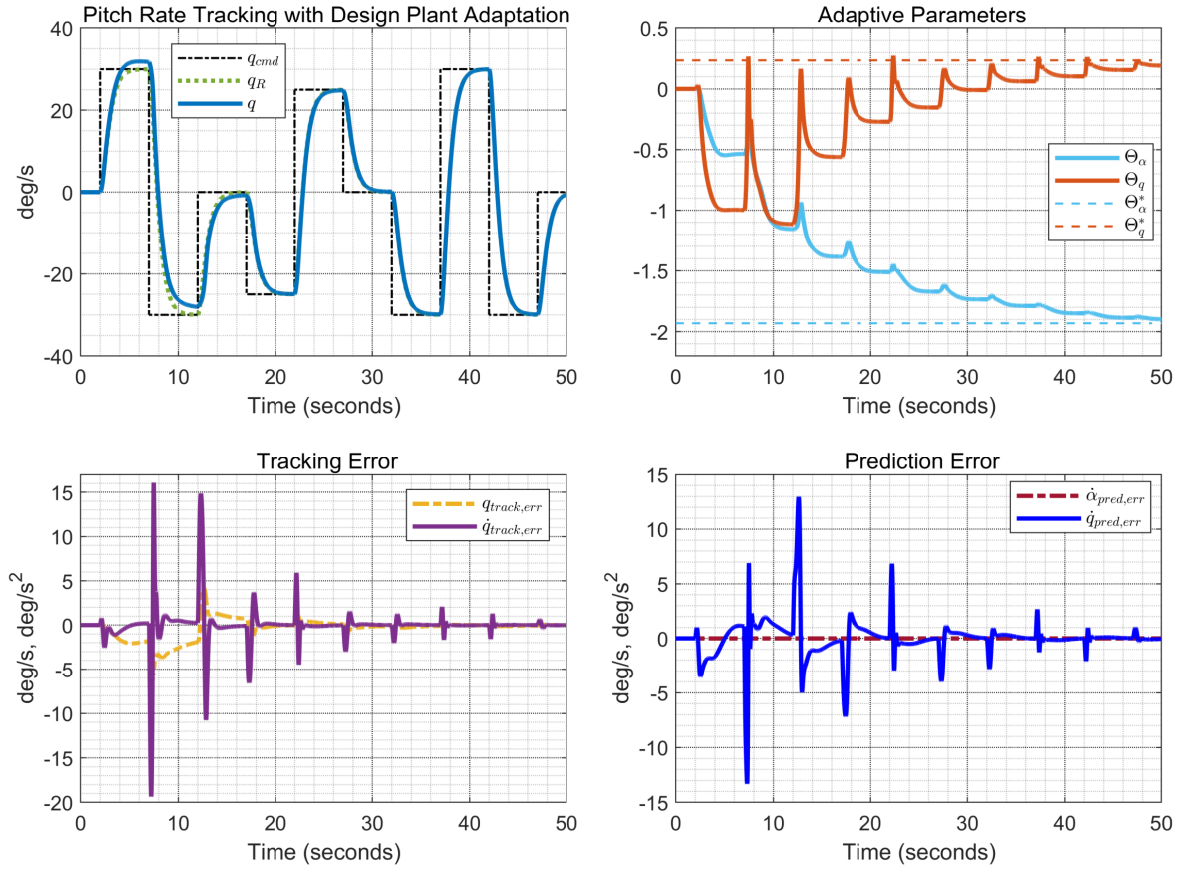


Fig. 6 Control Signals for Pitch Rate Command Responses with Design Plant Adaptation

parameterization of the state matrix A_v converge to their ideal values Θ_v^* . Consequently, as the estimated parameters $\hat{\Theta}_v$ converge towards their ideal values, the tracking performance with respect to the commanded reference trajectory q_R improves. This is corroborated by the pitch rate and pitch acceleration tracking errors that constitute the error controller pseudo control derivative \dot{v}_e .

The tracking errors and hence $\dot{v}_e = 0$ converge to zero because the parameters $\hat{\Theta}_v$ converge towards their ideal values, and therefore the closed loop system runs on the feedforward signal alone. Lastly, with the parameter convergence, the prediction error in $v = \dot{q}$ also goes to zero. As the auxiliary equation for the angle-of-attack only depends on unmatched parameters, which are assumed to have no uncertainty in this scenario, the resulting prediction error is permanently zero.

To improve the convergence behavior, the extended update law Eq. (29) can be used. In the data stack, a maximum of $p_{max} = 50$ points were stored. The adaptation rate for the concurrent update was defined as $\Gamma_2 = 0.1\Gamma_1$. The resulting adaptive parameter trajectories and the tracking errors are depicted in Fig. 7.

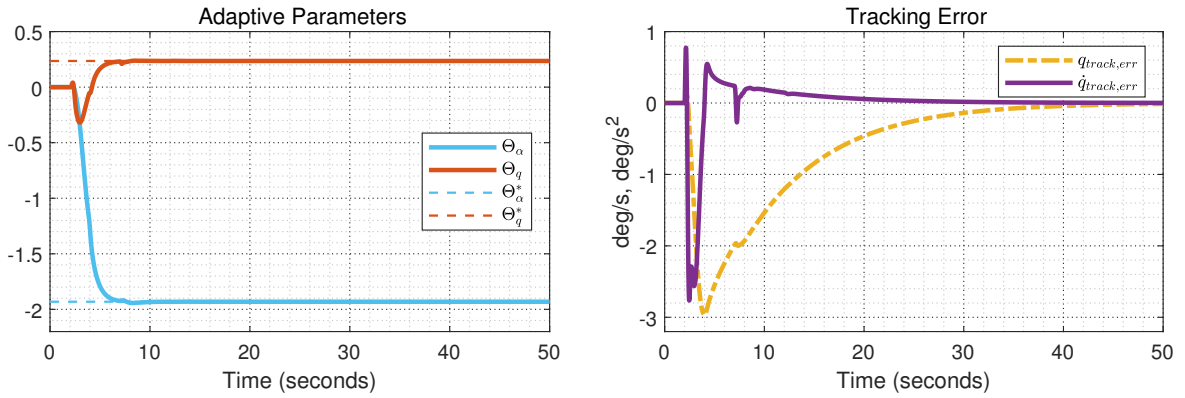


Fig. 7 Control Signals for Pitch Rate Command Responses with Concurrent Design Plant Adaptation

In comparison to Fig. 6, the convergence of $\hat{\Theta}_v$ towards Θ_v^* is smoother and, more importantly, significantly faster when leveraging concurrent data. As a result, the tracking error in pitch rate and pitch acceleration is lower in magnitude and converges faster towards zero.

VI. Conclusion

Design plant adaptation for a jerk-level higher order reference model based on a state predictor has been proposed in this article. The difference between the design plant and the true plant was identified, which was then used to update the design plant parameters. Consequently, the adaptation of the design plant led to generation of an augmented feedforward pseudo control derivative command. It was established that by adapting the design plant parameters with the estimates of the true plant, the generated feedforward command enhanced the reference tracking of the closed loop system. Furthermore, the parameter and error convergence was accelerated by additionally storing and leveraging concurrent data points. Compensation of second order actuators and consideration of dirt-effects in measurements will be dealt with in future works.

References

- [1] Smith, P., "A simplified approach to nonlinear dynamic inversion based flight control," *23rd Atmospheric Flight Mechanics Conference*, 1998, p. 4461. doi:10.2514/6.1998-4461.
- [2] Bacon, B., and Ostroff, A., "Reconfigurable flight control using nonlinear dynamic inversion with a special accelerometer implementation," *AIAA Guidance, Navigation, and Control Conference and Exhibit*, 2000, p. 4565. doi:10.2514/6.2000-4565.
- [3] Sieberling, S., Chu, Q. P., and Mulder, J. A., "Robust Flight Control Using Incremental Nonlinear Dynamic Inversion and Angular Acceleration Prediction," *Journal of Guidance, Control, and Dynamics*, Vol. 33, No. 6, 2010, pp. 1732–1742. doi:10.2514/1.49978.

- [4] Bhardwaj, P., Raab, S., Zhang, J., and Holzapfel, F., "Integrated Reference Model for a Tilt-rotor Vertical Take-off and Landing Transition UAV," *2018 AIAA Aviation, Applied Aerodynamics Conference*, American Institute of Aeronautics and Astronautics, Reston, Virginia, 2018, p. 3479.
- [5] Raab, S., Zhang, J., Bhardwaj, P., and Holzapfel, F., "Proposal of a Unified Control Strategy for Vertical Take-off and Landing Transition Aircraft Configurations," *2018 AIAA Aviation, Applied Aerodynamics Conference*, American Institute of Aeronautics and Astronautics, Reston, Virginia, 2018.
- [6] Bhardwaj, P., Akkinapalli, V. S., Zhang, J., Saboo, S., and Holzapfel, F., "Adaptive augmentation of Incremental Nonlinear Dynamic Inversion controller for an Extended F-16 model," *AIAA Scitech 2019 Forum*, Reston, Virginia, 2019, p. 1923.
- [7] Raab, S., Zhang, J., Bhardwaj, P., and Holzapfel, F., "Consideration of Control Effector Dynamics and Saturations in a extended INDI Approach," *2019 AIAA Aviation*, American Institute of Aeronautics and Astronautics, Reston, Virginia, 2019.
- [8] Bhardwaj, P., Raab, S., Zhang, J., and Holzapfel, F., "Thrust command based Integrated Reference Model with Envelope Protections for Tilt-rotor VTOL Transition UAV," *2019 AIAA Aviation*, American Institute of Aeronautics and Astronautics, Reston, Virginia, 2019.
- [9] Holzapfel, F., "Nichtlineare adaptive Regelung eines unbemannten Fluggerätes," Ph.D. thesis, Technische Universität München, 2004.
- [10] Bhardwaj, P., Raab, S. A., and Holzapfel, F., "Higher Order Reference Model for Continuous Dynamic Inversion Control," *AIAA Scitech 2021 Forum*, American Institute of Aeronautics and Astronautics, Reston, Virginia, 2021, p. 1130.
- [11] Lavretsky, E., Gadiant, R., and Gregory, I. M., "Predictor-based model reference adaptive control," *Journal of guidance, control, and dynamics*, Vol. 33, No. 4, 2010, pp. 1195–1201.
- [12] Nguyen, N. T., "Model-reference adaptive control," *Model-Reference Adaptive Control*, Springer, 2018, pp. 83–123.
- [13] Narendra, K. S., and Annaswamy, A. M., *Stable Adaptive Systems*, Dover Publications, Inc., 2005.
- [14] Slotine, J.-J. E., Li, W., et al., *Applied nonlinear control*, Vol. 199, Prentice hall Englewood Cliffs, NJ, 1991.
- [15] Hovakimyan, N., and Cao, C., *L₁ adaptive control theory - Guaranteed robustness with fast adaptation*, Vol. 21, Society for Industrial and Applied Mathematics, 2010.
- [16] Khalil, H. K., *Nonlinear systems*, 3rd ed., Prentice Hall, Upper Saddle River, N.J. and London, 2002.
- [17] Chowdhary, G., and Johnson, E., "Concurrent learning for convergence in adaptive control without persistency of excitation," *49th IEEE Conference on Decision and Control (CDC)*, 2010, pp. 3674–3679. doi:10.1109/CDC.2010.5717148.
- [18] Chowdhary, G., and Johnson, E., "Theory and Flight-Test Validation of a Concurrent-Learning Adaptive Controller," *Journal of Guidance, Control, and Dynamics*, Vol. 34, No. 2, 2011, pp. 592–607. doi:10.2514/1.46866.
- [19] Akkinapalli, V. S., and Holzapfel, F., "Incremental Dynamic Inversion based Velocity Tracking Controller for a Multicopter System," *2018 AIAA Guidance, Navigation, and Control Conference*, American Institute of Aeronautics and Astronautics, Reston, Virginia, 2018. doi:10.2514/6.2018-1345.
- [20] Zhang, J., Bhardwaj, P., Raab, S., and Holzapfel, F., "Control Allocation Framework with SVD-based Protection for a Tilt-rotor VTOL Transition Air Vehicle," *2019 AIAA Aviation*, American Institute of Aeronautics and Astronautics, Reston, Virginia, 2019.
- [21] Stengel, R. F., *Flight Dynamics*, Princeton University Press, Princeton, 2004.

Bibliography

- [1] International Civil Aviation Organisation (ICAO), “The World of Air Transport in 2019.” <https://www.icao.int/annual-report-2019/Pages/the-world-of-air-transport-in-2019.aspx>. Accessed: 25-Jan-2022.
- [2] J. Holden and N. Goel, “Uber elevate: Fast-Forwarding to a Future of On-Demand Urban Air Transportation.,” 2016.
- [3] R. Rothfeld, A. Straubinger, M. Fu, C. Al Haddad, and C. Antoniou, “Chapter 13 - Urban Air Mobility,” in *Demand for Emerging Transportation Systems* (C. Antoniou, D. Efthymiou, and E. Chaniotakis, eds.), pp. 267–284, Elsevier, 2020.
- [4] M. J. Duffy, S. R. Wakayama, and R. Hupp, “A study in reducing the cost of vertical flight with electric propulsion,” in *17th AIAA Aviation Technology, Integration, and Operations Conference*, p. 3442, 2017.
- [5] M. D. Moore and B. Fredericks, “Misconceptions of Electric Aircraft and their Emerging Aviation Markets,” in *52nd Aerospace Sciences Meeting*, 2014.
- [6] National Interagency Fire Center, “Helicopter Services.” <https://www.fs.usda.gov/sites/default/files/2021-02/feb%202021%20Contracts%20Awarded%202018-2021.pdf>. Accessed: 28-Dec-2021.
- [7] N. K. Borer, M. D. Patterson, J. K. Viken, M. D. Moore, J. Bevirt, A. M. Stoll, and A. R. Gibson, “Design and Performance of the NASA SCEPTOR Distributed Electric Propulsion Flight Demonstrator,” in *16th AIAA Aviation Technology, Integration, and Operations Conference*, p. 3920, 2016.
- [8] M. Söpper, J. Zhang, N. Bähr, and F. Holzzapfel, “Required Moment Sets: Enhanced Controllability Analysis for Nonlinear Aircraft Models,” *Applied Sciences*, vol. 11, no. 8, 2021.
- [9] A. M. Stoll, J. Bevirt, M. D. Moore, W. J. Fredericks, and N. K. Borer, “Drag Reduction through Distributed Electric Propulsion,” in *14th AIAA aviation technology, integration, and operations conference*, p. 2851, 2014.
- [10] H. D. Kim, A. T. Perry, and P. J. Ansell, “A review of Distributed Electric Propulsion Concepts for Air Vehicle Technology,” in *2018 AIAA/IEEE Electric Aircraft Technologies Symposium (EATS)*, pp. 1–21, IEEE, 2018.

- [11] Autel Robotics, "Dragonfish Lite." <https://dronexl.co/2020/09/28/autel-robotics-launches-autel-dragonfish-vtol-fixed-wing-drone-in-china/>. Accessed: 03-Feb-2022.
- [12] Phoenix-Wings GmbH, "PWOne." <https://phoenix-wings.de/pwone/>. Accessed: 03-Feb-2022.
- [13] Volocopter GmbH, "VoloCity." <https://www.volocopter.com/solutions/velocity/>. Accessed: 03-Feb-2022.
- [14] Lilium GmbH, "Lilium Jet." <https://lilium.com/>. Accessed: 03-Feb-2022.
- [15] Joby Aviation GmbH, "Pre-production Prototype." <https://www.jobyaviation.com/about/>. Accessed: 03-Feb-2022.
- [16] Autoflight, "Prosperity I, GEN 4 aircraft." <https://autoflight.com/en/press/>. Accessed: 08-Sep-2023.
- [17] C. Silva, W. R. Johnson, E. Solis, M. D. Patterson, and K. R. Antcliff, "VTOL Urban Air Mobility Concept Vehicles for Technology Development," in *2018 Aviation Technology, Integration, and Operations Conference*, 2018.
- [18] A. Straubinger, R. Rothfeld, M. Shamiyeh, K.-D. Büchter, J. Kaiser, and K. O. Plötner, "An overview of current research and developments in urban air mobility – Setting the scene for UAM introduction," *Journal of Air Transport Management*, vol. 87, p. 101852, 2020.
- [19] A. Cohen and S. Shaheen, "Urban Air Mobility: Opportunities and Obstacles," in *International Encyclopedia of Transportation* (R. Vickerman, ed.), pp. 702–709, Oxford: Elsevier, 2021.
- [20] European Union Aviation Safety Agency (EASA), "Urban Air Mobility." <https://www.easa.europa.eu/what-is-uam>. Accessed: 01-Jan-2022.
- [21] C. Al Haddad, E. Chaniotakis, A. Straubinger, K. Plötner, and C. Antoniou, "Factors affecting the adoption and use of urban air mobility," *Transportation Research Part A: Policy and Practice*, vol. 132, pp. 696–712, 2020.
- [22] A. Bauranov and J. Rakas, "Urban air mobility and manned eVTOLs: safety implications," in *2019 IEEE/AIAA 38th Digital Avionics Systems Conference (DASC)*, pp. 1–8, 2019.
- [23] C. Reiche, A. P. Cohen, and C. Fernando, "An Initial Assessment of the Potential Weather Barriers of Urban Air Mobility," *IEEE Transactions on Intelligent Transportation Systems*, vol. 22, no. 9, pp. 6018–6027, 2021.
- [24] M. Bahr, U. Hebbar, E. Ferede, and F. Gandhi, "Multi-rotor eVTOL Flight Simulation and Assessment under Atmospheric Turbulence," *Proceedings of the 77th Vertical Flight Society Annual Forum, Virtual*, 2021.

-
- [25] S. P. Boyd and C. H. Barratt, *Linear Controller Design: Limits of Performance*, vol. 7. Prentice-Hall, 1991.
- [26] J. Roskam, *Airplane Flight Dynamics and Automatic Flight Controls*. Design, Analysis and Research Corporation (DARcorporation), 1995.
- [27] B. L. Stevens, F. L. Lewis, and E. N. Johnson, *Aircraft Control and Simulation: Dynamics, Controls Design, and Autonomous Systems*. John Wiley & Sons, 2015.
- [28] K. Muraoka, N. Okada, and D. Kubo, "Quad Tilt Wing VTOL UAV: Aerodynamic Characteristics and Prototype Flight," in *AIAA Infotech@Aerospace Conference*, 2009.
- [29] G. Notarstefano and J. Hauser, "Modeling and Dynamic Exploration of a Tilt-Rotor VTOL Aircraft," *IFAC Proceedings Volumes*, vol. 43, no. 14, pp. 119–124, 2010. 8th IFAC Symposium on Nonlinear Control Systems.
- [30] E. Cetinsoy, S. Dikyar, C. Hancer, K. Oner, E. Sirimoglu, M. Unel, and M. Aksit, "Design and construction of a novel quad tilt-wing UAV," *Mechatronics*, vol. 22, no. 6, pp. 723–745, 2012. Special Issue on Intelligent Mechatronics (LSMS2010 & ICSEE2010).
- [31] A. Vuruskan, B. Yuksek, U. Ozdemir, A. Yukselen, and G. Inalhan, "Dynamic modeling of a fixed-wing VTOL UAV," in *2014 International Conference on Unmanned Aircraft Systems (ICUAS)*, pp. 483–491, 2014.
- [32] P. Pradeep and P. Wei, "Energy Optimal Speed Profile for Arrival of Tandem Tilt-Wing eVTOL Aircraft with RTA Constraint," in *2018 IEEE CSAA Guidance, Navigation and Control Conference (CGNCC)*, pp. 1–6, 2018.
- [33] G. P. Falconí and F. Holzapfel, "Position tracking of a hexacopter using a geometric backstepping control law - Experimental results," in *2014 IEEE International Conference on Aerospace Electronics and Remote Sensing Technology*, pp. 20–25, 2014.
- [34] V. S. Akkinapalli, G. P. Falconí, and F. Holzapfel, "Attitude control of a multicopter using L1 augmented quaternion based backstepping," in *2014 IEEE International Conference on Aerospace Electronics and Remote Sensing Technology*, pp. 170–178, 2014.
- [35] G. P. Falconí, V. A. Marvakov, and F. Holzapfel, "Fault tolerant control for a hexarotor system using Incremental Backstepping," in *2016 IEEE Conference on Control Applications (CCA)*, pp. 237–242, 2016.
- [36] M. Oishi and C. Tomlin, "Switched nonlinear control of a VSTOL aircraft," in *Proceedings of the 38th IEEE Conference on Decision and Control (Cat. No.99CH36304)*, vol. 3, pp. 2685–2690 vol.3, 1999.
- [37] X. Shi, K. Kim, S. Rahili, and S.-J. Chung, "Nonlinear Control of Autonomous Flying Cars with Wings and Distributed Electric Propulsion," in *2018 IEEE Conference on Decision and Control (CDC)*, pp. 5326–5333, 2018.

- [38] G. R. Flores-Colunga and R. Lozano-Leal, "A Nonlinear Control Law for Hover to Level Flight for the Quad Tilt-rotor UAV," *IFAC Proceedings Volumes*, vol. 47, no. 3, pp. 11055–11059, 2014. 19th IFAC World Congress.
- [39] J. Escareno, S. Salazar, and R. Lozano, "Modelling and Control of a Convertible VTOL Aircraft," in *Proceedings of the 45th IEEE Conference on Decision and Control*, pp. 69–74, 2006.
- [40] J.-J. E. Slotine and W. Li, *Applied Nonlinear Control*, vol. 199. Prentice Hall Inc., Englewood Cliffs, NJ, 1991.
- [41] H. K. Khalil, *Nonlinear Systems*, ch. 13, pp. 505–550. Prentice Hall Inc., Upper Saddle River, NJ, Third ed., 2002.
- [42] A. Isidori, E. Sontag, M. Thoma, and J. van Schuppen, *Nonlinear Control Systems*, ch. 4, pp. 137–211. Springer, London, Third ed., 2000.
- [43] N. B. Silva, J. V. Fontes, R. S. Inoue, and K. R. Branco, "Dynamic Inversion and Gain-Scheduling Control for an Autonomous Aerial Vehicle with Multiple Flight Stages," *Journal of Control, Automation and Electrical Systems*, vol. 29, no. 3, pp. 328–339, 2018.
- [44] A. Das, K. Subbarao, and F. Lewis, "Dynamic inversion with zero-dynamics stabilisation for quadrotor control," *IET control theory & applications*, vol. 3, no. 3, pp. 303–314, 2009.
- [45] J. Wang, T. Bierling, L. Höcht, F. Holzapfel, S. Klose, and A. Knoll, "Novel Dynamic Inversion Architecture Design for Quadcopter Control," in *Advances in Aerospace Guidance, Navigation and Control* (F. Holzapfel and S. Theil, eds.), (Berlin, Heidelberg), pp. 261–272, Springer Berlin Heidelberg, 2011.
- [46] J. Wang, T. Bierling, M. Achtelik, L. Hocht, F. Holzapfel, W. Zhao, and T. Hiong Go, "Attitude Free Position Control of a Quadcopter using Dynamic Inversion," in *Infotech@Aerospace 2011*, American Institute of Aeronautics and Astronautics, 2011.
- [47] M. L. Ireland, A. Vargas, and D. Anderson, "A Comparison of Closed-Loop Performance of Multirotor Configurations Using Non-Linear Dynamic Inversion Control," *Aerospace*, vol. 2, no. 2, pp. 325–352, 2015.
- [48] J. Hauser, S. Sastry, and G. Meyer, "Nonlinear control design for slightly non-minimum phase systems: Application to V/STOL aircraft," *Automatica*, vol. 28, no. 4, pp. 665–679, 1992.
- [49] Y. Patel and P. R. Smith, "Translational Motion Control of Vertical Takeoff Aircraft Using Nonlinear Dynamic Inversion," *Journal of Guidance, Control, and Dynamics*, vol. 21, no. 1, pp. 179–182, 1998.

-
- [50] F. Wang, P. Wang, H. Deng, and B. Chen, "Nonlinear Dynamic Inversion Control of VTOL Tilt-Wing UAV," in *2018 Eighth International Conference on Instrumentation Measurement, Computer, Communication and Control (IMCCC)*, pp. 1170–1174, 2018.
- [51] F. Holzapfel, *Nichtlineare adaptive Regelung eines unbemannten Fluggerätes*. PhD thesis, Technische Universität München, 2004.
- [52] J. Reiner, G. J. Balas, and W. L. Garrard, "Robust Dynamic Inversion for Control of Highly Maneuverable Aircraft," *Journal of Guidance, Control, and Dynamics*, vol. 18, no. 1, pp. 18–24, 1995.
- [53] J. Valasek, D. Ito, and D. Ward, *Robust dynamic inversion controller design and analysis for the X-38*. 2001.
- [54] E. N. Johnson and A. J. Calise, "Pseudo-Control Hedging: A New Method for Adaptive Control," in *Advances in navigation guidance and control technology workshop*, pp. 1–2, Citeseer, 2000.
- [55] T. Lombaerts and G. Looye, "Design and flight testing of nonlinear autoflight control laws," in *AIAA Guidance, Navigation, and Control Conference*, 2012.
- [56] P. Smith, "A simplified approach to nonlinear dynamic inversion based flight control," in *23rd Atmospheric Flight Mechanics Conference*, 1998.
- [57] B. Bacon and A. Ostroff, "Reconfigurable flight control using nonlinear dynamic inversion with a special accelerometer implementation," in *AIAA Guidance, Navigation, and Control Conference and Exhibit*, 2000.
- [58] P. Simplício, M. Pavel, E. van Kampen, and Q. Chu, "An acceleration measurements-based approach for helicopter nonlinear flight control using Incremental Nonlinear Dynamic Inversion," *Control Engineering Practice*, vol. 21, no. 8, pp. 1065–1077, 2013.
- [59] S. Sieberling, Q. P. Chu, and J. A. Mulder, "Robust Flight Control Using Incremental Nonlinear Dynamic Inversion and Angular Acceleration Prediction," vol. 33, pp. 1732–1742, 2010.
- [60] E. J. J. Smeur, Q. Chu, and G. C. H. E. de Croon, "Adaptive Incremental Nonlinear Dynamic Inversion for Attitude Control of Micro Air Vehicles," *Journal of Guidance, Control, and Dynamics*, vol. 39, no. 3, pp. 450–461, 2016.
- [61] E. Smeur, G. de Croon, and Q. Chu, "Cascaded incremental nonlinear dynamic inversion for MAV disturbance rejection," *Control Engineering Practice*, vol. 73, pp. 79–90, 2018.
- [62] V. S. Akkinapalli and F. Holzapfel, "Incremental Dynamic Inversion based Velocity Tracking Controller for a Multicopter System," in *2018 AIAA Guidance, Navigation, and Control Conference*.

- [63] C. Cakiroglu, E.-J. Van Kampen, and Q. P. Chu, "Robust Incremental Nonlinear Dynamic Inversion Control Using Angular Accelerometer Feedback," in *2018 AIAA Guidance, Navigation, and Control Conference*.
- [64] P. Bhardwaj, V. S. Akkinapalli, J. Zhang, S. Saboo, and F. Holzapfel, "Adaptive Augmentation of Incremental Nonlinear Dynamic Inversion Controller for an Extended F-16 Model," in *AIAA Scitech 2019 Forum*.
- [65] X. Wang, E. Van Kampen, Q. P. Chu, and R. De Breuker, "Flexible Aircraft Gust Load Alleviation with Incremental Nonlinear Dynamic Inversion," *Journal of Guidance, Control, and Dynamics*, vol. 42, no. 7, pp. 1519–1536, 2019.
- [66] R. Steffensen, A. Steinert, and F. Holzapfel, "Longitudinal Incremental Reference Model for Fly-By-Wire Control Law using Incremental Non-Linear Dynamic Inversion," in *AIAA SCITECH 2022 Forum*.
- [67] F. Grondman, G. Looye, R. O. Kuchar, Q. P. Chu, and E.-J. Van Kampen, "Design and Flight Testing of Incremental Nonlinear Dynamic Inversion-based Control Laws for a Passenger Aircraft," in *2018 AIAA Guidance, Navigation, and Control Conference*.
- [68] T. Lombaerts, J. Kaneshige, S. Schuet, G. Hardy, B. L. Aponso, and K. H. Shish, "Nonlinear Dynamic Inversion Based Attitude Control for a hovering quad tiltrotor eVTOL vehicle," in *AIAA Scitech 2019 Forum*.
- [69] T. Lombaerts, J. Kaneshige, S. Schuet, B. L. Aponso, K. H. Shish, and G. Hardy, "Dynamic Inversion based Full Envelope Flight Control for an eVTOL Vehicle using a Unified Framework," in *AIAA Scitech 2020 Forum*.
- [70] G. Di Francesco, M. Mattei, and E. D'Amato, "Incremental Nonlinear Dynamic Inversion and Control Allocation for a Tilt Rotor UAV," in *AIAA Guidance, Navigation, and Control Conference*, 2014.
- [71] G. Di Francesco and M. Mattei, "Modeling and Incremental Nonlinear Dynamic Inversion Control of a Novel Unmanned Tiltrotor," *Journal of Aircraft*, vol. 53, no. 1, pp. 73–86, 2016.
- [72] E. J. J. Smeur, M. Bronz, and G. C. H. E. de Croon, "Incremental Control and Guidance of Hybrid Aircraft Applied to a Tailsitter Unmanned Air Vehicle," *Journal of Guidance, Control, and Dynamics*, vol. 43, no. 2, pp. 274–287, 2020.
- [73] J. J. Harris, "F-35 Flight Control Law Design, Development and Verification," in *2018 Aviation Technology, Integration, and Operations Conference*.
- [74] J. F. Horn, "Non-Linear Dynamic Inversion Control Design for Rotorcraft," *Aerospace*, vol. 6, no. 3, 2019.

- [75] M. McFarland and S. Hoque, "Robustness of a nonlinear missile autopilot designed using dynamic inversion," in *AIAA Guidance, Navigation, and Control Conference and Exhibit*, 2000.
- [76] F. Holzapfel and G. Sachs, "Dynamic Inversion Based Control Concept with Application to an Unmanned Aerial Vehicle," in *AIAA Guidance, Navigation, and Control Conference and Exhibit*, 2004.
- [77] F. Peter, M. Leitão, and F. Holzapfel, "Adaptive Augmentation of a New Baseline Control Architecture for Tail-Controlled Missiles Using a Nonlinear Reference Model," in *AIAA Guidance, Navigation, and Control Conference*, 2012.
- [78] F. Zhang, F. Holzapfel, and M. Heller, "Nonlinear Non-cascaded Reference Model Architecture for Flight Control Design," in *Advances in Aerospace Guidance, Navigation and Control*, pp. 407–425, Springer, 2013.
- [79] M. Leitão, F. Peter, and F. Holzapfel, "Adaptive Augmentation of a Fighter Aircraft Autopilot Using a Nonlinear Reference Model," in *Proceedings of the EuroGNC, 2nd CEAS Specialist Conference, Delft, Netherlands*, 2013.
- [80] F. Zhang and F. Holzapfel, "Flight Control Using Physical Dynamic Inversion," in *AIAA Guidance, Navigation, and Control Conference*, 2015.
- [81] A. C. Gabrys, R. Steffensen, R. de Angelis Cordeiro, J. R. Azinheira, A. Moutinho, and F. Holzapfel, "Integration of Phase Plane Flight Envelope Protections in Cascaded Incremental Flight Control," *IFAC-PapersOnLine*, vol. 52, no. 12, pp. 429–435, 2019. 21st IFAC Symposium on Automatic Control in Aerospace ACA 2019.
- [82] P. Bhardwaj, S. A. Raab, J. Zhang, and F. Holzapfel, "Integrated Reference Model for a Tilt-rotor Vertical Take-off and Landing Transition UAV," in *2018 Applied Aerodynamics Conference*.
- [83] J. Angelov and F. Holzapfel, "A Novel Command Concept for Simplified Vehicle Operations of Onboard Piloted VTOL Transition Aircraft," *Deutsche Gesellschaft für Luft-und Raumfahrt*, 2021.
- [84] "ADS-33E-PRF - Aeronautical Design Standard, Performance Specification, Handling Qualities Requirements for Military Rotorcraft," Technical Report, United States Army Aviation and Missile Command Aviation Engineering Directorate, 2000. URL: <https://www.avmc.army.mil/Portals/51/Documents/TechData%20PDF/ads33.pdf>.
- [85] MIL-STD-1797A, "Flying qualities of piloted vehicles," Military Standard, 1990.
- [86] S. A. Raab, J. Zhang, P. Bhardwaj, and F. Holzapfel, "Consideration of Control Effector Dynamics and Saturations in an Extended INDI Approach," in *AIAA Aviation 2019 Forum*.

- [87] P. Bhardwaj, S. A. Raab, J. Zhang, and F. Holzapfel, "Thrust command based Integrated Reference Model with Envelope Protections for Tilt-rotor VTOL Transition UAV," in *AIAA Aviation 2019 Forum*.
- [88] S. A. Raab, J. Zhang, P. Bhardwaj, and F. Holzapfel, "Proposal of a Unified Control Strategy for Vertical Take-off and Landing Transition Aircraft Configurations," in *2018 Applied Aerodynamics Conference*.
- [89] R. Steffensen, A. Steinert, and E. J. J. Smeur, "Nonlinear Dynamic Inversion with Actuator Dynamics: An Incremental Control Perspective," *Journal of Guidance, Control, and Dynamics*, vol. 46, no. 4, pp. 709–717, 2023.
- [90] P. Bhardwaj, S. A. Raab, and F. Holzapfel, "Higher Order Reference Model for Continuous Dynamic Inversion Control," in *AIAA Scitech 2021 Forum*.
- [91] S. H. Schot, "Jerk: The time rate of change of acceleration," *American Journal of Physics*, vol. 46, no. 11, pp. 1090–1094, 1978.
- [92] S. A. Frank, "Time delays," in *Control Theory Tutorial: Basic Concepts Illustrated by Software Examples*, p. 96, Cham: Springer International Publishing, 2018.
- [93] M. S. Fadali and A. Visioli, "Chapter 12 - practical issues," in *Digital Control Engineering (Third Edition)* (M. S. Fadali and A. Visioli, eds.), p. 572, Academic Press, third edition ed., 2020.
- [94] M. J. Pelgrom, "Analog-to-digital conversion," in *Analog-to-Digital Conversion*, pp. 325–418, Springer, New York, NY, second edition ed., 2013.
- [95] L. Ren, M. Castillo-Effen, H. Yu, Y. Yoon, T. Nakamura, E. Johnson, and C. Ippolito, "Small Unmanned Aircraft System (sUAS) Trajectory Modeling in Support of UAS Traffic Management (UTM)," in *17th AIAA Aviation Technology, Integration, and Operations Conference*, 2017.
- [96] C. A. Ippolito, K. S. Krishnakumar, V. Stepanyan, A. Bencomo, S. Hening, and J. Baculi, "Autonomous UAS Operations in High-Density Low-Altitude Urban Environments," in *AIAA Scitech 2019 Forum*, 2019.
- [97] C. Reiche, C. McGillen, J. Siegel, and F. Brody, "Are We Ready to Weather Urban Air Mobility (UAM)?," in *2019 Integrated Communications, Navigation and Surveillance Conference (ICNS)*, pp. 1–7, 2019.
- [98] D. P. Thippavong, R. Apaza, B. Barmore, V. Battiste, B. Burian, Q. Dao, M. Feary, S. Go, K. H. Goodrich, J. Homola, H. R. Idris, P. H. Kopardekar, J. B. Lachter, N. A. Neogi, H. K. Ng, R. M. Oseguera-Lohr, M. D. Patterson, and S. A. Verma, "Urban Air Mobility Airspace Integration Concepts and Considerations," in *2018 Aviation Technology, Integration, and Operations Conference*.
- [99] S. Schatz, *Development and Flight-Testing of a Trajectory Controller Employing Full Nonlinear Kinematics*. Dissertation, Technische Universität München, 2018.

-
- [100] Zhufeng Xie, Yuanqing Xia, and Mengyin Fu, "Robust trajectory-tracking method for UAV using nonlinear dynamic inversion," in *2011 IEEE 5th International Conference on Cybernetics and Intelligent Systems (CIS)*, pp. 93–98, 2011.
- [101] W. Haitao and G. Jinyuan, "Trajectory tracking control for uninhabited air vehicles," in *2006 International Conference on Computational Intelligence for Modelling Control and Automation and International Conference on Intelligent Agents Web Technologies and International Commerce (CIMCA'06)*, pp. 236–236, 2006.
- [102] M. Azam and S. N. Singh, "Invertibility and trajectory control for nonlinear maneuvers of aircraft," *Journal of Guidance, Control, and Dynamics*, vol. 17, no. 1, pp. 192–200, 1994.
- [103] P. Sujit, S. Saripalli, and J. B. Sousa, "Unmanned Aerial Vehicle Path Following: A Survey and Analysis of Algorithms for Fixed-Wing Unmanned Aerial Vehicles," *IEEE Control Systems Magazine*, vol. 34, no. 1, pp. 42–59, 2014.
- [104] K. Enomoto, T. Yamasaki, H. Takano, and Y. Baba, "Guidance and Control System Design for Chase UAV," in *AIAA Guidance, Navigation and Control Conference and Exhibit*, 2008.
- [105] T. Yamasaki, H. Takano, and Y. Baba, "Robust Path-Following for UAV Using Pure Pursuit Guidance," in *Aerial Vehicles*, InTech, 2009.
- [106] F. Balampanis, A. P. Aguiar, I. Maza, and A. Ollero, "Path tracking for waypoint lists based on a pure pursuit method for fixed wing UAS," in *2017 Workshop on Research, Education and Development of Unmanned Aerial Systems (RED-UAS)*, pp. 55–59, 2017.
- [107] Y. Zhang, Y. Zhang, Z. Liu, Z. Yu, and Y. Qu, "Line-of-Sight Path Following Control on UAV with Sideslip Estimation and Compensation," in *2018 37th Chinese Control Conference (CCC)*, pp. 4711–4716, 2018.
- [108] T. I. Fossen, K. Y. Pettersen, and R. Galeazzi, "Line-of-Sight Path Following for Dubins Paths With Adaptive Sideslip Compensation of Drift Forces," *IEEE Transactions on Control Systems Technology*, vol. 23, no. 2, pp. 820–827, 2015.
- [109] D. Nelson, D. Barber, T. McLain, and R. Beard, "Vector field path following for small unmanned air vehicles," in *2006 American Control Conference*, pp. 7 pp.–, 2006.
- [110] D. R. Nelson, D. B. Barber, T. W. McLain, and R. W. Beard, "Vector Field Path Following for Miniature Air Vehicles," *IEEE Transactions on Robotics*, vol. 23, no. 3, pp. 519–529, 2007.
- [111] J. P. Wilhelm and G. Clem, "Vector Field UAV Guidance for Path Following and Obstacle Avoidance with Minimal Deviation," *Journal of Guidance, Control, and Dynamics*, vol. 42, no. 8, pp. 1848–1856, 2019.

- [112] K. Do and J. Pan, "State- and output-feedback robust path-following controllers for underactuated ships using Serret–Frenet frame," *Ocean Engineering*, vol. 31, no. 5, pp. 587–613, 2004.
- [113] D. Jung and P. Tsiotras, "Bank-to-Turn Control for a Small UAV using Backstepping and Parameter Adaptation," *IFAC Proceedings Volumes*, vol. 41, no. 2, pp. 4406–4411, 2008. 17th IFAC World Congress.
- [114] J. Osborne and R. Rysdyk, "Waypoint Guidance for Small UAVs in Wind," in *Infotech@Aerospace*, 2005.
- [115] I. Kaminer, A. Pascoal, E. Hallberg, and C. Silvestre, "Trajectory Tracking for Autonomous Vehicles: An Integrated Approach to Guidance and Control," *Journal of Guidance, Control, and Dynamics*, vol. 21, no. 1, pp. 29–38, 1998.
- [116] R. Rysdyk, "UAV Path Following for Constant Line-of-Sight," in *2nd AIAA "Unmanned Unlimited" Conf. and Workshop & Exhibit*, 2003.
- [117] V. Schneider, N. C. Mumm, and F. Holzapfel, "Trajectory generation for an integrated mission management system," in *2015 IEEE International Conference on Aerospace Electronics and Remote Sensing Technology (ICARES)*, pp. 1–7, 2015.
- [118] V. Schneider, *Trajectory Generation for Integrated Flight Guidance*. Dissertation, Technische Universität München, München, 2018.
- [119] N. C. Mumm, V. Schneider, and F. Holzapfel, "Nonlinear continuous and differentiable 3D trajectory command generation," in *2015 IEEE International Conference on Aerospace Electronics and Remote Sensing Technology (ICARES)*, pp. 1–9, 2015.
- [120] M. Sun, R. Zhu, and X. Yang, "UAV Path Generation, Path Following and Gimbal Control," in *2008 IEEE International Conference on Networking, Sensing and Control*, pp. 870–873, 2008.
- [121] D. Muniraj, M. C. Palframan, K. T. Guthrie, and M. Farhood, "Path-following control of small fixed-wing unmanned aircraft systems with H_∞ type performance," *Control Engineering Practice*, vol. 67, pp. 76–91, 2017.
- [122] I. Rhee, S. Park, and C.-K. Ryoo, "A tight path following algorithm of an UAS based on PID control," in *Proceedings of SICE Annual Conference 2010*, pp. 1270–1273, 2010.
- [123] C. Liu, J. Pan, and Y. Chang, "PID and LQR trajectory tracking control for an unmanned quadrotor helicopter: Experimental studies," in *35th Chinese Control Conference (CCC)*, pp. 10845–10850, IEEE, 2016.
- [124] R. Cunha, C. Silvestre, and A. Pascoal, "A path following controller for model-scale helicopters," in *2003 European Control Conference (ECC)*, pp. 2248–2253, 2003.

- [125] A. Ratnoo, P. Sujit, and M. Kothari, "Adaptive Optimal Path Following for High Wind Flights," *IFAC Proceedings Volumes*, vol. 44, no. 1, pp. 12985–12990, 2011. 18th IFAC World Congress.
- [126] I. Kaminer, A. Pascoal, E. Xargay, N. Hovakimyan, C. Cao, and V. Dobrokhodov, "Path Following for Small Unmanned Aerial Vehicles Using L1 Adaptive Augmentation of Commercial Autopilots," *Journal of Guidance, Control, and Dynamics*, vol. 33, no. 2, pp. 550–564, 2010.
- [127] J. Fang, C. Miao, and Y. Du, "Adaptive nonlinear path following method for fix-wing micro aerial vehicle," *Industrial Robot: An International Journal*, 2012.
- [128] T. Raffler, J. Wang, and F. Holzapfel, "Path Generation and Control for Unmanned Multicopter Vehicles Using Nonlinear Dynamic Inversion and Pseudo Control Hedging," *IFAC Proceedings Volumes*, vol. 46, no. 19, pp. 194–199, 2013. 19th IFAC Symposium on Automatic Control in Aerospace.
- [129] G. V. Raffo, M. G. Ortega, and F. R. Rubio, "Backstepping/nonlinear H_∞ control for path tracking of a quadrotor unmanned aerial vehicle," in *American Control Conference*, pp. 3356–3361, 2008.
- [130] M. Ahmed and K. Subbarao, "Nonlinear 3-D trajectory guidance for unmanned aerial vehicles," in *11th International Conference on Control Automation Robotics Vision*, pp. 1923–1927, 2010.
- [131] M. Labbadi, Y. Boukal, and M. Cherkaoui, "Path following control of quadrotor UAV with continuous fractional-order super twisting sliding mode," *Journal of Intelligent & Robotic Systems*, vol. 100, no. 3, pp. 1429–1451, 2020.
- [132] M. Z. Shah, R. Samar, and A. I. Bhatti, "Cross-track control of UAVs during circular and straight path following using sliding mode approach," in *2012 12th International Conference on Control, Automation and Systems*, pp. 185–190, 2012.
- [133] Y. Mao, Q. Chen, Z. Hou, and G. Zheng, "An improved nonlinear guidance law for unmanned aerial vehicles path following," in *34th Chinese Control Conference (CCC)*, pp. 5271–5276, 2015.
- [134] S. Park, J. Deyst, and J. P. How, "Performance and Lyapunov Stability of a Nonlinear Path Following Guidance Method," *Journal of Guidance, Control, and Dynamics*, vol. 30, no. 6, pp. 1718–1728, 2007.
- [135] European Union Aviation Agency (EASA), "Second Publication of Proposed Means of Compliance with the Special Condition VTOL." <https://www.easa.europa.eu/document-library/product-certification-consultations/special-condition-vtol>, 2021. Accessed: 16-Feb-2022.
- [136] P. Piprek, M. M. Marb, P. Bhardwaj, and F. Holzapfel, "Trajectory/Path-Following Controller Based on Nonlinear Jerk-Level Error Dynamics," *Applied Sciences*, vol. 10, no. 23, 2020.

BIBLIOGRAPHY

- [137] P. R. Grant and B. Haycock, "Effect of Jerk and Acceleration on the Perception of Motion Strength," *Journal of Aircraft*, vol. 45, no. 4, pp. 1190–1197, 2008.
- [138] K. Kyriakopoulos and G. Saridis, "Minimum jerk path generation," in *Proceedings. 1988 IEEE International Conference on Robotics and Automation*, pp. 364–369 vol.1, 1988.
- [139] E. Tal and S. Karaman, "Accurate Tracking of Aggressive Quadrotor Trajectories Using Incremental Nonlinear Dynamic Inversion and Differential Flatness," *IEEE Transactions on Control Systems Technology*, vol. 29, no. 3, pp. 1203–1218, 2021.
- [140] E. A. Tal and S. Karaman, "Global Trajectory-tracking Control for a Tailsitter Flying Wing in Agile Uncoordinated Flight," in *AIAA AVIATION 2021 FORUM*.
- [141] Mark Alis, "VTOL V48 - Night Eagle Model." <https://www.cgtrader.com/free-3d-models/aircraft/military-aircraft/vtol-v48-night-eagle>. Accessed: 09-Feb-2023.
- [142] Andrés Iborra López, "Eagle E-4 VTOL Cargo Drone Model." <https://grabcad.com/library/eagle-e-4-vtol-cargo-drone-1>. Accessed: 10-Feb-2023.
- [143] F. Holzapfel, "Lecture notes in Flight Dynamics Stability and Control," June 2022.
- [144] R. C. Nelson, *Flight Stability and Automatic Control*, vol. 2. WCB/McGraw-Hill New York, 1998.
- [145] W. Durham, *Aircraft Flight Dynamics and Control*. John Wiley & Sons, 2013.
- [146] R. W. BEARD and T. W. McLAIN, *Small Unmanned Aircraft: Theory and Practice*. Princeton University Press, 2012.
- [147] J. M. Cooke, M. J. Zyda, D. R. Pratt, and R. B. McGhee, "NPSNET: Flight Simulation Dynamic Modeling Using Quaternions," *Presence: Teleoperators and Virtual Environments*, vol. 1, pp. 404–420, 11 1992.
- [148] D. Dollinger, T. Fricke, and F. Holzapfel, "Control Inceptor Design for Remote Control of a Transition UAV," in *AIAA Aviation 2019 Forum*.
- [149] D. Dollinger, P. Reiss, J. Angelov, D. Löbl, and F. Holzapfel, "Control Inceptor Design for Onboard Piloted Transition VTOL Aircraft Considering Simplified Vehicle Operation," in *AIAA Scitech 2021 Forum*.
- [150] B. Yuksek, A. Vuruskan, U. Ozdemir, M. Yukselen, and G. Inalhan, "Transition Flight Modeling of a Fixed-Wing VTOL UAV," *Journal of Intelligent & Robotic Systems*, vol. 84, no. 1, pp. 83–105, 2016.
- [151] R. Czyba, M. Lemanowicz, Z. Gorol, and T. Kudala, "Construction Prototyping, Flight Dynamics Modeling, and Aerodynamic Analysis of Hybrid VTOL Unmanned Aircraft," *Journal of Advanced Transportation*, vol. 2018, 2018.

-
- [152] C. Wang, Z. Zhou, and R. Wang, "Research on Dynamic Modeling and Transition Flight Strategy of VTOL UAV," *Applied Sciences*, vol. 9, no. 22, 2019.
- [153] F. Zhang, *Physically Integrated Reference Model based Flight Control Design*. Dissertation, Technische Universität München, München, 2017.
- [154] J. Reiner, G. J. Balas, and W. L. Garrard, "Flight control design using robust dynamic inversion and time-scale separation," *Automatica*, vol. 32, no. 11, pp. 1493–1504, 1996.
- [155] P. Menon, V. Iragavarapu, and E. Ohlmeyer, "Nonlinear missile autopilot design using time-scale separation," in *Guidance, Navigation, and Control Conference*, 1997.
- [156] Y. Lin, E. Baumann, D. M. Bose, R. Beck, and G. Jenney, "Tests And Techniques For Characterizing And Modeling X-43a Electromechanical Actuators," tech. rep., 2008.
- [157] T. Lombaerts, J. Kaneshige, and M. Feary, "Control concepts for simplified vehicle operations of a quadrotor evtol vehicle," in *AIAA AVIATION 2020 FORUM*.
- [158] A. van der Schaft, "Linearization and input-output decoupling for general nonlinear systems," *Systems & Control Letters*, vol. 5, no. 1, pp. 27–33, 1984.
- [159] M. A. Henson and D. E. Seborg, "Input-output Linearization of General Nonlinear Processes," *AIChE Journal*, vol. 36, no. 11, pp. 1753–1757, 1990.
- [160] S. Sastry, *Nonlinear Systems: Analysis, Stability, and Control*, vol. 10. Springer Science & Business Media, 2013.
- [161] F. Holzapfel, "Lecture notes in Nonlinear Flight Control," June 2022.
- [162] R. M. Robinson, D. R. R. Scobee, S. A. Burden, and S. S. Sastry, "Dynamic inverse models in human-cyber-physical systems," in *Micro- and Nanotechnology Sensors, Systems, and Applications VIII* (T. George, A. K. Dutta, and M. S. Islam, eds.), vol. 9836, p. 98361X, International Society for Optics and Photonics, SPIE, 2016.
- [163] M. Zeitz, "CANONICAL FORMS FOR NONLINEAR SYSTEMS," in *Nonlinear Control Systems Design 1989* (A. ISIDORI, ed.), IFAC Symposia Series, pp. 33–38, Oxford: Pergamon, 1990.
- [164] B. Schwartz, A. Isidori, and T. J. Tarn, "Global normal forms for MIMO nonlinear systems, with applications to stabilization and disturbance attenuation," *Mathematics of Control, Signals and Systems*, vol. 12, pp. 121–142, 1999.
- [165] L. Höcht, *Advances in Stability Analysis for Model Reference Adaptive Control Systems and Application to Unmanned Aerial Systems*. Dissertation, Technische Universität München, 2014.
- [166] F. Garces, V. M. Becerra, C. Kambhampati, and K. Warwick, *Introduction to Feedback Linearisation*, pp. 27–60. London: Springer London, 2003.

- [167] H. B. Chen and S. G. Zhang, "Robust dynamic inversion flight control law design," in *2008 2nd International Symposium on Systems and Control in Aerospace and Astronautics*, pp. 1–6, IEEE, 2008.
- [168] W. C. Durham, "Constrained control allocation," *Journal of Guidance, Control, and Dynamics*, vol. 16, no. 4, pp. 717–725, 1993.
- [169] W. C. Durham, "Constrained control allocation - Three-moment problem," *Journal of Guidance, Control, and Dynamics*, vol. 17, no. 2, pp. 330–336, 1994.
- [170] W. Durham, K. A. Bordignon, and R. Beck, *Aircraft Control Allocation*. John Wiley & Sons, 2017.
- [171] T. Lombaerts, G. Looye, P. Chu, and J. A. Mulder, "Pseudo Control Hedging and its Application for Safe Flight Envelope Protection," in *AIAA Guidance, Navigation, and Control Conference*, 2010.
- [172] N. Sahani and J. Horn, "Command Limiting for Full-Envelope Guidance and Control of Rotorcraft," in *AIAA Guidance, Navigation, and Control Conference and Exhibit*, p. 6348, 2005.
- [173] I. Yavrucuk, J. Prasad, and S. Unnikrishnan, "Envelope protection for autonomous unmanned aerial vehicles," *Journal of guidance, control, and dynamics*, vol. 32, no. 1, pp. 248–261, 2009.
- [174] H. Duda, "Effects of Rate Limiting Elements in Flight Control Systems-A New PIO-Criterion," in *Guidance, Navigation, and Control Conference*, p. 3204, 1995.
- [175] J. Berg, K. Hammett, C. Schwartz, and S. Banda, "An analysis of the destabilizing effect of daisy chained rate-limited actuators," *IEEE Transactions on Control Systems Technology*, vol. 4, no. 2, pp. 171–176, 1996.
- [176] F. Zhang, S. Braun, and F. Holzapfel, "Physically Integrated Reference Model and Its Aids in Validation of Requirements to Flight Control Systems," in *AIAA Guidance, Navigation and Control Conference*, pp. 2014–0962, 2014.
- [177] H. Bouadi, M. Bouchoucha, and M. Tadjine, "Modelling and Stabilizing Control Laws Design Based on Sliding Mode for an UAV Type-Quadrotor," *IFAC Proceedings Volumes*, vol. 40, no. 15, pp. 245–250, 2007. 6th IFAC Symposium on Intelligent Autonomous Vehicles.
- [178] T. Luukkonen, "Modelling and control of quadcopter," *Independent research project in applied mathematics, Espoo*, vol. 22, no. 22, 2011.
- [179] A. Koehl, H. Rafaralahy, M. Boutayeb, and B. Martinez, "Aerodynamic Modelling and Experimental Identification of a Coaxial-Rotor UAV," *Journal of Intelligent & Robotic Systems*, vol. 68, pp. 53–68, 2012.

- [180] D. Mellinger, N. Michael, and V. Kumar, "Trajectory generation and control for precise aggressive maneuvers with quadrotors," *The International Journal of Robotics Research*, vol. 31, no. 5, pp. 664–674, 2012.
- [181] G. P. Falconí, C. D. Heise, and F. Holzapfel, "Fault-tolerant position tracking of a hexacopter using an Extended State Observer," in *2015 6th International Conference on Automation, Robotics and Applications (ICARA)*, pp. 550–556, 2015.
- [182] M. Euston, P. Coote, R. Mahony, J. Kim, and T. Hamel, "A complementary filter for attitude estimation of a fixed-wing UAV," in *2008 IEEE/RSJ International Conference on Intelligent Robots and Systems*, pp. 340–345, 2008.
- [183] T. S. Yoo, S. K. Hong, H. M. Yoon, and S. Park, "Gain-Scheduled Complementary Filter Design for a MEMS Based Attitude and Heading Reference System," *Sensors*, vol. 11, no. 4, pp. 3816–3830, 2011.
- [184] H. G. Min and E. T. Jeung, "Complementary Filter Design for Angle Estimation using MEMS Accelerometer and Gyroscope," *Department of Control and Instrumentation, Changwon National University, Changwon, Korea*, pp. 641–773, 2015.
- [185] M. Kollar and L. Michaeli, "Noise Consideration for Micromachined Digital Accelerometers," in *2006 IEEE Instrumentation and Measurement Technology Conference Proceedings*, pp. 507–512, 2006.
- [186] J. M. Buffington, "Tailless aircraft control allocation," in *Guidance, Navigation, and Control Conference*, 1997.
- [187] M. Bodson, "Evaluation of optimization methods for control allocation," *Journal of Guidance, Control, and Dynamics*, vol. 25, no. 4, pp. 703–711, 2002.
- [188] O. Harkegard, "Efficient active set algorithms for solving constrained least squares problems in aircraft control allocation," in *Proceedings of the 41st IEEE Conference on Decision and Control, 2002.*, vol. 2, pp. 1295–1300 vol.2, 2002.
- [189] J. Zhang, P. Bhardwaj, S. A. Raab, S. Saboo, and F. Holzapfel, "Control Allocation Framework for a Tilt-rotor Vertical Take-off and Landing Transition Aircraft Configuration," in *2018 Applied Aerodynamics Conference*.
- [190] J. Zhang, P. Bhardwaj, S. A. Raab, and F. Holzapfel, "Control Allocation Framework with SVD-based Protection for a Tilt-rotor VTOL Transition Air Vehicle," in *AIAA Aviation 2019 Forum*.
- [191] E. H. Moore, "On the reciprocal of the general algebraic matrix," *Bull. Am. Math. Soc.*, vol. 26, pp. 394–395, 1920.
- [192] "A generalized inverse for matrices," *Mathematical Proceedings of the Cambridge Philosophical Society*, vol. 51, no. 3, p. 406–413, 1955.

- [193] R. Penrose, "On best approximate solutions of linear matrix equations," *Mathematical Proceedings of the Cambridge Philosophical Society*, vol. 52, no. 1, p. 17–19, 1956.
- [194] J. C. A. Barata and M. S. Hussein, "The moore–penrose pseudoinverse: A tutorial review of the theory," *Brazilian Journal of Physics*, vol. 42, no. 1, pp. 146–165, 2012.
- [195] J. Virnig and D. Bodden, "Multivariable control allocation and control law conditioning when control effectors limit," in *Guidance, navigation, and control conference*, p. 3609, 1994.
- [196] M. W. Oppenheimer, D. B. Doman, and M. A. Bolender, "Control Allocation for Over-actuated Systems," in *2006 14th Mediterranean Conference on Control and Automation*, pp. 1–6, 2006.
- [197] R. Rysdyk, "Unmanned Aerial Vehicle Path Following for Target Observation in Wind," *Journal of Guidance, Control, and Dynamics*, vol. 29, no. 5, pp. 1092–1100, 2006.
- [198] A. Brezoescu, R. Lozano, and P. Castillo, "Bank to turn approach for airplane translational motion in unknown wind," in *2013 International Conference on Unmanned Aircraft Systems (ICUAS)*, pp. 1022–1029.
- [199] R. F. Stengel, *Flight Dynamics*. Princeton university press, 2022.
- [200] V. A. Marvakov and F. Holzapfel, "Defining Robust Transition and Re-Transition Procedures for Unmanned Fixed-Wing VTOL Aircraft," in *AIAA Scitech 2021 Forum*.
- [201] D. Dollinger, V. A. Marvakov, and F. Holzapfel, "Increasing Operator Situational Awareness During Transition Procedures for Fixed-Wing VTOL UAV Operations," in *AIAA Scitech 2021 Forum*.
- [202] F. Holzapfel, F. Schuck, L. Höcht, and G. Sachs, "Flight Dynamics Aspects of Path Control," in *AIAA Guidance, Navigation and Control Conference and Exhibit*.
- [203] V. A. Marvakov, *Automating the Transition of Lift-to-Cruise eVTOL Aircraft*. PhD thesis, Technische Universität München, 2023.
- [204] D. Surmann and S. Myschik, "Flugleistungsbetrachtung eines eVTOLs mit Schubvektorsteuerung und inkrementeller nichtlinearen dynamischen Inversion als Regelungsstrategie," in *Deutscher Luft- und Raumfahrtkongress 2021*.
- [205] D. Surmann, M. Zrenner, and S. Myschik, "Flight Performance Evaluation of a Conceptual eVTOL System using Nonlinear Simulations," in *AIAA SCITECH 2022 Forum*.
- [206] D. Surmann and S. Myschik, "Gain Design of an INDI-based Controller for a Conceptual eVTOL in a Nonlinear Simulation Environment," in *AIAA SCITECH 2023 Forum*.

- [207] P. Bhardwaj, P. Müller, and F. Holzapfel, "Design Plant Adaptation in Jerk-level Reference Model," in *AIAA SCITECH 2022 Forum*.
- [208] J. Wood and J. Hodgkinson, "Definition of Acceptable Levels of Mismatch for Equivalent Systems of Augmented CTOL (Conventional Take-off and Landing) Aircraft," tech. rep., McDonnell Aircraft Corporation, St. Louis, Missouri, 1980.
- [209] C. Miller, "Nonlinear Dynamic Inversion Baseline Control Law: Architecture and Performance Predictions," in *AIAA Guidance, Navigation, and Control Conference*, 2012.
- [210] S. Fasiello, T. Lu, D. M. Pool, and M. M. van Paassen, "Manual control adaptation to variations in short-period natural frequency and damping," in *AIAA Scitech 2019 Forum*.
- [211] Y. Li, X. Liu, P. Lu, Q. He, R. Ming, and W. Zhang, "Angular acceleration estimation-based incremental nonlinear dynamic inversion for robust flight control," *Control Engineering Practice*, vol. 117, p. 104938, 2021.
- [212] S. Ovaska and S. Valiviita, "Angular acceleration measurement: A Review," in *IMTC/98 Conference Proceedings. IEEE Instrumentation and Measurement Technology Conference. Where Instrumentation is Going (Cat. No.98CH36222)*, vol. 2, pp. 875–880 vol.2, 1998.
- [213] Y. Jiali and Z. Jihong, "An angular acceleration estimation method based on the complementary filter theory," in *2016 IEEE International Instrumentation and Measurement Technology Conference Proceedings*, pp. 1–6, 2016.
- [214] K. Gade, "A Non-singular Horizontal Position Representation," *Journal of Navigation*, vol. 63, no. 3, p. 395–417, 2010.
- [215] S. Scherer, P. Bhardwaj, M. Speckmaier, D. Gierszewski, M. Rosenbauer, and F. Holzapfel, "Flight Guidance command generation for an automatic flight mission in areas difficult to access," in *AIAA AVIATION 2023 Forum*, 2023 - to be published.
- [216] P. Piprek, H. Hong, and F. Holzapfel, "Optimal Trajectory Design Accounting for Robust Stability of Path-Following Controller," *Journal of Guidance, Control, and Dynamics*, vol. 45, no. 8, pp. 1385–1398, 2022.